Physics of the Solid State, Vol. 46, No. 11, 2004, pp. 1985–1993. Translated from Fizika Tverdogo Tela, Vol. 46, No. 11, 2004, pp. 1921–1929.
Original Russian Text Copyright © 2004 by Vlasova, Drichko, Petrov, Semkin, Zhilyaeva, Lyubovskaya, Olejniczak, A. Kobayashi, H. Kobayashi.

METALS AND SUPERCONDUCTORS

Optical Properties of New Organic Conductors Based on the BEDT-TSeF Molecule (the κ-(BETS)$_4$Hg$_{2.84}$Br$_8$ Superconductor and κ-(BETS)$_4$Hg$_3$Cl$_8$ Metal) in the Range 300–15 K

R. M. Vlasova*, N. V. Drichko*, B. V. Petrov*, V. N. Semkin*, E. I. Zhilyaeva, R. N. Lyubovskaya**, I. Olejniczak***, A. Kobayashi****, and H. Kobayashi*******

**Ioffe Physicotechnical Institute, Russian Academy of Sciences, Politekhnicheskaya ul. 26, St. Petersburg, 194021 Russia*
e-mail: rema.vlasova@mail.ioffe.ru
***Institute of Problems in Chemical Physics, Russian Academy of Sciences, Chernogolovka, Moscow oblast, 142432 Russia*
****Institute of Molecular Physics, Polish Academy of Sciences, Poznan, 60-179 Poland*
*****University of Tokyo, Hongo, Bankyo-ku, Tokyo, 113-0033 Japan*
******Institute of Molecular Science, Okazaki, 444 Japan*

Received March 18, 2004

Abstract—Polarized reflectance and optical conductivity spectra of single crystals of two new isostructural organic conductors based on the BEDT-TSeF molecule, namely, the κ-(BETS)$_4$Hg$_{2.84}$Br$_8$ superconductor (T_c = 2 K) and the κ-(BETS)$_4$Hg$_3$Cl$_8$ metal, which undergoes a smooth transition to the dielectric state near 35 K, have been obtained in the spectral region 700–6500 cm^{-1} at temperatures of 300–15 K. At 300 K, the spectra of both compounds are nearly identical and differ from the Drude spectrum characteristic of metals. The nature of the observed difference is discussed, and the spectra are described in terms of a cluster approach with inclusion of electron–electron correlations in the Hubbard approximation combined with the Drude model. The parameters of the theory were determined, including the electron transfer integrals between molecules in a cluster. The spectra in the conducting plane of the crystals were found to be essentially anisotropic, which should be assigned to specific features of in-plane interaction between molecules. The spectra of the superconductor and the metal become increasingly different as the temperature is lowered. The spectra of the metal obtained for T < 150 K exhibit splitting of the broad electronic maximum in the mid-IR region into two bands, which is accompanied by a splitting of a vibronic feature deriving from electron interaction with intramolecular BETS vibrations of $\nu_3(A_g)$ symmetry. No such splitting is observed in the superconductor spectra with decreasing temperature. *© 2004 MAIK “Nauka/Interperiodica”.*

1. INTRODUCTION

Quasi-two-dimensional organic conductors based on the bis(ethylenedithio)tetrathiafulvalene molecule (BEDT–TTF) and its derivatives are presently attracting considerable interest spurred by their unique electronic properties and the relation of these properties to compound structures. The crystal structure of these compounds (radical-ion salts) is an array of alternating cation and anion layers. Depending on the actual pattern of molecular stacking in the conducting cation layers (α, β, λ, θ, and κ phases), the chemical composition of the anion, and the specific features of interaction between molecules in a layer and between layers, these compounds exhibit a rich variety of electronic properties, including metallic behavior within a broad spectral region, superconductivity (with a highest critical temperature T_c = 12.3 K at normal pressure), metal–insulator transitions of various types, giant magnetoresistance, and antiferromagnetism (see, e.g., [1–3]). These molecular conductors have the following characteristic features: (i) electron interaction with intramolecular vibrations (IMV), which gives rise to coupled electronic–vibrational states, and strong electron–electron correlations and (ii) instability of the electron system to the formation of charge or spin density waves. The formation of the latter, accounted for by the low dimensionality of the electronic structure in these crystals, inhibits the appearance of the superconducting state.

Salts based on bis(ethylenedioxy)tetrathiafulvalene (BEDO–TTF) [4–6] and bis(ethylenedithio)tetraselenafulvalene (BETS) [7–11] molecules (Fig. 1) exhibit the most stable metallic state among these compounds. In BETS-based salts, this is accounted for by the following factors: first, by the stronger overlap of the higher occupied BETS molecular orbitals in the conducting crystal layers (compared to BEDT–TTF salts) due to the radius of Se (in BETS) being larger than that of the S atom (in BEDT–TTF) and, second, by the Coulomb repulsion of two electrons in a molecule being

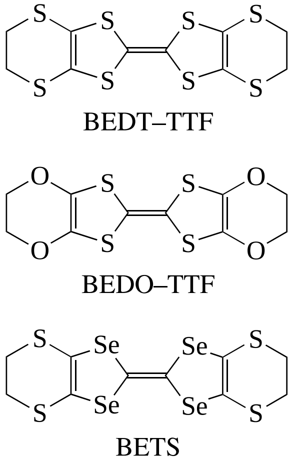

Fig. 1. Structural formulas of bis(ethylenedithio)tetrathiafulvalene (BEDT–TTF), bis(ethylenedioxy)tetrathiafulvalene (BEDO'–TTF), and bis(ethylenedithio)tetraselenafulvalene (BETS) molecules.

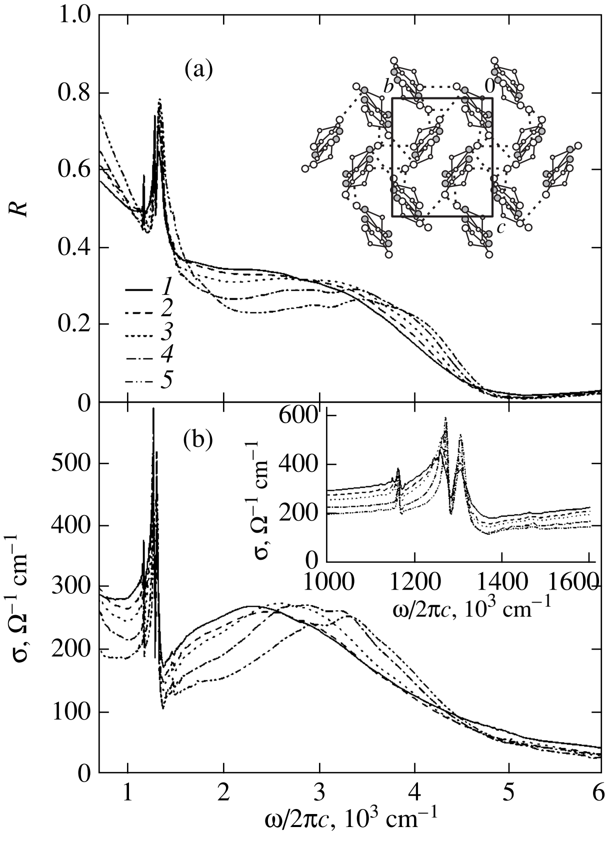

Fig. 2. (a) Reflectance and (b) optical conductivity spectra of the κ-$(BETS)_4Hg_{2.84}Br_8$ superconductor obtained in the **E** || *b* polarization at various temperatures *T*: (*1*) 300, (*2*) 200, (*3*) 150, (*4*) 80, and (*5*) 15 K. Insets: (a) structure of the $BETS_2^+$ conducting layer and (b) optical conductivity spectra measured in the vibronic frequency region.

weaker because of the difference between the first and second ionization potential in BETS (0.22 eV) being smaller than that in BEDT–TTF (0.28 eV). Some BETS salts have a superconducting ground state [12–15]. The λ-$BETS_2FeCl_4$ salt has an insulating ground state because of iron spins in the anions being antiferromagnetically ordered and because of the localized magnetic moments interacting with conduction electrons in the BETS layers [16, 17]. It is the rich diversity of properties of BETS-based salts and the possibility of controlling them by changing the chemical nature of the anion properly that account for the interest in these compounds.

Two new molecular conductors based on this molecule, κ-$(BETS)_4Hg_3Cl_8$ and κ-$(BETS)_4Hg_{2.84}Br_8$, have recently been synthesized [18, 19]. The salt with Cl, judging from the pattern of the temperature behavior of its electrical resistivity in the range 295–32 K, is a metal; as the temperature is lowered still further, the resistivity begins to grow smoothly [18]. The salt with Br is a superconductor with a superconducting transition temperature $T_c = 2$ K. It appears of interest to learn the difference in the electronic structure and electronic interactions between these compounds that are so similar in chemical and crystal structure.

It is known that valuable information on the electronic structure, the nature of the ground state, and electron interactions in quasi-two-dimensional molecular compounds based on BEDT–TTF and BEDO–TTF molecules can be gained from optical studies (see, e.g., [20–22] and our publications [23–26]). Optical properties of BETS-based salts have been investigated on κ-$(BETS)_2FeCl_4$ [10], α-$BETS_2I_3$ [27], and θ-$(BETS)_4HgBr_4(C_6H_5Cl)$ [28]; the last compound revealed an instability in the electronic metallic state induced by unstable structural distortions along the BETS molecule stacks.

We report here on a study of polarized reflectance and optical conductivity spectra of single crystals of κ-$(BETS)_4Hg_3Cl_8$ and κ-$(BETS)_4Hg_{2.84}Br_8$ measured in the spectral region 700–6500 cm^{-1} at temperatures ranging from 300 to 15 K and in the range 9000–40000 cm^{-1} at room temperature with the aim of obtaining information on the specific features of the electronic system in these compounds and of revealing differences in this information between the metal and superconductor within the temperature range covered.

2. EXPERIMENTAL

The crystals of both compounds under study were thin plates shaped as incompletely faceted rhombs measuring 0.5 × 0.5 × 2 mm. The main crystallographic data for κ-$(BETS)_4Hg_3Cl_8$ (BETS-Cl subsequently) are as follows [18]: monoclinic symmetry, $a = 38.23(4)$ Å, $b = 8.694(6)$ Å, $c = 11.37(1)$ Å, $\beta = 106.55(9)°$, $V = 3623.8$ Å^3, and $Z = 2$. The crystallographic data obtained by us for κ-$(BETS)_4Hg_{2.84}Br_8$ (BETS-Br in what follows) are the following: monoclinic symmetry, $a = 39.34$ Å, $b = 8.63$ Å, $c = 11.51$ Å, and $\beta = 106.2°$. The conducting layers of BETS molecules in both crystals are oriented parallel to the major face, (100) (*bc*). The BETS molecules in the conducting layers are stacked to form mutually perpendicular pairs $(\mathrm{BETS})_2^+$ (dimers) in the manner characteristic of the κ phase (see inset in Fig. 2a) [18, 19].

Polarized reflectance spectra $R(\omega)$ obtained under normal incidence of light onto the major crystal face, (100), were measured in the range 700–6500 cm^{-1} at temperatures of 300–15 K and in the range 9000–40000 cm^{-1} at room temperature. The largest anisotropy of reflectance spectra $R(\omega)$ obtained in the range 700–6500 cm^{-1} was observed in the polarizations where the electric vector of the light wave **E** was aligned with the long or the short rhomb axis. By varying the crystal orientation in the light wave field, it was shown that the largest reflectance $R_{\max}(\omega)$ is observed for both crystals in the $\mathbf{E} \parallel b$ polarization and the minimum reflectance $R_{\min}(\omega)$, in the $\mathbf{E} \parallel c$ polarization.

The experimental techniques employed were described by us in [26, 28]. The optical conductivity spectra $\sigma(\omega)$ were extracted from the corresponding reflectance spectra using the Kramers–Kronig relations. Extrapolation to the high frequency range was done using the $R(\omega)$ spectra obtained by us in the range 9000–40000 cm^{-1}.

3. RESULTS

3.1. κ-$(BETS)_4Hg_{2.84}Br_8$

Figures 2a and 2b present $R(\omega)$ and $\sigma(\omega)$ spectra of the BETS-Br superconductor, respectively, obtained in the $\mathbf{E} \parallel b$ polarization in the spectral range 700–6000 cm^{-1} for the (100) major conducting face of the crystal in the temperature interval 300–15 K. Figure 3 displays similar data for the $\mathbf{E} \parallel c$ polarization. We readily see that the $R(\omega)$ and $\sigma(\omega)$ spectra for the two polarizations differ appreciably from the Drude ("metallic") pattern. This difference, as discovered earlier, is typical of all salts of the BEDT–TTF κ phase, both for conductors and superconductors (see, e.g., [21–25]). On the other hand, in contrast to the BEDT–TTF κ-phase salts, for which the optical anisotropy in the conducting plane is small, κ-BETS-Br exhibits a noticeable optical anisotropy; indeed, the spectra obtained in the $\mathbf{E} \parallel b$ and $\mathbf{E} \parallel c$ polarizations differ markedly.

The $R(\omega)$ spectra obtained in the $\mathbf{E} \parallel b$ polarization qualitatively resemble those of salts of the BEDT–TTF κ phase. The similarity increases with decreasing temperature; indeed, a broad maximum appears in the range 3000–40000 cm^{-1} and shifts slightly toward higher frequencies with decreasing temperature; at low frequencies, 700–1000 cm^{-1}, R is observed to grow with decreasing frequency, a feature characteristic of metals (for $T = 15$ K, $R = 0.7$ at 700 cm^{-1}). Against this background of electronic reflectance, one clearly sees strong vibrational features at 1330, 1220, and 1165 cm^{-1} deriving from the electron–vibration interaction, which, as pointed out in Section 1, is typical of molecular conductors.

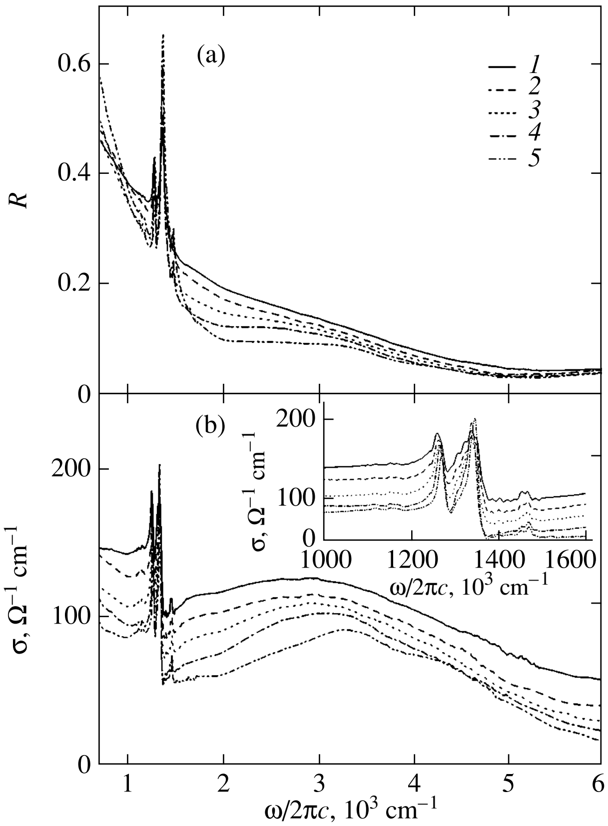

Fig. 3. (a) Reflectance and (b) optical conductivity spectra of the κ-$(BETS)_4Hg_{2.84}Br_8$ superconductor obtained in the $\mathbf{E} \parallel c$ polarization at various temperatures T: (*1*) 300, (*2*) 200, (*3*) 150, (*4*) 80, and (*5*) 15 K. Inset: optical conductivity spectra measured in the vibronic frequency region.

The $R(\omega)$ spectra measured in the $\mathbf{E} \parallel c$ polarization have a different pattern: weak reflectance ($R = 0.05$–0.13 in the range 6000–3000 cm^{-1}) grows gradually with decreasing frequency up to $R = 0.5$ at 700 cm^{-1}. As the temperature is lowered, R falls off over nearly all the frequency range covered, a plateau forms in the range 2000–3000 cm^{-1}, and, at low frequencies (1000–700 cm^{-1}), R increases when the temperature is lowered from 150 to 15 K, a feature that likewise resembles the metallic pattern. Two vibrational features are seen at frequencies of 1360 and 1277 cm^{-1}.

The $\sigma(\omega)$ spectra in both polarizations exhibit a very broad electronic maximum: in the range 2000–3000 cm^{-1} for $\mathbf{E} \parallel b$ and 2000–4000 cm^{-1} for $\mathbf{E} \parallel c$; this maximum is also characteristic of the spectra of all salts of the BEDT–TTF κ phase (see, e.g., [21, 22]). As seen from Figs. 2 and 3, the electronic maximum shifts

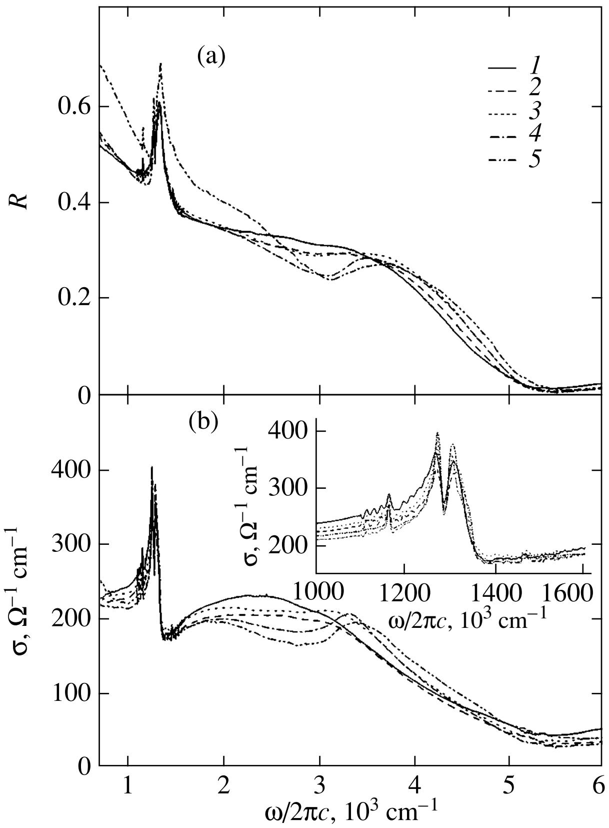

Fig. 4. Spectra of (a) reflectance and (b) optical conductivity of κ-$(BETS)_4Hg_3Cl_8$ metal measured in the **E** || *b* polarization at various temperatures *T*: (*1*) 300, (*2*) 200, (*3*) 150, (*4*) 80, and (*5*) 15 K. Inset: optical conductivity spectra obtained in the vibronic frequency region.

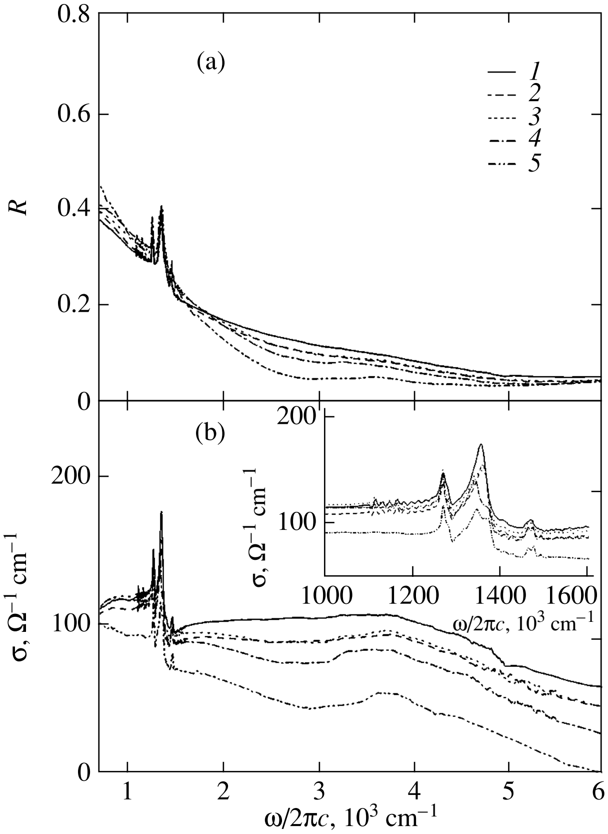

Fig. 5. Spectra of (a) reflectance and (b) optical conductivity of the κ-$(BETS)_4Hg_3Cl_8$ metal measured in the **E** || *c* polarization at various temperatures *T*: (*1*) 300, (*2*) 200, (*3*) 150, (*4*) 80, and (*5*) 15 K. Inset: optical conductivity spectra obtained in the vibronic frequency region.

slightly with decreasing temperature toward higher frequencies (up to ~3400 cm^{-1}) and has a doublet pattern at 80 and 15 K. The intensities and widths of the maximum measured in the **E** || *b* and **E** || *c* polarizations differ considerably more greatly than is the case with the BEDT–TTF salts. A similar behavior of the maximum in the σ(ω) spectra was also observed for κ-$(BETS)_2FeCl_4$ [10].

Strong vibronic features in the σ(ω) spectra are observed in the **E** || *b* polarization at frequencies of 1304, 1260, and 1164 cm^{-1} and in the **E** || *c* polarization at 1347 and 1265 cm^{-1}. As the temperature decreases, the vibrational bands narrow considerably, with the band at 1260 cm^{-1} (**E** || *b*) exhibiting a slight high-frequency shift (+15 cm^{-1}).

3.2. κ-$(BETS)_4Hg_3Cl_8$

Figures 4 and 5 display *R*(ω) and σ(ω) spectra of the BETS-Cl metal measured in the same polarizations and within the same temperature interval. We readily see that these spectra also differ from the Drude profile and exhibit a noticeable anisotropy. At 300 K, the spectra of both salts are qualitatively similar and the σ(ω) spectrum in the **E** || *b* polarization has a broad maximum in the mid-IR region (2000–3000 cm^{-1}).

However, the changes observed to occur in the BETS-Cl spectra with decreasing temperature differ substantially from those seen in the BETS-Br spectra; namely, the broad maximum in the σ(ω) spectra seen for $T < 150$ K at 2000–3000 cm^{-1} in the **E** || *b* polarization splits into two broad bands peaking at 1900 and 3500 cm^{-1}. For **E** || *c*, the intensity of the broad IR maximum decreases substantially at low temperatures and is also seen to split. At low frequencies (1000–700 cm^{-1}), σ is seen to grow slightly with decreasing frequency at 15 K, in accordance with the increase in *R* predicted by the Drude model.

Vibronic features in the *R*(ω) spectra are observed in the **E** || *b* polarization at 1340, 1280, and 1165 cm^{-1} and in the **E** || *c* polarization at 1340 and 1280 cm^{-1}.

The σ(ω) spectra reveal such features for **E** || *b* at 1308, 1268, and 1165 cm^{-1} and for **E** || *c* at 1357 and 1272 cm^{-1}. For $T < 150$ K, the vibronic features at 1308 cm^{-1} (**E** || *b*) and 1357 cm^{-1} (**E** || *c*) split into two components (1306 and 1321 cm^{-1} for **E** || *b* and 1346 and 1374 cm^{-1} for $\mathbf{E} \parallel c$) and the electronic maximum at 2000–3000 cm^{-1} also splits.

4. DISCUSSION OF THE RESULTS

4.1. Electronic Phenomena

The presence of a broad maximum in the mid-IR region (near 2200 and 3500 cm^{-1}, depending on the polarization) and the increase in conductivity with decreasing frequency at low frequencies (<800 cm^{-1}) and low temperatures (<50 K) are characteristic features of optical conductivity spectra of molecular conductors of the BEDT–TTF-based κ phase [21, 22, 29]. Our spectra displayed in Figs. 2 and 3, as well as the data reported in [10], indicate that a similar maximum is observed in the spectra of conductors of the BETS-based κ phase. The spectra of the latter compounds are, however, strongly anisotropic, so this maximum differs in intensity and width between the two major directions in the conducting plane of the crystals.

As pointed out in [18], the main difference in the structure of conducting layers between salts of the BEDT–TTF- and BETS-based κ phase consists in the absence of shortened S…S contacts in the $(\text{BEDT–TTF})_2^+$ dimer, whereas in the $(\text{BETS})_2^+$ dimer there are shortened Se…Se contacts (as compared to van der Waals contacts). It is this difference that probably accounts for the larger anisotropy of the spectra of these salts in the IR region. The same factor is apparently also responsible for the higher optical conductivity at low frequencies (below 1000 cm^{-1}) near room temperature in the BETS salts studied by us (as compared to the optical conductivity of their structural analogs based on the BEDT–TTF molecule [22]).

In the literature, the following views can be found concerning the possible nature of the maximum in the mid-IR spectral region (for the κ-(BEDT–TTF)$_2$Cu(SCN)$_2$ superconductor):

(1) The maximum derives from electronic transitions between the lower occupied bands below the Fermi level and the upper unfilled band in the electronic structure of these compounds (on which intraband electronic transitions in the upper band, which determine the low-frequency part of the spectra [21], are superimposed);

(2) From the molecular-physics viewpoint, it is assumed that the maximum originates from charge transfer between the dimers [22];

(3) The maximum is assigned in [30] to absorption by localized small-radius polarons, which form as a result of strong interaction of electrons with intramolecular vibrations (the metallic behavior at low temperatures is explained in terms of coherent motion of large-radius polarons).

Although these explanations are physically reasonable, they do not take into account the strong electronic correlations characteristic of low-dimensional molecular conductors (see, e.g., [31]) and cannot be applied to describe $R(\omega)$ and $\sigma(\omega)$ spectra with vibronic features.

Two alternate approximations have been used in an attempt to describe the optical spectra of low-dimensional molecular conductors with vibronic features, namely, the theory of phase phonons [32] and cluster models [31]. The former theory assumes that the electrons are delocalized and that electronic correlations can be taken into account in the mean-field approximation. The simplest model of the conducting layer proposed in the cluster approximation for κ-phase molecular conductors [24] is given by two orthogonal $(\text{BETS})_2^+$ dimers with two holes in the outer BETS molecular orbitals (see inset to Fig. 6b). The model considers electronic correlations in the Hubbard approximation and includes interaction of electrons with intramolecular vibrations.

In an attempt to quantitatively describe our $R(\omega)$ and $\sigma(\omega)$ spectra of BETS-Br in the spectral region covered (700–6500 cm^{-1}), we used a combination of these theories, similar to what we did earlier to explain the optical properties of the molecular superconductor κ-(BEDT–TTF)$_2$Cu[N(CN)$_2$]Cl$_{0.5}$Br$_{0.5}$ [33]. For delocalized electrons, however, we invoked the simple relation from the Drude model $\varepsilon = \varepsilon_\infty - \omega_p^2/(\omega^2 + i\Gamma_D\omega)$, because application of the phase phonon concept to the case in question failed to describe the experimental spectrum.

The cluster approximation model includes the Coulomb repulsion U between two electrons (holes) located on the same molecule and transfer integrals between BETS molecules in a dimer, t, and between molecules belonging to neighboring dimers, t' (see inset to Fig. 6b). The model also includes the extreme case of $U \longrightarrow \infty$ (where two electrons (holes) cannot occupy the same molecular orbital) [25] and is described by Eqs. (1)–(6) presented below [24]:

$$H = H_e + H_V + \sum_{\alpha, i} g_{\alpha, i} n_i Q_{\alpha, i} - \mathbf{p} \cdot \mathbf{E}, \qquad (1)$$

where the first two terms relate to the electrons (holes) and intramolecular vibrations in each molecule in the absence of electron–vibration interaction, respectively, and the third term describes electron–vibration interaction in the linear approximation; $g_{\alpha, i}$ are the electron–vibration coupling constants of the electronic density n_i of holes on the ith molecule and vibrational mode α (A_g) of this molecule characterized by a dimensionless coordinate $Q_{\alpha, i}$. The last term in Eq. (1) is the interaction energy of the electric dipole moment $\mathbf{p}$ of the tetramer induced by the displacement of the electronic density of holes in an external electric field $\mathbf{E}$. In the

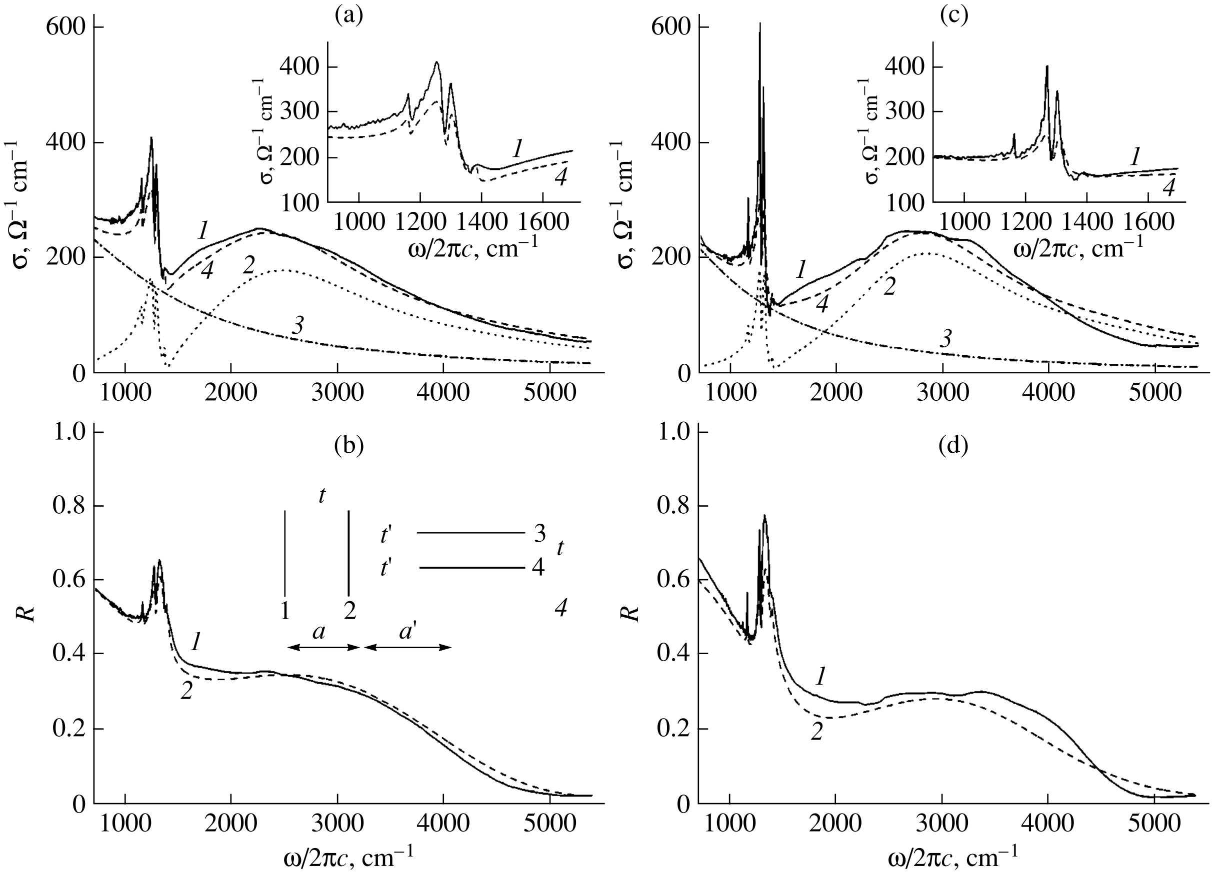

Fig. 6. Theoretical and experimental $\sigma(\omega)$ and $R(\omega)$ spectra of the κ-$(\text{BETS})_4\text{Hg}_{2.84}\text{Br}_8$ superconductor obtained for $\mathbf{E} \parallel b$ at 300 and 80 K. (a) (*1*) experimental $\sigma(\omega)$ spectrum obtained at 300 K and (*2*) calculated $\sigma(\omega)$ graph based on the cluster model with parameters $t = 1570$ cm^{-1} (0.195 eV), $t'/t = 0.45$, $\Gamma_{21} = \Gamma_{51} = 2280$ cm^{-1}, $g_3 = 550$ cm^{-1} ($\nu_3(A_g)$), $g_5 = 100$ cm^{-1} ($\nu_5(A_g)$), $g_7 = 60$ cm^{-1} ($\nu_7(A_g)$), $\gamma_{3,5,7} = 10$ cm^{-1}, $a = 3.52$ Å, $a'/a = 1.17$, and $N = 5.5 \times 10^{20}$ cm^{-3} (*2*). The frequencies ν_3, ν_5, and ν_7 are listed in the table. (*3*) Plot of the Drude formula with $\varepsilon_\infty = 3$, $\omega_p = 4832$ cm^{-1}, and $\Gamma_D = 1260$ cm^{-1} and (*4*) total calculated spectrum; inset: $\sigma(\omega)$ in the vibronic frequency region. (b) (*1*) Experimental $R(\omega)$ spectrum obtained at 300 K and (*2*) theoretical $R(\omega)$ spectrum constructed using the parameters presented in the caption to panel (a); inset: tetramer model used in the calculations. (c) (*1*) Experimental $\sigma(\omega)$ spectrum obtained at 80 K and (*2*) calculated $\sigma(\omega)$ graph based on the cluster model with parameters $t = 1740$ cm^{-1} (0.216 eV), $t'/t = 0.36$, and $\Gamma_{21} = \Gamma_{51} = 1980$ cm^{-1} and with all other parameters being identical to those presented in the caption to panel (a); (*3*) plot of the Drude relation constructed with $\varepsilon_\infty = 3$, $\omega_p = 4416$ cm^{-1}, and $\Gamma_D = 990$ cm^{-1}; and (*4*) total calculated spectrum; inset: $\sigma(\omega)$ spectrum in the vibronic frequency region. (d) (*1*) Experimental $R(\omega)$ spectrum obtained at 80 K and (*2*) calculated $R(\omega)$ spectrum constructed using the parameters presented in the caption to panel (c); the parameters obtained for $\mathbf{E} \parallel c$ at 300 K are as follows: $t = 1720$ cm^{-1}, $t'/t = 0.26$, $\Gamma_{21} = \Gamma_{51} = 3859$ cm^{-1}, $\varepsilon_\infty = 3$, $\omega_p = 3550$ cm^{-1}, and $\Gamma_D = 1200$ cm^{-1}.

limiting case of $U \longrightarrow \infty$, two particles cannot occupy the same molecular orbital, which simplifies the electronic Hamiltonian of the tetramer to

$$H_e = -t(c_1^+ c_2 + c_3^+ c_4 + \text{H.c.}) - t'(c_2^+ c_3 + c_2^+ c_4 + \text{H.c.}) \tag{2}$$

(where c_i^+ (c_i) is the operator of creation (annihilation) of a hole on molecule i) and allows analytical solution.

The complex conductivity of the κ-phase crystal is given by

$$\sigma_{\text{tetra}}(\omega) = -i\omega N(\mathbf{p}, [\mathbf{I} - \chi \cdot \text{diag}\,\mathbf{D}]^{-1} \cdot \chi \cdot \mathbf{p}), \tag{3}$$

$$\mathbf{p} = \begin{pmatrix} 2(a + a') \\ ea \\ 0 \\ 0 \end{pmatrix}, \tag{4}$$

where N is the tetramer concentration; a and a' are the distances between BETS molecules inside a dimer and between the dimers, respectively; $\mathbf{I}$ is the unit matrix; diag$\mathbf{D}$ is a diagonal matrix with components

$$D_i(\omega) = \sum_\alpha \frac{2g^2_{\alpha,i}\omega_{\alpha,i}}{\omega^2_{\alpha i} - \omega^2 - i\omega\gamma_{\alpha i}}, \tag{5}$$

Features of electron–vibration interaction (EVI) and their assignment

Frequencies of EVI features in $\sigma(\omega)$, cm^{-1}				Frequencies of the BETS^0 and BEDT–TTF^0 features (cm^{-1}) and their assignment [10]		
k-(BETS)$_4$Hg$_{2.84}$Br$_8$		k-(BETS)$_4$Hg$_3$Cl$_8$				
E || b	**E** || c	**E** || b	**E** || c			
1304	1341	1308	1356	1493	$\nu_3(A_g)$	ν(C=C)*
1260	1263	1268	1272	1282	$\nu_5(A_g)$	ν(C–C)**
1164	–	1165	–	1195	$\nu_7(A_g)$	δ(C–C–H)***

* Stretching vibrations of central and ring C=C bonds.

** Stretching vibrations of C–C bonds in ethylene groups.

*** Bending vibrations of C–C–H bonds in BEDT–TTF^0 (for D_2 symmetry) [37].

and χ is the electronic polarizability matrix with elements

$$\chi_{ij} = \sum_{\beta} \frac{\langle 1|n_i|\beta\rangle\langle\beta|n_j|1\rangle 2\omega_{\beta 1}}{\omega_{\beta 1}^2 - \omega^2 - i\omega\Gamma_\beta}. \tag{6}$$

In Eq. (5), $\omega_{\alpha i}$ and $\gamma_{\alpha i}$ are the frequency and decay coefficient of the A_g-IMV α mode, respectively. In Eq. (6), Γ_β is a phenomenological decay coefficient of charge transfer electronic excitation with energy $\omega_{\beta 1} = E_\beta - E_1$, E_β and $|\beta\rangle$ are the eigenvalues and eigenfunctions of the electronic Hamiltonian H_e in Eq. (1), and $\beta = 1$ corresponds to the ground state.

According to [25], two allowed transitions, ω_{21} and ω_{51}, contribute to $\sigma(\omega)$.

The total conductivity of the crystal was determined from the relation

$$\sigma(\omega) = \sigma_{\text{tetra}} + \sigma_{\text{Drude}}. \tag{7}$$

Figure 6 shows calculated and experimental $\sigma(\omega)$ and $R(\omega)$ spectra of the BETS-Br superconductor obtained for **E** || b at 300 and 80 K; the corresponding fitting parameters are specified in the figure captions. The proposed combined model is seen to fit the experimental spectra satisfactorily, including the vibronic region, and suggests the presence of two groups of electrons in the molecular conductors studied, namely, electrons delocalized in the conducting plane and localized on two orthogonal dimers (similar to [33]). As the temperature is lowered, the transfer integral between BETS molecules in the dimer (t) increases, whereas the ratio t'/t decreases slightly. This gives us grounds to conjecture that the shift of the maximum in the experimental $\sigma(\omega)$ spectra observed to occur in the mid-IR region toward high frequencies (Fig. 2b), which also takes place in salts of the BEDT–TTF κ phase with decreasing temperature, indicates charge transfer between molecules in the dimer to be the main factor causing this maximum to appear.

As already mentioned, the changes induced in spectra of the BETS-Cl metal by a decrease in temperature differ substantially from those observed in superconductor spectra. The splitting of the electronic maximum in the $\sigma(\omega)$ spectra at 2000–3000 cm^{-1} into two broad bands (at 1900 and 3500 cm^{-1}), which is accompanied by splitting of the vibronic features at 1308 cm^{-1} (for **E** || b) and 1356 cm^{-1} (for **E** || c) [mode $\nu_3(A_g)$, see below] into two components at $T < 150$ K, indicates a change in the electronic structure and in its symmetry occurring at low T, and it is apparently this change that inhibits the onset of superconductivity in this molecular metal.

The change in the electronic structure may be associated with changes in the crystal lattice. For instance, the Hg sublattice in the organic superconductor (BEDT–TTF)$_4$Hg$_{2.84}$Br$_8$ with a similar structure undergoes a transition at a low temperature, in which the Hg columns gradually shift parallel to the column axis [34], but this transition does not inhibit the onset of superconductivity. Another factor responsible for causing the change in the BETS-Cl electronic structure with decreasing T could be redistribution of charges localized on the $(\text{BETS})_2^+$ dimers or $(\text{BETS})_4^{+2}$ tetramers, which is caused by their interaction on neighboring molecules and is not included in [24, 25]. The Coulomb interaction of charges localized on nearest neighbors, which brings about a specific ordering on the lattice, is considered, in particular, in [35].

4.2. Vibrational Features

Our assignment of the vibronic features in the spectra was based, as that in [28], on Raman spectra of the neutral molecule BETS^0 [10] and on the corresponding data available on salts of BEDT–TTF [36, 37] (see table).

The strong bands seen in the $\sigma(\omega)$ spectra of BETS-Br at 1304 cm^{-1} (for **E** || b) and 1341 cm^{-1} (for **E** || c) and in the $\sigma(\omega)$ spectra of BETS-Cl at 1308 cm^{-1} (**E** || b) and 1356 cm^{-1} (**E** || c) derive from the interaction of electrons with stretching vibrations of the central and ring

C=C bonds, the $\nu_3(A_g)$ mode of $BETS^0$ (1493 cm^{-1}). The low-frequency shift of this feature can be attributed to the shift of the $\nu_3(A_g)$ frequency caused by the molecule ionization, as well as to the corresponding shift induced by electron–vibration interaction, as was observed earlier in BEDT–TTF salts [36]. (Note that the BETS molecule does not have optically active vibrations in the range 1350–1390 cm^{-1}.) The bands at 1260 cm^{-1} ($\mathbf{E} \parallel b$) and 1263 cm^{-1} ($\mathbf{E} \parallel c$) for BETS-Br and at 1268 and 1272 cm^{-1} for BETS-Cl derive from electron interaction with stretching vibrations of the C–C bonds in ethylene groups [the $\nu_5(A_g)$ mode of $BETS^0$ at 1282 cm^{-1}]. We assign the weaker feature at 1165 cm^{-1} seen in the spectra of both salts only in the $\mathbf{E} \parallel b$ polarization to the $\nu_7(A_g)$ mode (at 1195 cm^{-1}, bending vibrations of the C–C–H bonds), which was observed in the Raman spectra of salts of BEDT–TTF and was also obtained theoretically for the D_2 symmetry of this molecule. It is less likely that this band belongs to the vibration of B_{2g} symmetry observed in the Raman spectra of $BETS^0$ at 1173 cm^{-1} [10], because B_g vibrations usually do not couple to the electronic system.

Note the large difference in the frequency of the vibrational feature associated with the $\nu_3(A_g)$ mode and measured in the $\mathbf{E} \parallel b$ and $\mathbf{E} \parallel c$ polarizations, namely, 37 and 48 cm^{-1} for BETS-Br and BETS-Cl, respectively. We believe that this difference is due to the large anisotropy of the electronic band (the maxima in the IR region) and indicates strong electron coupling to the $\nu_3(A_g)$ mode. This difference is substantially larger than that observed in the spectra of θ-$(BETS)_4HgBr_4(C_6H_5Cl)$ (3 cm^{-1} in the $R(\omega)$ spectra), where the anisotropy of the electronic system is very small [28]. The vibronic features seen in the $\sigma(\omega)$ spectra of κ-BETS-Br, κ-BETS-Cl, and θ-$(BETS)_4HgBr_4(C_4H_5Cl)$ also differ in shape; indeed, these features are strong bands on the low-frequency wing of the electronic band for salts of the κ phase and dips in the electronic spectrum for the θ phase. This difference is accounted for by marked differences in the electronic spectra between salts of the κ and θ phases, as well as by the fact that the vibronic features of the θ phase lie practically at the center of the electronic band and those of the κ phase, on its low-frequency wing.

As already mentioned, at $T < 150$ K the BETS-Cl metal exhibits a splitting of the vibronic $\nu_3(A_g)$ features (at 1308 cm^{-1} for $\mathbf{E} \parallel b$ and at 1357 cm^{-1} for $\mathbf{E} \parallel c$) into two components, in addition to the splitting of the electronic maximum at 2000–3000 cm^{-1}.

5. CONCLUSIONS

Thus, we have carried out comparative optical studies ranging in frequency from 700 to 6500 cm^{-1} in polarized light at temperatures of 300–15 K on two new organic isostructural conductors based on the BETS molecule, which differ in the nature of the ground state, namely, a κ-$(BETS)_4Hg_{2.84}Br_8$ superconductor (T_c = 2 K) and a κ-$(BETS)_4Hg_3Cl_8$ metal that transfers to the insulating state at 35 K. It was shown that the room-temperature spectra of reflectance, $R(\omega)$, and optical conductivity, $\sigma(\omega)$, are nearly identical for the two compounds and differ from the Drude spectrum characteristic of metals. The nature of the observed difference is discussed, and the $\sigma(\omega)$ spectra are quantitatively described in terms of a cluster model (taking into account electron–electron correlations in Hubbard approximation) and the Drude model; this approach suggests the presence of two groups of electrons in the molecular conductors investigated, more specifically, electrons delocalized in the conducting plane of the crystal (*bc*) and localized on two orthogonal dimers. For κ-$(BETS)_4Hg_{2.84}Br_8$, theoretical parameters were determined, including the electron transfer integrals between molecules inside a dimer and between dimers; for $T = 300$ K, the parameters are $t = 0.195$ eV and $t'/t = 0.45$ (for $\mathbf{E} \parallel b$) and $t = 0.21$ eV and $t'/t = 0.26$ (for $\mathbf{E} \parallel c$); for 80 K, $t = 0.216$ eV and $t'/t = 0.36$ for $\mathbf{E} \parallel b$. The conclusion has been drawn that the broad electronic maximum observed in the spectra of the crystals under study in the range 2000–3000 cm^{-1} originates primarily from charge transfer between molecules inside a dimer. This conclusion is apparently also applicable to other salts of the κ phase. The anisotropy of the spectra in the conducting plane of the crystal was found to be larger than that seen in related salts of the κ phase based on the BEDT–TTF molecule, which can apparently be assigned to the difference in the intermolecular separations between dimers of the corresponding molecules in the crystal structure.

The variation of the $R(\omega)$ and $\sigma(\omega)$ spectra induced by a decrease in temperature was found to be radically different in the superconductor and the metal undergoing a transition to the insulating state. The spectra of the metal (κ-$(BETS)_4Hg_3Cl_8$) cooled down to 150 K reveal splitting of the broad electronic maximum in the range 2000–3000 cm^{-1} into two bands, which is accompanied by splitting of the vibronic feature deriving from electron interaction with intramolecular $\nu_3(A_g)$ vibrations of $BETS^0$. The observed changes suggest a substantial rearrangement of the electronic structure, which brings about a transition to the dielectric state when the temperature is lowered to 35 K and inhibits the onset of superconductivity.

ACKNOWLEDGMENTS

The authors are deeply indebted to N.F. Kartenko and A.S. Kolosova for determining the unit cell parameters of the κ-$(BETS)_4Hg_{2.84}Br_8$ superconductor and for their assistance in crystal orientation in the light wave field and to V.M. Yartsev for valuable comments and helpful discussions.

This study was supported by the Department of Physical Sciences of the Russian Academy of Sciences, program NSh-2200.2003.2, and in part by the Russian Foundation for Basic Research (project no. 04-03-32296).

REFERENCES

1. T. Ishiguro, K. Yamaji, and G. Saito, *Organic Superconductors*, 2nd ed. (Springer, Berlin, 1998).
2. G. Saito, A. Otsuka, and A. A. Zakhidov, Mol. Cryst. Liq. Cryst. **284**, 3 (1996).
3. H. Kobayashi, H. Akutsu, H. Tanaka, A. Kobayashi, M. Tokumoto, L. Borssard, and P. Cassoux, Synth. Met. **102**, 1654 (1999).
4. F. Wudl, H. Yamochi, T. Suzuki, H. Isotalo, C. Fite, H. Kasmai, K. Liou, G. Srdanov, P. Coppens, K. Maly, and A. Frost-Jensen, J. Am. Chem. Soc. **118**, 2461 (1990).
5. H. Yamochi, T. Nakamuram, G. Saito, T. Kikuchi, S. Sato, K. Nozava, M. Kinoshita, T. Sugano, and F. Wudl, Synth. Met. **41–43**, 1741 (1991).
6. S. Horiuchi, H. Yamochi, G. Saito, K. Sakaguchi, and M. Kusunoki, J. Am. Chem. Soc. **118**, 8604 (1996).
7. T. Naito, A. Miyamoto, H. Kobayashi, R. Kato, and A. Kobayashi, Chem. Lett. 1945 (1991).
8. A. Kobayashi, R. Kato, T. Naito, and H. Kobayashi, Synth. Met. **56**, 2078 (1993).
9. R. B. Lyubovskii, S. I. Pesotskii, S. V. Konovalikhin, G. V. Shylov, A. Kobayashi, H. Kobayashi, V. I. Nizhankovskii, J. A. A. J. Perenboom, O. A. Bogdanova, E. I. Zhilyaeva, and R. N. Lyubovskaya, Synth. Met. **123**, 149 (2001).
10. I. Olejniczak, A. Graja, N. D. Kushch, P. Cassoux, and H. Kobayashi, J. Phys. I **6**, 1631 (1996).
11. B. Zn. Narymbetov, N. D. Kushch, L. V. Zorina, S. S. Khasanov, R. P. Shibaeva, T. G. Togonidze, A. E. Kovalev, M. V. Kartsovnik, L. I. Buravov, E. B. Yagubskii, E. Canadell, A. Kobayashi, and H. Kobayashi, Eur. Phys. J. B **5**, 179 (1998).
12. H. Kobayashi, T. Udagawa, H. Tomita, K. Bun, T. Naito, and A. Kobayashi, Chem. Lett. 1559 (1993).
13. L. K. Montgomery, T. Burgin, J. C. Huffman, J. Ren, and M.-H. Whangbo, Physica C (Amsterdam) **219**, 490 (1994).
14. H. Kobayashi, H. Tomita, T. Naito, H. Tanaka, A. Kobayashi, and T. Saito, J. Chem. Soc. Chem. Commun. 1225 (1995).
15. H. Kobayashi, H. Tomita, T. Naito, A. Kobayashi, F. Sakai, T. Watanabe, and P. Cassoux, J. Am. Chem. Soc. **118**, 368 (1996).
16. Chisa Hotta and Hidetoshi Fukuyama, Synth. Met. **120**, 895 (2001).
17. H. Tanaka, T. Adachi, E. Ojima, H. Fujiwara, K. Kato, H. Kobayashi, A. Kobayashi, and P. Cassoux, J. Am. Chem. Soc. **121**, 11243 (1999).
18. E. I. Zhilyaeva, O. A. Bogdanova, V. V. Gritsenko, O. A. Dyachenko, R. B. Lyubovskii, K. V. Van, A. Kobayashi, H. Kobayashi, and R. N. Lyubovskaya, Synth. Met. **139** (2), 535 (2003).
19. E. Zhilyaeva, O. Bogdanova, R. Lyubovskaya, R. Lyubovskii, J. Perenboom, S. Konovalikhin, G. Shilov, A. Kobayashi, and H. Kobayashi, Synth. Met. **120**, 1089 (2001).
20. C. S. Jacobsen, D. B. Tanner, J. M. Williams, U. Geiser, and H. H. Wang, Phys. Rev. B **35**, 9605 (1987).
21. K. Kornelsen, J. E. Eldridge, H. H. Wang, and J. M. Williams, Phys. Rev. B **44**, 5235 (1991).
22. K. Kornelsen, J. E. Eldridge, C. C. Homes, H. H. Wang, and J. M. Williams, Solid State Commun. **72**, 475 (1989).
23. R. M. Vlasova, S. Ya. Priev, V. N. Semkin, R. N. Lyubovskaya, E. I. Zhilyaeva, E. B. Yagubskii, and V. M. Yartsev, Synth. Met. **48**, 129 (1992).
24. V. M. Yartsev, O. O. Drozdova, V. N. Semkin, and R. M. Vlasova, J. Phys. I **6**, 1673 (1996).
25. V. M. Yartsev, O. O. Drozdova, V. N. Semkin, R. M. Vlasova, and R. N. Lyubovskaya, Phys. Status Solidi B **209**, 471 (1998).
26. N. V. Drichko, R. M. Vlasova, V. N. Semkin, O. A. Bogdanova, E. I. Zhilyaeva, R. N. Lyubovskaya, R. B. Lyubovskii, and A. Graja, Phys. Status Solidi B **236** (3), 668 (2003).
27. M. Inokuchi, H. Tajima, A. Kobayashi, T. Ohta, H. Kuroda, R. Kato, T. Naito, and H. Kobayashi, Bull. Chem. Soc. Jpn. **68**, 547 (1995).
28. R. M. Vlasova, N. V. Drichko, B. V. Petrov, V. N. Semkin, E. I. Zhilyaeva, O. A. Bogdanova, R. N. Lyubovskaya, and A. Graja, Fiz. Tverd. Tela (St. Petersburg) **44** (1), 9 (2002) [Phys. Solid State **44**, 8 (2002)].
29. K. Kornelsen, J. E. Eldridge, H. H. Wang, H. A. Charlier, and J. M. Williams, Solid State Commun. **81** (4), 343 (1992).
30. N. L. Wang, B. P. Clayman, H. Mori, and S. Tanaka, J. Phys.: Condens. Matter **12**, 2867 (2000).
31. V. M. Yartsev, *Materials and Measurements in Molecular Electronics*, Ed. by K. Kajimura and S. Kuroda (Springer, Tokyo, 1996), Springer Proc. Phys., Vol. 81, p. 189.
32. M. J. Rice, Phys. Rev. Lett. **37**, 36 (1976).
33. B. V. Petrov, V. N. Semkin, R. M. Vlasova, V. M. Yartsev, N. D. Kushch, and A. Graja, in *Proceedings of NATO Advanced Research Workshop on Molecular Low Dimensional and Nanostructured Materials for Advanced Applications* (Poznan, Poland, 2001), pp. 259–261.
34. R. Li, V. Petricek, G. Yang, P. Coppen, and M. Naughton, Chem. Mater. **10**, 1521 (1998).
35. R. Citro and M. Marinaro, Eur. Phys. J. B **22**, 343 (2001).
36. J. E. Eldridge, Y. Xie, H. H. Wang, J. M. Williams, A. M. Kini, and J. A. Schlueter, Spectrochim. Acta A **52**, 45 (1996).
37. M. Meneghetti, R. Bozio, and C. Pecile, J. Phys. (Paris) **47**, 1377 (1986).

Translated by G. Skrebtsov

Physics of the Solid State, Vol. 46, No. 11, 2004, pp. 1994–1997. Translated from Fizika Tverdogo Tela, Vol. 46, No. 11, 2004, pp. 1930–1933.
Original Russian Text Copyright © 2004 by Medvedeva, Finkel'shteĭn, Shamin, Lyakhovskaya, Kurmaev.

Chemical Shifts in the X-ray Emission Spectra of MgB_2 and Their Correlation with the Electronic Structure

N. I. Medvedeva*, L. D. Finkel'shteĭn, S. N. Shamin**,**
I. I. Lyakhovskaya*, and É. Z. Kurmaev****
** Institute of Solid-State Chemistry, Ural Division, Russian Academy of Sciences,*
Pervomaĭskaya ul. 91, Yekaterinburg, 620219 Russia
e-mail: medvedeva@ihim.uran.ru
*** Institute of Metal Physics, Ural Division, Russian Academy of Sciences,*
ul. S. Kovalevskoĭ 18, Yekaterinburg, 620219 Russia
**** Fock Institute of Physics, St. Petersburg State University, Ul'yanovskaya ul. 1, St. Petersburg, 198504 Russia*

Received March 23, 2004

Abstract—The x-ray emission spectra of magnesium diboride MgB_2 are measured. It is found that the Mg $L_{2,3}$ and B K_α emission lines are shifted with respect to the spectra of the pure metals toward the low-energy range. The band calculations of the MgB_2 diboride in the framework of the full-potential linearized muffin-tin orbital (LMTO) method demonstrate that the electron populations of the shells in both components of MgB_2 are higher than those of pure metals. This increase in the electron populations is associated with the crystal contraction and manifests itself in low-energy shifts of the emission lines. *© 2004 MAIK "Nauka/Interperiodica".*

1. INTRODUCTION

The discovery of superconductivity in magnesium diboride MgB_2 [1] has stimulated intensive investigations into the electronic structure of this compound and the microscopic nature of its superconducting (and other) properties (see the review by Ivanovskiĭ *et al.* [2]). The electronic structure and chemical bonding in the MgB_2 diboride have been investigated theoretically [3–7] and experimentally [8–10] using x-ray emission, absorption, and photoemission spectroscopy. Calculations of the band structure have demonstrated that the energy spectrum of the valence band of the MgB_2 compound is predominantly determined by the B $2p$ states, which form two groups of energy bands of the $\sigma(2p_{x,y})$ and $\pi(p_z)$ types and for which the dependences $E(k)$ differ significantly. An important feature of the electronic structure of the MgB_2 diboride is that the hole quasi-two-dimensional B $2p_{x,y}$ states are localized along the Γ–A direction of the Brillouin zone. These bands reflect the distribution of electron states of boron atoms in the planar graphite-like networks. Two B $2p_{x,y}$ bands intersect the Fermi level E_F and make a substantial contribution to the density of states at the Fermi level. As was shown by An and Pickett [5] and Kong *et al.* [11], the hole nature of the B $2p_{x,y}$ states at the Γ point of the Brillouin zone is a necessary condition for superconductivity in the MgB_2 diboride. The B $2p_z$ bands are responsible for weaker pp_π interactions between the atomic planes. These bands (of the 3D type) are characterized by a maximum dispersion along the k_z (Γ–A) direction.

At present, it has been established that the state of magnesium ions in the form Mg^{2+}, which appears as a result of electron transfer from magnesium atoms to boron atoms, plays an important role in the formation of the electronic structure of the MgB_2 diboride. Band calculations carried out for the MgB_2 compound and isoelectronic systems (graphite C_2, hypothetical diboride $\square^{2+}B_2$) [5] showed that the presence of the Mg^{2+} ions in the structure brings about the lowering of the B $\pi(2p_z)$ nonbonding bands with respect to the B $\sigma(2p_{x,y})$ bonding bands as compared to graphite, which, in turn, leads to the σ–π electron transfer and the emergence of holes in the σ band. For the MgB_2 compound, the electron transfer from magnesium atoms to boron atoms is confirmed by theoretical calculations [12, 13] and experimental data on x-ray diffraction [13].

It should be noted that the direction of the charge transfer in borides has been a topic of discussion in the literature for a long time [14, 15]. It has been established that the metal is a donor in diborides and higher borides, whereas boron is an acceptor of electrons. In lower borides, the direction of the electron transfer is inverse. It is believed that, in higher borides, charge transfer stems from the necessity of supplying electrons for the formation of strong covalent B–B bonds. The results of investigating the direction of charge transfer in terms of the sign of the chemical shift with the use of x-ray emission and photoelectron spectroscopy are contradictory. For the TiB_2 compound, the B K_α emission line [16] and the Ti $L_{2,3}$ emission line [17] are shifted to the low-energy range. This indicates an increase in the electron density for atoms of both components as compared to the corresponding metals. The photoelectron spectrum is characterized by a high-energy shift of the Ti $2p_{3/2}$ level [17]. However, it should be remembered that the x-ray photoelectron spectra substantially depend on the surface condition. For example, the x-ray photoelectron spectra of inner levels in diborides exhibit an additional peak caused by strong oxidation of the surface [15, 17]. Moreover, theoretical and experimental investigations of the surface of titanium [18, 19] revealed that the charge states of atoms at the surface and in the bulk differ significantly. Therefore, x-ray photoelectron spectroscopy can also provide incorrect information on the bulk charge states. In this work, the charge state of magnesium and boron ions and the direction of charge transfer in the MgB_2 compound are investigated using x-ray photoelectron spectroscopy (which provides information on the bulk state) and band calculations for the MgB_2 compound and pure magnesium and boron metals.

2. CHEMICAL SHIFTS OF THE EMISSION LINES

The spectra of Mg $L_{2,3}$ (the $3s3d$–$2p$ transition) and B K_α (the $2p$–$1s$ transition) x-ray emission were measured on a spectrometer with a diffraction grating and electron excitation. The energy resolution was 0.3–0.4 eV. Figure 1 shows the Mg $L_{2,3}$ and B K_α x-ray emission spectra of the MgB_2 diboride and its constituent pure metals. It is found that the x-ray emission spectra of both components in the MgB_2 compound are shifted with respect to the spectra of pure magnesium and boron metals toward the low-energy range: the low-energy chemical shift is equal to 0.5 eV for Mg $L_{2,3}$ and 0.3 eV for B K_α. The chemical shifts reflect the variation in the electron population near the corresponding component through the mechanism of screening of the x-ray hole. Therefore, we investigated the electronic structure of the MgB_2 compound, calculated the energies of core levels and the populations of magnesium and boron shells for different radii, and constructed the charge density maps.

The band structures of the MgB_2 compound and metallic magnesium and boron were calculated by the full-potential method of muffin-tin (MT) orbitals, which does not involve approximations accounting for the shape of the potential and charge density [20]. In order to interpret the chemical shifts, we compared the energies of the Mg $2p$ and B $1s$ core levels, as well as the electron populations in the shells of magnesium and boron atoms in the MgB_2 compound and the corresponding metals (magnesium with a hexagonal structure and boron with an α-B_{12} structure) for two radii of Mg MT shells, R_{Mg} = 2.83 and 2.00 au. The radius of boron atoms was taken to be constant and equal to 1.65 au. As can be seen from the table, the results of calculations substantially depend on the radii chosen for the Mg MT shells. For R_{Mg} = 2.83 au, the change in the energy of the Mg $2p$ level in the MgB_2 compound with respect to the pure metal is determined to be Δ_{Mg2p} = 1.1 eV. The corresponding change in the energy of the B $1s$ level is Δ_{B1s} = 0.7 eV. For R_{Mg} = 2.00 au, these changes are considerably smaller: Δ_{Mg2p} = 0.4 eV and Δ_{B1s} = 0.3 eV. It should be emphasized that, for two radii of MT shells, the core levels of both magnesium and boron atoms are shifted toward lower energies, which corresponds to directions of the shifts determined in our experiments.

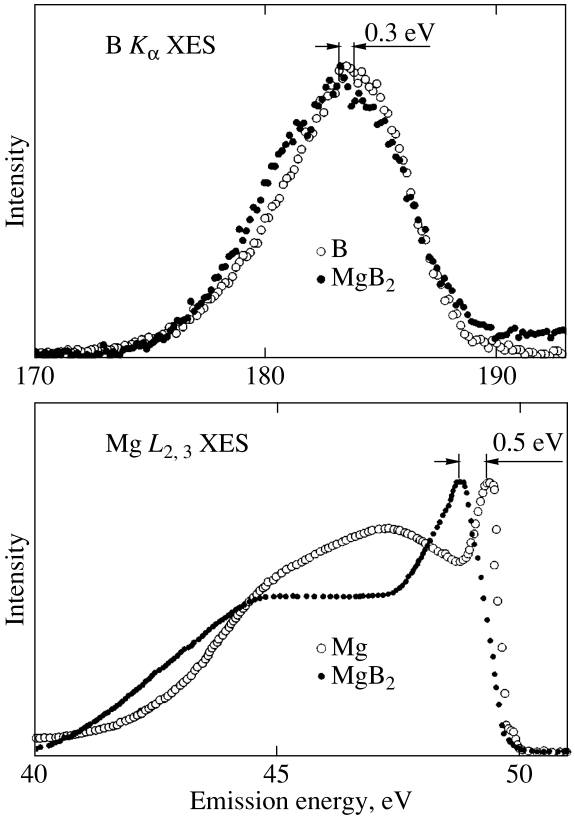

Fig. 1. Mg $L_{2,3}$ and B K_α x-ray emission spectra of the MgB_2 compound and its constituent pure metals.

Analysis of the data presented in the table shows that, for both radii of magnesium, the total populations q_{tot} in the magnesium and boron shells in the MgB_2 compound exceed those in metallic magnesium and boron. For R_{Mg} = 2.83 au, the increase in the population of the shells is equal to 0.5e and 0.02e for magnesium and boron, respectively. For R_{Mg} = 2.00 au, these quantities are equal to 0.1e and 0.04e, respectively. Considering the changes in the orbital populations, it is worth noting that the populations of the Mg $3s$ states decrease and the populations of the Mg $3p$ and Mg $3d$ states increase in the MgB_2 compound as compared to metallic magnesium for both MT radii. This is also confirmed by the map of the valence charge density, which is determined as the difference between the change

Energies E_{core} (eV) of Mg 2*p* and B 1*s* core levels and populations of orbitals q_l and atoms q_{tot} (electrons/atom)

	MgB$_2$				Mg		B
	R_{Mg} = 2.83 au R_{B} = 1.65 au		R_{Mg} = 2.00 au R_{B} = 1.65 au		R_{Mg} = 2.83 au	R_{Mg} = 2.00 au	R_{B} = 1.65 au
	Mg	B	Mg	B			
$-E_{\text{core}}$	42.36	168.49	37.67	168.95	43.49	38.08	169.22
q_s	0.506	0.581	0.153	0.587	0.600	0.173	0.573
q_p	0.785	1.028	0.185	1.041	0.522	0.129	1.018
q_d	0.392		0.064		0.075	0.011	
q_{tot}	1.683	1.609	0.402	1.628	1.197	0.313	1.591

densities in the MgB$_2$ compound and metallic magnesium (Fig. 2).

Most likely, the increase in the electron population of the magnesium and boron shells is caused by the crystal chemical contraction of the hexagonal lattice: the lattice parameter is equal to 6.042 au for Mg and decreases to 5.834 au for MgB$_2$. As regards boron atoms, the loose-packed structure of elemental boron transforms into the hexagonal close-packed structure of the MgB$_2$ compound. Upon crystal contraction, the electron density per unit volume increases. Therefore, the electron population in equivalent volumes of the shells in the MgB$_2$ compound also increases as compared to that of the pure metal. It should be noted that the electron population in magnesium shells increases at the expense of the *p* and *d* states. This indicates that the crystal contraction is due to the enhancement of the interatomic interaction (as compared to the initial elements) involving the *d* states, which are vacant in magnesium atoms in a free state. The calculations of the energy of the core levels for metallic magnesium with the lattice parameters of the MgB$_2$ diboride also revealed crystal contraction. The calculated energies of the Mg 2*p* level are equal to 43.12 eV (R_{Mg} = 2.83 au) and 37.67 eV (R_{Mg} = 2.00 au) and correspond to low-energy shifts of 0.4 eV.

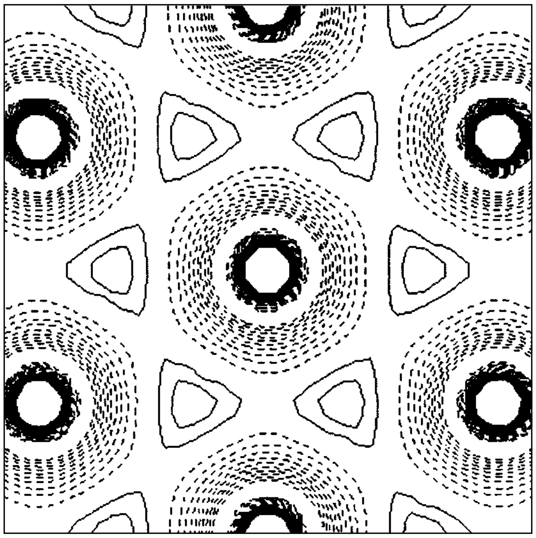

Fig. 2. Difference charge density for the MgB$_2$ compound in the *xy* plane. Dashed and solid lines correspond to a decrease and an increase in the charge density of the compound as compared to metallic magnesium (lattice parameter $a_{\text{Mg}} = a_{\text{MgB}_2}$), respectively.

3. CHARGE TRANSFER

Analysis of the difference charge-density maps (Fig. 3) demonstrates that, in the MgB$_2$ compound, the charge is transferred from magnesium atoms to boron atoms. It is worth noting that, according to these maps, the charge density changes upon the formation of diboride as compared to free atoms. The direction of the chemical shift is determined by comparing the x-ray emission spectra of the components of the diboride and metallic magnesium and boron.

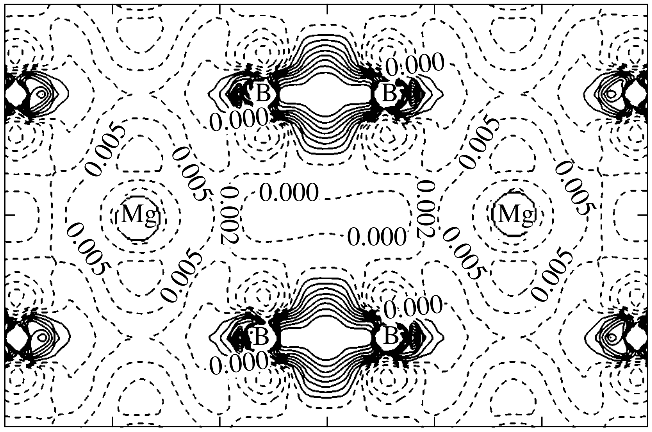

Fig. 3. Difference charge density for the MgB$_2$ compound in the *xz* plane. Dashed and solid lines correspond to a decrease and an increase in the charge density of the compound as compared to free atoms, respectively.

The calculated total populations q_{tot} for the case of close radii of the magnesium and boron atoms (R_{Mg} = 2.00 au, R_{B} = 1.65 au) are equal to 0.4*e* (Mg) and 1.6*e* (B). These values correspond to the ionic formula $\mathrm{Mg}^{+1.6}\mathrm{B}_2^{-0.8}$, which is in excellent agreement with the formula obtained in [12]: $\mathrm{Mg}^{+1.68}\mathrm{B}_2^{-0.84}$. This formula suggests that the charge is transferred from magnesium to boron atoms and that the magnesium atom losses approximately 1.6*e* upon the formation of the diboride, whereas two boron atoms acquire this charge. The same value for charge transfer (1.5–1.6*e*) was obtained by Tsirelson *et al.* [13].

4. CONCLUSIONS

Thus, the experimental and theoretical investigations demonstrated that the electron population in magnesium and boron shells of the $\mathrm{MgB_2}$ diboride is higher than that in pure metals. This manifests itself in low-energy shifts of the emission lines. The low-energy shift is due to a more effective screening of the inner-shell x-ray hole in the $\mathrm{MgB_2}$ compound. The chemical shift in $\mathrm{MgB_2}$ is caused primarily not by the charge transfer, which should lead to different shifts for magnesium and boron atoms, but by the crystal chemical contraction of the lattice upon changing over from the pure metals to $\mathrm{MgB_2}$.

ACKNOWLEDGMENTS

This work was supported by the Russian Foundation for Basic Research (project no. 02-03-32971), the Council on Grants from the President of the Russian Federation for the Support of Leading Scientific Schools of the Russian Federation (project nos. NSh-1026.2003.2 and NSh-829.2003.3), and the Ministry of Industry and Science of the Russian Federation (project “Superconductivity of Mesoscopic and Strongly Correlated Systems”).

REFERENCES

1. J. Akimitsu, in *Proceedings of Symposium on Transition Metal Oxides* (Sendai, 2001); J. Nagamatsu, N. Nakagawa, T. Muranaka, Y. Zenitani, and J. Akimitsu, Nature **410**, 63 (2001).
2. A. L. Ivanovskiĭ, N. I. Medvedeva, V. G. Zubkov, and V. G. Bamburov, Zh. Neorg. Khim. **47**, 661 (2002).
3. J. Kortus, I. I. Mazin, K. D. Belashchenko, V. P. Antropov, and L. L. Boyer, Phys. Rev. Lett. **86**, 4656 (2001).
4. K. D. Belashchenko, M. van Schilfgaarde, and V. P. Antropov, Phys. Rev. B **64**, 092503 (2001).
5. J. M. An and W. E. Pickett, Phys. Rev. Lett. **86**, 4366 (2001).
6. N. I. Medvedeva, A. L. Ivanovskii, J. E. Medvedeva, and A. J. Freeman, Phys. Rev. B **64**, 020502 (2001).
7. N. I. Medvedeva, Yu. E. Medvedeva, A. L. Ivanovskiĭ, V. G. Zubkov, and A. Friman, Pis’ma Zh. Éksp. Teor. Fiz. **73**, 378 (2001) [JETP Lett. **73**, 336 (2001)].
8. E. Z. Kurmaev, I. I. Lyakhovskaya, J. Kortus, N. Miyata, M. Demeter, M. Neumann, M. Yanagihara, M. Watanabe, M. Muranaka, and J. Akimitsu, Phys. Rev. B **65**, 134509 (2001).
9. T. A. Callcott, L. Lin, G. T. Woods, G. P. Zhang, J. P. Thompson, M. Paranthaman, and D. L. Erderer, Phys. Rev. B **64**, 132504 (2001).
10. T. Takahashi, T. Sato, S. Souma, T. Muranako, and J. Akimitsu, Phys. Rev. Lett. **86**, 4915 (2001).
11. Y. Kong, O. V. Dolgov, O. Jepsen, and O. K. Andersen, Phys. Rev. B **64**, 020501 (2001).
12. D. Bagayoko and G. L. Zhao, Int. J. Mod. Phys. B **16**, 571 (2002).
13. V. Tsirelson, A. Stash, M. Kohout, H. Rosner, H. Mori, S. Sato, S. Lee, A. Yamamoto, S. Tajima, and Y. Grin, Acta Crystallogr. B **859**, 575 (2003).
14. G. V. Samsonov, T. I. Serebryakova, and V. A. Neronov, *Borides* (Atomizdat, Moscow, 1975) [in Russian].
15. T. I. Serebryakova, V. A. Neronov, and P. D. Peshev, *High-Temperature Borides* (Metallurgiya, Moscow, 1991) [in Russian].
16. I. I. Lyakhovskaya, T. M. Zimkina, and V. A. Fomichev, Fiz. Tverd. Tela (Leningrad) **12**, 174 (1970) [Sov. Phys. Solid State **12**, 138 (1970)].
17. L. Remqvist, B. Ekstig, E. Kaline, E. Noreland, and R. Manne, J. Phys. Chem. Solids **30**, 1835 (1969).
18. M. V. Kuznetsov, E. V. Shalaeva, N. I. Medvedeva, and A. L. Ivanovskiĭ, *Chemistry of the Titanium–Gas Interface: Experiment and Theory* (Yekaterinburg, 1999) [in Russian].
19. N. I. Medvedeva, D. P. Frikkel’, M. V. Kuznetsov, and A. L. Ivanovskiĭ, Fiz. Met. Metalloved. **86** (3), 14 (1998) [Phys. Met. Metallogr. **86**, 232 (1998)].
20. M. Methfessel, C. O. Rodriguez, and O. K. Andersen, Phys. Rev. B **40**, 2009 (1989).

Translated by N. Korovin

Physics of the Solid State, Vol. 46, No. 11, 2004, pp. 1998–2001. Translated from Fizika Tverdogo Tela, Vol. 46, No. 11, 2004, pp. 1934–1936.

METALS AND SUPERCONDUCTORS

London Limit for the Lattice Model of a Superconductor

S. A. Ktitorov[1, 2]

[1] *Ioffe Physicotechnical Institute, Russian Academy of Sciences, Politekhnicheskaya ul. 26, St. Petersburg, 194021 Russia*

[2] *Electrotechnical University, St. Petersburg, 197376 Russia*

e-mail: ktitorov@mail.ioffe.ru

Received March 30, 2004

Abstract—The electromagnetic properties of superconductors are investigated as a function of the discreteness of the crystal lattice in the London limit. The dependence of the superconducting current on the magnitude of the order parameter is obtained in the framework of the lattice model. The dependence of the critical current on the degree of deviation from the continuous approximation is calculated. © *2004 MAIK "Nauka/Interperiodica".*

1. INTRODUCTION

The effect of an external magnetic field on the superconducting state near the upper critical field for type-II superconductors has been intensively investigated in recent years. In particular, Brezin *et al.* [1] demonstrated that, in a strong magnetic field, fluctuations of the order parameter near the upper critical field become substantially stronger due to their quasi-one-dimensionality. The nonrenormalizability of the relevant theory makes the use of the renormalization-group method ineffective. In our earlier work [2], we established that the breakdown of the continuous translational symmetry of the crystal lattice recovers the renormalizability of the theory. The kinetic term of the effective action takes the form of a Harper operator. Consequently, the fluctuations have three-dimensional character in the case where the magnetic flux through the lattice plaquette is comparable to the London flux quantum. On the other hand, the shift of the superconducting transition toward higher temperatures has given impetus to the development of new approaches with inclusion of the strong-coupling approximation, which is most appropriate for the use of lattice models. In their pioneering work [3], Nozieres and Schmitt-Rink considered the problem of strong coupling in the theory of superconductivity and also noted that inclusion of the discreteness of the translational symmetry in explicit form is of fundamental importance. In this respect, it is of interest to analyze all the possible physical consequences of this form of the Ginzburg–Landau action in a more general context, i.e., in terms of the boundedness of the spectrum of the corresponding operator due to the translational symmetry of the superconducting crystal. However, the complex mathematical character of this operator makes it very difficult to solve the problem. Another important aspect of our problem is to investigate the stability of the superconducting state when an electric current flows through the studied crystal. In the most consistent form, the current in a superconductor as a thermodynamic variable was studied by Kudinov [4]. In the present work, the phenomenological approach applied to a superconductor with strong coupling is similar to the approach used in the theory of stability of the current state, which is based on the Ginzburg–Landau equation in the London limit [5].

2. ELECTRODYNAMIC EQUATIONS FOR A NARROW-BAND-GAP SUPERCONDUCTOR

Our analysis is based on a phenomenological approach similar to that used in the monograph by de Gennes [5].

The lattice version of the Ginzburg–Landau equation was derived from the microscopic theory in our previous work [6]. The free energy functional has the form

$$F = \int d\mathbf{x}\left[\psi^*(\mathbf{x})\varepsilon\left(-i\hbar\nabla - \frac{2e}{c}\mathbf{A}(\mathbf{x})\right)\psi(\mathbf{x}) + \tau\psi^*(\mathbf{x})\psi(\mathbf{x})\right] + \frac{g}{2}\int d\mathbf{x}\left[(\psi^*(\mathbf{x})\psi(\mathbf{x}))^2 + \frac{\mathbf{B}^2}{8\pi}\right], \quad (1)$$

where $\mathbf{B} = \mathrm{curl}\mathbf{A}$ is the magnetic induction, $\tau = \alpha(T - T_c)/T_c$, T_c is the temperature of the superconducting transition in the self-consistent field approximation in the absence of an external field and current, and $\varepsilon\mathbf{p}$ is the function of the quasi-wave vector with periods $(2\pi)/a_1$, $(2\pi)/a_2$, and $(2\pi)/a_3$. The operators ∇ and $\mathbf{A}(\mathbf{x})$ commute in the case where we choose the gauge

$\operatorname{div}\mathbf{A} = 0$. This functional can also be written in the Bloch representation:

$$F = \sum_{\mathbf{k}}\left[\varphi_{\mathbf{k}}^{*}\varepsilon\left(\mathbf{k} - \frac{2e}{\hbar c}\mathbf{A}\left(i\frac{\partial}{\partial\mathbf{k}}\right)\right)\varphi_{\mathbf{k}} + \tau\varphi_{\mathbf{k}}^{*}\varphi_{\mathbf{k}}\right] + \sum_{\mathbf{k}_1+\mathbf{k}_2+\mathbf{k}_3+\mathbf{k}_4=0}\frac{g}{2}\varphi_{\mathbf{k}_1}^{*}\varphi_{\mathbf{k}_2}\varphi_{\mathbf{k}_3}^{*}\varphi_{\mathbf{k}_4} + \int d\mathbf{x}\frac{\mathbf{B}^2}{8\pi}. \qquad (2)$$

The vectors **m** enumerate the lattice sites in the plane perpendicular to the magnetic field. By varying expression (1) with respect to the vector potential $\mathbf{A}(\mathbf{x})$, we obtain the Maxwell equation

$$\frac{c}{4\pi}\operatorname{curl}\mathbf{B} = \mathbf{j} \qquad (3)$$

with the density of the electric current

$$\mathbf{j} = \frac{e}{2}\left(\psi^{*}(\mathbf{x})\mathbf{v}\left(-i\hbar\nabla - \frac{2e}{c}\mathbf{A}(\mathbf{x})\right)\psi(\mathbf{x}) + \psi^{*}(\mathbf{x})\mathbf{v}\left(i\hbar\nabla - \frac{2e}{c}\mathbf{A}(\mathbf{x})\right)\psi(\mathbf{x})\right), \qquad (4)$$

where $\mathbf{v}(\mathbf{p}) = (\partial\varepsilon)/(\partial\mathbf{p})$ is the group velocity of the wave packet of the order parameter. Let us represent the complex order parameter $\psi(\mathbf{x})$ in the form

$$\psi(\mathbf{x}) = R(\mathbf{x})e^{i\varphi(\mathbf{x})}, \qquad (5)$$

where $R^2 = n_s$ is the density of superconducting electrons. When the coherence length is small as compared to the depth of current penetration, the quantity τ is relatively large, which is equivalent to the presence of a small parameter in the kinetic term. In this case, the spatially homogeneous solution to Eq. (1) can be taken as a magnitude of the order parameter:

$$\tau(T)R_0 = -gR_0^3, \qquad (6)$$

which is valid almost everywhere. The last remark follows from the well-known fact that the small parameter before the higher derivative does not guarantee complete spatial homogeneity of the solution; it is owing to this loophole that the eddy solutions exist in the London limit. Under the assumption that the magnitude of the order parameter is constant and that the phase varies slowly, we obtain the following expression for the current in the London limit:

$$\mathbf{j} = en_s^0\mathbf{v}\left(\nabla\varphi - \frac{2e}{\hbar c}\mathbf{A}(\mathbf{x})\right), \qquad (7)$$

where $n_s^0 = R_0^2$. By introducing the gauge–invariant vector field

$$\mathscr{A} = \mathbf{A} - \frac{\hbar c}{2e}\nabla\varphi, \qquad (8)$$

we can rewrite the Maxwell equation (3) in the form

$$\frac{c}{4\pi}\operatorname{curl}\operatorname{curl}\mathscr{A} = -eR_0^2\mathbf{v}\left(\frac{2e}{\hbar c}\mathscr{A}\right). \qquad (9)$$

In the continuous approximation $\mathbf{v}(\mathbf{p}) = \mathbf{p}/m$, expression (9) can easily be reduced to the standard Londons' equation

$$\delta^2\nabla^2\mathbf{A} - \mathbf{A} = 0, \qquad (10)$$

where $\delta^2 = (mc^2)/(4\pi e^2R^2)$ and $m^{-1} = (\Delta a^2)/\hbar^2$. Let us now use relationship (9) to analyze the classical problem of a critical current in order to elucidate the specific features that arise when the translation symmetry in the crystal is reduced.

3. CRITICAL CURRENT IN A THIN FILM

We consider a crystal with tetragonal symmetry and with a kinetic term of the form

$$\varepsilon(\mathbf{p}) = \Delta_{\perp}\left(2 - \cos\frac{p_xa}{\hbar} - \cos\frac{p_ya}{\hbar}\right) + \Delta_{\parallel}\left(1 - \cos\frac{p_zb}{\hbar}\right). \qquad (11)$$

It is assumed that the electric current **j** flows through a film with thickness d in a direction parallel to the x axis. Let us also assume that $d \ll \xi(T)$ and $d \ll \delta(T)$, where $\xi(T)$ is the coherence length. These conditions ensure the homogeneity of the order parameter R and the density of the current **j** over the thickness of the film, respectively. By using relationships (1), (5), (7), and (8), we can write the following conditions for the minimum of the free energy (here, we disregard the effect of the magnetic field, as is usually done in the theory of a critical current):

$$j_x = -eR^2v_x\left(\frac{2e}{\hbar c}\mathscr{A}\right), \qquad (12)$$

$$\varepsilon_x\left(\frac{2e}{\hbar c}\mathscr{A}\right)R + \tau R + gR^3 = 0. \qquad (13)$$

Here,

$$\varepsilon_x(k_x) = \Delta_{\perp}(1 - \cos k_xa), \qquad (14)$$

$$v_x(k_x) = \hbar^{-1}\partial\varepsilon_x(k_x)/(\partial k_x) = (a\Delta_{\perp}/\hbar)\sin k_xa. \qquad (15)$$

Now, we eliminate the quantities v_x and ε_x from relationships (14) and (15) with the use of the expression

$$\varepsilon_x = \Delta_{\perp}\left[1 - \sqrt{1 - \left(\frac{hv_x}{a\Delta_{\perp}}\right)^2}\right], \qquad (16)$$

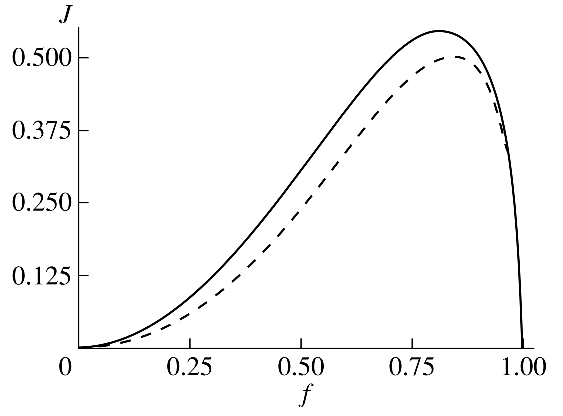

Fig. 1. Dependences of the dimensionless current J on the dimensionless order parameter f for a thin film in the continuum limit at $k \longrightarrow 0$ (solid line) and in the case of a narrow band at $k = 1$ (dashed line). The maxima of the curves correspond to the critical currents.

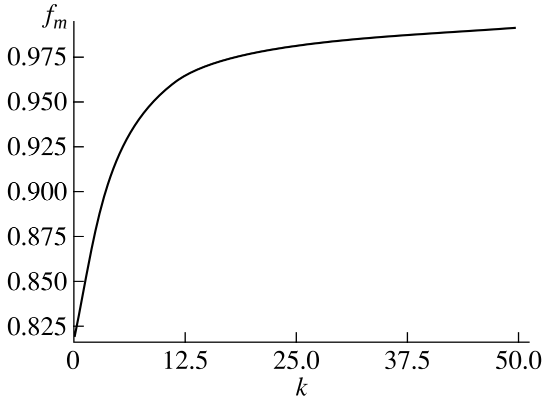

Fig. 2. Maximum of the dimensionless order parameter f_m as a function of k.

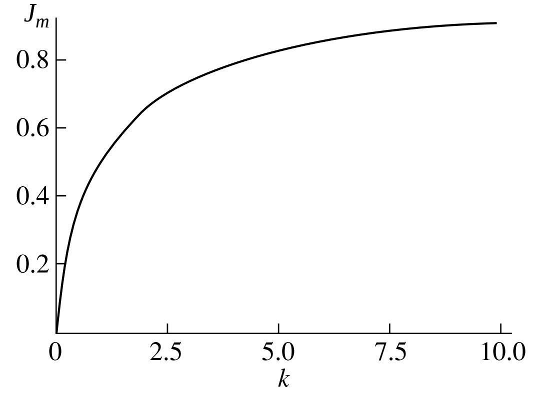

Fig. 3. Dimensionless critical current J_m as a function of k.

and derive the following relationship between the current j_x and the order parameter R:

$$\Delta_\perp R\left(1 - \sqrt{1 - \left(\frac{\hbar}{ea\Delta_\perp}\right)^2 \frac{j_x^2}{R^4}}\right) - |\tau| R + gR^3 = 0. \quad (17)$$

Next, we introduce the dimensionless variables J and f according to the formulas

$$j_x = \frac{ea\Delta_\perp R_0^2}{\hbar} J, \quad (18)$$

$$R = fR_0. \quad (19)$$

As a result, we have

$$1 - \sqrt{1 - \frac{J^2}{f^4}} = k(1 - f^2), \quad (20)$$

where $k = |\tau|/(\Delta_\perp)$. In the limit $\hbar v_x/(a\Delta_\perp) \longrightarrow 0$ and, hence, $k \longrightarrow 0$, relationship (20) transforms into the standard expression, which holds in the continuous approximation [5]:

$$J^2 = 2kf^4(1 - f^2). \quad (21)$$

Figure 1 shows the dependences of the dimensionless current J on the dimensionless order parameter f in the cases $k \longrightarrow 0$ and $k = 1$. The maxima of the dimensionless order parameter f_m and the dimensionless current J_m as a function of k are presented in Figs. 2 and 3, respectively.

4. PENETRATION OF THE MAGNETIC FIELD

Let us return to the Maxwell equation (9). In the case when the kinetic term has the form of relationship (11), the Maxwell equation (9) can be rewritten as

$$\frac{c}{4\pi} \mathrm{curl\,curl}\, \mathcal{A} = -eR_0^2 \mathbf{v}\left(\frac{2d}{\hbar c}\mathcal{A}\right) \quad (22)$$

or, with the London gauge $\mathrm{div}\,\mathcal{A} = 0$, in the form

$$\frac{c}{4\pi}\nabla^2 \mathcal{A} - eR_0^2 \mathbf{v}\left(\frac{2e}{\hbar c}\mathcal{A}\right) = 0. \quad (23)$$

Under the assumption that the dispersion law (11) holds, expression (23) for the x component can be represented in the form

$$\nabla^2 \mathcal{A}_x - \frac{4\pi e R_0^2 a\Delta}{\hbar c} \sin\left(\frac{2\pi}{\Phi_0}\mathcal{A}_x a\right) = 0, \quad (24)$$

where $\Phi_0 = (2\pi\hbar c)/(2e)$ is the London–Onsager flux quantum. In the weak-field limit, this expression takes the form of the Maxwell equation (10). Here, it is appropriate to introduce a new variable,

$$\frac{2\pi}{\Phi_0}\mathcal{A}_x a = \chi. \tag{25}$$

As a result, relationship (24) takes the form

$$\nabla^2\chi - \frac{1}{\delta^2}\sin\chi = 0. \tag{26}$$

Let us now consider the classical problem of penetration of a magnetic field [5] in terms of relationship (24). In the one-dimensional case, relationship (24) has the form

$$\frac{d^2\chi}{dx^2} - \frac{1}{\delta^2}\sin\chi = 0. \tag{27}$$

This is a standard equation that differs from the equation of pendulum only in sign. The one-dimensional penetration of a magnetic field can be described by the solution [7]

$$\chi = \arcsin\left\{\pm\mathrm{cn}\left[-\frac{x - x_0}{\kappa\delta};\ \kappa\right]\right\}, \tag{28}$$

where $cn(x)$ is the elliptic cosine and κ is the elliptic modulus. It is worth noting that the problem under consideration is mathematically similar to the problem of a fluxon in the one-dimensional Josephson contact.

In conclusion, it should be noted that, according to expression (18), the critical current in a superconductor with strong coupling tends to zero as the width of the allowed band Δ approaches zero. However, in this case, there can appear a strong lattice pinning of vortices, which will be considered in a separate paper.

ACKNOWLEDGMENTS

The author would like to thank E.K. Kudinov, B.N. Shalaev, and Yu.I. Kuz'min for their participation in discussions of the results and helpful remarks.

This work was supported by the Russian Foundation for Basic Research, project no. 02-02-17667.

REFERENCES

1. E. Brezin, D. R. Nelson, and A. Thiaville, Phys. Rev. B **31** (11), 7124 (1985).
2. S. A. Ktitorov, B. N. Shalaev, and L. Jastrabik, Phys. Rev. B **49** (21), 15248 (1994).
3. P. Nozieres and S. Schmitt-Rink, J. Low Temp. Phys. **59**, 195 (1985).
4. E. K. Kudinov, Fiz. Tverd. Tela (Leningrad) **30**, 2594 (1988) [Sov. Phys. Solid State **30**, 1493 (1988)].
5. P. G. de Gennes, *Superconductivity of Metals and Alloys* (Benjamin, New York, 1966; Mir, Moscow, 1968).
6. S. A. Ktitorov, V. S. Sherstinov, L. Jastrabik, and L. Soukup, in *Proceedings of the Seventh International Symposium on Weak Superconductivity*, Ed. by S. Benachka, P. Seidel, and V. Strib (Dept. of Cryoelectronics, Bratislava, 1994), pp. 300–305.
7. S. P. Novikov, S. V. Manakov, L. P. Pitaevskiĭ, and V. E. Zakharov, *Theory of Solitons: the Inverse Scattering Method* (Nauka, Moscow, 1980; Consultants Bureau, New York, 1984).

Translated by O. Moskalev

Physics of the Solid State, Vol. 46, No. 11, 2004, pp. 2002–2007. Translated from Fizika Tverdogo Tela, Vol. 46, No. 11, 2004, pp. 1937–1941.
Original Russian Text Copyright © 2004 by Mustafaeva, Gasanov.

SEMICONDUCTORS AND DIELECTRICS

Relaxation Phenomena in $TlGa_{0.99}Fe_{0.01}Se_2$ Single Crystals

S. N. Mustafaeva and A. I. Gasanov
Institute of Physics, National Academy of Sciences of Azerbaijan, pr. Dzhavida 33, Baku, 1143 Azerbaijan
e-mail: itpcht@itpcht.ab.az

Received January 12, 2004

Abstract—The relaxation electronic phenomena occurring in $TlGa_{0.99}Fe_{0.01}Se_2$ single crystals in an external dc electric field are investigated. It is established that these phenomena are caused by electric charges accumulated in the single crystals. The charge relaxation at different electric field strengths and temperatures, the hysteresis of the current–voltage characteristic, and the electric charge accumulated in the $TlGa_{0.99}Fe_{0.01}Se_2$ single crystals are consistent with the relay-race mechanism of transfer of a charge generated at deep-lying energy levels in the band gap due to the injection of charge carriers from the electric contact into the crystal. The parameters characterizing the electronic phenomena observed in the $TlGa_{0.99}Fe_{0.01}Se_2$ single crystals are determined to be as follows: the effective mobility of charge carriers transferred by deep-lying centers $\mu_f = 5.6 \times 10^{-2}$ cm^2/(V s) at 300 K and the activation energy of charge transfer $\Delta E = 0.54$ eV, the contact capacitance of the sample $C_c = 5 \times 10^{-8}$ F, the localization length of charge carriers in the crystal $d_c = 1.17 \times 10^{-6}$ cm, the electric charge time constant of the contact $\tau = 15$ s, the time a charge carrier takes to travel through the sample $t_t = 1.8 \times 10^{-3}$ s, and the activation energy of traps responsible for charge relaxation $\Delta E_\sigma = \Delta E_Q = 0.58$ eV. *© 2004 MAIK "Nauka/Interperiodica".*

1. INTRODUCTION

Single crystals of the $TlGa_{0.99}Fe_{0.01}Se_2$ compound belong to the class of layered semiconductors. These materials are characterized by a rather high electrical resistivity ($\rho = 1.3 \times 10^8$ Ω cm at 298 K). Earlier [1], we found that, at temperatures $T < 250$ K, $TlGa_{0.99}Fe_{0.01}Se_2$ single crystals in a dc electric field possess variable-range-hopping conduction. The density of states in the vicinity of the Fermi level was estimated as $N_F = 5.6 \times 10^{17}$ eV^{-1} cm^{-3}.

Investigations into the electrical properties of $TlGa_{0.99}Fe_{0.01}Se_2$ single crystals have revealed that, at an applied dc voltage, the samples undergo transient processes resulting in changes in the electric current with time.

The purpose of this work was to investigate experimentally the relaxation phenomena occurring in $TlGa_{0.99}Fe_{0.01}Se_2$ single crystals and to elucidate their mechanisms.

2. SAMPLE PREPARATION AND EXPERIMENTAL TECHNIQUE

Samples of the composition $TlGa_{0.99}Fe_{0.01}Se_2$ were synthesized by alloying initial components of high-purity grade (no less than 99.99) in silica glass ampules evacuated to a residual pressure of 10^{-3} Pa. Single crystals were grown using the Bridgman–Stockbarger method [1].

The $TlGa_{0.99}Fe_{0.01}Se_2$ samples used in electrical measurements were obtained by cleaving bulk single crystals along the natural cleavage planes. The thickness of the samples was approximately equal to 100 μm. The ohmic contacts were produced by soldering indium in the samples. For these experiments, samples were prepared in the form of a sandwich in such a way that the dc electric field applied to the sample would be directed parallel to the *C* axis of the crystal.

Immediately prior to measurement, the samples were placed in a shielded vacuum cryostat equipped with a temperature regulator. The temperature was kept constant to within 0.02 K. All the measurements were performed under vacuum at a residual pressure of $\sim 10^{-2}$ Pa.

The dark current passing through samples of the In–$TlGa_{0.99}Fe_{0.01}Se_2$–In system at an applied dc voltage was accompanied by charge relaxation. The time dependence of the dark current was investigated in different external dc electric fields. The charge relaxation in the studied samples was controlled by the applied voltage.

3. RESULTS AND DISCUSSION

The time dependences of the dark current in the $TlGa_{0.99}Fe_{0.01}Se_2$ single crystal at different applied dc voltages ranging from 1.0 to 50 V are shown in Fig. 1. It can be seen from curves *1–5* in Fig. 1 that, at relatively low voltages, the dark current decays with time and reaches a steady-state value 100–120 s after the

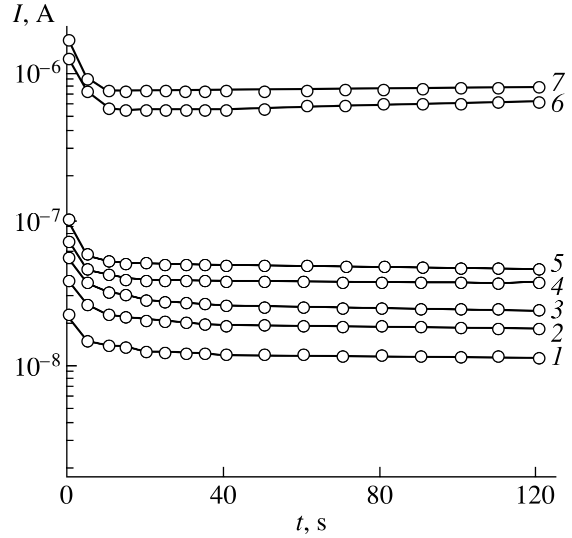

Fig. 1. Relaxation of the dark current in the $TlGa_{0.99}Fe_{0.01}Se_2$ single crystal at different applied voltages. U = (*1*) 1.0, (*2*) 1.5, (*3*) 2.0, (*4*) 3.0, (*5*) 4.0, (*6*) 40, and (*7*) 50 V. T = 300 K.

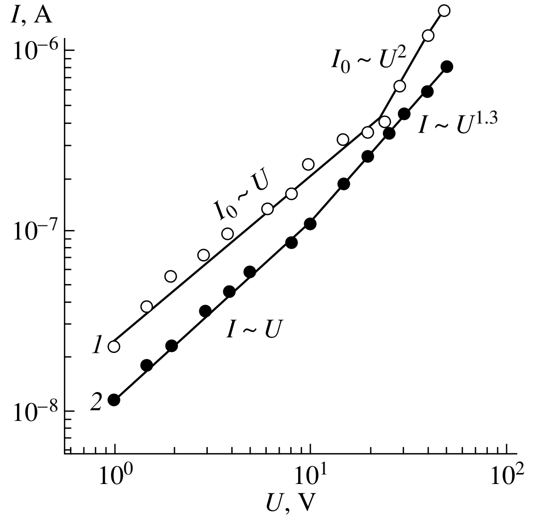

Fig. 2. Current–voltage characteristics of the In–$TlGa_{0.99}Fe_{0.01}Se_2$–In system: (*1*) the initial current I_0 and (*2*) the steady-state current I measured 120 s after the onset of the experiment.

onset of the experiment. The decay curves of charge relaxation are observed up to a voltage of 40 V. Beginning with this voltage, the dark current first decreases to a minimum and then increases to a steady-state value (Fig. 1, curves *6*, *7*). As can be seen, the dark current first decays for 40–50 s and then slightly increases. At higher voltages, no decay of the dark current occurs with time; on the contrary, the current only increases.

Since the electric current changes with time, the current–voltage characteristics of the samples studied exhibit a hysteresis. Figure 2 depicts the current–voltage characteristics constructed from the initial currents I_0 (curve *1*) and the steady-state currents I measured 120 s after the onset of the experiment (curve *2*). In the case when the voltage is applied to the sample for a longer time, the current–voltage characteristic is shifted toward weaker currents. Curve *1* has a linear portion $I_0 \sim U$ up to a voltage of 25 V and a quadratic portion $I_0 \sim U^2$ at higher voltages ($U > 25$ V). Curve *2* has a shorter linear portion at voltages $U < 10$ V and a portion $I \sim U^{1.3}$ at voltages $U > 10$ V.

The decay of charge relaxation observed in samples of the In–$TlGa_{0.99}Fe_{0.01}Se_2$–In system is accompanied by the accumulation of electric charge. After the external voltage was switched off and the electrodes were short-circuited, the circuit experienced a discharge current flow whose direction was opposite to the direction of the current passing through the sample when the voltage was switched on. The sample was completely discharged either under heating at a high temperature or under exposure to light. The electric charge accumulated in the system was calculated from the area under the current–time curve according to the formula $Q = \int_0^t I dt$.

Figure 3 shows the experimental time dependences of the electric charge accumulated in the $TlGa_{0.99}Fe_{0.01}Se_2$ single crystal at different applied dc voltages. It can be seen from Fig. 3 that, as the time of exposure to an external dc electric field increases, the electric charge accumulates more slowly and gradually reaches saturation.

A change in the dc voltage applied to the sample for the same time leads to a variation in the accumulated

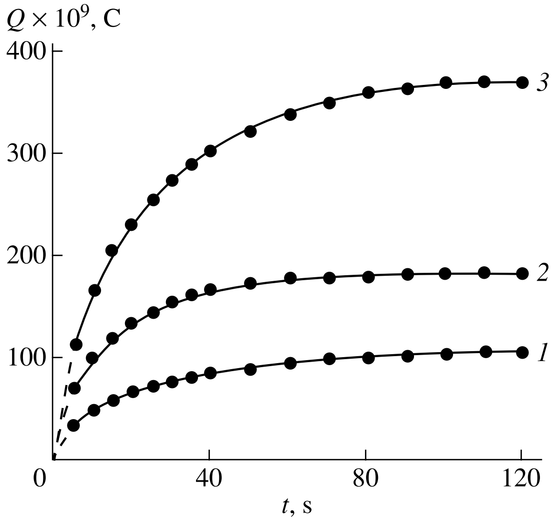

Fig. 3. Time dependences of the electric charge Q accumulated in the $TlGa_{0.99}Fe_{0.01}Se_2$ single crystal at different applied voltages. U = (*1*) 1.0, (*2*) 1.5, and (*3*) 2.0 V.

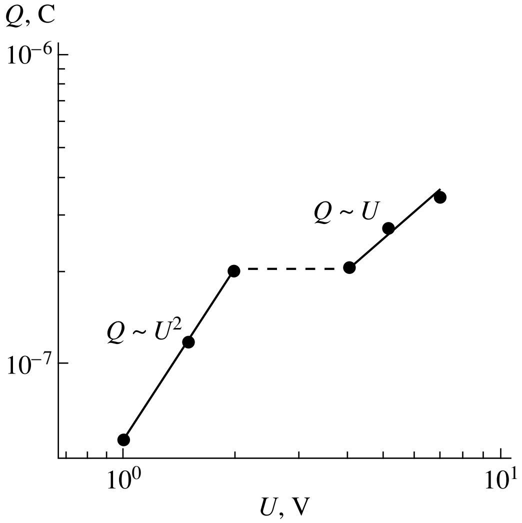

Fig. 4. Dependence of the electric charge Q accumulated in the $TlGa_{0.99}Fe_{0.01}Se_2$ single crystal for time $t = 15$ s on the applied voltage U.

charge. Figure 4 depicts the dependence of the accumulated charge on the voltage applied to the sample for a constant time $t = 15$ s. It can be seen from Fig. 4 that, at low applied voltages, the accumulated charge rapidly increases as the square of the voltage: $Q \sim U^2$. As the applied voltage increases, the accumulation of the electric charge occurs more slowly. At higher voltages ($U >$ 4 V), the accumulated charge is linearly proportional to the voltage: $Q \sim U$.

The experimental results obtained in this study were interpreted within a model according to which the transfer of an electric charge injected into a crystal occurs through the relay-race mechanism [2] and which accounts for the above specific features of the electric current flowing through a metal–semiconductor–metal system. This model implies that the crystal under consideration involves centers with deep-lying trapping levels responsible for hopping conduction. When the concentration of deep-lying centers is sufficiently high for the transfer of an electric charge injected into the crystal, it is this charge transfer that makes a dominant contribution to the electrical conduction of the crystal. According to the model proposed by Timan [2], the charge transfer provided by these local centers is accompanied by the formation of an energy barrier at the boundary with the anode, which hinders the transfer of electrons (injected from the cathode) to the anode. The energy barrier at the boundary with the anode arises from the energy difference between the electron affinity for the local center and the work function of the anode metal. Consequently, the electric current is limited by both the space charge in the bulk of the semiconductor and the energy barrier at the boundary with the anode. This brings about the accumulation of an excess charge in the vicinity of the anode, which, in turn, leads to a redistribution of the voltage across the crystal. As a result, the potential difference across the contact should increase with time, whereas the electric current passing through the crystal should decrease.

A theory of unsteady injection current with allowance made for trapping levels in the band gap of crystals was developed earlier by Many and Rakavy [3]. However, according to this theory and inferences made by Lampert and Mark [4], the injection current is caused by charge transfer through the conduction band of the crystal. An important feature of the current limited by the space charge [3, 4] is that the electric charge in this case cannot exceed the quantity C_gU, where C_g is the geometric capacitance of the sample and U is the voltage imposed across the sample. For the samples studied in the present work, the geometric capacitance was estimated at ~6×10^{-12} F. The maximum voltage across the sample at which the decay of charge relaxation was observed in $TlGa_{0.99}Fe_{0.01}Se_2$ single crystals amounted to 50 V. This means that the greatest possible charge Q accumulated in the system is equal to 3×10^{-10} C. However, in our experiments, the maximum charges Q accumulated in the crystal are significantly greater than the above value even at lower voltages (Figs. 3, 4).

According to Timan [2], the accumulated charge at short times of polarization can be given by the following relationship:

$$Q = \mu_f \varepsilon \varepsilon_0 S \frac{U^2}{L^3} t, \qquad (1)$$

where μ_f is the mobility of charge carriers transferred through the band gap of the crystal, ε_0 is the permittivity of free space, ε is the permittivity of the crystal, S is the contact area, L is the thickness of the crystal, U is the polarizing voltage, and t is the polarization time.

The experimental dependence $Q(U)$ measured at low voltages (Fig. 4) is adequately described by expression (1). The mobility of charge carriers transferred by local centers through the band gap of the $TlGa_{0.99}Fe_{0.01}Se_2$ single crystal was estimated from the slope of the quadratic portion $Q \sim U^2$ in the voltage dependence of the accumulated charge as follows: $\mu_f = 5.6 \times 10^{-2}$ cm^2/(V s). At higher voltages, the accumulated charge varies according to the law $Q \sim U$ (Fig. 4), which is also consistent with the theory presented in [2]:

$$Q = C_c U. \qquad (2)$$

From formula (2), the contact capacitance of the sample was estimated as $C_c = 5 \times 10^{-8}$ F. By substituting the contact capacitance C_c into expression $C_c = \varepsilon\varepsilon_0 S/d_c$, we determined the localization length of charge carriers in the crystal: $d_c = 1.17 \times 10^{-6}$ cm.

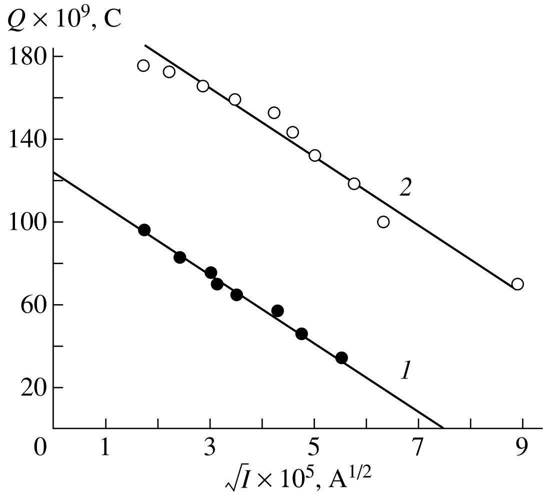

Fig. 5. Dependences of the electric charge Q accumulated in the In—In system on the current $\sqrt{I}$ at different applied voltages. U = (*1*) 1.0 and (*2*) 1.5 V.

The electric charge time constant of the contact τ = 15 s was calculated from the relationship [2]

$$\tau = \frac{L^3}{\mu_f d_c U}. \tag{3}$$

The time a charge carrier takes to travel through the sample,

$$t_t = \frac{\tau d_c}{L}, \tag{4}$$

was found to be equal to 1.8×10^{-3} s. It should be noted that the time t_t is approximately one order of magnitude longer than the Maxwell relaxation time $t_M = \varepsilon\varepsilon_0/\sigma = 2.4 \times 10^{-4}$ s.

As follows from the theory developed in [2], the electric current passing through the system and the accumulated charge are related by the expression

$$Q = UC_c - \sqrt{\frac{C_c L^3 I}{\mu_f d_c}}. \tag{5}$$

It can be seen from expression (5) that, at each instant of time, the accumulated charge is proportional to the square root of the current flowing through the system. Relationship (5) holds for the voltages and times corresponding to the descending branches of the relaxation characteristics. It is worth noting that the lower the voltage and the shorter the time, the better the fit of relationship (5) to the experimental data.

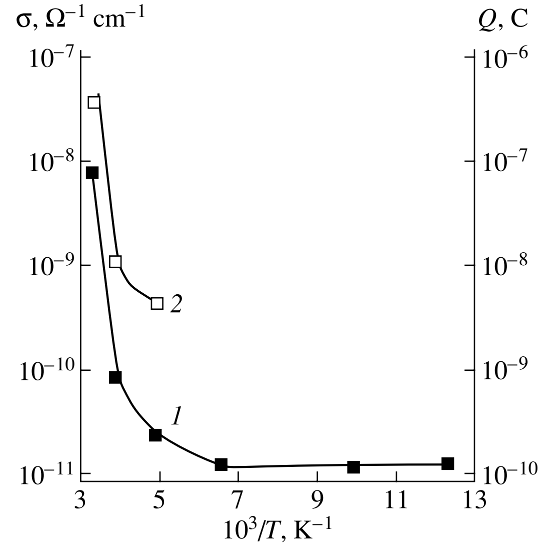

Fig. 6. Temperature dependences of (*1*) the electrical conductivity σ and (*2*) the charge Q accumulated in the $TlGa_{0.99}Fe_{0.01}Se_2$ single crystal at a polarizing voltage U = 2 V and polarization time t = 120 s.

Figure 5 shows the experimental dependences of the charge accumulated in the In–$TlGa_{0.99}Fe_{0.01}Se_2$–In system within different time intervals on the electric current measured at the same times. These dependences were obtained at applied dc voltages U = 1.0 (curve *1*) and 1.5 V (curve *2*) in the range of the descending branches of the relaxation characteristics. In this case, the currents I are the experimental values after subtracting the background current I_b, which corresponds to the leakage current. The background current I_b was chosen equal to the minimum value in the descending branch of the relaxation characteristic at a specified voltage and a longer time. The dependences constructed in the $\sqrt{I}$–Q coordinates in Fig. 5 exhibit linear behavior in accordance with relationship (5). Extrapolation of curve *1* in Fig. 5 gives the cutoff current $I_c = 5.6 \times 10^{-9}$ A at Q = 0. As a result, from relationship (5), we obtain the following expression for the charge-carrier mobility:

$$\mu_f = \frac{L^3 I_c}{U^2 C_c d_c}. \tag{6}$$

After substituting the known parameters into expression (6), we have $\mu_f = 9.6 \times 10^{-2}$ cm²/(V s), which coincides in order of magnitude with the charge-carrier mobility μ_f determined from formula (1).

The above results were obtained at room temperature. In order to elucidate the nature of the observed phenomena, we considered it expedient to compare the magnitudes of the activation energy of electrical conduction ΔE_σ and the activation energy of charge generation ΔE_Q. For this purpose, we measured the temperature dependences of the electrical conductivity σ and the charge Q accumulated in the $TlGa_{0.99}Fe_{0.01}Se_2$ single crystal (Fig. 6). The dependence of logσ on $10^3/T$ is characterized by an extended exponential portion in the temperature range 250–300 K. This portion corresponds to a deep-lying trapping level with the activation

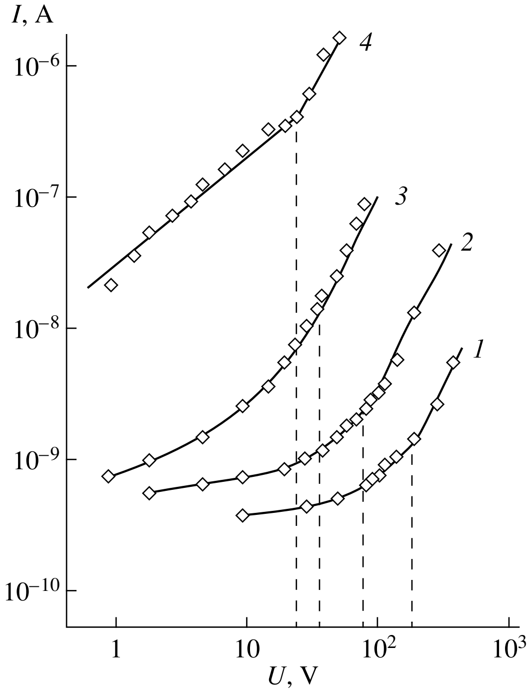

Fig. 7. Current–voltage characteristics of the In–$TlGa_{0.99}Fe_{0.01}Se_2$–In system at different temperatures. T = (*1*) 150, (*2*) 200, (*3*) 250, and (*4*) 300 K.

energy ΔE_σ = 0.58 eV. As the temperature decreases below 250 K, the slope of the temperature dependence of the electrical conductivity is ever changing; i.e., the activation energy of electrical conduction decreases progressively with a decrease in the temperature to 150 K. As was noted above, the $TlGa_{0.99}Fe_{0.01}Se_2$ single crystals at low temperatures possess hopping conduction.

It is known that the electric charge accumulated at shallow-lying trapping levels is only slightly or not at all dependent on the temperature. On the other hand, the temperature dependence of the electric charge accumulated at deep-lying trapping levels exhibits exponential behavior. The activation energy determined from the slope of this dependence plotted in the Arrhenius coordinates virtually coincides with the energy location of the corresponding trapping level. These results were confirmed in our experiments. The temperature dependence of the electric charge Q (Fig. 6, curve *2*) accumulated in the $TlGa_{0.99}Fe_{0.01}Se_2$ single crystals is similar to the dependence $\sigma(T)$; i.e., the accumulated charge Q increases drastically at temperatures $T > 250$ K with the activation energy $\Delta E_Q = \Delta E_\sigma = 0.58$ eV. At lower temperatures $T < 250$ K, the dependence $Q(T)$ becomes smoother. The equality of the activation energy of electrical conduction and the activation energy of charge generation indicates that the processes of charge generation and electrical conduction occur through mechanisms of the same nature.

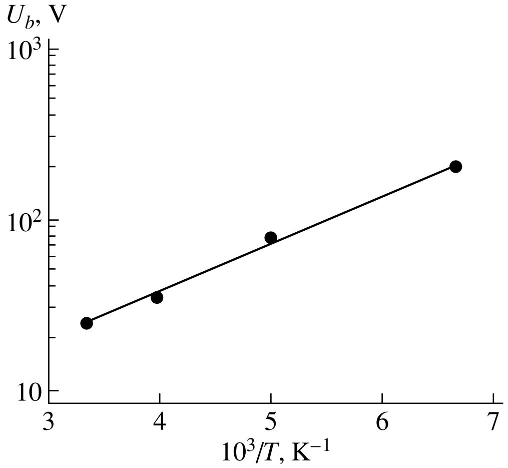

Fig. 8. Temperature dependence of the voltage U_b corresponding to the crossover from the ohmic to quadratic current–voltage characteristic of the $TlGa_{0.99}Fe_{0.01}Se_2$ single crystal.

The current–voltage characteristics of the In–$TlGa_{0.99}Fe_{0.01}Se_2$–In system at different temperatures (from 150 to 300 K) are depicted in Fig. 7. These curves are constructed from the initial values of the current passing through the system, i.e., at $t < \tau$. At temperatures $T < 300$ K, the current–voltage characteristics involve sublinear portions that transform first into linear portions and then into quadratic portions. At low temperatures ($T < 150$ K), no quadratic portions are revealed in the current–voltage characteristics of the sample up to a voltage of 400 V. In Fig. 7, the dashed lines issuing out of the points corresponding to the crossover from the ohmic to quadratic current–voltage characteristic of the sample are perpendicular to the abscissa axis. It can be seen from this figure that, with a decrease in the temperature, the voltage U_b of the crossover from the ohmic to quadratic current–voltage characteristic shifts toward larger values. The temperature dependence of the voltage U_b is plotted in the Arrhenius coordinates in Fig. 8. As the temperature decreases from 300 to 150 K, the voltage U_b increases from 25 to 200 V. It can be seen that this dependence exhibits exponential behavior: $U_b \sim \exp(W/kT)$, where $W = 0.05$ eV.

The presence of quadratic portions $I \sim U^2$ in the current–voltage characteristics follows from the relationship [2]

$$I = UC_c\frac{\tau}{(\tau + t)^2}. \tag{7}$$

At $t \ll \tau$, relationship (7) takes the form

$$I = \mu_f\varepsilon\varepsilon_0 S\frac{U^2}{L^3}. \tag{8}$$

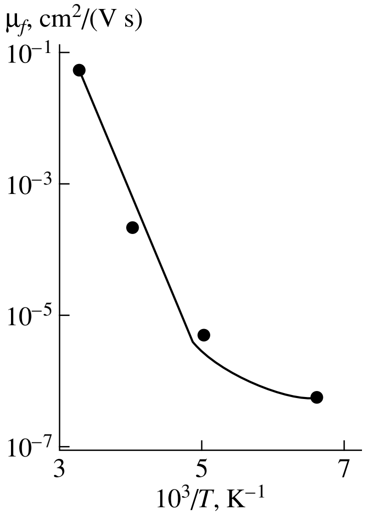

Fig. 9. Temperature dependence of the mobility of charge carriers in the band gap of the $TlGa_{0.99}Fe_{0.01}Se_2$ single crystal.

Expression (8) bears a resemblance to the Lampert formula [4] for an electric current limited by the space charge. However, as was already mentioned, according to the theory developed in [4], the injection current is caused by charge transfer through the conduction band of the crystal. If the electrical conduction is provided by states localized in energy bands, the temperature dependence of the conductivity is determined primarily by the temperature dependence of the charge-carrier concentration and, hence, the temperature dependence of the charge-carrier mobility can be disregarded ($\sigma = ne\mu$). In the case when charge transfer over localized states occurs through the hopping or relay-race mechanism, the main contribution to the electrical conductivity is made by the thermal activation of the mobility [5]:

$$\mu_f \sim \exp(-\Delta E/kT), \tag{9}$$

where ΔE is the activation energy of charge transfer.

The temperature dependence of the mobility of charge carriers transferred by local centers through the band gap of the $TlGa_{0.99}Fe_{0.01}Se_2$ single crystal is shown in Fig. 9. The dependence of $\log\mu_f$ on $10^3/T$ is characterized by an extended exponential portion with slope $\Delta E = 0.54$ eV. Within the limits of experimental error, the activation energy ΔE coincides with the activation energies $\Delta E_\sigma = \Delta E_Q = 0.58$ eV.

4. CONCLUSIONS

Thus, the experimental results obtained in the above investigation of the relaxation processes occurring in $TlGa_{0.99}Fe_{0.01}Se_2$ single crystals in an external dc electric field are in agreement with the relay-race mechanism of transfer of a charge generated in deep traps due to the injection of charge carriers from the electric contact into the crystal.

REFERENCES

1. S. N. Mustafaeva, A. I. Gasanov, and É. M. Kerimova, Izv. Nats. Akad. Azerb., Ser. Fiz.–Mat. Tekh. Nauk **23**, 117 (2003).
2. B. L. Timan, Fiz. Tekh. Poluprovodn. (Leningrad) **7**, 225 (1973) [Sov. Phys. Semicond. **7**, 163 (1973)].
3. A. Many and G. Rakavy, Phys. Rev. **126**, 1980 (1962).
4. M. A. Lampert and P. Mark, *Current Injection in Solids* (Academic, New York, 1970; Mir, Moscow, 1973).
5. N. F. Mott and E. A. Davis, *Electronic Processes in Non-Crystalline Materials* (Clarendon, Oxford, 1971; Mir, Moscow, 1974).

Translated by O. Borovik-Romanova

Physics of the Solid State, Vol. 46, No. 11, 2004, pp. 2008–2011. Translated from Fizika Tverdogo Tela, Vol. 46, No. 11, 2004, pp. 1942–1945.
Original Russian Text Copyright © 2004 by Grachev.

SEMICONDUCTORS AND DIELECTRICS

Recombination Mechanism of the Spin-Galvanic Effect

A. I. Grachev
Ioffe Physicotechnical Institute, Russian Academy of Sciences, Politekhnicheskaya ul. 26, St. Petersburg, 194021 Russia
e-mail: grach.shuv@mail.ioffe.ru

Received February 5, 2004

Abstract—The mechanism responsible for the spin-galvanic effect is considered. According to this mechanism, the current is generated as a result of the difference between the rates of spontaneous radiative transitions of charge carriers with oppositely directed spins. This difference arises when a spatially uniform nonequilibrium spin orientation of thermalized electrons (holes) is provided by any known method. © *2004 MAIK "Nauka/Interperiodica".*

1. INTRODUCTION

Recently, Ganichev *et al.* [1] experimentally observed the phenomenon referred to as the spin-galvanic effect (see also references in review [2]). In essence, this effect consists in exciting an electric current in a bulk semiconductor (or a heterostructure) when a nonequilibrium spin orientation of charge carriers is provided, for example, by uniform optical generation [1]. The origin of the current associated with the spin-galvanic effect was explained by the asymmetry of spin-flip scattering of thermalized charge carriers with oppositely directed spins [1]. It should be noted that the spin-galvanic effect caused by spin-dependent scattering processes was previously considered in [3–5]. In particular, Averkiev and D'yakonov [5] discussed the effect (more recently observed experimentally in [6]) governed by the spin diffusion due to a spatially nonuniform optical orientation of spins of charge carriers.

Ganichev and Prettl [2] noted that the spin-galvanic effect can be treated as an inverse (conjugate) effect with respect to the current-induced spin polarization of charge carriers, which would be reasonably termed the galvanospin effect. The galvanospin effect was theoretically considered by Aronov and Lyanda-Geller [7], Edelstein [8], and even earlier by Levitov *et al.* [9]. In the last work, this effect was called the kinetic magnetoelectric effect. Note that the conjugate effect, i.e., the spin-galvanic effect, was also analyzed in [9]. In all the above works, the appearance of spin polarization was explained by spin-dependent scattering of charge carriers. However, quite recently, Mal'shukov and Chao [10] theoretically described the mechanism of current-induced spin polarization due to the difference between the radiative-recombination rates for electrons with oppositely oriented spins. By analogy with the spin-galvanic and galvanospin effects caused by spin-dependent scattering, the question arises as to whether the spin-galvanic effect can be associated with a similar recombination mechanism.

In the present work, the recombination mechanism of the spin-galvanic effect is considered within a microscopic model. According to this mechanism, the current is generated as a result of the difference between the rates of spontaneous radiative transitions for charge carriers with oppositely directed spins. The difference in the radiative recombination arises when a nonequilibrium spin orientation of electrons (or holes) is ensured by any method known to date. Since the purpose of this work is to illustrate the main features of the recombination mechanism of the spin-galvanic effect, the model under consideration is not related to any specific bulk semiconductor or semiconductor heterostructure.

2. MODEL

Let us consider a sample of a semiconductor material whose symmetry allows for the existence of terms linear in the wave vector **k** in a Hamiltonian describing the energy spectrum of this sample. For example, these terms can have the form

$$H_{c,v} = \beta_{zx}^{c,v}\sigma_z k_x, \tag{1}$$

where subscripts x and z denote the corresponding crystallographic axes of the sample, σ_z is the Pauli matrix, and the quantities $\beta_{zx}^{c,v}$ are related to the spin splitting of the conduction and valence bands due to the spin–orbit interaction. For bulk semiconductors or heterostructures, the symmetry necessary for terms similar to term (1) to exist is well known [11]. A number of simplifying assumptions can be introduced into the model of the recombination mechanism without a loss of generality.

(i) We will consider a *p*-type degenerate semiconductor with allowance made for the spin polarization of only the conduction band electrons, because their spin relaxation time τ_s^e is assumed to be considerably longer than the spin relaxation time of holes τ_s^h.

(ii) It is assumed that the states with the angular-momentum projection $m_z = \pm 3/2$ (the subband of heavy holes) are dominant in the vicinity of the valence band top.

(iii) The hierarchy of relaxation times for conduction band electrons is assumed to satisfy the following inequalities: $\tau_p \ll \tau_\varepsilon \ll \tau_r$ and $\tau_s^e \ll \tau_{nr}$, where τ_p is the momentum relaxation time, τ_ε is the energy relaxation time, and τ_r and τ_{nr} are the radiative and nonradiative recombination times, respectively.

(iv) The spin orientation of conduction band electrons is provided through interband optical transitions induced by circularly polarized (left circularly polarized) light propagating along the z axis.

(v) Optical transitions occur from valence band states lying below the quasi-Fermi level of heavy holes under illumination. It is assumed that the temperatures are sufficiently low.

(vi) We also assume that the degree of spin polarization of electrons, i.e., the relative population of the s_+ and s_- spin branches (electrons with $s_z = \pm 1/2$) of the conduction band, is determined primarily by the ratio between $\tau_s^e = \tau_s$ and $\tau_0 = \tau_r\tau_{nr}/(\tau_r + \tau_{nr}) \sim \tau_r$.

A schematic diagram of the band structure satisfying the above conditions is depicted in the figure. This figure also shows the asymmetry in the stationary population of spin-split branches in the conduction band with nonequilibrium electrons (n_+, n_-) upon exposure to light under the above conditions. In order to compare the proposed mechanism of the spin-galvanic effect with the mechanism considered in [1], the spontaneous radiative transitions and the transitions with spin-flip scattering of electrons are represented in the figure. It is assumed that these processes make the determining contributions to spin relaxation.

3. RESULTS AND DISCUSSION

Since the radiative and direct interband transitions obey the same optical selection rules, the radiative recombination and spin-flip scattering are spin-dependent processes. As for the spin-galvanic effect associated with the spin-dependent scattering [1], the recombination contribution to the generation of an electric current is made by electrons of the s_+ branch lying above the quasi-Fermi level for electrons of the s_- branch. However, unlike the situation analyzed in [1], there are only three types of radiative transitions. The transitions of the first two types, which occur for both branches (arrows *2*, *3* in figure), make mutually compensating contributions to the electric current, because, after the recombination event, electrons with equal but oppositely directed wave vectors are removed from the electron gas. For transitions from the s_+ branch (arrow *1* in figure), the corresponding transitions are absent in the s_- branch. Therefore, the processes of radiative recombination from this branch (as well as the corresponding processes of scattering [1]) are accompanied by the generation of a current j^r. However, the contributions made by scattering and recombination to the spin-galvanic current differ significantly. Let us now turn to the discussion of these differences.

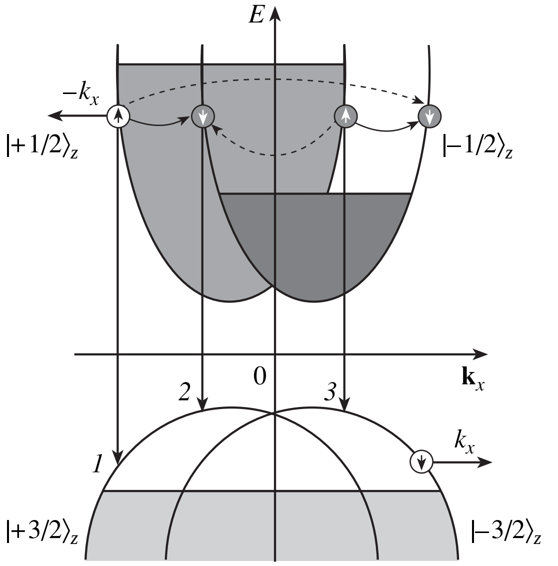

Schematic diagram of the band structure and electron transitions within the microscopic model of the recombination mechanism of the spin-galvanic effect. Radiative transition *1* leads to the generation of the spin-galvanic current, whereas transitions *2* and *3* do not result in the generation of a current. Curved arrows indicate spin-flip scattering of electrons for comparison with the mechanism of the spin-galvanic effect considered in [1]. Open circles correspond to a hypothetical "hole" in the conduction band and a real hole in the valence band. These holes make contributions (opposite in sign) to the recombination component of the spin-galvanic current.

In the case of scattering, the removal of an electron characterized by a parameter $-k_x$ from the region of the s_+ branch (this process can be treated as the formation of a positively charged hypothetical "hole" with the same wave vector) is accompanied by the creation of an electron with the vector k_x in the s_- branch. The contributions of the aforementioned hole and electron to the current coincide both in sign and in magnitude [1]. The event of radiative recombination involving the same electron, first, leads to the creation of a similar hole in the electron gas of the conduction band. Second, the real hole with vector $-k_x$ is removed from the hole gas of the valence band due to the recombination. This brings about the generation of an uncompensated hole flux with oppositely directed wave vectors (see figure). Unlike the scattering mechanism, the contributions of the hypothetical and real holes to the recombination current have opposite signs. It should be noted that a similar situation is observed for the circular photogalvanic current j^{ex} generated upon interband transitions. In this case, the resultant current is proportional to the average total velocity of charge carriers [2]:

$$\left|\mathbf{v}_{\Sigma}^{\mathrm{ex}}\right| = (2/\hbar)[(\beta_c m_e - \beta_v m_h)/(m_e + m_h)]. \qquad (2)$$

However, the expression for the average total velocity determining the current j^r has a form different from the expression for the current j^{ex}. The total velocity of charge carriers during the recombination event shown in the figure can be written in the form

$$\left|\mathbf{v}_{\Sigma}^{r}\right| = \hbar|\mathbf{k}_x|(m_e^{-1} - m_h^{-1}) = \hbar|\mathbf{k}_x|[(m_h - m_e)/m_e m_h]. \qquad (3)$$

The general relationship for the current determined by the recombination mechanism can be derived in the framework of the model under consideration with the use of balance equations for the concentrations of nonequilibrium electrons n_+ and n_- with spins of +1/2 and –1/2, respectively. According to assumption (vi), the balance equations can account for only the processes of radiative recombination and spin-flip scattering of electrons:

$$dn_+/dt = G_+ - (n_+/\tau_r) - (n_+ - n_-)/\tau_s, \qquad (4)$$

$$dn_-/dt = (n_-/\tau_r) + (n_+ - n_-)/\tau_s, \qquad (5)$$

where G_+ is the rate of optical generation of spin-polarized electrons. From this system of equations, it is easy to obtain the following expressions for n_+ and n_-:

$$n_+ = G_+\tau_r(\tau_r + \tau_s)(\tau_s + 2\tau_r)^{-1}, \qquad (6)$$

$$n_- = G_+\tau_r^2(\tau_s + 2\tau_r)^{-1}. \qquad (7)$$

In order to simplify further calculations, we assume that the intensity of light is such that the maximum population of any spin branch with nonequilibrium electrons does not exceed the energy level specified by the point of intersection of the branches at $\mathbf{k} = 0$. Then, the analysis of the recombination from both spin branches clearly demonstrates that the radiative transitions from these branches are characterized, on the average, by the wave vector corresponding to the extremum of the given spin branch $k_{\min} = \pm(m_e\beta_c/\hbar^2)$. Next, from formulas (3), (6), and (7) with due regard for the condition that the momentum relaxation times for electrons and holes are approximately equal to each other, it is easy to find the current

$$j^r \sim e(\beta_c/\hbar)G_+\tau_p[(m_h - m_e)/m_h]\tau_s(\tau_s + 2\tau_r)^{-1}. \qquad (8)$$

Moreover, it is expedient to give the expression derived for the current j^{sc} in the framework of our model; that is,

$$j^{\mathrm{sc}} \sim e(2\beta_c/\hbar)G_+\tau_p\tau_r(\tau_s + 2\tau_r)^{-1}. \qquad (9)$$

Note that, in the expressions for the spin-galvanic current in real samples, it is necessary to take into account the distribution of charge carriers in the **k** and **s** spaces.

First and foremost, it can be seen from relationship (8) that, as should be expected, the current j^r is maximum when the recombination rate is considerably higher than the scattering rate, i.e., at $\tau_s \gg \tau_r$ (it is quite reasonable that the reverse holds true for the current j^{sc}).

Depending on the ratio between the effective masses of electrons and holes, the sign of the current j^r can be different; namely, it can either coincide or differ from the sign of the current j^{sc}. Certainly, this circumstance can complicate the interpretation of the results of experimental investigations into the spin-galvanic effect. Note also that one more difference between the two mechanisms of generation of spin-galvanic current should be taken into account.

In [1], it was emphasized that, upon elastic spin-flip scattering, the current j^{sc} is not spin polarized, because the hole and the electron generated in the s_+ and s_- branches have oppositely directed spins. Although the real hole in the valence band and the hypothetical hole in the conduction band for the recombination mechanism also have oppositely directed spins (for the real hole, this is the angular momentum projection, which differs in magnitude from the spin of conduction band electrons), the total current j^r can turn out to be spin polarized. Moreover, the polarization, like the current, can be opposite in sign.

Therefore, the recombination component of the current of the spin-galvanic effect, like the current of the circular photogalvanic effect, can be considered a source of the current of spin-polarized charge carriers. Furthermore, the use of methods based on the recombination mechanism of the spin-galvanic effect makes it possible to detect the current of spin-polarized charge carriers. Indeed, the spin-dependent recombination of thermalized charge carriers, which leads to the generation of the current j^r (in a gyrotropic medium), is attended by a circular polarization of recombination radiation [12]. It is known (see, for example, [13]) that the measurement of the ellipticity of this radiation is used in so-called spin LED detectors (spin-polarized light-emitting diodes) to determine the degree of spin polarization of electrically injected charge carriers. However, the use of the purely electrical method (i.e., measurement of the current j^r) can offer certain advantages over the optical measurement technique. It should be noted that the aforementioned condition for the most effective generation of the recombination current ($\tau_s \gg \tau_r$) is consistent with the specific feature of spintronics according to which the spin relaxation time of charge carriers should be as long as possible.

4. CONCLUSIONS

Thus, a microscopic model was proposed for the recombination mechanism of spin-galvanic current. This current arises as a result of the difference between the rates of spontaneous radiative transitions for charge carriers with oppositely directed spins under the conditions of a spatially uniform nonequilibrium spin orientation of thermalized carriers. It was shown that the use of methods based on this mechanism makes it possible to generate and detect spin-polarized charge carriers.

REFERENCES

1. S. D. Ganichev, E. L. Ivchenko, V. V. Bel'kov, S. A. Tarasenko, M. Solinger, D. Weiss, W. Wegscheider, and W. Prettl, Nature **417**, 153 (2002).
2. S. D. Ganichev and W. Prettl, J. Phys.: Condens. Matter **15**, R935 (2003).
3. E. L. Ivchenko, Yu. B. Lyanda-Geller, and G. E. Pikus, Pis'ma Zh. Éksp. Teor. Fiz. **50**, 156 (1989) [JETP Lett. **50**, 175 (1989)].
4. E. L. Ivchenko, Yu. B. Lyanda-Geller, and G. E. Pikus, Zh. Éksp. Teor. Fiz. **98**, 989 (1990) [Sov. Phys. JETP **71**, 550 (1990)].
5. N. S. Averkiev and M. I. D'yakonov, Fiz. Tekh. Poluprovodn. (Leningrad) **17**, 629 (1983) [Sov. Phys. Semicond. **17**, 393 (1983)].
6. A. A. Bakun, B. P. Zakharchenya, A. A. Rogachev, M. I. Tkachuk, and V. G. Fleĭsher, Pis'ma Zh. Éksp. Teor. Fiz. **40**, 464 (1984) [JETP Lett. **40**, 1293 (1984)].
7. A. G. Aronov and Yu. B. Lyanda-Geller, Pis'ma Zh. Éksp. Teor. Fiz. **50**, 398 (1989) [JETP Lett. **50**, 431 (1989)].
8. V. M. Edelstein, Solid State Commun. **73**, 233 (1990).
9. L. S. Levitov, Yu. V. Nazarov, and G. M. Éliashberg, Zh. Éksp. Teor. Fiz. **88**, 229 (1985) [Sov. Phys. JETP **61**, 133 (1985)].
10. A. G. Mal'shukov and K. A. Chao, Phys. Rev. B **65**, 241308 (2002).
11. E. L. Ivchenko and G. E. Pikus, *Superlattices and Other Heterostructures: Symmetry and Optical Phenomena* (Springer-Verlag, Berlin, 1997).
12. M. I. D'yakonov and V. I. Perel', Zh. Éksp. Teor. Fiz. **60**, 1954 (1971) [Sov. Phys. JETP **33**, 1053 (1971)].
13. R. Fiederling, M. Keim, G. Reuscher, W. Ossau, G. Schmidt, A. Wang, and L. W. Molenkamp, Nature **402**, 787 (1999).

Translated by N. Korovin

Physics of the Solid State, Vol. 46, No. 11, 2004, pp. 2012–2014. Translated from Fizika Tverdogo Tela, Vol. 46, No. 11, 2004, pp. 1946–1948.

SEMICONDUCTORS AND DIELECTRICS

Charge Transport in $PbMoO_4$ Crystals

M. D. Volnyanskiĭ, A. Yu. Kudzin, S. N. Plyaka, and Z. Balasme
Dnepropetrovsk National University, Dnepropetrovsk, 320625 Ukraine
e-mail: SPlyaka@ff.dsu.dp.ua
Received March 17, 2004

Abstract—Dc and ac electrical conductivity of lead molybdate crystals is studied in the temperature range 300–550 K. The electrical conductivity was shown to have electronic (hole) impurity character. The *I–V* characteristics are typical of a space charge–limited current. The carrier mobility was estimated to be 10^{-5} cm^2 V^{-1} s^{-1} at $T = 300$ K. The results of the study suggest the hopping mechanism of conduction in $PbMoO_4$ crystals. *© 2004 MAIK "Nauka/Interperiodica".*

1. INTRODUCTION

Lead molybdate crystals have been a subject of intense research for over three decades. The reason for this lies in the fact that $PbMoO_4$ crystals possess a combination of physical properties that makes them promising for use in acoustooptical devices, for instance, in acoustooptical deflectors and modulators [1]. The velocities of sound for various types of waves, the dependence of acoustic losses on frequency, the photoelastic constants, and other characteristics listed in [1] suggest that these crystals can be employed to advantage at ultrasonic frequencies below 500 MHz in the spectral range 0.45–4 μm. Melt-grown $PbMoO_4$ crystals are most frequently of yellow color because of absorption in the ~0.45-μm region. The intensity of coloring is governed by many factors, such as the actual oxide ratio in the charge, the gas environment during the growth, the gas ambient and temperature of annealing, and impurities. $PbMoO_4$ crystals become colored under illumination (photochromic effect). Color centers form and transform under the action of various factors through charge transport (ions, electrons) and are related to disordering in the crystal lattice.

The processes occurring in $PbMoO_4$ crystals at high temperatures have been studied in considerable detail (see, e.g., [2]). The photochromic effect [3] and photoluminescence [4, 5] have attracted great interest. Considerable effort has been devoted to growing perfect crystals [6–8]. Charge transport has been studied as a function of temperature, partial oxygen pressure, and stoichiometry [2]. It has been established that, at low temperatures, $PbMoO_4$ supports primarily electron (hole) conduction, but no discussion of the electron transport mechanisms has been undertaken. We report here on a study of the dc and ac electrical conductivity of $PbMoO_4$ crystals at temperatures substantially below the melting point in order to determine specific features of the charge transport mechanism.

2. MEASUREMENT TECHNIQUE

The $PbMoO_4$ crystals studied by us were Czochralski-grown in air from OSCh-grade MoO_3 and PbO oxides taken in stoichiometric proportion. The samples for measurement were plane-parallel, (001)-oriented plates 0.1-cm thick. Pt electrodes were applied by vacuum deposition.

Dc measurements were performed using a voltmeter and an ammeter in electric fields ranging from 10 V/cm to 10 kV/cm, and ac measurements were carried out by the bridge technique in a weak field in the frequency range ν from 200 Hz to 16 kHz. All measurements were carried out in the temperature interval 300–550 K.

3. EXPERIMENTAL RESULTS AND DISCUSSION

Figure 1 depicts plots of the electrical conductivity versus temperature obtained in a weak electric field

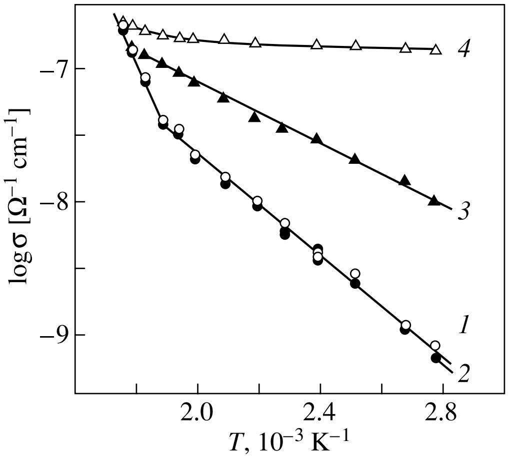

Fig. 1. Temperature dependence of the electrical conductivity of $PbMoO_4$ crystals: (*1*, *2*) dc measurements (direct and reverse runs, respectively) and (*3*, *4*) measurements at a frequency of 8 kHz of (*3*) Reσ and (*4*) Imσ.

1063-7834/04/4611-2012$26.00 © 2004 MAIK "Nauka/Interperiodica"

(curve *1*). The dc electrical conductivity σ exhibits the standard activated behavior with temperature. There are two temperature regions differing in activation energy: $E_a = 0.38$ eV at $T < 520$ K and $E_a = 1.02$ eV at $T > 520$ K. Heating–cooling runs performed within the temperature interval of the measurements did not affect the crystal parameters, which is indicated by the coincidence of the $\sigma(T)$ graphs measured under heating and cooling (Fig. 1).

Some limited information concerning the electrical conductivity of lead molybdate can be found in [2, 9]. According to [2], the conduction at temperatures above 800 K is largely ionic, although the authors of the aforementioned work believe that the conductivity is intrinsic at these temperatures. At low temperatures ($T < 700$ K), the ionic component of the current does not exceed 0.01–0.02% and the activation energy is 0.36 eV. The data from [9] suggest that, within the range 300–100 K, conduction is also of activated nature, with an activation energy of 0.24 eV. Photoconductivity was observed in the same temperature interval, which indicates that the conduction is electronic in character. The band gap in lead molybdate crystals is in excess of 3 eV; therefore, the conductivity observed in this work and in [2, 9] is extrinsic. The similarity between the activation energies obtained in studies of samples with different impurity concentrations and in different temperature intervals provides reason to believe that the electronic character of charge transport in $PbMoO_4$ is accounted for not by impurities but rather by native lattice defects.

Figure 1 plots temperature dependences of the real (Reσ) and imaginary (Imσ) parts of the complex conductivity measured at 8 kHz (curves *3*, *4*). In the high-temperature domain, the values of the dc conductivity σ nearly coincide with those of Re(σ) and their activation energies are also similar. At lower temperatures, the activation energy for Re(σ) is slightly lower. Im(σ) is practically frequency-independent, thus reflecting the weak temperature dependence of permittivity, which is determined primarily by ionic displacement polarization.

The frequency dependences of Re(σ) measured at different temperatures are displayed in Fig. 2. At low frequencies, Re(σ) is almost entirely independent of frequency, while for $\nu \geq 1$ kHz it can be fitted by the relation

$$\sigma \sim \nu^s, \tag{1}$$

where s grows weakly with temperature. The imaginary part Imσ above 1 kHz can also be fitted by a power-law dependence on frequency, with an exponent that is close to unity.

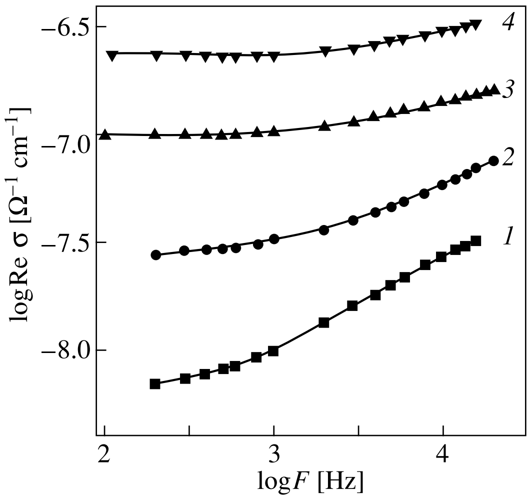

Fig. 2. Frequency dependence of the real part of complex conductivity of $PbMoO_4$ crystals obtained at different temperatures: (*1*) 360, (*2*) 453, (*3*) 520, and (*4*) 563 K.

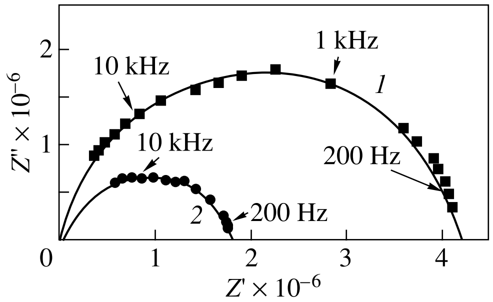

Fig. 3. Z'–Z'' diagrams of lead molybdate crystals at (*1*) 520 and (*2*) 560 K.

The frequency dependence of complex conductivity can be determined both by the properties of the material and by other factors. These include inhomogeneities of the conductivity over the volume and electrode processes. The parts played by these factors can be conveniently estimated by plotting the conductivity measurements in the Z'–Z'' plane of complex impedance [10]. Figure 3 displays the dependence of Z'' on Z' measured for $PbMoO_4$ crystals at two temperatures. The $Z''(Z')$ graphs take the form of circular arcs with the centers lying below the Z' axis. The dependences thus obtained suggest that near-contact phenomena and macroscopic volume inhomogeneities play a negligible role in crystal conductivity. This gives us grounds to maintain that the observed behavior of Reσ and Imσ is accounted for by the bulk properties of the crystals.

The conductivity of a material is determined by the type of charges and their concentration and mobility. There are efficient methods for determining these parameters in classical semiconductors. These methods are inapplicable to complex oxides (to which $PbMoO_4$ belongs), because they have a high electrical resistivity and a low charge mobility. To estimate the transport parameters, we used the method of space charge–limited currents (SCLC) [11]. The *I*–*V* characteristics of $PbMoO_4$ obtained at different temperatures are typical of SCLC in insulators containing traps. The carrier mobility extracted from these *I*–*V* curves is ~10^{-5} cm^2 V^{-1} s^{-1} at T = 300 K. The mobility grows exponentially with increasing temperature. Estimation of the carrier concentration yields 10^{12} cm^{-3}. The low carrier mobility and its exponential growth with temperature are characteristic of the hopping mechanism of conduction.

The problem of hopping conduction in disordered systems is treated in a number of papers in the cluster approximation (see, e.g., [12, 13]). In this model, clusters are approximated by variable-length chains connecting accessible carrier positions. Carrier motion within a cluster occurs by activated hopping with an activation energy E_3. The electrical resistivity decreases exponentially with increasing chain length. This cluster model was invoked to determine the form of the frequency dependence of complex conductivity. It was found in [12] that, in different frequency intervals, the conductivity is determined by clusters of different length. In particular, at very low frequencies, transport occurs over clusters comparable in size to the sample. At higher frequencies, transport takes place over clusters of a finite size. In this frequency range, the exponent s in Eq. (1) grows slowly with increasing frequency at constant temperature but remains less than unity. It was demonstrated that the temperature dependence of conductivity of $PbMoO_4$ crystals has an activated character and that its variation with frequency implies the hopping mechanism of carrier transport along finite clusters. Clusters in $PbMoO_4$ can have the form of agglomerates of native point defects.

Lattice defects in $PbMoO_4$ have aroused particular interest [2, 14] in connection with the nature of their coloring and luminescence [4]. Data obtained on the self-diffusion of Mo ions indicate that defect agglomerates are likely to exist [2]. Such agglomerates may be a pair of vacancies on the molybdenum and oxygen sublattices, lead with a valence greater than two, and trapped electrons, as well as extended defects. The electronic states of these defects have not been studied. According to [9], however, the optical absorption spectrum is strongly broadened near the absorption edge and varies substantially with temperature in accordance with Urbach's rule. Rather than being determined by impurities, these electronic states are related primarily to native lattice defects, because the absorption spectrum of $PbMoO_4$ depends noticeably on crystal annealing [3].

4. CONCLUSIONS

Thus, the results obtained in our study of the temperature and frequency dependences of electrical conductivity in $PbMoO_4$ crystals can be qualitatively described by multiple jumps of carriers over finite clusters, which are probably defect agglomerates.

REFERENCES

1. G. A. Coquin, D. A. Pinnow, and A. W. Warner, J. Appl. Phys. **42** (6), 2162 (1971).
2. A. Ya. Neĭman, E. V. Tkachenko, L. M. Fedorova, A. N. Petrov, V. T. Gabriélyan, and S. M. Karagbedyan, Neorg. Mater. **16** (11), 2025 (1980).
3. T. M. Bochkova, M. D. Volnyanskiĭ, D. M. Volnyanskiĭ, and V. S. Shchetinkin, Fiz. Tverd. Tela (St. Petersburg) **45** (2), 235 (2003) [Phys. Solid State **45**, 244 (2003)].
4. W. Van Loo, Phys. Status Solidi A **27**, 565 (1975).
5. W. Van Loo, Phys. Status Solidi A **28**, 227 (1975).
6. N. Senguttuvan, S. M. Babu, and R. Dhanasekaran, Mater. Chem. Phys. **49** (2), 120 (1997).
7. H. C. Zeng, J. Cryst. Growth **171** (1), 136 (1997).
8. L. C. Lim, L. K. Tan, and H. C. Zeng, J. Cryst. Growth **167** (3), 686 (1996).
9. Hj. Bernhardt, Phys. Status Solidi A **40**, 257 (1977).
10. A. West, *Solid State Chemistry and Its Applications* (Wiley, Chichester, 1984; Mir, Moscow, 1988), Vol. 2.
11. M. A. Lampert and P. Mark, *Current Injection in Solids* (Academic, New York, 1970; Mir, Moscow, 1973).
12. H. Bettger and V. V. Bryksin, Phys. Status Solidi B **113**, 9 (1982).
13. B. I. Shklovskiĭ and A. L. Éfros, *Electronic Properties of Doped Semiconductors* (Nauka, Moscow, 1979; Springer, New York, 1984).
14. A. Ya. Neĭman, L. M. Fedorov, and A. A. Afanas'ev, Neorg. Mater. **22** (5), 811 (1986).

Translated by G. Skrebtsov

Physics of the Solid State, Vol. 46, No. 11, 2004, pp. 2015–2020. Translated from Fizika Tverdogo Tela, Vol. 46, No. 11, 2004, pp. 1949–1954.
Original Russian Text Copyright © 2004 by Purskiĭ, Zholonko.

SEMICONDUCTORS AND DIELECTRICS

Heat Transfer in the High-Temperature Phase of Solid SF_6

O. I. Purskiĭ and N. N. Zholonko
Cherkasy National University, Cherkasy, 18031 Ukraine
e-mail: Pursky_O@ukr.net

Received January 27, 2004

Abstract—The temperature dependences of the thermal conductivity are calculated for solid SF_6 and Xe. The influence of thermal pressure in a crystal on the isochoric thermal conductivity is investigated. The contributions of the phonon–phonon and phonon–rotation interactions to the total thermal resistance of solid SF_6 are calculated using a modified method of reduced coordinates. The temperature dependence of the isochoric thermal conductivity of SF_6 is explained by a combined effect of thermal pressure and phonon–rotation interaction.

1. INTRODUCTION

At present, there are many works concerned with the thermal properties of rare-gas crystals [1–4]. The thermal properties of molecular crystals have not been adequately investigated to date. However, molecular crystals are of considerable research interest, because they are characterized by different types of thermal molecular motion, which, in many cases, can have a substantial effect on the temperature dependence of the thermal conductivity. Additional mechanisms that, in principle, can affect the thermal conductivity are associated with the processes of orientational disordering and intramolecular vibrations. However, the frequencies of intramolecular vibrations in the majority of molecular crystals are sufficiently high. Consequently, this type of thermal motion does not significantly affect the heat transfer in solid phases.

It should be noted that, in an equilibrium state, no phase transformations are revealed in classical atomic crystals with central interactions. By contrast, the majority of molecular crystals can have several solid phases [5] that substantially differ in terms of the character of orientational disordering. At temperatures above the Debye temperature, the heat transfer in simple molecular crystals is governed, to a great extent, not only by translational motion but also by rotational motion of molecules at lattice sites [5]. The contribution from rotational molecular motion to the heat transfer is insignificant, whereas the contribution from phonon scattering by rotational excitations of molecules can be of the order of the contribution from phonon–phonon scattering. However, up to now, there has not been a practically applicable consistent microscopic theory that would adequately describe the influence of the above factors on the thermal properties of molecular crystals. The development of such a theory is a fairly complex problem. This is primarily due to a large number of elementary excitations existing at high temperatures, which extremely complicates microscopic analysis. Therefore, the initial problem, as always, consists in accumulating reliable data over a wide range of temperatures for crystals with different symmetries. This will make it possible to investigate different types of molecular motion in order to separate the contributions of the aforementioned factors and to establish their correlation with thermodynamic parameters of the studied materials.

2. THE OBJECT OF INVESTIGATION

Sulfur hexafluoride SF_6 was chosen as the object of our investigation. This compound is frequently assigned to materials with plastic crystalline phases. However, the nature of orientational disordering in the high-temperature phase of SF_6 somewhat differs from that in plastic phases of other molecular crystals in which the symmetries of the molecules and environment do not coincide with each other. As a rule, in crystals formed by molecules with orientational freedom, there exist a number of possible molecular orientations and the molecules can execute a reorientational motion. In some cases, this reorientational motion can transform into continuous rotation. In general, an increase in the rotational mobility of molecules is associated with the phase transition. The presence or absence of the phase transition depends on whether the possible orientations of molecules can be distinguished in the lattice.

For solid sulfur hexafluoride SF_6, the high-temperature β phase is observed over an unusually wide range of temperatures. The crystallization temperature of SF_6 is equal to 222.4 K, whereas the phase transition accompanied by a reduction of the symmetry of the translational and orientational subsystems in the crystal occurs only at 94.3 K [6, 7]. In this temperature range, molecules of solid SF_6 have octahedral symmetry. The Debye characteristic temperature $\theta_D = 62$ K is considerably lower than the temperature of the phase transition to the plastic phase [8]. According to [9, 10], the

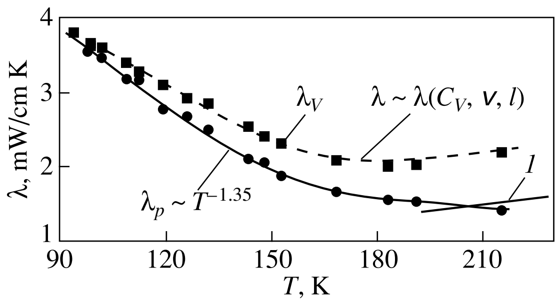

Fig. 1. Temperature dependences of the isochoric λ_V and isobaric λ_p thermal conductivities of solid SF_6. Points indicate experimental data on the isobaric thermal conductivity [20] and the isochoric thermal conductivities calculated from formula (1). The solid line shows the smoothed experimental dependence. The dashed line represents the temperature dependence of the thermal conductivity λ calculated from formula (2). Line *1* corresponds to the data obtained in direct investigations of the isochoric thermal conductivity of solid SF_6 [17] for samples with the molar volume V_{mol} = 62.2 cm^3/mol.

symmetry of the crystal is reduced to trigonal at temperatures below the phase transition point and then to monoclinic or even triclinic at $T < 50$ K. Structural investigations revealed that the high-temperature phase of SF_6 has a body-centered cubic structure with space symmetry I_m3_m and that the S–F bonds at temperatures in the vicinity of the phase transition temperature are oriented along the principal directions of the lattice [10–12].

In cubic crystals of the AX_6 type, the symmetries of individual molecules and their lattice sites are identical and the plastic properties manifest themselves due to the quasi-sphericity of molecules that execute large-amplitude librations and reorientations [13, 14]. According to Dove and Pawley [15], the interaction between the nearest neighbors in the body-centered cubic phase of SF_6 favors the ordering of S–F bonds in molecules along the {100} planes, whereas the repulsion dominates in the interaction with the next-to-nearest neighbors (between fluorine atoms). Therefore, the noncentral interaction in SF_6 encourages orientational ordering in the first coordination sphere and orientational disordering in the second coordination sphere [11]. This character of the interaction with an increase in the temperature leads to a considerable increase in the libration amplitude and facilitates the molecular reorientation [8, 11, 16, 17].

The analysis of the experimental data [8] demonstrated that SF_6 is characterized by a strong orientational order at temperatures immediately above the phase transition point. This distinguishes SF_6 among the other plastic crystals (such as CH_4, CCl_4, adamantane, etc.) in which the long-range orientational order is disturbed immediately after the phase transition [18]. X-ray diffraction investigations revealed that the intensities of particular reflections, especially of the {*h*00} and {*hk*0} types, begin to decrease and approach the values calculated within the model of orientational disordering of molecules only at temperatures above 150 K. A decrease in the intensity of the x-ray reflections indicates that the orientational disorder becomes more pronounced. This increase in the degree of orientational disordering with an increase in the temperature does not result from a simple increase in the libration amplitude but is associated with the dynamic reorientations, which are assisted by the frustration of the intermolecular interaction [8, 15, 16, 19]. It is of interest that the experimental data on neutron scattering in SF_6 at premelting temperatures indicate the absence of collective excitations [11, 12]. From the aforesaid, it is clear that SF_6 is a convenient material for analyzing the dependence of the thermal properties of a single-phase system on the rotational state of molecules in a wide range from almost complete orientational order to virtually free rotational motion.

To date, the isobaric thermal conductivity of solid SF_6 has been experimentally studied over the entire temperature range of existence of the high-temperature phase [20] and the isochoric thermal conductivity has been directly investigated at premelting temperatures [17]. The obtained data on the thermal conductivity of equilibrium samples of solid SF_6 are presented in Fig. 1.

3. RESULTS AND DISCUSSION

The isobaric thermal conductivity λ_p (Fig. 1, solid line) decreases with an increase in the temperature as $\lambda_p \sim T^{-1.35}$. The isochoric thermal conductivities λ_V at given temperatures were obtained by recalculating the experimental data on the isobaric thermal conductivity for a constant volume V_{mol} = 58.25 cm^3/mol, which is occupied by the samples immediately above the phase transition temperature. The calculations were performed according to the formula [1]

$$\lambda_V = \lambda_p\left(\frac{V_m(T)}{V_{m0}}\right)^g, \qquad (1)$$

where $V_m(T)$ is the molar volume of the free sample as a function of temperature, V_{m0} is the molar volume of the sample for which the recalculation is carried out, and $g = -(\partial \ln\lambda/\partial \ln V)_T$ is the Bridgman coefficient taken equal to 5.2 [17]. As the temperature increases, the isochoric thermal conductivity λ_V of solid SF_6 (Fig. 1) initially decreases, passes through a flattened minimum, and then increases. This behavior is inconsistent with the theoretical predictions according to which the thermal conductivity in the given temperature range should decrease as 1/*T*. In our earlier work [21], such an increase in the thermal conductivity of solid SF_6 was explained by the defreezing of molecular motion, which results in a weakening of libron scattering.

It is important that the temperature dependence of the isochoric thermal conductivity for rare-gas crystals [1] (in which rotational degrees of freedom are absent) and some molecular crystals that consist of strongly asymmetric molecules and retain orientational ordering up to the melting temperature [22, 23] is also weaker than $1/T$. This indicates that the deviation from the law $1/T$ cannot be explained by the influence of the phonon–rotation interaction alone.

In the isochoric experiments performed upon heating, the measuring cell, which is only slightly susceptible to thermal expansion, prevents thermal expansion of the studied sample; as a result, the thermal pressure increases in the crystal structure [1, 17, 22]. This can lead to an additional increase in the isochoric thermal conductivity as compared to that predicted by the dependence $\lambda(1/T)$.

The isochoric thermal conductivity with due regard for the thermal pressure can be calculated using the standard gas-kinetic relationship

$$\lambda = 1/3(C_V v l), \tag{2}$$

where C_V is the isochoric heat capacity, v is the velocity of sound, and l is the mean free path. In isochoric investigations, a crystal sample upon heating experiences an increasing pressure produced by a measuring cell that is only slightly susceptible to thermal expansion. This process is similar to uniform compression with negative sign, because the thermal pressure is associated with the thermal expansion of the studied sample. Upon uniform compression, the same pressure directed normally to the surface acts on each unit area of a polycrystal. This completely corresponds to the conditions arising in isochoric experiments.

The temperature dependences of the thermal pressure (Fig. 2) in SF_6 solid samples with the given constant molar volumes were calculated from the relationship [24]

$$\left(\frac{\partial P}{\partial T}\right)_V = \frac{\gamma C_V}{V_{\text{mol}}}. \tag{3}$$

The molar volumes V_{mol}, the temperature dependences of the Grüneisen coefficient γ, and the isochoric heat capacities C_V were taken from [8].

It can be seen from Fig. 2 that the thermal pressure in the isochoric sample changes by more than two orders of magnitude in the temperature range under investigation. The molar volumes of the samples depend on their growth temperature. The results of calculations are in good agreement with the data obtained from direct measurements of the thermal pressure in solid SF_6 [17] for samples with a molar volume V_{mol} = 62.2 cm^3/mol (Fig. 2, solid line *1*).

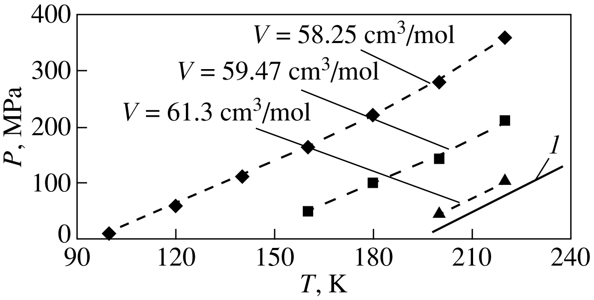

Fig. 2. Calculated temperature dependences of the thermal pressure for solid SF_6 (dashed lines). Solid line *1* shows the experimental data taken from [17] for samples with the molar volume V_{mol} = 62.2 cm^3/mol.

As follows from the theory [25], the phonon velocity in dielectric crystals under isochoric conditions is virtually independent of temperature and is equal to the mean velocity of sound. Unfortunately, no experimental data on the velocity of sound in solid SF_6 under isochoric conditions are available in the literature. In this respect, the isochoric phonon velocity was calculated from the data on the thermal pressure (Fig. 2) and the thermal expansion [8]. The diagonal elements C_{11}^p and C_{44}^p of the stress tensor for free samples of solid SF_6 (necessary for evaluating the effect of the thermal pressure on the phonon velocity under isochoric conditions) were calculated from the expressions [26]

$$\begin{aligned} C_{11} &= v_l^{p^2}\rho, \\ C_{44} &= v_t^{p^2}\rho, \end{aligned} \tag{4}$$

where v_l^p and v_t^p are the longitudinal and transverse phonon velocities for free samples, respectively, and ρ is their density [8].

It is known [26] that, upon uniform compression, the stress tensor is uniquely determined by the diagonal elements and is related to the strain tensor through the expression $C_{ii} = 3Ku_{ii}$, where $K = -\frac{1}{V}\left(\frac{\partial V}{\partial P}\right)_T$ is the compressibility factor. The diagonal elements of the strain tensor were calculated according to the data taken from [8]. The dependence $\left(\frac{\partial V}{\partial P}\right)_T$ was obtained using the data on the thermal pressure (Fig. 2) and the molar volume [8]. The diagonal elements C_{11}^V and C_{44}^V of the stress tensor (determined with allowance made for the thermal pressure) were used to calculate the temperature dependences of the longitudinal and transverse phonon velocities under isochoric conditions from expressions (4).

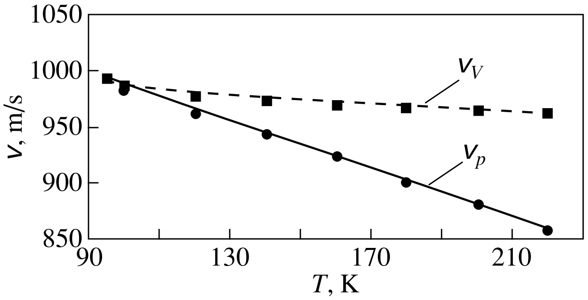

Fig. 3. Temperature dependences of the isobaric v_p [8] and isochoric v_V velocities of sound in solid SF_6.

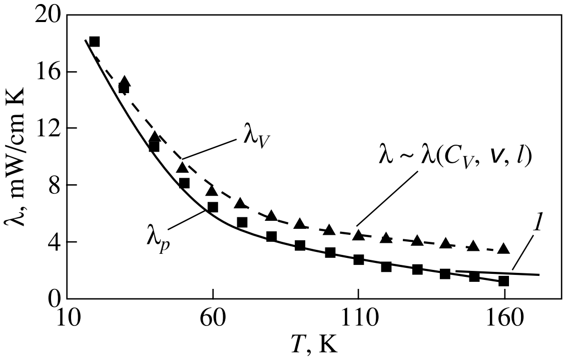

Fig. 4. Temperature dependences of the isochoric λ_V and isobaric λ_p thermal conductivities of solid Xe. Symbols indicate experimental data on the isobaric thermal conductivity [28] and the isochoric thermal conductivities calculated from formula (1). The solid line shows the smoothed experimental dependence. The dashed line represents the temperature dependence of the thermal conductivity λ calculated from formula (2) for solid Xe. Line *1* corresponds to the data obtained in direct investigations of the isochoric thermal conductivity of solid Xe [1] for samples with the molar volume $V_{\text{mol}} = 37.4$ cm^3/mol.

The mean (according to Debye) isochoric phonon velocity v_V (Fig. 3) at a specified temperature was computed from the relationship

$$\frac{3}{v_V^3} = \frac{1}{3v_l^{V^3}} + \frac{2}{v_t^{V^3}}, \tag{5}$$

where v_l^V and v_t^V are the longitudinal and transverse phonon velocities in the crystal under isochoric conditions. The temperature dependence of the mean free path was determined from the experimental data on the isochoric thermal conductivity (corresponding to the beginning of the fulfillment of the isochoric conditions) under the assumption that the thermal conductivity in the temperature range $T > \theta_D$ is inversely proportional to the temperature. Finally, the temperature dependence of the thermal conductivity λ (Fig. 1, dashed line) with due regard for the effect of the thermal pressure was obtained from formula (2) using the calculated data on the isochoric phonon velocity and the mean free path and also the isochoric heat capacities taken from [8].

It should be noted that, in this work, we extended the field of application of formula (2) and used it for calculating the thermal conductivity of molecular crystals, even though this formula within the traditional theory is used only to calculate the lattice thermal conductivity [25]. The curve calculated without fitting parameters (Fig. 1) adequately describes the behavior of the temperature dependence of the isochoric thermal conductivity λ_V and agrees with the results of direct investigations into the isochoric thermal conductivity [17] (making allowance for different molar volumes of the studied samples). In our case, C_V is the volume isochoric heat capacity of the system and contains the following components under the additivity condition:

$$C_V = C_{\text{tr}} + C_{\text{rot}} + C_{\text{in}}, \tag{6}$$

where C_{tr} is the translational heat capacity, C_{rot} is the rotational heat capacity, and C_{in} is the intramolecular heat capacity. However, separating these contributions is quite problematic [5].

The analysis of the obtained results on the basis of the relationship $\lambda = 1/3(C_V v l)$ shows that, at $v = \text{const}$ and $l \sim 1/T$, the increase in the thermal conductivity at premelting temperatures is caused by the increase in the heat capacity C_V. The lattice heat capacity in the given temperature range ($T > \theta_D$) obeys the Dulong–Petit law, and the frequencies of intramolecular vibrations are so high that the interaction of phonons with these excitations of the crystal lattice does not satisfy the law of conservation of energy. Therefore, we can assume that the decisive factor responsible for the anomalous behavior of the isochoric thermal conductivity is the phonon–rotation interaction. This inference is consistent with the results obtained in our previous work [27], in which the increase in the isochoric thermal conductivity of solid SF_6 was explained by the decrease in the contribution of phonon scattering from rotational excitations of the crystal lattice. Moreover, this is also confirmed by the results of the calculations performed in [8], according to which the rotational heat capacity varies significantly with a variation in the temperature.

Of particular interest is a comparison of the results obtained with the calculated data for atomic crystals, because there are no orientational excitations of their crystal lattices and this factor does not affect the behavior of the isochoric thermal conductivity. Solid xenon, whose mass is closest to the mass of the SF_6 molecule, was chosen for comparison. The results of the calculations carried out with the use of the data taken from [28–30] are presented in Fig. 4. It can be seen from Fig. 4 that the results obtained taking into account the influence of the thermal pressure fit the experimental dependence well and the maximum differences do not exceed 5%. This explains why the temperature dependence of the isochoric thermal conductivity for solid xenon deviates from the law $1/T$. It is quite reasonable to assume that similar deviations (caused by the thermal pressure) should also be observed for molecular crystals.

However, this circumstance does not allow us to explain the increase in the isochoric thermal conductivity of solid SF_6 at premelting temperatures. In order to elucidate the origin of the increase in the isochoric thermal conductivity, we separate the contributions of the phonon–phonon and phonon–rotation interactions to the total thermal resistance of solid SF_6. It is assumed that the heat is predominantly transferred by translational vibrations regardless of the orientational ordering. The role of librations in the heat transfer is insignificant due to the low group velocity of librons, whereas the contribution from phonon scattering by rotational excitations of the crystal lattice can be of the order of the contribution from phonon–phonon scattering. Under the assumption that the contributions of the phonon–phonon W_{pp} and phonon–rotation W_{pr} interactions to the total thermal resistance $1/\lambda = W$ are additive, we separate out the phonon–rotation contribution. The calculations are performed by the modified method of reduced coordinates [27]. It should be emphasized that, in this case, there is no need to invoke a particular approximate model of heat transfer. By assuming that, in the reduced coordinates ($W^* = W/W_{\mathrm{mol}}$, $T^* = T/T_{\mathrm{mol}}$), the thermal resistance associated with the phonon–phonon scattering W_{pp} is identical to that of solidified rare gases, we can separate out the phonon–rotation contribution W_{pr} to the thermal resistance of solid SF_6 at equal reduced volumes $V^* = V/V_{\mathrm{mol}}$.

As a rule, the quantities $T_{\mathrm{mol}} = \varepsilon/k_{\mathrm{B}}$, $\lambda_{\mathrm{mol}} = k_{\mathrm{B}}/\sigma^2\sqrt{\varepsilon/\mu}$, and $V_{\mathrm{mol}} = N\sigma^3$ are used as reduced parameters. Here, σ and ε are the parameters of the Lennard-Jones potential, μ is the molar weight, and N is the Avogadro number. The temperatures T_{cr} and the molar volumes V_{cr} for SF_6 and solidified rare gas xenon Xe at the critical points [1, 8, 17, 31] were chosen as the reduced parameters T_{mol} and V_{mol}. The choice of these coordinates is motivated by the fact that, for simple molecular compounds, the critical parameters T_{cr} and V_{cr} are proportional to ε and σ^3, respectively. However, the accuracy in the determination of the critical parameters is considerably higher than that of the parameters of the binomial potential. Note also that the values of σ and ε depend significantly on the choice of the binomial potential and the method of its determination.

The results of the calculations are presented in Fig. 5. It is interesting to note that the phonon–phonon component of the thermal resistance is virtually independent (within 2–3%) of the choice of the particular rare gas for comparison. An increase in the temperature initially leads to a slow increase in the thermal resistance component corresponding to the rotational degrees of freedom of molecules in solid SF_6. This behavior of the thermal conductivity can be explained by the increase in the contribution of phonon scattering from collective rotational excitations, whose density increases with an increase in the temperature. This agrees well with the data obtained in [8] on a rather strong orientational order in solid SF_6 at temperatures close to the phase transition point but contradicts the results of inelastic neutron scattering measurements and molecular dynamics calculations [14, 15]. The phonon–rotation contribution to the thermal resistance passes through a maximum at approximately 170 K and begins to decrease. This is in agreement with the data obtained by Isakina and Prokhvatilov [8], according to which the orientational disordering in the crystalline β phase of SF_6 becomes more pronounced at temperatures above 150 K.

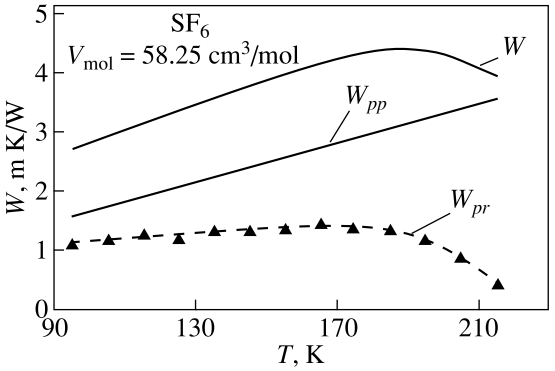

Fig. 5. Contributions of the phonon–phonon W_{pp} and phonon–rotation W_{pr} interactions to the total thermal resistance W of solid SF_6 in the framework of the additive model.

Note also that the temperature dependence of the phonon–rotation contribution to the thermal resistance of solid SF_6 is similar to the dependence observed for the low-temperature phase of solid CCl_4 [32]. Hence, it follows that, as for solid CCl_4, the observed increase in the isochoric thermal conductivity can be explained by the decrease in the contribution of phonon scattering from collective orientational excitations of SF_6 molecules upon defreezing of their rotational motion. The additional contribution due to the rotational degrees of freedom to the thermal resistance is approximately equal to 30% of the phonon–phonon component. According to the Brillouin scattering data [16], the translation–rotation coupling in solid SF_6 is weaker than that in solid methane and other cubic crystals. Thus, the data obtained on the isochoric thermal conductivity in the high-temperature β phase of solid SF_6 can be explained by the combined effect of the thermal pressure and the phonon–rotation interaction on the heat transfer processes.

REFERENCES

1. V. A. Konstantinov, V. G. Manzheliĭ, M. L. Strzhemechnyĭ, and S. A. Smirnov, Fiz. Nizk. Temp. **14** (1), 90 (1988) [Sov. J. Low Temp. Phys. **14**, 48 (1988)].
2. F. Clayton and D. Batchelder, J. Phys. Chem. **6** (7), 1213 (1973).
3. A. I. Bondarenko, V. G. Manzheliĭ, V. A. Popov, *et al.*, Fiz. Nizk. Temp. **8** (11), 1215 (1982) [Sov. J. Low Temp. Phys. **8**, 617 (1982)].
4. I. N. Krupskiĭ and V. G. Manzheliĭ, Zh. Éksp. Teor. Fiz. **55** (6), 2075 (1968) [Sov. Phys. JETP **28**, 1097 (1968)].
5. A. F. Prikhot'ko, V. G. Manzheliĭ, I. Ya. Fugol', *et al.*, *Cryocrystals*, Ed. by B. I. Verkin and A. F. Prikhot'ko (Naukova Dumka, Kiev, 1983) [in Russian].
6. B. G. Parsonage and A. K. Staveley, *Disorder in Crystals* (Clarendon, Oxford, 1978).
7. A. P. Isakina, A. I. Prokhvatilov, and J. Rodriguez-Carvajal, Fiz. Nizk. Temp. **26** (4), 404 (2000) [Low Temp. Phys. **26**, 296 (2000)].
8. A. P. Isakina and A. I. Prokhvatilov, Fiz. Nizk. Temp. **19**, 201 (1993) [Low Temp. Phys. **19**, 142 (1993)].
9. V. G. Manzhelii and Y. A. Freiman, *Physics of Cryocrystals* (AIP, Woodbury, N. Y., 1997).
10. G. Raynard and J. Venables, Ultramicroscopy **23** (10), 433 (1987).
11. G. Dolling, B. Powell, and V. Sears, Mol. Phys. **37** (6), 1859 (1979).
12. M. T. Dove, G. S. Pawley, G. Dolling, and B. M. Powell, Mol. Phys. **57** (4), 865 (1986).
13. Y. N. Sherwood, *Orientationally-Disordered Crystals* (Wiley, Chichester, 1979).
14. M. C. Roufosse and P. G. Klemens, J. Geophys. Res. **79** (5), 703 (1974).
15. M. T. Dove and G. S. Pawley, J. Phys. Chem. **17** (36), 6581 (1984).
16. H. Kiefte, R. Penny, and M. Clouter, J. Chem. Phys. **88** (9), 5846 (1988).
17. A. V. Konstantinov, V. G. Manzheliĭ, and S. A. Smirnov, Fiz. Nizk. Temp. **18** (1), 1290 (1992) [Sov. J. Low Temp. Phys. **18**, 902 (1992)].
18. V. A. Konstantinov, Funct. Mater. **6** (2), 335 (1999).
19. M. T. Dove and G. S. Pawley, J. Phys. Chem. **16** (31), 5969 (1983).
20. O. I. Purs'kiĭ, Ukr. Fiz. Zh. **45** (9), 1076 (2000).
21. O. I. Purskii, N. N. Zholonko, and V. A. Konstantinov, Fiz. Nizk. Temp. **29** (9), 1021 (2003) [Low Temp. Phys. **29**, 771 (2003)].
22. V. A. Konstantinov, V. G. Manzheliĭ, V. P. Revyakin, and S. A. Smirnov, Fiz. Nizk. Temp. **21** (1), 102 (1995) [Low Temp. Phys. **21**, 78 (1995)].
23. O. I. Purs'kiĭ, M. M. Zholonko, and V. V. Tsibulin, Ukr. Fiz. Zh. **46** (3), 337 (2001).
24. V. A. Konstantinov, V. G. Manzheliĭ, and S. A. Smirnov, Fiz. Nizk. Temp. **17** (7), 883 (1991) [Sov. J. Low Temp. Phys. **17**, 462 (1991)].
25. R. Berman, *Thermal Conduction in Solids* (Clarendon, Oxford, 1976; Mir, Moscow, 1979).
26. L. D. Landau and E. M. Lifshitz, *Course of Theoretical Physics*, Vol. 7: *Theory of Elasticity,* 4th ed. (Nauka, Moscow, 1987; Pergamon, New York, 1986).
27. O. I. Purskiĭ, N. N. Zholonko, and V. A. Konstantinov, Fiz. Nizk. Temp. **26** (4), 380 (2000) [Low Temp. Phys. **26**, 278 (2000)].
28. V. G. Manzheliĭ, A. M. Tolkachev, and V. G. Gavrilko, Fiz. Kondens. Sostoyaniya, No. 2, 41 (1968).
29. V. G. Manzheliĭ and I. N. Krupskiĭ, Fiz. Kondens. Sostoyaniya, No. 2, 3 (1968).
30. P. A. Bezuglyĭ, L. M. Tarasenko, and O. I. Baryshevskiĭ, Fiz. Tverd. Tela (Leningrad) **13**, 2392 (1971) [Sov. Phys. Solid State **13**, 2841 (1971)].
31. *Tables of Physical Data: Reference Book*, Ed. by I. K. Kikoin (Atomizdat, Moscow, 1976) [in Russian].
32. O. I. Purs'kiĭ, M. M. Zholonko, and V. A. Konstantinov, Ukr. Fiz. Zh. **46** (7), 740 (2001).

Translated by O. Borovik-Romanova

Physics of the Solid State, Vol. 46, No. 11, 2004, pp. 2021–2025. Translated from Fizika Tverdogo Tela, Vol. 46, No. 11, 2004, pp. 1955–1959.
Original Russian Text Copyright © 2004 by Patrakov, Gritsenko, Zhidomirov.

DEFECTS, DISLOCATIONS, AND PHYSICS OF STRENGTH

Interaction with Charge Carriers and the Optical Absorption Spectrum of an Associate Formed by Elementary Defects (an Oxygen Vacancy and a Silylene Center) in SiO_2

A. E. Patrakov*, V. A. Gritsenko*, and G. M. Zhidomirov**
** Institute of Semiconductor Physics, Siberian Division, Russian Academy of Sciences,*
pr. Akademika Lavrent'eva 13, Novosibirsk, 630090 Russia
e-mail: m_patrakov@mail.ru
*** Boreskov Institute of Catalysis, Siberian Division, Russian Academy of Sciences,*
pr. Akademika Lavrent'eva 5, Novosibirsk, 630090 Russia

Received December 9, 2003

Abstract—The ability of intrinsic defects in SiO_2 to capture electrons and holes is investigated by quantum-chemical methods. It is established that a twofold-coordinated silicon atom with two unpaired electrons, namely, the silylene center =Si:, and a silicon–silicon bond, namely, the oxygen vacancy ≡Si–Si≡, are electron–hole traps in SiO_2. The properties of a defect in the form of an associate of the two above centers are studied. It is shown that this defect can capture electrons and holes; i.e., it is an amphoteric defect in SiO_2. The optical absorption spectrum of the studied associate virtually coincides with that of the oxy radical (≡Si–$O^{\bullet}$) in silicon dioxide. *© 2004 MAIK "Nauka/Interperiodica".*

1. INTRODUCTION

Amorphous SiO_2 and Si_3N_4 have been widely used as materials for modern semiconductor electronic devices. In this respect, it is important to elucidate the influence of external factors on the physical characteristics of dielectrics. In particular, dielectric materials subjected to strong electric fields (up to 10^8 V/m) or exposed to ionizing radiation and high temperatures undergo structural transformations with the formation of defect centers, such as electron and hole traps. Electric charges induced in a dielectric material or at an Si–SiO_2 interface can bring about a shift in the threshold voltage of metal–insulator–semiconductor transistors, parasitic leakage in *p*–*n* junctions, and a decrease in the gain of bipolar transistors. For silicon devices at a standard supply voltage $U = 3$ V, the field strength in the dielectric is approximately equal to 10^8 V/m and the mean field strength in the channel amounts to $1–5 \times 10^6$ V/m. In such strong fields, the following phenomena can be observed in a dielectric material: (i) electrons and holes can be injected from contacts, (ii) surface states can be generated, and (iii) injected charge carriers can be trapped by deep-level centers.

A large number of theoretical and experimental works have been devoted to the identification and investigation of defects in SiO_2. In the present work, we studied two intrinsic defects in SiO_2, namely, the silylene center =Si: and the oxygen vacancy ≡Si–Si≡. Hereafter, the symbols (–), (:), and (·) denote a chemical bond, a lone electron pair, and an unpaired electron, respectively. For convenience, we introduce the following designations: *S* is a silylene center, *V* is an oxygen vacancy, and *VS* is an associate formed by a silylene center and an oxygen vacancy. Earlier [1–3], it was shown that the Si–Si bond can capture a hole. A similar inference regarding the *S* center was made in [4, 5]. The purpose of this work was, first, to refine the results obtained in our previous studies of the *V* and *S* centers and, second, to elucidate how direct contact between these defects affects their parameters, i.e., to investigate the electronic structure and optical properties of the *VS* center. This center is an oxygen vacancy in which one of the two silicon atoms is coordinated by the other silicon atom and by one oxygen atom. The structural formula of this defect has the form –Si:–Si≡.

2. COMPUTATIONAL TECHNIQUE

We carried out *ab initio* calculations in the framework of the density-functional theory according to the Gaussian98 program package. All the calculations were performed in the cluster approximation with the use of two variants of the cluster model. This made it possible to investigate the properties of defects located both in the bulk of the dielectric material and near the surface. In order to simulate the bulk of SiO_2 and bulk defects, we used fragments of crystalline α-quartz. Dangling bonds at the cluster boundary were saturated with hydrogen atoms whose positions were fixed in the course of the geometric optimization (search for the minimum in the hypersurface of the total electronic energy of the system). The bulk oxygen vacancy was

1063-7834/04/4611-2021$26.00 © 2004 MAIK "Nauka/Interperiodica"

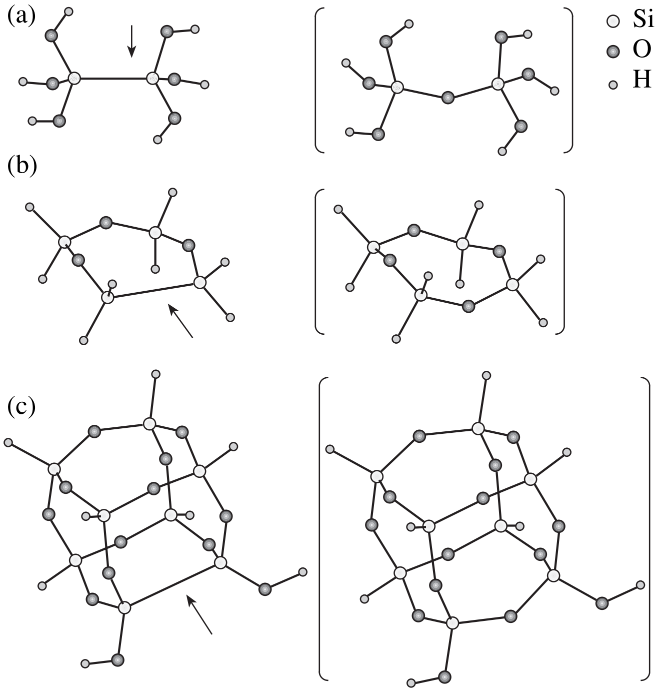

Fig. 1. Cluster models of an oxygen vacancy in SiO_2: (a) $Si_2O_6H_6$ [$Si_2O_7H_6$], (b) $Si_4O_3H_8$ [$Si_4O_4H_8$], and (c) $Si_8O_{13}H_8$ [$Si_8O_{14}H_8$]. The corresponding model of the regular structure is given in brackets to the right of the structure containing the defect (indicated by an arrow).

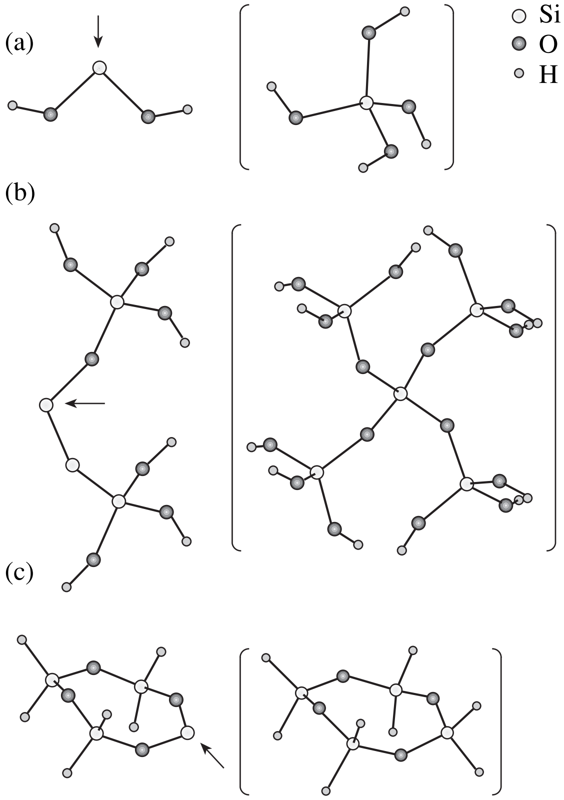

Fig. 2. Cluster models of a silylene center in SiO_2: (a) $Si(OH)_2$ [$Si(OH)_4$], (b) $Si_3O_8H_6$ [$Si_5O_{16}H_{12}$], and (c) $Si_4O_4H_6$ [$Si_4O_4H_8$]. The corresponding model of the regular structure is given in brackets to the right of the structure containing the defect (indicated by an arrow).

simulated by the $Si_2O_6H_6$ [$Si_2O_7H_6$] clusters (Fig. 1a) (hereafter, the corresponding models of the regular structures are given in square brackets). The silylene center was simulated using the $Si(OH)_2$ [$Si(OH)_4$] and $Si_3O_8H_6$ [$Si_5O_{16}H_{12}$] clusters (Figs. 2a, 2b). When simulating the surface defects, we used the $Si_4O_3H_8$ [$Si_4O_4H_8$] and $Si_8O_{13}H_8$ [$Si_8O_{14}H_8$] clusters for the oxygen vacancy (Figs. 1b, 1c) and the $Si_4O_4H_6$ [$Si_4O_4H_8$] clusters for the silylene center (Fig. 2b). These clusters consisted of one or several closed rings. Such structures enabled us to arrange the defect centers on the "surface" of the cluster model. The sole exception is the bulk silylene center, whose geometry makes it impossible to construct a cluster in which a defect can be positioned at the center of a regular coordination sphere (in accordance with the geometry of crystalline α-quartz). However, it should be remembered that the method used for determining the energy gain due to capture of charge carriers by a defect involves calculation of the total energy of two structures, namely, a regular structure (which either has the geometry of α-quartz in the case of bulk defects or contains closed rings formed by ≡Si–O–Si≡ fragments in the case of surface defects) and the corresponding defect-containing structure in different charge states. For this reason, as was noted above, we used fragments of crystalline α-quartz, namely, the $Si(OH)_4$ and $Si_5O_{16}H_{12}$ clusters, as models of regular structures for studying the bulk silylene center. In the clusters simulating surface defects, the positions of the hydrogen atoms were not fixed.

The Kohn–Sham molecular orbitals were constructed using the split-valence (double-zeta) basis set augmented with 3*d* polarization functions (the standard 6–31G* basis set) for all the silicon atoms. The positions of all the Si and O atoms were optimized with the B3LYP gradient-corrected exchange–correlation functional [6, 7].

The energy gain due to capture of charge carriers (an electron and a hole) by a defect was determined from the following relationships:

$$\Delta E^e = (E^0_{\mathrm{bulk}} + E^-_{\mathrm{def}}) - (E^-_{\mathrm{bulk}} + E^0_{\mathrm{def}}), \qquad (1)$$

$$\Delta E^h = (E^0_{\mathrm{bulk}} + E^+_{\mathrm{def}}) - (E^+_{\mathrm{bulk}} + E^0_{\mathrm{def}}). \qquad (2)$$

Here, E^0_{bulk}, E^-_{bulk}, and E^+_{bulk} are the energies of the neutral, negatively charged, and positively charged clusters simulating the bulk of the dielectric, respectively; and E^0_{def}, E^-_{def}, and E^+_{def} are the energies of the neutral, negatively charged, and positively charged

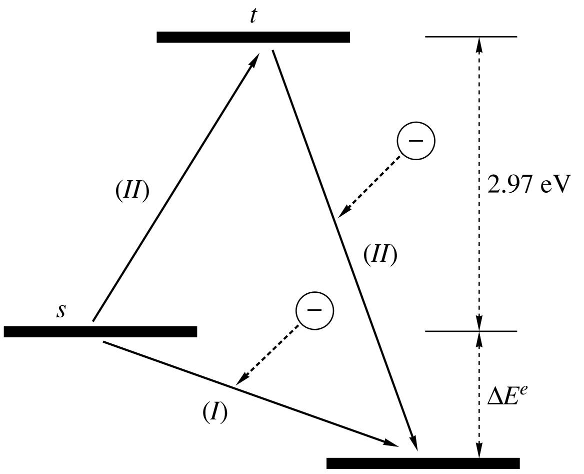

Fig. 3. Schematic diagram of the electronic structure of a =Si: defect in SiO_2. Designations: *s* is the ground (singlet) state of the silylene center, and *t* is the excited (triplet) state. Solid arrows indicate the possible paths of the reaction $=\mathrm{Si}\colon + e \longrightarrow =\mathrm{Si}\colon$ (*I*) capture of an electron in the ground state of the defect with a decrease in the energy of the system by 1.16 eV and (*II*) excitation of the defect (E_{ex} = 2.97 eV) with subsequent capture of an electron and a decrease in the energy of the system by 4.05 eV.

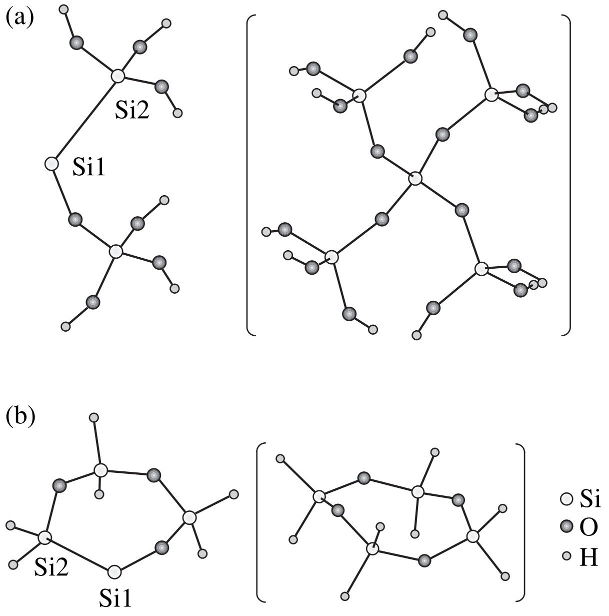

Fig. 4. Cluster models of a *VS* defect (an associate formed by an oxygen vacancy and a silylene center) in SiO_2: (a) $Si_3O_7H_6$ [$Si_5O_{16}H_{12}$] and (b) $Si_{14}O_3H_6$ [$Si_4O_4H_8$]. The corresponding model of the regular structure is given in brackets to the right of the structure containing the defect.

clusters simulating the defect, respectively. An electron (hole) is captured when the quantity ΔE^e (ΔE^h) is negative in sign.

3. RESULTS AND DISCUSSION

The results of our calculations are presented in Table 1. It was assumed that the silylene center can exist in two states in which the total spin of the electronic system is equal to zero (singlet state) and unity (triplet state). The triplet state is an excited state, and the excitation energy is equal to 2.97 eV. The two possible paths of the reaction $=\mathrm{Si}\colon + e \longrightarrow =\mathrm{Si}^{\cdot}$ are shown in Fig. 3. A similar situation occurs with the capture of a hole.

From analyzing the results presented in Table 1, we can make the inference that the quantities ΔE^e and ΔE^h characterizing the energy location of the electron and hole traps do not depend on the location of defects with respect to the cluster boundaries (for bulk and surface defects, the values of ΔE^e and ΔE^h are nearly identical).

In order to investigate the properties of the *VS* defect, which is an associate formed by an oxygen vacancy *V* and a silylene center *S*, we used the $Si_4O_3H_6$ [$Si_4O_4H_8$] and $Si_3O_7H_6$ [$Si_5O_{16}H_{12}$] cluster models for the surface and bulk defects, respectively (Figs. 4a, 4b). As in the case of the *S* center, the calculations were performed for the triplet and singlet states. It was found that the energy of the singlet state of the defect is 1 eV less than the energy of the triplet state. The calculated energy gains due to the capture of an electron and a hole are listed in Table 2.

The Si–Si bond length in the neutral $Si_4O_3H_8$ cluster is equal to 2.37 Å. The capture of an electron does not lead to considerable structural distortions, whereas the capture of a hole results in an increase in the length of the Si–Si bond to 2.61 Å. A somewhat different situation arises with the $Si_8O_{13}H_8$ and $Si_2O_6H_6$ clusters. The capture of an electron leads to an increase in the Si–Si bond length from 2.33 to 2.48 Å in the $Si_8O_{13}H_8$ cluster

Table 1. Energy gains due to capture of an electron (ΔE^e) and a hole (ΔE^h) by an oxygen vacancy and a silylene center in SiO_2 according to calculations from formulas (1) and (2)

Defect	Cluster	ΔE^e (eV)	ΔE^h (eV)
V	$Si_4O_3H_8$ [$Si_4O_4H_8$]	–0.63	–0.98
	$Si_8O_{13}H_8$ [$Si_8O_{14}H_8$]	–0.61	–0.95
	$Si_2O_6H_6$ [$Si_2O_7H_6$]	–0.59	–0.97
S	$Si_4O_4H_6$ [$Si_4O_4H_8$]	–1.16(*s*)	–1.12(*s*)
		–4.05(*t*)	–4.1(*t*)
	Si(OH)$_2$ [Si(OH)$_4$]	–1.45(*s*)	–1.62(*s*)
		–4.2(*t*)	–4.3(*t*)
	$Si_3O_8H_6$ [$Si_5O_{16}H_{12}$]	–1.19(*s*)	–1.35(*s*)

Note: (*s*) and (*t*) stand for the singlet and triplet states of the silylene center, respectively. The models of bulk defects are marked with bold type.

Table 2. Energy gains due to capture of an electron (ΔE^e) and a hole (ΔE^h) by a *VS* defect (an associate formed by an oxygen vacancy and a silylene center) in SiO_2 according to calculations from formulas (1) and (2)

Defect	Cluster	ΔE^e (eV)	ΔE^h (eV)
VS	$Si_4O_3H_6$ [$Si_4O_4H_8$]	–2.16(*s*)	–2.39(*s*)
		–3.24(*t*)	–3.3(*t*)
	$Si_3O_7H_6$ [$Si_5O_{16}H_{12}$]	–2.15(*s*)	–2.37(*s*)

Table 3. Energies T_{ex} of optical transitions for an oxygen vacancy *V*, a silylene center *S*, and an associate *VS* according to the TD–DFT (B3LYP/6–31*G**) calculations

Defect	Cluster	Transition	T_{ex} (eV)	*f*
V	$Si_2O_6H_6$	$S_0 \longrightarrow S_1$	7.04	0.1
		$S_0 \longrightarrow S_2$	7.11	0.13
		$S_0 \longrightarrow T_1$	5.1	0.0
	$Si_8O_{13}H_8$	$S_0 \longrightarrow S_1$	7.17	0.06
		$S_0 \longrightarrow S_2$	7.6	0.0006
		$S_0 \longrightarrow T_1$	5.3	0.0
S	$Si_3O_8H_6$	$S_0 \longrightarrow S_1$	4.86	0.1
		$S_0 \longrightarrow S_2$	5.66	0.003
		$S_0 \longrightarrow T_1$	3.0	0.0
	$Si_4O_4H_6$	$S_0 \longrightarrow S_1$	5.19	0.1
		$S_0 \longrightarrow S_2$	6.04	0.005
		$S_0 \longrightarrow T_1$	2.9	0.0
VS	$Si_3O_7H_6$	$S_0 \longrightarrow S_1$	1.7	0.002
		$S_0 \longrightarrow S_2$	4.2	0.01
	$Si_4O_4H_6$	$S_0 \longrightarrow S_1$	2.02	0.003
		$S_0 \longrightarrow S_2$	4.16	0.02
		$S_0 \longrightarrow T_1$	1.0	0.0

and from 2.48 to 3.00 Å in the $Si_2O_6H_6$ cluster. The capture of a hole also results in an increase in the Si–Si bond length from 2.33 to 2.58 Å in the $Si_8O_{13}H_8$ cluster and from 2.48 to 2.90 Å in the $Si_2O_6H_6$ cluster. The attractive forces between the silicon atom of the defect and the oxygen atoms of the nearest environment and an increase in the repulsive force (in the case of the hole capture) between the silicon atoms can lead to an increase in the length or even to the breaking of the Si–Si bond with the formation of a positively charged *E*' center [2, 3]. However, in the framework of our model, we can only be sure that the Si–Si bond length increases by ~12% of the initial length in the case of the hole capture and by ~5% of the initial length for the electron capture. For both defects, the spin density distribution is symmetric with respect to the plane perpendicular to the Si–Si bond and, hence, there are no grounds to believe that the Si–Si bond is broken.

In the neutral $Si_4O_3H_6$ cluster simulating the *VS* surface defect, the Si–Si bond length is equal to 2.46 Å. Structural relaxation due to the capture of an electron or a hole is insignificant. The Si–Si bond lengths in the $Si_4O_3H_6$ cluster upon capture of an electron and a hole are equal to 2.41 and 2.56 Å, respectively. The behavior of the bulk defect does not differ radically from that of the surface defect. However, it should be noted that the spin density distribution is nonsymmetric for the bulk defect. In particular, the spin density in the $Si_4O_3H_6$ cluster is approximately equal to 0.86 at the Si1 atom and 0.1 at the Si2 atom for the electron capture and 0.52 at the Si1 atom and 0.3 at the Si2 atom for the hole capture. Therefore, the captured charge carrier is predominantly localized at the silylene center of the associate.

The optical properties of the defects, namely, the energies and intensities of the electron transitions, were calculated in the framework of the time-dependent density functional response theory (TD–DFT). This approach offers new possibilities for investigating the properties of excited states of defects in dielectric materials. Although the TD–DFT method was devised rather recently, it has managed to show good performance in the study of the optical properties of point defects in SiO_2 [8]. The energies of optical transitions were calculated in the adiabatic approximation; i.e., upon excitation of the electronic system, the geometric parameters of the cluster models remained unchanged. For each of the three defects (*S*, *V*, or *VS*), we calculated the excitation energies T_{ex} and the oscillator strengths *f* for the two lowest singlet ⟶ singlet transitions ($S_0 \longrightarrow S_1$ and $S_0 \longrightarrow S_2$) and one singlet ⟶ triplet transition ($S_0 \longrightarrow T_1$). The results of the calculations are given in Table 3. It can be seen from the data presented in Table 3 that the calculated energy of the $S_0 \longrightarrow S_1$ transition for the oxygen vacancy almost coincides with the experimental value (7.6 eV) [9]. It should be noted that the augmentation of the basis set with *s* and *p* polarization functions, i.e., the use of the standard 6–31G* basis set in the quantum-chemical calculations (which we performed only for the oxygen vacancy), leads to slightly underestimated energies of the optical transitions as compared to the experimental values. For example, we obtained the excitation energy $T_{ex} = 6.57$ eV ($f = 0.2$) for the $S_0 \longrightarrow S_1$ transition. This discrepancy suggests that the inclusion of the polarization functions in the basis set used in calculating the optical absorption spectrum of oxygen-deficient defects is not necessary and, in some cases, is even deleterious. The data calculated for the silylene center are in reasonable agreement with the results obtained in [8, 10, 11]. The optical absorption spectrum of the *VS* defect is of particular interest because the energy of the $S_0 \longrightarrow S_1$ transition coincides with the energy of the $D_0 \longrightarrow D_2$ (doublet ⟶ doublet) transition for another intrinsic defect in SiO_2, namely, the $\equiv$Si–O$^\bullet$ oxy radical ($f \sim 0$ for the $D_0 \longrightarrow D_1$ transition), whose optical spectrum has been repeatedly investigated theoretically [8, 12] and experimentally [13, 14]. Therefore, although this coincidence, in our opinion, is accidental, it indicates that the identification of defects only on the basis of the optical absorption spectra can be problematic.

In an earlier work [4], we noted that the method for calculating the energy gain upon interaction of defects with charge carriers on the basis of formulas (1) and (2) disregards the long-range Coulomb polarization induced in the lattice by a charged defect. However, the correction to the energy gain for lattice polarization can be estimated in the framework of the classical Born model [15]. For the cluster models used, this correction falls in the range from ~–0.4 to ~–0.5 eV. Therefore, the error of the method almost coincides in magnitude with the energy gain ΔE^e for the oxygen vacancy. Hence, we cannot draw correct inference concerning the role played by the V defect in the accumulation of negative charges in SiO_2. On the other hand, as follows from our data, the S defect is an electron–hole trap in SiO_2. By analogy with the capture of a hole [4], the capture of an electron by a neutral diamagnetic center brings about the formation of a negatively charged S center, i.e., a twofold-coordinated silicon atom with an unpaired electron. The direct contact of the oxygen vacancy and the silylene center also results in the formation of an electron–hole trap whose depth (i.e., the energy gains ΔE^e and ΔE^h) is considerably greater than the depths (energy gains) of the constituent elementary defects.

ACKNOWLEDGMENTS

This work was supported by the Siberian Division of the Russian Academy of Sciences, project no. 116.

REFERENCES

1. G. Pacchioni and G. Ierano, Phys. Rev. Lett. **79** (4), 753 (1997).
2. J. K. Rudra and W. B. Fowler, Phys. Rev. B **35** (15), 8223 (1987).
3. T. E. Tsai, D. L. Criscom, and E. J. Frieble, Phys. Rev. Lett. **61** (4), 444 (1988).
4. A. V. Shaposhnikov, V. A. Gritsenko, G. M. Zhidomirov, and M. Roger, Fiz. Tverd. Tela (St. Petersburg) **44** (6), 985 (2002) [Phys. Solid State **44**, 1028 (2002)].
5. T. Uchino, M. Takahashi, and T. Yoko, Appl. Phys. Lett. **78** (18), 2730 (2001).
6. A. D. Becke, Phys. Rev. A **38** (6), 3098 (1988).
7. C. Lee, W. Yang, and R. G. Parr, Phys. Rev. B **37** (2), 785 (1988).
8. K. Raghavachari, D. Ricci, and G. Pacchioni, J. Chem. Phys. **116** (2), 825 (2002).
9. H. Hosono, Y. Abe, H. Imagawa, H. Imai, and K. Arai, Phys. Rev. B **44** (21), 12043 (1991).
10. L. Skuja, J. Non-Cryst. Solids **149**, 77 (1992).
11. G. Pacchioni and R. Ferrario, Phys. Rev. B **58** (10), 6090 (1998).
12. C. de Graaf, C. Sousa, and G. Pacchioni, J. Chem. Phys. **114** (14), 6259 (2001).
13. L. Skuja, J. Non-Cryst. Solids **179**, 51 (1994).
14. L. Skuja, K. Tanimura, and N. Itoh, J. Appl. Phys. **80** (6), 3518 (1996).
15. D. Erbetta, D. Ricci, and G. Pacchioni, J. Chem. Phys. **113** (23), 10744 (2000).

Translated by O. Borovik-Romanova

Physics of the Solid State, Vol. 46, No. 11, 2004, pp. 2026–2029. Translated from Fizika Tverdogo Tela, Vol. 46, No. 11, 2004, pp. 1960–1963.
Original Russian Text Copyright © 2004 by Tetelbaum, Mendeleva.

DEFECTS, DISLOCATIONS, AND PHYSICS OF STRENGTH

A Mechanical Model of Amorphization under Ion Bombardment

D. I. Tetelbaum and Yu. A. Mendeleva
Physicotechnical Research Institute, Nizhni Novgorod State University,
pr. Gagarina 23/3, Nizhni Novgorod, 603950 Russia
e-mail: Tetelbaum@phys.unn.ru

Received February 10, 2004

Abstract—A mechanical model is proposed for the amorphization of solids. The model is based on a concept according to which the accumulation of radiation-induced defects gives rise to forces and force moments that act on local volumes of the material and are responsible for fragmentation. The estimates obtained demonstrate that the proposed model can adequately describe the amorphization of solids only with allowance made for strain waves generated during reactions between defects. This model is consistent with the paracrystalline structure of silicon layers transformed into the amorphous state under ion bombardment. *© 2004 MAIK "Nauka/Interperiodica".*

1. INTRODUCTION

It is known [1] that, under ion bombardment, a surface layer in crystalline solids of different types, in particular, covalent semiconductors, undergoes amorphization, i.e., a transition to an amorphous state. This phenomenon plays an important role in the case of ion implantation. There exist two basic models of amorphization. According to the model proposed by Parsons [2], the formation of an ion track is accompanied by melting of the material along the track followed by solidification. Since the cooling rate is very high, the molten region has no time to crystallize and retains the amorphous structure. In our opinion, this model is valid only for the heaviest ions. Christel *et al.* [3] proposed a more general model, according to which the crystal region exposed to irradiation spontaneously transforms into an amorphous state after reaching a sufficiently high (critical) concentration of radiation-induced defects. Despite the large number of works dealing with the amorphization, the mechanism of the transition to the amorphous state in the latter case is still not clearly understood.

In this work, we proposed the simplest (mechanical) model of a transition from a crystalline state to an amorphous state due to the attainment of a critical concentration of radiation-induced defects.

2. THE MODEL OF AMORPHIZATION

The model is based on the concept that an amorphous material is a conglomerate of mutually misoriented small-sized crystals, i.e., nanocrystals. It is obvious that this model, which was proposed even tens years ago by Valenkov and Porai-Koshits [4], is significantly simplified. For example, structural, optical, and electron diffraction investigations revealed that the degree of short-range order in the structure of amorphous silicon (*a*-Si) prepared by several methods differs from the degree of short-range order in the structure of crystalline silicon but, in both materials, tetrahedra are the main structural units [5]. It is generally believed that the structure of amorphous silicon can be best described in the framework of the random network model [6]. However, the degree of short-range order cannot serve as a criterion for validity of a particular model, because the fraction of atoms located at interfaces or in their vicinity in a conglomerate composed of small-sized nanocrystals is rather large. Moreover, it should be remembered that, for the most part, the works concerned with the structural investigation of amorphous materials have not covered ion-irradiated semiconductors. Information on the structure of amorphous films formed by ion-irradiated semiconductor materials is very scarce. In their recent work, Cheng *et al.* [7] analyzed the results obtained using a new technique, namely, fluctuation electron microscopy, and demonstrated that the structure of *a*-Si films synthesized through ion implantation at low temperatures can be adequately described within the so-called paracrystalline model. According to this model, the short-range order is not perfect and, unlike the random network model, there also exists a medium-range (intermediate-range) order, which makes it possible to distinguish and characterize grain (block) boundaries. Note that the diameter of grains lies in the range 1–3 nm. Only after annealing of the material at a temperature of 500°C or higher does the structure become similar to that described in terms of the random network model. These results suggest that, in the case of ion bombardment (at least, at low temperatures), the concept of an amorphous layer being formed by a set of misoriented blocks can hold true.

Let us assume that ion-beam amorphization leads to the fragmentation of a surface layer of the crystal, during which each fragment (block) is rotated through a sufficiently large angle. In contrast to the fragmentation under mechanical treatment (for example, mechanical dispersion in ball mills), ion-beam amorphization does not result in fracture of the material: after the reorientation, fragments form new interatomic bonds with each other along the interfaces. In the framework of our model, the fragmentation is caused by the local stresses associated with the high concentration of radiation-induced point defects, such as vacancies, interstitial atoms, and their complexes (divacancies, di-interstices, multivacancies, multi-interstitial complexes). Each fragment (a local volume of the crystal) experiences a force exerted by adjacent blocks, so that the resultant force and its moment are not equal to zero due to fluctuations in the distribution of defects. Apart from the static forces, the block subjected to ion bombardment experiences a dynamic action due to the generation of strain waves in the course of reactions between defects, for example, during recombination of Frenkel pairs [8]. It has been demonstrated that such waves can bring about atomic displacements [8]. Consequently, these waves can initiate reactions between defects, which, in turn, generate secondary strain waves. As a result, there arises a chain process that enhances the action of strain waves. When the strain waves reach the boundaries of a particular block, they produce a nonuniform pressure that results in rotation of the block.

Of course, blocks in an original (ideal) crystal are virtual. In our model, the sizes (and shape) of the blocks are postulated. Intuitively, it is clear that the macroscopic approach is not appropriate for very small blocks and that rotations of very large blocks cannot occur without disruption of the medium (accommodation). As follows from the results of structural investigations, the sizes of regions with short-range order in amorphous materials, for example, in silicon, are approximately equal to 1–2 nm [5]. For our estimates, the block size will be taken equal to 2 nm.

Now, we divide a volume of the irradiated layer into blocks. For convenience, these blocks are assumed to be identical and cubic in shape (with the size $a = 2$ nm). It is also assumed that the blocks are arranged in a brick masonry (see figure), even though the block arrangement is of no fundamental importance in our model. Below, we will estimate the threshold concentration of defects necessary for amorphization in the static and dynamic cases.

2.1. *The Static Case*

Let the mean number of defects in each block be equal to N. For a Gaussian statistics and a sufficiently large N, the root-mean-square deviation of the number of defects is equal to $\sqrt{N}$. It is this quantity that plays the role of the effective number of defects when estimating (in order of magnitude) the mean force or the mean force moment acting on the given block from adjacent blocks, because the forces for equal numbers of defects in all blocks are balanced and the resultant moment of the forces is equal to zero. Each defect induces an elastic-stress field in its environment [9, 10]. If the stresses generated by $\sqrt{N}$ defects located in block *1* (see figure) are summed, the resultant force vector **F** will be applied at the point indicated in the figure. This force produces the moment M with respect to the center of the cube. The moments of forces exerted by the other adjacent blocks can be determined in a similar manner (the forces exerted by more distant blocks are ignored in rough estimates). The inclusion of the other blocks (except for block *1*) surrounding block *2* in our calculation leads to a decrease in the force moment and to an increase in the critical concentration of defects. (This circumstance only supports the inference made below.)

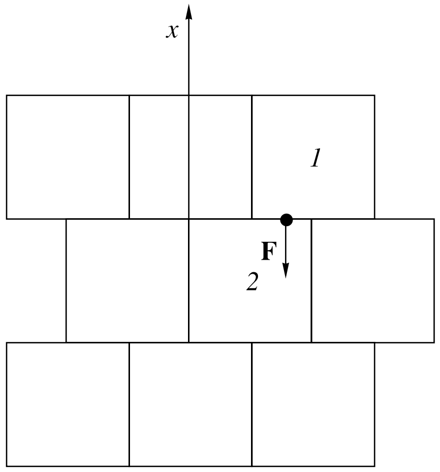

Schematic diagram of crystal blocks in the initial state. **F** is the resultant force acting on block *2* from block *1*.

According to the schematic diagram depicted in the figure, we can write the following relationship:

$$M = \frac{1}{4}Fa = \frac{1}{8}\sigma a^3, \qquad (1)$$

where σ is the stress. By equating $\sigma = \sigma_{\mathrm{cr}}$ (where σ_{cr} is the ultimate stress), we obtain the critical moment

$$M_{\mathrm{cr}} = \frac{1}{8}\sigma_{\mathrm{cr}} a^3. \qquad (2)$$

On the other hand, the effective stress for block *1* containing $\sqrt{N}$ defects, according to the elasticity theory, can be represented in the form

$$\sigma \approx \varepsilon B = \frac{\beta\sqrt{N}B}{3a^3}, \qquad (3)$$

where B is the bulk modulus and β is the change in the volume due to the presence of a single point defect in the block. Now, we substitute expression (3) into relationship (1) at the standard values of $\sigma_{\mathrm{cr}} = 0.05B$ and $\beta = 3 \times 10^{-24}$ cm^{-3} [10]. Here, the theoretical ultimate stress is taken as σ_{cr}. Why is specifically the theoretical ultimate stress used? This can be explained by the fact that the block size is considerably smaller than the dislocation spacing typical of semiconductors, for example, silicon (>10^{-4} cm); hence, the fragmentation is not related to the dislocation motion and, unlike the dislocation mechanism of fracture, requires the breaking of all interatomic bonds at the block boundary. From relationships (1)–(3), we obtain the critical concentration of point defects $n_{\mathrm{cr}} = N/a^3 \sim 10^{25}$ cm^{-3}. This value is two orders of magnitude greater than the atomic concentration in silicon, which has no physical meaning. Therefore, the static stresses caused by the radiation-induced defects are not sufficient for fragmentation.

2.2. The Dynamic Case

In the course of ion bombardment, radiation-induced defects can undergo transformations, such as the formation of more complex defects, reorientation, recombination, etc. These transformations are accompanied by changes in the local strain fields and, hence, by the generation of strain waves. In turn, the interaction of strain waves with defects can initiate reactions between the defects with the generation of secondary strain waves. (This process was described in detail in [11].) Therefore, the crystal subjected to ion bombardment experiences “radiation shaking” [8], whose amplitude increases with an increase in the defect concentration. Any separated volume of the crystal is in the field of strain waves. These waves produce a pressure that is not uniform and, hence, induces the moment of the force acting on this volume. The same is true for nanovolumes (blocks). Let us now estimate the defect concentration at which the pressure exceeds the theoretical ultimate stress and, consequently, initiates fragmentation.

For a sufficiently high concentration of defects (sources of strain waves), summation can be replaced by integration. In this case, the pressure that is associated with the defects involved in block *1* and acts on the right half of the upper face of block *2* can be written in the form

$$P = \int_0^a \int_0^{1/2} \frac{2\pi r p_0 r_0 n}{(r^2 + x^2)^{1/2}} dx dr = 2.5\pi p_0 r_0 a n. \qquad (4)$$

Here, the x axis is directed upward (see figure) and r is the radial coordinate in the plane perpendicular to the x axis. In relationship (4), we introduced the following designations: n is the mean concentration of radiation-induced point defects, $p_0 = B\varepsilon_0$ is the pressure inside the source of strain waves (the source is assumed to be spherical in shape), ε_0 is the local strain caused by the point defect, and r_0 is the effective radius of the locally strained region. The typical values of the above parameters are as follows [10, 12]: $r_0 = 0.1$ nm and $\varepsilon_0 = 10^{-2}$. Relationship (4) was derived under the assumption that the distribution of defects is uniform, the amplitude of strain waves decreases in inverse proportion to the distance from the point defect, and the dissipation of the energy of the strain waves at distances of the order of a can be disregarded.

By equating the pressure P to the critical pressure determined by the theoretical ultimate stress σ_{cr}, i.e., $P = \sigma_{\mathrm{cr}} = 0.05B$, we obtain $n_{\mathrm{cr}} \approx 10^{20}$ cm^{-3}. The experimental value of n_{cr} for silicon amounts to approximately 10% of the atomic concentration, i.e., to ~5×10^{21} cm^{-3} [3]. However, our estimate of the critical concentration n_{cr} is rather low. This is associated with the fact that, in general, the strain waves arriving at the face of block *2* from point defects are shifted in phase and can partially cancel each other. Furthermore, as was noted above, the forces acting on the given block from other (adjacent) blocks partially balance each other. These factors are difficult to take into account with high accuracy. However, the estimate obtained indicates that the dynamic model is at least not in contradiction with the experimental data.

3. DISCUSSION

The amorphization can be explained in the framework of the mechanical model but only in terms of the dynamic variant, i.e., with due regard for strain waves excited upon transformation of radiation-induced defects. Of course, this model raises a number of questions.

It is not quite clear how an individual block can rotate with respect to a surrounding material without disruption of the medium. It seems likely that the adjacent blocks rotate in a correlated fashion: the mutual accommodation of individual blocks is attended by the breaking of the already existing bonds and the formation of new bonds. (A similar situation is observed upon the formation of rolling textures. In this case, the sense of rotation of the stacks composed of atomic planes (grains) is specified by the rolling direction and the process occurs through the dislocation mechanism.) Note that the amorphization is accompanied by a slight fracture of the material: the amorphous structure, as a rule, contains pores, which can be interpreted as a result of imperfect accommodation.

As was noted above, the initial crystal (prior to fragmentation), in the general case, does not involve nanoblocks (not to be confused with “blocks” in mosaic single crystals, which are usually of considerably larger size and are not necessarily formed). In our case, the notion of blocks suggests that the ion bombardment induces nonuniform stress fields responsible for the generation of forces that act on local crystal regions and, thus, initiate fragmentation. The block size (~2 nm) is comparable to the distance between subcascades in displacement cascades [13]; i.e., it is actually comparable to the characteristic scale of fluctuations in the defect distribution. Therefore, we can assume that, although these fluctuations themselves do not bring about the fragmentation (see Section 2), they produce "weak sites" (in regions with an increased defect concentration) through which the fragmentation proceeds within the framework of the dynamic model.

The mechanical model under consideration does not allow one to determine the dose dependence of the volume fraction of the amorphous phase. Within this model, the amorphization is treated as a unit event that covers the regions in which the mean defect concentration reaches a critical value. This is the disadvantage of the model.

At the same time, the advantage of the model is its better agreement with the paracrystalline structure of amorphous layers [7] as compared to the hypothesis for the gradual disturbance of the long-range order in the course of defect accumulation.

As regards the role played by strain waves in amorphization, it is pertinent to note that a similar concept was used to explain the so-called long-range interaction upon ion bombardment [11]. In our opinion, strain waves play an important role in many processes occurring in solids, such as plastic deformation, fracture, phase transitions, etc. (i.e., processes attended by rapid local transformations of atomic configurations). Unfortunately, this circumstance has received little attention in the theory of solids. Apparently, the traditional phonon formalism, even with allowance made for the anharmonicity, is not appropriate for considering similar phenomena due to the strong nonlinearity of the processes. The other methods indented for describing dynamic processes (for example, the soliton formalism) have been rarely used and lack generality. Most likely, it would be expedient to use the molecular dynamics method for simulating processes in large-sized blocks. (Here, unlike the above consideration, the term "block" implies a model crystal in the sense common for molecular dynamics.) Attempts to perform the molecular dynamics simulation (only for relatively small-sized blocks however) have already demonstrated the possibility of revealing new previously unpredicted interesting phenomena under bombardment of solids with low-energy ions [14]. However, calculations of this type as applied to amorphization were not carried out.

4. CONCLUSIONS

Thus, it was demonstrated that the proposed model is consistent with the concept according to which amorphization is treated as a spontaneous phase transition occurring after reaching a critical concentration of point defects [1, 3]. The above model is a step forward in the development of this concept and makes it possible to elucidate the mechanism of transformation. The estimates obtained serve as a basis for more accurate mathematical development of the model (possibly with the use of computer calculations).

REFERENCES

1. E. I. Zorin, P. V. Pavlov, and D. I. Tetelbaum, *Ion Doping of Semiconductors* (Énergiya, Moscow, 1976) [in Russian].
2. J. R. Parsons, Philos. Mag. **12** (120), 1159 (1965).
3. L. A. Christel, J. F. Gibbons, and T. W. Sigmon, J. Appl. Phys. **52** (12), 7143 (1981).
4. N. Valenkov and E. Porai-Koshits, Z. Kristallogr. **95** (1/4), 195 (1937).
5. V. P. Zakharov and V. S. Gerasimenko, *Structural Features of Semiconductors in the Amorphous State* (Naukova Dumka, Kiev, 1976) [in Russian].
6. D. Polk and D. S. Bondreax, Phys. Rev. Lett. **31** (2), 92 (1973).
7. Ju. Yin Cheng, J. M. Gibson, P. M. Baldo, and B. J. Kestel, J. Vac. Sci. Technol. A **20** (6), 1855 (2002).
8. V. L. Indenbom, Pis'ma Zh. Tekh. Fiz. **5** (8), 489 (1979) [Sov. Tech. Phys. Lett. **5**, 200 (1979)].
9. J. D. Eshelby, in *Continuous Theory of Dislocations* (Inostrannaya Literatura, Moscow, 1966).
10. A. C. Damask and G. J. Dienes, *Point Defects in Metals* (Gordon and Breach, New York, 1963; Mir, Moscow, 1966).
11. P. V. Pavlov, Yu. A. Semin, V. D. Skupov, and D. I. Tetelbaum, Fiz. Tekh. Poluprovodn. (Leningrad) **20** (3), 503 (1986) [Sov. Phys. Semicond. **20**, 315 (1986)].
12. M. W. Thompson, *Defects and Radiation Damage in Metals* (Cambridge Univ. Press, Cambridge, 1969; Mir, Moscow, 1971).
13. V. L. Vinetskiĭ and G. A. Kholodar', *Radiation Physics of Semiconductors* (Naukova Dumka, Kiev, 1979) [in Russian].
14. I. V. Tereshko, V. I. Khodyrev, É. A. Lipskiĭ, Zh. A. Rymkevich, V. V. Glushchenko, V. N. Konchalenko, and D. L. Vinogradov, Vestn. Nizhegorod. Univ. im. N. I. Lobachevskogo, Fiz. Tverd. Tela, No. 2, 131 (1998).

Translated by O. Borovik-Romanova

Physics of the Solid State, Vol. 46, No. 11, 2004, pp. 2030–2034. Translated from Fizika Tverdogo Tela, Vol. 46, No. 11, 2004, pp. 1964–1967.
Original Russian Text Copyright © 2004 by Gorlov.

DEFECTS, DISLOCATIONS, AND PHYSICS OF STRENGTH

Ligand Electron–Nuclear Double Resonance of T_1 Trigonal Gd^{3+} Centers in CaF_2 with a Mixed Oxygen–Fluorine Environment

A. D. Gorlov
Research Institute of Physics and Applied Mathematics, Ural State University,
pr. Lenina 51, Yekaterinburg, 620083 Russia
e-mail: Anatoliy.Gorlov@usu.ru

Received April 13, 2004

Abstract—This paper reports on the results of ligand electron–nuclear double resonance (ENDOR) investigations of T_1 trigonal $^{157}Gd^{3+}$ centers in the CaF_2 compound. It is experimentally found that the nearest environment of an impurity center contains only one ^{19}F ion. Anions in the other coordination shells are identical to those in the pure CaF_2 crystal. However, ^{19}F ions in these shells are displaced from their ideal positions in the lattice. The parameters of the ligand hyperfine interaction (LHFI) for ^{19}F nuclei and their coordinates and displacements with respect to the positions in the lattice of the pure CaF_2 crystal are determined. It is demonstrated that the unusual isotropic LHFI constant $A_s > 0$ for Gd^{3+} ions in the lattice with a mixed oxygen–fluorine nearest environment can be associated with the strong polarization of impurity centers in accordance with the empirical model proposed in [1], provided the structural model of the nearest environment of impurities in the T_1 centers [2] is correct. This structural model is confirmed by the analysis of the isotropic hyperfine constant $A(s)$ for $^{157}Gd^{3+}$ centers. © *2004 MAIK “Nauka/Interperiodica”.*

1. INTRODUCTION

Early investigations of the optical and electron paramagnetic resonance (EPR) spectra of MeF_2 compounds [2–8] have revealed a great diversity of impurity centers with trigonal local symmetry. It has been established that the formation of impurity centers differing in local symmetry is determined by the conditions of crystal growth. The spectra of these centers are characterized by crystal-field parameters and initial splittings that differ in magnitude and sign. This indicates considerable changes in the nearest environment of impurities. Among the proposed structural models of these centers, only the models according to which ions with nonzero nuclear spin serve as compensators can be directly confirmed by ligand electron–nuclear double resonance (ENDOR) spectroscopy [1, 2, 7].

The most complete and consistent EPR investigation of T_1 trigonal Gd^{3+} centers in MeF_2 (Me = Ca, Sr, Ba) was performed by Yang *et al.* [6]. It was found that the observed ligand hyperfine structure of the EPR lines is in agreement with the structural model proposed in [2] for the nearest environment of impurity centers. This model is based on the results of the sole ENDOR investigation of T_1 trigonal Yb^{3+} centers in a CaF_2 compound for which impurities were introduced in the form of $Yb_2^{17}O_3$ and the nature of compensators was studied. It was assumed that the nearest environment of impurity centers contains one ^{19}F ion and four ^{17}O ions, of which three ions form a triangle with the plane perpendicular to the C_3 trigonal axis of the crystal and one ion rests on the C_3 axis. However, no data on more distant ligands were reported.

The main objective of the present work was to perform a detailed ENDOR investigation of T_1 trigonal Gd^{3+} centers in CaF_2 in order to elucidate the nature of anions in the second and more distant coordination shells, to estimate their displacements, and to answer the question as to why the isotropic constant of the ligand hyperfine interaction (LHFI) for the nearest ^{19}F nucleus is positive in sign. It should be noted that the positive isotropic constant of the LHFI interaction is not characteristic of rare-earth ions in the ground S state in fluorites [1, 9].

2. EXPERIMENTAL TECHNIQUE, RESULTS AND DISCUSSION

The ligand hyperfine interaction of ^{19}F nuclei (nuclear spin $I = 1/2$) in T_1 trigonal Gd^{3+} centers (electron spin $S = 7/2$) in CaF_2 crystals was investigated using nutation ENDOR spectroscopy [8]. CaF_2 crystals doped with $^{157}Gd_2O_3$ (0.01 wt % in the batch) were grown by the Czochralski technique. The EPR spectra of doped CaF_2 crystals are characterized by two Gd^{3+}

Ligand hyperfine constants (kHz); spherical coordinates of fluorine nuclei in the second, third, and fourth coordination shells of T_1 trigonal Gd^{3+} centers in CaF_2; and deviations (Å) $\Delta R = R - R_0$, $\Delta = z - z_0$ ($z = R\cos\theta + \delta$, where δ is the displacement of the impurity center), and $\Delta\theta = \theta - \theta_0$

Shell	Type of nuclei (their number)	A_s	A_p	R	θ, deg	$\Delta R \times 10^2$	$\Delta\theta$, deg	$\Delta \times 10^2$
2	311(3)	0(3)	857.1(36)	4.42(1)	29.9(3)	–10(1)	0.4(3)	8(2)
	$1\bar{1}3$(3), $31\bar{1}$(3)	0(3)	849.3(39)	4.43(1)	59.4(3)	–9(1)	0.9(4)	7(2)
	$\bar{1}\bar{1}3$(3)	–4(4)	810.4(26)	4.59(2)	78.5(2)	7(2)	–1.5(3)	31(3)
	$1\bar{3}1$(3)	0(5)	767.5(36)	4.59(2)	98.3(4)	7(2)	–1.7(4)	30(3)
	$1\bar{3}\bar{1}$(3), $\bar{1}1\bar{3}$(3)	7(6)	795.9(85)	4.53(3)	122.3(4)	1(3)	0.6(5)	13(4)
	$\bar{1}\bar{3}\bar{1}$ (3)	14(4)	740.3(50)	4.64(3)	148.6(4)	12(3)	–1.9(5)	15(4)
3	313(3)	0	380.1(22)	5.80(2)	22.9(3)	–13(3)	0.9(3)	2(3)
	$3\bar{1}3$(3)	0	372.3(36)	5.84(2)	48.2(4)	–9(3)	0.0(4)	14(4)
	$1\bar{3}3$(3), $3\bar{3}1$(3)	0	348.5(32)	5.97(3)	84.3(12)	4(5)	1.8(15)	–1(2)
	$\bar{1}\bar{3}3$(3), $3\bar{3}\bar{1}$(3)	0	349.3(40)	5.98(3)	97.5(14)	5(5)	0.1(16)	19(3)
	$\bar{3}\bar{3}1$(3)	0	358(4)	5.91(3)	131.9(3)	–2(4)	0.4(3)	16(4)
	$\bar{3}\bar{3}\bar{1}$(3)	0	332(4)	6.07(3)	158.9(4)	13(4)	0.9(4)	2(4)
4	333(1)	0	218.9(19)	6.97(3)	0	–8(4)	0	8(4)
	$\bar{3}\bar{3}\bar{3}$(1)	0	194.1(12)	7.25(3)	0	18(4)	0	0(4)

signals with an intensity ratio of 1 : 1, which corresponds to the T_1 and T_2 trigonal centers [8]. The EPR signals of these centers at a temperature $T = 1.8$ K are adequately described by the standard spin Hamiltonian with the parameters taken from [8] in the coordinate system in which the principal symmetry axis of the center has the orientation $Z \parallel C_3 \parallel [111]$ and the other axes are oriented as follows: $X \parallel [\bar{1}\bar{1}2]$ and $Y \parallel [\bar{1}10]$.

For the most part, the ENDOR measurements were carried out in an external magnetic field **H** aligned parallel to the symmetry axes of the crystal (C_3, C_2, C_4). Moreover, if required, we investigated the angular dependences in the vicinity of these axes. For each EPR transition, the experimental nutation ENDOR spectra associated with the ligands contain a set of resonance signals in the form of decaying periodic distortions of the absorption signal (periodic nutations) and aperiodic distortions of the level of the absorbed microwave power. For a small constant amplitude of the radio-frequency field applied to the sample, the periodic-nutation signals are primarily observed for nuclear spins with large LHFI parameters. This is explained by the radio-frequency field gain at nuclei of ligands [8]. For any EPR transition, there are no more than two ENDOR signals in the form of periodic nutations and their angular dependences in any crystallographic plane of the CaF_2 crystal indicate that these periodic nutations are always single signals. This means that only one ion with nuclear spin $I = 1/2$ and large LHFI constants is located in the vicinity of the impurity center. The sets of all observed ENDOR frequencies are adequately described when the nuclear Zeeman frequency ν_F is determined by the nuclear g factor of ^{19}F. Therefore, the number of signals, their positions, and splitting into a particular number of components upon deviation from the principal orientations uniquely indicate that the nearest environment of impurity centers involves only one fluorine ion. On the other hand, as in the lattices of pure MeF_2, the second and more distant coordination shells consist of ^{19}F ions.

The above findings directly confirm the structural model for the T_1 center, according to which only one fluorine ion is located in the nearest environment of a Gd^{3+} ion (see Fig. 1 in [8], where a fragment of the hypothetical environment of a Gd^{3+} ion is shown), providing that the $Me^{2+}F_8^-$ complex is replaced by the $Gd^{3+}F^-O_4^{2-}$ complex if the atmosphere during the crystal growth contains water vapor or oxygen [2, 3, 5, 6].

The ENDOR frequency spectrum was analyzed by a standard method on the basis of the complete spin Hamiltonian corresponding to trigonal symmetry of the impurity center and local symmetry of ^{19}F in the coordinate system of the chosen nucleus according to the technique described in [1]. The set of frequencies (~200) for different orientations of the external magnetic field is adequately described by the LHFI constants listed in the table.

The calculations demonstrate that, irrespective of the local symmetry of nuclei, all the ENDOR frequencies corresponding to aperiodic signals are described by axially symmetric LHFI tensors with the hyperfine constants $-2A_{xx} = -2A_{yy} = A_{zz} = 2A_p$ and $A_s \sim 0$, as is usually the case with all Gd^{3+} and Eu^{2+} centers in MeF$_2$ [9]. This indicates that the fluorine ions in the second and more distant coordination shells are involved in the magnetodipole ligand hyperfine interaction. On this basis, we determined the coordinates of these ligands (with respect to the impurity centers). The table presents these coordinates and the calculated distances $R(Gd^{3+}-{}^{19}F)$, which are compared with the distances $R_0(Me^{2+}-{}^{19}F)$ in the lattices of the pure CaF_2 compound. The type of nuclei is determined by the Miller indices in the cubic lattice.

The experimental ENDOR frequencies were assigned to specific types of nuclei under the following assumptions. Previous investigations [1, 7, 9] revealed that, when impurity centers are formed with local compensation in MeF$_2$, lattice relaxation decays rapidly in the range far from charge-compensating ions. On this basis, we assume that nuclei of the $\bar{3}\bar{3}\bar{3}$ type occupy positions identical to those in the pure CaF_2 compound. An excess negative charge of the oxygen ion should lead to displacement of the impurity center along the C_3 axis toward O^{2-}. In this case, we have $R(333) < R(\bar{3}\bar{3}\bar{3})$. The cation displacements should only slightly affect the positions of these nuclei. These nuclei are characterized by single signals, which are observed in the vicinity of the Zeeman frequency of ^{19}F nuclei and can be easily separated by analyzing the angular dependences of the ENDOR spectra. The remaining spectra were identified with due regard for the displacement of the impurity center.

In the table, the polar coordinates of anions do not contain azimuthal angles, because they coincide with the lattice angles to within the limits of experimental error. It can be seen from the data presented in the table that, in the second shell, ^{19}F nuclei are characterized by $R < R_0$ at $\theta < 80°$ (where θ is the angle between the axis $Z \parallel C_3$ and the axis of the $Gd^{3+}-{}^{19}F$ pair) and, conversely, $R \geq R_0$ at $\theta > 120°$ due to the displacement of the impurity center toward oxygen. From here, it is necessary to exclude the fluorine nuclei with θ close to 90°, because their displacement most strongly depend on the Coulomb interaction with three O^{2-} ions (located in the vicinity of the XY plane) and on the cation displacement.

Unfortunately, we failed to identify all the frequencies attributed to ^{19}F nuclei located in the fourth coordination shell, because the resolution of the nutation ENDOR technique is lower than that of the stationary technique. However, the locations determined from the experimental constants for two nuclei in this shell demonstrate that the distortions of the shells are insignificant. By assuming that the fluorine ion of the $\bar{3}\bar{3}\bar{3}$ type is not displaced, we found that the Gd^{3+} ion is displaced toward the O^{2-} ion along the C_3 axis by $\delta = 0.18(4)$ Å, where δ is the displacement of the impurity center with respect to the Ca^{2+} position in the undistorted lattice.

The relaxation of the nearest anion environment of the Gd^{3+} ion can be more clearly demonstrated by analyzing the displacements of the planes containing fluorine nuclei that are equivalent from the standpoint of the parameters R and θ (these planes are perpendicular to the Z axis). The displacements of these planes can be characterized by the quantities $\Delta = z + \delta - z_0$, where z and z_0 are the coordinates of the centers of the panes in the lattices of doped and pure CaF_2, respectively. The positive sign of the quantity Δ indicates displacement away from the already existing center at $\theta < 90°$ and displacement toward this center at $\theta > 90°$.

It was found that $\Delta > 0$ (see table). As a result, in the region far from the oxygen ion, all the anions are displaced toward the already existing center. On the other hand, the nuclei located close to the O^{2-} ion are displaced from the center. Therefore, the experimental data show that all the nuclei in the second shell and a number of nuclei in the third shell are displaced in the same manner and accompany the displacement of the impurity center and cations toward the oxygen ion. This regularity can be broken only for ^{19}F nuclei with angles θ close to 90°, because their displacements are affected not only by cations displacements but also by the fact that the number of anions (located in the same region in pure CaF_2) nearest to the impurity center is halved.

In our opinion, the most surprising result obtained in this work is the positive sign of the constant A_s = 1.114 MHz for the fluorine ion nearest to the Gd^{3+} ion [8]. This is quite unusual for rare-earth ions in the S state [1, 9–11]. Without aiming for quantitative agreement, we attempted to use the model described in [1], which relates the isotropic LHFI constants to the quantities R through the dipole moments D and d induced at the Gd^{3+} and F^- ions, and to obtain a positive constant $A_s > 0$. Making allowance for the directions of the displacement of the impurity center and fluorine ions of distant shells and also for the changes in the distances to them, we assumed that $R(111) \geq 2.5$ Å (the change in R by ±0.05 Å leads to a change in the magnitude but not in the sign of the constant A_s). The distances to the axial oxygen ion were determined as the sum of the ionic radii. As in [8], the superposition model for the parameters of the initial splitting and the crystal filed was used for calculating the parameters for the oxygen ions of the triangle: $R \approx 2.42$ Å and $\theta \approx 95°$ (unlike Fig. 1 in [8], the Z axis is directed at the O^{2-} ion). According to

[1], the projections of the dipole moments D and d along the bond axis were estimated within the point-charge model without regard for cation displacements. As a result, we obtain $d \approx -0.05\ e$Å for ^{19}F ions of the $\bar{1}\bar{1}\bar{1}$ type and $D \approx -0.09\ e$Å (e is the magnitude of the elementary charge). It should be noted that the negative sign of the dipole moments is governed by the axial O^{2-} ion. The expression for the constant A_s is written in a form similar to expression (3) in [1]; that is,

$$A_s = A_s(R_0)(1 + ad + AD)(R_0/R)^{13} \qquad (1)$$

for the model parameters $A_s(R_0) = -4.058(2)$ MHz at $R_0 = 2.37$ Å, $K_s = a = -4.1(1)\ (e\text{Å})^{-1}$, and $K_s'/A_s(R_0) = A = 25(3)\ (e\text{Å})^{-1}$ [10]. On the basis of these data, we find that $A_s \leq 2.1$ MHz; i.e., the constant under consideration has the positive sign. Note that we modified relationship (3) obtained in [1], because our last calculations of isotropic contributions based on theoretical estimates of the dipole moments R and d for the nearest ligands of impurity centers with different symmetries in crystals having a CaF_2-type structure [10] demonstrated that the radial dependence is given by a single-power function and expression (1) adequately describes all the measured isotropic constants.

The result obtained allows us to make the inference that the positive sign of the constant A_s is associated with the large contribution of the positive spin density at the fluorine nucleus due to the overlap of the electron shells of the anion and the excited states of the impurity center. For example, the electron density arises at the 5*d* orbital due to the mixing with the 4*f* and 5*p* states by a strong negative (with respect to the direction of the Gd^{3+}–^{19}F bond) odd electric field. This field is antiparallel to the bond in the T_1 center and is one order of magnitude stronger than that in the fluorine trigonal center [1]. Undeniably, this effect enhances the state mixing proportional to matrix elements of the $\langle 4f, 5p|D|5d\rangle$ type. The contribution made to the constant A_s by the polarization of the ^{19}F ion turns out also to be negative and considerably smaller than those in other MeF$_2$ crystals [1, 9–11].

According to the data obtained in [8] for the hyperfine interaction of $^{157}Gd^{3+}$ ions, these ions are characterized by the isotropic hyperfine constant $A(s) = 9.505(8)$ MHz. It is well known that this constant for impurity centers of the iron group depends heavily on the number of the nearest ligands and their type [12]. A similar regularity is observed for $^{155}Gd^{3+}$ and $^{157}Gd^{3+}$ ions in different materials [13]. The smallest constant $A(s) = 8.3$ MHz was determined for $^{157}Gd^{3+}$ in ZnO, in which the impurity centers are surrounded by four O^{2-} ions [14]. This constant is close to that obtained in the present work. Therefore, by ignoring the radial dependence of the constant $A(s)$ due to a change in the covalence parameters and the degree of overlap of the electronic states of impurity centers and ligands in isostructural crystals, the analysis of the data available in the literature [11, 13, 14] within the model proposed in [12] enables us to argue that, compared to ZnO, the degree of covalence of the complex studied in the present work is lower, if for no other reason than the presence of an additional F^- ion, which results in an increase in $A(s)$. Hence, it is clear that the number of nearest O^{2-} anions in the T_1 center satisfies the condition $4 < n < 6$. Consequently, there exists a sole variant with $n = 5$ and, according to the ENDOR data, the ^{19}F ion is the ligand nearest to the impurity center. Therefore, the coordination of the T_1 trigonal $^{157}Gd^{3+}$ center in CaF_2 is once again confirmed.

3. CONCLUSIONS

Thus, the results obtained in this work can be summarized as follows.

(1) Ligand ENDOR investigations of T_1 trigonal $^{157}Gd^{3+}$ centers in CaF_2 revealed that the second and more distant anion shells are composed of fluorine ions and the nearest environment of impurity centers contains only one ^{19}F ion.

(2) The LHFI constants and the spherical coordinates of distant fluorine nuclei were determined reasoning from the fact that the ligand hyperfine interaction is described as the interaction of two magnetic point dipoles.

(3) The analysis of the ligand displacements showed that the complex as a whole, including distant ^{19}F ions (up to the third anion shell), is displaced in the direction positive with respect to the Z axis, even though the displacements of ^{19}F ions decrease with an increase in the distance to the impurity center and O^{2-} ions.

(4) A comparison of the experimental and calculated anisotropic constants A_s for the ^{19}F ion nearest to the center demonstrated that the change in the sign of the constant A_s is predominantly associated with the mixing of electronic states of the impurity center due to its polarization by a negative odd electric field induced by the environment.

(5) The small value of the constant $A(s)$ for $^{157}Gd^{3+}$ ions in T_1 centers was explained by the decrease in the number of nearest ligands. This constant can be predicted with a high accuracy when $^{157}Gd^{3+}F^-O_4^{2-}$ complexes are formed in crystals.

REFERENCES

1. A. D. Gorlov, V. B. Guseva, A. P. Potapov, and A. I. Rokeakh, Fiz. Tverd. Tela (St. Petersburg) **43** (3), 456 (2001) [Phys. Solid State **43**, 473 (2001)].
2. T. Rs. Reddy, E. R. Davis, J. M. Baker, D. H. Chambers, R. C. Newman, and B. Osbay, Phys. Lett. A **36** (3), 231 (1971).

3. I. V. Stepanov and P. P. Feofilov, Dokl. Akad. Nauk SSSR **108** (4), 615 (1956).
4. A. A. Antipin, in *Paramagnetic Resonance* (Kazan. Gos. Univ., Kazan, 1969), No. 5, pp. 74–100 [in Russian]; F. Z. Gil'fanov and A. L. Stolov, in *Paramagnetic Resonance* (Kazan. Gos. Univ., Kazan, 1970), No. 6, pp. 56–100 [in Russian].
5. J. Sierro, J. Chem. Phys. **34** (6), 2183 (1961).
6. Chi-Chung Yang, Sook Lee, and A. J. Bevolo, Phys. Rev. B **12** (11), 4887 (1975).
7. B. G. Berulava, R. I. Mirianashvili, O. V. Nazarova, and T. I. Sanadze, Fiz. Tverd. Tela (Leningrad) **19** (6), 1771 (1977) [Sov. Phys. Solid State **19**, 1033 (1977)].
8. A. D. Gorlov, A. P. Potapov, and L. I. Levin, Fiz. Tverd. Tela (St. Petersburg) **34** (10), 3179 (1992) [Sov. Phys. Solid State **34**, 1701 (1992)].
9. J. M. Baker, J. Phys. C: Solid State Phys. **12** (19), 4039 (1979).
10. A. D. Gorlov, Yu. V. Leskova, A. E. Nikiforov, and V. A. Chernyshev, Fiz. Tverd. Tela (St. Petersburg) (in press).
11. A. D. Gorlov, V. B. Guseva, A. Yu. Zakharov, A. E. Nikiforov, A. I. Rokeakh, V. A. Chernyshov, and S. Yu. Shashkin, Fiz. Tverd. Tela (St. Petersburg) **40** (12), 2172 (1998) [Phys. Solid State **40**, 1969 (1998)]; A. D. Gorlov, A. P. Potapov, V. I. Levin, and V. A. Ulanov, Fiz. Tverd. Tela (Leningrad) **33** (5), 1422 (1991) [Sov. Phys. Solid State **33**, 801 (1991)].
12. E. Simanek and K. A. Muller, J. Phys. Chem. Solids **31** (5), 1027 (1970).
13. D. van Ormondt, K. V. Reddy, and M. A. van Ast, J. Magn. Reson. **37** (1), 195 (1980).
14. A. Hausmann, Solid State Commun. **7** (8), 579 (1969).

Translated by O. Borovik-Romanova

Physics of the Solid State, Vol. 46, No. 11, 2004, pp. 2035–2041. Translated from Fizika Tverdogo Tela, Vol. 46, No. 11, 2004, pp. 1968–1974.
Original Russian Text Copyright © 2004 by Malygin.

DEFECTS, DISLOCATIONS, AND PHYSICS OF STRENGTH

Analysis of the Parameters of a Submicron Dislocation Structure in Metals Subjected to Severe Plastic Deformation

G. A. Malygin
Ioffe Physicotechnical Institute, Russian Academy of Sciences,
Politekhnicheskaya ul. 26, St. Petersburg, 194021 Russia
e-mail: malygin.ga@mail.ioffe.ru

Received March 9, 2004

Abstract—Equations of dislocation kinetics are used to quantitatively compare the mechanisms of formation and evolution (with deformation) of cellular dislocation structures at moderate strains and of submicron block dislocation structures at high plastic strains. In both cases, the formation of nonuniform dislocation structures is a result of dislocation self-organization, more specifically, the self-organization of statistically random dislocations during the formation of cellular structures and the self-organization of geometrically necessary dislocations (which appear due to the nonuniform character of plastic deformation on the micron scale) during the formation of block structures. *© 2004 MAIK "Nauka/Interperiodica".*

1. INTRODUCTION

The mechanisms of strain hardening and evolution of a dislocation structure in metals subjected to severe plastic deformation are being extensively studied experimentally [1–5] and theoretically [6–10]. This problem is of interest because severe plastic deformation by, e.g., equal-channel angular pressing [3] produces ultrafine-grained materials (with nano- or submicrograins) that have a higher strength than the respective coarse-grained materials. These features result from the formation of a block (fragmented) dislocation structure with high (>1°) misorientation angles between neighboring fragments (blocks) in a material at shear strains $\gamma > 0.5$.

There exist a number of assumptions and hypotheses regarding the causes of the high strength of severely deformed metals. They can be divided into three groups. One group contains hypotheses that the high strength σ of a material after its severe plastic deformation is caused by the small size Λ and high misorientation angle ω of crystal fragments according to the Hall–Petch relation $\sigma \sim \Lambda^{-1/2}$ [2]. This mechanism is supported by the fact that severe deformations ($\gamma > 10$–20) result in a subgrain structure with mean misorientation angles of ≈45° between crystal fragments [11, 12]. Another group of hypotheses assumes that the high strength of severely deformed materials is related to high internal stresses due to the nonequilibrium boundaries of highly misoriented fragments [7, 13, 14]. Finally, according to the third group of hypotheses, a high strength after severe plastic deformation is caused by strain hardening of the material, that is, by the high density of dislocations ($\approx 10^{15}$–10^{16} m^{-2}), which are mainly concentrated in fragment boundaries [6, 9, 10].

Another frame of questions that are being discussed now is the mechanism of formation of block dislocation structures in a severely deformed material. As for cellular dislocation structures, their formation is known to be related to the process of self-organization of dislocations in a deformed crystal [15]. This circumstance explains why cellular structures change self-similarly, by retaining the relations between their parameters [2, 10, 15] and the character (law) of the statistical size and misorientation-angle distributions of cells (scaling of cellular structures [4, 5]). There are a number of experimental facts indicating that strongly misoriented (to at least $\omega < 15°$–$30°$) block structures are also formed due to the self-organization of dislocations. This hypothesis is confirmed by the fact that such structures obey the laws of self-similarity [2, 10, 16] and scaling [2, 4, 5].

In this work, we continue the comparison of the mechanisms of formation of cellular and block dislocation structures and of their parameters that was started in [9, 10, 16]. In those studies, we assumed that the additional hardening induced by severe plastic deformation and the appearance of the fourth and fifth strengthening stages in the stress–strain curves of fcc metals were caused by the generation of geometrically necessary dislocations (GNDs) due to nonuniform plastic deformation at a microscopic level and by the formation of block boundaries from GNDs. In Section 2, we analyze data on the evolution of the dislocation-cell (block) size with strain. In Section 3, we perform a similar analysis for the evolution of the misorientation angles of cells and blocks with strain. In Section 4, we discuss the possible causes of the low annihilation coefficients of geometrically necessary dislocations as compared to those of statistically random dislocations, which are involved in the formation of cellular dislocation structures and are responsible for the appearance of

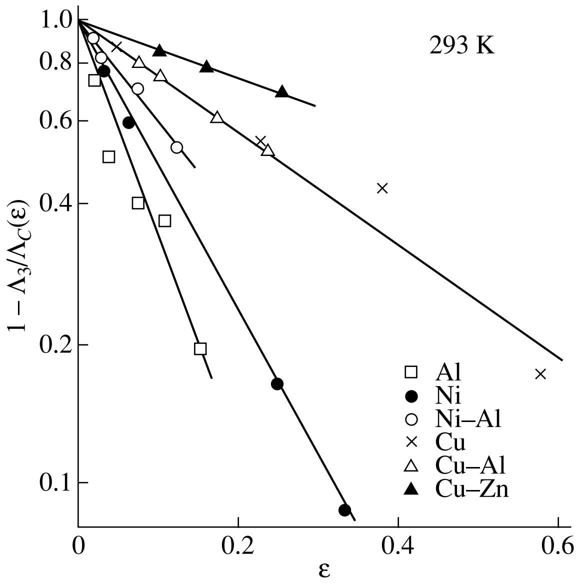

Fig. 1. Strain dependence of the dislocation-cell size Λ_C according to Eq. (6) in Al [19], Ni [20], Cu [21], and in Ni–Al, Cu–Al, and Cu–Zn alloys [22].

the second and third stages in the stress–strain curves of fcc metals. In the final section, we discuss the formation of dislocation block structures and the related strain hardening.

2. EVOLUTION OF THE DISLOCATION-CELL AND DISLOCATION-BLOCK SIZES WITH STRAIN

According to the two-phase model [9, 16], the total dislocation density ρ in a crystal subjected to plastic deformation in the range from the second to the fifth stage in a stress–strain curve is the sum of the densities of statistically random (ρ_C) and geometrically necessary (ρ_B) dislocations concentrated in dislocation-cell and dislocation-block boundaries, respectively:

$$\rho(\gamma) = f_C\rho_C(\gamma) + f_B\rho_B(\gamma), \tag{1}$$

where γ is the shear strain; $f_C = \Delta\Lambda_C(\gamma)/\Lambda_C(\gamma)$ and $f_B = \Delta\Lambda_B(\gamma)/\Lambda_B(\gamma)$ are the strain-independent volume fractions of cell and block boundaries, respectively, in the dislocation structure [2, 10]; $\Delta\Lambda_C$ and $\Delta\Lambda_B$ are the widths of the cell and block boundaries, respectively; and Λ_C and Λ_B are the cell and block sizes, respectively. The dislocation density (1) defines the flow stress

$$\tau(\gamma) = \alpha\mu b\rho^{1/2}(\gamma), \tag{2}$$

where α is the dislocation interaction constant, μ is the shear modulus, and b is the Burgers vector. The stress (2) corresponds to the square law of summation of flow stresses:

$$\tau(\gamma) = [\tau_C^2(\gamma) + \tau_B^2(\gamma)]^{1/2}, \tag{3}$$

where $\tau_C(\gamma) = \alpha_C\mu b\rho_C^{1/2}(\gamma)$ and $\tau_B(\gamma) = \alpha_B\mu b\rho_B^{1/2}(\gamma)$ are the contributions of the cell and block boundaries to the total flow stress, respectively; $\alpha_C = \alpha f_C^{1/2}$; and $\alpha_B = \alpha f_B^{1/2}$. The square law of summation is known to define the flow stress in the presence of dislocation-motion obstacles having strongly different strengths. In the case under analysis, block boundaries are stronger obstacles for dislocations than cell boundaries.

The dislocation density in dislocation-cell boundaries increases with strain according to the law [15]

$$\rho_C(\gamma) = \left(\frac{5}{6}\right)^2\rho_S(\gamma) = \rho_3\left[1 - \exp\left(-\frac{1}{2}k_a\gamma\right)\right]^2,$$

$$\rho_3 = \left(\frac{6}{5}\right)^2\left(\frac{k_f}{k_a}\right)^2, \tag{4}$$

where ρ_3 is the equilibrium dislocation density in cell boundaries at the end of the third stage in the strain-hardening curve (the first stage of dynamic recovery). This density depends on the coefficient k_f (which determines the intensity of dislocation multiplication by forest dislocations) and the coefficient of annihilation of the screw segments of dislocation loops k_a according to the kinetic equation for the dislocation density at the second and third stages of the strain-hardening curve [17]:

$$\frac{d\rho_S}{d\gamma} = k_f\rho_S^{1/2} - k_a\rho_S. \tag{5}$$

By solving Eq. (5), we obtain the law of evolution of the dislocation density with strain given by Eq. (4). The additional factor $(6/5)^2$ is the result of the self-organization of dislocations during the formation of a cellular dislocation structure [15]. Since $bk_f \approx 10^{-2}$ and $k_a \approx 4$–8 at 293 K [15], the dislocation density at the end of the third stage is $\rho_3 \approx 10^{13}$–10^{14} m^{-2}.

According to the principle of similitude of cellular dislocation structures, the cell size and dislocation density at different strains are connected by the relation $\Lambda_C(\gamma) = K_2\rho_S^{-1/2}(\gamma)$, where $K_2 \approx 8$–10 is a certain scale factor [18]. Thus, taking into account Eq. (4), we have

$$\Lambda_C(\gamma) = \frac{\Lambda_3}{1 - \exp\left(-\frac{1}{2}k_a\gamma\right)}, \tag{6}$$

where $\Lambda_3 = K_2\rho_S^{-1/2} \approx 1$–2 μm is the cell size at the end of the third stage. Figure 1 shows the results of processing the experimental $\Lambda_C(\varepsilon)$ dependences for Al [19], Ni [20], and Cu [21] metals and Ni–2% Al, Cu–2.8% Al, and Cu–10% Zn [22] alloys in the $\log(1 - \Lambda_3/\Lambda_C(\varepsilon))$ versus ε coordinates using Eq. (6), where $\varepsilon = \gamma/m$ is the tensile strain and $m \approx 3$ is the Taylor factor for polycrystals. The experimental points in these coordinates are seen to fall on straight lines, whose slopes increase with the dislocation annihilation coefficient k_a. In the case of fcc metals, this coefficient increases with the stacking fault energy γ_D [15], which is confirmed by the data from Fig. 1. For Al, Ni, and the Ni–Al alloy, γ_D = 140–180 mJ m^{-2}, whereas for Cu and the Cu–Al and Cu–Zn alloys we have γ_D = 20–60 mJ m^{-2}. Table 1 shows the parameters of evolution of the dislocation-cell size with strain for the metals under analysis. The strain $\varepsilon_3 = 2/mk_a$ characterizes the duration of the third stage of strain hardening (the first stage of dynamic recovery).

Geometrically necessary dislocations differ from statistically random dislocations in their source, since they appear as a result of elastic-stress relaxation associated with nonuniform plastic deformation at the micron level (at the level of the dislocation-cell size in the case under study) [23]. Another difference from statistically random dislocations consists in the fact that dislocations of the same sign and the same orientation of the Burgers vector with respect to the dislocation line are predominantly generated in certain local regions. As for the other features (participation in the processes of multiplication and annihilation), the geometrically necessary dislocations are qualitatively similar to statistically random dislocations. This behavior allows us to write the following kinetic equation for the density of GNDs [10]:

$$\frac{d\rho_G}{d\gamma} = \frac{2(1-\beta_i)}{b\Lambda_C(\gamma)} + k_4\rho_G^{1/2} - k_5\rho_G, \qquad (7)$$

where β_i is the coefficient of immobilization of dislocations at obstacles, which exclude dislocations from the processes of multiplication by forest dislocations (the second term in the right-hand side of Eq. (7)) and of annihilation (the third term). According to Eq. (7), at the end of the third stage of strain hardening (at $\beta_i = 0.9$, $b = 0.25$ nm, $\Lambda_3 = 1$ μm, $\gamma_3 = 0.5$), the density of GNDs is equal to $\rho_G = [2(1-\beta_i)/b\Lambda_3]\gamma_3 \approx 4 \times 10^{14}$ m^{-2} and becomes comparable to the density of statistically random dislocations. As a result, the additional forth and fifth hardening stages appear in the strain-hardening curve at high strains ($\gamma > \gamma_3$).

The GND density in dislocation-block boundaries increases with strain according to the following law [10] (which is analogous to Eq. (4)):

$$\rho_B(\gamma) = \left(\frac{6}{5}\right)^2\rho_G(\gamma) = \rho_5\left[1-\exp\left(-\frac{1}{2}k_5\gamma\right)\right]^2, \qquad (8)$$
$$\rho_5 = \left(\frac{6}{5}\right)^2\left(\frac{k_4}{k_5}\right)^2,$$

where ρ_5 is the dislocation density at the end of the fifth strain-hardening stage (the second stage of dynamic recovery). According to the principle of similitude of block dislocation structures $\Lambda_B = K_2/\rho_G^{1/2}$, the evolution of the block size with strain should be described by the following formula, similar to Eq. (6):

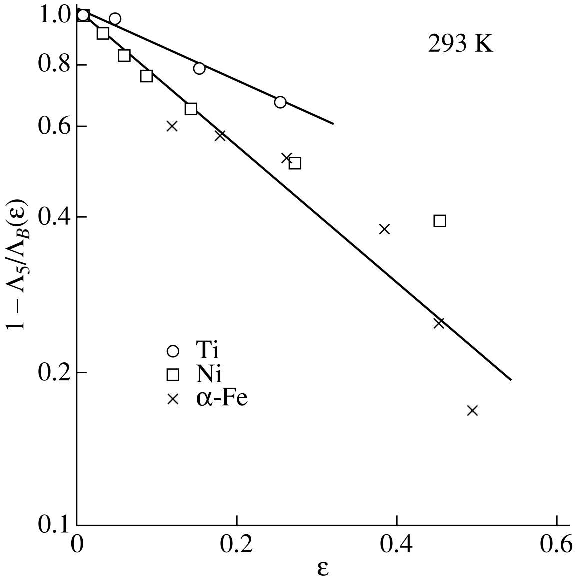

Fig. 2. Strain dependence of the dislocation-block size Λ_B according to Eq. (9) in Ni [2], Ti [24], and α-Fe [25].

$$\Lambda_B(\gamma) = \frac{\Lambda_5}{1-\exp\left(-\frac{1}{2}k_5\gamma\right)}, \qquad (9)$$

where $\Lambda_5 = K_2/\rho_5^{1/2}$ is the equilibrium block size at the end of the fifth hardening stage. Figures 2 and 3 show the results of processing the experimental $\Lambda_B(\varepsilon)$ dependences for Ni [2], Ti [24], α-Fe [25] and the Al–0.13% Mg and Al–1.3% Fe alloys [3] in the $\log(1 - \Lambda_5/\Lambda_B(\varepsilon))$ versus ε coordinates by using Eq. (9). It is seen that, despite the scatter of the experimental data, especially at high strains (Fig. 2), Eq. (9) agrees with experiment.

The steplike character of Eq. (9) plotted for the Al–Mg alloy in Fig. 3 is likely to be related to the fact that magnesium atoms strongly pin dislocations in aluminum in the temperature range 200–350 K as a result of dynamic strain aging, which causes a delay in the for-

Table 1. Parameters of the evolution of the dislocation-cell size with strain

Metal	Reference	Λ_3, μm	$\varepsilon_3 = 2/mk_a$	k_a
Al 99.995%	[19]	1.6	0.10	6.7
Ni	[20]	0.14	0.15	4.5
Ni–2%Al	[22]	0.14	0.20	3.3
Cu	[21]	0.14	0.36	1.8
Cu–2.8%Al	[22]	0.14	0.36	1.8
Cu–10%Zn	[22]	0.12	0.83	0.8

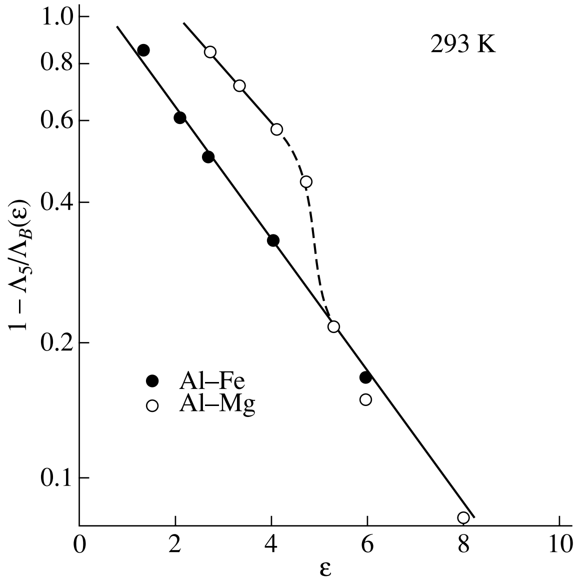

Fig. 3. Strain dependence of the dislocation-block size Λ_B according to Eq. (9) in Al–Mg and Al–Fe alloys [3].

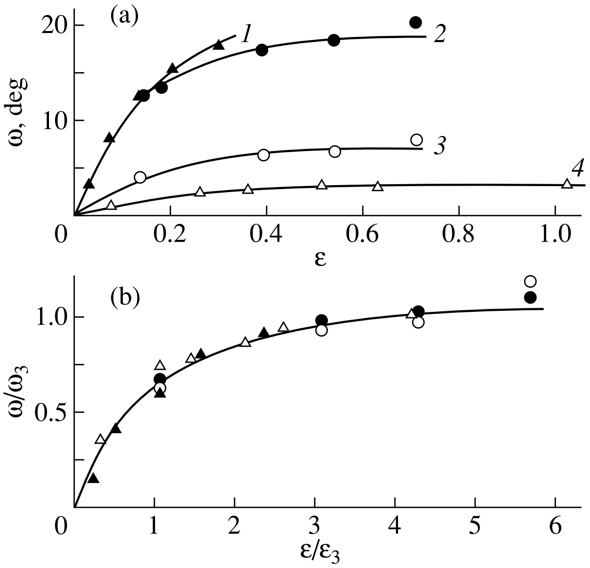

Fig. 4. (a) Strain dependence of the misorientation angle of dislocation cells ω_C for (*1*) Al 99.995% [26], (*2*, *3*) Al 99.9% [27], and (*4*) Ni_3Fe [11]. (b) The same dependence plotted in dimensionless variables using Eq. (10).

mation of both cellular and block dislocation structures [3]. This delay is small in the case of the Al–Fe alloy, since iron atoms interact weakly with dislocations in aluminum and form Al_3Fe precipitates approximately 2 μm in size in the aluminum matrix [3]. Table 2 gives the parameters of the evolution of a block structure with strain in the metals and alloys in question. A comparison of the dislocation annihilation coefficients given in Tables 1 and 2 indicates that the effective annihilation coefficient for GNDs (k_5) is about an order of magnitude lower than that for statistically random dislocations (k_a) (Table 2, last column). The possible causes of this difference are discussed in Section 4.

3. EVOLUTION OF THE MISORIENTATION ANGLES OF DISLOCATION CELLS AND BLOCKS WITH STRAIN

Analysis of the experimental data shows that the mean dislocation-cell size Λ_C and the mean misorientation angle ω_C are connected by the relation $\Lambda_C(\gamma)\omega_C(\gamma) = \text{const}$ [2, 10, 16], which means that the cell size varies with strain as $\omega_C = K_3 b\rho_S^{1/2}$ or

$$\omega_C(\varepsilon) = \omega_3\left[1-\exp\left(-\frac{1}{2}k_a m\varepsilon\right)\right], \qquad (10)$$

where $\omega_3 = K_3 b\rho_3^{1/2}$ is the equilibrium misorientation angle of cells at the end of the third hardening stage, K_3 is a certain constant, and $\varepsilon = \gamma/m$. Figure 4a shows experimental strain dependences of the misorientation angle of cells in aluminum of different purity [25, 26] and in a Ni_3Fe alloy [11]. Curves *2* and *3* correspond to the maximum and average misorientation angles of cells in Al, respectively [26]. Figure 4b shows the results of processing these dependences in terms of dimensionless variables according to Eq. (10). The calculated (solid) curve is seen to agree with the experimental data. Table 3 gives the values of the parameters ω_3, ε_3, and k_a that control the evolution of the average misorientation angle of dislocation cells with strain in the metals under study.

Table 2. Parameters of the evolution of the dislocation-block size with strain

Metal	Reference	Λ_5, μm	$\varepsilon_5 = 2/mk_5$	k_5	$\beta = k_5/k_a$
Ni 99.99%	[2]	0.1	3.1	0.21	0.05
α-Fe	[25]	0.1	3.1	0.21	–
Ti	[24]	0.32	6.25	0.11	–
Al–0.13%Mg	[3]	0.42	3.0	0.22	0.03
Al–1.3%Fe	[3]	0.40	3.0	0.22	0.03

Experimental data regarding the evolution of the misorientation angle of dislocation blocks with strain in Ni [2], Al [28], and α-Fe [25] are shown in Fig. 5a. For blocks, in a first approximation, the relation $\Lambda_B(\gamma)\omega_B(\gamma) = \text{const}$ between the mean block size and the mean misorientation angle holds true [10, 16]. Therefore, the evolution of the angle ω_B with strain should be described by a relation similar to Eq. (10):

$$\omega_B(\varepsilon) = \omega_5\left[1-\exp\left(-\frac{1}{2}k_5 m\varepsilon\right)\right], \qquad (11)$$

where $\omega_5 = K_3 b\rho_5^{1/2}$ is the equilibrium misorientation angle of blocks at the end of the fifth hardening stage. Figure 5b illustrates the results of processing the experimental data from Fig. 5a by using Eq. (11). It is seen that, apart from the two experimental points corresponding to the highest strains, the points fall on the calculated (solid) curve. Table 4 lists the values of the parameters ω_5, ε_5, and k_5 that control the evolution of the mean misorientation angle of dislocation blocks with strain in the metals under study. As is the case with the block sizes (Table 2), the dislocation annihilation coefficient k_5 at high strains is an order of magnitude smaller than the dislocation annihilation coefficient k_a in the third stage of the strain-hardening curve.

4. ANNIHILATION OF GEOMETRICALLY NECESSARY DISLOCATIONS

There can be several causes of the fact that the dislocation annihilation coefficient at high strains (k_5) is an order of magnitude smaller than the dislocation annihilation coefficient k_a in the third stage of the strain-hardening curve (the first stage of dynamic recovery).

In writing kinetic equations (5) and (7), we assumed that the densities of dislocations of opposite sign in the crystal are the same. This is true for the case of statistically random dislocations in the second and third stages. However, the situation is different in the case of geometrically necessary dislocations: in local regions, dislocations of one sign dominate over dislocations of the other sign. As a consequence, dislocation blocks where sign-uncompensated dislocations are concentrated become strongly misoriented. In the case where dislocations of one sign dominate, the effective dislocation annihilation coefficient that controls the second stage of dynamic recovery (the fifth stage of strain hardening) is obviously smaller than that in the third hardening stage. If we assume that the ratio of the densities of positive and negative dislocations at large strains is constant ($\beta = \rho_-/\rho_+ = \text{const}$) [10], then, taking into account the experimental values of β (Tables 2, 4), we can conclude that the relative fraction of dislocations of opposite sign does not exceed ten percent at the given strains.

The low values of the annihilation coefficient of GNDs can also be related to the physical mechanism of dislocation annihilation that controls the dynamic recovery of a plastically deformed metal at low and moderate temperatures. According to [29, 30], the effective annihilation coefficient of screw dislocations during dynamic recovery is specified by the formula

$$k_a = \frac{\omega_s^{5/2}}{2\pi^2 p\alpha}\left(\frac{\mu}{\tau_c}\right), \tag{12}$$

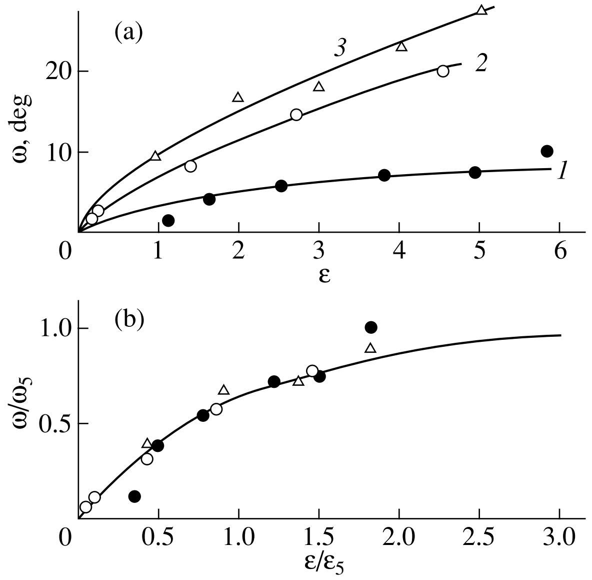

Fig. 5. (a) Strain dependence of the misorientation angle of dislocation blocks ω_B for (*1*) α-Fe [25], (*2*) Ni [2], and (*3*) Al [28]. (b) The same dependence plotted in dimensionless variables using Eq. (11).

where ω_s is the fraction of screw segments in expanding dislocation loops, p is the number of operating slip systems, and τ_c is the friction stress, which determines the critical distance for the spontaneous annihilation of screw dislocations of opposite sign. In the case of bcc metals at temperatures $T < 0.15T_m$, the friction stress corresponds to the Peierls stress [30].

For fcc metals, the stress τ_c is the stress τ_{III} that is required for a screw dislocation to go from the slip

Table 3. Parameters of the evolution of the misorientation angle of dislocation cells with strain

Metal	Reference	ω_3, deg	$\varepsilon_3 = 2/mk_a$	k_a
Al 99.995%	[26]	20.0	0.125	5.3
Al 99.9% (Fig. 4a)	[27]			
Curve *2*		18.3	0.125	5.3
Curve *3*		6.7	0.125	5.3
Ni_3Fe	[11]	3.25	0.24	2.8

Table 4. Parameters of the evolution of the misorientation angle of dislocation blocks with strain

Metal	Reference	ω_5, deg	ε_5	k_5	$\beta = k_5/k_a$
Ni 99.99%	[2]	26	3.3	0.21	0.08
α-Fe	[25]	10	3.2	0.22	–
Al 99%	[28]	25	2.2	0.3	0.06

plane to the plane of cross slip to meet a screw dislocation of the opposite sign [31]:

$$\tau_{III}(T) = \tau_{III}(0)\exp\left(-\frac{kT}{A}\ln\frac{\dot{\gamma}_0}{\dot{\gamma}}\right), \tag{13}$$

where $\tau_{III}(0)$ is the stress τ_{III} at $T = 0$, A is a parameter dependent on the stacking fault energy, $\dot{\gamma}$ is the plastic-strain rate, $\dot{\gamma}_0$ is the preexponential factor, and k is the Boltzmann constant. By substituting Eq. (13) into Eq. (12), we obtain the temperature–rate dependence of the annihilation coefficient of screw dislocations:

$$k_a(T) = k_a(0)\exp\left(\frac{kT}{A}\ln\frac{\dot{\gamma}_0}{\dot{\gamma}}\right),$$
$$k_a(0) = \frac{\omega_s^{5/2}}{2\pi^2 p\alpha}\left(\frac{\mu}{\tau_{III}(0)}\right). \tag{14}$$

Analysis of the experimental data indicates [10, 16] that the ratio of the dislocation annihilation coefficients in the first and second stages of dynamic recovery (k_5/k_a) is temperature-independent. This means that the lower values of the annihilation coefficient of GNDs $k_5 = \beta k_a$ (as compared to the annihilation coefficient of statistically random dislocations k_a) are related to the preexponential factor $k_5(0) = \beta k_a(0)$, i.e., to the parameters ω_s, α, p, and $\tau_{III}(0)$ in the second formula in Eqs. (14).

Since the dislocation interaction constant α decreases at high dislocation densities, it cannot be a factor that decreases the parameter $k_5(0)$. The estimations made in [31] show that $\tau_{III}(0) \approx 0.1\mu/n$, where $n \approx$ 20–30 is the number of screw dislocations required in a pileup to activate the cross slip of the leading dislocation of the pileup. Since $k_a(0) \sim n$, the decrease in the number of dislocations in pileups in a nano- or submicrometer (subgrain) dislocation structure at high strains can substantially decrease the probability of GND annihilation. It is also known that, at high strains, the number of operating slip systems p increases; according to the second relation in Eq. (14), this increase should also cause the annihilation coefficient of geometrically necessary dislocations to decrease. Finally, if elastic lattice bends dominate over elastic lattice rotations during microscopically nonuniform plastic deformation, the fraction of screw segments in dislocation loops ω_s will decrease, which, according to Eqs. (14), should additionally decrease the annihilation coefficient of GNDs.

5. DISCUSSION OF THE RESULTS

In conclusion, we will discuss a number of the specific features of the formation of block dislocation structures and the related strain hardening. Block structures are secondary formations; they appear after (and as a result of) the formation of a cellular dislocation structure in a material. This circumstance explains why the strain hardening due to the formation of block structures becomes noticeable only at sufficiently high strains. As was shown above and in [10, 16], this hardening is related to the high GND density in block boundaries. Such discrete dislocation boundaries can be boundaries with misorientation angles of less than 15°–30°.

The contribution of block boundaries with misorientation angles above 30° to the strain hardening of a severely deformed material is less understood. If the blocks are submicron subgrains with equilibrium boundaries, it is natural to assume that their contribution to the hardening of a severely deformed material is described by the Hall–Petch relation $\sigma \sim \Lambda_B^{-1/2}$, as has been assumed by many authors. However, the Hall–Petch hardening is known to control not only the initial deformation stage (the yield strength), but also to affect (intensify) the strain hardening of a polycrystalline material. However, experiments show that, at shear strains $\gamma > 5$, the strain hardening of a material ceases to occur and the flow stress and microhardness reach saturation [1, 3, 32]. This means that, at such strains, there exists a dynamic equilibrium between the processes of dislocation multiplication and annihilation (hardening and recovery, respectively). Since dislocations are concentrated in the boundaries of strongly misoriented blocks, dynamic equilibrium exists in them as well.

Under this equilibrium, however, the boundaries do not become equilibrium in the thermodynamic sense, as is the case after high-temperature annealing. The presence of sufficiently high local stresses near block boundaries [14] indicates their disordering. The spatial disordering of the boundaries manifests itself in the fact that, in terms of dislocations, they behave as dislocation obstacles with a dislocation density that is higher than that in cell boundaries. This circumstance can explain why the flow stress of a material at high strains is determined by the relation $\sigma \sim \Lambda_B^{-1}$ [25, 32] (as in the case of dislocation-cell boundaries) rather than by the Hall–Petch relation.

However, if a material with a submicron dislocation structure is annealed to remove an excess dislocation density, to order block boundaries, and to subject them to partial recrystallization, then, during plastic deformation, the annealed material with a submicron or micron structure undergoes strong strain hardening and its yield strength (the stress at the initial deformation stage) varies with grain size according to the Hall–Petch law [33].

REFERENCES

1. M. Zehebetbauer and V. Seumer, Acta Metall. Mater. **41** (2), 577 (1993).
2. D. A. Hughes and N. Hansen, Acta Metall. Mater. **48** (11), 2958 (2000).
3. P. J. Apps, J. R. Bowen, and P. B. Prangnell, Acta Mater. **51** (10), 2811 (2003).

4. D. A. Hughes, Q. Liu, D. C. Chrzan, and N. Hansen, Acta Metall. Mater. **45** (1), 105 (1997).
5. D. A. Hughes, Scr. Mater. **47** (10), 697 (2002).
6. Y. Estrin, L. S. Toth, A. Molinari, and Y. Brechet, Acta Mater. **46** (15), 5509 (1998).
7. M. Seefeldt, Rev. Adv. Mater. Sci. **2** (1), 44 (2001).
8. N. Hansen and D. Kuhlmann-Wilsdorf, Mater. Sci. Eng. **81** (1/2), 141 (1986).
9. G. A. Malygin, Fiz. Tverd. Tela (St. Petersburg) **43** (10), 1832 (2001) [Phys. Solid State **43**, 1909 (2001)].
10. G. A. Malygin, Fiz. Tverd. Tela (St. Petersburg) **44** (11), 1979 (2002) [Phys. Solid State **44**, 2072 (2002)].
11. V. V. Rybin, *Large Plastic Deformations and Fracture of Metals* (Metallurgiya, Moscow, 1986) [in Russian].
12. A. P. Zhilyaev, G. V. Nurislamova, B. K. Kim, *et al.*, Acta Mater. **51** (3), 753 (2003).
13. N. A. Koneva and É. V. Kozlov, Izv. Vyssh. Uchebn. Zaved., Fiz. **33** (2), 89 (1990).
14. A. A. Popov, I. Yu. Pyshmintsev, R. Z. Valiev, *et al.*, Scr. Metall. Mater. **37** (7), 1089 (1997).
15. G. A. Malygin, Usp. Fiz. Nauk **169** (6), 979 (1999) [Phys. Usp. **42**, 887 (1999)].
16. G. A. Malygin, in *Problems in Materials Technology* (Prometeĭ, St. Petersburg, 2003), No. 1(33), p. 278 [in Russian].
17. U. F. Kocks, J. Eng. Mater. Technol. **98** (1), 76 (1976).
18. F. Prinz and A. S. Argon, Phys. Status Solidi A **57** (2), 741 (1980).
19. T. Tabata, S. Yamanaka, and H. Fujita, Acta Metall. **26** (3), 405 (1978).
20. A. S. Rubtsov and V. V. Rybin, Fiz. Met. Metalloved. **44** (3), 611 (1977).
21. I. A. Gindin, Ya. D. Starodubtsev, and V. K. Aksenov, Metallofizika (Kiev) **8** (12), 49 (1980).
22. L. A. Kornienko, G. P. Bakach, and E. F. Dudarev, in *Plastic Deformation of Alloys* (Tomsk. Gos. Univ., Tomsk, 1986), p. 219 [in Russian].
23. J. S. Stölken and A. G. Evans, Acta Mater. **46** (14), 5109 (1998).
24. G. A. Malygin, S. V. Zherebtsov, and S. Yu. Mironov, in *Problems in Materials Technology* (Prometeĭ, St. Petersburg, 2003), No. 1(33), p. 175 [in Russian].
25. G. Langford and M. Cohen, Metall. Trans. A **6** (4), 901 (1975).
26. A. Kelly, Acta Crystallogr. **7** (8/9), 554 (1954).
27. N. Yu. Zolotorevskiĭ, Yu. F. Titovets, and N. Yu. Ermakova, in *Problems in Materials Technology* (Prometeĭ, St. Petersburg, 2002), No. 1(29), p. 290 [in Russian].
28. Q. Liu, X. Huang, D. J. Lloyd, and N. Hansen, Acta Mater. **50** (15), 3789 (2002).
29. L. E. Popov, V. S. Kobytev, and T. A. Kovalevskaya, *Plastic Deformation of Alloys* (Tomsk. Gos. Univ., Tomsk, 1984) [in Russian].
30. G. A. Malygin, Fiz. Tverd. Tela (St. Petersburg) **34** (9), 2882 (1992) [Sov. Phys. Solid State **34**, 1543 (1992)].
31. R. Berner and G. Kronmüller, *Plastische Verformung von Einkristallen* (Springer, Berlin, 1965; Mir, Moscow, 1969).
32. A. Belyakov, T. Sakai, H. Miura, and K. Tsuzaki, Philos. Mag. A **81** (11), 2629 (2001).
33. M. M. Myshlyaev and S. Yu. Mironov, Fiz. Tverd. Tela (St. Petersburg) **44** (4), 711 (2002) [Phys. Solid State **44**, 738 (2002)].

Translated by K. Shakhlevich

Physics of the Solid State, Vol. 46, No. 11, 2004, pp. 2042–2052. Translated from Fizika Tverdogo Tela, Vol. 46, No. 11, 2004, pp. 1975–1985.
Original Russian Text Copyright © 2004 by Gutkin, Ovid'ko, Skiba.

DEFECTS, DISLOCATIONS, AND PHYSICS OF STRENGTH

Emission of Partial Dislocations by Grain Boundaries in Nanocrystalline Metals

M. Yu. Gutkin, I. A. Ovid'ko, and N. V. Skiba

Institute of Problems of Mechanical Engineering, Russian Academy of Sciences,
Vasil'evskiĭ Ostrov, Bol'shoĭ pr. 61, St. Petersburg, 199178 Russia
e-mail: ovidko@def.ipme.ru

Received March 23, 2004

Abstract—A theoretical model is proposed to describe the emission of partial dislocations by grain boundaries in nanocrystalline materials during plastic deformation. Partial dislocations are assumed to be emitted during the motion of grain-boundary disclinations, which are carriers of rotational plastic deformation. The ranges of the parameters of a defect structure in which the emission of partial dislocations by grain boundaries in nanocrystalline metals are energetically favorable are calculated. It is shown that, as the size of a grain decreases, the emission of partial dislocations by its boundary becomes more favorable as compared to the emission of perfect lattice dislocations. *© 2004 MAIK "Nauka/Interperiodica".*

1. INTRODUCTION

The mechanisms of plastic deformation in nanocrystalline materials (NCMs) have been extensively studied (see, e.g., [1–17]). Some NCMs have significantly higher values of yield strength and ultimate strength as compared to their coarse-grained analogs; in addition, they retain high plastic properties [3, 4]. This combination of high mechanical properties of NCMs is mainly caused by the fact that the dislocation activity typical of coarse-grained materials is suppressed in nanograins and other mechanisms of plastic deformation become operative [1, 2, 6–17]. One of such mechanisms is the experimentally observed emission of partial Shockley dislocations by grain boundaries followed by the formation of stacking faults and twins in nanocrystalline aluminum [13–15] and copper [16, 17]. However, the microscopic mechanisms and basic laws of this emission remain unknown. Computer simulations [8–12] and experimental observations [12–17] are insufficient for explaining the characteristic features of this process.

Generally speaking, the emission of both partial and perfect dislocations by grain boundaries is well known [18, 19]. In particular, the emission of partial Shockley dislocations by grain boundaries has been established to account for the heterogeneous nucleation of twin layers and martensitic plates in some fcc metals [18, 20]. In this case, stress concentrators can be lattice dislocations trapped by grain boundaries. Splitting of these dislocations into two partial Shockley dislocations, one of which is retained in the grain boundary and the other glides far into the grain, is the well-known microscopic mechanism of emission of partial dislocations in coarse-grained metals [20]. In NCMs, the density of ordinary lattice dislocations is low; however, grain boundaries, as a rule, have nonequilibrium structures [2, 21–24]. Grain boundaries can pass to a nonequilibrium state due to disordered absorption of lattice dislocations during severe plastic deformation used to produce NCMs [25]. In particular, the nonequilibrium state manifests itself in sharp changes in the misorientation angle of a boundary, which can be described in terms of grain-boundary disclinations [24, 26–28]. Grain-boundary (and junction) disclinations can be stress concentrators and dislocation sources in grain boundaries in NCMs. In our recent studies [29–31], we considered the emission of pairs of perfect lattice dislocations by partial wedge grain-boundary disclinations and showed that this emission causes effective disclination motion and, correspondingly, rotational plastic deformation of NCMs. The emission of partial Shockley dislocations by grain-boundary disclinations was studied in [32–34], as applied to the problem of heterogeneous nucleation of the ε martensite in coarse-grained fcc metals (this nucleation is also sensitive to the stress fields of immobile dislocations [35]).

The purpose of this work is to develop a theoretical model to describe the emission of partial Shockley dislocations by grain-boundary disclinations in nanocrystalline fcc metals. This model is used to calculate and compare the critical stresses for emission of partial and perfect dislocations with allowance made for the orientation (the orientation angles of a slip plane and the disclination dipole arm) and scale (the nanograin size) factors.

2. DISLOCATION EMISSION BY GRAIN BOUNDARIES: MODEL

Let us consider a two-dimensional model of an NCM in which rectilinear positive and negative partial

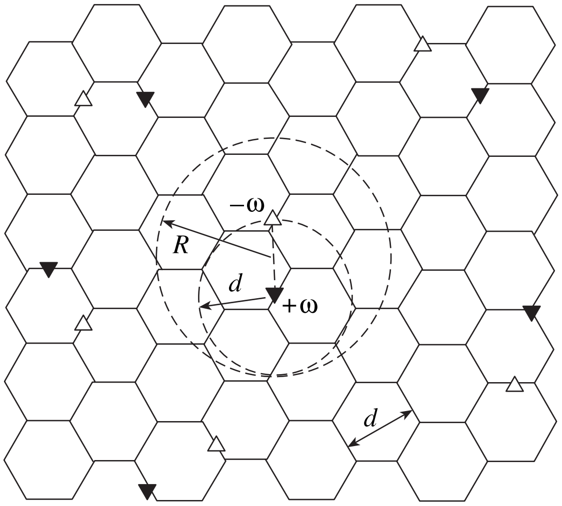

Fig. 1. The model of an NCM having positive and negative wedge disclinations distributed over grain boundaries. The dashed lines show the circular region of radius R where the elastic field of a disclination dipole in a random disclination ensemble of the dipole type is screened and a circle of radius d specifying the possible position of the negative disclination near the positive one.

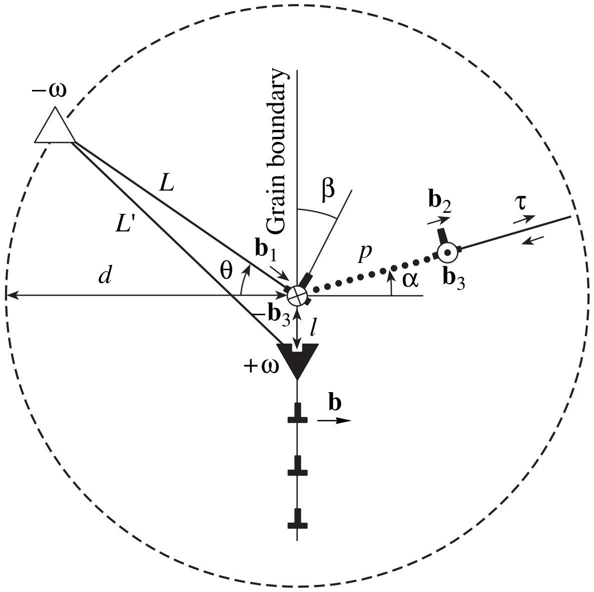

Fig. 2. Emission of a partial Shockley dislocation by a grain boundary when a grain-boundary disclination moves.

wedge disclinations having a mean strength of $+\omega$ and $-\omega$, respectively, are distributed over grain boundaries (Fig. 1). These disclinations simulate sharp changes in the misorientation angles of tilt boundaries, and their density can serve as a measure of equilibrium in the grain-boundary structure of an NCM. In our model, an ensemble of such grain-boundary disclinations consists of individual disclination dipoles; that is, we analyze a nonequilibrium but relatively low-energy disclination structure, each of whose elements (disclination dipoles) has a low-energy self-screened defect configuration. It is assumed that the dipole distribution and orientation are random and that the average distance between dipoles is substantially (several times) greater than the average distance L between disclinations of a dipole (dipole arm). In such an ensemble, in a rough approximation, the effective screening length R of the dipole elastic fields can be half the distance between dipoles (Fig. 1). The length L is assumed to be approximately equal to the nanograin size d.

With these assumptions, we can restrict our analysis to a model of an individual dipole of partial wedge disclinations in considering the emission of a dislocation by a grain-boundary disclination. In the initial state, the positive disclination (with strength ω) of the dipole is assumed to be located in a grain boundary at the center of an imaginary circle with a radius equal to the dipole arm $L = d$. Figure 2 shows the semi-infinite wall of excess edge grain-boundary dislocations (having a Burgers vector $\mathbf{b}$ and a period l) that forms this disclination. The position of the negative disclination in this circle is specified by azimuthal angle θ (Fig. 2). Physically, the negative disclination can be either a grain-boundary or junction disclination [24, 26–28].

Let the positive disclination emit a partial dislocation under the action of an external shear stress τ. The microscopic mechanism of such emission in an fcc crystal can be the splitting of the extreme grain-boundary dislocation with Burgers vector $\mathbf{b}$ in the wall into a partial Shockley dislocation with Burgers vector $\mathbf{b}'_1 = (a/6)[112]$ and a difference grain-boundary dislocation with Burgers vector $(\mathbf{b} - \mathbf{b}'_1)$, with the $\mathbf{b}'_1$ dislocation gliding deep into the grain. This process can be described as displacement of the positive disclination through a distance l (Fig. 2). As a result of the splitting, a new defect structure forms; it consists of a disclination dipole having an arm L', an edge difference dislocation with Burgers vector $\mathbf{b}_1$, a partial edge dislocation with Burgers vector $\mathbf{b}_2$, and a dipole of partial screw dislocations with Burgers vectors $\pm\mathbf{b}_3$. The edge $\mathbf{b}_1$ dislocation and the screw $-\mathbf{b}_3$ dislocation form a $(\mathbf{b} - \mathbf{b}'_1)$ difference dislocation, and the edge $\mathbf{b}_2$ dislocation and the screw $+\mathbf{b}_3$ dislocation form a partial Shockley dislocation. The Burgers vector $\mathbf{b}_1$ makes an angle $\pi/2 - \beta$ with the plane of the grain boundary. The partial Shockley dislocation moves on its slip plane and forms a stacking fault of length p behind it. The position of the slip plane is specified by angle α (Fig. 2). Note that the external shear stress τ in our model is always oriented along this plane.

3. CHANGE IN THE ENERGY OF THE SYSTEM CAUSED BY EMISSION OF A SHOCKLEY DISLOCATION

We now consider a change in the total energy of the defect system caused by the emission of partial Shockley dislocation by a positive grain-boundary disclination. This process is energetically favorable if the difference between the total energies (per unit disclination or dislocation length) after (W_2) and before (W_1) the spitting of the **b** dislocation $\Delta W = W_2 - W_1$ is negative ($\Delta W < 0$).

The energy of the system in the initial state is the elastic self-energy of the disclination dipole with arm L [28]:

$$W_1 = E_1^{\Delta} = \frac{D\omega^2 L^2}{2}\left(\ln\frac{R}{L} + \frac{1}{2}\right), \tag{1}$$

where $D = G/[2\pi(1-\nu)]$, G is the shear modulus, ν is the Poisson ratio, and the screening length R is taken to be equal to kd (where $k \gg 1$).

The total energy of the system in the final state, W_2, can be written as

$$\begin{aligned} W_2 = {} & E_2^{\Delta} + E^{b_1} + E^{b_2} + E^{b_3} + E_c + E_{\mathrm{int}}^{b_1-b_2} \\ & + E_{\mathrm{int}}^{\Delta-b_1} + E_{\mathrm{int}}^{\Delta-b_2} + E_{\gamma} + E_{\tau}, \end{aligned} \tag{2}$$

where E_2^{Δ}, E^{b_1}, E^{b_2}, and E^{b_3} are the elastic self-energies of the disclination dipole, $\mathbf{b}_1$ dislocation, $\mathbf{b}_2$ dislocation, and the dipole of the $\pm\mathbf{b}_3$ screw dislocations, respectively; E_c is the contribution from the dislocation cores to the energy; $E_{\mathrm{int}}^{b_1-b_2}$ is the elastic interaction energy between the $\mathbf{b}_1$ and $\mathbf{b}_2$ edge dislocations; $E_{\mathrm{int}}^{\Delta-b_1}$ and $E_{\mathrm{int}}^{\Delta-b_2}$ are the energies of elastic interaction of the disclination dipole with the $\mathbf{b}_1$ and $\mathbf{b}_2$ edge dislocations, respectively; E_{γ} is the stacking-fault energy; and E_{τ} is the energy of interaction of the shear stress τ with the $\mathbf{b}_2$ edge dislocation.

Let us consider the energies entering into Eq. (2). The elastic energy of the disclination dipole E_2^{Δ} is

$$E_2^{\Delta} = E_1^{\Delta}(L \longrightarrow L'), \tag{3}$$

where $L'^2 = L^2 + l^2 + 2Ll\sin\theta$. The elastic components of the self-energy of the $\mathbf{b}_1$ and $\mathbf{b}_2$ edge dislocations are [18]

$$E^{b_i} = \frac{Db_i^2}{2}\ln\frac{R}{r_{c_i}}, \tag{4}$$

where $i = 1, 2$; $r_{c_i} \approx b_i$ is the core radius of the $\mathbf{b}_i$ edge dislocation; and $b_1^2 = b^2 + b_2^2 - 2bb_2\cos\alpha$.

The elastic energy of the dipole of screw dislocations can be calculated as the work done in producing the dipole in its own stress field and is equal to

$$E^{b_3} = D(1-\nu)b_3^2\ln\frac{p - r_{c_3}}{r_{c_3}}, \tag{5}$$

where $r_{c_3} \approx b_3$ is the core radius of the screw dislocation with Burgers vector $\mathbf{b}_3$.

In calculating the contribution of the dislocation cores to the energy (2), we can take into account only the cores of the edge and screw components of the glide partial Shockley dislocation. It is difficult to correctly estimate the change in the energy of the core of the grain-boundary dislocation. We assume that this change is negligible as compared to the core energy of the lattice partial dislocation and neglect it to a first approximation. The contribution from the core of the partial Shockley dislocation to the energy is [18]

$$E_c = \frac{D}{2}[b_2^2 + (1-\nu)b_3^2]. \tag{6}$$

The interaction energies $E_{\mathrm{int}}^{b_1-b_2}$ and $E_{\mathrm{int}}^{\Delta-b_i}$ are [31]

$$E_{\mathrm{int}}^{b_1-b_2} = -Db_1b_2\cos(\alpha+\beta)\ln\frac{R+p}{p}, \tag{7}$$

where $\beta = \arcsin(b_2/b_1\sin\alpha)$;

$$E_{\mathrm{int}}^{\Delta-b_1} = \frac{D\omega b_1}{2}\Psi(0,\beta), \tag{8}$$

where

$$\begin{aligned} & \Psi(p,\beta) \\ & = -L\sin(\theta-\beta)\ln\left[\frac{L^2 + R^2 + 2LR\cos(\theta-\beta)}{L^2 + p^2 + 2Lp\cos(\theta+\beta)}\right] \\ & \quad - l\cos\beta\ln\left[\frac{R^2 + l^2 + 2Rl\sin\beta}{p^2 + l^2 + 2pl\sin\beta}\right], \end{aligned} \tag{9}$$

$$E_{\mathrm{int}}^{\Delta-b_2} = -\frac{D\omega b_2}{2}\Psi(p,\pi-\alpha). \tag{10}$$

The stacking-fault energy E_{γ} is given by

$$E_{\gamma} = \gamma p, \tag{11}$$

where γ is the specific surface stacking-fault energy.

The work E_{τ} done by the external shear stress τ on the Shockley dislocation to move it a distance p is

$$E_{\tau} = -\tau b_2 p. \tag{12}$$

Using Eqs. (1)–(12), the change in the total energy of the system $\Delta W = W_2 - W_1$ as a result of the emission of a Shockley dislocation can be found to be

$$\begin{aligned}\Delta W = \frac{D}{2}\Bigg(&\omega^2\left(L^2\ln\frac{R}{L} - L'^2\ln\frac{R}{L'}\right)\\ &+ (3-2\nu)\sum_{i=1}^{3}\left(b_i^2\ln\frac{R}{b_i}\right) + b_2^2 + (1-\nu)b_3^2\\ &+ \omega b_1\Psi(0,\beta) - \omega b_2\Psi(p,\pi-\alpha)\\ &- 2b_1b_2\cos(\alpha+\beta)\ln\frac{R+p}{p}\Bigg) + \gamma p - \tau b_2 p.\end{aligned} \tag{13}$$

4. CALCULATION RESULTS

Now, we analyze the change in the energy characteristics of the defect structure (Fig. 2) formed when the $\mathbf{b}_1'$ partial dislocation travels a distance p into the grain. As noted above, the splitting of the **b** grain-boundary dislocation is energetically favorable under the condition $\Delta W < 0$. This condition, however, is only a necessary condition for the beginning of motion of the $\mathbf{b}_1'$ dislocation, since it contains no direct information on the variation in the total system energy with increasing distance p traveled by this dislocation. To unambiguously determine whether a further displacement of the $\mathbf{b}_1'$ dislocation is energetically favorable, it is necessary to analyze the variation of ΔW with p. For this analysis, it is convenient to use the thermodynamic driving force F, which is defined as [34]

$$F = -\frac{\partial\Delta W}{\partial p}. \tag{14}$$

At $F > 0$, an increase in the splitting length p is energetically favorable, whereas at $F < 0$ its decrease is energetically favorable. Thus, both conditions $\Delta W < 0$ and $F > 0$ are necessary for the nucleation and development of the defect structure at hand (Fig. 2).

Let us use nanocrystalline Al as an example. Its shear modulus G and Poisson ratio ν are 26.5 GPa and 0.34, respectively [18]. For the Burgers vector **b** of the grain-boundary dislocation, we take the characteristic value $b = 0.1$ nm [19]. The Burgers vector magnitudes of the partial edge dislocation (b_2) and the partial screw dislocation (b_3) can be determined from the crystallography of the fcc lattice [18] and are equal to 0.143 and 0.022 nm, respectively. The stacking fault energy is taken to be $\gamma = 120$ mJ/m^2; this value corresponds to the upper limit of the calculated values of γ (from 104 to 122 mJ/m^2) and to the lower limit of the experimental values of γ (from 120 to 142 mJ/m^2) in pure Al [8–10]. The strength ω of the disclination dipole is taken to be $\omega = 0.1$ ($\approx 6°$), which is typical of NCMs.

4.1. Possible Scenarios for the Emission and Motion of a Shockley Dislocation

We consider the $\Delta W(p)$ and $F(p)$ dependences at a fixed grain size ($d = 30$ nm) and different values of the shear stress τ and azimuthal angles α and θ. Our calculations indicate that, under the necessary condition $\Delta W(p = b_2) < 0$, there are $\Delta W(p)$ and $F(p)$ curves of four different types (constructed for $\tau = 0$, 0.25, 0.50, 0.75, 1, and 1.25 GPa in Fig. 3) corresponding to various combinations of the angles α and θ.

$\Delta W(p)$ and $F(p)$ curves of the first type are shown in Figs. 3a and 3b, respectively, for angles $\alpha = 10°$ and $\theta = 180°$. All the $\Delta W(p)$ curves are seen to have three inflection points, which correspond to two minima (at $p = p_{\min 1}$ and $p = p_{\min 2}$) and one maximum in the $F(p)$ curves. The $\Delta W(p)$ curves can have the first minimum (in the range $\tau = 0$–1 GPa in Fig. 3) at $p \approx 1$ nm and the second minimum (for $\tau \approx 1.1$ GPa; it is not shown in Fig. 3) at $p = 10$–20 nm or can have no minimum (at $\tau = 1.25$ GPa). These curves can also have one maximum (for $\tau = 1$ GPa at $p \approx 28$ nm) or two maxima (for $\tau = 1.1$ GPa at $p \approx 5$ nm and $p \approx 29$ nm; not shown in Fig 3). Naturally, these minima and maxima meet the condition $F = 0$ and determine the positions of stable and unstable equilibrium, respectively, for the glide partial Shockley dislocation.

$\Delta W(p)$ and $F(p)$ curves of the second type are shown in Figs. 3c and 3d, respectively, for angles $\alpha = 10°$ and $\theta = 120°$. $\Delta W(p)$ curves of this type have two inflection points, which correspond to a minimum at $p = p_{\min 1}$ and a maximum in the $F(p)$ curves. The $\Delta W(p)$ curves can have only the first minimum (in the range $\tau = 0$–0.5 GPa in Fig. 3) at ≈ 1 nm; the first and second minima (for $\tau \approx 0.6$ GPa; not shown in Fig. 3) at $p \approx 1$ nm and $p \approx 10$–12 nm, respectively; only the second minimum (for $\tau = 0.75$ and 1 GPa at $p \approx 15$ and 25 nm, respectively); and no minimum (for $\tau = 1.25$ GPa). Moreover, these curves can have only one maximum (for $\tau \approx 0.6$ GPa; not shown in Fig. 3) at $p \approx 3$–4 nm.

$\Delta W(p)$ and $F(p)$ curves of the third type are shown in Figs. 3e and 3f, respectively, for angles $\alpha = 10°$ and $\theta = 200°$). All the $\Delta W(p)$ curves have only one inflection point, which corresponds to a minimum at $p = p_{\min 1}$ in the $F(p)$ curves. The $\Delta W(p)$ curves can have one minimum (in the range $\tau = 0$–1 GPa) at $p \le 1$ nm or have no minima (for $\tau = 1.25$ GPa). Maxima can also exist for relatively high values of τ (in Fig. 3, for $\tau = 0.75$ GPa at $p \approx 28$ nm and for $\tau = 1$ GPa at $p \approx 22$ nm). For lower values of τ, the $\Delta W(p)$ curves increase monotonically at $p > 1$ nm.

$\Delta W(p)$ and $F(p)$ curves of the fourth type are shown in Figs. 3g and 3h, respectively, for angles $\alpha = 30°$ and $\theta = 180°$. $\Delta W(p)$ curves of this type have no inflection points, which corresponds to the absence of extrema in the $F(p)$ curves. The $\Delta W(p)$ curves either increase monotonically at relatively low τ (up to 0.5 GPa in Fig. 3) or reach a maximum and then decrease at high τ.

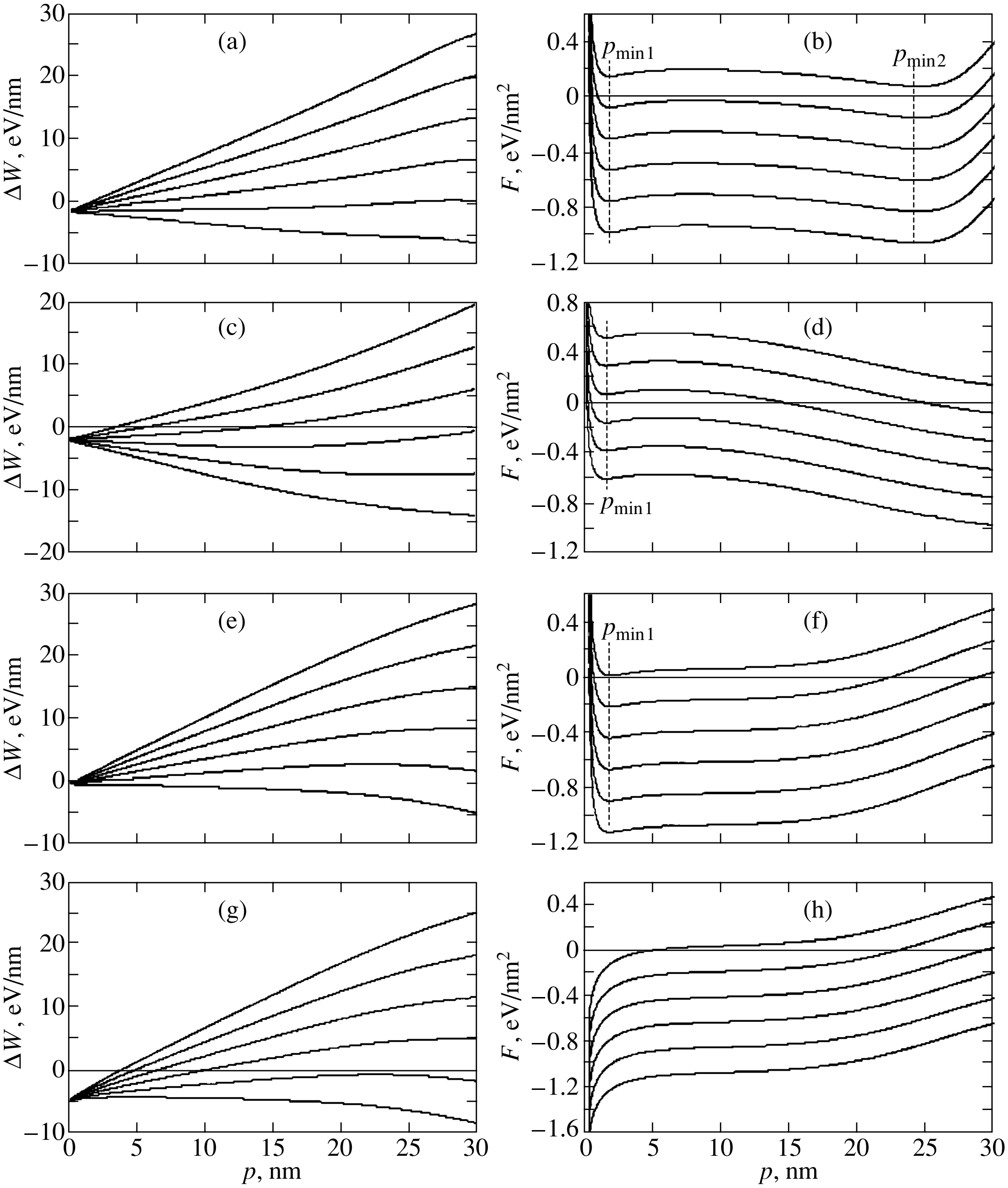

Fig. 3. Dependences of (a, c, e, g) the energy difference ΔW and (b, d, f, h) the thermodynamic driving force F on the distance p traveled by an emitted Shockley dislocation for pure Al at a grain size d = 30 nm; applied shear stresses τ = 0, 0.25, 0.50, 0.75, 1, and 1.25 GPa [from top to bottom for (a, c, e, g) and from bottom to top for (b, d, f, h)]; and various azimuthal angles α and θ: (a, b) α = 10°, θ = 180°; (c, d) α = 10°, θ = 120°; (e, f) α = 10°, θ = 200°; and (g, h) α = 30°, θ = 180°.

Note an important feature of curves of the first, second, and third types. Since the term given by Eq. (12) (describing the work done by the external stress τ on the Shockley dislocation to move it) varies linearly with displacement p, its derivative with respect to p gives a constant term in the $F(p)$ function. Correspondingly, the extrema of $F(p)$ (the inflection points in the $\Delta W(p)$ curves) do not change position as τ is varied (Figs. 3a–3f). As will be shown below, this finding allows us to easily formulate the conditions for emission and subsequent changes in the motion of the Shockley dislocation.

The $\Delta W(p)$ and $F(p)$ dependences discussed above allow us to consider several possible scenarios for the emission of a partial Shockley dislocation by a grain-boundary disclination depending on the stress τ applied in the slip plane and on the azimuthal angles α and θ. Obviously, these scenarios correspond to the four types of $\Delta W(p)$ and $F(p)$ curves considered above.

In the first case ($\alpha = 10°$, $\theta = 180°$), the grain-boundary dislocation splits and a Shockley dislocation is emitted even in the absence of stress τ. A Shockley dislocation is emitted and occupies the position of stable equilibrium in the vicinity of the boundary. As τ increases, this position moves gradually to the point $p = p_{\min 1} \approx 2$ nm. At this point, τ reaches a certain critical value τ_{c1}, which meets the condition $F(p = p_{\min 1}) = 0$ (in Fig. 3b, $\tau_{c1} \approx 1.15$ GPa), and the Shockley dislocation again begins to move until it reaches a new position of stable equilibrium at a point $p \approx 17$ nm. As τ increases further, this position shifts gradually toward larger values of p. Finally, when τ reaches a second critical value τ_{c2}, which meets the condition $F(p = p_{\min 2}) = 0$ (in Fig. 3b, $\tau_{c2} \approx 1.2$ GPa), the Shockley dislocation breaks away from this equilibrium position and rapidly reaches the opposite boundary of the grain (the circle of radius d). Thus, in this scenario, three stable positions of the emitted Shockley dislocation are possible, depending on the external stress. The first position is near the point of splitting, the second is approximately at the center of the grain, and the third is at the opposite boundary (which is not covered by our model). Correspondingly, we can distinguish three possible characteristic states of the defect structure in the grain: state I, in which grain boundaries emit very short (as short as 1 nm) stacking faults; state II, in which these stacking faults reach the central region of the grain; and state III, in which the stacking faults pass through the entire grain.

In the second case ($\alpha = 10°$, $\theta = 120°$), the system initially follows the first scenario. The grain-boundary dislocation splits in the absence of an applied stress τ, and the Shockley dislocation occupies the first stable equilibrium position near the boundary. As τ increases, this equilibrium position shifts gradually from the boundary toward the point $p = p_{\min 1} \approx 2$ nm and reaches this point at $\tau = \tau_{c1}$ (in Fig. 3d, $\tau_{c1} \approx 0.7$ GPa), when the Shockley dislocation breaks away from the first position of stable equilibrium and goes to the second position, which is located at point $p \approx 12$ nm at this stress. The Shockley dislocation cannot break away from this equilibrium position; it can only move gradually with this position as τ increases further. The dislocation reaches the opposite grain boundary at a certain critical stress $\tau = \tau'_{c2}$ (in Fig. 3d, $\tau'_{c2} \approx 1.1$ GPa). This second critical stress can be found from the condition $F(p = d) = 0$. By comparing the critical stresses for the first and second scenarios, one can see that the second scenario requires substantially lower critical stresses ($\tau_{c1} \approx 0.7$ GPa instead of 1.15 GPa, and $\tau'_{c2} \approx 1.1$ GPa instead of $\tau_{c2} \approx 1.2$ GPa). Unlike the first scenario, where the transition from structure II to structure III occurs in a jump at $\tau = \tau_{c2}$, in the second scenario, structure II transforms into structure III smoothly as the stress τ reaches τ'_{c2}.

In the third scenario ($\alpha = 10°$, $\theta = 200°$), the situation develops according to the first scenario; namely, the grain-boundary dislocation splits spontaneously and the Shockley dislocation goes into a state of stable equilibrium near the boundary. As the applied stress τ increases, this equilibrium position again shifts and reaches the point $p = p_{\min 1} \approx 2$ nm at $\tau = \tau_{c1}$ (in Fig. 3f, $\tau_{c1} \approx 1.25$ GPa). At this instant of time, the Shockley dislocation breaks away from the equilibrium position and reaches the opposite boundary. Thus, in the third scenario, the second position of stable equilibrium for the dislocation (in the central zone of the grain) and the second critical stress do not exist. Correspondingly, intermediate defect structure II should not form in this case. Note that the transition from structure I to structure III requires the highest stress τ among all the stresses analyzed.

Finally, the fourth case ($\alpha = 30°$, $\theta = 180°$) corresponds to the situation where the grain-boundary dislocation can split and emit a Shockley dislocation only at a very high applied stress ($\tau = \tau''_c \approx 2$ GPa), which is determined by the condition $F(p = b_2) = 0$. The Shockley dislocation has no intermediate equilibrium positions and goes through the entire grain at once. In this case, defect structure III is immediately formed in the system.

Thus, when splitting itself is energetically favorable, i.e., $\Delta W(p = b_2) < 0$, the choice of the pair of azimuthal angles α and θ specifies one of the four possible scenarios of the development of the defect structure in a nanograin of size $d = 30$ nm. To consider the influence of the nanograin size d on the situation, we will study the behavior of the critical stresses, which are the basic parameters characterizing each scenario.

4.2. Critical Stresses

In the previous subsection, we discussed the critical stresses that determine the state of the defect structure when a partial Shockley dislocation is emitted by a grain-boundary disclination. In general, these stresses are given by the equation $F(p = p^*) = 0$, which can easily be solved for the critical stress τ_c:

$$\tau_c = \frac{Db_3^2(1-\nu)}{b_2(p^*-b_3)} - \frac{Db_1\cos(\alpha+\beta)R}{p^*(p^*+R)} - \frac{D\omega}{2}\frac{\partial\Psi(p,\pi-\alpha)}{\partial p}\bigg|_{p=p^*} + \frac{\gamma}{b_2}. \quad (15)$$

By substituting successively $p_{\min 1}$, $p_{\min 2}$, d, and b_2 for p^* in Eq. (15), we find τ_{c1}, τ_{c2}, τ'_{c2}, and τ''_c, respectively.

Using Eq. (15), we plot the dependence of the critical shear stress τ_c on the angle θ at $\alpha = 10°$ and $d = 10$, 20, and 30 nm (Figs. 4a, 4b, 4c, respectively). Here, the $\tau_c(\theta)$ dependences are shown for only the angles θ at

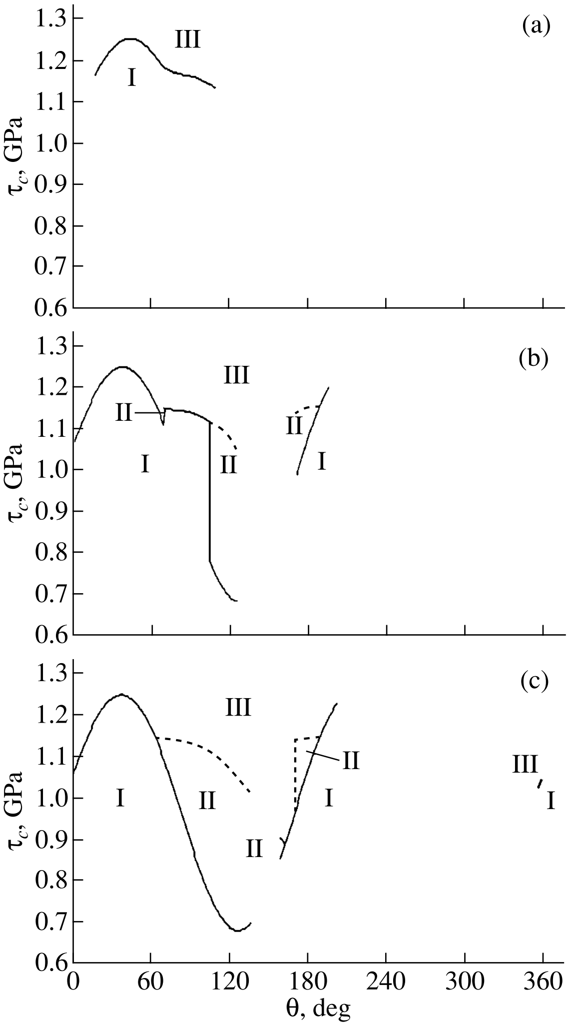

Fig. 4. Dependence of the critical applied stress τ_c on the azimuthal angle θ at various grain sizes d: (a) 10, (b) 20, and (c) 30 nm. Roman numerals mark the following states of the defect structure in the grain: (I) partial Shockley dislocations are located at a distance $p \le 2$ nm from the emission points in grain boundaries, (II) partial Shockley dislocations are located inside the grain, and (III) partial Shockley dislocations reach the opposite grain boundary.

which the emission of a Shockley dislocation is energetically favorable (i.e., under the condition $\Delta W(p \approx b_2) < 0$). Regions with different defect structures are marked as I, II, and III. Each defect structure forms in certain stress τ ranges, whose boundaries are characterized by three critical stresses: τ_{c1} for the boundaries between regions I and II, τ_{c2} for the boundaries between regions II and III, and τ'_{c2} for the boundaries between regions I and III. As noted above, the critical stress τ''_c, which specifies the state of the system for the fourth scenario (see Subsection 4.1), is substantially higher than the other critical stresses; therefore, it is not shown here.

Figure 4 demonstrates that the $\tau_c(\theta)$ diagram substantially depends on the grain size d. At $\alpha = 10°$ and $d = 10$ nm (Fig. 4a), only defect structures I and III can exist, and they exist in a relatively narrow θ range (here, from ≈15° to ≈105°). As the grain size increases, structure II can appear (Figs. 4b, 4c) and the θ range where all three structures can exist becomes significantly wider. On the whole, at low (here, from 0° to ≈65°) and high θ angles (here, from 355° to 360°), only defect structures I and III can form. In the angular ranges $\theta \approx$ 65°–140° and $\theta \approx$ 160°–190°, all three types of defect structures can form in the material.

Thus, as follows from Fig. 4, an increase in the grain size d results in widening of the θ angular range in which a grain-boundary $\mathbf{b}$ dislocation can split to form a Shockley dislocation. As d increases, the $\tau_c(\theta)$ curves split into branches that correspond to τ_{c1} and to τ_{c2} or τ'_{c2}, which leads to the possible formation of all three types of defect structures in the material. The critical stresses decrease with increasing d.

4.3. Comparison of the Characteristics of the Emission of Partial Shockley Dislocations and Perfect Dislocations by Grain Boundaries

Let us assume now that a grain-boundary dislocation splits to form a perfect lattice dislocation with Burgers vector $\mathbf{b}''_1$ rather than a partial Shockley dislocation. We compare the critical shear stresses that are required for the emission of a perfect and partial dislocation. The calculation of the energy characteristics of the emission of the perfect $\mathbf{b}''_1$ dislocation is similar to the calculation performed for the $\mathbf{b}'_1$ partial dislocation. We have only to replace the Burgers vector $\mathbf{b}'_1$ of the partial dislocation by the Burgers vector $\mathbf{b}''_1$ of the perfect dislocation, which is equal to double the Burgers vector of the edge component of the $\mathbf{b}'_1$ partial Shockley dislocation ($\mathbf{b}''_1 = 2\mathbf{b}_2$), as follows from the crystallography of the fcc lattice [18]. Moreover, in the calculation for the $\mathbf{b}''_1$ perfect dislocation, the contributions from the dipole of screw partial dislocations and from the stacking fault to the complete energy of the system disappear. In this case, the critical shear stress τ_c^{perf} for the emission of a $\mathbf{b}''_1$ perfect dislocation by a grain boundary can be found to be

$$\tau_c^{\text{perf}} = -\frac{Db_1\cos(\alpha+\beta)R}{p^*(p^*+R)} - \frac{D\omega}{2}\frac{\partial\Psi(p,\pi-\alpha)}{\partial p}\bigg|_{p=p^*}, \qquad (16)$$

where $b_1^2 = b^2 + 4b_2^2 - 4bb_2\cos\alpha$.

Using Eqs. (15) and (16), we plot the $\tau_c(\theta)$ and $\tau_c^{\text{perf}}(\theta)$ dependences at various angles α and grain sizes d for the emission of a partial and perfect dislocation, respectively. These dependences are shown in Fig. 5 for

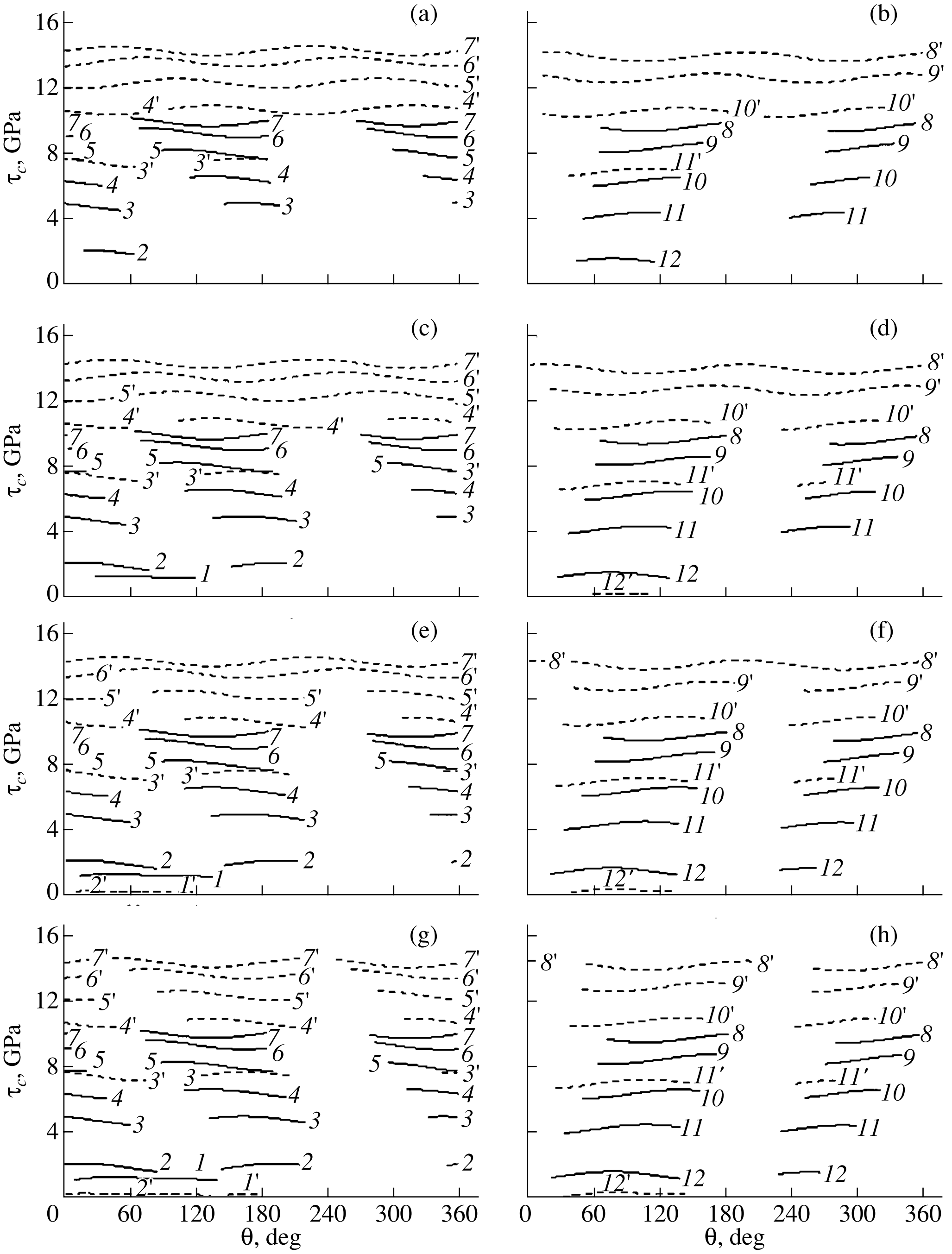

Fig. 5. $\tau_c(\theta)$ (solid lines) and $\tau_c^{\text{perf}}(\theta)$ dependences (dashed lines) for partial and perfect dislocations, respectively, at grain sizes d equal to (a, b) 5, (c, d) 10, (e, f) 20, and (g, h) 30 nm. The azimuthal angle α is (*1, 1'*) 0°, (*2, 2'*) 30°, (*3, 3'*) 60°, (*4, 4'*) 90°, (*5, 5'*) 120°, (*6, 6'*) 150°, (*7, 7'*) 180°, (*8, 8'*) 210°, (*9, 9'*) 240°, (*10, 10'*) 270°, (*11, 11'*) 300°, and (*12, 12'*) 330°.

a grain size (a, b) $d = 5$, (c, d) 10, (e, f) 20, and (g, h) 30 nm. Figures 5a, 5c, 5e, and 5g show the $\tau_c(\theta)$ (solid lines) and $\tau_c^{\text{perf}}(\theta)$ (dashed lines) dependences for the angle α increasing from 0° to 180° in 30° steps. Figures 5b, 5d, 5f, and 5h show these curves for α increasing from 210° to 330° in the same steps. When plotting the $\tau_c(\theta)$ and $\tau_c^{\text{perf}}(\theta)$ curves, we do not show the branching points (for the sake of simplicity) and take only the critical stresses τ_{c2}, τ'_{c2}, and τ''_c at which defect structure III can form in the material (when the emitted partial or perfect dislocation reaches the opposite grain boundary). The ranges of admissible θ and α

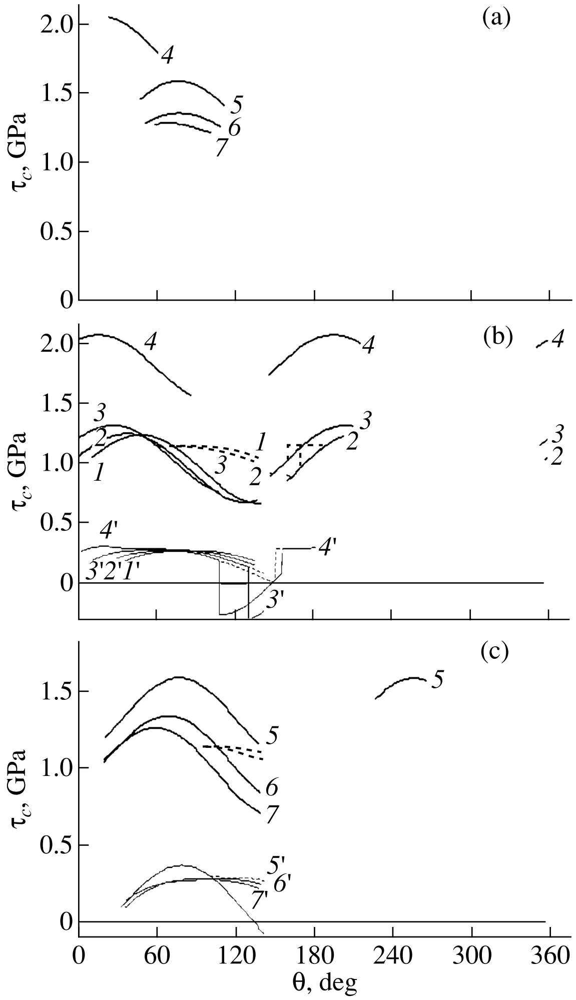

Fig. 6. $\tau_c(\theta)$ (heavy solid and dashed lines) and $\tau_c^{\text{perf}}(\theta)$ dependences (thin solid and dashed lines) at $\tau \le 2$ GPa for partial and perfect dislocations, respectively, at grain sizes d equal to (a) 5 and (b, c) 30 nm. The azimuthal angle α is (*1*, *1*') 0°, (*2*, *2*') 10°, (*3*, *3*') 20°, (*4*, *4*') 30°, (*5*, *5*') 330°, (*6*, *6*') 340°, and (*7*, *7*') 350°. The solid lines show the boundaries between defect structure I and defect structure II or III. The dashed lines show the boundaries between defect structures II and III.

angles were determined from the conditions $\Delta W(p \approx b_2) \le 0$ for the partial dislocation and $\Delta W(p \approx 2b_2) \le 0$ for the perfect dislocation, i.e., from the conditions under which the defect configurations in question are energetically favorable. Therefore, the $\tau_c(\theta)$ and $\tau_c^{\text{perf}}(\theta)$ curves have discontinuities for the majority of the angles α.

Most $\tau_c(\theta)$ and $\tau_c^{\text{perf}}(\theta)$ curves shown here lie at very high stresses, which are virtually unachievable in real nanocrystalline aluminum. The only purpose was to demonstrate, first, the dependence of the critical stresses on the angles θ and α and, second, the relation between the quantities $\tau_c(\theta)$ and $\tau_c^{\text{perf}}(\theta)$ over the entire admissible range of these angles. The maximum shear stresses that can be achieved in nanocrystalline aluminum in practice are likely to be 1–1.5 GPa [8–10].

Let us compare the $\tau_c(\theta)$ and $\tau_c^{\text{perf}}(\theta)$ dependences at various grain sizes d. At $d = 5$ nm, the $\tau_c^{\text{perf}}(\theta)$ curves are significantly higher than the corresponding $\tau_c(\theta)$ curves for all values of angles α and θ (Figs. 5a, 5b). This means that, at a grain size $d \le 5$ nm, the emission of partial Shockley dislocations by grain boundaries always requires a lower external shear stress than does the emission of perfect lattice dislocations.

When the grain size increases to 10 nm (Figs. 5c, 5d) at high α angles ($\alpha = 330°$ for curve *12*' in Fig. 5d), there appears a θ range (60°–110°) in which perfect dislocations can be emitted at lower shear stresses as compared to the emission of partial dislocations. As the grain size increases further and becomes equal to 20 nm (Figs. 5e, 5f), a θ angular range ($\theta \approx 10°$–120°) where perfect dislocations should first be emitted appears even at low α angles ($\alpha = 0°$–30° for curves *1*' and *2*' in Fig. 5e).

A further increase in the grain size to 30 nm (Figs. 5g, 5h) causes no qualitative changes. Only the θ angular range where the $\tau_c(\theta)$ and $\tau_c^{\text{perf}}(\theta)$ curves lie at relatively low stresses (up to 2 GPa) becomes gradually wider and the θ angular range where the $\tau_c(\theta)$ and $\tau_c^{\text{perf}}(\theta)$ curves lie at high stresses (from 2 to 15 GPa) becomes narrower.

Now, we consider the range of real stresses (up to ≈2 GPa) in more detail for two characteristic cases: d = 5 nm (Fig. 6a) and 30 nm (Figs. 6b, 6c). Figure 6a shows the $\tau_c(\theta)$ curves (the $\tau_c^{\text{perf}}(\theta)$ curves lie above and do not fall within this range of relatively low stresses) for an increase in the angle α from 0° to 30° and from 330° to 350° in 10° steps. Figure 6b gives the $\tau_c(\theta)$ (heavy solid and dashed lines) and $\tau_c^{\text{perf}}(\theta)$ dependences (thin solid and dashed lines) for an increase in the angle α from 0° to 30° in 10° steps. Figure 6c demonstrates the corresponding curves for an increase in the angle α from 330° to 350° in the same steps. The solid lines indicate the boundaries between defect structure I and defect structure II or III. The dashed lines show the boundaries between defect structures II and III.

As is seen from Fig. 6a for a grain size $d = 5$ nm, only partial Shockley dislocations are emitted at applied shear stresses $\tau \le 2$ GPa, whereas the emission of perfect dislocations is completely suppressed here. The ranges of admissible values of the angle α are rather narrow: emission is possible at $\alpha \approx 30°$ and 330°–350°. For a grain size $d = 30$ nm, the emission of perfect dislocations dominates over almost the entire range of angles α and θ (Figs. 6b, 6c), because the emission of partial dislocations requires application of higher shear stresses. Note that, at certain combinations of the angles α and θ, the critical stress τ_c^{perf} for the emission of perfect dislocations becomes negative; that is, spontaneous emission of perfect dislocations can occur even when a low opposed stress is applied.

4.4. Emission of Extended Dislocations by Grain Boundaries

Apart from the emission of single partial Shockley dislocations and perfect dislocations by grain boundaries, extended dislocations can also be emitted. Such a configuration consists of two partial Shockley dislocations (leading and trailing dislocations) connected by a stacking-fault strip. Extended dislocations are formed in two stages. First, a leading partial Shockley dislocation is emitted; it moves away from the emission point (grain boundary) and forms a stacking fault behind it. This stage was considered in detail in the previous sections. In the second stage, the trailing partial Shockley dislocation (in which the stacking fault extending from the leading Shockley dislocation terminates) splits off from the grain boundary.

Our calculations of the change in the system energy caused by the emission of such split dislocation configurations show that there are no ranges of the system parameters where this emission is energetically favorable. Only in the parameter ranges where the emission of perfect dislocations should be predominant (Subsection 4.3) does the emission of extended dislocations also become possible. The equilibrium length of their splitting (the distance between the leading and trailing Shockley dislocations) is very small, so the extended dislocations do not differ from perfect dislocations either in terms of their energy characteristics or critical stresses. In the parameter ranges where the emission of leading partial Shockley dislocations should prevail (Subsection 4.3), the splitting off of their trailing partial Shockley dislocations from the boundary is energetically unfavorable.

5. CONCLUSIONS

It has been shown that the deformation mechanism that occurs via the emission of partial Shockley dislocations by grain-boundary disclinations can effectively operate in fcc nanocrystalline materials when an external shear stress reaches a certain critical value τ_c. The type of defect structure formed is determined by the external shear stress τ operating in the slip plane of a Shockley dislocation. At $0 < \tau < \tau_{c1}$, a defect structure of type I forms; it is characterized by the emission of short stacking faults (as short as 2 nm) at grain boundaries. At $\tau_{c1} \le \tau < \tau_{c2}$ or $\tau < \tau_c'$, a defect structure of type II forms; it is characterized by more extended (as compared to structure I) stacking faults. At $\tau \ge \tau_{c2}$ or $\tau \ge \tau_c'$, a defect structure of type III forms; here, stacking faults intersect entire grains. Note that all types of defect structures were observed upon two-dimensional [8–10] and three-dimensional [11, 12] molecular-dynamics simulations of the plastic deformation of NCMs.

As follows from our model, two characteristic critical grain sizes ($d_{c1} \approx 5$ nm, $d_{c2} \approx 30$ nm) can be distinguished in nanocrystalline aluminum. At $d \le d_{c1}$, grain boundaries emit partial Shockley dislocations at lower values of τ as compared to the emission of perfect dislocations over the entire range of admissible angles α and θ. At $d \ge d_{c2}$, the emission of perfect dislocations becomes energetically favorable over the entire range of admissible angles α and θ (in the range of real $\tau \le$ 1 GPa). In grains of intermediate size (at $d_{c1} < d < d_{c2}$), both partial and perfect dislocations can be emitted, depending on the angles α and θ.

ACKNOWLEDGMENTS

This work was supported by INTAS (project no. 03-51-3779), the Russian Foundation for Basic Research (project no. 04-01-00211), the Ministry of Education and Science of the Russian Federation (program "Physics of Solid-State Nanostructures"), the Foundation for Assistance to Russian Science, the RAS program "Structural Mechanics of Materials and Members of Constructions," the Office of US Naval Research (project no. 00014-01-1-1020), the program "Integration" (project no. B0026), and the St. Petersburg Scientific Center of the Russian Academy of Sciences.

REFERENCES

1. *Mechanical Properties of Nanostructured Materials and Nanocomposites*, Ed. by I. A. Ovid'ko, C. S. Pande, R. Krishnamoorti, E. Lavernia, and G. Skandan (MRS, Warrendale, 2004), Mater. Res. Soc. Symp. Proc., Vol. 791.
2. M. Yu. Gutkin and I. A. Ovid'ko, *Plastic Deformation in Nanocrystalline Materials* (Springer, Berlin, 2004).
3. R. Z. Valiev, I. A. Alexandrov, Y. T. Zhu, and T. C. Lowe, J. Mater. Res. **17** (1), 5 (2002).
4. K. S. Kumar, S. Suresh, M. F. Chisholm, J. A. Horton, and P. Wang, Acta Mater. **51** (2), 387 (2003).
5. D. V. Shtanskiĭ, S. A. Kulinich, E. A. Levashov, and J. J. Moore, Fiz. Tverd. Tela (St. Petersburg) **45** (6), 1122 (2003) [Phys. Solid State **45**, 1177 (2003)].
6. I. A. Ovid'ko, Science **295** (5569), 2386 (2002).
7. M. Yu. Gutkin, I. A. Ovid'ko, and N. V. Skiba, Acta Mater. **52** (6), 1711 (2004).
8. V. Yamakov, D. Wolf, M. Salazar, S. R. Phillpot, and H. Gleiter, Acta Mater. **49** (14), 2713 (2001).
9. V. Yamakov, D. Wolf, S. R. Phillpot, A. K. Mukherjee, and H. Gleiter, Nature Mater. **1** (1), 45 (2002).
10. V. Yamakov, D. Wolf, S. R. Phillpot, and H. Gleiter, Acta Mater. **50** (20), 5005 (2002).

11. P. M. Derlet and H. van Swygenhoven, Scr. Mater. **47** (11), 719 (2002).
12. P. M. Derlet, A. Hasnaoui, and H. van Swygenhoven, Scr. Mater. **49** (7), 629 (2003).
13. M. Chen, E. Ma, K. J. Hemker, H. Sheng, Y. Wang, and X. Cheng, Science **300** (5623), 1275 (2003).
14. X. Z. Liao, F. Zhou, E. J. Lavernia, S. G. Srinivasan, M. I. Baskes, D. W. He, and Y. T. Zhu, Appl. Phys. Lett. **83** (4), 632 (2003).
15. X. Z. Liao, F. Zhou, E. J. Lavernia, D. W. He, and Y. T. Zhu, Appl. Phys. Lett. **83** (24), 5062 (2003).
16. X. Z. Liao, Y. H. Zhao, S. G. Srinivasan, Y. T. Zhu, R. Z. Valiev, and D. V. Gunderov, Appl. Phys. Lett. **84** (4), 592 (2004).
17. O. V. Klyavin, V. I. Nikolaev, L. V. Khabarin, Yu. M. Chernov, and V. V. Shpeĭzman, Fiz. Tverd. Tela (St. Petersburg) **45** (12), 2187 (2003) [Phys. Solid State **45**, 2292 (2003)].
18. J. P. Hirth and J. Lothe, *Theory of Dislocations*, 2nd ed. (McGraw-Hill, New York, 1982; Atomizdat, Moscow, 1972).
19. A. P. Sutton and R. W. Balluffi, *Interfaces in Crystalline Materials* (Clarendon, Oxford, 1995).
20. G. B. Olson and M. Cohen, Metall. Trans. A **7** (12), 1897 (1976).
21. R. Z. Valiev, N. A. Krasilnikov, and N. K. Tsenev, Mater. Sci. Eng. A **137**, 35 (1991).
22. R. Z. Valiev, F. Chmelik, F. Bordeaux, G. Kapelski, and B. Baudelet, Scr. Metall. Mater. **27** (7), 855 (1992).
23. J. Languillaume, F. Chmelik, G. Kapelski, F. Bordeaux, A. A. Nazarov, G. Canova, C. Esling, R. Z. Valiev, and B. Baudelet, Acta Metall. Mater. **41** (10), 2953 (1993).
24. A. A. Nazarov, A. E. Romanov, and R. Z. Valiev, Nanostruct. Mater. **6** (5–8), 775 (1995).
25. G. A. Malygin, Fiz. Tverd. Tela (St. Petersburg) **37** (8), 2281 (1995) [Phys. Solid State **37**, 1248 (1995)].
26. V. V. Rybin, *Large Plastic Deformations and Fracture of Metals* (Metallurgiya, Moscow, 1986) [in Russian].
27. M. Yu. Gutkin and I. A. Ovid’ko, Rev. Adv. Mater. Sci. **4** (2), 79 (2003).
28. A. E. Romanov and V. I. Vladimirov, in *Dislocations in Solids*, Ed. by F. R. N. Nabarro (North-Holland, Amsterdam, 1992), Vol. 9, pp. 191–402.
29. M. Yu. Gutkin, I. A. Ovid’ko, and N. V. Skiba, Pis’ma Zh. Tekh. Fiz. **28** (10), 78 (2002) [Tech. Phys. Lett. **28**, 437 (2002)].
30. M. Yu. Gutkin, A. L. Kolesnikova, I. A. Ovid’ko, and N. V. Skiba, Philos. Mag. Lett. **82** (12), 651 (2002).
31. M. Yu. Gutkin, I. A. Ovid’ko, and N. V. Skiba, Mater. Sci. Eng. A **339** (1/2), 73 (2003).
32. M. Yu. Gutkin, K. N. Mikaelyan, and V. E. Verijenko, Scr. Mater. **45** (8), 939 (2001).
33. M. Yu. Gutkin, K. N. Mikaelyan, and V. E. Verijenko, Acta Mater. **49** (18), 3811 (2001).
34. M. Yu. Gutkin, K. N. Mikaelyan, V. E. Verijenko, and L. D. Thompson, Metall. Mater. Trans. A **3** (5), 1351 (2002).
35. G. A. Malygin, Fiz. Tverd. Tela (St. Petersburg) **45** (2), 327 (2003) [Phys. Solid State **45**, 345 (2003)].

Translated by K. Shakhlevich

Physics of the Solid State, Vol. 46, No. 11, 2004, pp. 2053–2057. Translated from Fizika Tverdogo Tela, Vol. 46, No. 11, 2004, pp. 1986–1990.
Original Russian Text Copyright © 2004 by Bobylev, Gutkin, Ovid'ko.

DEFECTS, DISLOCATIONS, AND PHYSICS OF STRENGTH

Chain Decay of Low-Angle Tilt Boundaries in Nanocrystalline Materials

S. V. Bobylev, M. Yu. Gutkin, and I. A. Ovid'ko
Institute of Problems of Mechanical Engineering, Russian Academy of Sciences,
Vasil'evskiĭ Ostrov, Bol'shoĭ pr. 61, St. Petersburg, 199178 Russia
e-mail: gutkin@def.ipme.ru

Received April 22, 2004

Abstract—In terms of two-dimensional dislocation–disclination dynamics, a theoretical model is developed to describe the decay of a low-angle tilt boundary in a deformed nanocrystalline material under the action of an externally applied elastic stress and of the elastic field of a neighboring decayed boundary. The critical external stresses are calculated at which the boundary decays and the dislocations making up this boundary either are trapped by the boundary that decayed earlier or break away from both boundaries. The decay of a low-angle tilt boundary is shown to result in a substantial decrease in the critical decay stresses for the neighboring boundaries, which can cause an avalanche-like chain decay of low-angle boundaries yielding high-density ensembles of mobile dislocations capable of carrying substantial plastic deformations and of forming shear bands in deformed nanocrystalline materials. *© 2004 MAIK "Nauka/Interperiodica".*

1. INTRODUCTION

Nanocrystalline materials (NCMs) have unique mechanical properties, whose mechanisms of formation are being extensively studied [1–18]. Many NCMs are very hard and brittle [19], whereas others can be subjected to superplastic deformation [20–24]. The characteristic feature of plastic deformation of many NCMs is its strong nonuniformity: a plastic flow is localized in shear bands [25]. On the whole, the mechanisms of plastic and superplastic deformation in NCMs can be divided into ordinary dislocation glide [1–4], diffusion creep along grain boundaries [5–9] and triple junctions [6], rotation deformation [7–10], grain-boundary sliding [10–14], and twinning [15]. The activation of these mechanisms is substantially determined by the grain size d in NCMs [18].

In this work, we consider plastically deformable NCMs with a relatively large grain size ($100 \geq d \geq 30$ nm). In such NCMs, intragrain dislocation glide is predominant. To discuss the specific features of plastic deformation in these materials, it is necessary to consider dislocation sources in them. Indeed, the operation of ordinary Frank–Read dislocation sources can be hindered or even suppressed because of a small grain size and the strong effect of grain boundaries [26]. Under these conditions, alternative sources of lattice dislocations can be grain boundaries [9, 10], whose volume fraction in NCMs is very high. The theoretical models developed in [9, 10] assume that the emission of lattice dislocations from high-angle grain boundaries could be controlled by the motion and transformation of grain-boundary dislocations and disclinations. However, these processes are too slow to form an ensemble of mobile dislocations having a high density and thus being capable of carrying severe plastic deformation in shear bands. At the same time, nanocrystalline metals have a significant amount of low-angle boundaries formed by lattice dislocations [27]. Low-angle boundaries are known to be able to undergo substantial rearrangement under the action of internal and external stresses in coarse-grained polycrystals [28–30]. It is natural to assume that they also undergo similar transformations in NCMs.

In [31], we proposed a model to describe the decay of a single low-angle tilt boundary under the action of an applied stress. The trajectories of glide edge dislocations making up a low-angle tilt boundary in the fields of internal and external elastic stresses were studied in the context of two-dimensional dislocation–disclination dynamics similar to that considered in [32]. The critical external stress τ_c for the decay of such a boundary was calculated, and this decay was found to result in the formation of an ensemble of mobile lattices dislocations, which can carry substantial plastic deformation [31].

In this work, we develop the model described in [31]; namely, we study the decay of a low-angle tilt boundary in the elastic-stress field of a decayed neighboring boundary. It is shown that the decay of the former boundary can lead to an avalanche-like chain decay of the neighboring low-angle boundaries, which should cause substantial changes in the shape and size of grains in shear bands in NCMs (grains become extended along the direction of development of the shear bands). These changes were experimentally observed in [33].

1063-7834/04/4611-2053$26.00 © 2004 MAIK "Nauka/Interperiodica"

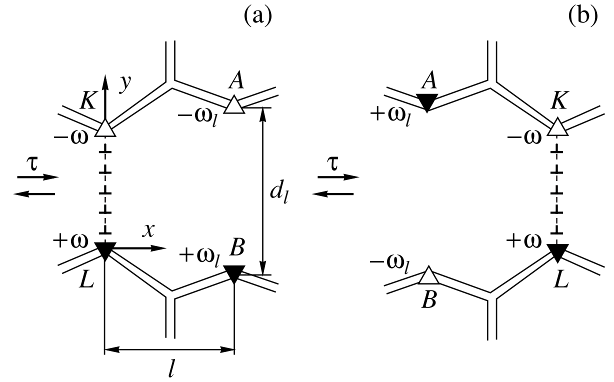

Fig. 1. Possible positions of low-angle tilt boundary *KL* with a misorientation angle ω near decayed low-angle tilt boundary *AB* with a misorientation angle ω_l in the case when the dislocations of decayed boundary *AB* move away from boundary *KL*.

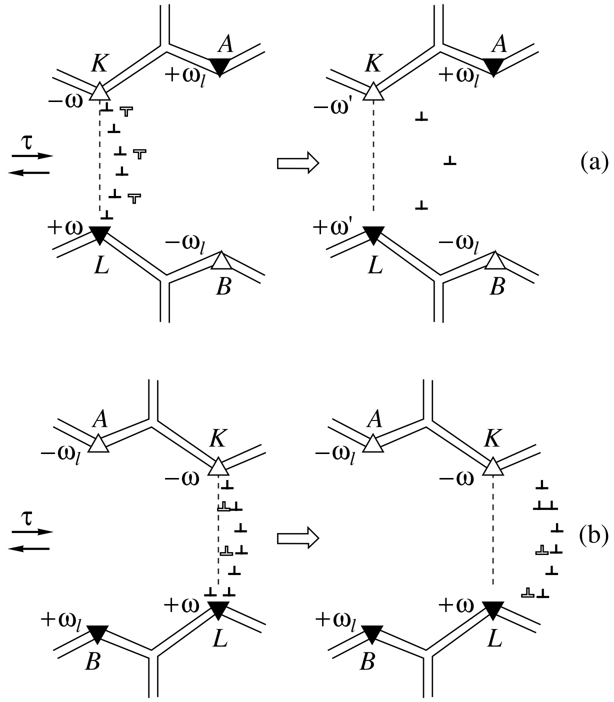

Fig. 2. Interaction of the dislocations from decayed boundary *AB* (open symbols) with the dislocations of neighboring boundary *KL*.

2. MODEL FOR THE DECAY OF A LOW-ANGLE TILT BOUNDARY

As was shown in [31], the decay of a low-angle tilt boundary is accompanied by the formation of grain-boundary junctions with uncompensated misorientation angles, which are sources of elastic stresses of the disclination-dipole type. Indeed, after the dislocations making up a tilt boundary move far away from its initial plane, two partial wedge disclinations having opposite signs and strengths $\pm\omega_l$ (where ω_l is the misorientation angle of the initial tilt boundary, *AB* in Fig. 1) form in the neighboring, former triple grain-boundary junctions. This disclination dipole interacts elastically with the surrounding defects. Depending on its position, the dipole either attracts or repulses the lattice dislocations making up the neighboring low-angle boundaries. Obviously, this interaction should strongly affect the decay of these boundaries.

Figure 1 shows possible positions of decayed boundary *AB* (which is represented in the form of a dipole of disclinations having strengths $\pm\omega_l$ and separated by a distance d_l) with respect to a probe low-angle boundary *KL* with a misorientation angle ω. The dislocations formed during the decay of boundary *AB* move away from boundary *KL* and do not participate in the decay of boundary *KL*. In the case shown in Fig. 1a, disclination dipole *AB* attracts the lattice dislocations of boundary *KL*, thereby facilitating its decay (the critical decay stress τ_c decreases). This critical stress also decreases in the case shown in Fig. 1b. Here, disclination dipole *AB* repulses the dislocations; however, since this dipole is located on the other side of boundary *KL*, its stress field again facilitates the decay of this boundary.

Radically different kinds of defect configurations are shown in Fig. 2. Here, the dislocations from decayed boundary *AB* (marked by open symbols) approach boundary *KL* and take part in its decay. Figure 2a shows the situation where the dislocations and both boundaries opposite in sign interact with each other. Obviously, some dislocations should annihilate. This would result in a decrease in the dislocation density in boundary *KL*, i.e., in a decrease in its misorientation angle ($\omega' < \omega$) and, hence, a decrease in the critical stress τ_c. In the right-hand side of Fig. 2a, this is shown as an increase in the flexure of boundary *KL*. Note that only the case of $\omega_l < \omega$ is of interest, since a stress that breaks a boundary with a misorientation angle ω_l will, of course, break a boundary with a lower misorientation angle. Thus, the number of dislocations that made up decayed boundary *AB* should be smaller than the number of dislocations in boundary *KL*. Therefore, the dislocations of boundary *AB* cannot annihilate completely with the dislocations of boundary *KL*.

Figure 2b shows the interaction of the dislocations of both boundaries when they have the same sign. The dislocations of decayed boundary *AB* abut against boundary *KL* and either increase its flexure (Fig. 2b, right-hand side) or break it when their amount is sufficiently high ($\omega_l \approx \omega$). In any case, we can also conclude that the dislocations of the decayed boundary cause a decrease in the critical stress τ_c for the decay of the neighboring boundary.

Thus, the disintegration of a low-angle grain boundary should lead to a decrease in the critical stresses for the decay of the neighboring boundaries.

We now go from a qualitative analysis of the decay of low-angle boundaries to its quantitative description. We estimate the change in the critical stress τ_c for the decay of a low-angle boundary in the presence of a neighboring decayed boundary using the configuration shown in Fig. 1a as an example. Let dipole *AB* of wedge disclinations having strengths $\pm\omega_l$ and separated by a distance d_l be located at a distance l from dislocation wall *KL* consisting of N lattice dislocations. To analyze the decay dynamics of boundary *KL*, we apply the approach developed in [31] to describe the decay of a single low-angle boundary. In the context of this approach, the glide of the lattice dislocations making up the low-angle boundary is described by the equations of motion

$$m\frac{d^2x_i}{dt^2} + \beta\frac{dx_i}{dt} = F_i, \quad i = 1, 2, \ldots, N, \qquad (1)$$

where x_i is the coordinate of the *i*th dislocation in the boundary, $m = \rho b^2/2$ is the effective dislocation mass [34], ρ is the material density, b is the Burgers vector of a lattice dislocation, β is the dynamic-friction coefficient of the lattice (the coefficient of viscosity), and F_i is the elastic force acting on the *i*th dislocation. The force F_i is specified by the superposition of the external shear stress τ and the shear-stress fields of the neighboring dislocations [35] and disclination dipoles *AB* and *KL* [36]. This force can be written as

$$F_i = b\left[\tau + \sum_{\substack{k=1\\ k\neq i}}^{N}\sigma_{xy}(x_i - x_k, y_i - y_k) - \frac{G\omega}{2\pi(1-\nu)}\left(\frac{x_i y_i}{x_i^2 + y_i^2} - \frac{x_i(y_i - d)}{x_i^2 + (y_i - d)^2}\right) - \frac{G\omega_l}{2\pi(1-\nu)}\left(\frac{(x_i - l)(y_i + d_l/2 - d/2)}{(x_i - l)^2 + (y_i + d_l/2 - d/2)^2} - \frac{(x_i - l)(y_i - d_l/2 - d/2)}{(x_i - l)^2 + (y_i - d_l/2 - d/2)^2}\right)\right], \qquad (2)$$

where $\sigma_{xy} = Gbx(x^2 - y^2)/(2\pi(1 - \nu)(x^2 + y^2)^2)$ is the shear component of the stress tensor of an edge dislocation, G is the shear modulus, and ν is the Poisson ratio.

3. CRITICAL DECAY STRESSES OF A LOW-ANGLE BOUNDARY

Equations (1), with the right-hand side defined by Eq. (2), were solved numerically for nanocrystalline iron as an example at various values of the parameters ω_l, d_l, and l. For iron, the parameters were taken to be the following: $G = 82$ GPa, $\nu = 0.29$, the lattice parameter is $a = 2.87$ Å, the typical Burgers vector is $b = (a/2)\langle 111\rangle \approx 2.5$ Å, $\rho = 7800$ kg m^{-3}, $m = 2.4 \times 10^{-16}$ kg m^{-1}, and $\beta \approx 5 \times 10^{-5}$ Pa s [34]. Figure 3 shows the calculated dependence of the critical stress τ_c for the decay of boundary *KL* on the angle of its initial misorientation ω for the case of $l = 50$ nm and $d_l = d$. The uppermost curve corresponds to the $\tau_c(\omega)$ dependence at $\omega_l = 0$, i.e., in the absence of disclination dipole *AB*. Then, from top to bottom, we plot the curves that show how the $\tau_c(\omega)$ dependence varies with the strength of dipole *AB* at $\omega_l = 1°, 3°$, and $5°$ (these curves are plotted in the range $\omega_l \le \omega \le 10°$). As was expected, the critical stress τ_c decreases with increasing ω_l, and this decrease can be rather significant at certain values of the parameters ω and ω_l. For example, at $\omega = 8.5°$ and $\omega_l = 5°$, the critical stress τ_c decreases by approximately 40% as compared to the case of $\omega_l = 0$.

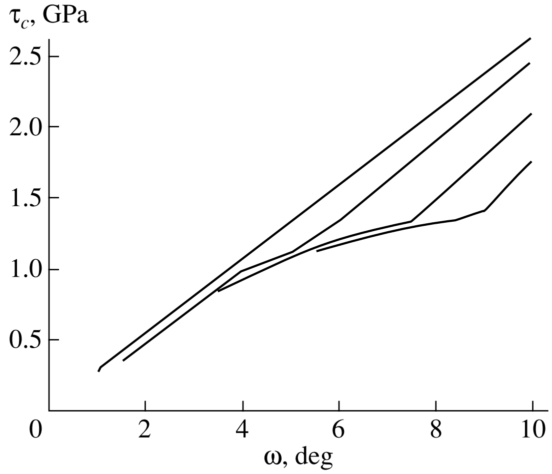

Fig. 3. Dependences of the critical stress τ_c for the decay of low-angle boundary *KL* on its misorientation angle ω at various values of the misorientation angle ω_l of decayed boundary *AB*: $\omega_l = 0°, 1°, 3°$, and $5°$ (from top to bottom).

It should be noted that there is an important distinction between the model of the decay of a low-angle boundary in the field of a decayed boundary and the model of the decay of a single boundary developed in [31]. Indeed, in the latter case, the critical decay stress is unambiguously defined as the stress at which dislocations break away irreversibly from the boundary and go to infinity (to the outer boundary of the crystal), whereas a more complex situation may occur in the model considered in this paper. In the field of an applied stress, the dislocations of boundary *KL* can reach the line of decayed boundary *AB* rather than go to infinity. This situation can naturally be treated as a transition of dislocations from one boundary to another, since the dislocations no longer belong to their parent boundary *KL*. The stress at which this situation is realized can be taken as the critical stress for the decay of boundary *KL*. We will call it the first critical stress τ_{c1}. By the second

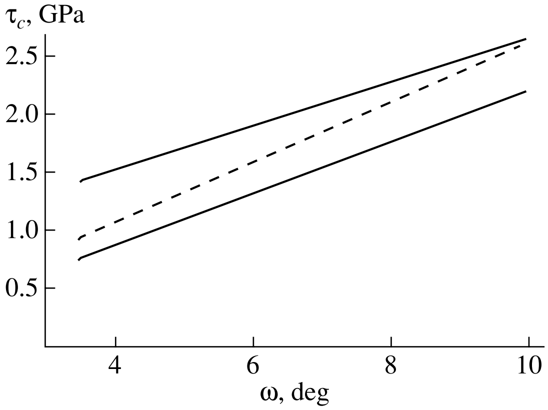

Fig. 4. Dependences of the first (τ_{c1}) and second (τ_{c2}) critical decay stresses of low-angle boundary *KL* on its misorientation angle ω (the lower and upper solid lines, respectively) at $\omega_l = 3°$, $d_l = d$, and $l = d$. The dashed line shows the $\tau_c(\omega)$ dependence for the decay of a single boundary.

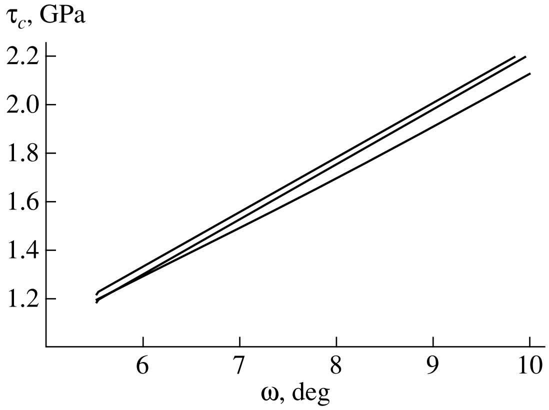

Fig. 5. Dependence of the critical decay stress τ_c of low-angle boundary *KL* on its misorientation angle ω at $\omega_l = 5°$, $l = d$, and $d_l/d = 1$, 0.5, and 1.5 (from bottom to top, respectively).

critical stress τ_{c2} will be meant the stress at which dislocations also break away from the second boundary (here, boundary *AB*) and go to infinity. It is important that τ_{c2} exists always, whereas τ_{c1} appears only at certain values of the parameters of the system. As follows from the definitions of τ_{c1} and τ_{c2}, τ_{c1} is always lower than τ_{c2}. In the situations where both τ_{c1} and τ_{c2} exist, by the critical stress will be meant the lowest quantity, namely, τ_{c1}.

Detailed calculations show that the first critical stress τ_{c1} is realized when either the strengths of dipoles *AB* and *KL* are similar ($\omega \approx \omega_l$) or the dipoles are located close to each other ($l \approx d$). At high values of ω, the transition from the first to second critical stress almost always occurs, which is clearly seen from the curves shown in Fig. 3. The breaks in the curves are related to this transition. These curves also indicate that, contrary to the second critical stress τ_{c2}, the first critical stress τ_{c1} (the curve segments on the left of the breaks) only weakly depends on ω_l (the curves for different values of ω_l almost coincide in these segments).

If dipoles *AB* and *KL* are located close to each other, the first critical stress τ_{c1} is realized over the whole ω range. This situation takes place when, for example, $l = d$, $\omega_l = 3°$, and $d_l = d$. Figure 4 shows the $\tau_{c1}(\omega)$ and $\tau_{c2}(\omega)$ curves. The second critical stress τ_{c2} turns out to be even higher than the critical stress for the decay of a single boundary (Fig. 4, dashed line). This can be explained by the fact that, at the instant of breakaway from the strongly bent wall *KL*, its dislocations are on the right-hand side of decayed boundary *AB*; therefore, the boundary elastic field hinders rather than facilitates this breakaway.

Now, let us consider the dependence of the critical stress on the length d_l of decayed boundary *AB*. In this case, it is of no importance which of the critical stresses (τ_{c1} or τ_{c2}) is realized, since the critical stress τ_c is the lowest of them. In the case analyzed above, where $l = d$ and $d_l = d$, the maximum of the shear stress field of decayed boundary *AB* is exactly at the center of boundary *KL* [36]. If d_l decreases or increases at fixed *d* and *l*, this maximum shifts to the right or to the left of boundary *KL*, respectively, which would increase τ_c. This conclusion is fully confirmed by calculations. Figure 5 shows the $\tau_c(\omega)$ dependence for three cases: $d_l/d = 0.5$, 1, and 1.5 at $l = d$ and $\omega_l = 5°$. For the configurations with $d_l/d = 0.5$ and 1.5, the critical stress τ_c increases, with the increase in the latter case being greater. This behavior is explained by the fact that, in the former case, the maximum of the field of decayed boundary *AB* shifts to the right and dislocations can reach it, whereas in the latter case this maximum shifts to the left and the field of decayed boundary *AB* weakens in the zone between boundaries *AB* and *KL*.

4. CONCLUSIONS

This study of the effect of a decayed grain boundary on the decay of a low-angle tilt boundary has shown that, in general, the presence of a decayed boundary results in a decrease in the critical decay stresses of the neighboring boundaries. This decrease can serve as a prerequisite for the chain decay of low-angle boundaries to form high-density ensembles of mobile dislocations, which can carry substantial plastic deformation in shear bands in NCMs.

ACKNOWLEDGMENTS

This work was supported by INTAS (project no. 03-51-3779), the Russian Foundation for Basic Research (project no. 04-01-00211), the Ministry of Education and Science of the Russian Federation (program "Physics of Solid-State Nanostructures"), the Foundation for

Assistance to Russian Science, the RAS program "Structural Mechanics of Materials and Construction Members," the Office of US Naval Research (project no. 00014-01-1-1020), the program "Integration" (project no. B0026), and the St. Petersburg Scientific Center of the RAS.

REFERENCES

1. C. S. Pande, R. A. Masumura, and R. W. Armstrong, Nanostruct. Mater. **2** (3), 323 (1993).
2. G. A. Malygin, Fiz. Tverd. Tela (St. Petersburg) **37** (8), 2281 (1995) [Phys. Solid State **37**, 1248 (1995)].
3. K. S. Kumar, S. Suresh, M. F. Chisholm, J. A. Horton, and P. Wang, Acta Mater. **51** (3), 387 (2003).
4. K. S. Kumar, S. Suresh, and H. Swygenhoven, Acta Mater. **51** (12), 5743 (2003).
5. R. A. Masumura, P. M. Hazzledine, and C. S. Pande, Acta Mater. **46** (13), 4527 (1998).
6. A. A. Fedorov, M. Yu. Gutkin, and I. A. Ovid'ko, Scr. Mater. **47** (1), 51 (2002).
7. M. Murayama, J. M. Howe, H. Hidaka, and S. Takaki, Science **295** (5564), 2433 (2002).
8. I. A. Ovid'ko, Science **295** (5564), 2386 (2002).
9. M. Yu. Gutkin, A. L. Kolesnikova, I. A. Ovid'ko, and N. V. Skiba, Philos. Mag. Lett. **82** (12), 651 (2002).
10. M. Yu. Gutkin, I. A. Ovid'ko, and N. V. Skiba, Acta Mater. **51** (14), 4059 (2003).
11. H. Hahn, P. Mondal, and K. A. Padmanabhan, Nanostruct. Mater. **9** (1–8), 603 (1997).
12. H. Hahn and K. A. Padmanabhan, Philos. Mag. B **76** (4), 559 (1997).
13. D. A. Konstantinidis and E. C. Aifantis, Nanostruct. Mater. **10** (7), 1111 (1998).
14. A. A. Fedorov, M. Yu. Gutkin, and I. A. Ovid'ko, Acta Mater. **51** (4), 887 (2003).
15. M. Chen, E. Ma, K. J. Hemker, H. Sheng, Y. Wang, and X. Cheng, Science **300** (5623), 1275 (2003).
16. D. V. Shtanskiĭ, S. A. Kulinich, E. A. Levashov, and J. J. Moore, Fiz. Tverd. Tela (St. Petersburg) **45** (6), 1122 (2003) [Phys. Solid State **45**, 1177 (2003)].
17. O. V. Klyavin, V. I. Nikolaev, L. V. Khabarin, Yu. M. Chernov, and V. V. Shpeĭzman, Fiz. Tverd. Tela (St. Petersburg) **45** (12), 2187 (2003) [Phys. Solid State **45**, 2292 (2003)].
18. M. Yu. Gutkin and I. A. Ovid'ko, *Plastic Deformation in Nanocrystalline Materials* (Springer, Berlin, 2004).
19. F. A. Mohamed and Y. Li, Mater. Sci. Eng. A **298**, 1 (2001).
20. S. X. McFadden, R. S. Mishra, R. Z. Valiev, A. P. Zhilyaev, and A. K. Mukherjee, Nature **398** (6729), 684 (1999).
21. R. Z. Valiev, C. Song, S. X. McFadden, A. K. Mukherjee, and R. S. Mishra, Philos. Mag. A **81** (1), 25 (2001).
22. A. K. Mukherjee, Mater. Sci. Eng. A **322** (1–2), 1 (2002).
23. R. Z. Valiev, I. V. Alexandrov, Y. T. Zhu, and T. C. Lowe, J. Mater. Res. **17** (1), 5 (2002).
24. A. K. Mukherjee, in *Creep Deformation: Fundamentals and Applications*, Ed. by R. S. Mishra, J. C. Earthman, and S. V. Raj (TMS, Warrendale, 2002), p. 3.
25. D. Jia, K. T. Ramesh, and E. Ma, Acta Mater. **51** (12), 3495 (2003).
26. J. R. Weertman and P. G. Sanders, Solid State Phenom. **35–36** (1), 249 (1994).
27. S. Zghal, M. J. Hytch, J.-P. Chevalier, R. Twesten, F. Wu, and P. Bellon, Acta Mater. **50** (19), 4695 (2002).
28. A. P. Sutton and R. W. Balluffi, *Interfaces in Crystalline Materials* (Clarendon, Oxford, 1995).
29. M. Yu. Gutkin and I. A. Ovid'ko, Phys. Rev. B **63** (6), 064515 (2001).
30. S. V. Bobylev and I. A. Ovid'ko, Phys. Rev. B **67** (13), 132506 (2003).
31. S. V. Bobylev, M. Yu. Gutkin, and I. A. Ovid'ko, J. Phys. D: Appl. Phys. **37** (2), 269 (2004).
32. K. N. Mikaelyan, M. Seefeldt, M. Yu. Gutkin, P. Klimanek, and A. E. Romanov, Fiz. Tverd. Tela (St. Petersburg) **45** (11), 2002 (2003) [Phys. Solid State **45**, 2104 (2003)].
33. Q. Wei, D. Jia, K. T. Ramesh, and E. Ma, Appl. Phys. Lett. **81** (8), 1240 (2002).
34. U. F. Kocks, A. S. Argon, and M. F. Ashby, Prog. Mater. Sci. **19** (5), 1 (1975).
35. J. P. Hirth and J. Lothe, *Theory of Dislocations* (McGraw-Hill, New York, 1967; Atomizdat, Moscow, 1972).
36. V. I. Vladimirov and A. E. Romanov, *Disclinations in Crystals* (Nauka, Leningrad, 1986) [in Russian].

Translated by K. Shakhlevich

Physics of the Solid State, Vol. 46, No. 11, 2004, pp. 2058–2062. Translated from Fizika Tverdogo Tela, Vol. 46, No. 11, 2004, pp. 1991–1995.

DEFECTS, DISLOCATIONS, AND PHYSICS OF STRENGTH

Micrometer-Scale Deformation Jumps at Different Stages of Creep in Solids

N. N. Peschanskaya, V. V. Shpeĭzman, A. B. Sinani, and B. I. Smirnov

Ioffe Physicotechnical Institute, Russian Academy of Sciences,
Politekhnicheskaya ul. 26, St. Petersburg, 194021 Russia
e-mail: shpeizm.v@mail.ioffe.ru

Received March 23, 2004

Abstract—Laser interferometry is used to study micrometer-scale creep-strain nonuniformities (jumps) that occur during compression of metals (Ag, Al, Bi, Cu, Pb, Sn, Zn) and LiF : Mg crystals. The strain rate is found to vary periodically. The average magnitude of deformation *L* over one period and the variation of *L* with the total strain are determined. Correlations are found to exist between *L* and the Mg content in the LiF crystals, between *L* and the grain size in the metals, and between the magnitude of small jumps and the Burgers vector in the metals. *© 2004 MAIK “Nauka/Interperiodica”.*

1. INTRODUCTION

The concepts of a multilevel character of deformation and its localization at different levels have been developed in many works [1–4]. However, in the traditional techniques of recording deformation, its microscopic nonuniformity is often averaged, since the recording precision does not allow one to resolve small-scale local displacements. One of the manifestations of deformation localization during creep is its nonuniformity (serrated creep), which was detected when the strain rate changed during compression of amorphous and amorphous–crystalline polymers for small changes in the sample length [5–7]. A new method of recording deformation with a laser interferometer and precision measurement of the strain rate and its change make it possible to study deformation jumps on the micrometer scale. A characteristic feature of the deformation of polymers is alternation of creep segments with relatively high and low rates. Experiments show that the periods of creep instability measured in terms of deformation units (the jump length) correlate with the size of inhomogeneities in the polymer structure on the micrometer scale [6–9]. It was shown in [10, 11] that serrated creep is characteristic of different types of solids; however, the nature of creep nonuniformity in metals and crystals has not been studied.

In this work, we study the effect of different structural factors on the deformation nonuniformity in solids using the techniques applied for polymers in [5–9]. Particular emphasis was placed on the dependence of the deformation nonuniformity on the grain size, using tin, lead, and microcrystalline aluminum as an example. We also study the effect of preliminary deformation, impurities, and the type of crystal lattice on the average magnitude of micrometer-scale deformation jumps.

2. EXPERIMENTAL

We studied creep in Ag, Al, Bi, Cu, Pb, Sn, Zn, and LiF subjected to constant compressive stresses at 290 K. Aluminum, tin, lead, and lithium fluoride were studied in more detail. Aluminum samples were prepared from single crystals and microcrystalline Al. The latter was produced by multiple equal-channel angular pressing (ECAP). The grain size after ECAP was 1–2 μm. The grain size in tin (β modification) was 50–70 μm, and that in lead was 90–110 μm.

The LiF single crystals differed in Mg impurity concentration (c = 0.0024, 0.007, 0.03 wt %). The single crystals were grown by the Kyropoulos method, annealed at 1020 K for 48 h, and then cooled at a rate of 5 K/h. The crystals were cleaved along the {100} planes to produce 4 × 4 × 10-mm samples. Metallic samples were 3 mm in diameter and 6 mm in height.

The variation of deformation with time was recorded with a laser interferometer; one of its mirrors was connected rigidly with a movable grip to track the deformation of a sample. The creep interferogram consists of sequential beats each of which corresponds to a deformation increment of 0.3 μm [5–9]. The strain rate is determined from the formula $\dot{\varepsilon} = \lambda_0 \nu / 2 l_0$, where λ_0 = 0.63 μm is the laser wavelength, ν is the beat frequency in the interferogram, and l_0 is the initial sample length. The recording technique makes it possible to measure the strain rate with an accuracy of 1–5% when deformation changes by 0.15–0.30 μm; that is, one can study deformation kinetics on the micrometer and submicrometer scales.

To reveal periodic changes in the strain rate (deformation jumps), the rate was measured in each sequential beat in an interferogram and the dependence of the strain rate $\dot{\varepsilon}$ on the deformation increment (which was a multiple of 0.3 μm) was plotted (Figs. 1, 2). The measurements are related to short deformation segments at different time stages of creep. The deformation periods (measured in micrometers) of oscillations in the strain rate (Figs. 1, 2) were determined as $L = 0.3n$, where n is the number of beats over a given period (the number of points), and the average values of L were calculated, as a rule, for several sequential periods at a given preliminary macrodeformation.

Depending on the structure and deformation stage, the strain-rate oscillations can have various shapes. We distinguish small deformation jumps $L_{\min}$, which are usually equal to 0.6–1.2 μm; medium jumps L_{med}, which are equal to several micrometers and consist of small simple jumps); and large jumps $L_{\max}$, equal to tens of micrometers and consisting of small and medium jumps.

3. RESULTS AND DISCUSSION

3.1. Correlation between the Jump Length and the Grain Size

Figure 1 shows examples of changes in the strain rate during creep in Al single crystals and in polycrystals with fine (1–2 μm) grains. The measurements were performed both in the initial creep stage (at a strain of 3–5%) and after significant deformation (26–35%). Preliminary deformation of the microcrystalline aluminum (26%) was accomplished on a universal Instron 1342 machine at loads exceeding the macroscopic yield stress $\sigma_y = 440$ MPa. The measured average magnitudes of small creep deformation jumps are given in Table 1.

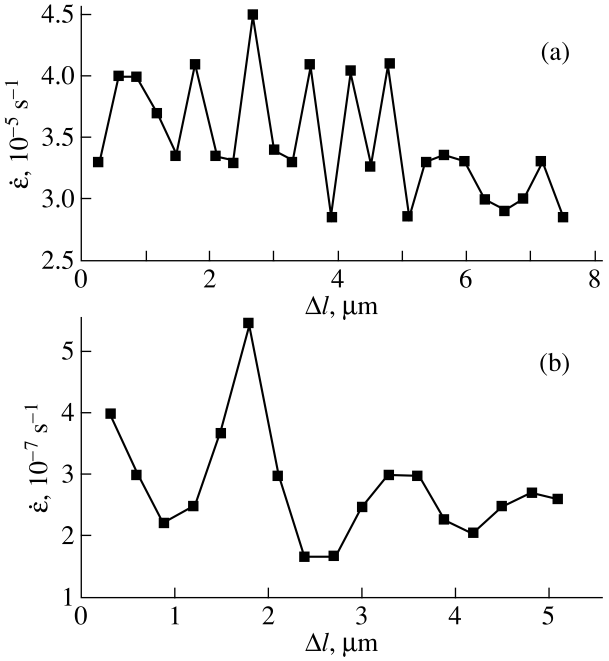

Fig. 1. Dependence of the creep rate in (a) single-crystal and (b) microcrystalline Al on the deformation increment. The preliminary strain ε is (a) 35 and (b) 3%. The stress σ is (a) 40 and (b) 200 MPa. The mean oscillation period L of the creep rate is (a) 0.8 and (b) 1.7 μm.

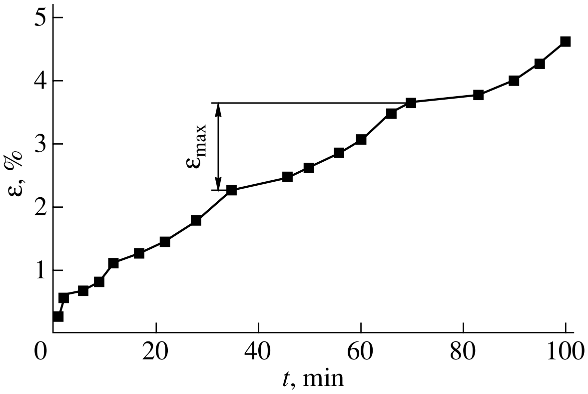

Fig. 2. Creep curve of β-Sn with a grain size of 50–70 μm at a stress σ = 10 MPa. The successive strain rate periods correspond to $L_{\max}$ = 30, 60, 80, and 80 μm. $\varepsilon_{\max} = L_{\max}/l_0$, where l_0 is the initial sample length.

Microcrystalline Al samples were tested in the creep mode at stresses of 30–200 MPa. The creep rate at these stresses was low (on the order of 10^{-7} s^{-1}). At a stress of 200 MPa, the initial strain was 3% and the creep strain after 100 min was 0.1%. Creep-rate oscillations correspond to the period $L_{\min}$ = 1.2 μm for very low stresses and 1.7 μm for higher stresses, approximately equal to half the yield stress. As the initial deformation was increased to 26%, the average deformation jump remained almost unchanged.[1] This value of $L_{\min}$ at high stresses (200 MPa) virtually coincides with the grain size in Al. It is likely that creep starts in coarser grains whose size is close to 2 μm and that the dislocation path length is equal to the grain size. In this case, a correlation between the grain size and the jump magnitude (and even their approximate equality for the corresponding calculated dislocation density) can exist. A lower value of $L_{\min}$ at very low stresses can indicate that deformation occurs either in finer grains or in the same coarse grains that are operative at high stresses, but these stresses are insufficient to move a dislocation through the whole grain.

As compared to microcrystalline Al, the creep rate in Al single crystals is two orders of magnitude higher, the average value of $L_{\min}$ is smaller, and $L_{\min}$ decreases with increasing strain (Table 1). Based on the relation between $L_{\min}$ and the dislocation path length, we can assume that barriers for dislocation motion are created by the deformation itself (e.g., during the intersection

---

[1] The absence of the effect of preliminary deformation on the jump magnitude is likely due to the fact that an additional deformation of 26% is negligibly small as compared to the deformation produced by ECAP.

Table 1. Deformation jumps in materials with different grain sizes subjected to different deformations

Material	Strain, %	$L_{\min}$, μm	L_{med}, μm	$L_{\max}$, μm
Al (single crystal)	3	1.1		
	20	0.9		
	35	0.8		
Al (after ECAP, grain size 1–2 μm)	3 (σ = 30 MPa)	1.2		
	3 (σ = 200 MPa)	1.7		
	26* (σ = 200 MPa)	1.6		
Pb (grain size 90–110 μm	3.5	1.3		
	58	0.9	2.7	
	3.5–5.1			100
				120
Sn (grain size 50–70 μm)	1.0	1.4	4.2	
			4.8	
	4.0	1.2	4.5	
			2.1	
			1.8	
	0.5–4.6			30
				60
				80
				80

* Preliminary deformation was performed at stresses exceeding the yield stress σ_y = 440 MPa.

Table 2. Comparison of the deformation jump *L* with the mean distance *d* between impurity atoms in a slip plane for LiF + Mg (the average jumps *L* are measured at stresses corresponding to the yield stress for each crystal (7, 12, 42 MPa) and strains of 2–5%)

Mg concentration, wt %	*L*, μm	*d*, nm
0.0024	1.0–1.5	95
0.007	0.9–1.3	56
0.03	0.8–1.1	27

of dislocations belonging to different slip systems) and that the interbarrier distance decreases with increasing strain.

Figure 2 shows a creep curve for polycrystalline tin with a grain size of 50–70 μm. In this case, we did not plot the curve in the rate–strain coordinates, since small jumps could blur the large-period pattern. As seen from Fig. 2, the large periods of strain-rate oscillations are clearly visible in the ordinary strain–time curve for creep. Thus, deformation develops with periodic accelerations and decelerations and the rate oscillation periods are equal to tens of micrometers (for example, four sequentially measured deformation jumps are 30–60–80–80 μm), which corresponds to the coarse-grain sizes in Sn (Table 1).

Similar data were obtained for coarse-grained lead with a grain size of about 100 μm. As seen from Table 1, $L_{\max}$ for Pb corresponds to the coarse-grain sizes. Strain rate–strain curves plotted for sequential strain increments of 0.3 μm show that micrometer-scale jumps are typical of the creep in Sn and Pb, as well as in other metals, with small jumps transforming into larger ones. The data from Figs. 1 and 2 and Table 1 prove that the magnitude of jumps corresponds to the size of structural inhomogeneities characteristic of a material.

3.2. Effect of Impurities on Serrated Deformation of LiF Crystals

When analyzing the creep in LiF crystals, the authors of [10] considered the deviations of experimental values of the strain rate from a logarithmically decaying curve. The authors believed that, because of the high measurement accuracy, the experimental error did not contribute to the calculated rate deviation. Therefore, the mean deviation from the true strain rate at different times (or the mean strain deviation calculated using the known law) can be a characteristic of the time creep nonuniformity. However, the authors of [10] did not take into account that the simple logarithmic creep law is approximate and that the application of a more complex law would result in changes in the characteristic of deformation nonuniformity. The calculation of the nonuniformity performed in this work is not related to any creep law. Moreover, we detect deformation nonuniformity (the step height in a stress–strain curve) rather than time nonuniformity.

In Table 2, the results of measuring the jump deformation are compared with the mean distance *d* between Mg impurity atoms in a slip plane, which is determined by the impurity concentration. Both characteristics are seen to decrease with increasing impurity concentration. For the time nonuniformity of deformation (see [10]), the relation between its value and the impurity concentration would be inverse, which is mainly due to the fact that the yield stress and the flow stress increase with the Mg concentration [12]. Hence, the time and strain nonuniformities of deformation behave differently upon alloying. This finding can be interpreted as follows: at a low Mg concentration (Mg atoms play the role of barriers), the dislocation path lengths are large; therefore, the deformation jumps *L* are large and rate changes in the jumps are small [10]. On the contrary, at a high Mg concentration, rate changes in the jumps are large and occur more frequently, which results in a greater scatter of the data [10] and a smaller period *L* (Table 2). Thus, the time nonuniformity of deformation on the mesoscale correlates with the force characteristic (the yield stress or the flow stress) and the deformation nonuniformity correlates with the geometrical (structural) characteristic, (the impurity interatomic distance *d*).

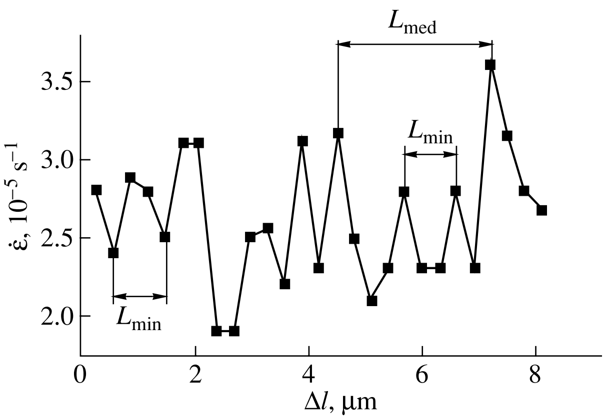

Fig. 3. Dependence of the creep rate of lead on the deformation increment on the micrometer scale. The total initial strain is $\varepsilon = 58\%$, the stress is $\sigma = 9$ MPa, and the creep-rate oscillation periods are $L_{min} = 0.9$ μm and $L_{med} = 2.7$ μm.

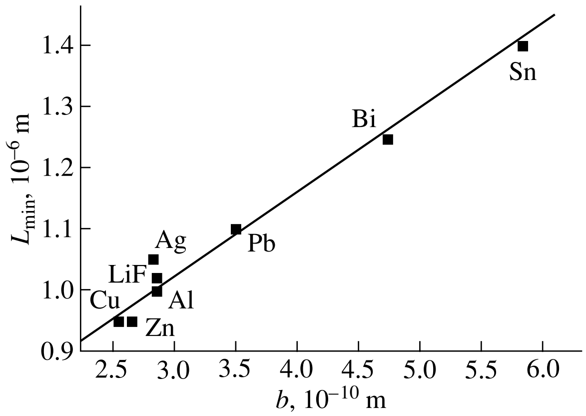

Fig. 4. Relation between the average length L_{min} of simple jumps and the Burgers vector for various materials under similar deformation conditions.

Assuming that the basic deformation mechanism in this stage is the broadening of slip bands [12], we can estimate the number of broadening slip bands that form a step in the creep curve. The axial strain in a jump L can be expressed as $L = m\gamma s/\sqrt{2}$, where m is the number of the bands, γ is the shear in the band, and s is the average displacement of the band edge in the direction normal to the slip plane (which can be taken to be equal to d for LiF). Substituting the values given in Table 2 and taking into account that a slip band can grow from both sides, we obtain $m = 150$–250. This value corresponds to an interband distance of 40–70 μm, which is admissible for this level of deformation.

Therefore, as in Subsection 3.1, L allows us to distinguish the basic structural characteristic of deformation on the mesoscale, namely, the displacement of an active deformation element. The scatter and large oscillation of this quantity during deformation (Table 2) are likely related to the random character of impurity distributions in the crystals.

3.3. Serrated Creep in Metals

Figure 3 shows an example of the variation of the creep rate in Pb with the deformation increment Δl on the micrometer scale. The total strain at which the $\dot{\varepsilon}$–Δl curve is plotted is given in the figure caption. Each point corresponds to an increment of deformation of 0.3 μm (0.005%). Similar curves were plotted for all the materials under study for different creep segments. It is seen from Fig. 3 and Table 1 that, as the strain increases, the sizes of small jumps L_{min} can change and, simultaneously, more complex jumps (L_{med}, L_{max}) can form from the small ones.

Let us consider the relations between the magnitude of small jumps L_{min} at the initial deformation stage and the characteristic distances in the structure of the material. Since all the materials were annealed, the dislocation density in them can be assumed to be approximately the same in the strain range under study. Therefore, we can suppose that the mean path lengths of dislocations l_d in the initial stage are also approximately the same; in this case, the characteristic deformation $\varepsilon = \rho b l_d$, to which the jump magnitude L_{min} is compared, should be proportional to the Burgers vector magnitude b.

As follows from Fig. 4, the values of L_{min} and b do correlate with each other: the greater b is, the larger the deformation jumps. If L_{min} and b are measured in the same length units (e.g., micrometers), the straight line in Fig. 4 can be described as $L_{min} = 0.6 + 1400b$. Here, 0.6 μm is obviously a characteristic of the device (its limiting resolution) and a small jump corresponds to an elementary deformation act on the mesoscale.

4. CONCLUSIONS

Thus, the deformation jumps (nonuniformities), which indicate cooperative motion of interrelated structural defects, are caused by ordered formations at different structural levels. We can state that, if repeated morphological inhomogeneities exist or are created by deformation, jumps on the same scale should appear in creep and that, vice versa, deformation jumps indicate the presence of ordered structural elements of a size similar to that of the jumps. For example, small jumps observed in metals and crystals indicate the existence of a characteristic deformation size of 1 μm and large jumps correspond to grain sizes. There can also occur smaller jumps that cannot be resolved by this technique and well-known macroscopic jumps that result from macroscopic localization of deformation [13, 14].

As noted above, the jumps characterize not only initial inhomogeneities but also the structural evolution during deformation. Hence, the experiments performed on the crystals and metals confirm the conclusion drawn for polymers: the inhomogeneity of a medium is the cause of jumplike cooperative displacements [9, 11]. The jump characteristics can be used to estimate the structural parameters of solids that determine deformation and to track their variation during structural evolution.

ACKNOWLEDGMENTS

This work was supported in part by the Ministry of Education and Science of the Russian Federation (program “Solid-State Nanostructures”).

REFERENCES

1. V. E. Panin, V. A. Likhachev, and Yu. V. Grinyaev, *Structural Deformation Levels of Solids* (Nauka, Novosibirsk, 1985) [in Russian].
2. S. V. Kolupaeva, V. A. Starenchenko, and L. E. Popov, *Instabilities of Plastic Deformation in Crystals* (Tomsk. Gos. Univ., Tomsk, 1994) [in Russian].
3. V. I. Vladimirov, in *Problems in the Theory of Crystal Defects* (Nauka, Leningrad, 1987), p. 43 [in Russian].
4. M. M. Myshlyaev, V. V. Shpeĭzman, and M. M. Kamalov, Fiz. Tverd. Tela (St. Petersburg) **43** (11), 2015 (2001) [Phys. Solid State **43**, 2099 (2001)].
5. N. N. Peschanskaya and P. N. Yakushev, Fiz. Tverd. Tela (Leningrad) **30** (7), 2196 (1988) [Sov. Phys. Solid State **30**, 1264 (1988)].
6. N. N. Peschanskaya, L. P. Myasnikova, and A. B. Sinani, Fiz. Tverd. Tela (Leningrad) **33** (10), 2948 (1991) [Sov. Phys. Solid State **33**, 1665 (1991)].
7. N. N. Peschanskaya, Fiz. Tverd. Tela (St. Petersburg) **35** (11), 3019 (1993) [Phys. Solid State **35**, 1484 (1993)].
8. N. N. Peschanskaya, Fiz. Tverd. Tela (St. Petersburg) **43** (8), 1418 (2001) [Phys. Solid State **43**, 1478 (2001)].
9. N. N. Peschanskaya, P. N. Yakushev, V. M. Egorov, V. A. Bershteĭn, and L. Bokobza, Fiz. Tverd. Tela (St. Petersburg) **44** (9), 1609 (2002) [Phys. Solid State **44**, 1684 (2002)].
10. V. V. Shpeĭzman, N. N. Peschanskaya, and B. I. Smirnov, Fiz. Tverd. Tela (St. Petersburg) **40** (4), 690 (1998) [Phys. Solid State **40**, 634 (1998)].
11. N. N. Peschanskaya, Doctoral Dissertation (Physicotechnical Inst., Russian Academy of Sciences, St. Petersburg, 1999).
12. B. I. Smirnov, *Dislocation Structure and Hardening of Crystals* (Nauka, Leningrad, 1981) [in Russian].
13. V. I. Startsev, V. Ya. Il’ichev, and V. V. Pustovalov, *Plasticity and Strength of Metals and Alloys at Low Temperatures* (Metallurgiya, Moscow, 1975) [in Russian].
14. V. V. Shpeĭzman, V. I. Nikolaev, B. I. Smirnov, A. B. Lebedev, and V. I. Kopylov, Fiz. Tverd. Tela (St. Petersburg) **42** (6), 1034 (2000) [Phys. Solid State **42**, 1066 (2000)].

Translated by K. Shakhlevich

Physics of the Solid State, Vol. 46, No. 11, 2004, pp. 2063–2066. Translated from Fizika Tverdogo Tela, Vol. 46, No. 11, 2004, pp. 1996–1999.

DEFECTS, DISLOCATIONS, AND PHYSICS OF STRENGTH

Dynamics of Slip Lines on the Surface of Polycrystalline Copper

V. I. Vettegren* and V. N. Svetlov

Ioffe Physicotechnical Institute, Russian Academy of Sciences,
Politekhnicheskaya ul. 26, St. Petersburg, 194021 Russia
**e-mail: Victor.Vettegren@mail.ioffe.ru*

Received March 25, 2004

Abstract—Tunneling microscopy is used to study the geometry and dynamics of slip lines on the surface of cold-rolled polished copper during steady-state creep at room temperature. Dislocation sources in a 200- to 300-nm-thick surface layer are found to be initially activated under stresses. As a result, a large number of lines are formed whose lengths vary from several tens to several hundreds of nanometers. Then, dislocation sources located in deeper layers become operative, which results in the formation of slip lines as long as ≈8–9 μm. The formation, evolution, and disappearance of slip lines are caused by the motion of bands having a width of several nanometers. *© 2004 MAIK "Nauka/Interperiodica".*

1. INTRODUCTION

Dislocation motion along several slip planes is known to result in a deformation relief on the crystal surface. Studies of the dynamics of relief formation in the nanometer range have shown that, during plastic deformation of metals (Cu, Au, Mo, etc.), defects in the form of individual pits, whose walls are parallel to dislocation slip lines, form on their surfaces at the beginning of steady-state creep [1–6]. As the strain increases, slip lines form on the surfaces [1]. This work is a continuation of a series of such studies. In this paper, we describe the results of studying the formation and evolution of slip lines.

2. EXPERIMENTAL

The surface profiles of commercial 60-μm-thick cold-rolled copper (99.96% purity) ribbons were studied. Strips 6-mm wide (parallel to the rolling axis) were cut from the ribbons. To localize the deformation zone, half-round notches 1.5 mm in radius were made at the edges of the strips. The gauge length of a sample was 12 mm. For loading, we used a spring device [1] designed at the laboratory; it was fixed on the microscopic stage of an RTP-1 scanning tunneling profilometer [1].

In this profilometer, a measuring tip can travel no more than 1 μm normally to the surface to be studied. To remove microasperities higher than 1 μm, the samples were mirror-polished with a GOI paste before measurements. To remove the rest of the paste and other impurities from the surface, the samples were rinsed in acetone and alcohol. The chemical composition of the sample surfaces before and after measurements was controlled with an LH-10 Auger spectrometer. The sample surfaces were found to be covered with a ≈2-nm-thick oxide layer.

The measurement window was 10 × 10 μm, and the time of recording a complete topogram was about 40 min. Because of creep, the area under study moves gradually with respect to the profilometer tip. In order to obtain a high-quality image of the surface under such conditions, the absolute displacement of the surface in recording must be at least 10–100 times smaller than the linear dimensions of the area under study; that is, it must be smaller than ≈100 nm/h. The low creep rate caused the experiments to be long in duration, covering up to 30 days.

To minimize the distortions induced by the residual deformation of piezoengines and the measuring tip, we took periodic breaks in the experiments to control the quality of surface images by recording a test grid. To prevent the formation of an electrolyte on the sample surface, the measuring device with the piezoengines was covered by a polyurethane cap, through which dry nitrogen was blown.

3. GEOMETRY OF DEFORMATION NANODEFECTS AND THE MECHANISMS OF THEIR FORMATION

Figure 1 shows the time variation of the position of a microdefect produced on the surface by the measuring tip. The experimental points are seen to fall on a straight line; hence, the topograms recorded are related to steady-state creep. The creep rate determined from the slope of this line is ≈1.6 nm/h.

Figure 2a shows a fragment of a topogram of the copper surface obtained 2 h after a tensile stress of 400 MPa was applied. It contains individual defects,

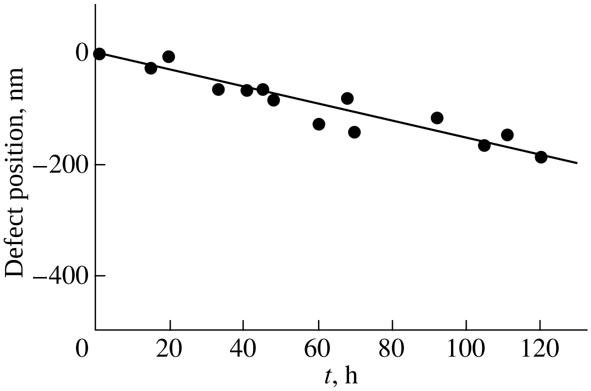

Fig. 1. Displacement of a microdefect on the copper surface with time under a stress of 400 MPa.

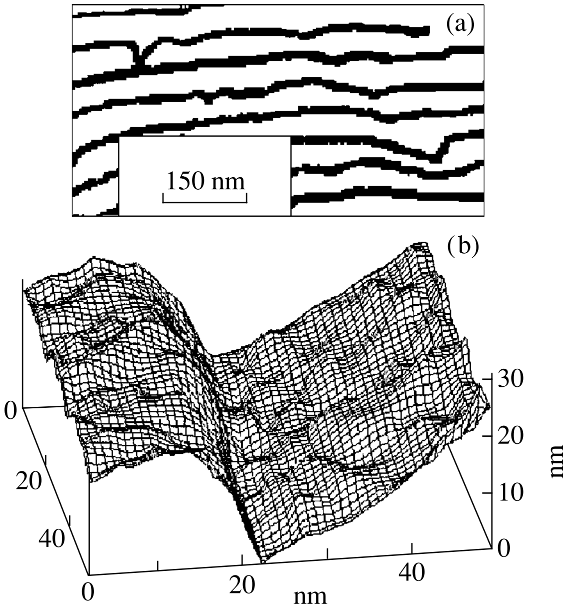

Fig. 2. Defects forming on the copper surface within two hours after a tensile stress of 400 MPa is applied: (a) fragment of a surface topogram and (b) a scaled up nanodefect.

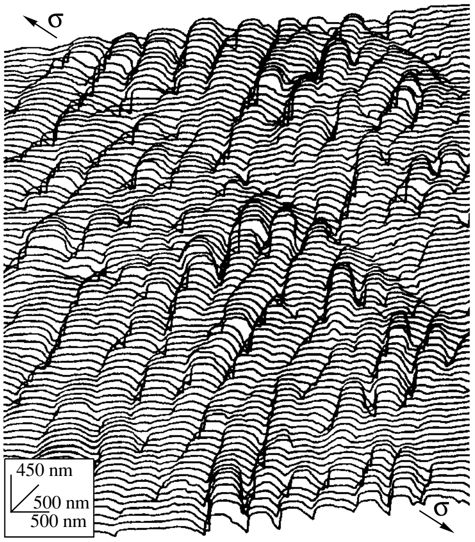

Fig. 3. Slip lines forming on the copper surface within 450 h after a tensile stress of 400 MPa is applied.

which are magnified in Fig. 2b. The defect sizes are the following: the depth is d = 10–20 nm, the wall length is l = 30–50 nm, and the width is h = 25–35 nm. The apex angle of the nanodefects is ≈70°, with one of the walls being approximately perpendicular to the surface and the other wall making an angle of ≈20°–30°. This orientation of the defect walls coincides with that of the (111) easy-slip planes in copper after cold rolling. Therefore, the defects were assumed to be formed during dislocation motion along the easy-slip planes [1]. A theory on the formation of nanodefects by dislocations reaching the surface was developed in [7].

The defect sizes increase with time, and the wall length increases faster than the depth and width. As a result, slip lines in the form of grooves are formed. Before fracture, their length reaches ≈8–9 μm (Fig. 3). The walls of grooves are irregular, their depths vary from several tens of nanometers to one micrometer or larger, and their axes are curved. The angle between the line axis and the tensile direction is 60° ± 20°.

4. SLIP-LINE DYNAMICS

To study the dynamics of slip lines, we recorded topograms over 452 h in steps of ≈1 h. The time to fracture was 454 h.

We found that, if the groove length does not exceed a critical value $l_c \approx 2.5$–3 μm, grooves grow and disappear with time (Fig. 4). Simultaneously, their depth increases. In time, a valley forms, which, as a rule, is located in the central portion of the line (Fig. 5).

To study the line growth mechanism, we recorded line cross sections in intervals of 40 s (Fig. 6). Analysis shows that the lines grow and disappear due to the displacement of 5-nm-wide bands in directions normal to the surface or at an angle of ≈30° with the surface.

Lines whose lengths are larger than 3 μm are formed upon the coalescence of two or three sequentially arranged lines shorter than 3 μm. Analysis indicates that there are three deep sites (deeper than 1 μm) at the bottom of lines (grooves) 7–9 μm long (Fig. 7). Since the measuring tip cannot travel more than 1 μm, we failed to measure the depths of these sites.

5. MECHANISM OF SLIP-LINE FORMATION

According to modern concepts [8, 9], slip lines form when dislocation loops generated by dislocation

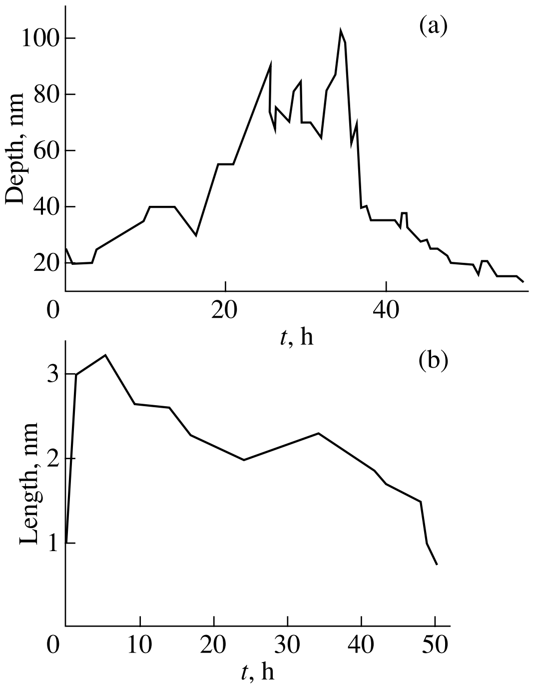

Fig. 4. Time dependences of (a) the depth and (b) the length of a slip line on the copper surface.

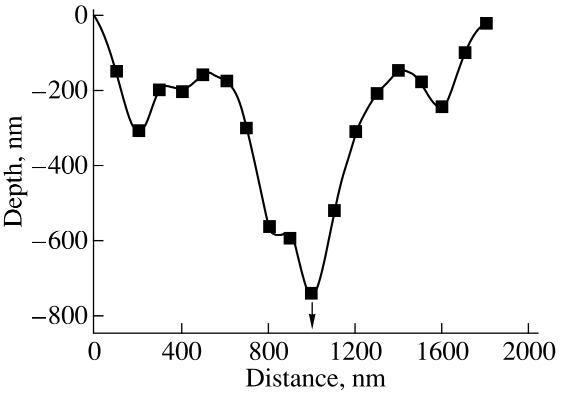

Fig. 5. Variation of the line depth along a slip line on the copper surface. The arrow shows the possible position of a dislocation source.

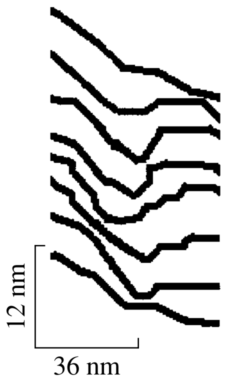

Fig. 6. Time evolution of the cross section of a slip line on the copper surface. Sections are recorded in steps of 40 s. The time increases from bottom to top.

sources reach the surface. As noted above, we studied samples subjected to a high degree of preliminary deformation (cold rolling). Therefore, a large number of dislocations moving in different slip planes are involved in a slip.

Moreover, the samples were polished before measurements, which additionally increased the number of dislocation sources in the surface layer.

In such samples, sources in the polished surface layer are initially activated under the action of mechanical stress. As a result, a large number of individual defects having a depth of 10–20 nm and a wall length of 30–50 nm are formed. Some of them disappear, and the others transform into slip lines 0.5–1.5 μm long and ≈100–200 nm deep.

As these sources are exhausted, sources in deeper subsurface layers become operative, which results in the formation of longer and deeper slip lines. Their lengths vary from 2–2.5 to 8–9 μm, and their depths are 1 μm or greater.

As noted above, one deep valley exists inside a slip line ≈2.5–3 μm long and three such valleys exist inside a slip line 8–9 μm long. The positions of these valleys are likely to reflect the positions of dislocation sources in a sample. Therefore, the mean intervalley distance corresponds to the mean distance between dislocation sources (≈3 μm). Interestingly, a theoretical analysis of nanodefect formation on the surface of copper [7] also gave the same intersource distance (≈3 μm).

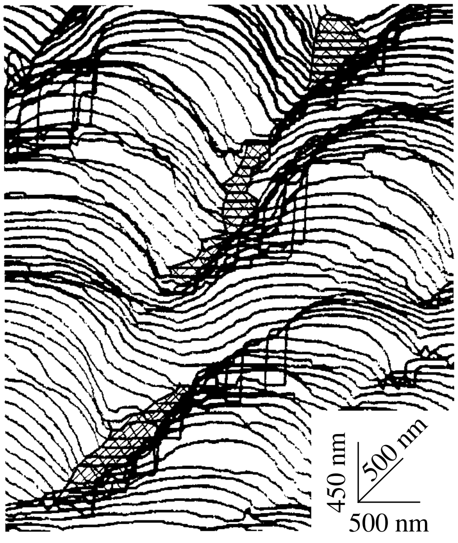

Fig. 7. Slip line ≈8 μm long on the copper surface. The regions located deeper than 1 μm are crosshatched. In these regions, the measuring tip cannot reach the surface.

6. CONCLUSIONS

The results obtained indicate that, as cold-rolled polished copper is stretched, dislocation sources in the polished surface layer are initially activated; this leads to the formation of a large number of slip lines in the form of grooves 100–200 nm deep with lengths varying from several tens to several hundreds of nanometers. Then, sources located in deeper layers become operative, which results in the formation of slip lines as deep as 1 μm or deeper and ≈8–9 μm long. The distance between sources in these layers is ≈3 μm. The formation, evolution, and disappearance of slip lines are caused by the motion of material bands several nanometers wide.

REFERENCES

1. V. I. Vettegren, S. Sh. Rakhimov, and V. N. Svetlov, Fiz. Tverd. Tela (St. Petersburg) **37** (4), 913 (1995) [Phys. Solid State **37**, 495 (1995)]; Fiz. Tverd. Tela (St. Petersburg) **37** (12), 3635 (1995) [Phys. Solid State **37**, 2001 (1995)]; Fiz. Tverd. Tela (St. Petersburg) **40** (4), 2180 (1998) [Phys. Solid State **40**, 1977 (1998)].
2. J. Plessing, Ch. Achmus, H. Neuhauser, B. Schonfeld, and G. Kostorz, Z. Metallkd. **88** (8), 630 (1997).
3. V. I. Vettegren, S. Sh. Rakhimov, and V. N. Svetlov, Proc. SPIE **3345**, 226 (1998).
4. V. I. Vettegren, V. L. Gilyarov, S. Sh. Rakhimov, and V. N. Svetlov, Fiz. Tverd. Tela (St. Petersburg) **40** (4), 668 (1998) [Phys. Solid State **40**, 614 (1998)].
5. V. I. Vettegren, S. Sh. Rakhimov, and V. N. Svetlov, Neorg. Mater. **35** (6), 756 (1999).
6. Kh. G. Kilian, V. I. Vettegren, and V. N. Svetlov, Fiz. Tverd. Tela (St. Petersburg) **42** (11), 2024 (2000) [Phys. Solid State **42**, 2083 (2000)]; Fiz. Tverd. Tela (St. Petersburg) **43** (11), 2107 (2001) [Phys. Solid State **43**, 2199 (2001)].
7. G. A. Malygin, Fiz. Tverd. Tela (St. Petersburg) **43** (5), 822 (2001) [Phys. Solid State **43**, 854 (2001)].
8. B. I. Smirnov, *Dislocation Structure and Strengthening of Crystals* (Nauka, Leningrad, 1981) [in Russian].
9. V. I. Vladimirov, *Physics of Metal Fracture* (Metallurgiya, Moscow, 1984) [in Russian].

Translated by K. Shakhlevich

Physics of the Solid State, Vol. 46, No. 11, 2004, pp. 2067–2072. Translated from Fizika Tverdogo Tela, Vol. 46, No. 11, 2004, pp. 2000–2005.
Original Russian Text Copyright © 2004 by Aplesnin, Ryabinkina, Abramova, Romanova, Kiselev, Bovina.

Spin-Dependent Transport in α-MnS Single Crystals

S. S. Aplesnin, L. I. Ryabinkina, G. M. Abramova, O. B. Romanova,
N. I. Kiselev, and A. F. Bovina
Kirensky Institute of Physics, Siberian Division, Russian Academy of Sciences,
Akademgorodok, Krasnoyarsk, 660036 Russia
e-mail: lir@iph.krasn.ru

Received January 29, 2004

Abstract—The electrical resistivity of single crystal α-MnS in crystallographic directions [111] and [100] was found to be anisotropic in the temperature interval 77–300 K. The change in activation energy below the Néel temperature was determined. Magnetoresistance was revealed, and reversal of its sign in the (111) plane above the Néel point was found. The experimental data are analyzed in terms of the *s*–*d* model, with the manganese ion holes interacting with localized spins assumed to be free carriers. *© 2004 MAIK “Nauka/Interperiodica”.*

1. INTRODUCTION

A new direction in science, spintronics, has recently been undergoing explosive development [1]. Spintronics draws on the dependence of conductivity on magnetic structure, which changes when acted upon by an external magnetic field. The use of nanotechnology in electronic devices places constraints on the area of application of *p*–*n* junction–based semiconductors and calls for using alternative materials that have strongly interrelated magnetic and electronic properties. Manganites figure among such materials. They have the remarkable feature of exhibiting giant magnetoresistance at room temperature, with the resistivity in an external magnetic field varying over more than an order of magnitude. The effect of magnetic order on transport properties also becomes manifest in the sulfide systems $Me_xMn_{1-x}S$ (*Me* = Cr, Fe), which are prepared on the basis of the monosulfide α-MnS and exhibit colossal magnetoresistance [2]. Off-stoichiometry in the α-MnS magnetic semiconductor also brings about a change in the magnetic structure and a substantial variation in resistivity [3].

We report on a study of the relation between the magnetic, electronic, and elastic subsystems in the α-MnS magnetic semiconductor. The manganese monosulfide α-MnS is an antiferromagnet with an fcc lattice. Its magnetic structure combines ferromagnetic ordering of the magnetic moments of manganese ions in (111)-type planes and antiferromagnetic interplane ordering with a Néel temperature $T_N \approx 150$ K [3, 4]. Antiferromagnetic ordering is also observed to set in along the cube edges. It thus appeared reasonable to investigate the effect of magnetic ordering on the transport properties of an α-MnS single crystal in (111)- and (100)-type planes. The experimental data obtained are analyzed in terms of the *s*–*d* model in the strong-coupling limit, where the conduction band width $W \ll I$ (I is the *s*–*d* exchange integral), which is valid for magnetic semiconductors with a narrow conduction band.

2. EXPERIMENTAL TECHNIQUES AND EXPERIMENTAL RESULTS

An α-MnS single crystal was grown by saturating liquid manganese with sulfur at $T \sim 1245°$C. X-ray structural analysis was performed on a DRON-2.0 diffractometer with CuK_α radiation in the temperature interval 77–300 K. X-ray fluorescence analysis was carried out on a SPARK-1 x-ray spectrometer. The electrical resistivity in the (100) and (111) crystallographic planes was measured in zero magnetic field and in transverse magnetic fields of up to 15 kOe in the temperature interval 77–300 K. The magnetoresistance was calculated using the relation $\delta_H^{ex} = \dfrac{\rho(H) - \rho(H = 0)}{\rho(H)} \times 100\%$.

The x-ray diffraction measurements showed the α-MnS single crystal to have a NaCl-type fcc lattice with the parameter $a = 5.222 \pm 0.001$ Å, which agrees well with the data obtained on α-MnS single crystals grown using chemical transport reactions [5]. The x-ray fluorescence analysis suggests the absence of impurities in the α-MnS single crystal. Figure 1 shows the temperature dependence of the lattice parameter, which decreases nonlinearly with decreasing temperature. The variation in $a(T)$ is maximum in the region (166–125) ± 5 K, where the NaCl-type fcc lattice was shown in [5] to undergo a rhombohedral distortion.

Figure 2 plots the temperature dependence of electrical resistivity in the (111) and (100) crystallographic planes obtained in zero magnetic field in the temperature interval 77–300 K. When measured at ~300 K, the electrical resistivity of the crystal is 3.17×10^5 Ω cm in the (100) plane and 5.98×10^5 Ω cm in the (111) plane.

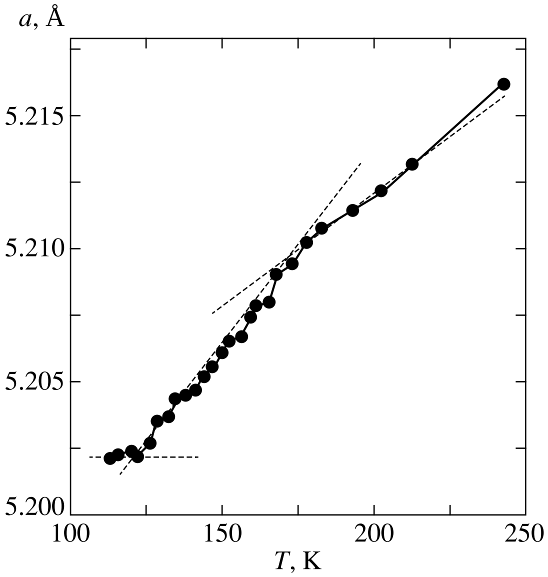

Fig. 1. Temperature dependence of the lattice parameter of a manganese monosulfide single crystal.

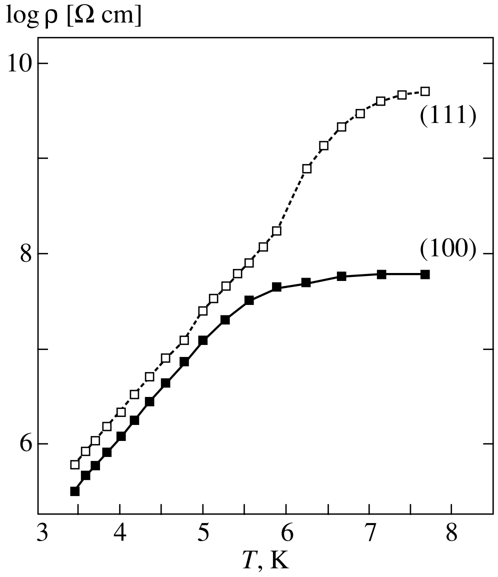

Fig. 2. Temperature dependence of the electrical resistivity of α-MnS in the (111) and (100) planes.

For temperatures $T \sim 170$–300 K, the conductivity can be fitted by a relation typical of semiconductors, $\sigma \sim \exp(-E_a/k_BT)$, with activation energy $E_a \sim 0.2$ eV. For $T < 160$ K, the electrical resistivity in the (111) plane increases, which is accompanied by the conductivity activation energy decreasing down to $E_a \sim 0.04$ eV below T_N. An analysis of the behavior of electrical resistivity in the (100) plane measured in zero magnetic field shows $\rho(T)$ not to be activated thermally for $T < T_N$.

The magnetoresistance of α-MnS was studied by measuring the electrical resistivity in the (111) and (100) planes in the temperature interval 77–300 K and magnetic fields of up to 15 kOe. Figures 3a and 3b plot temperature dependences of the magnetoresistance measured in the (111) and (100) planes of α-MnS, respectively, in a field of 10 kOe at temperatures of 100–300 K. It was established that the magnetoelectric properties, as well as the electrical properties, depend on crystallographic orientation. The negative magnetoresistance reaches –12% at 10 kOe and becomes most pronounced in the (111) plane at temperatures $T \sim 230$ K. The maximum positive magnetoresistance in the (100) plane in the same field is +11% in the region of the magnetic transition point. As the magnetic field increases, the minimum negative magnetoresistance in the (111) plane does not change in magnitude but shifts to low temperatures; indeed, in a field of 15 kOe, the minimum is seen at $T \sim 170$ K. The observed variation in magnetoresistance is reversible.

3. MODEL AND METHOD OF CALCULATION

Hall measurements performed for $T < 450$ K suggest [4] that the conduction in α-MnS is due to holes in the 3*d* levels of the manganese ion. This conclusion is also supported by calculations made using the electronic density functional method [6]. For instance, the hole concentration in the t_{2g} and e_g shells is 0.11 and 0.29 per Mn^{2+} ion, respectively. The rhombohedral distortion of the fcc lattice occurring near the Néel temperature brings about a weak overlap of the t_{2g} shells of neighboring manganese ions and the formation of a narrow energy band. For $T > T_N$, the low mobility of the holes caused by their being trapped by dynamic rhombohedral distortions supports the validity of assuming a narrow Mn^{2+} band.

Since the hole concentration is much less than unity, we neglect the Coulomb interaction of holes at a site and consider a gas of holes interacting with the localized manganese ion spins in the *s*–*d* model, an instructive approach that simplifies a qualitative understanding of the experimental results obtained.

We treat the magnetic and electronic properties in the adiabatic approximation. We define the magnetic structure in the Heisenberg model with antiferromagnetic interaction between the nearest (J_s) and next-to-nearest (K) neighbors mediated by sulfur ions:

$$H = -\sum_{i,j} J_{i,js}\mathbf{S}_i\mathbf{S}_j - \sum_{i,j} K_{i,j}\mathbf{S}_i\mathbf{S}_j - \sum_i H_i S_i, \qquad (1)$$

where H_i is an external magnetic field.

The electronic properties will be considered in terms of the *s*–*d* model with an Ising-type Hamiltonian [7]:

$$H = H_{\text{kin}} + H_{\text{int}}, \quad H_{\text{kin}} = \sum_{ij\sigma} t_{ij} a^{+}_{i\sigma} a_{i\sigma},$$
$$H_{\text{int}} \longrightarrow -\frac{1}{2} J_H \sum_{I} S^z_i (a^{+}_{i\uparrow} a_{i\uparrow} - a^{+}_{i\downarrow} a_{i\downarrow}), \tag{2}$$

where S^z_i is the operator of the z component of the localized spin at site i; J_H is the Hund exchange parameter; t_{ij} is the matrix element of hole transfer over the lattice, which depends on the mutual orientation of spins at sites i and j involved in the hole transfer; and $a^{+}_{i\sigma}$ ($a_{i\sigma}$) is the Fermi operator of creation (annihilation) of a hole with spin σ at site i. In second order of perturbation theory in parameter W/J_H (W is the band width), one can switch from the original Hamiltonian $H = H_{\text{kin}} + H_{\text{int}}$ with simplified interaction (2) to the effective Hamiltonian

$$H = -t \sum c^{+}_{i\sigma} c_{i\sigma} - \sum J^h_{ij} n_{i\sigma} n_{i\sigma}. \tag{3}$$

Here, J^h is the indirect interaction between the nearest neighbor sites ($J^h \sim t^2/J_H$), $n_{i\sigma} = c^{+}_{i\sigma} c_{i\sigma}$, and $c_{i\sigma}(c^{+}_{i\sigma})$ is the Fermi-like annihilation (creation) operator for a complex consisting of a localized spin at site i and a hole with a parallel spin,

$$c_{i\sigma} = \frac{1}{2}(1 + \sigma S^z_i) a_{i\sigma}. \tag{4}$$

The states of sites at which the spins in the complexes described by operators $(1/2)(1 - \sigma S^z_i) a_{i\sigma}$ are antiparallel are disregarded [8]. In the limit as $z \longrightarrow \infty$, the Hartree–Fock approximation of intersite interaction becomes exact; therefore, the exchange term in Eq. (3) can be linearized and the Hamiltonian can be recast in the form

$$H = \sum \varepsilon_\sigma c^{+}_{i\sigma} c_{i\sigma} - t \sum c^{+}_{i\sigma} c_{i\sigma}, \tag{5}$$

where $\varepsilon_\sigma = -\mu - \sum_j J^h_{ij} \langle n_{j\sigma} \rangle$ and μ is the chemical potential.

Using a special diagrammatic technique, Izyumov and Letfulov [8] obtained the following coupled equations to determine the magnetizations m^s and m^d of itinerant and localized spins, respectively, and the chemical potential μ:

$$m^d = \tanh \frac{1}{2} \lambda,$$

$$\lambda = \frac{1}{\pi} \int_0^{\pi} dt \ln \frac{1 + \exp \beta(\mu_r - \nu - a_{\uparrow} \cos t)}{1 + \exp \beta(\mu_r + \nu - a_{\downarrow} \cos t)},$$
$$m^s = n m^d + [1 - (m^d)^2] \sum_\sigma \sigma \frac{1}{\pi} \int_0^{\pi} dt \sin^2 t f(a_\sigma \cos t + \sigma \nu), \tag{6}$$
$$n = \sum_\sigma (1 + \sigma m^d) \frac{1}{\pi} \int_0^{\pi} dt \sin^2 t f(a_\sigma \cos t + \sigma \nu).$$

Here, $\mu_r = \mu + I_h n/2$, $n = \langle n_{i\uparrow} \rangle + \langle n_{i\downarrow} \rangle$, $\nu = (1/2) I_h m^s$, $I_h = z J^h$, $a^2_\sigma = (1/8) W^2 (1 + \sigma m^d)$, $\beta = 1/T$, and $f(x)$ is the Fermi distribution function.

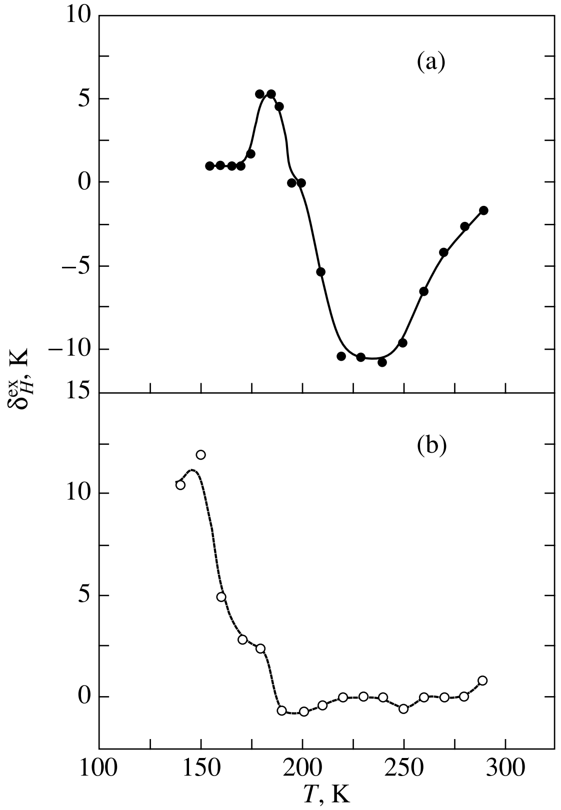

Fig. 3. Temperature dependence of the magnetoresistance $\delta^{\text{ex}}_H = [(\rho(H) - \rho(H = 0))/\rho(H)] \times 100\%$ of α-MnS in a magnetic field $H = 10$ kOe in (a) the (111) and (b) (100) planes.

We will use these equations to determine the chemical potential, bandwidth, and hole concentration as functions of localized spin magnetization in the (111) plane. For temperatures above the Néel point, we will include the interaction of holes with the short-range localized spin order, i.e., the parameter $(m^d)^2 = (4/L) \sum_r^{L/4} \langle S^z(0) S^z(r) \rangle$.

The magnetic structure and thermodynamic characteristics for localized spins were calculated using the

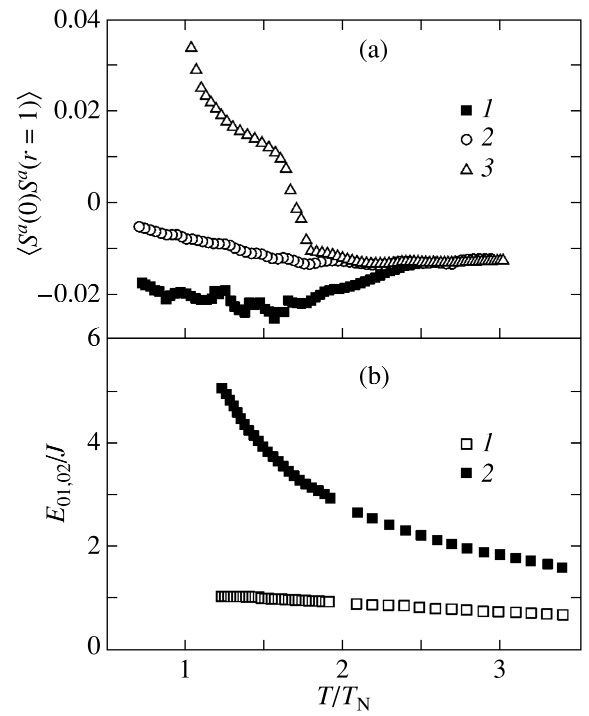

Fig. 4. (a) Spin–spin correlation function $\langle S^\alpha(0)S^\alpha(r=1)\rangle$ for nearest neighbors along the [011] direction calculated for (*1*) $\alpha = x$, (*2*) y, and (*3*) z. (b) Local spin interaction energies (*1*) $E_{01}/J = \sum_{\alpha=x,y,z}\sum_{h=1}^{12} S_0^\alpha S_h^\alpha$ and (*2*) $E_{02}/J = (K/J)\sum_{\alpha=x,y,z}\sum_{h=1}^{6} S_0^\alpha S_h^\alpha$ in the first and second coordination shells, respectively, plotted vs. normalized temperature T/T_N.

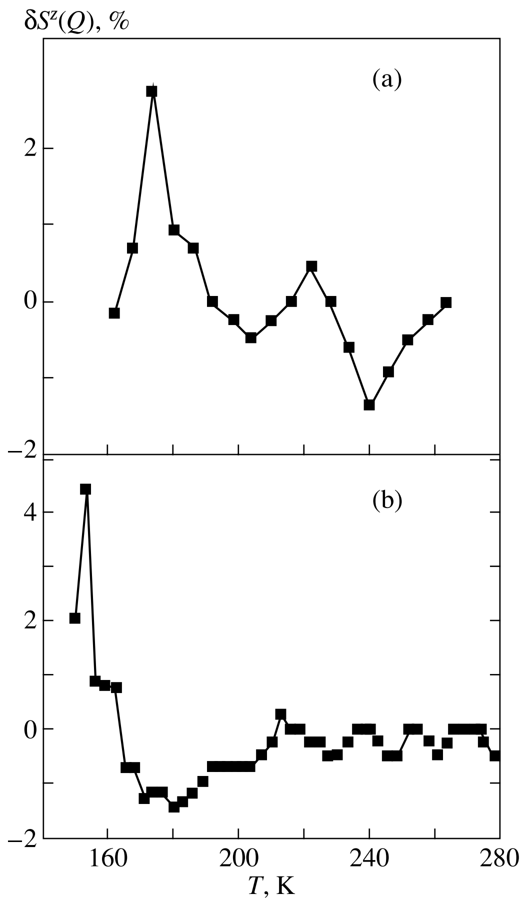

Fig. 5. Relative variation of the magnetic structural factor in the (111) plane, $\delta S^z = [(S^z(Q,H) - S^z(Q,H=0)/S^z(Q,H)] \times 100\%$, in a magnetic field (a) $H = 8$ and (b) 16 kOe plotted vs. temperature for wave vector $Q \leq 0$.

Monte Carlo technique (MC) in classical Heisenberg model (1) with the exchange energy ratio $K/J = 1.85$ determined earlier in [9]. The procedure used periodic boundary conditions imposed on a $20 \times 20 \times 20$ grid with 30000 MC steps per spin.

4. RESULTS AND DISCUSSION

The fcc lattice of α-MnS contains the maximum number of frustrated spin exchange bonds: the numbers of nearest neighbors with parallel spins and with antiparallel spins are equal, and the local energy for Ising spins is $E_{01}/J = \sum_{h=1}^{12} S_0 S_h = 0$.

In the classical Heisenberg model, frustration accounts for a noncollinear spin arrangement. For $T \ll T_N$, the contribution from the transverse spin components to $E_{0.1}/J$ is ≈2, which is approximately 3% of the maximum contribution, and their contribution to the exchange interaction energy in the second coordination shell $E_{02}/J = (K/J)\sum_{h=1}^{h=6} S_0 S_h$ is about 12%. For certain directions, the sign of the spin–spin correlation functions of transverse spin components does not coincide with the sign of the spin–spin correlation functions of longitudinal spin components calculated for the cube face diagonals. Figure 4a presents graphs of typical temperature dependences of the nearest neighbor correlation functions in the [011] direction. The transverse spin components in the (111) plane are possibly disordered.

As one crosses the Néel temperature, the short-range magnetic spin order for $T > T_N$ corresponds to the long-range magnetic order. The correlation length of the spin–spin correlation functions in the paramagnetic phase decreases following a power law. The exchange interaction energy in the second coordination shell E_{02} falls off rapidly, whereas the energy E_{01} is practically independent of temperature (Fig. 4b). In the vicinity of the temperature $T^* \approx 1.6T_N$, the type of short-range magnetic order changes. Indeed, as seen from Fig. 4a, the nearest neighbor spin–spin correlation function $\langle S^z(0)S^z(r=1)\rangle$ becomes negative in the (111) plane. An external magnetic field applied perpendicular to the (111) plane reduces the correlation length and decreases the temperature at which the type of short-range order changes. The magnetic structural factor in the (111) plane also decreases in magnitude. The corresponding relative change $\delta S^z(Q) = [S^z(Q, H) - S^z(Q, H = 0)]/S^z(Q, H)$ with temperature (Q is the wave vector) is displayed graphically in Fig. 5. Near the Néel temperature, the magnetic field suppresses a noncollinear spin arrangement and thereby increases the correlation functions of longitudinal components. This case is a typical for frustrated systems, where an external magnetic field brings about destruction of a noncollinear structure.

Using the known hole concentration $n \approx 0.1$ [4] at $T = 435$ K, we calculated the indirect interaction parameter $I_h = 9.3$ meV and the Hund exchange integral $J_H \approx 4$ eV. The calculated parameters correlate well with $J_H \approx 3.8$ eV and $W \approx 1$ eV from [3]. The interaction of the hole spins with localized spins exhibiting short-range magnetic order in the (111) plane splits the upper and lower hole band edges. This effect manifests itself particularly clearly below the Néel temperature, as seen from Fig. 6. Because of the strong s–d coupling, a localized spin is bonded in a complex with a band hole, which results in efficient attraction of the hole to the site and in a gap opening at the Fermi level below T_N in the (111) plane. The temperature dependence of the gap is shown in Fig. 7.

Manganese ions arranged along the cube edges are coupled by indirect antiferromagnetic exchange interaction mediated by sulfur ions, and hole hopping without spin flip is possible by the double exchange mechanism. The double-exchange model allows the formation of a weak ferromagnetic moment ($m_0 \ll m_d$) [7] and nonactivated conductivity in the [100] direction. In a magnetic field, the magnetic structural factor changes (Fig. 5) and the position of the chemical potential changes relative to the Fermi level (inset in Fig. 7). As a result, the electrical resistivity in the (111) plane undergoes a change, because $\ln\rho \sim (E_F - \mu)/k_BT$. The calculated temperature ranges corresponding to negative and positive changes in the quantity $\{(E_F - \mu)_H - (E_F - \mu)_{H=0}\}$ are in good agreement with those over which positive and negative values of magnetoresistance are observed.

The temperature derivative of the chemical potential $d\mu/dT$ has a minimum tending to zero at the Néel temperature. The temperature behavior of $\mu(T)$ is shown in Fig. 6. According to [8], the thermopower is proportional to $d\mu/dT$. The experimentally observed growth of thermopower for $T > T_N$ [4] agrees qualitatively with our results. The compressibility coefficient κ is defined as the second derivative with respect to energy and is given by

$$\frac{1}{\kappa} = \frac{\partial^2 E}{\partial n^2} = \left(\frac{\partial n}{\partial \mu}\right)^{-1}. \qquad (7)$$

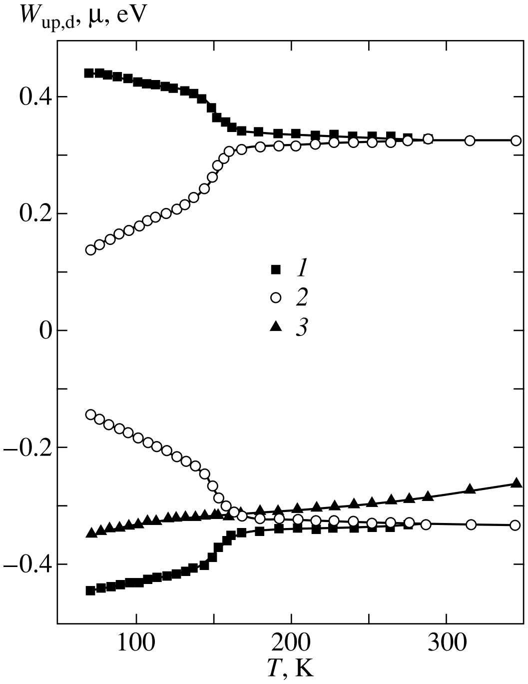

Fig. 6. Temperature dependences (*1*, *2*) of the upper and lower edges of the (*1*) spin-up and (*2*) spin-down subbands and (*3*) of the chemical potential.

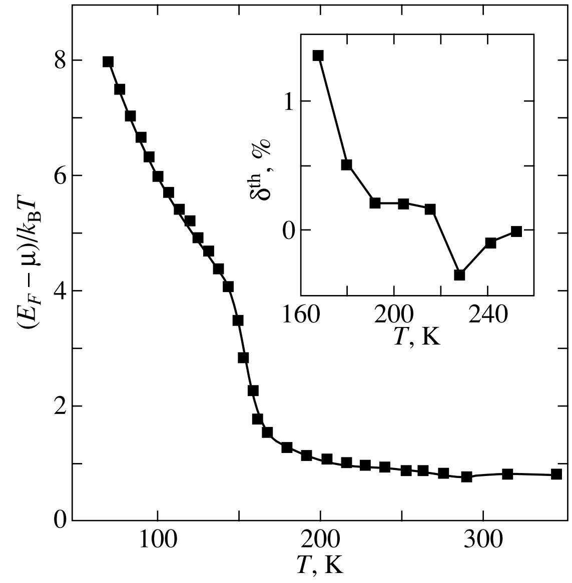

Fig. 7. Temperature dependence of the difference between the Fermi energy and the chemical potential. Inset: calculated shift in chemical potential relative to the Fermi level $\delta^{\rm th} = [\{(E_F - \mu)_H - (E_F - \mu)_{H=0}\}/(E_F - \mu)_H] \times 100\%$ in a magnetic field $H = 8$ kOe plotted vs. temperature.

The compressibility coefficient reverses sign from negative to positive near the Néel temperature at $T =$ 162 K. The dependence of the hole concentration on the chemical potential is presented graphically in Fig. 8. The negative compressibility coefficient in the temperature interval $125 < T < 162$ K should be attributed to

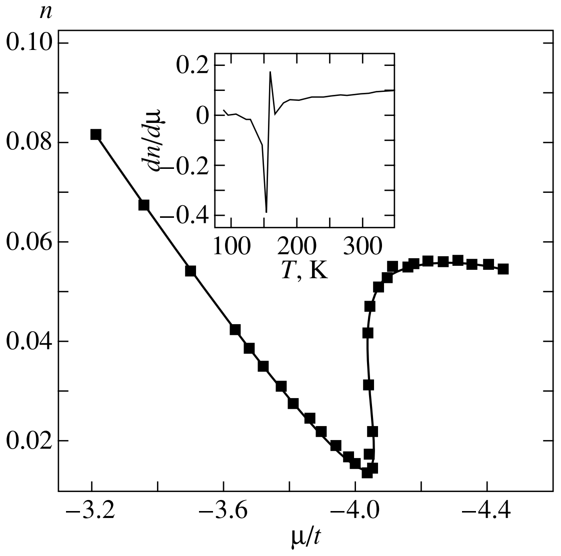

Fig. 8. Dependence of the hole concentration on the chemical potential normalized against the hopping integral t. Inset: temperature dependence of compressibility coefficient $dn/d\mu$ for a hole gas.

the sharp increase in the hole concentration. This brings about a decrease in Coulomb interaction between the ions and, possibly, a change in the elastic modulus of the α-MnS crystal. Furthermore, additional ferromagnetic exchange interaction mediated by delocalized holes appears between the localized spins in the (111) plane, which gives rise to a rhombohedral distortion of the fcc lattice observed to occur in α-MnS [4]. The distortion angle is directly proportional to the exchange interaction J^h and inversely proportional to the elastic modulus of the crystal [10]. Exchange-induced striction compresses the lattice. The calculated temperature interval over which the compressibility coefficient is negative correlates well with the temperature region in which the lattice constant is observed to undergo the maximum change (Fig. 1).

5. CONCLUSIONS

The pronounced increase in the resistivity anisotropy observed in an α-MnS single crystal below the Néel temperature is induced by the hole spins interacting with ferromagnetically ordered localized spins in the (111) plane and by gap formation at the Fermi level, which correlates qualitatively with the activated character of the conductivity in the (111) plane. The sign reversal of magnetoresistance in α-MnS in the (111) plane is initiated by a change in magnetic order for $T > T_N$; indeed, the disappearance of long-range magnetic order gives rise to positive magnetoresistance at $T \sim 160$ K and the destruction of short-range magnetic order causes negative magnetoresistance at $T \sim 230$ K. The additional exchange interaction created by the holes leads to compression and rhombohedral distortion of the lattice in the (111) plane below the Néel temperature.

ACKNOWLEDGMENTS

The authors are indebted to G.A. Petrakovskiĭ for helpful discussions and to G.V. Bondarenko for performing the x-ray fluorescence analysis.

This study was supported by the program of the Presidium of the Russian Academy of Sciences (project “New Materials for Technology”) and, in part, by the Russian and Belarussian Foundations for Basic Research (project no. 04-02-81018 Bel2004_a).

REFERENCES

1. A. V. Vedyaev, Usp. Fiz. Nauk **172** (12), 1458 (2002) [Phys. Usp. **45**, 1296 (2002)].
2. G. A. Petrakovskiĭ, L. I. Ryabinkina, G. M. Abramova, N. I. Kiselev, A. D. Velikanov, and A. F. Bovina, Pis’ma Zh. Éksp. Teor. Fiz. **69** (12), 895 (1999) [JETP Lett. **69**, 949 (1999)]; G. A. Petrakovskiĭ, L. I. Ryabinkina, G. M. Abramova, A. D. Balaev, D. A. Balaev, and A. F. Bovina, Pis’ma Zh. Éksp. Teor. Fiz. **72** (2), 99 (2000) [JETP Lett. **72**, 70 (2000)].
3. G. V. Loseva, S. G. Ovchinnikov, and L. I. Ryabinkina, Fiz. Tverd. Tela (Leningrad) **28** (7), 2048 (1986) [Sov. Phys. Solid State **28**, 1145 (1986)].
4. H. H. Heikens, C. F. van Bruggen, and C. J. Haas, J. Phys. Chem. Solids **39** (8), 833 (1978).
5. H. H. Heikens, G. A. Wiegers, and C. F. van Bruggen, Solid State Commun. **24** (3), 205 (1977).
6. R. Tappero and A. Lichanot, Chem. Phys. **236** (1), 97 (1998).
7. Yu. A. Izyumov and Yu. N. Skryabin, Usp. Fiz. Nauk **171** (2), 121 (2001) [Phys. Usp. **44**, 109 (2001)].
8. Yu. A. Izyumov and B. M. Letfulov, in *Magnetism of Transition Metals and Alloys* (Yekaterinburg, 2000), pp. 42–60 [in Russian].
9. G. A. Petrakovskiĭ, S. S. Aplesnin, G. V. Loseva, L. I. Ryabinkina, and K. I. Yanushkevich, Fiz. Tverd. Tela (Leningrad) **33** (2), 406 (1991) [Sov. Phys. Solid State **33**, 333 (1991)].
10. B. Morosin, Phys. Rev. B **1** (1), 236 (1970).

Translated by G. Skrebtsov

Physics of the Solid State, Vol. 46, No. 11, 2004, pp. 2073–2080. Translated from Fizika Tverdogo Tela, Vol. 46, No. 11, 2004, pp. 2006–2013.
Original Russian Text Copyright © 2004 by Shutyĭ, Sementsov.

MAGNETISM AND FERROELECTRICITY

Stochastic High-Frequency Precession of Magnetization in Layered Structures with Antiferromagnetic Ordering

A. M. Shutyĭ and D. I. Sementsov
Ulyanovsk State University, ul. L’va Tolstogo 42, Ulyanovsk, 432700 Russia
e-mail: shuty@mail.ru

Received October 16, 2003; in final form, February 15, 2004

Abstract—The conditions for the appearance of self-oscillating and stochastic regimes in an exchange-coupled multilayer structure in the presence of a longitudinal high-frequency magnetic field are studied. Bifurcational diagrams are constructed that reveal various types of dynamic states of magnetic moments in the multilayer structure and transitions between these states with varying the frequency of the ac field. Attractors of stochastic oscillations are studied, and Lyapunov exponents determining the divergence of their phase trajectories are numerically calculated. *© 2004 MAIK “Nauka/Interperiodica”.*

1. In recent years, special attention has been paid to various oscillating systems where, in addition to regular regimes, stochastic dynamic regimes are also possible [1]. Magnetically ordered structures, whose dynamics is related to precession of magnetization and is generally described by the Landau–Lifshitz nonlinear equation, are among the most extensively studied [2, 3]. There is currently a large interest in multilayer exchange-coupled structures, in which giant magnetoresistance is observed [4–6]. The presence of characteristic statistical and dynamic bistable states, near which the behavior of the magnetic subsystem is determined in many respects by self-organization of the magnetization in the presence of an ac magnetic field, can be important for wide practical applications of such structures [7, 8]. The magnitude and the type of coupling of magnetic moments of neighboring layers are expected to play a decisive role in such processes. In the studies available [9, 10] concerning the analysis of stochastic dynamics in layered structures, substantial simplifications are used (approximation of the planar motion of magnetic moments and dipole–dipole interaction of two magnetized layers); these simplifications do not allow one to describe the nonlinear dynamics of real structures adequately. The structures with antiferromagnetic ordering of the magnetic moments of the neighboring layers are of greatest interest for the realization of various equilibrium states [11]. In this paper, we study the nonlinear regular and stochastic dynamic regimes of magnetization that occur in a multilayer structure with exchange interlayer coupling of the antiferromagnetic type in the presence of a longitudinal ac magnetic field near the boundaries of an orientation hysteresis loop.

2. We assume that the structure consists of a large number of identical layers of a magnetic metal ($n \gg 1$) separated by nonmagnetic layers, which provide the antiferromagnetic type of ordering of the magnetic moments of the neighboring layers in the initial state. To avoid complications related to the roughness of interlayer boundaries, which can result in frustrations and splitting of ferromagnetic layers into domains [12, 13], we assume that the interlayer boundaries are sufficiently smooth and that each of the ferromagnetic layers is homogeneously magnetized. These approximations are widely used in the studies dealing with orientational phase transitions in multilayer nanostructures [14–16], and their correctness has been confirmed by experimental and theoretical studies of the ferromagnetic resonance in structures of the $(\mathrm{Fe/Cr})_n$ type [17]. In this case, the entire set of magnetic layers is divided into two subsystems ($j = 1, 2$) with identical behavior of the magnetic moments of the layers of each subsystem. For the structures under study, the contributions to magnetic anisotropy come from the induced uniaxial anisotropy of the “easy-axis” type and the crystallographic cubic anisotropy; the crystallographic [100] and [010] axes lie in the layer plane, and the easy magnetization axis of the induced anisotropy is directed normally to the layers. The free energy of the system per unit area is given by

$$E = d\frac{n}{2}\sum_{j=1,2}\Big[-(\mathbf{H}+\mathbf{h})\mathbf{M}_j + \frac{K_1}{4}(\sin^2 2\psi_j + \cos^4\psi_j \sin^2 2\varphi_j) + \frac{K_2}{16}\sin^2 2\psi_j \cos^2\psi_j \sin^2 2\varphi_j + (K_u - 2\pi M^2)\cos^2\psi_j\Big] + Jn\frac{\mathbf{M}_1\mathbf{M}_2}{M^2}, \quad (1)$$

where d is the magnetic layer thickness; $\mathbf{M}_j$ is the magnetization of the layers of the subsystem j; J is the bilinear exchange coupling constant of the magnetic

1063-7834/04/4611-2073$26.00 © 2004 MAIK “Nauka/Interperiodica”

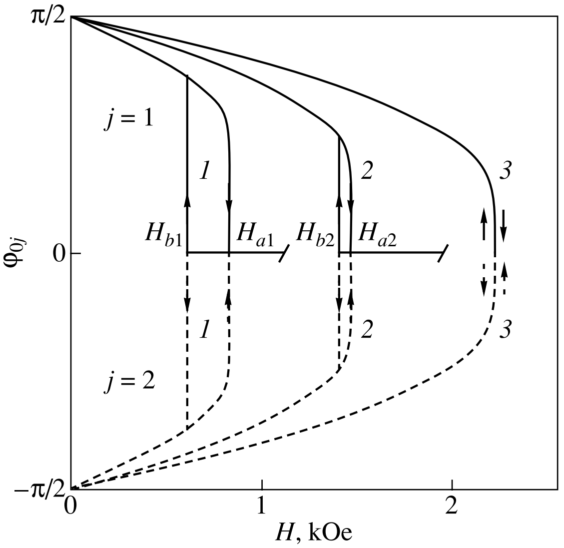

Fig. 1. Field dependence of the equilibrium azimuthal angle of the magnetic moments of the structure for (*1*) $J = 0.1$, (*2*) 0.17, and (*3*) 0.24 erg/cm^2.

moments of the nearest neighbor layers; K_1 and K_2 are the first and second constants of cubic anisotropy; K_u is the growth anisotropy constant; **H** and **h** are the static and high-frequency magnetic fields, respectively; φ_j is the azimuthal angle measured from the [100] axis and determines the orientation of the magnetic moment in the layer plane; and ψ_j is the angle between the vector $\mathbf{M}_j$ and the film plane.

The equations of motion for the magnetization vectors of each of the layers in the spherical system of coordinates have the form

$$\begin{aligned}\dot{\varphi}_j M d\cos\psi_j &= \gamma\frac{\partial E}{\partial\psi_j} + \frac{\lambda}{M}\frac{1}{\cos\psi_j}\frac{\partial E}{\partial\varphi_j},\\ \dot{\psi}_j M d &= \frac{\lambda}{M}\frac{\partial E}{\partial\psi_j} - \gamma\frac{1}{\cos\psi_j}\frac{\partial E}{\partial\varphi_j},\end{aligned} \tag{2}$$

where γ is the gyromagnetic ratio and λ is the decay parameter. For simulation, we use the parameters corresponding to a real (Fe/Cr)$_n$ structure. For the iron layers, we set $M = 1620$ G, $K_1 = 4.6 \times 10^5$ erg/cm^3, $K_2 = 1.5 \times 10^5$ erg/cm^3, $K_u = 2.06 \times 10^6$ erg/cm^3, $\lambda = 5 \times 10^7$ s^{-1}, $\gamma = 1.76 \times 10^7$ (Oe s)$^{-1}$, and $d = 21.2 \times 10^{-8}$ cm. We note that, for the chosen orientation of the crystallographic axes, the contribution to the free energy related to the second cubic anisotropy constant can be disregarded, since its effect on the magnetic properties of the structure is small. The layer parameters for chromium do not appear in Eqs. (1) explicitly, but they determine the magnitude of the coupling constant J [17].

3. In the absence of a high-frequency field ($h = 0$), with allowance for large demagnetizing fields ($4\pi M \gg 2K_u/M$, JM), the magnetic moments lie in the layer plane if the magnetic bias field lies in this plane; i.e., the equilibrium angles are $\psi_{0j} = 0$. The equilibrium azimuthal angles $\varphi_{0j}(H)$ are determined by the relations $\partial E/\partial\varphi_j = 0$ and $\partial^2 E/\partial\varphi_j^2 > 0$, which, in combination with Eq. (1), lead to the system of equations

$$\begin{aligned}&2HM\sin(\varphi_{0j} - \varphi_H) + K_1\sin 4\varphi_{0j}\\ &\quad - 2\bar{J}\sin(\varphi_{0j} - \varphi_{03-j}) = 0,\\ &HM\cos(\varphi_{0j} - \varphi_H) + 2K_1\cos 4\varphi_{0j}\\ &\quad - \bar{J}\cos(\varphi_{0j} - \varphi_{03-j}) > 0,\end{aligned} \tag{3}$$

where $j = 1, 2$; $\bar{J} = 2J/d$; and φ_H is the azimuthal angle measured from the [100] axis and determining the direction of the field **H** in the layer plane.

An analysis of these equations shows that, at small enough values of the coupling constant J, a change in the magnitude of the magnetic bias field is accompanied by orientational hysteresis loops and the related bistability. Figure 1 shows the bias field dependence of the equilibrium azimuthal angles of the magnetic moments of the first (solid curves) and second (dashed curves) subsystems of magnetic layers obtained for coupling constants $J = 0.1$, 0.17, and 0.24 erg/cm^2. For the initial orientation of the magnetic moments $\varphi_{0j} = \pm\pi/2$ and for the orientation of the bias field $\varphi_H = 0$, i.e., for $\mathbf{M}_{0j} \perp \mathbf{H}$, a noncollinear symmetric orientation of the magnetic moments of the neighboring layers ($\varphi_{02} = -\varphi_{01}$) occurs in the equilibrium state in the range $0 < H \le H_a$. In this range, an increase in the bias field results in a decrease in the angle between the magnetic moments of the neighboring layers $\Delta\varphi_0 = \varphi_{01} - \varphi_{02}$. When the field becomes equal to the critical value H_a, this angle reaches a minimum value

$$\Delta\varphi_0 = 2\varphi_a = 2\arccos\sqrt{\frac{\bar{J} + K_1}{6K_1}}. \tag{4}$$

This minimum angle decreases as the coupling constant increases until an orientational phase transition occurs and the magnetic moments are aligned with the bias field. With a decrease in the bias field from $H > H_a$, the state with codirected orientation of magnetic moments of the layers is conserved down to a value H_b. At $H = H_b < H_a$, a reverse phase transition occurs in which the vectors $\mathbf{M}_1$ and $\mathbf{M}_2$ cease to be collinear and their azimuthal angles change in a jump to the values $\pm\varphi_b$; i.e., $\Delta\varphi_0 = 2\varphi_b$. A further decrease in the bias field produces an increase in $\Delta\varphi_0$, and for $H = 0$, we have again $\Delta\varphi_0 = \pi$. The critical fields bounding the orientational hysteresis loop are given by

$$H_b = \frac{2}{M}(\bar{J} - K_1), \quad H_a = \frac{4}{3M}\sqrt{\frac{\bar{J} + K_1}{6K_1}}(\bar{J} + K_1). \tag{5}$$

As the coupling constant increases, the hysteresis loop narrows to collapse at $J = J_{ab}$, where J_{ab} is found from the equation $H_b = H_a$. For $J > J_{ab}$, the orientational states of the system are characterized by a single magnetization curve with a one-to-one correspondence between φ_{0j} and H.

4. The systems with narrow hysteresis loops are of special interest for the realization of different dynamic regimes. In the case where H corresponds to the center of the hysteresis loop and there is a longitudinal high-frequency field ($\mathbf{h} \parallel \mathbf{H}$) whose amplitude is close to the loop width ($h \geq H_a - H_b$), various high-amplitude self-oscillating and stochastic regimes appear in the system of layer magnetic moments. The most detailed information on the dynamic regimes in the structure considered in a wide frequency range can be obtained from the bifurcational diagram. Figure 2 shows the bifurcational diagram, where we plot the frequencies of the ac field as abscissas and the corresponding maximum and minimum values of the angles of the magnetic moments as ordinates; the data are obtained for the exchange coupling constant $J = 0.24$ erg/cm^2 (this value is close to $J_{ab} \approx 0.244$ erg/cm^2); magnetic bias field $H = 2227.4$ Oe, corresponding to the collinear equilibrium state with angles $\varphi_{0j} = 0$; and the amplitudes of the ac field $h = 0.2$ and 1.0 Oe, which exceed the value $H_a - H_b \approx 0.144$ Oe. For a fixed value of H, a single point with zero angle φ_{jm} implies the absence of oscillations, two points correspond to an oscillating regime with one maximum $\varphi_{j\,\max}$ and one minimum $\varphi_{j\,\min}$, a set of a greater countable number of points represents a more complicated oscillation, and a set of closely spaced points corresponds to stochastic dynamics of magnetic moments. Oscillations of the magnetic moments of the two subsystems are always in antiphase; therefore, in both the regular and stochastic regimes, the equality $\varphi_2(t) = -\varphi_1(t)$ is satisfied with high accuracy. It is seen in Fig. 2 that, as the frequency is varied, the transformation of one regular oscillatory regime into others, as a rule, occurs by passing over the frequency intervals corresponding to the stochastic dynamics of magnetic moments. Among regular regimes, there are both symmetric and asymmetric ones with respect to the axis with a zero azimuthal angle.

From the diagram, it is seen that, as the frequency decreases in the high-frequency region, the system first appears to be insensitive to the effect of an ac field. Then (after Hopf's bifurcation [1]) a limit cycle appears, whose amplitude increases with decreasing frequency. Next, at a low amplitude of the ac field (Fig. 2a), after a cascade of oscillation period doublings, the system attains a stochastic oscillatory regime. When the amplitude of stochastic oscillations becomes high enough, the magnetic moments enter the attraction zone of the attractor given by a high-amplitude limit cycle, resulting in new bifurcations and in the establishment of a self-oscillating regime. High-amplitude oscillations can also be established at higher frequencies but in the case of another initial orientation of the magnetic moments. Thus, in a certain frequency range, dynamic bistability occurs. At large amplitudes of the ac field (Fig. 2b), there is no time for stochastic dynamics to develop: the amplitude of the low-amplitude limit cycle that appears after Hopf's bifurcation is sufficient for the magnetic moments to be drawn by the attractor in the self-oscillating regime. The amplitude of self-oscillations weakly depends on the frequency of the ac field and, in all cases, appreciably exceeds the difference between the angles of the magnetic moments in the hysteresis loop ($\varphi_a \approx 6°$). The oscillation amplitude depends on h only weakly: an increase in h by a factor of 5 increases the amplitude of the angle φ_1 only by one-third. However, the frequency range corresponding to this regular regime significantly grows with increasing ac field and is displaced towards higher frequencies.

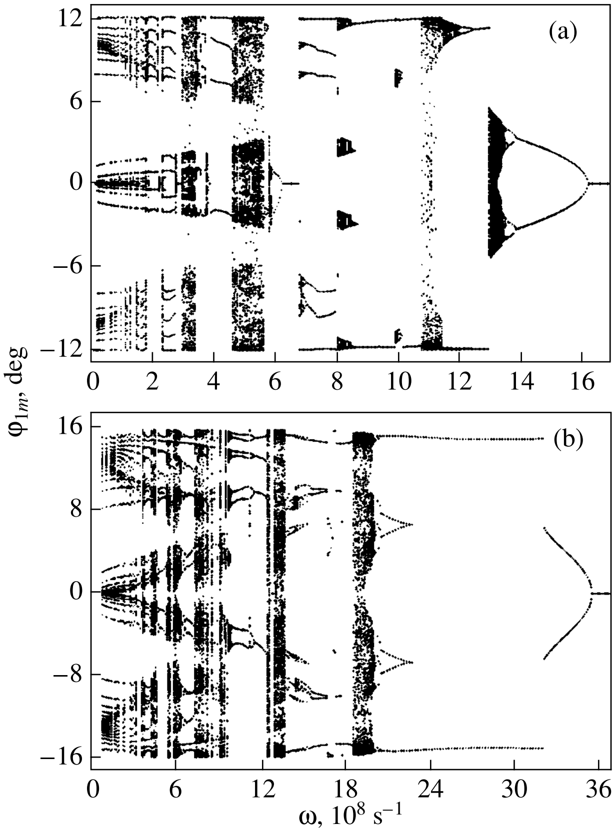

Fig. 2. Frequency dependence of the maximum and minimum values of the angle φ_1 (bifurcational diagram) for h equal to (a) 0.2 and (b) 1.0 Oe. $J = 0.24$ erg/cm^2, $H = 2227.4$ Oe.

In addition to wide frequency ranges corresponding to stochastic oscillations, in the diagram there are also narrow frequency intervals of stochastic regimes ($\Delta\omega \sim 10^7$ s^{-1}) outside which regular high-amplitude regimes are realized. With decreasing frequency, the stochastic

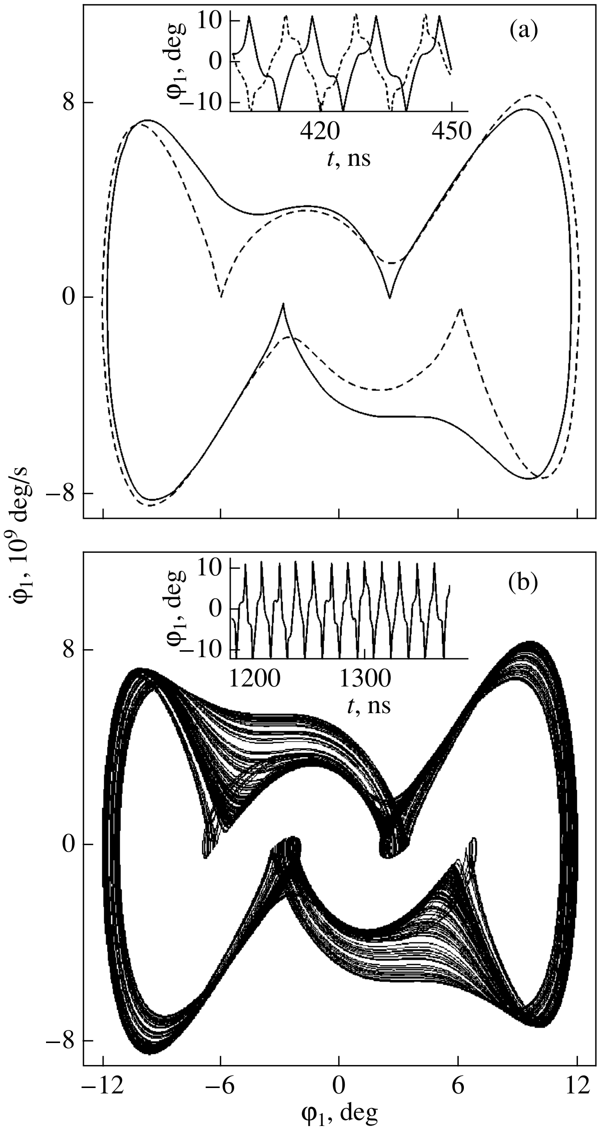

Fig. 3. Phase trajectories for (a) regular oscillations of the vector $\mathbf{M}_1$ for $\omega = 7.9 \times 10^8$ (dashed curve) and 8.7×10^8 s^{-1} (solid curve) and (b) stochastic oscillations for $\omega = 8.0 \times 10^8$ s^{-1}. $h = 0.2$ Oe. The insets show the $\varphi_1(t)$ dependence.

regimes are established in these narrow frequency ranges after a cascade of bifurcational period doublings, whereas the return of the system to the self-oscillating regime with a period equal to the period of the ac field occurs after only one bifurcation. The regular regimes occurring at frequencies above and below the interval corresponding to stochastic dynamics can both be very close and differ appreciably in terms of the phase trajectories.

Except for stochastic and regular oscillations, there are also frequency intervals of dynamic insensitivity (for example, at $h = 0.2$ Oe near the frequency $\omega = 6.5 \times 10^8$ s^{-1}), which narrow progressively and disappear with increasing h.

At low frequencies ($\omega \sim 10^7$ s^{-1}), regular dynamic regimes are realized in which there are time intervals with zero angle and with fast oscillations related to magnetization reversal (Fig. 2). At certain frequencies, we have asymmetric regimes with an oscillation period equal to the period of the ac field and at other frequencies we have a symmetric regime for which the signs of high-amplitude oscillations of the angle of the magnetic moment alternate, resulting in the period doubling. By changing the magnitude of the bias field by a small value $\Delta H \sim 0.1$ Oe, we can control the relative pulse duration for the regimes under study, i.e., change the duration of the periods with zero angle.

5. Let us consider two narrow frequency intervals corresponding to stochastic oscillations. Figure 3 shows the $\dot{\varphi}_1(\varphi_1)$ phase trajectories for the magnetic moments of the first subsystem of layers at an amplitude of the ac field $h = 0.2$ Oe and at frequencies corresponding to regular regimes (Fig. 3a) and to stochastic oscillations (Fig. 3b). The corresponding time dependence of $\varphi_1(t)$ is plotted in the insets. The phase trajectories for regular regimes at frequencies lying above and below the frequency interval corresponding to stochastic dynamics differ only slightly: both regimes have a high amplitude and are symmetric, and their period is equal to the period of the ac field. The amplitude of the stochastic regime that arises after a cascade of period doublings (as the frequency ω decreases), only slightly differs from the amplitude of self-oscillating regimes; the stochastic nature is mainly seen as smearing of the phase trajectory of the limit cycle.

This regime is sensitive to the variation in the bias field. Decreasing H only by 0.01 Oe with respect to the value indicated above brings the system from the stochastic to the self-oscillating regime, which is also realized only in a very small interval of bias fields ($\Delta H \sim 0.02$ Oe). Then again the stochasticity is developed to cover the entire angular range of oscillations of the magnetic moment. When the bias field approaches the boundary of the hysteresis loop, low-amplitude regular oscillations are established corresponding to noncollinear equilibrium orientation of the magnetic moments of the system. With increasing H, the stochasticity first grows and then the system becomes insensitive to the ac field, since the bias field magnitude lies outside the hysteresis loop and corresponds to a collinear codirected orientation of the magnetic moments. At other frequencies close to the chosen one, the main features of the bias-field dependence of the magnetic moment dynamics is similar to that just described.

In Fig. 4, phase trajectories of the magnetic moment $\mathbf{M}_1$ are plotted for $h = 1.0$ Oe and $\omega = (12.2, 12.3) \times 10^8$ s^{-1}. The phase attractor of stochastic oscillations (Fig. 4b) is symmetric and is formed in the merging and smearing of two asymmetric limit cycles, more specifically, a phase trajectory of the adjoining (with a close frequency) regular regime (Fig. 5a) and the phase trajectory that is symmetric to it and corresponds to the dynamics of the magnetic moment $\mathbf{M}_2$. At higher frequencies, the region of stochastic oscillations passes, after only one bifurcation, to the region of dynamic insensitivity (Fig. 2a) corresponding to the absence of magnetic moment oscillations induced by an ac field. These regimes also appear to be rather sensitive to a change in the bias field because of the narrowness of the hysteresis loop corresponding to these regimes.

For clarity, it is convenient to represent complicated phase trajectories as a set of points obtained in time steps equal to the period of the ac field (an analog of Poincaré diagrams [18]). In Fig. 5, a discrete (in time) representation of phase portraits of the stochastic dynamics of the magnetic moment is shown on the $(\varphi_1, \dot{\varphi}_1)$ plane for $h = 0.2$ Oe and various frequencies of the ac field. In the insets, the corresponding $\varphi_1(t)$ dependences are plotted. The dynamic regime near the frequency $\omega = 5.0 \times 10^8$ s^{-1} (Fig. 5a) arises via intermittency; however, "laminar" phases (high-amplitude angle oscillations either in the positive or in the negative half-plane) consist only of several periods. The phase portrait for this regime is a union of two funnel-shaped attractors joined to each other in the central region of the phase plane. The regime at the frequency $\omega = 1.1 \times 10^9$ s^{-1} (Fig. 5c) also has laminar phases, alternating with bursts of turbulence and characterized by a certain angular interval of disorder in the oscillation amplitude. As the frequency increases, the bursts of turbulence stop and a stochastic regime is established with an attractor not involving the central region of the phase plane (a similar attractor is shown in Fig. 3a). In the case shown in Fig. 5b, stochasticity manifests itself only in a small interval of azimuthal angles of the magnetic moment and its first derivative, i.e., in slight smearing of the trajectory of the limit cycle. This regime has an asymmetric attractor and is realized in a narrow frequency interval (Fig. 2a). In the case shown in Fig. 5d, stochastic dynamics has developed as a result of a cascade of period doublings and after the reverse cascade [18] corresponding to merging of the "noise" intervals of the angle φ_1; therefore, stochasticity covers the entire angular range of oscillations of the magnetic moment.

The attractors corresponding to the stochastic dynamics of magnetization have regions of strong compression (or folds) and regions of expansion. This feature causes sensitivity of the phase trajectories to the initial conditions. Figure 6 shows the time dependences of the natural logarithm, $\ln(\delta/\delta_0)$, of the relative distance between two points of phase trajectories of the magnetic moment $\mathbf{M}_1$ on the $(\varphi_1, \dot{\varphi}_1)$ plane, which are initially close to each other ($\delta = \delta_0$ at $t = 0$), for the cases considered in Fig. 5. The curves are shifted along the time axis, since, for convenience, the initial times were chosen to be different for them. From Fig. 6, we see that the average distance between the points first increases according to an exponential law $\delta = \delta_0 \exp(\zeta t)$, where ζ is the largest Lyapunov exponent, equal to the slope of the straight line fitting the divergence of the phase trajectories (the dashed line plotted for curve *a*). After diverging to the attractor scale, δ begins to oscillate about a value determined by the size of the attractor itself. An analysis of phase portraits for the corresponding regimes shows that the Lyapunov exponent grows as the attractor expands (and, hence, the noise intervals increase). When the attractor covers the central region of the phase plane (curves *a*, *c*, *d*), the rate of divergence of trajectories close to each other is much greater than in the case where stochasticity manifests itself only in smearing of the trajectory of the limit cycle (curve *b*).

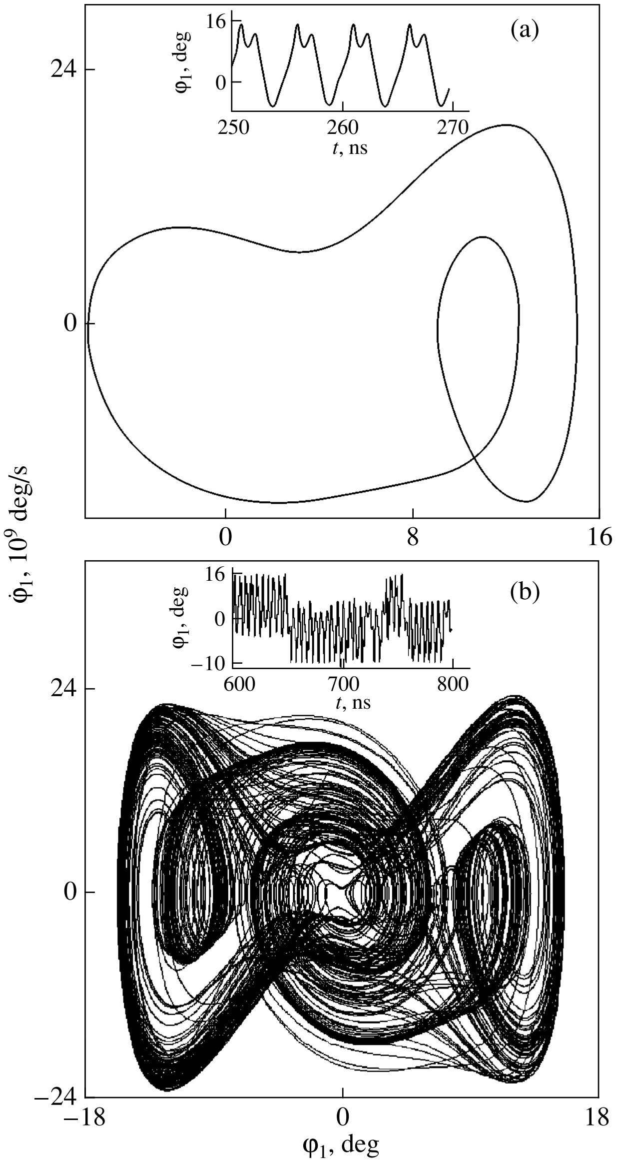

Fig. 4. Phase trajectories for (a) regular oscillations ($\omega = 12.2 \times 10^8$ s^{-1}) and (b) stochastic oscillations ($\omega = 12.3 \times 10^8$ s^{-1}) of the magnetic moment $\mathbf{M}_1$ for $h = 1.0$ Oe. The insets show the $\varphi_1(t)$ dependence.

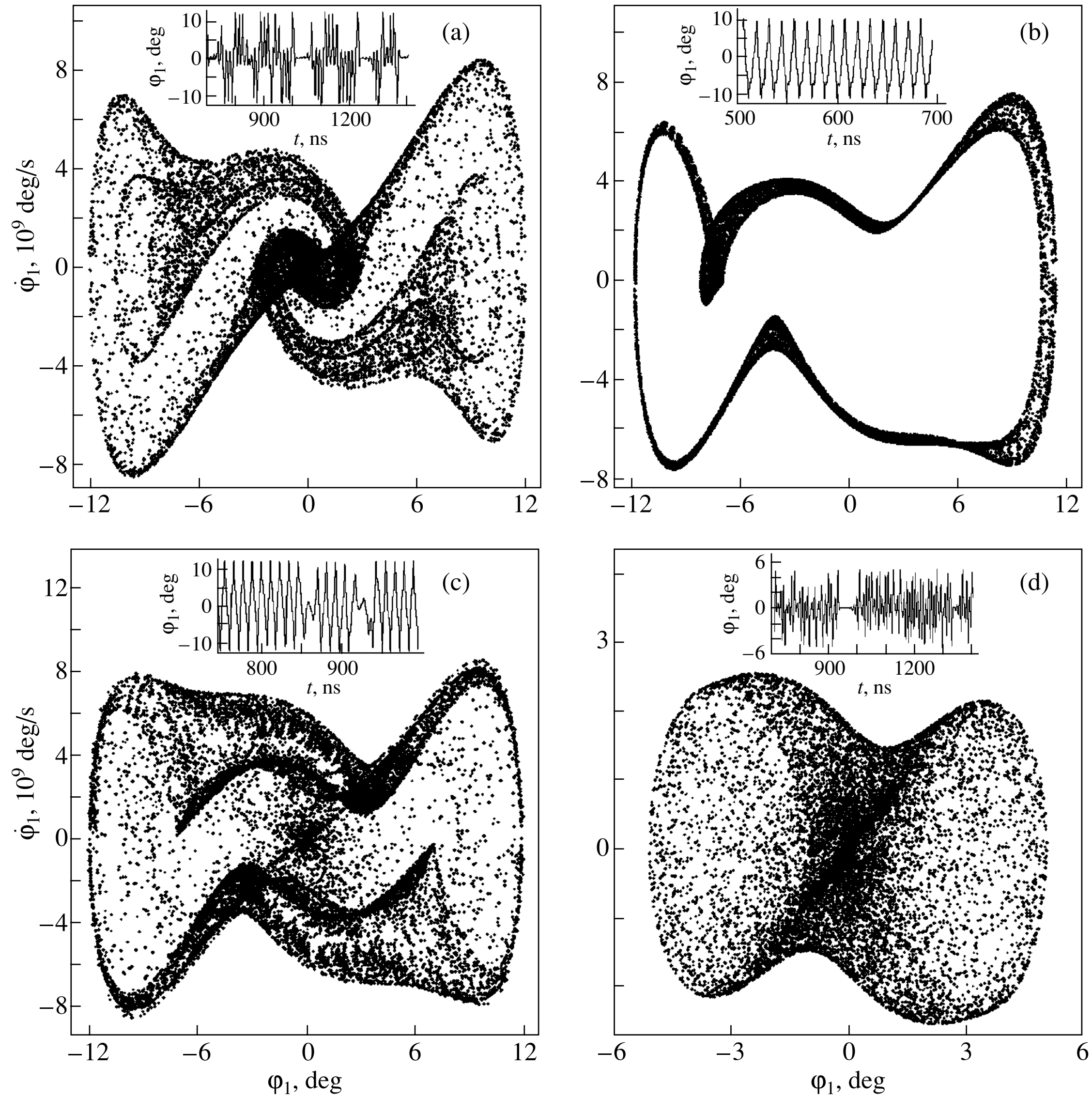

Fig. 5. Discrete-time representation (with a step of $\Delta t = 2\pi/\omega$) of phase trajectories of the magnetic moment at $h = 0.2$ Oe and different values of ω (10^8 s^{-1}): (a) 5.0, (b) 9.95, (c) 11.0, and (d) 13.1. The $\varphi_1(t)$ dependence is shown in the insets.

For $\omega = 11 \times 10^8$ s^{-1} (curve *c*), the rate of divergence of the trajectories is determined by two rates: the low rate in the laminar phase and the high rate during the bursts of turbulence. As the frequency increases, the time of existence of laminar phases grows; therefore, the rate decreases and the $\delta(t)$ dependence becomes smoother. For the cases considered, $\zeta \approx (12.7, 3.8, 9.8, 15.2) \times 10^7$ s^{-1}.

6. With the relations $4\pi M^2 \gg 2K_1$ and $\lambda \ll \gamma M$, which are obeyed well, equation of motion (2) can be transformed to the following system [3]:

$$\begin{aligned} \ddot{\varphi}_j + 4\pi\lambda\dot{\varphi}_j + \frac{4\pi\gamma^2}{d}\frac{\partial E}{\partial \varphi_j} &= 0, \\ \dot{\psi}_j &= -\frac{\ddot{\varphi}_j}{4\pi M_j}. \end{aligned} \tag{6}$$

Because of the symmetric orientation of the bias and high-frequency fields with respect to the crystallographic and growth anisotropy axes, as well as the character of interaction of the magnetic moments of the neighboring layers, symmetry takes place for the deviation angles from the layer plane ($\psi_1 = -\psi_2 = \psi$) and for the azimuthal angles ($\varphi_1 = -\varphi_2 = \varphi$), which was confirmed above by numerically solving Eqs. (2). Using this asymmetry, we can reduce the system of four equations (6) to two equations for the angles φ and ψ. Further simplification of the problem is based on the fact that the angle ψ that the magnetic moments make with the layer plane is small because of the high demagnetizing fields (for the parameters of the system indicated above, $\psi(t)_{\max} \sim 10^{-2}$ deg). For $\psi \approx 0$, the derivative $\partial E/\partial\varphi$ becomes independent of the angle ψ; therefore, when analyzing the azimuthal motion, we can replace spatial precession of the magnetic moments with their planar oscillatory motion. In this case, the equation for the azimuthal angle takes the form

$$\begin{gathered}\ddot{\varphi} + 4\pi\lambda\dot{\varphi} + 4\pi\gamma^2[(H + h\sin\omega t)M\cos\varphi \\ + (K_1\cos 2\varphi - \bar{J})\sin 2\varphi] = 0.\end{gathered} \tag{7}$$

However, a comparative analysis of the azimuthal motion of the magnetic moments shows that, if precession is neglected, the solutions in a number of frequency intervals differ strongly from those described above and obtained from the initial equations of motion (2). This is especially true for stochastic dynamics. In particular, for h = 0.2 Oe, there are no stochastic regimes for $\omega \cong (10, 11) \times 10^8$ s^{-1} (Figs. 5b, 5c) and $\omega \cong 3 \times 10^8$ s^{-1} (Fig. 2a) and there are no regular asymmetric regimes for $\omega \cong 7.5 \times 10^8$ s^{-1}. Nevertheless, many self-oscillating and stochastic regimes, for example, for $\omega \cong (5.0, 13.5) \times 10^8$ s^{-1} (Figs. 5a, 5d), are obtained by solving only the first equation in system (6).

From the above analysis, it follows that, in the structure under study with the antiferromagnetic type of coupling, in the presence of a longitudinal ac magnetic field, various types of stochastic and regular high-amplitude regimes are established, depending on the ac field frequency, for certain parameters of the magnetic subsystem and bias fields. The widths of the frequency ranges corresponding to different regimes can be both appreciable and rather small. The scenarios of the appearance of stochasticity, and therefore the number of bifurcations giving rise to stochasticity, may also be different. High sensitivity of the dynamic regimes to a change in the bias field is caused by the narrowness of the orientational hysteresis loop; near the loop limits, nonlinear oscillations of the magnetic moments are excited by a weak ac field. The variety of possible oscillation regimes makes such structures rather promising both for practical applications and for experimental studies of nonlinear dynamics.

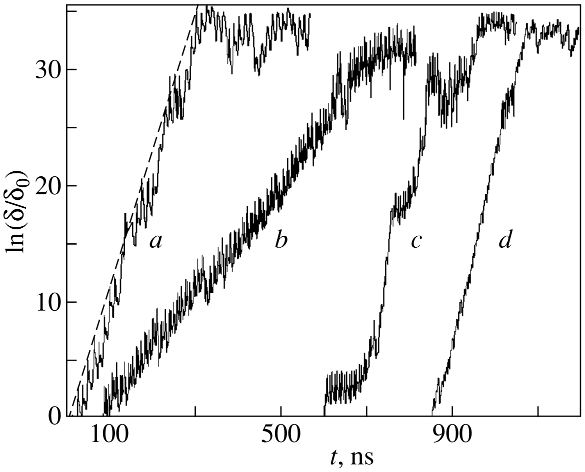

Fig. 6. Time dependence of the distance between two initially closely spaced phase points.

In the approximation of two magnetic subsystems, which is valid if the number of identical ferromagnetic layers is sufficiently large, the expression for the energy and the equation of motion of the magnetic moments are analogous to the corresponding equations for a two-sublattice antiferromagnet. However, for realizing the dynamic regimes discussed above, the numerical values of the parameters of the magnetic system play a decisive role. By varying the ratios of these parameters, we can obtain sufficiently narrow hysteresis loops with greatly different equilibrium angles in the region of orientation bistability; this is necessary for obtaining large amplitudes of the precession of the magnetic moments. Compared to the multilayer structure considered, uniaxial growth anisotropy is not important in antiferromagnets and the exchange energy is greater by two to three orders of magnitude. Therefore, in antiferromagnets, orientational hysteresis is absent or the difference between the equilibrium angles in the region of bistability is very small. In this respect, a special additional study is required in order to search for and analyze the features of stochastic and regular nonlinear dynamics of magnetization in antiferromagnets.

Our model of a multilayer structure is rather simplified. In addition to the interface roughness, in real structures, there are deviations of the coupling constants and magnetization from their average values because of, in particular, the presence of defects in the films and the limited number of layers. In addition, the interlayer coupling can differ from bilinear exchange interaction [13, 16]. Allowing for these factors should essentially complicate the analysis of nonlinear regular and stochastic dynamics of the magnetic moments and considerably increase the variety of dynamic regimes. Nevertheless, the results obtained correctly reflect the basic features of dynamic behavior of real multilayer systems with narrow hysteresis loops.

ACKNOWLEDGMENTS

This study was supported by the Ministry of Education of the Russian Federation, grant no. PD02-1.2-72.

REFERENCES

1. G. G. Malinetskiĭ and A. B. Potapov, *Modern Problems in Nonlinear Dynamics* (Editorial URSS, Moscow, 2002) [in Russian].
2. S. M. Rezende and F. M. de Aguiar, Proc. IEEE **78** (6), 893 (1990).
3. A. G. Gurevich and G. A. Melkov, *Magnetic Oscillations and Waves* (Nauka, Moscow, 1994).
4. V. V. Ustinov, M. M. Kirillova, I. D. Lobov, V. M. Maevskiĭ, A. A. Makhnev, V. I. Minin, L. N. Romashev, A. R. Del', A. V. Semerikov, and E. I. Shreder, Zh. Éksp. Teor. Fiz. **109** (2), 477 (1996) [JETP **82**, 253 (1996)].

5. V. V. Kostyuchenko and A. K. Zvezdin, Phys. Rev. B **57** (6), 5951 (1998).
6. G. S. Patrin, N. V. Volkov, and V. P. Kononov, Pis'ma Zh. Éksp. Teor. Fiz. **68** (5), 287 (1998) [JETP Lett. **68**, 307 (1998)].
7. A. M. Shutyĭ and D. I. Sementsov, Fiz. Met. Metalloved. **95** (3), 211 (2003) [Phys. Met. Metallogr. **95**, 211 (2003)].
8. D. I. Sementsov and A. M. Shutyĭ, Fiz. Tverd. Tela (St. Petersburg) **45** (5), 878 (2003) [Phys. Solid State **45**, 922 (2003)].
9. F. V. Lisovskiĭ and O. P. Polyakov, Pis'ma Zh. Éksp. Teor. Fiz. **68** (12), 643 (1998) [JETP Lett. **68**, 679 (1998)].
10. F. V. Lisovskiĭ and O. P. Polyakov, Pis'ma Zh. Éksp. Teor. Fiz. **73** (9), 546 (2001) [JETP Lett. **73**, 483 (2001)].
11. D. I. Sementsov and A. M. Shutyĭ, Pis'ma Zh. Éksp. Teor. Fiz. **75** (5), 287 (2002) [JETP Lett. **75**, 242 (2002)].
12. A. I. Morozov and A. S. Sigov, Fiz. Tverd. Tela (St. Petersburg) **41** (7), 1240 (1999) [Phys. Solid State **41**, 1130 (1999)].
13. V. D. Levchenko, A. I. Morozov, and A. S. Sigov, Zh. Éksp. Teor. Fiz. **121** (5), 1149 (2002) [JETP **94**, 985 (2002)].
14. A. K. Zvezdin and V. V. Kostyuchenko, Fiz. Tverd. Tela (St. Petersburg) **39** (1), 178 (1997) [Phys. Solid State **39**, 155 (1997)].
15. M. I. Kurkin and D. Z. Khusainov, Fiz. Tverd. Tela (St. Petersburg) **41** (4), 660 (1999) [Phys. Solid State **41**, 595 (1999)].
16. S. O. Demokritov, A. V. Drovosekov, N. M. Kreĭnes, H. Nembach, M. Rickart, and D. I. Kholin, Zh. Éksp. Teor. Fiz. **122**, 1233 (2002) [JETP **95**, 1062 (2002)].
17. A. B. Drovosekov, O. V. Zhotikova, N. M. Kreĭnes, V. F. Meshcheryakov, M. A. Milyaev, L. N. Romashev, V. V. Ustinov, and D. I. Kholin, Zh. Éksp. Teor. Fiz. **116**, 1817 (1999) [JETP **89**, 986 (1999)].
18. P. Bergé, Y. Pomeau, and C. Vidal, *L'ordre dans le Chaos. Vers une Approche Deterministe de la Turbulence* (Hermann, Paris, 1988; Mir, Moscow, 1991).

Translated by I. Zvyagin

Physics of the Solid State, Vol. 46, No. 11, 2004, pp. 2081–2085. Translated from Fizika Tverdogo Tela, Vol. 46, No. 11, 2004, pp. 2014–2017.
Original Russian Text Copyright © 2004 by Men'shenin.

MAGNETISM AND FERROELECTRICITY

Antiferromagnetic Photogalvanic Effect in Orthoaluminates

V. V. Men'shenin

Institute of Metal Physics, Ural Division, Russian Academy of Sciences,
ul. S. Kovalevskoĭ 18, Yekaterinburg, 620219 Russia
e-mail: menshenin@imp.uran.ru

Received January 12, 2004; in final form, March 19, 2004

Abstract—The antiferromagnetic photogalvanic effect in gadolinium, dysprosium, and terbium orthoaluminates is described within the phenomenological approach. The cases of linear and circular polarization of light are considered. *© 2004 MAIK "Nauka/Interperiodica".*

1. INTRODUCTION

The antiferromagnetic photogalvanic effect consists in generating direct electric current in centroantisymmetric antiferromagnets under exposure to light in the absence of an external dc electric field and spatial inhomogeneities. The phenomenological theory of the antiferromagnetic photogalvanic effect in tetragonal and trigonal antiferromagnets was developed earlier in [1]. The microscopic phonon mechanism of the origin of this phenomenon was proposed in [2].

Phenomenologically, the antiferromagnetic photogalvanic effect is characterized by the following feature: in centroantisymmetric antiferromagnets, the transformation of the antiferromagnetic vector **L** through symmetry operations of the medium can reverse the sign of the vector. This transformation takes place in the situation where all magnetic atoms occupy identical positions in the lattice and the symmetry operations transfer atoms from positions in one magnetic sublattice to positions in another magnetic sublattice. In particular, this permutation of atoms can occur in centroantisymmetric antiferromagnets in which the center of symmetry becomes the center of antisymmetry due to magnetic ordering and for which the antiferromagnetic vector **L** obeys the equality

$$\bar{1}\mathbf{L} = -\mathbf{L}. \tag{1}$$

Therefore, centroantisymmetric antiferromagnets are the only materials for which the density of the photogalvanic current can be written in the form

$$j_i = \beta_{ijkl} L_j e_k e_l^* J, \tag{2}$$

where β_{ijkl} is the antiferromagnetic photogalvanic tensor, **e** is the polarization vector of light, and J is the intensity of light.

In our earlier work [1], we analyzed the linear antiferromagnetic photogalvanic effect in trirutiles, orthophosphates, orthovanadates, and Cr_2O_3. In these materials, the electric current can be generated by linearly polarized light. The antiferromagnetic photogalvanic tensor β_{ijkl}^L can be represented by the expression

$$\beta_{ijkl}^L = \operatorname{Re}\beta_{ijkl}. \tag{3}$$

This tensor determines the relation between the direction of the photocurrent, the orientation of the antiferromagnetic vector **L**, and the direction of the polarization of the electromagnetic wave. The antiferromagnetic photogalvanic tensor coincides in symmetry with the piezomagnetic tensor.

Let us also call attention to the specific features of the phonon mechanism responsible for the antiferromagnetic photogalvanic effect. The point is that, unlike nonmagnetic media in which a photogalvanic current has been observed in experiments, centroantisymmetric antiferromagnets do not exhibit a piezoelectric effect but are characterized by a magnetoelectric effect. Consequently, the long-range part of the electron–phonon interaction in centroantisymmetric antiferromagnets can be caused by two factors: (i) polarization of the medium in response to an external magnetic field due to the magnetoelectric effect and (ii) phonon-assisted modulation of the medium.

It is of interest to extend the list of materials in which the antiferromagnetic photogalvanic effect can be observed in the experiment. The orthoaluminates we are interested in also belong to this class of materials. The magnetoelectric effect and magnetic properties of orthoaluminates have been studied in sufficient detail, and the literature on the magnetic and magnetoelectric properties of these materials is quite extensive. It should be noted that the conditions used for exciting a linear photocurrent in orthoaluminates with low symmetry are less diverse than those for tetragonal antiferromagnets. In this respect, it is necessary to investigate the manifestation of both the linear and circular antiferromagnetic photogalvanic effects in orthoaluminates.

Table 1. Permutation relationships for ions located in the 4*c* positions

g	$\bar{1}$	2_{1x}	2_{1y}
1	2	3	4
2	1	4	3
3	4	1	2
4	3	2	1

Table 2. Irreducible representations of the *Pbnm* group

Γ	$\bar{1}$	2_{1x}	2_{1y}	2_{1z}	Combinations of basis vectors	Magnetic point group
Γ_1	+1	+1	+1	+1		$m_x m_y m_z$
Γ_2	+1	+1	–1	–1		$m_x m'_y m'_z$
Γ_3	+1	–1	+1	–1		$m'_x m_y m'_z$
Γ_4	+1	–1	–1	+1		$m'_x m'_y m_z$
Γ_5	–1	+1	+1	+1	a_x, g_y	$m'_x m'_y m'_z$
Γ_6	–1	–1	–1	+1	g_x, a_y	$m_x m_y m'_z$
Γ_7	–1	–1	+1	–1	a_z	$m_x m'_y m_z$
Γ_8	–1	+1	–1	–1	g_z	$m'_x m_y m_z$

2. EXCHANGE MAGNETIC STRUCTURES

Compounds of the general formula $R\text{AlO}_3$, where R is a rare-earth metal ion (Gd^{3+}, Dy^{3+}, Tb^{3+}) located in the 4*c* position, have the symmetry $Pbnm(D_{2h}^{16})$. It is assumed that the crystallographic axes are aligned parallel to the twofold axes. Table 1 presents the permutation relationships for ions located in the 4*c* positions. As can be seen from Table 1, orthoaluminates of gadolinium, dysprosium, and terbium have two exchange magnetic structures (EMS) (with oppositely oriented magnetizations of the magnetic sublattices) that are odd with respect to the inversion. The first exchange magnetic structure is even with respect to the 2_{1x} screw axis of the crystal and belongs to structures of the *a* type. The second exchange magnetic structure is even with respect to the 2_{1y} screw axis and belongs to structures of the *g* type. For these structures, we can write the following relationships [3]:

$$\begin{aligned} &\text{OMC}\,\bar{1}(-)2_x(+)2_y(-), \quad \mathbf{a} = M_1 - M_2 + M_3 - M_4, \\ &\text{OMC}\,\bar{1}(-)2_y(+)2_z(-), \quad \mathbf{g} = M_1 - M_2 - M_3 + M_4, \end{aligned} \tag{4}$$

where M_i ($i = 1, \ldots, 4$) is the local sublattice magnetization. Table 2 presents the irreducible representations of the *Pbnm* group with components of the basis vectors **a** and **g** that are transformed by these representations. It should be noted that the other two possible exchange magnetic structures are even with respect to the inversion and, consequently, are of no interest to us.

3. GADOLINIUM ORTHOALUMINATE

Gadolinium orthoaluminate GdAlO_3 in the ground state is characterized by the Γ_5 representation. The results of investigating the magnetoelectric effect indicate that the GdAlO_3 compound has an exchange magnetic structure with magnetic sublattices in the $a_x g_y$ orientation state (the cross type) in the *xy* plane [3]. However, since the component χ_{xx} of the magnetic susceptibility of the GdAlO_3 compound tends to zero at $T \longrightarrow 0$ and a spin-flop transition occurs in an external magnetic field **H** aligned with the *x* axis, the vector $\mathbf{a} \parallel Ox$ is the maximum antiferromagnetic vector and the g_y component of the exchange magnetic structure can exist only in the form of a small addition [3].

Let us first consider the situation where the g_y component of the exchange magnetic structure is absent. In this case, the density components of the linear photogalvanic current can be represented in the form

$$\begin{gathered} j_x = 2\beta^{L(a)}_{xxyz} e_y e_z a_x J, \quad j_y = 2\beta^{L(a)}_{yxzx} e_z e_x a_x J, \\ j_z = 2\beta^{L(a)}_{zxxy} e_x e_y a_x J, \end{gathered} \tag{5}$$

where $\beta^{L(a)}_{ijkl} = Re\beta^{(a)}_{ijkl}$ are the components of the real part of the antiferromagnetic photogalvanic tensor. As was noted above, the antiferromagnetic photogalvanic tensor $\beta^{L(a)}_{ijkl}$ coincides in symmetry with the piezomagnetic tensor. The superscript *a* in parentheses indicates that these tensors refer to the exchange magnetic structure $\bar{1}(-)2_x(+)2_y(-)$. It follows from relationships (5) that the photocurrent passing through the GdAlO_3 sample is directed perpendicularly to the plane of the polarization of the electromagnetic wave, provided one of the components of the polarization vector is equal to zero and the other two components are nonzero. The electric current can be generated along an arbitrary crystallographic axis with appropriate choice of the direction of the electromagnetic wave polarization.

Next, we analyze how the expression for the electric current can transform depending on whether the g_y component of the exchange magnetic structure is present or absent. An exchange magnetic structure of the *g* type can be represented by the second equality in relationships (4). This structure differs from the exchange magnetic structure of the *a* type by the parity of the 2_y screw axis. Hence, the other components of the real part of the antiferromagnetic photogalvanic tensor are also nonzero. The photogalvanic current density related to the vector **g** ∥ *Oy* is given by the following expressions:

$$\begin{gathered} j_x = 2\beta^{L(g)}_{xyzy}e_z e_y g_y J, \quad j_y = 2\beta^{L(g)}_{yyzx}e_z e_x g_y J, \\ j_z = (\beta^{L(g)}_{zyxx}e_x^2 + \beta^{L(g)}_{zyyy}e_y^2 + \beta^{L(g)}_{zyzz}e_z^2)g_y J. \end{gathered} \tag{6}$$

A comparison of relationships (5) and (6) shows that the expressions for the components j_z of the photogalvanic current density differ significantly. Actually, in the case when the g_y component does not contribute to the magnetic structure, the photocurrent j_z is generated along the z axis of the crystal for the polarization of light $\mathbf{e} = (e_x, e_y, 0)$. If the g_y component makes a contribution to the magnetic structure, the photocurrent j_z is generated for the polarization of the electromagnetic wave along an arbitrary coordinate axis. Therefore, the manifestation of the antiferromagnetic photogalvanic effect can provide direct evidence of the presence or absence of a contribution from the g_y component to magnetic ordering of the $GdAlO_3$ compound.

4. DYSPROSIUM AND TERBIUM ORTHOALUMINATES

The neutron diffraction data and results of investigating the optical transitions between multiplet layers [4–6] give grounds to believe that dysprosium and terbium orthoaluminates have a noncollinear exchange magnetic structure with four magnetic sublattices in the $a_x g_y$ orientation state; i.e., as in the preceding case, the compounds are characterized by the Γ_5 representation. Earlier [3], it was shown that the exchange magnetic structure of these orthoaluminates in the $a_x g_y$ orientation state can be represented in the form of two antiferromagnetic configurations with the antiferromagnetic vectors

$$\mathbf{L}_1 = \mathbf{M}_1 - \mathbf{M}_2, \quad \mathbf{L}_2 = \mathbf{M}_3 - \mathbf{M}_4, \tag{7}$$

which are inserted into each other. The vectors $\mathbf{L}_1$ and $\mathbf{L}_2$ are oriented along the principal axes of the g tensors of the ions related through the inversion. In this case, we obtain

$$\mathbf{a} = \mathbf{L}_1 + \mathbf{L}_2, \quad \mathbf{g} = \mathbf{L}_1 - \mathbf{L}_2. \tag{8}$$

Here, we have the vectors $\mathbf{L}_1 + \mathbf{L}_2 \parallel x$ and $\mathbf{L}_1 - \mathbf{L}_2 \parallel y$ in the ground state. It is evident that, for the $DyAlO_3$ and $TbAlO_3$ orthoaluminate compounds, the expression describing the components of the photogalvanic current density is a combination of equalities (5) and (6) in which a_x and g_y are replaced by $(\mathbf{L}_1 + \mathbf{L}_2)_x$ and $(\mathbf{L}_1 - \mathbf{L}_2)_y$, respectively.

5. CIRCULATING ANTIFERROMAGNETIC PHOTOGALVANIC CURRENT

In the preceding sections, we analyzed the case of linearly polarized light. Now, we consider the situation where the light is circularly polarized. For circularly polarized light, the expression describing the density of the photogalvanic current involves only the imaginary part of the antiferromagnetic photogalvanic tensor:

$$\operatorname{Im}\beta_{ijkl} = \beta_{ijs}\varepsilon_{skl}, \tag{9}$$

where the tensor β_{ijs} does not possess any properties associated with the permutation of the subscripts. In order to determine nonzero components of the antiferromagnetic photogalvanic tensor β_{ijs}, we use the relationship for the circulating electric current,

$$\begin{gathered} j_i = (\beta^{(a)}_{ijs}\{\mathbf{L}_1 + \mathbf{L}_2\}_j[\mathbf{e}, \mathbf{e}^*]_s \\ + \beta^{(g)}_{ijs}\{\mathbf{L}_1 - \mathbf{L}_2\}_j[\mathbf{e}, \mathbf{e}^*]_s)J, \end{gathered} \tag{10}$$

and the rule following which each material tensor can be transformed through the symmetry operations of the medium according to the rule of transformation of the quantities related by this tensor; i.e., the tensor can be transformed as a product of these quantities. Therefore, the antiferromagnetic photogalvanic tensor β_{ijs} can be transformed by the symmetry operations as the product $j_i L_j[\mathbf{e}, \mathbf{e}^*]_s$. In equality (10), the superscripts (a) and (g) refer to the exchange magnetic structures characterized by the vectors $\mathbf{L}_1 + \mathbf{L}_2$ and $\mathbf{L}_1 - \mathbf{L}_2$, respectively.

Let us determine the nonzero components of the antiferromagnetic photogalvanic tensor $\beta^{(a)}_{ijs}$. Since the sum of the vectors $\mathbf{L}_1 + \mathbf{L}_2$ has a sole nonzero projection onto the x axis, it is sufficient to consider only the quantities $\beta^{(a)}_{ixs}$. Recall that the exchange magnetic structure is even with respect to the 2_x screw axis of the crystal. On this basis, we can easily verify that the antiferromagnetic photogalvanic tensor has the following nonzero components:

$$\beta^{(a)}_{xxx}, \quad \beta^{(a)}_{yxy}, \quad \beta^{(a)}_{zxz}.$$

For exchange magnetic structures of the g type, the antiferromagnetic photogalvanic tensor has the nonzero components

$$\beta^{(g)}_{xyx}, \quad \beta^{(g)}_{yyy}, \quad \beta^{(g)}_{zyz}.$$

As a consequence, the components of the density of the photogalvanic current for circularly polarized light can be represented by the expressions

$$\begin{gathered} j_x = (\beta^{(a)}_{xxx}\{\mathbf{L}_1 + \mathbf{L}_2\}_x + \beta^{(g)}_{xyx}\{\mathbf{L}_1 - \mathbf{L}_2\}_y) \\ \times(e_y e_z^* - e_z e_y^*)J, \\ j_y = (\beta^{(a)}_{yxy}\{\mathbf{L}_1 + \mathbf{L}_2\}_x + \beta^{(g)}_{yyy}\{\mathbf{L}_1 - \mathbf{L}_2\}_y) \\ \times(e_z e_x^* - e_x e_z^*)J, \\ j_z = (\beta^{(a)}_{zxz}\{\mathbf{L}_1 + \mathbf{L}_2\}_x + \beta^{(g)}_{zyz}\{\mathbf{L}_1 - \mathbf{L}_2\}_y) \\ \times(e_x e_y^* - e_y e_x^*)J. \end{gathered} \tag{11}$$

For the gadolinium orthoaluminate compound under the condition that the g_y component of the exchange magnetic structure is absent ($g_y = 0$), expressions (11) involve only the terms proportional to the quantities $\beta^{(a)}_{xxx}$, $\beta^{(a)}_{yxy}$, and $\beta^{(a)}_{zxz}$. It follows from expressions (11) that, for circular polarization of the electromagnetic wave, the photogalvanic current is directed perpendicularly to the plane of wave polarization. This inference holds true where the polarization of the electromagnetic wave has only two nonzero components.

Now, we consider the significant difference in the manifestation of the antiferromagnetic photogalvanic effect and the photogalvanic effect in nonmagnetic crystals. For this purpose, we will analyze how the operation of time inversion can transform the right-hand and left-hand sides of equality (2). With the replacement $t \longrightarrow -t$, the current density $\mathbf{j}$ and the antiferromagnetic vector $\mathbf{L}$ reverse sign and the polarization vector of the electromagnetic wave changes as follows: $\mathbf{e} \longrightarrow \mathbf{e}^*$. In this case, the sign of the antiferromagnetic photogalvanic tensor β^{L}_{ijkl} should remain unchanged, whereas the imaginary part of the tensor $\mathrm{Im}\beta_{ijkl}$ reverses sign. Consequently, the antisymmetric part of the antiferromagnetic photogalvanic tensor should become zero, provided the dissipation of light energy is disregarded. Therefore, we can infer that, in the case of the antiferromagnetic photogalvanic effect, the nondissipative current can be generated only by linearly polarized light. In nonmagnetic media, the nondissipative current is generated by circularly polarized light.

6. RESULTS AND DISCUSSION

Thus, the linear and circulating photogalvanic currents in gadolinium, dysprosium, and terbium orthoaluminates were analyzed within the phenomenological approach.

First and foremost, we note that the question as to whether the gadolinium orthoaluminate in the ground state has an exchange magnetic structure $\bar{1}(-)2_y(+)2_z(-)$ remains open. In principle, this problem can be solved in terms of the antiferromagnetic photogalvanic effect: if the photocurrent is generated in a direction parallel to the z axis of the crystal upon exposure to light that is linearly polarized along an arbitrary coordinate axis, the $GdAlO_3$ compound has an exchange magnetic structure $\bar{1}(-)2_y(+)2_z(-)$. In the absence of an exchange magnetic structure in the $GdAlO_3$ compound, the linear photocurrent is directed perpendicularly to the plane of the polarization of the electromagnetic wave.

In the $DyAlO_3$ and $TbAlO_3$ orthoaluminate compounds, there can exist two possible centroantisymmetric exchange magnetic structures. In this respect, the photocurrent generated in dysprosium and terbium orthoaluminate crystals is most conveniently observed under conditions where the polarization of the electromagnetic wave and the photocurrent are directed along the same axis (namely, the z axis). For any other polarization of the electromagnetic wave, the photocurrent is directed perpendicularly to the plane of the wave polarization and can be determined from equalities (5) and (6) with due regard for the aforementioned replacement (8).

A number of remarks concerning the order of magnitude of generated currents need to be made. It should be noted that, in the case under consideration, the photocurrent is generated through the phonon mechanism. Therefore, the qualitative assessment obtained in [2] for the photocurrent is also valid for dysprosium and terbium orthoaluminates in which the photogalvanic current is directed along the z axis of the crystal. In actual fact, the metamagnetic transition from the antiferromagnetic to ferromagnetic exchange magnetic structure in the $DyAlO_3$ and $TbAlO_3$ orthoaluminate compounds occurs in a magnetic field $H \sim 5$ kOe. Hence, the magnetic field $H \sim 1$ kOe used in [2] can also be applied to the $DyAlO_3$ and $TbAlO_3$ compounds. The temperature range of manifestation of the antiferromagnetic order in dysprosium and terbium orthoaluminate crystals coincides with that used in [2] for evaluating the photocurrent density. As a result, we obtain $j(\mathrm{CGS}) \sim 10^{-5}J$ (erg/cm^2 s), where J is the intensity of light.

In [7–9], when studying electron–hole correlations in "exciton" dielectrics, considerable attention was given to the current states and, in particular, the photogalvanic effect. The origin of these states can be associated with the instability of the system with respect to the electron–hole pairing in the course of electron scattering by holes. It was demonstrated that the bulk photogalvanic effect is caused by the interband transitions responsible for the appearance of the imaginary part of the singlet order parameter in the system. On the macroscopic level, the existence of the imaginary part of the singlet order parameter is equivalent to the existence of the antisymmetric components of the magnetoelectric tensor of the medium. For orthorhombic crystals, the photogalvanic effect can manifest itself through the above mechanism in the case when the point magnetic symmetry in the ground state is $mmm'(D_{2h}(C_{2v}))$. However, the orthoaluminate crystals in the ground state considered in this paper have the point magnetic symmetry $m'm'm'(D_{2h}(D_2))$; i.e., the orthoaluminate crystals in the ground state are characterized only by the symmetric magnetoelectric tensor. Consequently, the factors responsible for the photogalvanic effect [7–9] do not manifest themselves in the studied orthoaluminates until the magnetic state of the crystal changes.

In this respect, we should note that, in an external magnetic field, the $GdAlO_3$ orthoaluminate compound undergoes a spin-flop transition to the a_z magnetic state with the point magnetic symmetry $mm'm(D_{2h}(C_{2v}))$. In this situation, when the magnetic field does not substantially affect the electron–hole pairing, the photogalvanic effect can occur through the mechanism proposed in [7–9]. In an external magnetic field, the $DyAlO_3$ and $TbAlO_3$ orthoaluminate compounds undergo a transition to an intermediate state characterized by the off-diagonal components α_{13} and α_{31} of the magnetoelectric tensor [3]. Therefore, under the condition $\alpha_{13} = -\alpha_{31}$ for the $DyAlO_3$ and $TbAlO_3$ orthoaluminates in the intermediate state, the photogalvanic effect can also occur through the mechanism proposed in [7–9]. However, the equality $\alpha_{13} = -\alpha_{31}$ must be verified in the experiment.

REFERENCES

1. V. V. Men'shenin and E. A. Turov, Pis'ma Zh. Éksp. Teor. Fiz. **72** (1), 23 (2000) [JETP Lett. **72**, 14 (2000)].
2. V. V. Men'shenin, Fiz. Tverd. Tela (St. Petersburg) **45** (11), 2028 (2003) [Phys. Solid State **45**, 2131 (2003)].
3. E. A. Turov, A. V. Kolchanov, V. V. Men'shenin, I. F. Mirsaev, and V. V. Nikolaev, *Symmetry and Physical Properties of Antiferromagnets* (Fizmatlit, Moscow, 2001) [in Russian].
4. L. Schuchert, S. Hufner, and R. Faulhaber, Z. Phys. **222** (1), 105 (1969).
5. R. Bidaux and P. Meriel, J. Phys. (Paris) **29** (2–3), 220 (1968).
6. J. Bielen, J. Mareschal, and J. Sivardiere, Z. Angew. Phys. **23** (4), 243 (1967).
7. A. A. Gorbatsevich, Yu. V. Kopaev, and V. V. Tugushev, Zh. Éksp. Teor. Fiz. **85**, 1107 (1983) [Sov. Phys. JETP **58**, 643 (1983)].
8. Yu. A. Artamonov, A. A. Gorbatsevich, and Yu. V. Kopaev, Zh. Éksp. Teor. Fiz. **101** (2), 557 (1992) [Sov. Phys. JETP **74**, 296 (1992)].
9. Yu. A. Artamonov and A. A. Gorbatsevich, Zh. Éksp. Teor. Fiz. **89**, 1078 (1985) [Sov. Phys. JETP **62**, 621 (1985)].

Translated by O. Borovik-Romanova

Physics of the Solid State, Vol. 46, No. 11, 2004, pp. 2086–2093. Translated from Fizika Tverdogo Tela, Vol. 46, No. 11, 2004, pp. 2018–2024.
Original Russian Text Copyright © 2004 by Baĭkov, Nikulin, Melekh, Egorov.

MAGNETISM AND FERROELECTRICITY

Conductivity, Magnetoresistance, and Specific Heat of Oxygen-Deficient $La_{0.67}Sr_{0.33}MnO_{3-\alpha}$ $(0 \le \alpha \le 0.16)$

Yu. M. Baĭkov, E. I. Nikulin, B. T. Melekh, and V. M. Egorov
Ioffe Physicotechnical Institute, Russian Academy of Sciences, Politekhnicheskaya ul. 26, St. Petersburg, 194021 Russia
e-mail: baikov.solid@mail.ioffe.ru

Received March 19, 2004

Abstract—Oxygen-deficient $La_{0.67}Sr_{0.33}MnO_{3-\alpha}$ solid solutions have been studied. A comparison is made with the results obtained in an earlier study of a similar lanthanum–calcium manganite series. The physical characteristics of both series are accounted for as being due to a change in the Mn^{3+}/Mn^{4+} ratio caused by oxygen removal. The differences between the strontium and calcium series originate from differences in both the bulk properties of the original oxygen-stoichiometric materials and their texture. In the strontium series, the texture manifests itself in intergrain magnetoresistance, which exceeds in magnitude the colossal magnetoresistance caused by bulk properties of the material. Study of the oxygen-deficient $La_{0.67}Sr_{0.33}MnO_{3-\alpha}$ compound revealed specific features in the dependence of the electrophysical parameters on temperature and the Mn^{4+} fractional content that were not observed in the $La_{0.67}Ca_{0.33}MnO_{3-\alpha}$ compound studied by us earlier and in $La_{1-x}Sr_xMnO_3$ samples described in the literature. The physics underlying these differences is discussed. A modified phase diagram relating the phase transition temperature to the Mn^{4+} fraction is proposed. © *2004 MAIK “Nauka/Interperiodica”.*

1. FORMULATION OF THE PROBLEM

The physics underlying the phenomenon of colossal magnetoresistance (CMR) in solid solutions of alkaline- and rare-earth (AE and RE, respectively) manganites is currently fairly clear (see reviews [1–6]). The concepts involved rest on the idea of a mixed valence state (MVS) of the manganese ions (Mn^{3+}/Mn^{4+}). All the other features of the structure and spin, orbital, and charge ordering may play an important and even decisive role, but only in the formation of the manganese MVS. Basic research and applications in the area of the physics and chemistry of manganites depend crucially on the possibility of controlling this state.

The method most widely used to control the manganite MVS is based on varying the cation ratio in a solid solution, e.g., in $La_{1-x}Sr_xMnO_3$. A modification of this approach consists in synthesizing nonstoichiometric solid solutions deficient in one of the cations. This technique enjoys wide use in studies of simple manganites, e.g., $La_{1-x}MnO_3$ [7]. It has also been found that the manganites, including their simple structures, tend to form defect compounds of the type of $La_{1-x}Mn_{1-x}O_3$; these compounds are actually oxygen-rich manganites defined customarily by the formula $LaMnO_{3+\delta}$ (see, e.g., [8]). This property vanishes in solid solutions with the AE manganites [9].

Controlling the manganese MVS by producing oxygen deficiency is a much less popular approach [10–14]. This should be attributed to the difficulties involved in varying the oxygen content, because the oxygen in manganites is bound much more strongly than, say, in oxide superconductors. At the same time, investigating oxygen-deficient manganites could substantially broaden experimental possibilities for fine tailoring of the characteristics of a material to a specific basic study or an application. Our preceding investigation [10] showed that the changes in the physical characteristics of the $La_{0.67}Ca_{0.33}MnO_{3-\alpha}$ series $(0 \le \alpha \le 0.34)$ are qualitatively similar to those obtained when the cation composition x is varied. For instance, as α is increased, the semiconductor–metal transition point, the maximum in the magnitude of the CMR, and the region where the specific heat exhibits anomalous behavior shift toward lower temperatures, just as has been observed when x is reduced. There is, however, no quantitative coincidence between these shifts obtained for the same Mn^{3+}/Mn^{4+} ratio by varying the La/Sr cation ratio and producing an oxygen deficiency, i.e., where $|\Delta\alpha| = 2|\Delta x|$. To gain a deeper understanding of these phenomena, it appeared necessary to continue the investigation of the part played by oxygen deficiency in an apparently similar series, $La_{0.67}Sr_{0.33}MnO_{3-\alpha}$.

The lanthanum–strontium manganites have been studied to a greater extent than the lanthanum–calcium manganites. Despite their similar chemical compositions, the Ca, Sr, and Ba series differ both quantitatively and qualitatively in terms of their physical characteristics, including the conductivity and CMR. Some reviews stress the large difference in conduction band width between the materials of these series, a factor that

1063-7834/04/4611-2086$26.00 © 2004 MAIK “Nauka/Interperiodica”

Characteristics of $La_{0.67}Sr_{0.33}MnO_{3-\alpha}$ samples: oxygen deficiency α and phase transition temperatures as derived from electrical, magnetoresistance, and calorimetric measurements

Sample no.	α	z	$T_{CMR, HT}$, K	$T_{CMR, LT}$, K	$T_{\rho, HT}$, K	$T_{\rho, LT}$, K	|CMR|, %	maxC_p, K	E_{act}, meV
1	0.000	0.33	352	n/obs	352	n/obs	10	356	35*
2	0.010	0.31	344	n/obs	341	n/obs	8.0	348	47*
3	0.016	0.298	339	250	345	250	5.8	340	52*
4	0.030	0.27	326	220	325	220	4.0	n/obs	70*
5	0.034	0.262	322	200	320	200	4.0	n/obs	80
6	0.040	0.25	318	180	315	180	4.0	n/obs	80*
7	0.070	0.19	265	140	n/obs	n/obs	2.3	n/obs	120
8	0.100	0.13	238	n/obs	n/obs	n/obs	1	n/obs	150
9	0.16	0.01	n/obs	n/obs	n/obs	n/obs	n/obs	n/obs	220*

Note: $z = 0.33 - 2\alpha$; $T_{CMR, HT}$ and $T_{CMR, LT}$ are positions of the high- and low-temperature maxima in the magnitude of CMR, respectively; $T_{\rho, HT}$ and $T_{\rho, LT}$ are positions of the high- and low-temperature maxima in resistivity, respectively; C_p is the specific heat above 100 K; E_{act} is the activation energy for conductivity in the semiconducting region (asterisks refer to the values calculated using data from [16]); and n/obs stands for not observed experimentally.

is also apparent in the diagram of the magnetic phases and metal–semiconductor transitions (see, e.g., [6]). Our earlier study revealed different crystallization patterns for calcium and strontium samples prepared by direct cold-crucible high-frequency melting. Strontium-based samples are an agglomerate of heavily intergrown needle-shaped crystals, 10–15 mm long and ~1–2 mm in diameter (in contrast to the smaller crystals of the calcium series).

Because no comprehensive investigation of oxygen-deficient $La_{0.67}Sr_{0.33}MnO_{3-\alpha}$ samples has thus far been carried out experimentally, let alone theoretically, this study was aimed primarily at establishing the general pattern of changes that the conductivity, magnetoresistance, and heat capacity undergo within the range of Mn^{4+} fractions from 0.33 to zero. (This fraction is found from the charge neutrality condition.) The study is logically concluded with a comparison with measurements where the variation of the Mn^{4+} fraction was attained in a different way (rather than by removing oxygen), as well as with works where the oxygen content was not varied methodically [11–15].

2. EXPERIMENTAL TECHNIQUES

The techniques used to prepare the starting material; remove the oxygen by various physicochemical procedures; and measure the electrical conductivity, magnetoresistance, and heat capacity were described in our earlier paper [10]. The table lists characteristics of the samples studied by us. To make our presentation more revealing, we drop from the subsequent consideration (particularly in the figures) data on several of the samples. This relates to samples with similar characteristics (primarily, samples 1, 2, and 4–6).

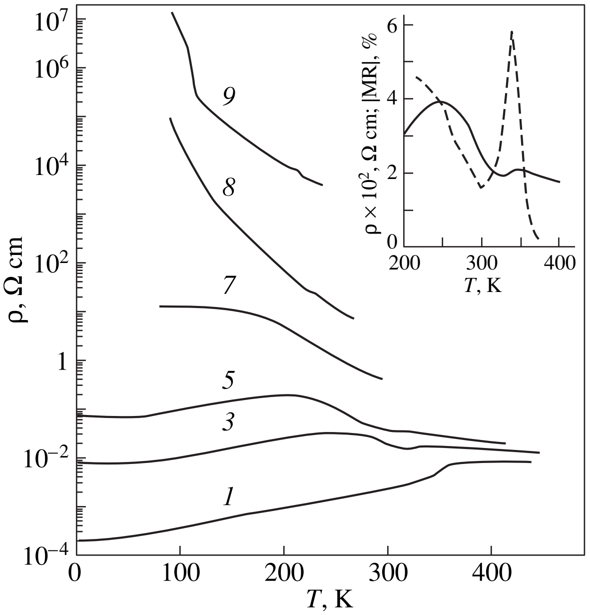

Fig. 1. Temperature behavior of the electrical resistivity ρ of $La_{0.67}Sr_{0.33}MnO_{3-\alpha}$ for various values of α: (*1*) 0, (*3*) 0.016, (*5*) 0.034, (*7*) 0.070, (*8*) 0.100, and (*9*) 0.160. The numerals adjacent to the curves refer to the sample numbers (see table). Inset: data for sample 3 obtained in the region of the feature in the ρ(*T*) course (solid line) and the magnetoresistance curve (dashed line).

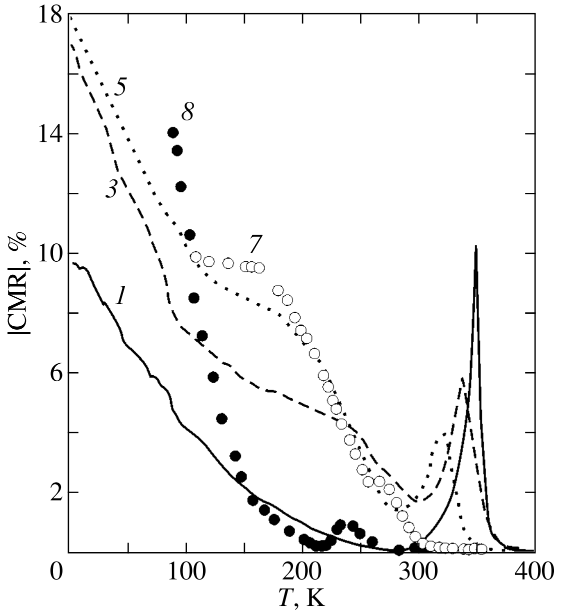

Fig. 2. Temperature dependence of magnetoresistance of $La_{0.67}Sr_{0.33}MnO_{3-\alpha}$ for various values of α: (*1*) 0, (*3*) 0.016, (*5*) 0.034, (*7*) 0.070, and (*8*) 0.100. The numerals adjacent to the curves refer to sample numbers (see table).

3. EXPERIMENTAL RESULTS

3.1. Electrical Conductivity

The temperature dependence of electrical resistivity ρ for increasing values of the oxygen deficiency is plotted in Fig. 1 in the logρ vs. *T* coordinates. The nine samples studied can be divided into three groups according to the magnitude and temperature behavior of their conductivity.

Below 360 K, samples 1 and 2 (see table) transfer from a high-conductivity state (where $\partial\rho/\partial T \approx 0$ in the range 400–550 K) to another, higher conductivity state, which can be called metal-like, because $\partial\rho/\partial T > 0$ and the resistivity is $\sim 10^{-4}\ \Omega$ cm at low (liquid-helium) temperatures.

The temperature dependence of the resistivity of samples 3–6 (see table) exhibits extrema; i.e., the derivative $\partial\rho/\partial T$ changes sign. Also, additional extrema can be isolated on both sides of the main hump in ρ(*T*). For illustration, the inset in Fig. 1 shows the temperature behavior of the derivative $\partial\rho/\partial T$ obtained for sample 3 in the range 200–400 K; the less pronounced feature in $\partial\rho/\partial T$ near 340 K correlates with the distinct peak in magnetoresistance (the same behavior is characteristic of samples 4–6). Turning now to the low-temperature side of the main hump, i.e., below 250 ± 5 K for sample 3 and below 200 ± 20 K for samples 4–6, we see that the curve describing the metal-like decrease in the resistivity with decreasing temperature ($\partial\rho/\partial T > 0$) passes through a broad minimum near 30 K; i.e., $\partial\rho/\partial T$ switches sign. A comparison of the behavior of the ρ(*T*) curves obtained for samples 4–6 indicates a good accuracy and reproducibility of the measurements, which was particularly evident in the sensitivity to small changes in the oxygen content: 2.970, 2.966, and 2.960 for samples 4–6, respectively. Therefore, to make the curves more revealing and to facilitate subsequent discussion of the main features present in the high-temperature part of the curves, we will use only the curve for sample 5.

The third group of samples (7–9, see table) exhibits only semiconducting behavior ($\partial\rho/\partial T < 0$), although sample 7 suggests the formation of a plateau in the range 70–150 K. For sample 9, the ρ(*T*) curve exhibits an inflection point near 100 K; however, the measurement accuracy in this region is poor and no refinement of the curve behavior was undertaken.

Both the clearly pronounced features in the temperature behavior of ρ(*T*) (which were used to classify the samples) and the peculiarities requiring a more careful analysis are compared with CMR data and available literature data in Section 4.

3.2. Magnetoresistance

The magnetoresistance is defined as $\{\rho(H) - \rho(H = 0)\}/\rho(H = 0)$, where the magnetic field is $H = 0.65$ T in our experiments. Considered physically, this quantity in our manganites is negative; in Fig. 2, which shows the temperature course of the CMR (as well as in the inset to Fig. 1), the absolute values of the corresponding quantities (|CMR| and |MR|, respectively) are given. To make the plots more revealing, the group of curves for samples 4–6 is not presented in full; in fact, there are only data for sample 5 (as in the case of electrical resistivity). The data on the two other samples are qualitatively very similar, and the quantitative changes are small and what should be expected. For the same reason, we do not display the curve for sample 2; indeed, its CMR temperature dependence behaves qualitatively similar to what we see for sample 1.

The CMR of the oxygen-deficient $La_{0.67}Sr_{0.33}MnO_{3-\alpha}$ samples exhibits three distinct features. One of them is associated with the presence of an extremum near and above room temperature. The CMR of samples 1–3, 5, and 8 reaches a maximum in magnitude at temperatures 352 ± 1, 344 ± 1, 339 ± 2, 322 ± 1, and 238 ± 8 K, respectively. An inflection point, barely discernible on the scale of Fig. 2 but nevertheless distinct, is seen in the graph for sample 7 at 265 ± 5 K. Another feature is a monotonic (but fairly steep) growth of CMR in magnitude for the same samples observed as the temperature is lowered still further, so that the CMR at liquid-helium temperature is even larger than that at the maximum of the peak. The third feature is a clearly pronounced change in the temperature behavior of the CMR exhibited by samples 3–8 in the range 100–250 K. The CMR curves of these samples can be represented phenomenologically as the sum of two curves, one of which grows monotonically with increasing temperature and the other passes through a maximum (we consider the magnitude of CMR). Sample 7 exhibits, starting from 160 K, a broad plateau extending down to 70 K, after which the temperature behavior of CMR becomes poorly reproducible, and therefore we neither present nor discuss it here. It may be conjectured that the chemical composition forming at an oxygen content corresponding to an index of 2.93 (or $\alpha = 0.07$) is poorly reproducible, so the properties of the manganite become intermediate between those observed in the third group of the samples (without the characteristic transition to metallic conduction) and in the first and second groups, which feature such a transition (see Subsection 3.1).

3.3. Specific-Heat Anomaly

Differential scanning calorimetry spectra showed an anomalous temperature behavior of the heat capacity in samples with $\alpha < 0.05$ in the range 320–350 K, where the CMR passes through a maximum and/or $\partial\rho/\partial T$ either switches sign or varies in magnitude. The heat capacity did not feature anomalies as distinctly as the conductivity and magnetoresistance do when the temperature is lowered to 100 K.

4. DISCUSSION OF THE RESULTS

We start the analysis of the conductivity and magnetoresistance of our $La_{0.67}Sr_{0.33}MnO_{3-\alpha}$ samples with a general comparison with our earlier data on $La_{0.67}Ca_{0.33}MnO_{3-\alpha}$ (the calcium series) [10]. Ignoring quantitative differences (in the magnitude of ρ and the temperatures of the conductivity and CMR extrema), similarity in the behavior of the characteristics of these two series can be noticed only for samples with extreme oxygen deficiencies, i.e., for samples with the lowest ($\alpha = 0$ for both series, $\alpha = \alpha_{Ca} = 0.006$ for the Ca series, and $\alpha = \alpha_{Sr} = 0.01$ for the Sr series) and the largest ($\alpha = 0.16$ for both series) deficiency levels. The strongly oxygen-deficient samples of the Ca and Sr series, as should be expected for manganites with a close-to-zero Mn^{4+} content, exhibit the lowest semiconductor-type conductivity without CMR (at least in the experimentally covered temperature regions). Samples that are nearly or fully stoichiometric in oxygen reveal a classical transition to the metallic state and CMR. The transition temperatures are close to those quoted in the literature. (It should be noted that the changes in T_c observed by us in samples with low oxygen off-stoichiometry could account for the scatter in the literature data!)

Samples of the two series under study with intermediate oxygen-deficiency levels exhibit distinct qualitative differences. For instance, the $\rho(T)$ curve for the sample with $\alpha_{Ca} = 0.017 \pm 0.001$ in the calcium series exhibits an inflection point, correlating with the maximum in CMR (165 K), below which the temperature behavior changes from $\ln\rho \sim 1/T$ to $\ln\rho \sim 1/T^{1/4}$, a pattern that persists down to liquid-helium temperatures. The behavior of $\rho(T)$ of sample 3 in the strontium series (with $\alpha_{Sr} = 0.016 \pm 0.001$) and of the sample with $\alpha_{Ca} = 0.017 \pm 0.001$ in the calcium series at relatively high temperatures are qualitatively similar ($\partial\rho/\partial T < 0$). Furthermore, the extremum observed for the strontium sample in the 323- to 345-K interval could be identified with the above-mentioned inflection point for the calcium series. Below 250 K, however, the character of the $\rho(T)$ dependence of the strontium sample switches to metallic, i.e., to a pattern radically different from that of its counterpart in the calcium series.

A similar conclusion can be drawn from comparing samples of both series that are off-stoichiometric in oxygen ($0.03 \le \alpha \le 0.04$). The calcium series exhibits in this case only a transition from one type of semiconducting conductivity to another, and this transition occurs in the temperature region where CMR reaches a maximum in magnitude. Judging from the sign of its derivative, the temperature dependence of conductivity in samples of the strontium series having the same oxygen off-stoichiometry radically changes its pattern below ~200 K (Fig. 1). While the conductivity below this temperature is no longer metallic, it nevertheless is higher by one and a half to two orders of magnitude than that for the calcium samples.

Samples 7 and 8, just as the calcium samples with similar oxygen off-stoichiometry ($\alpha_{Ca} = 0.06, 0.10$), reveal a semiconducting behavior. However, two differences should be pointed out. First, the $\rho(T)$ dependence for the Ca sample with $\alpha_{Ca} = 0.06$ does not show a tendency toward the formation of a plateau, in contrast to that for the Sr sample with $\alpha_{Sr} = 0.07$. Second, the Ca sample with $\alpha_{Ca} = 0.10$ does not exhibit CMR, in contrast to the Sr sample with $\alpha_{Sr} = 0.10$, which certainly reveals not only intergrain CMR but also bulk CMR, with a maximum at 238 ± 8 K.

Thus, a purely phenomenological comparison of the two oxygen-deficient series shows that substitution of Sr for Ca, a simple procedure at first glance, produces different responses to oxygen loss. The strontium series retains the metallic-like and ferromagnetic state to heavier oxygen deficiencies than the calcium series.

A more comprehensive analysis of our results and comparing them with other available data would require knowledge of the numerical parameters describing the dependence of conductivity on temperature and the Mn^{4+} content, which is dictated by the Sr and/or oxygen content. It turned out very hard, however, to locate in the numerous reviews that have appeared in recent years [1–6] the numerical parameters corresponding to the universally accepted analytical forms of the $\rho(T)$ relation. Therefore, the information necessary for performing a comparative quantitative analysis is taken primarily from the graphs presented in various papers and the analytical description is of a phenomenological character and based on the present authors' concepts rather than on those put forward in the cited papers.

The only publication that presents analytical temperature dependences of $\sigma(T) = 1/\rho(T)$ for a broad range of variations of both the cation composition and oxygen off-stoichiometry for $La_{1-x}Sr_xMnO_{3-\alpha}$ is [16]. Regretfully, the temperature range of 600 to 1400 K covered there lies substantially higher than the region where the phase transitions and CMR occur. In this range, the conduction is treated in [16] in terms of the small-polaron model. To compare these results with our data on the conductivity of the strontium series, we extrapolated the data from [16] to temperatures of 300–500 K using the corresponding relations. Attention is focused on the temperature behavior of ρ rather than on its magnitude. The fact is that the values of the conductivity quoted in the literature are poorly reproducible, because they depend strongly on technological factors. This dependence was demonstrated earlier in [17] for $La_{0.67}Sr_{0.33}MnO_3$-based samples studied by us by comparing the conductivities of a single crystal and two ceramic samples of composition $La_{0.67}Sr_{0.33}MnO_3$ prepared at different anneal temperatures. Above 400 K, the single crystal and the ceramic sample annealed at 1973 K have a fairly similar resistivity, which is lower by about a factor of 1.5 than the values obtained by us and those reported in [18], but these differences decrease to ~10% with a decrease in temperature. The ceramic sample annealed at 1573 K has an electrical resistivity at 400 K differing from our data by no more than 10%, but as the temperature is lowered, this difference reaches an order of magnitude (the conductivity of the ceramic sample becomes lower). Our oxygen-stoichiometric sample 1 features approximately the same temperature behavior of CMR as the ceramic samples studied in [17]; namely, the CMR grows in magnitude continuously as the temperature is decreased to 4.2 K and its values are similar in both cases at the same magnetic fields (10% in the present work and ~20% in [17]).

In view of the part played by technological factors and the temperature range covered in [16], it appeared only natural to compare the temperature behavior in the temperature regions where the conductivity follows a semiconducting pattern. The data obtained for the second and third groups of samples, which feature temperature regions with semiconducting behavior, are most appropriate for this purpose. It was found that in these groups the temperature dependences of $\rho(T)$ obtained experimentally on samples 4–8 and calculated for the same compositions using the equations from [16] are similar. However, in order to match the data on ρ, the prefactor given in [16] had to be multiplied by factors of 4.3, 4.8, 5.7, 17, and 31, respectively. Also, this procedure is efficient for samples 4–6 above 360 K ($E_{act} \approx$ 80 meV), for sample 7 above 200 K ($E_{act} \approx 120$ meV), and for sample 8 above 150 K ($E_{act} \approx 150$ meV). For samples 3 and 9, the activation energies quoted in [16] differ from $\partial \ln\rho/\partial(T^{-1})$ for our samples (above 360 K for the former sample and above 150 K for the latter) by a factor of approximately 2, which makes matching the data of the two studies by varying the prefactor impossible.

The electrical resistivity of samples 1 and 2 (making up the first group) at temperatures above 400 K is five times higher than that calculated using the equations from [16]. However, because of the smallness of the activation energies (35 and 47 meV, respectively [16]), the function $\rho = (\rho_0/T)\exp(E_{act}/T)$ in this temperature region features a broad minimum for $T_{min} = E_{act}$ resembling a plateau. This does not permit us to unambiguously conclude whether the conductivities obtained in the semiconducting region for our oxygen-stoichiometric samples and calculated from data from [16] are consistent or not.

Let us turn now to studies dealing with the temperature region where electrical and magnetic phase transitions and CMR occur. For comparison, we chose publications [9, 18], which reported on a comprehensive study of the temperature and concentration dependences of the conductivity. Those studies dealt, however, with samples of lanthanum–strontium manganites which had variable cation composition but were oxygen stoichiometric. It is customarily believed that the conductivity of the manganites under study depends primarily on the Mn^{4+} fraction, which is determined either by the fraction of Sr (or another AE element) substituting for lanthanum or by oxygen off-stoichiometry [1–6]. Therefore, we make a comparison of our date with experimental data from the literature by reducing the oxygen off-stoichiometry α to the Mn^{4+} fraction, which we denote by z. For samples with a Sr fraction of x, we have $z = x - 2\alpha$. The corresponding values of z for our samples are listed in the table.

Let us turn to the temperature dependences described in different publications. In all three studies under discussion (in the present paper and in [9, 18]), one can isolate two main types of $\rho(T)$ behavior, namely, a monotonic (or nearly monotonic) behavior, where the $\partial\rho/\partial T$ derivative does not change sign, and dependences with maxima and minima, which can be absolute or relative in the temperature interval covered. The nearly monotonic course is characteristic of the samples that transfer to the metallic state. We note immediately that $La_{0.67}Sr_{0.33}MnO_3$ exhibits, as a rule, metallic-like behavior slightly above the transition temperature, although this conclusion is based rather on the specific features of the $\rho(T)$ course for the small-polaron conduction (see above). Nearly monotonic behavior is seen clearly in our samples 1 and 2 (Fig. 1), for which $z = 0.33$ and 0.31, respectively (see table), and for the samples with $z \geq 0.175$ studied in [9, 18], where $z = x$. We stress immediately that the cation-variable series from [9, 18] differ from our oxygen-deficient system, where $\rho(T)$ follows a different course already for $z < 0.3$ (see below). A monotonic course of $\rho(T)$ is also characteristic of samples with a purely semiconducting behavior and is observed for samples with $z = 0.05$ and 0 [18] and for our samples 8 ($z = 0.13$) and 9 ($z = 0.01$).

A nonmonotonic $\rho(T)$ dependence with a relative maximum and minimum was seen for $z = 0.15$ in [18] and over the interval $0.125 \leq z \leq 0.175$ in [9] (where 11 samples were studied with a step of $\Delta z = 0.005$). In addition, the $\rho(T)$ curves from [9] exhibit a distinct plateau or inflection points within the interval $0.10 \leq z \leq 0.12$. Our sample 7 ($z = 0.19$) also reveals a clearly pronounced plateau, so it can be placed in the group of samples with nonmonotonic behavior. Thus, the $\rho(T)$ dependence for our samples 1, 2, and 7–9 coincides with that identified in the literature as characteristic of samples with variable cation composition and, most essentially, within the corresponding intervals of z.

The situation with our oxygen-deficient samples 3–6, whose Mn^{4+} fraction varies within the interval $0.25 \leq z \leq 0.3$, is more complicated. According to the above classification, they exhibit a $\rho(T)$ dependence with extrema; this feature is unique for the reason alone that it was not reported in the publications we are familiar with from reviews [1–6], primarily in [18]. (In [9], such compositions were not studied.) The uniqueness of this behavior consists in that oxygen-deficient samples in the above z interval pass through an absolute resistivity maximum at 180–250 K. This maximum is preceded on the high-temperature side by a relative maximum for sample 3 ($z = 0.298$) and by inflection points in the $\rho(T)$ dependence for the other samples (see above). It is also essential that the temperature region where the relative maximum in ρ is observed coincides with the region of the peak in CMR (Fig. 2) and of the anomalous temperature behavior of the heat capacity. We believe that this feature should be assigned to the unconventional method of manganese MVS control used in our study. The low-temperature part of the $\rho(T)$ curve (i.e., below the temperature of the absolute maximum) for the group of samples being discussed exhibits a weakly pronounced minimum near 30 K (see above), which was mentioned in some publications dealing with manganites and assigned to electron correlation at liquid-helium temperatures. This effect is usually observed, however, for close-to-metallic conductivities, while the conductivity of oxygen-deficient samples is substantially lower than metallic. More detailed experimental data, which may be obtained already in the near future, are needed to better understand the nature of this $\rho(T)$ minimum.

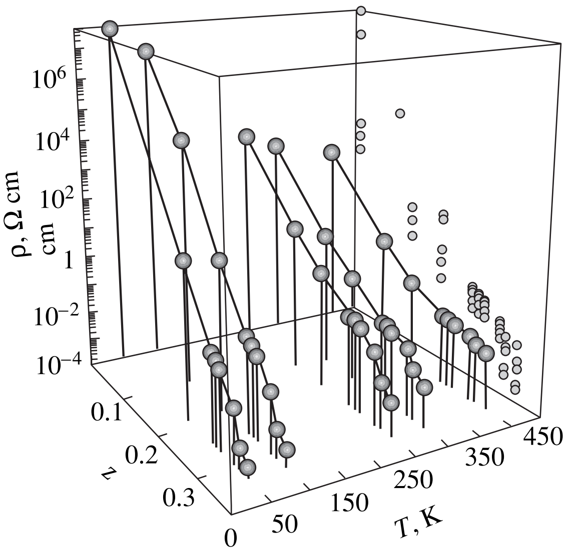

Fig. 3. Isotherms of the electrical resistivity ρ of $La_{0.67}Sr_{0.33}MnO_{3-\alpha}$ samples plotted vs. the Mn^{4+} fraction z.

Let us turn now to the concentration dependence of $\rho(z, T)$, i.e., the dependence of the conductivity on the Mn^{4+} fraction. Figure 3 plots isotherms of the concentration dependences derived from our measurements. Their main feature is a clearly nonlinear, exponential-like behavior of $\rho(z)$. Of particular interest is a still steeper course observed in the case of Mn^{4+} fractions near $z = 0.3$, where at all temperatures presented in Fig. 3 except 400 K the metal–semiconductor transition takes place. This effect is also evident when all experimental data are projected onto the xz plane (Fig. 3). The concentration dependence of conductivity is discussed primarily qualitatively in all experimental studies of which we are aware. We succeeded in extracting the $\rho(z)$ dependence from [9, 18] and compared it with our data. In view of the above differences in the conductivity attributable to technological factors, we focused attention on the general pattern of this relation. It turned out that the corresponding curves behave in a similar manner, including the sharper variation in the interval

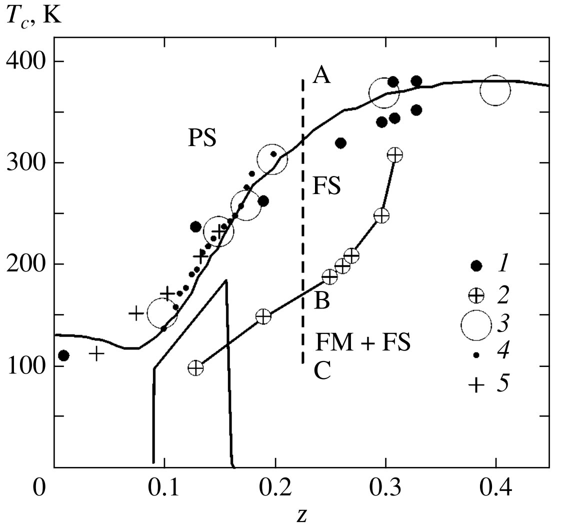

Fig. 4. Modification of the phase diagram relating the phase transition temperature T_c to the Mn^{4+} fraction z for $La_{0.67}Sr_{0.33}MnO_{3-\alpha}$. PS stands for paramagnetic semiconductor, FS for ferromagnetic semiconductor, and FM for ferromagnetic metal; (*1*, *2*) our data for the high- and low-temperature branches, respectively, and data from (*3*) [18], (*4*) [9], and (*5*) [15].

$z = 0.25–0.3$. The patterns of $\rho(z)$ curves for oxygen-deficient samples (our data) and samples with varied cation composition [9, 18] differ, however, in two respects. First, the latter samples with $z > 0.25$ exhibit, in effect, a jump to metallic-like conductivity. Second, because the $\rho(T)$ dependences of samples of both types for $0.04 < z < 0.3$ exhibit a complex behavior with extrema located at different temperatures (for example, at 300 K, one part of the curves relates already to a metal-like state while the other relates to the semiconducting state), the similarity in the behavior of the curves obtained in different studies is of a conceptual rather than quantitative character. For temperatures near 400 K, however, the curves can be approximately described by a parabolic relation of the type $\ln\rho(400\ K) = 3.7 - 49z + 68z^2$, which passes through a minimum near $z \sim 0.36$. According to the phase diagrams available in the literature, at the Mn^{4+} contents $z = 0.3–0.4$, T_c reaches a maximum for $La_{1-x}Sr_xMnO_3$ (see, e.g., [5, 6]).

In concluding this section, we discuss the modified phase diagram of the lanthanum–strontium manganites (Fig. 4) constructed with allowance for the two phase transitions that occur in oxygen-deficient samples (see table). A number of features for $z > 0.5$ given in reviews [1–6] are dropped here, but for $z < 0.5$ the diagram contains all the experimental points presented in the publications discussed in this paper. A three-dimensional diagram $T_c(x, \alpha)$ would certainly provide more information; nevertheless, we can state with confidence that the establishment of a second curve (at lower temperatures) was possible only due to the nonstandard manner in which the manganese MVS was varied in this study. The identification of the magnetic and electrical phases was made from experimental data. The simplest interpretation of the A–B–C cut of the diagram in Fig. 4 is as follows: a paramagnetic semiconductor (PS) transfers, with decreasing temperature, to a ferromagnetic semiconductor (FS) and only after that to a ferromagnetic metal (FM). The latter assignment cannot, however, be considered to be supported fully by experiment; indeed, while $\partial\rho/\partial T$ follows a metallic behavior, the magnitude of ρ is far from the values characteristic of metals. It appears therefore more reasonable to suggest that, in actual fact, phase separation (electronic or microheterogeneous) occurs at point B; to stress this point, an FM + FS state is shown under the low-temperature phase diagram line.

5. CONCLUSIONS

The electrophysical and magnetic properties of oxygen-deficient $La_{0.67}Sr_{0.33}MnO_{3-\alpha}$ ($\alpha \le 0.16$) have been studied in the temperature range from 4.2 to 550 K. The changes in conductivity induced by varying both the concentration of carriers (holes, Mn^{4+}) and the number of Mn–O–Mn bonds differ from those obtained by varying the cation composition. Furthermore, the conductivity changes differ from those observed to occur in $La_{0.67}Ca_{0.33}MnO_{3-\alpha}$. In particular, the metal-like behavior of strontium-based samples persists down to larger oxygen deficiencies. Invoking the concept of phase separation provides a basis for deeper insight into the behavior of conductivity and the features in the diagram relating the phase transition temperature to the Mn^{4+} fraction. The potential inherent in the method of “soft” oxygen removal for controlling the properties of manganites for basic science and applications is demonstrated; indeed, with no need for high-temperature synthesis, it has become possible to lower the metal–semiconductor and ferromagnet–paramagnet transition temperatures by more than 100 K (360–238 K) and to change the conductivity by several orders of magnitude (7 and 11 orders of magnitude at room temperature and 100 K, respectively).

ACKNOWLEDGMENTS

This study was supported by INTAS, grant no. 00-0728.

REFERENCES

1. J. M. D. Coey, M. Viret, and S. Von Molnar, Adv. Phys. **48** (2), 167 (1999).
2. E. L. Nagaev, Phys. Rep. **346**, 387 (2001).

3. Y. Tokura and Y. Tomioka, J. Magn. Magn. Mater. **200** (1), 1 (1999).
4. M. B. Salamon and M. Jaime, Rev. Mod. Phys. **73** (7), 583 (2001).
5. M. Ziese, Rep. Prog. Phys. **65**, 143 (2002).
6. E. Dagotto, T. Hotta, and A. Moreo, Phys. Rep. **344**, 1 (2001).
7. E. A. Gan'shina, I. K. Rodin, O. Yu. Gorbenko, and A. R. Kaul, J. Magn. Magn. Mater. **239**, 537 (2002).
8. M. Muroi and R. Street, Aust. J. Phys. **52**, 205 (1999).
9. B. Dabrovski, X. Xiong, Z. Bukovski, R. Dybzinski, P. W. Klamut, J. E. Siewenie, O. Chmaissen, J. Shaffer, C. W. Kinball, J. D. Jorgensen, and S. Short, Phys. Rev. B **60** (10), 7006 (1999).
10. E. I. Nikulin, V. M. Egorov, Yu. M. Baĭkov, B. T. Melekh, Yu. P. Stepanov, and I. N. Zimkin, Fiz. Tverd. Tela (St. Petersburg) **44** (5), 881 (2002) [Phys. Solid State **44**, 920 (2002)].
11. H. L. Ju, J. Gopalakrishnan, J. L. Peng, Qi Li, G. C. Xiong, T. Venkatesan, and R. L. Green, Phys. Rev. B **51** (9), 6143 (1995).
12. A. M. De Leon-Guevara, P. Berthet, J. Berthon, F. Millot, A. Revcoltvshi, A. Anane, C. Dupas, K. Le Dang, J. P. Renard, and P. Veillet, Phys. Rev. B **56** (10), 6031 (1997).
13. C. Jardon, M. A. Lopez-Quintela, D. Caiero, C. Vazquez-Vazquez, F. Rivadulla, J. Rivas, L. E. Hueso, and R. D. Sanchez, J. Magn. Magn. Mater. **189** (3), 321 (1998).
14. I. O. Troyanchuk, S. V. Trukhanov, D. D. Khalyavin, N. V. Pushkarev, and G. Szymczak, Fiz. Tverd. Tela (St. Petersburg) **42** (2), 297 (2000) [Phys. Solid State **42**, 305 (2000)].
15. L. Malavasi, M. C. Mozzati, C. B. Azzoni, G. Chiodelli, and G. Flor, Solid State Commun. **123** (8), 321 (2002).
16. J. Mizusaki, Y. Yonemura, H. Kamata, K. Ohyama, N. Mori, H. Takai, H. Tagawa, M. Dokiya, K. Naraya, T. Sasamoto, H. Inaba, and T. Hashimoto, Solid State Ionics **132**, 167 (2000).
17. H. Y. Hwang, S. W. Cheong, N. P. Ong, and B. Battlog, Phys. Rev. Lett. **77**, 2041 (1996).
18. A. Urushibara, Y. Moritomo, T. Arima, A. Asamitsu, G. Kido, and Y. Tokura, Phys. Rev. B **51**, 14103 (1995).

Translated by G. Skrebtsov

Physics of the Solid State, Vol. 46, No. 11, 2004, pp. 2094–2102. Translated from Fizika Tverdogo Tela, Vol. 46, No. 11, 2004, pp. 2025–2032.
Original Russian Text Copyright © 2004 by Gudenko, Yakubovskiĭ, Gorbenko, Kaul.

MAGNETISM AND FERROELECTRICITY

EPR Study of the Spin Dynamics of the $(La_{1-y}Pr_y)_{0.7}Ca_{0.3}MnO_3$ System

S. V. Gudenko*, A. Yu. Yakubovskiĭ*, O. Yu. Gorbenko, and A. R. Kaul****

**Russian Science Center Kurchatov Institute, pl. Kurchatova 1, Moscow, 123182 Russia*
e-mail: gudenko@imp.kiae.ru
***Moscow State University, Vorob'evy gory, Moscow, 119899 Russia*

Received March 23, 2004

Abstract—The EPR of Mn ions in the $(La_{1-y}Pr_y)_{0.7}Ca_{0.3}MnO_3$ system has been studied within a broad range of temperatures ($4 < T < 600$ K) and Pr concentrations ($0 \le y \le 1$), as well as under isotope substitution of ^{18}O for ^{16}O. All compositions were shown to undergo transitions to a magnetically ordered state with decreasing temperature. Magnetic phase diagrams were constructed for systems with different oxygen isotopes. The diagrams include paramagnetic, ferromagnetic, and antiferromagnetic regions. In the paramagnetic region, at temperatures not too close to the phase transition points, the Mn ion linewidth $\Delta H_{pp}(T)$ is related to the magnetic susceptibility $\chi(T)$ through the relation $\Delta H_{pp}(T) = [\chi_0/\chi(T)]\Delta H_{pp}(\infty) + \Delta H_0$, where $\Delta H_{pp}(\infty)$ is the width of the exchange-narrowed line in the high-temperature approximation, $\chi_0 \propto 1/T$ is the susceptibility of noninteracting ions, and ΔH_0 is the residual width originating from the sample porosity and resonance-field scatter in unoriented grains of a powder sample. An analysis of the data on $\Delta H_{pp}(\infty)$, ΔH_0, and $\chi(T)$ made it possible to estimate the symmetric and antisymmetric exchange interaction of Mn ions and of the noncubic crystal-field component of the oxygen ions. These parameters were found to be independent of the oxygen isotope species to within experimental error. *© 2004 MAIK “Nauka/Interperiodica”.*

1. INTRODUCTION

The recent intense investigation of perovskite manganites with the general formula $A_{1-x}A'_xMnO_3$ (A = La, Pr, or another rare-earth element; A' = Ca, Sr, Ba) should be attributed to the fact that the colossal magnetoresistance effect has been revealed in them [1–3]. These compounds show a close relation between the transport, magnetic, and structural properties. The level of doping by divalent cations A' determines the fractional content of the Mn^{3+} and Mn^{4+} ions, and the average cation ionic radius $\langle r_A \rangle$ determines the extent of deviation of the structure from a perfect cubic perovskite.

The doping level in the $(La_{1-y}Pr_y)_{0.7}Ca_{0.3}MnO_3$ compound remains constant as the Pr concentration y is varied from 0 to 1, and the average cationic radius $\langle r_A \rangle$ decreases, accordingly, from 1.21 to 1.18 Å. This entails a substantial change in the low-temperature phase state; indeed, for $0 < y < 0.6$, the compound is a ferromagnetic (FM) metal; for $0.6 \le y \le 0.8$, it is an inhomogeneous mixture of FM and antiferromagnetic (AFM) regions (conducting and insulating, respectively); and for $0.8 < y \le 1.0$, it is a canted antiferromagnetic (CAFM) dielectric. Within the interval $0.6 \le y \le 0.8$, the material is very sensitive to various external disturbances; in particular, the metallic state may switch to dielectric in response to even such a weak perturbation as substitution of the ^{18}O isotope for ^{16}O [4]. The properties of magnetically ordered phases in this compositional region have been studied in considerable detail by neutron diffraction [5, 6]. This communication reports on an EPR study of the magnetic properties of the $(La_{1-y}Pr_y)_{0.7}Ca_{0.3}MnO_3$ system.

The EPR signal in the manganites was shown to be generated by all manganese ion species present in a sample, namely, Mn^{3+} and Mn^{4+} [7]. These ions are coupled by exchange interaction strongly enough to favor the realization of phonon bottleneck conditions, which accounts for the observation of one common exchange-narrowed line. By neglecting spin–lattice relaxation, the temperature dependence of the width of this line can be described by [8]

$$\Delta H_{pp}(T) = \frac{\chi_0(T)}{\chi(T)}\Delta H_{pp}(\infty). \qquad (1)$$

Here, $\Delta H_{pp}(T)$ is the linewidth (field separation between the peaks in the derivative of the absorption curve) measured at temperature T; $\chi_0(T) \propto 1/T$ is the magnetic susceptibility of noninteracting spins; $\chi(T)$ is the experimentally observed susceptibility; and $\Delta H_{pp}(\infty)$ is the width of the exchange-narrowed line in the high-temperature limit, where most of the eigenvalues of the Hamiltonian of isotropic exchange interaction between Mn spins

$$H_{ex} = -\sum_{i<j} J_{ij}\mathbf{S}_i\mathbf{S}_j \qquad (2)$$

are much less than k_BT (k_B is the Boltzmann constant). The linewidth $\Delta H_{pp}(\infty)$ is given by the well-known relation [9]

$$\Delta H_{pp}(\infty) \simeq \left(\frac{\hbar}{g\mu_B}\right)\frac{\alpha M_2}{\omega_{ex}}, \qquad (3)$$

where M_2 is the second moment of the line, $\omega_{ex} \simeq J/\hbar$ is a characteristic exchange frequency, μ_B is the Bohr magneton, g is the magnetic-splitting factor, $\hbar$ is the Planck constant, and α is a dimensionless constant of order unity, whose value may differ slightly in various theories concerning exchange-induced narrowing.

It was shown in [8, 10] that the second moment M_2 in compounds with nonmagnetic ions A and A' is determined primarily by the Dzyaloshinskiĭ–Moriya antisymmetric exchange interaction

$$H_{DM} = \sum_{i<j} D_{DMij}[\mathbf{S}_i \times \mathbf{S}_j] \qquad (4)$$

and the noncubic crystal-field component, which is caused by deformation of the oxygen octahedra surrounding the Mn ions. Analyzing the experimental data on $\Delta H_{pp}(\infty)$ allowed us to estimate the parameters of these interactions and their dependence on temperature and the composition of the systems under study.

We carried out EPR measurements on two lots of powder samples of $(La_{1-y}Pr_y)_{0.7}Ca_{0.3}MnO_3$, with the oxygen isotopic composition corresponding to a natural ^{16}O abundance or a composition enriched in the ^{18}O isotope and with y = 0.0, 0.25, 0.5, 0.6, 0.7, 0.75, and 1.0 (which are subsequently designated as LPCM-100y-16(18)). At temperatures not too close to the phase transition points, the experimentally observed temperature dependence of the linewidth for powder samples with $0 \le y \le 1$ is related to the magnetic susceptibility $\chi(T)$ (obtained by integrating the spectrum) by a slightly modified form of Eq. (1),

$$\Delta H_{pp}(T) = \frac{\chi_0}{\chi(T)}\Delta H_{pp}(\infty) + \Delta H_0. \qquad (5)$$

We measured the dependences of $\Delta H_{pp}(\infty)$ and ΔH_0 on y and the oxygen isotopic composition and estimated the parameters governing these quantities. The characteristic variations in the EPR spectra and in the magnetic susceptibility $\chi(T)$ were used to derive the transition temperatures to the ferromagnetic (T_{FM}) and antiferromagnetic (T_{AFM}) states and to construct a magnetic phase diagram of the system.

2. SAMPLES AND MEASUREMENT TECHNIQUE

2.1. Sample Preparation

$(La_{1-y}Pr_y)_{0.7}Ca_{0.3}MnO_3$ samples with Pr contents y = 0.0, 0.25, 0.5, 0.6, 0.7, 0.75, and 1.0 were prepared in the form of a powder using the so-called paper synthesis. A water solution comprising nitrates of La, Pr, Ca, and Mn mixed in required proportion was deposited on ashless paper filters, which were burnt after drying at 120°C. The oxides thus prepared were calcined in air at 700°C for two hours. The final powder product was pelletized and calcined subsequently in air for 12 h at 1200°C.

The pellets intended for EPR measurements were ground to powder with a characteristic grain size of a few microns. Enrichment with oxygen isotopes was carried out at 950°C at an oxygen pressure of 1 atm. Two samples of the same composition were annealed simultaneously, one of them in an ^{16}O environment (99.7% enrichment), and the other, in an ^{18}O atmosphere (enrichment 93%). Platinum crucibles with powders were placed in two quartz tubes fixed in a furnace parallel to each other. Each tube was actually part of a closed circuit, with ^{16}O and ^{18}O, respectively, circulating through them. Samples were annealed for 48 h at 950°C and subsequently cooled slowly to room temperature. The ^{18}O content in the samples, derived from the change in their weight after isotope enrichment, was never less than 80%. Samples with y = 0.75 were checked for oxygen stoichiometry by neutron diffraction (in powder form) and iodometric titration. The difference in oxygen content in samples with different isotopes did not exceed 0.002.

X-ray diffraction was employed to verify that samples of all compositions were single phase. The same method showed that all the samples had an orthorhombic P_{nma} crystal structure (no. 62). The unit cell parameters in this space group are related to the lattice parameter of the cubic perovskite $a_c \approx 3.8$ Å by the relations $a \approx c \approx \sqrt{2}a_c$ and $b \approx 2a_c$.

The results obtained in structural, transport, and magnetic-structure studies of samples of this system are reported in [5, 6, 11]. The orthorhombicity, defined as the relative deviation of the lattice parameters a, c, and $b/\sqrt{2}$ from one another, did not exceed 0.5–0.6% throughout the temperature range covered, 4.2–300 K, and for the Pr content y varied from 0 to 1. The largest deviation was observed for compositions with $y \ge 0.75$. The crystal structure differs from that of an ideal perovskite, besides in the cell parameters not being equal, in that the Mn–O–Mn valence angle is not equal to 180° because the oxygen octahedra are tilted. Indeed, the average room-temperature valence angle in samples with $y = 0$ is $\varphi = 160.1°$ and decreases linearly with increasing Pr content down to $\varphi = 156.5°$ for $y = 1.0$. At room temperature, the oxygen octahedra are close to regular; i.e., the three independent bond lengths Mn–O1 (along the b axis), Mn–O21, and Mn–O22 (in the a–c plane) only slightly differ from one another. As the temperature decreases and approaches the phase transi-

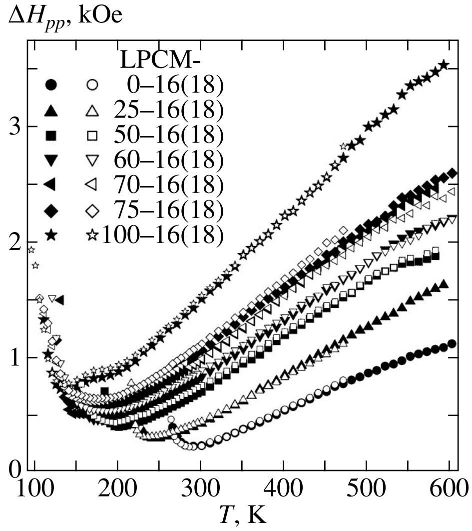

Fig. 1. Temperature dependence of EPR linewidth ΔH_{pp} obtained at frequency $\nu \cong 9.4$ GHz on $(La_{1-y}Pr_y)_{0.7}Ca_{0.3}MnO_3$ samples with oxygen isotopes ^{16}O and ^{18}O (LPCM-100y-16(18)). Filled symbols refer to samples with the ^{16}O isotope, and open symbols, to samples with the ^{18}O oxygen.

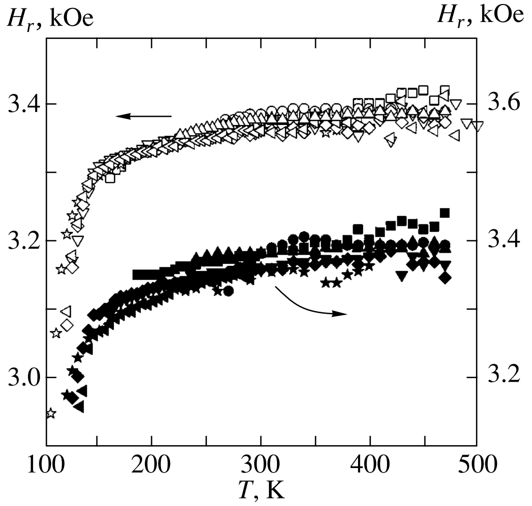

Fig. 2. Resonance field H_r at frequency $\nu \cong 9.4$ GHz plotted vs. temperature for $(La_{1-y}Pr_y)_{0.7}Ca_{0.3}MnO_3$ samples. Notation is the same as that in Fig. 1.

tion points, Jahn–Teller distortions of the lattice appear. For samples with $y \geq 0.5$, the parameter

$$\sigma_{JT} = \sqrt{\frac{\sum_i [(\text{Mn–O})_i - \langle \text{Mn–O} \rangle]^2}{3}} \qquad (6)$$

reaches noticeable values on the order of 10^{-2} Å. Note also that, in the paramagnetic region, the difference in structural data between samples with different oxygen isotopes did not exceed the measurement error.

As the temperature decreases, samples of all compositions transfer to a magnetically ordered state, whose actual form depends on both the Pr content and the isotopic substitution [5, 6]. For $y \leq 0.5$, collinear FM structures arise, with the magnetic moment lying in the *a–c* plane in the *c* direction and reaching a value of $3.40\mu_B$ per Mn ion at saturation. For $y \geq 0.6$, samples with different oxygen isotopes exhibit substantial differences. In the $0.6 \leq y \leq 0.8$ interval, samples with the ^{16}O isotope undergo two successive transitions, first to a collinear AFM state with a pseudo-charge exchange (CE) structure and after that to an inhomogeneous state separated into AFM and FM domains. For $y > 0.8$, a homogeneous CAFM structure sets in below the second transition point. In samples with ^{18}O, an inhomogeneous state with phase separation into AFM and FM domains is observed to occur within the narrow concentration interval $0.5 \leq y < 0.6$, with no second transition seen for $y \geq 0.6$, so the magnetic structure remains a collinear antiferromagnet.

2.2. Measurement Technique

The spectra were recorded on a Bruker ESP-300 EPR spectrometer equipped with a helium-flow cryostat (Oxford Instruments). The measurements were performed at a frequency $\nu \cong 9.4$ GHz at temperatures ranging from 4 to 600 K. The derivative of the absorption signal was usually measured. The 0.5- to 3-mg powder samples intended for measurements were loaded in quartz ampoules. The powders prepared for measurements in the vicinity of the phase transitions and in magnetically ordered phases were fixed in the ampoules with molten paraffin.

3. EXPERIMENTAL RESULTS AND DISCUSSION

3.1. Paramagnetic Region

Figure 1 plots temperature dependences of the linewidth $\Delta H_{pp}(T)$ for samples of different compositions. Each curve passes through a minimum at a temperature T_{min}. As y increases, the value of T_{min} decreases by more than a factor of 2 and the rate of linewidth growth with temperature within the linear part of the graph increases by the same factor. Figure 2 contains data on the resonance fields H_r. In the temperature region where the linewidth grows linearly, the line position depends only weakly on temperature and corresponds to $g = 1.99 \pm 0.01$. The slightly larger scatter of the resonance fields can be traced to the resonance frequency varying from one sample to another and to a variation in the temperature.

The line shape in this temperature region is fitted well by a Lorentzian profile, irrespective of the composition and the isotope content. The peak ratio of the second derivative was close to 4. Only as the temperature

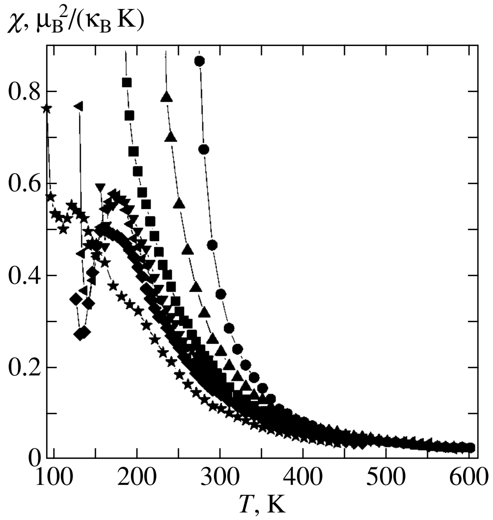

Fig. 3. Temperature dependence of magnetic susceptibility per Mn ion for samples of $(La_{1-y}Pr_y)_{0.7}Ca_{0.3}Mn^{16}O_3$. Notation is the same as that in Fig. 1.

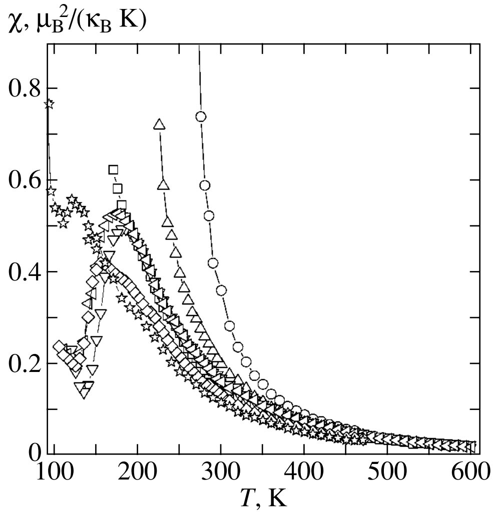

Fig. 4. Temperature dependence of magnetic susceptibility per Mn ion for samples of $(La_{1-y}Pr_y)_{0.7}Ca_{0.3}Mn^{18}O_3$. Notation is the same as that in Fig. 1.

was reduced to below T_{min} did this ratio for samples with $y \leq 0.5$ decrease to 3–3.5. (Recall that this ratio is 2.24 for a Gaussian curve and is exactly 4 for a Lorentzian.) Samples with a high Pr content ($y \geq 0.6$) cooled below T_{min} exhibited a decrease in the resonance field by 10–15%, but this did not entail a strong change in the line shape, which remained symmetric and close to Lorentzian.

Figures 3 and 4 plot the data on magnetic susceptibility χ (per Mn ion) obtained by double integration of the spectra. Note that double integration of spectra can only yield reliable information for lines that are not overly broad, where the integration range (8–10 kOe in our experiments) is substantially larger than the linewidth ΔH_{pp}. To reduce the line integration error for linewidths in excess of 0.5–1.0 kOe, the results were corrected assuming the line shape to remain Lorentzian not only within the integration region but also beyond it. At temperatures $T \geq$ 300–350 K, in the region of small Jahn–Teller deformations, the susceptibility data fit well to the Curie–Weiss law

$$\chi(T) = \frac{C}{T - \Theta_0} \tag{7}$$

with the constant

$$C = \frac{S(S+1)g^2\mu_B^2}{3k_B}. \tag{8}$$

For the effective value of the quantity $S(S + 1)$ in Eq. (8), we chose the composition-averaged value

$$S(S+1) = 0.3S_4(S_4+1) + 0.7S_3(S_3+1) = 5.325,$$

where, as is well known, $S_4 = 3/2$ for the Mn^{4+} ions and $S_3 = 2$ for Mn^{3+}. The Curie–Weiss temperature Θ_0 decreased with increasing Pr content from $\Theta_0 \cong 320$ K for $y = 0$ to $\Theta_0 \cong 260$ K for $y = 1$.

Using Eq. (1), one can derive the values of $\Delta H_{pp}(\infty)$ from experimental data on $\chi(T)$ and $\Delta H_{pp}(T)$ and draw a conclusion on possible contributions to the linewidth (estimate the second moment M_2 and the main parameters defining it). Equation (1), as already mentioned, is obtained neglecting the spin–lattice relaxation. Possible broadening mechanisms associated with sample inhomogeneities and the scatter of resonance fields in powder samples originating from the appearance of demagnetizing fields and from the presence of a noncubic crystal-field component are also disregarded. The contributions from these mechanisms to the linewidth, as a rule, are proportional to the magnetization and can be neglected for high temperatures. As the temperature decreases and approaches the phase transition region, however, these mechanisms may produce noticeable effects. It is no wonder, therefore, that we succeeded in achieving a good fit in describing the experimental linewidth $\Delta H_{pp}(T)$ in terms of the susceptibility $\chi(T)$ by merely introducing an additional term into the right-hand part of Eq. (1), the residual linewidth ΔH_0 (see Eq. (5)), which accounts for the influence of temperature-independent or weakly temperature-dependent broadening mechanisms.

Figure 5 compares the experimental linewidth relations with those obtained from susceptibility data by using Eq. (5). For samples with low Pr contents, the curves practically coincide. As the Pr content increases, the region of good fit narrows, but even for $y = 1.0$ there is an interval of about 200 K within which the agreement is quite satisfactory and one is still able to determine the parameters of interest. Note that this comparison is valid at sufficiently high temperatures, where the

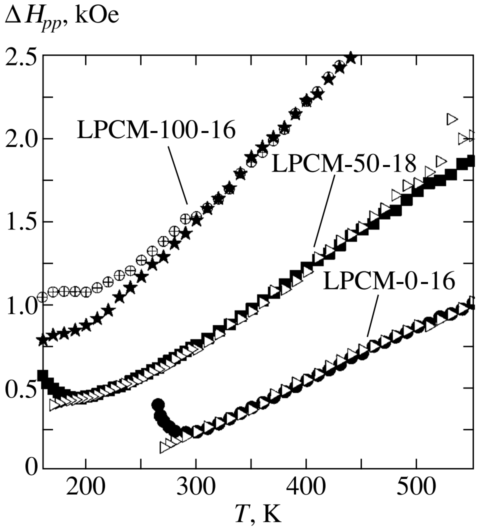

Fig. 5. Comparison of experimental linewidth ΔH_{pp} (filled symbols) with a plot of Eq. (5) (open symbols) for samples LPCM-0-16, LPCM-50-18, and LPCM-100-16.

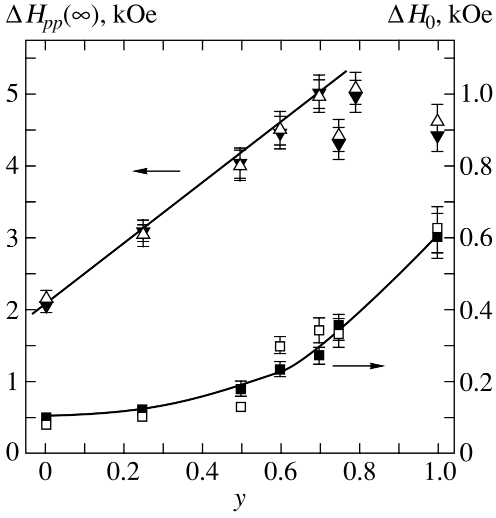

Fig. 6. Dependence of the parameters $\Delta H_{pp}(\infty)$ and ΔH_0, involved in Eq. (5), on Pr concentration. Filled symbols refer to samples with ^{16}O, and open symbols, to samples with ^{18}O. The lines are intended only to guide the eye.

quantity $\Delta H_{pp}(\infty)$ can still be considered temperature-independent, an assumption that, as in Eq. (7), is correct for small enough Jahn–Teller deformations. As for ΔH_0, the values thus obtained are characteristic primarily of a region near $T \approx T_{\min}$, where $\Delta H_{pp}(T) \approx \Delta H_0$, i.e., where ΔH_0 provides a major contribution to the linewidth.

Figure 6 plots the parameters $\Delta H_{pp}(\infty)$ and ΔH_0 as a function of Pr content obtained in comparing the $\Delta H_{pp}(T)$ and $\chi(T)$ dependences. $\Delta H_{pp}(\infty)$ is seen to exceed ΔH_0 by an order of magnitude or more. In the $0 \le y \le 0.7$ interval, $\Delta H_{pp}(\infty)$ grows practically linearly, to increase at $y = 0.7$ by nearly a factor of 2.5. After this, the growth stops, followed even by a certain falloff. As for the residual linewidth ΔH_0, it grows fairly sharply only for $y > 0.7$, i.e., exactly where $\Delta H_{pp}(\infty)$ stops increasing. The dependence on oxygen isotope substitution is fairly weak; indeed, the obtained parameters coincide to within experimental error.

Now, we consider the possible mechanisms of broadening that govern the magnitude of ΔH_0. As shown in [12, 13], the contribution to the linewidth due to the appearance of demagnetizing fields can be estimated from the expression

$$\Delta H_{0M} \approx 4\pi\chi H_r \rho / V_{\mathrm{Mn}}, \tag{9}$$

where $V_{\mathrm{Mn}} \cong a_c^3 \cong 57$ Å^3 is the volume per Mn ion and ρ is the sample porosity, i.e., the fractional volume of all pores and other nonmagnetic inclusions. The line broadening that is observed with reducing the temperature to below $T_{\min}$ and is accompanied by a deviation of the line shape from a Lorentzian implies that the contribution due to the first term on the right-hand side of Eq. (5) is no longer dominant. As is evident from Figs. 1, 3, and 4, $\chi(T_{\min}) \approx (0.4–0.6)\mu_{\mathrm{B}}^2 (k_{\mathrm{B}}\mathrm{K})^{-1}$ and depends only weakly on composition. From an analysis of the ferromagnetic resonance (FMR) spectra, the porosity was found to be $\rho \approx 0.3–0.4$. Substituting these values into Eq. (9) yields $\Delta H_{0M}(T_{\min}) \approx 100–150$ Oe. As seen from Fig. 6, ΔH_0 assumes approximately the same values for samples with $0 \le y \le 0.5$; i.e., ΔH_{0M} provides a major contribution to ΔH_0 already at $T_{\min}$. We also see that, for samples with $y > 0.7$, this contribution is clearly inadequate.

In addition to a change in the linewidth caused by the appearance of a second moment, the noncubic crystal-field component, as shown in [14, 15], leads to the resonance field becoming dependent on its orientation relative to the crystallographic axes of the crystal. Deformation of the oxygen octahedra in the orthorhombic *O*' phase derives primarily from the Jahn–Teller effect. Orbital ordering brings about the formation of macroscopic regions with preferred directions of deformation, in which an additional term appears in the spin Hamiltonian of the form [8]

$$H_{CF} = -D\sum_{i=1}^{N/2} S_{x(i)}^2 - D\sum_{j=1}^{N/2} S_{z(j)}^2. \tag{10}$$

The deviation from perfect cubic structure is described here by a sequence of (i, j) octahedra elongated alternately along the c and a axes; indices i and j refer to the Mn ions in these octahedra, N is the number of Mn ions, and D is the crystal field parameter. Using the results obtained in [14, 15], one can readily estimate the scatter in resonance fields for an interaction of the type of Eq. (10) and for randomly distributed orientations of the grain crystallographic axes in a powder sample to be

$$\Delta H_r \approx \frac{\chi H_r D}{g^2 \mu_B^2}. \qquad (11)$$

Accepting typical field parameters $D/k_B \approx 0.5$–1 K [10], the resonance field scatter at $T \approx T_{\min}$, depending on the actual orientation, amounts, according to Eq. (11), to $\Delta H_r \approx 150$–300 Oe, which is greater than ΔH_{0M}. In the case where the lines are originally not very broad, this will produce an additional linewidth contribution of the same order of magnitude for a nonoriented powder sample. This contribution is not related to the magnitude of exchange interactions and depends only on the crystal field parameters. The growth of ΔH_0 for $y > 0.7$ apparently indicates the appearance of noticeable noncubic distortions in these samples. This also correlates with the increase in the Jahn–Teller parameter (6) in this concentration region. Judging from the residual linewidth $\Delta H_0 \approx 300$–600 Oe, the parameter D/k_B may become as large as 1–2 K.

Let us consider now the quantity $\Delta H_{pp}(\infty)$ in Eq. (3) in more detail. The symmetric exchange interaction constant J, determining the exchange frequency $\omega_{ex} \simeq J/\hbar$, can be estimated by invoking experimental data on the Curie–Weiss temperature Θ_0. Assuming interaction only with the nearest neighbors (and neglecting the difference in this interaction among various neighbors, $J_{ij} \cong J$), J is given by [16]

$$J = \frac{3k_B\Theta_0}{zS(S+1)}, \qquad (12)$$

where $z = 6$ is the number of nearest neighbors for the Mn ions. As Θ_0 is varied from 320 to 260 K, J/k_B changes from $\cong$30 to $\cong$24 K; in other words, the average value of the symmetric-exchange constant drops by about 25% with y changing from 0 to 1.

The second moments M_{2DM} and M_{2CF} generated by the Dzyaloshinski–Moriya antisymmetric exchange interaction (4) and by single ion anisotropy with the interaction Hamiltonian (10) were derived in [8] under the assumption of anisotropic exchange interaction between Mn spins described by Eq. (2). The corresponding expressions are applicable for the P_{nma} crystal structure and, neglecting the difference between the components $|D_{DMij}| \approx D_{DM}$ [17], can be reduced, for homogeneous powders, to the form

$$\hbar^2 M_{2DM} = \frac{32}{9} S(S+1) D_{DM}^2, \qquad (13)$$

$$\hbar^2 M_{2CF} = \frac{8}{15}\left[S(S+1) - \frac{3}{4}\right] D^2. \qquad (14)$$

As follows from Eqs. (13) and (14), the relative contribution of M_{2CF} to the second moment is on the order of $0.1D^2/D_{DM}^2$. As will be shown later, $D_{DM}/k_B \approx 1$ K. On the other hand, in the temperature regions where the experimental data on $\Delta H_{pp}(T)$ and $\chi(T)$ were compared to determine $\Delta H_{pp}(\infty)$, the orthorhombic distortions for samples with $y \le 0.7$ are fairly small; therefore, $D \ll D_{DM}$ in this case. According to our preliminary estimates from the residual linewidth, only for samples with a high Pr content, $y \ge 0.75$, can the quantity D/k_B in the region where experimental data on $\Delta H_{pp}(T)$ and $\chi(T)$ were compared reach values of the order of 1–2 K. Even in this case, however, the relative contribution of M_{2CF} remains small. For $D \ll D_{DM}$, the coefficient α in Eq. (3) is approximately 0.5 and only slightly decreases as the ratio D/D_{DM} increases [8]. This allows us to estimate D_{DM} for the region of not very high Pr concentrations. For instance, for $y = 0$, we have $D_{DM}/k_B \cong 0.95 \pm 0.1$ K. The difference for different oxygen isotopes remains within experimental error. Similar values for this quantity, $D_{DM}/k_B \approx 0.8$ K, were obtained in [8, 10] for the systems $La_{1-y}Ca_xMnO_3$ and $LaMnO_{3+\delta}$, with the dependence on composition and temperature found to be very weak in both cases.

As follows from [18], the variation of D_{DM} with increasing Pr concentration should be associated primarily with the decrease in the average valence angle φ, according to the relation $D_{DM} \propto \sin 2\varphi(y)$. It follows from this relation that the increase in D_{DM}^2 should not exceed 25–30% with a variation in y from 0 to 1 and a corresponding variation in the average valence angle from 160.1° to 156.5°. Thus, in accordance with Eq. (3), variation of the parameters D, D_{DM}, and J with increasing Pr content can initiate an increase in $\Delta H_{pp}(\infty)$ by no more than a factor of 1.5–1.6, which is clearly not large enough to account for the experimentally observed growth by a factor of nearly 2.5 (Fig. 6).

Therefore, inclusion of other factors capable of strongly affecting the linewidth appears inevitable. Note the approximately linear rise of $\Delta H_{pp}(\infty)$ with Pr concentration (at least in the region $y \le 0.7$). Since the Pr^{3+} ions have a magnetic moment, the indirect exchange interaction appearing in these conditions and the associated additional relaxation may play a certain role.

3.2. Region of Magnetic Ordering

3.2.1. Observation of the FM transition. Near $T_{\min}$, samples with $y \le 0.5$ exhibit a fairly sharp growth of magnetic susceptibility with decreasing temperature (Figs. 3, 4). Here, the quantity χH_r, equal to the magnetic moment per Mn ion, reaches values (1–2)μ_B, which are comparable to the saturation magnetic moment μ_0. (Recall that the theoretical value of the saturation moment at a temperature tending to zero is $\mu_0 = g(0.7S_3 + 0.3S_4) = 3.7\mu_B$ and the experimental value quoted in [6] is $3.4\mu_B$.) The results obtained in [6] allow

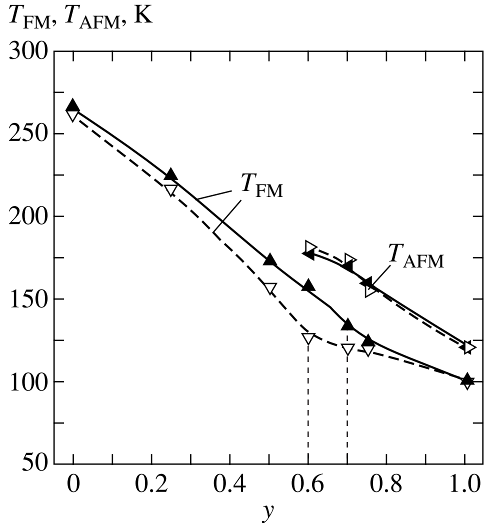

Fig. 7. Magnetic phase diagram of the $(La_{1-y}Pr_y)_{0.7}Ca_{0.3}MnO_3$ system. $T_{\rm FM}$ is the FM ordering temperature, and $T_{\rm AFM}$ is the AFM ordering temperature. Filled symbols refer to samples with the ^{16}O oxygen, and open symbols, to the ^{18}O samples. The lines are intended only to guide the eye. Vertical lines specify the Pr concentrations at which the fractional volume of the FM phase decreases sharply.

us to conclude that the samples transfer to the FM state. The transition temperature $T_{\rm FM}$ was defined as the temperature at which the EPR line broadened to the extent that it could no longer be observed. At this point, a new line characteristic of the FMR signal of a powder sample appeared in the absorption spectrum [19].

For $y \le 0.5$, isotopic substitution affects primarily the phase transition temperatures and has almost no influence on the pattern of spectral evolution.

3.2.2. Observation of the AFM transition. The broadening of the EPR line in samples with $y \ge 0.6$ observed to occur at temperatures below $T_{\rm min}$ is not accompanied by a sharp growth of susceptibility. By contrast, it ceases to increase at a certain temperature, experiences a subsequent falloff, and a characteristic maximum appears in the $\chi(T)$ graph (Figs. 3, 4). The line shape does not vary strongly and remains approximately Lorentzian. The resonance field H_r begins to decrease (Fig. 2); for samples with $y = 1$, this decrease can be as large as 300–400 Oe. This behavior of the spectra can be accounted for by assuming that part of the sample transfers to the AFM state, which does not contribute to the absorption signal (as a rule, because of a gap $\Delta E_g \gg h\nu$ present in the resonance mode spectrum [20]), and that the observed EPR signal is due to the sample regions that remained in the paramagnetic (PM) state. The decrease in the resonance field apparently indicates that these regions are extended along the field. For instance, the decrease in the resonance field applied along the z axis for regions of ellipsoidal shape with demagnetizing factors $N_z \ll N_x$, N_y will be [21]

$$\delta H_r \approx -(2\pi - 3N_z/2)\chi H_r/V_{\rm Mn} \approx -2\pi\chi H_r/V_{\rm Mn}.$$

In the transition region, we have $\chi \approx (0.4–0.6)\mu_{\rm B}^2(k_{\rm B}K)^{-1}$ and the decrease in the resonance field can be estimated as $\delta H_r \approx -(150–200)$ Oe. We note that the line shift should increase with decreasing temperature and increasing susceptibility inside the PM regions.

We accepted for the AFM transition point the temperature at which the formation of the AFM phase brought about a stop in the growth of the susceptibility, i.e., the temperature corresponding to the maximum in the $\chi(T)$ curve.

As the temperature is lowered still further, the susceptibility starts to grow again, but the line no longer has a Lorentzian shape. As at lower Pr concentrations, the EPR line vanishes and the FMR signal appears. However, in contrast to the case of lower Pr concentrations, χH_r is here substantially smaller. Only for the LPCM-60-16 sample does it reach a noticeable value of $\approx 0.7\mu_{\rm B}$, while for the other samples it does not exceed $\approx 0.2–0.3\mu_{\rm B}$, which corresponds to an FM fraction in the sample of about 10–20%.

3.2.3. Phase diagram. Figure 7 presents data on the temperatures of phase transitions to the FM state ($T_{\rm FM}$) and the AFM state ($T_{\rm AFM}$). The vertical lines identify the Pr concentrations at which the FM phase fraction decreases strongly in volume.

This phase diagram fits, on the whole, the neutron diffraction data obtained on this system [6]. One observes a monotonic decrease in $T_{\rm FM}$ with increasing Pr content and enhancement of the effect of oxygen isotope substitution; indeed, for $y = 0.5$, the difference $^{16}T_{\rm FM} - {}^{18}T_{\rm FM}$ is 16 K. Below $T_{\rm AFM}$, according to [6], samples with the ^{18}O isotope and $y \ge 0.6$ do not undergo any magnetic phase transitions, there is no FM component, and the AFM structure always remains collinear. The total ordered magnetic moment of this phase turns out, however, to be smaller by about 25% than that at lower Pr concentrations. In addition, the diffraction spectra revealed fairly intense additional peaks, whose origin remains unclear. This suggests the possible formation of one more phase, which accounts for the resonance absorption signal. We estimate the content of this phase as 10–20%, which is consistent with the jump in the magnetic moment of the AFM phase. This most probably also accounts for the appearance of the FMR signal in the LPCM-100-16 sample, which likewise exhibits a transition to a collinear AFM state with a reduced magnetic moment. As the temperature continues to decrease, this sample undergoes a second transition to the homogeneous canted AFM state [6]. The FM component of the magnetic moment is fairly large, $\mu_{CAFM} \approx 2.15\mu_{\rm B}$. In our experiments, the EPR spectra and, subsequently, FMR spectra for samples LPCM-

100-16 and LPCM-100-18 undergo practically the same evolution with decreasing temperature, which supports the assumption that the AFM phase does not contribute to the absorption signal whatsoever, even for a large canting of the magnetic sublattices.

The reason for the fairly small ordered magnetic moment of the FM phase in the inhomogeneous state in the LPCM-60-16 and, particularly, LPCM-75-16 samples remains unclear, although the transition itself to the FM state and the magnitude of the transition temperature T_{FM} agree well with neutron diffraction data [6].

We also readily see from Fig. 7 that T_{AFM} falls off monotonically with increasing y and does not depend, within experimental error, on oxygen isotope substitution.

4. CONCLUSIONS

We have studied the EPR of Mn ions in the $(La_{1-y}Pr_y)_{0.7}Ca_{0.3}MnO_3$ system within broad ranges of temperatures ($4 < T < 600$ K) and concentrations ($0 \le y \le 1$) and in the case of ^{18}O isotope substitution for ^{16}O. All compositions exhibited transitions to a magnetically ordered state with decreasing temperature. Magnetic phase diagrams were constructed for systems with different oxygen isotopes. The diagrams include paramagnetic, ferromagnetic, and antiferromagnetic regions.

Powder samples studied in the paramagnetic region at temperatures not too close to the phase transition points exhibit an absorption curve of Lorentzian shape, with the linewidth $\Delta H_{pp}(T)$ being related to the magnetic susceptibility $\chi(T)$, obtained by integrating the spectrum, by an equation of the type of Eq. (5). This relation was derived neglecting spin–lattice relaxation and with inclusion of the demagnetizing fields and the noncubic crystal-field component, which is responsible for the additional broadening due to the scatter of resonance fields caused by random orientation of the crystallographic axes in powder sample grains with respect to the external field. The experimental data on $\chi(T)$ and $\Delta H_{pp}(T)$ were employed to obtain the values of $\Delta H_{pp}(\infty)$ and ΔH_0. An analysis of the data on $\Delta H_{pp}(\infty)$, ΔH_0, and $\chi(T)$ provided an estimate of the symmetric (J) and antisymmetric (D_{DM}) exchange interactions of Mn ions with one another and of the noncubic crystal-field component of oxygen ions (D). The values thus obtained do not depend, within experimental error, on the oxygen isotope involved; J/k_B falls off practically monotonically in the range 30–24 K with the Pr content y increasing from 0 to 1, $D_{DM}(y = 0)/k_B \cong 0.95$ K, $D(0 \le y \le 0.7)/k_B \ll 1$ K, and $D(y \ge 0.75)/k_B$ may reach 1–2 K.

It has been shown that taking into account the variation of J, D, and D_{DM} only is clearly not sufficient to explain the experimentally observed growth of $\Delta H_{pp}(\infty)$ with Pr concentration by a factor of more than 2.5 and that one should invoke other broadening mechanisms. The linear dependence of $\Delta H_{pp}(\infty)$ on Pr concentration and the existence of spin on the Pr^{3+} ions give one grounds to assume that the additional relaxation may be induced by exchange interaction between the Mn and Pr ions.

The transition to the FM state was identified from the growth in magnetic susceptibility and a change in the absorption spectrum, more specifically, from the vanishing of the EPR line and appearance of the FMR signal. For $y > 0.6$, the volume fraction of the FM phase does not exceed 10–20%. For these compositions, the transition to the FM state is preceded by an AFM ordering region. The transition to the AFM state is accompanied by a marked decrease in susceptibility, with the Lorentzian line shape preserved; here, the absorption signal derives only from the fractional sample volume remaining in the paramagnetic state. An increase in the Pr concentration brings about a monotonic decrease in the magnetic phase transition temperatures (both T_{FM} and T_{AFM}), with the effect of oxygen isotope substitution, ^{18}O for ^{16}O, being the largest for T_{FM} for $y = 0.5$–0.6. In this case, ΔT_{FM} reaches values of approximately –(15–20) K.

ACKNOWLEDGMENTS

The authors are indebted to N.A. Babushkina and A.N. Taldenkov for assistance in preparing the samples and helpful discussions.

This study was supported by the Russian Foundation for Basic Research (project no. 02-02-16357), INTAS (project no. 01-2008), and CRDF (project no. RP2-2355-MO-02).

REFERENCES

1. V. M. Loktev and Yu. G. Pogorelov, Fiz. Nizk. Temp. **26** (3), 231 (2000) [Low Temp. Phys. **26**, 171 (2000)].
2. J. M. D. Coey, M. Viret, and S. Molnar, Adv. Phys. **48** (2), 167 (1999).
3. E. L. Nagaev, Phys. Rep. **346**, 387 (2001).
4. N. A. Babushkina, L. M. Belova, O. Yu. Gorbenko, A. R. Kaul, A. A. Bosak, V. I. Ozhogin, and K. I. Kugel, Nature **391** (6663), 159 (1998).
5. A. M. Balagurov, V. Yu. Pomjakushin, D. V. Sheptyakov, V. L. Aksenov, N. A. Babushkina, L. M. Belova, A. H. Taldenkov, A. V. Inyushkin, P. Fischer, M. Gutmann, L. Keller, O. Yu. Gorbenko, and A. R. Kaul, Phys. Rev. B **60** (1), 383 (1999).
6. A. M. Balagurov, V. Yu. Pomjakushin, D. V. Sheptyakov, V. L. Aksenov, P. Fisher, L. Keller, O. Yu. Gorbenko, A. R. Kaul, and N. A. Babushkina, Phys. Rev. B **64**, 024420 (2001).
7. M. T. Causa, M. Tovar, A. Caneiro, F. Prado, G. Ihañez, C. A. Ramos, A. Butera, A. Alascio, X. Obrados, S. Piňol, F. Rivadulla, C. Vázquez-Vázquez, M. A. Lypez-Quintela, J. Rivas, Y. Tokura, and S. B. Oseroff, Phys. Rev. B **58** (6), 3233 (1998).
8. D. L. Huber, G. Alejandro, A. Caneiro, M. T. Causa, F. Prado, M. Tovar, and S. B. Oseroff, Phys. Rev. B **60** (17), 12 155 (1999).

9. A. Abragam, *The Principles of Nuclear Magnetism* (Clarendon, Oxford, 1961; Inostrannaya Literatura, Moscow, 1963), p. 436.
10. M. Tovar, G. Alejandro, A. Butera, A. Caneiro, M. T. Causa, F. Prado, and R. D. Sánchez, Phys. Rev. B **60** (14), 10199 (1999).
11. A. M. Balagurov, V. Yu. Pomjakushin, D. V. Sheptyakov, V. L. Aksenov, N. A. Babushkina, L. M. Belova, O. Yu. Gorbenko, and A. R. Kaul, Eur. Phys. J. B **19**, 215 (2001).
12. F. Rivadulla, M. A. Lopez-Quintela, L. E. Hueso, J. Rivas, M. T. Causa, C. A. Ramos, R. D. Sánchez, and M. Tovar, Phys. Rev. B **60** (17), 11 922 (1999).
13. M. Sparks, J. Appl. Phys. **36**, 1570 (1965).
14. J. Deisenhofer, M. V. Eremin, D. V. Zakharov, V. A. Ivanshin, R. M. Eremina, H.-A. Krug von Nidda, A. A. Mikhnin, A. M. Balbashov, and A. Loidl, Phys. Rev. B **65**, 104440 (2002).
15. J. Deisenhofer, M. V. Eremin, D. V. Zakharov, V. A. Ivanshin, R. M. Eremina, H.-A. Krug von Nidda, A. A. Mikhnin, A. M. Balbashov, and A. Loidl, cond-mat/0108515 v 1 (2001).
16. S. V. Vonsovskiĭ, *Magnetism* (Nauka, Moscow, 1971; Wiley, New York, 1974).
17. I. Solovyev, N. Hamada, and K. Terakura, Phys. Rev. Lett. **76**, 4825 (1996).
18. A. S. Moskvin and I. G. Bostrem, Fiz. Tverd. Tela (Leningrad) **19** (9), 2616 (1977) [Sov. Phys. Solid State **19**, 1532 (1977)].
19. A. G. Gurevich, *Magnetic Resonance in Ferrites and Antiferromagnets* (Nauka, Moscow, 1973), p. 63 [in Russian].
20. S. Mitsudo, K. Hiramo, H. Nojiri, M. Motokava, K. Hirota, A. Nishizawa, N. Kaneko, and Y. Endoh, J. Magn. Magn. Mater. **177–181**, 877 (1998).
21. I. Svare and G. Seidel, Phys. Rev. [Sect. A] **134** (1), A172 (1964).

Translated by G. Skrebtsov

Physics of the Solid State, Vol. 46, No. 11, 2004, pp. 2103–2109. Translated from Fizika Tverdogo Tela, Vol. 46, No. 11, 2004, pp. 2033–2039.
Original Russian Text Copyright © 2004 by O. Tarasenko, S. Tarasenko, Yurchenko.

LATTICE DYNAMICS AND PHASE TRANSITIONS

Specific Features of the Propagation of a Shear Elastic Wave in an Acoustic Superlattice of the Magnet–Ideal Diamagnet Type: Localization Conditions

O. S. Tarasenko, S. V. Tarasenko, and V. M. Yurchenko

Donetsk Physicotechnical Institute, National Academy of Sciences of Ukraine, Donetsk, 83114 Ukraine
e-mail: tarasen@host.dipt.donetsk.ua

Received August 14, 2003; in final form, February 4, 2004

Abstract—The influence of gyrotropy on the conditions for propagation and localization of a shear elastic wave in a semi-infinite magnetic superlattice composed of ferromagnetic and superconducting layers is investigated by the effective-medium method. This method correctly takes into account the dynamic interaction between the spin and elastic subsystems. *© 2004 MAIK “Nauka/Interperiodica”.*

1. INTRODUCTION

In recent years, the dynamic properties of composite magnetic structures with a one-, two-, or three-dimensional translational invariance (magnetic photonic crystals [1]) have been investigated extensively. In the general case, a one-dimensional magnetic phonon–photon crystal can be considered a two-component magnetic superlattice that is composed of a set of alternating equidistant, acoustically coupled magnetic and nonmagnetic layers. Consistent theoretical treatment of the dynamics in this crystal is based on the simultaneous inclusion of the magnetoelastic and magnetodipole interactions. When the nonmagnetic component of the superlattice under consideration is an ideal diamagnet, for example, a superconductor ($2\lambda/t \longrightarrow 0$, where λ is the London penetration depth and t is the thickness of the superconducting layer), this structure should be treated as a one-dimensional magnetic phonon crystal, because the acoustic interlayer interaction is the sole mechanism responsible for the formation of the spectrum of collective excitations. However, even for a semi-infinite acoustic magnetic superlattice, calculation of the spectrum of normal elastic shear horizontal (SH) waves with due regard for the magnetoelastic and magnetodipole interactions and gyrotropy by the transfer matrix method requires the use of matrices no less than 4×4 in size [2]. On the other hand, at sufficiently small wave numbers (a thin-layer superlattice), the spectrum of collective excitations of an acoustic magnetic superlattice with allowance made for the finite dimensions of the real sample can be analyzed using the effective-medium method [3, 4].

Considerable research attention has been focused on the investigation of different classes of one-dimensional magnetic phonon crystals, in particular, acoustic superlattices of the ferromagnet–superconductor type. Traditionally, these superlattices (like superlattices of the antiferromagnet–superconductor type) have been studied only from the standpoint of the coexistence of magnetic and superconducting ordering. Note that, even in an infinite homogeneously magnetized easy-axis and elastically isotropic ferromagnet, the only geometry that allows for the propagation of an elastic SH wave with the wave vector $\mathbf{k}$, which is noncoincident with the direction of the equilibrium magnetization vector $\mathbf{M}$, must satisfy the condition $\mathbf{k} \perp \mathbf{M} \parallel \mathbf{u}$ (where $\mathbf{u}$ is the vector of elastic lattice displacements). However, the question as to the influence of gyrotropy on the conditions for propagation and localization of a shear elastic wave in the vicinity of the outer surface of a semi-infinite superlattice of the magnet–ideal diamagnet type remains open.

In this respect, the purpose of the present work was to reveal the gyrotropy-induced features in the propagation and localization of an elastic shear horizontal wave traveling along the surface of a semi-infinite acoustic superlattice of the “easy-axis ferromagnet–ideal superconductor” type. These investigations were performed using the effective-medium method.

2. BASIC RELATIONSHIPS

In our model, the magnetic superlattice under investigation is considered a set of equidistant ferromagnetic layers (medium *1*) of thickness d_1. These layers are acoustically coupled through identical ideal superconducting layers (medium *2*) of thickness d_2 (it is assumed that, in the superconductor, the London penetration depth λ obeys the inequality $2\lambda \ll d_2$ with good accuracy). It is known that, even in an infinite easy-axis ferromagnet, a shear linearly polarized acoustic wave can propagate only in the case when the vector of elastic displacements $\mathbf{u}$ and the wave vector $\mathbf{k}_\perp$ satisfy the condition $\mathbf{u} \parallel \mathbf{M} \perp \mathbf{k}_\perp$.

It is assumed that the magnetic medium in the superlattice can be adequately described within the one-sublattice model of easy-axis ferromagnets (*OZ* is the easy axis) [5] and that the elastic properties of the magnetic and nonmagnetic media are isotropic. For example, this situation corresponds to crystals with hexagonal symmetry when the *OZ* axis is a sixfold axis and the wave vector of shear acoustic vibrations lies in the *XY* plane. According to the one-sublattice model of uniaxial ferromagnetic crystals (medium *1*), the energy density *W*, with due regard for the interaction of the spin and elastic subsystems, can be written in the form [5]

$$W = -0.5bm_z^2 - mh_m + \gamma m_i m_k u_{ik} + \lambda_1 u_{ii}^2 + \mu_1 u_{ik}^2, \quad (1)$$

where b is the easy-axis anisotropy constant, γ is the isotropic magnetoelastic interaction constant, λ_1 and μ_1 are the Lamé coefficients of the magnetic medium, u_{ik} is the elastic strain tensor, and h_m is the magnetodipole field. In the model under consideration, the dynamics in the nonmagnetic medium (medium *2* with the Lamé coefficients λ_2 and μ_2) is described by the basic equation in elasticity theory. In the case of the magnetic medium (medium *1*), this equation is supplemented with the Landau–Lifshitz and magnetostatic equations. The requirement of the acoustic continuity at the boundary of the magnetic and nonmagnetic layers in the hybrid structure leads to the following relationships:

$$u_1 = u_2, \quad \xi = d_1 + N(d_1 + d_2), N(d_1 + d_2), \quad (2)$$

$$\begin{gathered} \sigma_{ik}^{(1)} n_k^{(1)} = \sigma_{ik}^{(2)} n_k^{(2)}, \\ \xi = d_1 + N(d_1 + d_2), N(d_1 + d_2). \end{gathered} \quad (3)$$

Here, $N = 0, 1, \ldots$, ξ is the current coordinate along the interface of the magnetic and nonmagnetic layers in the superlattice; σ_{ik} is the elastic stress tensor; and subscripts 1 and 2 indicate media *1* and *2*, respectively. Under the assumption that the superconducting medium is an ideal superconductor, the electrodynamic boundary conditions at the magnet–nonmagnet interface can be represented as follows [6]:

$$B_1 n = 0, \quad \xi = d_1 + N(d_1 + d_2), N(d_1 + d_2). \quad (4)$$

Therefore, the indirect interlayer interaction through the phonon field is the sole mechanism responsible for the formation of the collective excitation spectrum in the superlattice, which is a variant of magnetic phonon crystals.

Since, even for model (1) of the infinite easy-axis ferromagnet, the shear elastic wave can propagate only in the case when its wave vector is orthogonal to the easy axis and **u** || **M** || *OZ* [5, 7], the analysis is performed under the following assumptions. (1) $\mathbf{k} \in XY$. (2) The equilibrium magnetization directions in all the magnetic layers of the superlattice formed by the easy-axis (*OZ*) ferromagnet and superconductors are collinear and orthogonal to the normal **n** to the interface. (3) Owing to the isotropic properties of the magnet in the *XY* plane, the normal to the interface can be considered to be parallel to the *OX* axis (**n** || *OX*) without loss of generality. (4) At equilibrium, the magnetic moments of any pair of adjacent ferromagnetic layers are parallel to each other. From the viewpoint of translational symmetry, the elementary period *D* of the magnetic superlattice consists of two layers, namely, a magnetic layer (d_1 in thickness) and a superconducting layer (d_2 in thickness); i.e., $D = d_1 + d_2$. As was noted above, we restrict our consideration to the range of frequencies ω and wave vectors $\mathbf{k}_\perp$ for which the superlattice can be treated as a thin-layer superlattice [3, 4]. In particular, this implies that the normal (to the surface) component $\mathbf{k}_\|$ of the wave vector of the shear elastic wave in each layer forming the elementary period of the superlattice, i.e., in the magnetic ($\mathbf{k}_{\|,1}$) and superconducting ($\mathbf{k}_{\|,2}$) layers, is considerably less than the reciprocal of the corresponding layer thickness (d_1, d_2); that is,

$$k_{\|,1} d_1 \ll 1, \quad k_{\|,2} d_2 \ll 1. \quad (5)$$

As a consequence, this acoustic superlattice can be considered an effective spatially homogeneous medium, which is characterized by the elastic stress tensor components $\sigma_i(\langle\sigma_i\rangle)$ and the elastic strain tensor components $u_i(\langle u_i\rangle)$ averaged over the superlattice period *D*. By designating the relative thicknesses of the magnetic (medium *1*) and nonmagnetic (medium *2*) layers as

$$f_1 = \frac{d_1}{d_1 + d_2}, \quad f_2 = \frac{d_2}{d_1 + d_2}, \quad (6)$$

the physical quantity *P* averaged over the superlattice period can be represented in the form

$$\langle P \rangle = f_1 P_2 + f_2 P_2. \quad (7)$$

The relationship between the elastic stress tensor components $\langle\sigma_{ik}\rangle$ and the elastic strain tensor components $\langle u_{ik}\rangle$ (averaged with allowance made for the acoustic continuity of the layered structure, i.e., the continuity of σ_{ix} and u at the interfaces of adjacent layers) is determined by the effective elastic moduli c_{ik}. For the chosen geometry of propagating the elastic SH wave (**M** || **u** || *OZ*, $\mathbf{k} \in XY$, **n** || *OX*), the tensor components $\langle\sigma_i\rangle$ and $\langle u_i\rangle$ satisfy the following conditions:

$$\begin{gathered} \langle\sigma_4\rangle = f_1\sigma_4^{(1)} + f_2\sigma_4^{(2)}, \quad \langle\sigma_5\rangle = \sigma_5^{(1)} = \sigma_5^{(2)}, \\ \langle u_4\rangle = u_4^{(1)} = u_4^{(2)}, \quad \langle u_5\rangle = f_1 u_5^{(1)} + f_2 u_5^{(2)}. \end{gathered} \quad (8)$$

Therefore, for the acoustic magnetic superlattice whose elementary period $D = d_1 + d_2$ is formed by the superconducting layer (medium *2*) of thickness d_2 and the elastically isotropic easy-axis ferromagnetic layer (d_1 in thickness) rigidly coupled to the former layer, the effective elastic moduli $\bar{c}_{44}$, $\bar{c}_{55}$, $\bar{c}_{54}$, and $\bar{c}_{45}$ can be determined from the relationships

$$\begin{aligned} \langle\sigma_5\rangle &= \bar{c}_{55}\langle u_5\rangle + i\bar{c}_{54}\langle u_4\rangle, \\ \langle\sigma_4\rangle &= \bar{c}_{44}\langle u_4\rangle + i\bar{c}_{45}\langle u_5\rangle. \end{aligned} \tag{9}$$

As a result, we obtain

$$\begin{aligned} \bar{c}_{55} &= c_{55}^{(1)}c_{55}^{(2)}\Delta^{-1}, \quad \Delta \equiv f_2c_{55}^{(1)} + c_{55}^{(2)}f_1, \\ \bar{c}_{45} &= -\bar{c}_{54} = [f_1c_{45}^{(1)}c_{55}^{(2)} + f_2c_{55}^{(1)}c_{45}^{(2)}]\Delta^{-1}, \\ c_{44}^{(1)} &= f_1c_{44}^{(1)} + f_2c_{44}^{(2)} - f_1f_2[c_{45}^{(1)} - c_{45}^{(2)}]^2\Delta^{-1}. \end{aligned} \tag{10}$$

By assuming that $\mu_1 = \mu_2 = \mu$, in formulas (9) and (10) for the easy-axis ferromagnet–superconductor acoustic superlattice, we have

$$\begin{aligned} c_{44}^{(1)} &= c_{55}^{(1)} = \nu\mu, \quad c_{45}^{(1)} = \nu_*\mu, \\ c_{44}^{(2)} &= c_{55}^{(2)} = \mu, \quad c_{45}^{(2)} = c_{54}^{(2)} = 0. \end{aligned} \tag{11}$$

In relationships (11), we introduced the following designations:

$$\nu \equiv \frac{\omega_0(\omega_0 - \omega_{\mathrm{me}})\omega^2}{\omega_0^2 - \omega^2}, \quad \nu_* \equiv \frac{\omega\omega_{\mathrm{mc}}}{\omega_0^2 - \omega^2}. \tag{12}$$

Here, according to the notation used in [7], $\omega_{\mathrm{me}} \equiv gH_{\mathrm{me}4}$ is the magnetoelastic gap, $\omega_0 \equiv g(H_{\mathrm{A}} + H_{\mathrm{me}4})$ is the ferromagnetic resonance frequency, H_{A} is the uniaxial magnetic anisotropy field, $H_{\mathrm{me}4}$ is the magnetoelastic field, and g is the magnetomechanical ratio. The application of the effective-medium method to the analysis of the elastic dynamics in the magnet–ideal diamagnet acoustic superlattice means that condition (4) is satisfied in each magnetic layer. As a consequence, the inclusion of the magnetodipole interaction in this range of wave numbers does not lead to additional mechanisms (except for the magnetoelastic mechanism) responsible for the generation of time dispersion of the elastic moduli (10) and (11). For the chosen geometry of wave propagation ($\mathbf{k} \in XY$, $\mathbf{u} \parallel OZ$), this inclusion is reduced to renormalizing the uniaxial magnetic anisotropy constant $\beta \longrightarrow \beta - 4\pi$. Moreover, hereafter, we will assume that the densities of the magnetic medium ρ_1 and the nonmagnetic medium ρ_2 in the superlattice are equal to each other: $\rho_1 = \rho_2 = \rho$. As a result, within the effective-medium approximation, the spectrum of the elastic SH wave that propagates in the infinite acoustic superlattice of the easy-axis ferromagnet–ideal superconductor type at $\mathbf{k} \in XY$, $\mathbf{n} \parallel OX$, and $\mathbf{u} \parallel OZ$ with due regard for the magnetoelastic and magnetodipole interactions for both magnetic configurations is described by the expression

$$\omega^2 = s_t^2(c_\perp k_y^2 + c_\parallel k_x^2), \tag{13}$$

where $s_t^2 \equiv \mu/\rho$,

$$\begin{aligned} c_\parallel &= \bar{c}_{55}/\mu = \frac{\omega_0(\omega_0 - \omega_{\mathrm{me}}) - \omega^2}{\omega_0^2 - f_2\omega_0\omega_{\mathrm{me}} - \omega^2}, \\ c_\perp &= \bar{c}_{44}/\mu = \frac{\omega_0(\omega_0 - \omega_{\mathrm{me}}) - \omega^2 + \omega_{\mathrm{me}}^2 f_1 f_2}{\omega_0^2 - f_2\omega_0\omega_{\mathrm{me}} - \omega^2}, \\ c_* &= \bar{c}_{54}/\mu = \frac{f_1\omega\omega_{\mathrm{me}}}{\omega_0^2 - f_2\omega_0\omega_{\mathrm{me}} - \omega^2}. \end{aligned} \tag{14}$$

Therefore, unlike the elastic moduli $\tilde{c}_{44}$, $\tilde{c}_{55}$, and $\tilde{c}_{45}$ calculated disregarding the magnetodipole interaction for the infinite ferromagnet ($M \parallel OZ$),

$$\tilde{c}_{44} = \tilde{c}_{55} = \nu\mu, \quad \tilde{c}_{45} = -\tilde{c}_{54} = \nu_*\mu, \tag{15}$$

the effective moduli (14) for the acoustic magnetic superlattice not only possess the time dispersion but also depend substantially on the relative thicknesses of the magnetic and nonmagnetic layers (f_1, f_2).

It is easy to demonstrate that, without regard for the magnetoelastic interaction [upon the formal changeover in relationships (14) to the limit $\gamma \longrightarrow 0$, the obtained effective elastic moduli (14) coincide with the corresponding elastic moduli of the two-layer nonmagnetic superlattice [3].

From relationships (13) and (14), it follows that the shear elastic wave, with allowance made for the magnetoelastic and magnetodipole interactions, is a single partial wave characterized by the elastic tensor

$$\langle u_z\rangle = A\exp(ik_\parallel x)\exp(ik_\perp y - i\omega t). \tag{16}$$

The condition $k_\parallel^2 > 0$ ($k_\parallel^2 \equiv -\alpha^2k_\perp^2$) corresponds to the propagating volume (trigonometric) elastic SH wave. On the other hand, at $k_\parallel^2 < 0$, only the hyperbolic shear elastic wave with

$$\langle u_z\rangle \longrightarrow 0, \quad x \longrightarrow \infty \tag{17}$$

can propagate along the surface of the magnetic superlattice if it occupies the upper half-space $x > 0$.

When the quantities ω and $k_\perp$ in expressions (13), (14), and (16) are treated as specified external parameters, it is possible to determine the necessary conditions under which the propagating shear elastic wave can be localized in the vicinity of the surface of the magnetic sublattice.

The calculations demonstrate that the surface (hyperbolic) single partial elastic SH wave described by relationships (13), (14), and (16) can propagate only at $\alpha^2 > 0$, i.e., if the frequency ω and the wave number $k_\perp$ of this wave satisfy one of the following relationships:

$$\begin{aligned}
&k_\perp > k_{**}, \quad \omega_-(k_\perp) < \omega < \omega_+(k_\perp),\\
&k_\perp < k_{**}, \quad \omega_2(k_\perp) < \omega < \omega_+(k_\perp),\\
&k_\perp > k_{**}, \quad \omega < \omega_2(k_\perp),\\
&k_\perp < k_{**}, \quad \omega < \omega_-(k_\perp),
\end{aligned} \tag{18}$$

$$c_\parallel = \frac{\omega_2^2 - \omega^2}{\omega_1^2 - \omega^2}, \quad c_\perp = \frac{\omega_3^2 - \omega^2}{\omega_1^2 - \omega^2}, \quad c_* = \frac{f_1\omega\omega_{\rm me}}{\omega_1^2 - \omega^2},$$

where $\omega_3^2 \equiv \omega_0(\omega_0 - \omega_{\rm me}) + \omega_{\rm me}^2 f_1 f_2$, $\omega_1^2 \equiv \omega_0^2 - f_2\omega_0\omega_{\rm me}$, $\omega_2^2 \equiv \omega_0^2 - \omega_0\omega_{\rm me}$, $\omega_\pm^2(k_\perp) \equiv 0.5P_{\rm A} + \sqrt{0.25P_{\rm A}^2 - Q_{\rm A}}$, $P_{\rm A} \equiv \omega_1^2 + s_t^2k_\perp^2$, and $Q_{\rm A} \equiv \omega_3^2 s_t^2 k_\perp^2$. It can easily be shown that $\omega_1 > \omega_3 > \omega_2$. The wave number k_{**} is determined from the condition $\omega_2(k_{**}) = \omega_-(k_{**})$. When the quantities ω and $k_\perp$ do not satisfy conditions (18), the shear volume elastic wave cannot be localized in the vicinity of the surface of the magnetic superlattice [$k_\parallel^2 > 0$ in expression (16)].

However, relationships (18) are no more than necessary conditions for the generation of the surface elastic SH wave in the specified magnetic configuration. The dispersion relation for this wave is determined from the boundary conditions at the superlattice surface as the condition for the existence of a nontrivial solution to the corresponding boundary problem with respect to an arbitrary amplitude A of the elastic wave (16). Let us now assume that the surface $x = 0$ of the effective medium (thin-layer magnetic superlattice) occupying the upper half-space $x > 0$ is a slip boundary with the ideal superconductor occupying the lower half-space ($x < 0$); that is,

$$\langle \sigma_{xz} \rangle = 0, \quad x = 0. \tag{19}$$

The calculations with the use of expressions (13), (14), and (16) demonstrate that, under these conditions, the surface acoustic SH wave in the vicinity of the surface of the acoustic magnetic ferromagnet–superconductor superlattice can be generated only if the wave possesses an acoustic gyrotropy ($c_* \neq 0$). The corresponding dispersion relation, with allowance made for expressions (18), can be written in the form

$$k_\perp^2 = \omega^2[(c_\perp - c_\parallel\alpha^2)s_t^2]^{-1}, \quad \alpha \equiv \frac{\sigma f_1\omega\omega_{\rm me}}{\omega_2^2 - \omega^2}, \quad \sigma \equiv k_\perp/|k_\perp|. \tag{20}$$

As follows from Eq. (20), the spectrum of the shear surface acoustic wave $\Omega_s(k_\perp)$ is not symmetric with respect to the inversion of the propagation direction: $\Omega_s(k_\perp) \neq \Omega_s(-k_\perp)$. Note that, for the same magnitude of the wave number $k_\perp$, the degree of localization of elastic vibrations in the vicinity of the mechanically free surface of the superlattice appears to be different: $|k_\parallel(k_\perp)| \neq |k_\parallel(-k_\perp)|$ in relationship (16). At $\sigma = -1$, the surface acoustic wave has one branch and its dispersion relation at all $k_\perp$ satisfies the condition $\Omega_s(k_\perp) > \omega_2$. The corresponding dispersion curve at $k_\perp = 0$ emerges from the point $\omega^2 = \omega_0(\omega_0 - \omega_{\rm me})$ and, with an increase in $k_\perp$, asymptotically tends from below to the line described by

$$\omega^2 = s_t^2 k_\perp^2 \frac{\omega_3^2 - \omega^2}{\omega_1^2 - \omega^2}. \tag{21}$$

At $\sigma = 1$, the dispersion curve described by Eq. (20) for the shear surface acoustic wave at all permissible values of $k_\perp$ lies in the frequency range $\omega^2 < \omega_0(\omega_0 - \omega_{\rm me})$ and emerges from the point $\omega = 0$ at $k_\perp = 0$. With an increase in the wave number, the frequency of the wave tends from below to the frequency $\Omega_+ < \omega_2$, which is defined in the elastostatic limit ($\omega/s_tk_\perp \longrightarrow 0$) as

$$\Omega_+ \equiv \omega_2\omega_3/\omega_1. \tag{22}$$

In the limit $d_2/d_1 \longrightarrow 0$, we have $\Omega_+ \longrightarrow \omega_0 - \omega_{\rm me}$.

Since both of the aforementioned branches of the surface elastic SH wave (20) have only long-wavelength (rather than short-wavelength) end points, according to the terminology accepted in polariton dynamics [8], they can be assigned to shear surface acoustic waves of the first kind.

It is easy to show that the dispersion relation (20) in the limit $f_2/f_1 \longrightarrow 0$ coincides with the dispersion relation for a Parekh wave (generated in this geometry [7]) in which formal passage to the limit $4\pi \longrightarrow 0$ is performed (this corresponds to ignoring the magnetodipole interaction):

$$k_\perp^2 = \omega^2[(1 - \alpha^2)s_t^2]^{-1}, \quad \alpha \equiv \nu_*\sigma/\nu, \quad \sigma \equiv k_\perp/|k_\perp|. \tag{23}$$

Now, we consider the case where the outer surfaces of the effective medium $x > 0$ and the ideal semi-infinite elastically isotropic superconductor $x < 0$ (density ρ_*, the shear modulus μ_*, superscript $^<$ indicates quantities characterizing the lower half-space) at $x = 0$ are in continuous acoustic contact; that is,

$$\begin{aligned}
&\langle \sigma_{xi} \rangle = \sigma_{xi}^<, \quad x = 0, \quad \langle u_i \rangle = u_i^<,\\
&u_i^<(x \longrightarrow -\infty) \longrightarrow 0, \quad \langle u_i \rangle(x \longrightarrow \infty) \longrightarrow 0.
\end{aligned} \tag{24}$$

Then, the calculations with the use of expressions (13), (14), and (16) show that the dispersion relation for the shear surface acoustic wave generated at the interface can be represented in the following form:

$$k_\perp^2 = \omega^2[(c_\perp - c_\parallel\alpha^2)s_t^2]^{-1},$$

$$\alpha \equiv aq\frac{(\omega + \sigma\tilde{\omega}_-)(\omega - \sigma\tilde{\omega}_+)}{\omega_2^2 - \omega^2} > 0,$$

$$\sigma\tilde{\omega}_\pm \equiv \left(\frac{f_1^2\omega_{\rm me}^2}{4a^2q^2} + \omega_1^2\right)^{1/2} \mp \frac{f_1\omega_{\rm me}}{2aq}, \quad \sigma \equiv k_\perp/|k_\perp|, \tag{25}$$

$$c_\parallel = \frac{\omega_2^2 - \omega^2}{\omega_1^2 - \omega^2}, \quad c_\perp = \frac{\omega_3^2 - \omega^2}{\omega_1^2 - \omega^2},$$

where $q^2 \equiv 1 - \omega^2/(s_*^2 k_\perp^2) > 0$, $s_*^2 \equiv \mu_*/\rho_*$, $a \equiv \mu_*/\mu$, and $\mu_1 = \mu_2 = \mu \neq \mu_*$.

By passing to the limit $a \longrightarrow 0$ in expression (25) (slip boundary), we find that the relationship derived coincides with expression (20).

For the surface acoustic SH wave generated in the vicinity of the acoustically continuous interface ($x = 0$) between the nonmagnetic medium and the acoustic ferromagnet–superconductor superlattice with collinear ordering of the equilibrium magnetic moments in adjacent ferromagnetic layers, the dispersion relation (25) is not symmetric with respect to the inverse propagation direction: $\omega(k_\perp) \neq \omega(-k_\perp)$. At both $\sigma = -1$ and 1, these waves have one branch.

At $\sigma = -1$, the frequency of the branch of spectrum (25), as for spectrum (20), satisfies the inequality $\omega > \omega_2$. However, this branch can have not only a long-wavelength end point but also a short-wavelength end point whose wave number is determined from relationship (25) at $\omega = \tilde{\omega}_-$ ($\tilde{\omega}_- > \omega_1$). For $\sigma = 1$, it follows from relationship (25) that, at $a \neq 0$, the spectrum depends significantly on the ratio between $\tilde{\omega}_+$ ($\tilde{\omega}_+ < \omega_1$) and ω_2 and ω_3($\omega_2 < \omega_3$). The analysis of relationship (25) demonstrates that, as for the slip boundary, for the acoustically continuous interface at $\sigma = 1$, the surface acoustic wave has only one branch and its long-wavelength end point is determined from formula (25) at $q = 0$. If $\tilde{\omega}_+ > \omega_3$, the dispersion curve described by expression (25) for the surface SH wave lies in the frequency range $\omega > \omega_2$. This dispersion curve emerges from the line $q = 0$ and, with an increase in the wave number at $d_1 > d_2$, asymptotically tends to the frequency $\tilde{\Omega}_+$, which, in the elastostatic limit $\omega/s_t k_\perp \longrightarrow 0$ ($q \longrightarrow 1$) and $a \neq 1$ ($\mu_2 = \mu_*$, $\mu_1 = \mu$), is given by the formula

$$\tilde{\Omega}_+ = \omega_0 - \frac{\omega_{\rm me}}{1 + \alpha}. \tag{26}$$

In the specific case where $a = 1$ and $d_1 > d_2$, we obtain $\tilde{\Omega}_- = \omega_0 - 0.5\omega_{\rm me}$. In the limit $a \longrightarrow 0$, we have $\tilde{\Omega}_+ \longrightarrow \Omega_+$, where Ω_+ is defined by relationship (22).

For $\omega_2 < \omega < \omega_3$ and $\sigma = 1$, the dispersion curve under consideration has the long-wavelength end point determined from relationship (25) at $q = 0$ and also the short-wavelength end point. The wave number of this point is determined from the formula

$$\omega_+^2 = s_t^2 k_\perp^2 \frac{\omega_3^2 - \tilde{\omega}_-^2}{\omega_1^2 - \tilde{\omega}_-^2}. \tag{27}$$

Therefore, this branch corresponds to a shear surface acoustic wave of the second kind, whereas, at $\tilde{\omega}_+ > \omega_3$, it corresponds to a surface acoustic wave of the first kind.

Finally, at $\omega_2 > \tilde{\omega}_+$ and $\sigma = 1$, according to expression (25), the dispersion curve for the considered branch of the spectrum of the shear surface elastic wave at all wave numbers $k_\perp$ lies in the range $\omega < \omega_2$ and the long-wavelength end point of this curves corresponds to the frequency $\omega = \tilde{\omega}_+$. In the elastostatic limit, the dispersion curve tends to the frequency $\tilde{\Omega}_+$ defined by formula (26).

Thus, at $\sigma = 1$ and -1 ($\omega_2 < \tilde{\omega}_+ < \omega_3$), the dispersion curve described by relationship (25) corresponds to a shear surface acoustic wave of the second kind. In all other cases, the dispersion curves have only long-wavelength end points, which are characteristic of shear surface acoustic waves of the first kind.

The relationships derived make it possible to analyze the conditions for the localization of an elastic SH wave propagating in the vicinity of a planar superconducting defect embedded in an infinite acoustic magnetic superlattice of the type considered above (at $\mathbf{n} \parallel OX$, $\mathbf{u} \parallel OZ$, $\mathbf{k} \in XY$).

3. CONDITIONS FOR THE GENERATION OF A GAP SHEAR HORIZONTAL WAVE

Let us consider the situation where a planar nonmagnetic defect in the form of an infinite layer $2d$ in thickness ($-d < x < d$) is embedded in the superlattice under investigation. The defect is an ideal elastically isotropic superconductor with shear modulus μ_* and density ρ_*. When the elastic boundary conditions on both surfaces of this layer ($x = \pm d$) correspond to conditions (19) for the slip boundary, the conditions for the generation of a shear magnetoelastic surface acoustic wave in this structure in the long-wavelength limit do not differ from those in the aforementioned case of the slip boundary between a semi-infinite magnetic superlattice and a semi-infinite ideal superconductor with dispersion relation (20) at $x > d$ and $x < -d$.

Now, we assume that slip conditions (19) are satisfied at one boundary of the superconducting layer (for example, at $x = d$) and a continuous acoustic contact [conditions (24)] occurs at the second boundary (at $x = -d$). Then, in the long-wavelength limit, the conditions for localization of the elastic SH wave are determined by dispersion relation (20) for the semi-infinite ferromagnet–superconductor superlattice at $x > d$ and dispersion relation (25) at $x < -d$ with the change $aq \longrightarrow aq\tanh(qk_\perp 2d)$ (acoustic contact of the semi-infinite superlattice at $x < -d$ with a superconducting layer of thickness $2d$ whose outer surface at $x = d$ is mechanically free). In both cases, the field structure of the zth component of the elastic displacement vector $\mathbf{u}$ in the shear surface acoustic wave in the semi-infinite superlattice is determined with due regard for the magnetic configuration according to relationships (16), (17), (13), and (14). Note that the shear surface acoustic waves localized in the vicinity of the surface of the superconducting defect ($-d < x < d$) are independently generated in each half-space.

A qualitatively different situation is observed for rigid contact of both surfaces of a superconducting defect layer $2d$ thick with the surrounding acoustic magnetic superlattice, i.e., in the case when conditions (24) for the acoustic continuity are satisfied at $x = \pm d$. Hereinafter, the system composed of the superconducting layer *S* embedded in the magnetic superlattice is designated as *F–S–F*. The spatial structure of the lattice displacement vector u_z for the elastic SH wave with $\mathbf{u} \parallel OZ$ and $k_\perp \parallel OY \perp \mathbf{n}$ is determined by the expressions

$$\begin{aligned} u_z &= A_+\exp(ik_\parallel x + ik_\perp y - i\omega t), \quad x > d, \\ u_z &= A_0\exp(ik_\parallel x + ik_\perp y - i\omega t) \\ &\quad + B_0\exp(-ik_\parallel x + ik_\perp y - i\omega t), \\ &\qquad x > d, \\ u_z &= A_-\exp(ik_\parallel x + ik_\perp y - i\omega t), \quad x < -d, \end{aligned} \tag{28}$$

where ($\tilde{k}_\parallel^2 \equiv -q^2k_\perp^2$). In this case, the localization of the shear elastic wave in the vicinity of the superconducting defect ($-d < x < d$) does not occur in each half-space independently. This wave is referred to as a gap SH wave. With the use of expressions (14) and (28), the dispersion relation for the spectrum of this localized shear wave can be written in the form

$$\begin{gathered} (\beta_1 + \beta_2)\tilde{k}_\parallel\cot(2k_\parallel d) = \tilde{k}_\parallel^2 - \beta_1\beta_2, \\ \tilde{k}_\parallel^2 \equiv \omega^2/(s_* k_\perp)^2 - k_\perp^2, \\ \beta_1 \equiv (ac_\parallel - c_*\sigma)/a, \quad \beta_2 \equiv (\alpha c_\parallel + c_*\sigma)/a, \end{gathered} \tag{29}$$

where $\alpha^2 \equiv [c_\perp - \omega^2/(s_t^2k_\perp^2)]/c_\parallel$.

Let us now analyze the necessary conditions for the generation of the gap SH wave in the situation where both surfaces of the superconducting layer ($x = \pm d$) are in continuous acoustic contact with a semi-infinite acoustic magnetic superlattice in the *F–S–F* configuration. It follows from relationships (14) and (29) that, for the parameters ω and $k_\perp$ at which the inequalities

$$\alpha^2 > 0, \quad c_\parallel > 0 \tag{30}$$

are satisfied, the spectrum of the gap SH wave has only one branch, provided the following relationships hold:

$$|\alpha^2c_\parallel^2 - c_*^2|d > [\alpha a|c_\parallel|], \quad \alpha^2c_\parallel^2 < c_*^2. \tag{31}$$

In the case when

$$\alpha^2 > 0, \quad c_\parallel < 0, \tag{32}$$

the spectrum of the gap SH wave has two branches according to relationships (14) and (29), but only under the conditions

$$|\alpha^2c_\parallel^2 - c_*^2|d > [\alpha a|c_\parallel|], \quad \alpha^2c_\parallel^2 > c_*^2. \tag{33}$$

For $\alpha^2c_\parallel^2 < c_*^2$, the spectrum of the elastic SH wave localized in the vicinity of the superconducting layer ($-d < x < d$) for the parameters ω and $k_\perp$ corresponding to conditions (32) has only one branch.

In the limit $d \longrightarrow \infty$ (the thickness $2d$ of the embedded superconducting layer increases infinitely), relationship (29) for the spectrum of the gap SH wave transforms into relationship (25) for the spectrum of the shear surface acoustic wave that travels along the acoustically continuous interface between two half-spaces occupied by the magnetic superlattice and the superconductor.

4. CONCLUSIONS

Thus, the specific features in the propagation of a shear elastic wave along the surface of a semi-infinite acoustic superlattice of the easy-axis ferromagnet–ideal superconductor type were considered within the effective-medium approach with simultaneous inclusion of the magnetoelastic and magnetodipole interactions. The analysis was performed for parallel orientation of the equilibrium magnetic moments in adjacent tangentially magnetized ferromagnetic layers of the superlattice.

It was shown that, already in the case of a mechanically free surface, the gyrotropy leads to the generation of a shear surface acoustic wave of the first kind (only with a long-wavelength end point of the spectrum).

The above analysis demonstrated that a nonmagnetic coating characterized by a continuous acoustic contact with the surface of the magnetic superlattice can radically change the spectrum of the generated surface acoustic wave and lead to the appearance of both long-wavelength and short-wavelength end points in branches of the spectrum.

For the interface between the magnetic superlattice and nonmagnetic medium half-spaces, all the aforementioned effects upon a change in the sign of the projection of the wave vector of the elastic SH wave onto the surface of the superlattice differ from each other due to the gyrotropy.

It was revealed that the gap elastic SH wave can propagate in the vicinity of a nonmagnetic layer embedded in the magnetic superlattice under investigation and that the spectrum of this wave is symmetric with respect to the inversion of the propagation direction.

The influence of the intralayer inhomogeneous exchange interaction and specific features of reflection (refraction) of a volume elastic SH wave incident on the surface of an acoustic superlattice of the magnet–superconductor type will be investigated in a separate work.

ACKNOWLEDGMENTS

S.V. Tarasenko would like to thank I.E. Dikshteĭn for supporting the work and helpful discussions.

REFERENCES

1. Yu. I. Bespyatykh, I. E. Dikshteĭn, V. P. Mal'tsev, S. A. Nikitov, and V. Vasilevskiĭ, Fiz. Tverd. Tela (St. Petersburg) **45** (11), 2056 (2003) [Phys. Solid State **45**, 2160 (2003)].
2. M. G. Cottam and D. R. Tilley, *Introduction to Surface and Superlattice Excitations* (Cambridge Univ. Press, Cambridge, 1989).
3. S. M. Rytov, Akust. Zh. **2** (1), 72 (1956) [Sov. Phys. Acoust. **2**, 68 (1956)].
4. S. M. Rytov, Zh. Éksp. Teor. Fiz. **29** (5), 605 (1955) [Sov. Phys. JETP **2**, 466 (1956)].
5. E. A. Turov and V. G. Shavrov, Usp. Fiz. Nauk **140** (3), 429 (1983) [Sov. Phys. Usp. **26**, 593 (1983)].
6. V. I. Al'shits, A. S. Gorkunova, and A. L. Shuvalov, Zh. Éksp. Teor. Fiz. **110**, 924 (1996) [JETP **83**, 509 (1996)].
7. Yu. V. Gulyaev, I. E. Dikshteĭn, and V. G. Shavrov, Usp. Fiz. Nauk **167** (7), 735 (1997) [Phys. Usp. **40**, 701 (1997)].
8. *Surface Polaritons*, Ed. by V. M. Agranovich and D. L. Mills (North-Holland, Amsterdam, 1982; Nauka, Moscow, 1985).

Translated by O. Borovik-Romanova

Physics of the Solid State, Vol. 46, No. 11, 2004, pp. 2110–2114. Translated from Fizika Tverdogo Tela, Vol. 46, No. 11, 2004, pp. 2040–2044.
Original Russian Text Copyright © 2004 by Zadokhin, Solodovnik.

LATTICE DYNAMICS
AND PHASE TRANSITIONS

Simulation of the Dynamic Properties of Hg_2Hal_2 Crystals (Hal = Cl, Br, I)

B. S. Zadokhin and E. V. Solodovnik
Khabarovsk State Technical University, Khabarovsk, 680035 Russia
e-mail: zadokhin@khstu.ru

Received February 24, 2004

Abstract—The dispersion curves for crystal lattices of univalent mercury halides Hg_2Hal_2 (Hal = Cl, Br, I) are calculated from the experimental frequencies at singular points of the Brillouin zone and the velocities of sound in the framework of the valence–force field model. The results of calculating the dispersion branch of the *TA* soft mode along the Γ–*X* direction of the Brillouin zone and the calculated elastic moduli are presented. The calculated values are in good agreement with the experimental data. © *2004 MAIK "Nauka/Interperiodica".*

1. INTRODUCTION

Univalent mercury halides Hg_2Hal_2 (Hal = Cl, Br, I) belong to a new group of materials. In 1970, C. Barta [1], a Czech scientist, synthesized these compounds in a crystalline state. The unique properties of univalent mercury halides have attracted considerable research attention. Specifically, Hg_2Hal_2 crystals possess very strong elastic anisotropy (the velocities of transverse acoustic waves in the basal plane are the lowest among the known velocities in a condensed medium and are comparable in magnitude to the velocity of sound in air), well-pronounced acoustooptical properties, transparency over a wide range, and a record-high optical birefringence [2]. The above properties are of great practical importance. Moreover, owing to their simple crystal structure, univalent mercury halides are convenient model objects for use in studying general problems in solid-state physics.

Strong anisotropy of the physical properties of Hg_2Hal_2 crystals is associated with the specific features of their structure. At room temperature, the crystal lattice of univalent mercury halides consists of linear four-atom chains –*Hal*–Hg–Hg–*Hal*– aligned parallel to each other [3]. The Hg_2Hal_2 molecules form a body-centered lattice with space group D_{4h}^{17} ($I4/mmm$) and two molecules in the unit cell (Fig. 1). This lattice corresponds to the first Brillouin zone depicted in Fig. 2.

To date, there have appeared a large number of papers concerned with experimental and theoretical studies of the vibrational spectra of univalent mercury halides [4–10]. In particular, the normal lattice modes of Hg_2Hal_2 crystals were classified, the eigenvectors of the lattice vibrations at singular points of the Brillouin zone were determined, and the selection rules for optical processes were analyzed in the framework of the group theory [4].

The main objective of this work was to determine the parameters of the potential function of Hg_2Hal_2 crystals in the framework of the valence–force field model with the use of the experimental frequencies at singular points of the Brillouin zone and the velocities of sound in the studied crystals. The elastic moduli of the Hg_2Hal_2 crystals were also calculated within the chosen model.

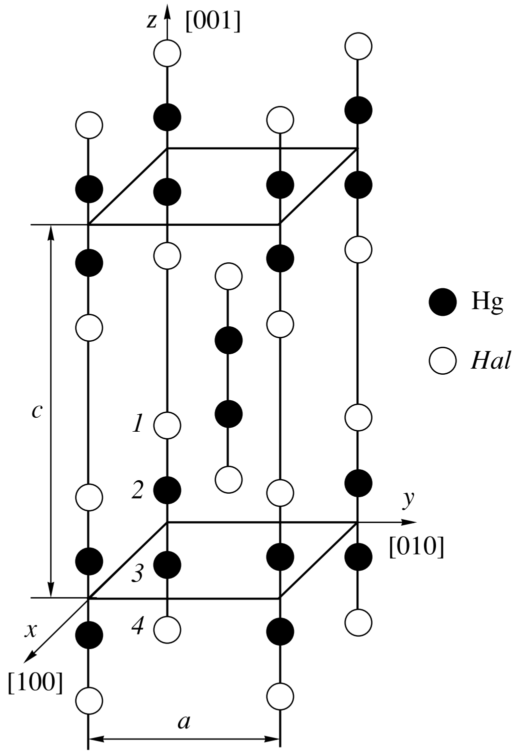

Fig. 1. Crystal lattice of the univalent mercury halides Hg_2Hal_2. Designations: *a* and *c* are the lattice parameters.

2. MATHEMATICAL MODEL

The dynamic properties of Hg_2Hal_2 crystals were calculated in the framework of the valence–force field model. The algorithm for determining the frequencies and modes of optical vibrations was constructed using the method proposed in the monograph by Lazarev and coauthors [11].

The eigenfrequencies and modes of vibrations can be determined by solving the eigenvalue problem for the matrices of the potential and kinetic energies K and G. The matrix elements of the potential energy are the force constants characterizing the interaction of atoms in the crystal. The diagonal matrix elements of the kinetic energy are determined as the inverse masses of the lattice atoms.

In the framework of the force-field model used in our calculations, it is expedient to construct the matrix K in natural coordinates, whereas the matrix G has the simplest form in Cartesian coordinates. Consequently, we will consider both systems of coordinates. For this purpose, we introduce the matrix B in order to change over from the displacements in the Cartesian coordinates x to the vibrations in the natural coordinates s: $B = \partial s/\partial x$.

When solving the problem of calculating the frequencies of the lattice vibrations, it is necessary to take into account the crystal symmetry. To accomplish this, the matrices G and K can be related to the translational symmetrical coordinates (TSC) through the matrix T. As a result, we obtain the matrices G_{TSC} and K_{TSC}:

$$G_{\mathrm{TSC}} = TG\tilde{T}^*, \tag{1}$$

$$K_{\mathrm{TSC}} = T\tilde{B}^*KB\tilde{T}^*. \tag{2}$$

The frequencies and modes of the vibrations can be determined by diagonalizing the matrices G_{TSC} and K_{TSC} specified in the translational symmetrical coordinates:

$$\tilde{L}^*G_{\mathrm{TSC}}L = I, \tag{3}$$

$$\tilde{L}^*F_{\mathrm{TSC}}L = \Lambda, \tag{4}$$

where I is the unit matrix. The matrix Λ obtained in such a manner contains squares of the vibrational frequencies ($\nu^2 = \lambda$). The matrix L is the matrix of vibrational modes.

The elastic constants of the crystal lattice were also calculated in the framework of the valence–force field model. The elastic constants were determined according to [12].

3. CALCULATION SCHEME

The frequencies and modes of lattice vibrations in Hg_2Hal_2 crystals for different values of the wave vector were determined from relationships (3) and (4). In order to calculate the force constants, we solved the

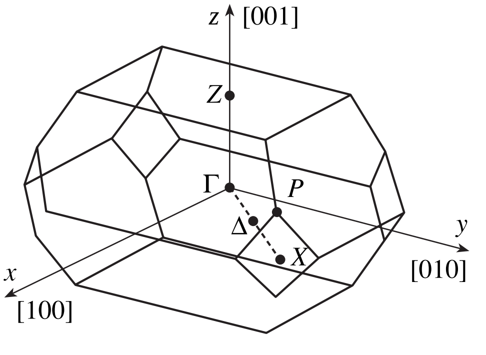

Fig. 2. The first Brillouin zone for the tetragonal lattice of Hg_2Hal_2 crystals.

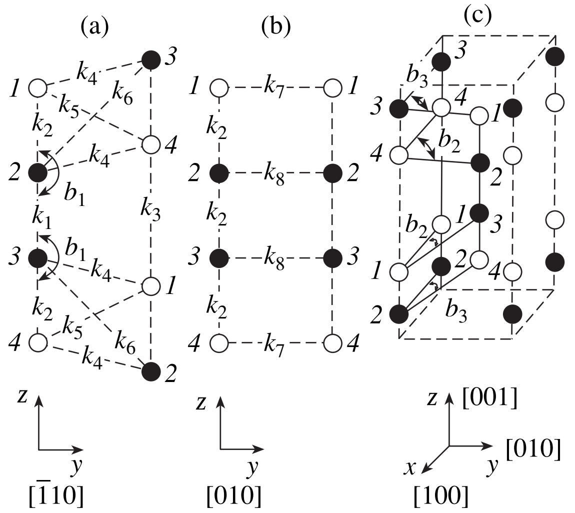

Fig. 3. Force constants for the lattice of the Hg_2Hal_2 crystal.

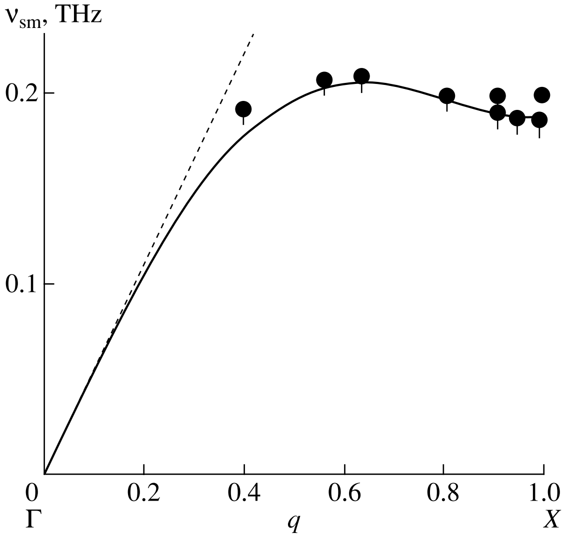

Fig. 4. Dependence of the soft-mode frequency ν_{sm} on the wave vector q along the (Γ–X) direction in the Hg_2Cl_2 crystal.

Table 1. Force constants for Hg_2Hal_2 crystals under normal pressure

Force constants	Bonds and angles	*Hal* = Cl		*Hal* = Br		*Hal* = I	
		numerical values of bond lengths* and angles	numerical values of force constants**	numerical values of bond lengths* and angles	numerical values of force constants**	numerical values of bond lengths* and angles	numerical values of force constants**
k_1	Hg2–Hg3	2.52	1.9	2.57	1.6	2.69	1.3
k_2	Hg2–*Hal*1	2.51	1.15	2.56	1.10	2.68	1.02
	Hg3–*Hal*4	2.51	1.15	2.56	1.10	2.68	1.02
k_3	*Hal*1–*Hal*4	3.37	0.008	3.43	0.05	3.55	0.10
k_4	Hg2–*Hal*4	3.1927	0.010	3.3266	0.018	3.5060	0.030
	Hg3–*Hal*1	3.1927	0.010	3.3266	0.018	3.5060	0.030
k_5	*Hal*1–*Hal*4	3.7895	0.002	3.9266	0.002	4.1460	0.001
k_6	Hg2–Hg3	4.3159	0.17	4.4521	0.13	4.6760	0.10
k_7	*Hal*1–*Hal*1	4.475	0.00070	4.665	0.00040	4.920	0.00035
	*Hal*4–*Hal*4	4.475	0.00070	4.665	0.00040	4.920	0.00035
k_8	Hg2–Hg2	4.475	0.00070	4.665	0.00040	4.920	0.00035
	Hg3–Hg3	4.475	0.00070	4.665	0.00040	4.920	0.00035
h_1	k_4–k_7	–	0.0035	–	0.0025	–	0.0017
h_2	k_4–k_8	–	0.0035	–	0.0025	–	0.0017
b_1	*Hal*1–Hg2–Hg3	180°	8.5	180°	4.3	180°	3.1
	Hg2–Hg3–*Hal*4	180°	8.5	180°	4.3	180°	3.1
b_2	*Hal*1–*Hal*1–Hg3	45.53°	0.09	45.50°	0.07	45.46°	0.07
	*Hal*4–*Hal*4–Hg2	45.53°	0.09	45.50°	0.07	45.46°	0.07
b_3	Hg2–Hg2–*Hal*4	45.53°	0.09	45.50°	0.07	45.46°	0.07
	Hg3–Hg3–*Hal*1	45.53°	0.09	45.50°	0.07	45.46°	0.07

* The lengths of the valence bonds are given in Å.

** The force constants k_1–k_8, h_1, and h_2 are given in 10^5 dyn/cm; and the force constants b_1–b_3 are expressed as 10^{-12} dyn/cm.

inverse problem. The force constants for Hg_2Cl_2, Hg_2Br_2, and Hg_2I_2 crystals were calculated with the Mathcad 7.0 mathematical program package and the Project program in such a way as to achieve the best agreement between the calculated and experimental values of both the frequencies of the vibrational spectrum at the Γ, *X*, *P*, *Z*, and Δ points of the Brillouin zone and the velocities of elastic waves. The experimental frequencies, velocities of sound, and elastic moduli were obtained in [4–10, 13]. When constructing the coordinate bases, we also used the CRYME program package [14].

The numerical calculation of the force constants is performed according to the following scheme.

(1) The matrices *G*, *B*, and *T* are formed as follows: (i) the diagonal matrix *G* of the inverse masses is constructed in the Cartesian coordinates with dimensions $3NM \times 3NM$ (where *N* is the number of atoms per primitive cell and *M* is the number of primitive cells), (ii) the matrix *B* is introduced to change over from atomic displacements in the Cartesian coordinates to vibrations in the natural coordinates and has dimensions $S \times 3NM$ (where *S* is the number of natural coordinates), and (iii) the translation matrix *T* has dimensions $3N \times 3NM$.

(2) An initial set of force constants is specified, and the force constants are used to form the matrix *K* with dimensions $S \times S$.

(3) The frequencies and modes of the vibrations and the velocities of elastic waves are determined according to relationships (1)–(4). This procedure makes it possible to determine the frequencies and modes of the vibrations at different points of the Brillouin zone.

(4) The calculated values are compared with the experimental data. The elements of the matrix *K* are fitted by iterations until the best agreement between the experimental and calculated data is achieved.

In order to determine the dispersion curves for the vibrational spectrum of univalent mercury halide crystals, we introduced the following force constants: the force constants k_1–k_8, which correspond to the diagonal two-center interactions; the force constants b_1–b_3, which account for the diagonal three-center interactions; and the force constants h_1–h_2, which characterize the nondiagonal multicenter interactions.

Table 2. Calculated and experimental frequencies (cm^{-1}) of the vibrational spectrum for the tetragonal phase of Hg$_2$*Hal*$_2$ crystals at singular points of the Brillouin zone

Frequencies of the spectrum	Hg_2Cl_2		Hg_2Br_2		Hg_2I_2	
	experiment	calculation	experiment	calculation	experiment	calculation
	Γ point of the Brillouin zone					
$\nu_1(E_g)$	40	48	36	40	30	35
$\nu_2(E_g)$	137	1337	91	91	74	75
ν_5–$\nu_6(E_u^{LO–TO})$	75	94	66	55	48	47
$\nu_3(A_{1g})$	167	167	135	129	113	105
$\nu_4(A_{1g})$	275	274	221	223	192	197
$\nu_7(A_{2u}^{LO–TO})$	254	256	197	183	150	149
	X point of the Brillouin zone					
$\nu_1(B_{2g})$	45.5	51	40.5	41	–	36
$\nu_2(B_{2g})$	148	137	–	92	–	76
$\nu_5(B_{3u})$	72	96	52	58	–	37
$\nu_6(B_{2u})$	144	95	97	56	–	48
$\nu_3(A_g)$	163	163	133	127	–	104
$\nu_4(A_g)$	288	273	225	220	–	194
$\nu_7(B_{1u})$	265	256	176	184	–	151
$TA_1(B_{3u})$	6.3	6.335	–	4.4	–	3.8
$TA_2(B_{1u})$	39	47	35	38	–	30
	P point of the Brillouin zone					
$TA_1(E)$	12.5	14.5	–	–	–	–
	Z point of the Brillouin zone					
$TA_1(E_u)$	25	17.8	–	–	–	–
	Δ point of the Brillouin zone					
$TA_1(B_1)$	6.5	6.5	–	–	–	–

More precisely, the force constants k_1–k_3 characterize the two-atom interactions along the chains; the force constants k_4–k_6 describe the nearest neighbor interactions in the (110) plane; the force constant b_1 accounts for the interactions in the linear angles *Hal*1–Hg2–Hg3 and Hg2–Hg3–*Hal*4 (Fig. 3a); the force constants k_7 and k_8 describe the interactions of atoms involved in the *Hal*–*Hal* and Hg–Hg bonds in the [010] direction (Fig. 3b); the force constant b_2 characterizes the angular interactions *Hal*1–*Hal*1–Hg3 and *Hal*4–*Hal*4–Hg2; b_3 accounts for the angular interactions Hg2–Hg2–*Hal*4 and Hg3–Hg3–*Hal*1 (Fig. 3c); the nondiagonal force constant h_1 describes the interactions of the *Hal*1–*Hal*1 and *Hal*1–Hg3 bonds and the *Hal*4–*Hal*4 and *Hal*4–Hg2 bonds, which have a common atom; and the force constant h_2 characterizes the interactions of the Hg2–Hg2 and Hg2–*Hal*4 bonds and the Hg3–Hg3 and Hg3–*Hal*1 bonds, which have a common atom.

4. RESULTS OF CALCULATIONS

The force constants providing the best fit of the calculated values to the experimental data for the Hg_2Cl_2, Hg_2Br_2, and Hg_2I_2 crystals are presented in Table 1. The calculated and experimental frequencies (Table 2), velocities of sound (Table 3), and elastic moduli (Table 4) are in good agreement. The dispersion curves for the Hg$_2$*Hal*$_2$ crystals were also calculated.

Figure 4 shows the calculated dispersion branch (TA_1) of the low-frequency transverse acoustic vibrations along the [110] direction for the Hg_2Cl_2 crystal. The closed circles indicate the frequencies determined from the data on inelastic neutron scattering [15]. The dashed line represents the experimental velocities of sound according to the data obtained in [13]. The solid line corresponds to the calculated results.

The force constants k_1, k_2, and b_1 corresponding to the intramolecular interactions considerably exceed the other force constants, which suggests a covalent character of the intramolecular bond and a weak intermo-

Table 3. Calculated and experimental velocities of sound (10^5 cm/s) in Hg_2Hal_2 crystals

Velocities of sound	Hg_2Cl_2		Hg_2Br_2		Hg_2I_2	
	experiment	calculation	experiment	calculation	experiment	calculation
$v\left[{001 \atop 001}\right]$	3.343	3.384	3.487	3.484	3.725	3.678
$v\left[{110 \atop 110}\right]$	2.054	2.011	1.914	1.801	1.790	1.736
$v\left[{110 \atop 110}\right]$	0.347	0.348	0.282	0.283	0.253	0.253
$v\left[{100 \atop 100}\right]$	1.622	1.6279	1.487	1.448	1.361	1.351
$v\left[{100 \atop 010}\right]$	1.305	1.261	1.249	1.188	1.204	1.176
$v\left[{100 \atop 001}\right]$	1.084	0.905	1.008	0.860	0.871	0.946

Table 4. Calculated and experimental elastic moduli (10^{10} dyn/cm^3) of Hg_2Hal_2 crystals

Elastic moduli	Hg_2Cl_2		Hg_2Br_2		Hg_2I_2	
	experiment	calculation	experiment	calculation	experiment	calculation
C_{11}	18.92	19.03	16.16	15.3	14.26	14.05
C_{33}	80.37	82.20	88.85	88.7	104.11	104.16
C_{44}	8.46	5.88	7.45	5.40	5.84	6.89
C_{66}	12.25	1140	11.19	10.30	11.17	10.65
C_{12}	17.12	18.16	15.00	14.7	13.28	13.56
C_{13}	15.63	23.70	18.88	17.20	24.06	15.00

lecular interaction [16]. The force constant k_6 corresponding to two-atom Hg–Hg interactions in the (110) plane was found to be one to two orders of magnitude greater than the force constants k_4 and k_5. This can be explained by the fact that one of the specific features of univalent mercury halides is the stable Hg–Hg bond, which is rare in occurrence. The force constants k_7, k_8, b_2, b_3, h_1, and h_2 predominantly affect the acoustic vibrations in the (001) plane. The nondiagonal force constants h_1 and h_2 indicate mutual influence of the bonds *Hal*1–*Hal*1 and *Hal*1–Hg3, *Hal*4–*Hal*4 and *Hal*4–Hg2, Hg2–Hg2 and Hg2–*Hal*4, and Hg3–Hg3 and Hg3–*Hal*1.

REFERENCES

1. C. Barta, Cryst. Tachnik **5** (4), 541 (1970).
2. *Proceedings of the Second International Symposium on Univalent Mercury Halides* (Trutnov, ČSSR, 1989).
3. R. J. Havighurst, J. Am. Chem. Soc. **48**, 2113 (1926).
4. B. S. Zadokhin, A. A. Kaplyanskiĭ, M. F. Limonov, and Yu. F. Markov, Fiz. Tverd. Tela (Leningrad) **29** (1), 187 (1987) [Sov. Phys. Solid State **29**, 103 (1987)].
5. C. Barta, M. F. Limonov, and Yu. F. Markov, Fiz. Tverd. Tela (Leningrad) **20** (12), 3724 (1978) [Sov. Phys. Solid State **20**, 2155 (1978)].
6. C. Barta, M. F. Limonov, Yu. F. Markov, and D. V. Nakhabtsev, Opt. Spektrosk. **55** (3), 580 (1983) [Opt. Spectrosc. **55**, 344 (1983)].
7. J. Petzelt, M. Matyas, J. Kroupa, and C. Barta, Czech. J. Phys. B **28**, 357 (1978).
8. C. Barta, A. A. Kaplyanskiĭ, and Yu. F. Markov, Fiz. Tverd. Tela (Leningrad) **15** (9), 2835 (1973) [Sov. Phys. Solid State **15**, 1896 (1973)].
9. C. Barta, A. A. Kaplyanskiĭ, V. V. Kulakov, and Yu. F. Markov, Opt. Spektrosk. **37** (1), 95 (1974).
10. C. Barta, A. A. Kaplyanskiĭ, V. V. Kulakov, and B. Z. Malkin, Zh. Éksp. Teor. Fiz. **70** (4), 1429 (1976) [Sov. Phys. JETP **43**, 744 (1976)].
11. A. N. Lazarev, A. P. Mirgorodskiĭ, and I. S. Ignat'ev, *Vibrational Spectra of Complex Oxides* (Nauka, Leningrad, 1975) [in Russian].
12. G. Leibfried, *Gittertheorie der Mechanischen und Thermischen Eigenschaft der Kristalle: Handbuch der Physik* (Springer, Berlin, 1955; GIFML, Moscow, 1963).
13. I. M. Sil'vestrova, C. Barta, G. F. Dobrzhanskiĭ, L. M. Belyaev, and Yu. V. Pisarevskiĭ, Kristallografiya **20** (2), 359 (1975) [Sov. Phys. Crystallogr. **20**, 221 (1975)].
14. M. B. Smirnov, Opt. Spektrosk. **65**, 311 (1988) [Opt. Spectrosc. **65**, 186 (1988)].
15. J. P. Benoit, G. Hauret, and J. Lefebvre, J. Phys. (Paris) **43** (4), 641 (1982).
16. D. A. Kleier and W. R. Wadt, J. Am. Chem. Soc. **102** (23), 6909 (1980).

Translated by O. Moskalev

Physics of the Solid State, Vol. 46, No. 11, 2004, pp. 2115–2120. Translated from Fizika Tverdogo Tela, Vol. 46, No. 11, 2004, pp. 2045–2050.
Original Russian Text Copyright © 2004 by Martyushev, Kuznetsova, Nazarova.

Morphological Phase Diagram of a Spherical Crystal Growing under Nonequilibrium Conditions at the Growth Rate as a Quadratic Function of Supersaturation

L. M. Martyushev, I. E. Kuznetsova, and A. S. Nazarova
Institute of Industrial Ecology, Ural Division, Russian Academy of Sciences, Yekaterinburg, 620219 Russia
e-mail: mlm@ecko.uran.ru

Received March 23, 2004

Abstract—The complete morphological diagram of a spherical nucleus growing from a solution under nonequilibrium conditions at a local growth rate as a quadratic function of supersaturation is calculated for the first time on the basis of a linear analysis for morphological stability and the principle of maximum entropy production. The results of calculations are compared with those obtained previously for a spherical particle in the case of a linear dependence of the growth rate on the supersaturation. *© 2004 MAIK “Nauka/Interperiodica”.*

1. INTRODUCTION

The problems associated with the morphological stability and coexistence of different crystalline phases during nonequilibrium crystallization are important from both the theoretical and technological standpoints [1–3]. One of the interesting problems that has arisen recently is the development of a method for calculating and predicting complete morphological phase diagrams (with the boundaries of metastable and labile regions). In our earlier works [4, 5], we proposed solving this problem on the basis of a linear analysis for morphological stability and the principle of maximum entropy production. The key idea in these works lies in the fact that the principle of maximum entropy production [6–8] allows one to determine the binodal of a nonequilibrium morphological transition (the point of instability with respect to small but finite perturbations) rather than the spinodal (the point of instability with respect to infinitesimal perturbations).

In [4, 5], such an approach was applied to solving the simplest problem concerning the growth of spherical and cylindrical crystals under the assumption of infinitely fast kinetic processes occurring at the surface (diffusion regime). Subsequently, this approach was generalized to crystallizing systems with an arbitrary kinetics of surface processes and a linear dependence of the local growth rate on the supersaturation for spherical [9] and cylindrical [10, 11] geometries. It was found that the crystal growth conditions substantially affect the type of morphological diagram. In particular, the number of phases coexisting under identical crystallization conditions can be infinitely large when a spherical particle grows in the kinetic and intermediate regimes and appears to be limited to two phases in the case of the diffusion regime.

However, apart from the linear dependence of the growth rate on the supersaturation, a quadratic dependence of the growth rate is rather frequently observed in the course of crystallization (for example, for the dislocation mechanism at small supersaturation) [12, 13]. In this respect, investigating the morphological stability in the case of a quadratic dependence of the growth rate on the supersaturation is an important and interesting problem.

The purpose of the present work was to perform a morphological analysis of a spherical crystal growing under nonequilibrium isotropic conditions at an arbitrary rate of kinetic processes at a crystal–solution interface for a quadratic dependence of the local growth rate on the supersaturation.

The paper consists of four sections. In the second section, we carry out a classical linear analysis for morphological stability. This analysis has not been previously performed for the problem of crystal growth from a solution. In the third and fourth sections, we calculate the entropy production upon crystallization for the first time and construct morphological phase diagrams of a crystal growing under nonequilibrium conditions.

2. LINEAR ANALYSIS FOR MORPHOLOGICAL STABILITY

A linear analysis for morphological stability in the case of a quadratic dependence of the growth rate on the supersaturation was earlier performed only for the growth of a spherical particle from a melt [14]. The solution of the problem for the growth of a weakly distorted spherical particle from a solution has specific mathematical features and, hence, will be briefly described below.

Let us consider the growth of a spherical particle from a solution under the assumption that the free surface energy and the kinetic coefficient are isotropic quantities. The mass transfer is described by the Laplace equation (i.e., it is assumed that the driving forces are weak) [15]

$$\left|\frac{C_\infty - C_{\mathrm{int}}}{C - C_{\mathrm{int}}}\right| \le \left|\frac{C_\infty - C_0}{C - C_0}\right| \ll 1, \qquad (1)$$

where C is the density of the crystal, C_∞ is the solute concentration far from the crystal, C_{int} is the solute concentration in the vicinity of a surface of an arbitrary shape, and C_0 is the equilibrium concentration at the plane boundary.

It is assume that an arbitrary small distortion of the sphere can be expanded into a series in terms of spherical harmonics. Now, we consider the behavior of the sole spherical harmonic Y_{lm}.

The solute concentration $c(r, \varphi, \theta)$ satisfies the following boundary conditions:

$$c(\infty) = C_\infty, \qquad (2)$$

$$V \equiv \dot{R} + \dot{\delta} Y_{lm} = \frac{D}{C}\frac{\partial c}{\partial r}\bigg|_{\rho} = \beta_2 \frac{(C_{\mathrm{int}} - C_{\mathrm{int\,eq}})^2}{C}, \qquad (3)$$

where $\rho = R(t) + \delta(t)Y_{lm}(\varphi, \theta)$ is the equation of the surface of the perturbed sphere, R is the radius of the unperturbed particle, δ is the perturbation amplitude, V is the local growth rate, $\dot{R} \equiv dR/dt$, $\dot{\delta} \equiv d\delta/dt$, φ and θ are the spherical coordinates, D is the diffusion coefficient, β_2 is the kinetic coefficient of crystallization, $C_{\mathrm{int\,eq}} = C_0(1 + \Gamma K)$ is the equilibrium solute concentration at the surface of an arbitrary shape (in linear order of the perturbation theory, this concentration is determined to be $C_0[1 + 2\Gamma/R + (l-1)(l+2)\Gamma\delta Y_{lm}(\varphi, \theta)/R^2]$ [15]), Γ is the capillary length proportional to the surface tension, K is the surface curvature, and $C_{\mathrm{int}} \equiv c|_\rho$.

The boundary condition (3) is written under the assumption that the solute concentration is negligible as compared to the crystal density. This assumption significantly simplifies the solution of the problem and is satisfied well for many real systems crystallizing from solutions.

By solving the formulated problem, we obtain

$$\begin{aligned} c(r, \Theta, \varphi) &= C_\infty - \frac{R}{r}(C_\infty - C_0) \\ &\times\left(1 - \frac{R^*}{R}\left(1 + \frac{\chi\alpha_2}{2}\right)\right) - \frac{R^l}{r^{l+1}}\frac{(C_\infty - C_0)\delta Y_{lm}}{1 + \dfrac{l+1}{\chi}} \\ &\times\left[\left(1 - \frac{R^*}{R}\left(1 + \frac{\chi\alpha_2}{2}\right)\right)\left(1 + \frac{2}{\chi}\right) - \frac{1}{2}\frac{R^*}{R}(l-1)(l+2)\right]. \end{aligned} \qquad (4)$$

Here, we introduced the following dimensionless parameters:

$$\alpha_2 = \frac{D}{\beta_2}\frac{1}{R^*(C_\infty - C_0)},$$

$$\chi = -1 + \sqrt{1 + \frac{4}{\alpha_2}\frac{R}{R^*}\left(1 - \frac{R^*}{R}\right)},$$

$R^* = 2\Gamma/\Delta$ is the radius of the critical nucleus of a new phase [15], and $\Delta = (C_\infty - C_0)/C_0$ is the relative supersaturation.

From relationships (3) and (4), we have

$$\dot{R} = \frac{D}{CR}(C_\infty - C_0)\left(1 - \frac{R^*}{R}\left(1 + \frac{\alpha_2\chi}{2}\right)\right), \qquad (5)$$

$$\begin{aligned} \dot{\delta} &= \frac{D}{C}\frac{(C_\infty - C_0)\delta}{R^2\left(\dfrac{l+1}{\chi} + 1\right)} \\ &\times (l-1)\left[1 - \frac{R^*}{R}\left(1 + \frac{\chi\alpha_2}{2} + \frac{(l+1)(l+2)}{2}\right)\right]. \end{aligned} \qquad (6)$$

Then, we equate the parameter $\dot{\delta}$ to zero. In this case, as can be seen from expression (6), the perturbation increases when the crystal radius becomes greater than the critical size:

$$R^S = \left[\left(\frac{(l+1)(l+2)}{2} + 1\right) + \sqrt{\alpha_2\frac{(l+1)(l+2)}{2}}\right]R^*. \qquad (7)$$

Taking into account the method of derivation, relationship (7) is an equation of the spinodal (the point of stability loss with respect to infinitesimal-amplitude perturbations of the shape) of the morphological transition from stable (spherical) growth to unstable (dendrite-like, skeletal) growth.

The difference between the critical size R^S for the quadratic growth kinetics and the radius at the spinodal point in the case of linear growth kinetics (according to the data obtained in [9]) is illustrated in Fig. 1. It can be seen from this figure that the nonlinearity in relationship (3) leads to an increase in the radius of stability loss R^S. This behavior can be explained as follows: at a relatively small supersaturation (considered in our case), the growth rate that is linearly dependent on the supersaturation is higher than the growth rate characterized by a quadratic dependence on the supersaturation. Since the local growth rate is the main destabilizing factor responsible for the loss of morphological stability [14, 15], the crystal in the case of the quadratic dependence of the growth rate on the supersaturation can remain stable for a longer time.

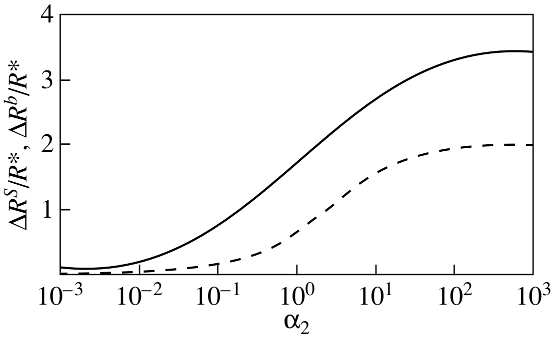

Fig. 1. Differences between the crystal radii at the spinodal point $\Delta R^S/R^*$ (solid line) and the crystal radii at the binodal point $\Delta R^b/R^*$ (dashed line) as a function of the parameter α_2 for the quadratic and linear dependences of the growth rate on the supersaturation. $l = 2$.

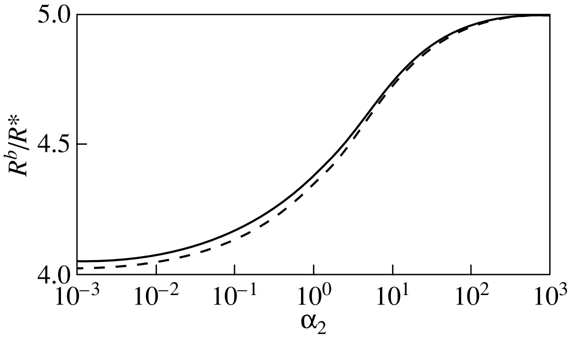

Fig. 2. Dependences of the radius R^b (in terms of R^*) on the parameter α_2. The solid line indicates the numerical solution of the equation $\Delta\Sigma = 0$, where $\Delta\Sigma$ is determined by expression (10). The dashed line is constructed according to the analytical relationship (11). $\Delta = 0.02$, $l = 2$.

3. THERMODYNAMIC ANALYSIS FOR MORPHOLOGICAL STABILITY

Now, we analyze the formulated problem within the thermodynamic approach.

The local entropy production in a volume element $r^2 d\Omega dr$, which is immediately adjacent to the crystal boundary ρ and is bounded by the solid angle $d\Omega$, can be written in the form [5, 9]

$$\Sigma \sim \frac{C^2 V^2}{C_{\text{int}} D} r^2 dr d\Omega. \tag{8}$$

Let us determine the difference $\Delta\Sigma$ between the entropy productions in the cases of growth of perturbed and unperturbed spherical crystals. As follows from expression (8), the difference $\Delta\Sigma$ can be represented in the following form:

$$\begin{aligned}\Delta\Sigma &\sim \frac{C^2}{D}\left\{\frac{V^2\rho^2}{C_{\text{int}}} - \frac{\dot{R}^2 R^2}{C_R}\right\} dr d\Omega \\ &= \frac{C^2 R\dot{R}}{C_R D}\left\{2Y_{lm}(R\dot{\delta} + \dot{R}\delta) - R\dot{R}\left(1 - \frac{C_R}{C_{\text{int}}}\right)\right\} dr d\Omega,\end{aligned} \tag{9}$$

where C_R is the solution concentration in the vicinity of the spherical particle. According to relationship (4), this concentration is equal to $C_0 + (C_\infty - C_0)(1 + 0.5\alpha_2\chi)R^*/R$.

Substituting relationships (5) and (6) into expression (9) gives

$$\begin{aligned}\Delta\Sigma \sim \frac{(l+1)\chi}{(l+1+\chi)}&\left[1 - \frac{R^*}{R}\left(1 + \frac{\chi\alpha_2}{2} + \frac{(l+1)(l+2)}{2}\right)\right] \\ &+ \left[1 - \frac{R^*}{R}\left(1 + \frac{\chi\alpha_2}{2}\right)\right] \\ &- \frac{(l-1)\chi\Delta\left[1 - \frac{R^*}{R}\left(1 + \frac{\chi\alpha_2}{2}\right)\right]}{4(l+1+\chi)\left[1 + \frac{\Delta R^*}{R}\left(1 + \frac{\chi\alpha_2}{2}\right)\right]} \\ &\times \left\{l + 2 + \frac{2}{\chi}\left(\frac{R}{R^*} - 1 - \frac{\chi\alpha_2}{2}\right)\right\}.\end{aligned} \tag{10}$$

Numerical analysis of relationship (10) demonstrates that the difference $\Delta\Sigma$ in the region of definition $[R^*, R^S]$ is an increasing function and vanishes when the size of the spherical crystal becomes equal to R^b. Therefore, for crystals with sizes larger than R^b, the local entropy production at the perturbed surface turns out to be greater than that in the vicinity of the unperturbed crystal surface. According to [4, 5, 9–11], this point will be referred to as the binodal point of the morphological transition under investigation.

The dependence of the radius R^b on the parameter α_2 is plotted in Fig. 2. This dependence is constructed by numerically solving the equation $\Delta\Sigma = 0$ with the MathCAD software package. It can be seen from Fig. 2 that, as the parameter α_2 increases, the radius R^b at the binodal point varies over a relatively narrow range. Note that the largest changes in the radius R^b are observed for parameters α close to unity.

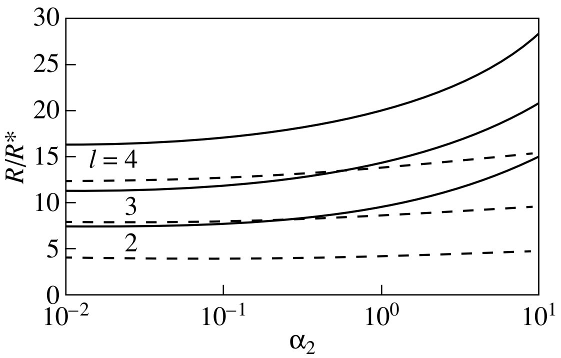

Fig. 3. Dependences of the crystal radius (in terms of R^*) at the binodal (dashed lines) and spinodal (solid lines) points on the parameter α_2 for different l.

In the limit $\Delta \ll 1$, the third term in expression (10) can be ignored and the radius R^b on the interval $[R^*, R^S]$ can be determined in explicit form:

$$R^b = R^*\left\{1 + \frac{l-1}{8l^2}[4l(l+1)(l+2) - \alpha_2(l+1) + \sqrt{\alpha_2^2(l+1)^2 + 8\alpha_2 l(l^2-1)(l+2)}]\right\}. \quad (11)$$

As can be seen from Fig. 2, the approximate expression (11) makes it possible to describe the exact numerical solution of the equation $\Delta\Sigma = 0$ at small supersaturations with good accuracy. Indeed, at $\Delta \le 0.1$, the difference between the radius R^b determined from relationship (11) and the radius obtained from numerical solution of the equation $\Delta\Sigma = 0$ does not exceed 4%. Note that the largest difference is observed for higher perturbing harmonics in the diffusion regime of crystal growth.

It should also be noted (Fig. 1) that, as in the case of stability loss with respect to an infinitesimal perturbation, the nonlinearity in the growth kinetics results in an increase in the radius at the binodal point (according to the data taken from [9]).

In the approximation of an infinitely high rate of surface reactions ($\alpha_2 \longrightarrow 0$), Eq. (11) can be rearranged to the form

$$R^{b\,\mathrm{diff}} = (2l)^{-1}R^*[l^3 + 2l^2 + l - 2].$$

This radius at the binodal point coincides with the radius determined in our previous work [5].

In the kinetic regime of crystal growth ($\alpha_2 \longrightarrow \infty$), the radius R^b at the binodal point reaches the asymptotic value

$$R^{b\,\mathrm{kin}} = R^*(l^2 + l - 1).$$

4. MORPHOLOGICAL DIAGRAMS OF A SPHERICAL CRYSTAL GROWING UNDER NONEQUILIBRIUM CONDITIONS

The equations obtained for the spinodal [expression (7)] and the binodal [expression (11)] can be used to construct complete morphological diagrams (see, for example, Fig. 3). It can be seen from Fig. 3 that, in the diffusion regime ($\alpha_2 < 0.1$), the metastable regions corresponding to different harmonics do not intersect. In the intermediate regime ($0.1 < \alpha_2 < 1$), the binodal of the $(l + 1)$st harmonic intersects the spinodal of the lth harmonic and the metastable regions of the neighboring harmonics overlap. A further increase in the parameter α_2 can lead to the overlapping of three or more metastable regions. As a consequence, in the intermediate and kinetic regimes of crystal growth, a large number of crystals with different shapes (morphological phases) can coexist and grow from a spherical nucleus (for example, the number of coexisting morphological phases is equal to six for $\alpha_2 = 150$ and nine for $\alpha_2 = 1000$).

Now, we examine the change in the crystal mass in the vicinity of the morphological transition from the spherical particle to a particle with developing perturbations. For this purpose, we consider the difference between the increments of the crystal mass (or, in other words, the flows of the material arriving at the crystal surface from the solution) for the perturbed $(dN/dt)_p$ and unperturbed $(dN/dt)_n$ crystals. As in the preceding case, this increment is calculated for the volume element $r^2 d\Omega dr$ near the crystal surface per unit time. As a result, we have

$$\begin{aligned}&(dN/dt)_p - (dN/dt)_n\\ &= (CV\rho^2 - C\dot{R}R^2)drd\Omega \sim (2\dot{R}\delta + R\dot{\delta})Y_{lm}drd\Omega\\ &\sim (l-1)\chi\left(\frac{R}{R^*} - 1 - \frac{\alpha_2\chi}{2} - \frac{(l+1)(l+2)}{2}\right)\\ &+ 2(l+1+\chi)\left(\frac{R}{R^*} - 1 - \frac{\alpha_2\chi}{2}\right).\end{aligned} \quad (12)$$

This difference is an increasing function of the crystal radius R and becomes equal to zero at the point

$$R^I = 0.5R^*l(l+1). \quad (13)$$

It is interesting to note that, unlike the case considered in [9], the radius R^I does not depend on the growth regime and is a function only of the perturbing harmonic.

The dependences of the radii R^S, R^b, and R^I on the parameter α_2 are depicted in Fig. 4. As can be seen from this figure, in any growth regime, the size at which the mass increment rate for the crystal with the perturbed surface becomes higher than that for the crystal with the unperturbed surface is always smaller then the radius at the binodal point. As a consequence, the increment rate of the crystal mass can only undergo a jumpwise increase at the morphological transition point lying in

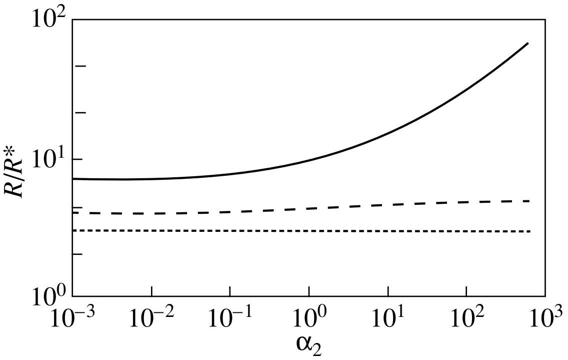

Fig. 4. Dependences of the radii R^S (solid line), R^b (dashed line), and R^I (dotted line) on the parameter α_2. $l = 2$.

the range from R^b to R^S depending on the perturbation amplitude.

Figures 5 and 6 show the dependences of the mass increment rate on the supersaturation and the crystal size in the vicinity of the morphological transition point (binodal point). These dependences are constructed with the use of formulas (11) and (12) for a constant amplitude δ. Such diagrams enable one to make inferences regarding the behavior of the jump in the crystal growth rate with a variation in the main parameters of the solution and to determine the parameters of the transition. Direct (even qualitative) comparison of these dependences with the corresponding dependences obtained in [9] for the linear growth kinetics is complicated, because the dimensionless parameters characterizing the growth regime differ from each other. The parameter α used in [9] and the parameter α_2 are related by the expression $\alpha = \alpha_2\beta_2(C_\infty - C_0)/\beta$, where β is the kinetic coefficient of crystallization. The dimension of this coefficient, which was introduced in [9], differs from that of the coefficient β_2. The above expression makes it possible to compare the behavior of dependences similar to those plotted in Figs. 5 and 6. Figures 7 and 8 show the dependences of the jump in the mass increment rate on the parameters α_2 and l at the binodal point for the linear and quadratic surface kinetics in the case when the dimensionless coefficient $\beta_2(C_\infty - C_0)/\beta$ is equal to unity (the same coeffi-

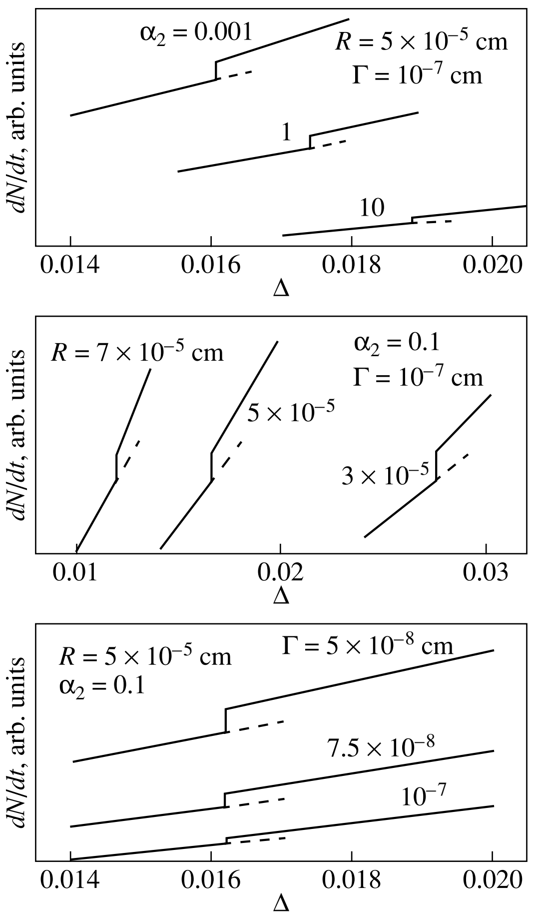

Fig. 5. Dependences of the mass increment rate dN/dt on the supersaturation Δ in the vicinity of the morphological transition point. $l = 2$.

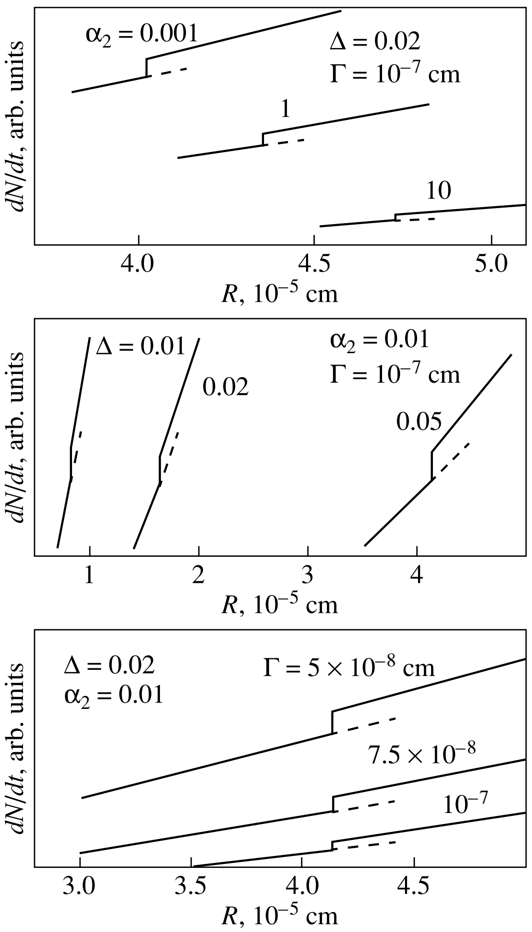

Fig. 6. Dependences of the mass increment rate dN/dt on the crystal size R in the vicinity of the morphological transition point. $l = 2$.

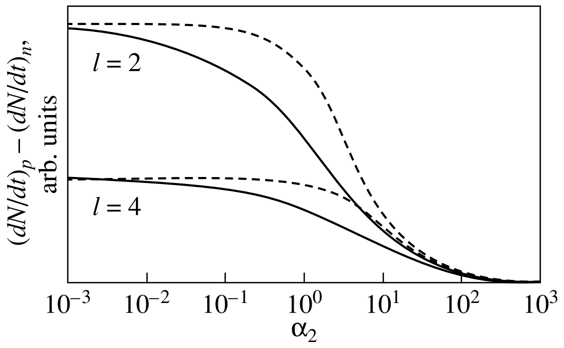

Fig. 7. Dependences of the jump in the mass increment rate $(dN/dt)_p - (dN/dt)_n$ on the parameter α_2 for the morphological transition at point R^b for the quadratic (solid line) and linear (dashed line) dependences of the growth rate on the supersaturation.

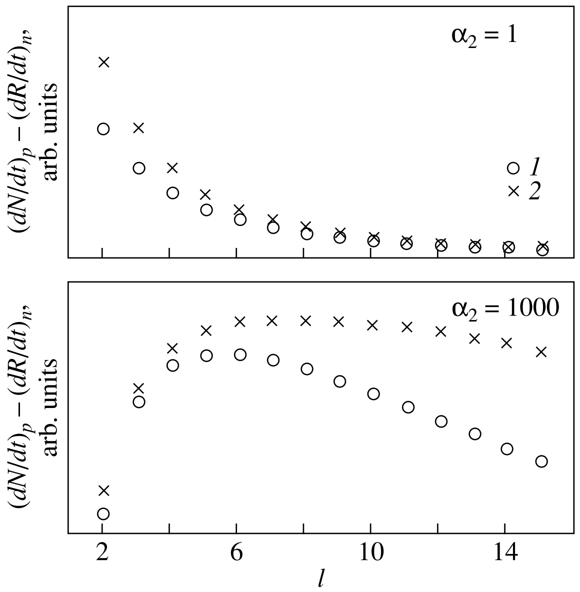

Fig. 8. Dependences of the jump in the mass increment rate $(dN/dt)_p - (dN/dt)_n$ on the number of the perturbing harmonic l for the morphological transition at point R^b for the (*1*) quadratic and (*2*) linear dependences of the growth rate on the supersaturation.

cient was used for constructing the dependences depicted in Fig. 1). It can be seen that the jumps in the mass increment rate depend substantially on the mechanism of surface kinetics.

5. CONCLUSIONS

Thus, the results of the above investigation demonstrated that nonlinear (quadratic) behavior of the dependence of the local growth rate on the supersaturation leads to considerable quantitative corrections to the morphological transition points (radii) and the jumps in the crystal growth rate obtained for linear behavior.

REFERENCES

1. M. C. Cross and P. C. Hohenberg, Rev. Mod. Phys. **65** (1), 851 (1993).
2. E. Ben-Jacob and P. Garik, Nature **343**, 523 (1990).
3. W. Kurz and D. J. Fisher, *Fundamentals of Solidification* (Trans. Tech., Zurich, 1992).
4. L. M. Martyushev and V. D. Seleznev, Dokl. Akad. Nauk **371** (4), 466 (2000) [Dokl. Phys. **45**, 129 (2000)].
5. L. M. Martyushev, V. D. Seleznev, and I. E. Kuznetsova, Zh. Éksp. Teor. Fiz. **118** (1), 149 (2000) [JETP **91**, 132 (2000)].
6. H. Ziegler, in *Progress in Solid Mechanics*, Ed. by I. N. Sneddon and R. Hill (North-Holland, Amsterdam, 1963; Mir, Moscow, 1966), Vol. 4.
7. H. Ziegler, *An Introduction to Thermomechanics* (North-Holland, Amsterdam, 1983).
8. Y. Sawada, J. Stat. Phys. **34**, 1039 (1984).
9. L. M. Martyushev, I. E. Kuznetsova, and V. D. Seleznev, Zh. Éksp. Teor. Fiz. **121** (2), 363 (2002) [JETP **94**, 307 (2002)].
10. L. M. Martyushev and E. M. Sal'nikova, Pis'ma Zh. Tekh. Fiz. **28** (6), 57 (2002) [Tech. Phys. Lett. **28**, 242 (2002)].
11. L. M. Martyushev and E. M. Sal'nikova, J. Phys.: Condens. Matter **15**, 1137 (2003).
12. J. W. Cahn, W. B. Hillig, and G. W. Seers, Usp. Fiz. Nauk **91** (4), 691 (1967); Acta Metall. **12**, 1421 (1964).
13. A. A. Chernov, Kristallografiya **16** (4), 842 (1971) [Sov. Phys. Crystallogr. **16**, 734 (1971)].
14. S. Corill and R. Parker, in *Proceedings of International Conference on Crystal Growth, Boston, 1966* (London, 1967; Mir, Moscow, 1968).
15. W. W. Mullins and R. F. Sekerka, J. Appl. Phys. **34**, 323 (1963).

Translated by O. Borovik-Romanova

Physics of the Solid State, Vol. 46, No. 11, 2004, pp. 2121–2125. Translated from Fizika Tverdogo Tela, Vol. 46, No. 11, 2004, pp. 2051–2055.

LATTICE DYNAMICS AND PHASE TRANSITIONS

Phase Stresses Induced by the $\gamma \longrightarrow \alpha$ Transformation in an Iron Polycrystal

A. A. Zisman[1,2] and A. A. Vasilyev[1]

[1]*St. Petersburg State Polytechnical University, Politekhnicheskaya ul. 29, St. Petersburg, 195251 Russia*

[2]*Prometeĭ Central Research Institute of Structural Materials, Shpalernaya ul. 49, St. Petersburg, 193015 Russia*

e-mail: vasilyev_aa@mail.ru

Received March 23, 2004; in final form, April 8, 2004

Abstract—The evolution of the phase stresses induced in the course of the $\gamma \Rightarrow \alpha$ transformation in polycrystalline iron is analyzed in the framework of the elastoplastic model of a spherical inclusion. The isolated regions of the α phase (ferrite) and the γ phase (austenite) are treated as inclusions at the initial and final stages of the transformation, respectively. The stresses are calculated with due regard for the plastic flow in a spherical layer (matrix) around these inclusions. The calculated dependence of the hydrostatic phase stresses on the volume fraction of ferrite suggests that these stresses retard the initial stage and promote the final stage of the transformation. *© 2004 MAIK “Nauka/Interperiodica”.*

1. INTRODUCTION

In iron and its alloys, the mean relative increase in volume upon the $\gamma \longrightarrow \alpha$ transformation in the characteristic temperature range (600–800°C) is approximately equal to 0.015 [1]. The stresses induced in this case are very strong and, consequently, lead to plastic flow of one of the phases (depending on the transformation stage). At the initial stage, when isolated nuclei of the α phase (ferrite) are subjected to uniform (hydrostatic) compression, considerable shear stresses and plastic flow predominantly occur in the surrounding layers of the γ phase (austenite). By contrast, at the final stage of the transformation, when “islands” of residual austenite appear to be isolated and are subjected to hydrostatic tension, shear stresses and plasticity are characteristic of the surrounding ferrite layers [1–3]. It should be noted that, at any stage, the magnitude of the stresses in both phases is controlled by the local flow stress in the phase forming a continuous matrix.

The hydrostatic stresses arising in the interacting phases change in the course of the transformation and can affect the relative thermodynamic stability of these phases and, hence, the kinetics of the transformation as a whole. This effect was indirectly confirmed in the experiments on the strong influence of external pressure on the rate of the $\gamma \longrightarrow \alpha$ transformation in iron and its alloys [1]. Moreover, according to recent experimental data [4], the specific features of the transformation kinetics cannot be explained without regard for the elastic energy associated with the phase stresses. However, up to now, no reliable correct estimates had been obtained for these stresses with allowance made for their variation depending on the morphology and the volume fraction of the transformed phase. This problem is important not only from the theoretical standpoint but is also of considerable practical interest due to the crucial role played by the $\gamma \longrightarrow \alpha$ transformation in the formation of steel structures under heat treatment.

In this work, we analyzed the phase stresses in the course of the $\gamma \longrightarrow \alpha$ transformation in the framework of a quantitative model that allows for their plastic accommodation depending on the morphological features of the two-phase structure at different stages of the transformation. For simplicity, we restricted our consideration to the specific case of the formation of the ferrite phase with polygonal (equiaxed) grains that predominantly nucleate at boundary junctions and boundaries between the original austenite grains.

2. STRESSES AND PLASTIC ACCOMMODATION IN THE SPHERICAL-INCLUSION MODEL

When simulating the morphology of a two-phase structure, we take into account that the ferrite phase predominantly nucleates at boundary junctions of austenite grains (Fig. 1a). The subsequent nucleus growth (proceeding at an increased rate along the grain boundaries) leads to the formation of a continuous ferrite framework with islands of residual austenite (Fig. 1b). Therefore, at the initial and final stages of the transformation, the structure of the material can be represented as a set of two-phase cells containing ferrite and austenite inclusions, respectively. By assuming that these cells are identical (Figs. 1c, 1d), we ignore their interaction; i.e., each cell is considered to be free. Furthermore, for simplicity, the cells are assumed to be spherical in shape (Figs. 1e, 1f). The stresses calculated for the model cells under consideration (Figs. 1e, 1f) should be matched for some volume fraction of the ferrite phase f^* at which the initially continuous austenite

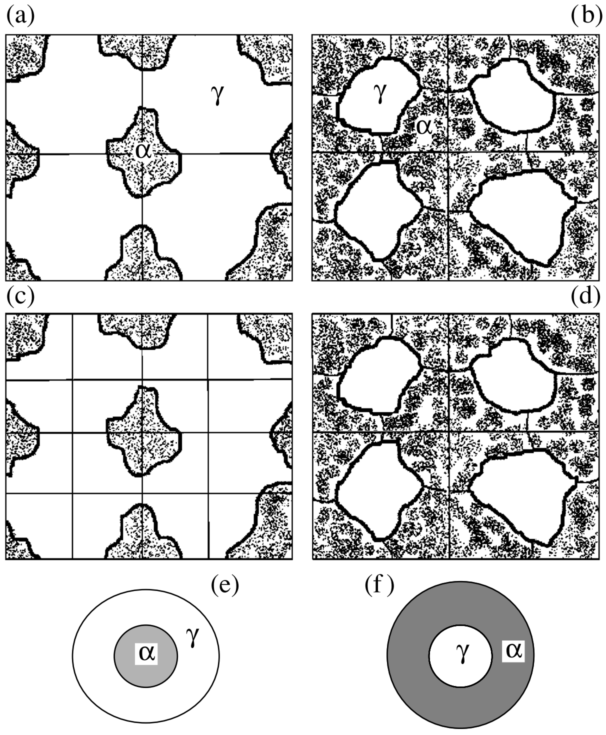

Fig. 1. Schematic two-dimensional representation of the morphology of the two-phase structure formed in the course of the $\gamma \Rightarrow \alpha$ transformation in an iron polycrystal: (a) initial and (b) final stages of the transformation (thin straight lines indicate the boundaries of austenite grains), (c, d) two-phase structural cells (straight lines), and (e, f) computational cells of the model two-phase structure.

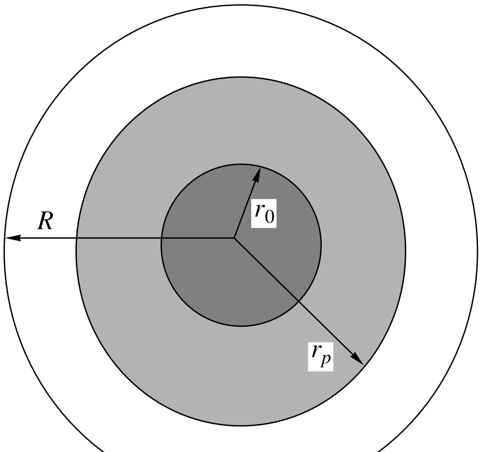

Fig. 2. Schematic drawing of the spherical two-phase cell consisting of an inclusion and the matrix with a zone of plastic accommodation of phase stresses. r_0, r_p, and R are the radii of the inclusion, the plastic accommodation zone, and the matrix, respectively.

matrix is separated into isolated quasi-spherical regions. According to an approximate geometric estimate, we have $f^* \approx 0.2$.

Let us consider a model spherical cell of radius R (Fig. 2). This cell contains a concentric inclusion of radius r_0, which was subjected to inelastic dilatation δ. The induced stresses can lead to plastic deformation of the matrix material in a spherical layer adjacent to the inclusion (Fig. 2). By virtue of the symmetry of the problem, the spherical stress components obey the following equalities: $\sigma_\varphi = \sigma_\theta = \sigma_r$ $(0 \le r < r_0)$ and $\sigma_\varphi = \sigma_\theta$ $(r_0 \le r \le R)$. Moreover, the plasticity condition $\sigma_{eq} = \sigma_\varphi - \sigma_r = \sigma_s$ (where σ_{eq} is the equivalent deforming stress and σ_s is the yield stress of the matrix material) [5] is satisfied in the plastic zone $(r_0 \le r \le r_p)$. With due regard for these relationships, the hydrostatic stresses $\sigma_0 = (\sigma_\varphi + \sigma_\theta + \sigma_r)/3$ inside the inclusion (σ_0^i) and in the plastic zone (σ_0^m) can be written in the form

$$\sigma_0^i = \sigma_\varphi = \sigma_\theta = \sigma_r, \quad 0 \le r < r_0, \tag{1}$$

$$\sigma_0^m = \sigma_r + \frac{2}{3}\sigma_s, \quad r_0 \le r \le r_p. \tag{2}$$

Now, we determine the stresses in the inclusion and the matrix layers adjacent to the inclusion with allowance made for their plastic accommodation. Under the plasticity condition, it follows from expressions (1) and (2) that, for all the stress components, the differences between their values at the boundary of the plastic zone and on the inclusion surface are identical: $\sigma_\varphi(r_p) - \sigma_\varphi(r_0) = \sigma_r(r_p) - \sigma_r(r_0) = \sigma_0(r_p) - \sigma_0(r_0) = \Delta\sigma$. According to [5], in order to calculate $\Delta\sigma$, the equation of elastic equilibrium in the plastic zone can be written in spherical coordinates in the following form:

$$\frac{\partial \sigma_r}{\partial r} - \frac{2\sigma_s}{r} = 0. \tag{3}$$

From this equation, we have $\Delta\sigma = 2\sigma_s \ln(r_p/r_0)$. On the basis of this result and relationships (1) and (2), we find the uniform stresses in the inclusion $(0 \le r < r_0)$,

$$\sigma_r = \sigma_\varphi = \sigma_0 = \sigma_r(r_p) - 2\sigma_s \ln\left(\frac{r_p}{r_0}\right), \tag{4}$$

and the local stresses at the inner boundary of the plastic zone $(r = r_0 + 0)$,

$$\sigma_r = \sigma_\varphi - \sigma_s = \sigma_0 - \frac{2}{3}\sigma_s = \sigma_r(r_p) - 2\sigma_s \ln\left(\frac{r_p}{r_0}\right). \tag{5}$$

Therefore, the problem regarding the stresses in the vicinity of the matrix–inclusion interface can be reduced to determining the radial stresses $\sigma_r(r_p)$ at the outer boundary of the plastic zone.

As the volume fraction of the inclusion $f = (r_0/R)^3$ increases, the boundary of the plastic zone approaches the outer boundary of the cell under consideration and reaches it ($r_p = R$) at $f = f_1$. Thereafter ($f \geq f_1$), taking into account relationships (4) and (5) and the absence of radial stresses on the free surface, the stresses in the vicinity of the inclusion boundary can be given by the expressions

$$\sigma_r = \sigma_\varphi = \sigma_0 = \frac{2}{3}\sigma_s \ln(f), \quad r < r_0, \tag{6}$$

$$\begin{gathered}\sigma_r = \sigma_\varphi - \sigma_s = \sigma_0 - \frac{2}{3}\sigma_s = \frac{2}{3}\sigma_s \ln(f), \\ r = r_0 + 0.\end{gathered} \tag{7}$$

It remains to find the quantity f_1 and to determine the stresses in the volume fraction range $0 \leq f < f_1$. For this purpose, the elastoplastic region of radius r_p is treated as an inclusion in the sphere of radius R. According to [6], the following expression holds in the vicinity of this inclusion ($r = r_p + 0$):

$$\frac{\sigma_\varphi}{\sigma_r} = -\frac{1/2 + r_p^3/R^3}{1 - r_p^3/R^3}. \tag{8}$$

From expression (8) with allowance made for the plasticity condition, we obtain

$$\begin{gathered}\sigma_r(r_p) = -\frac{2}{3}\sigma_s\left(1 - \frac{r_p^3}{R^3}\right), \\ \sigma_\varphi(r_p) = \frac{1}{3}\sigma_s\left(1 + \frac{2r_p^3}{R^3}\right).\end{gathered} \tag{9}$$

On the other hand, $\sigma_r(r_p)$ can be expressed through the dilatation δ^* of the effective inclusion of radius r_p as follows [6]:

$$\sigma_r(r_p) = -\frac{4}{9}\frac{G\delta^*(1+\nu)(1 - r_p^3/R^3)}{(1-\nu)}. \tag{10}$$

From formulas (9) and (10), we have

$$\delta^* = \frac{3}{2}\frac{\sigma_s(1-\nu)}{G(1+\nu)}. \tag{11}$$

The total dilatation δ^* of a free sphere with radius r_p [$\sigma_r(r_p) = 0$] is equal to the sum of the inelastic strain δ in the range $0 \leq r \leq r_0$ and the nonuniform elastic strain over the entire range $0 \leq r \leq r_p$. The radial elastic strain in the spherical layer $r_0 \leq r \leq r_p$ can be represented in the form

$$\varepsilon_r^{el}(r) = \frac{\sigma_s(1-2\nu)}{G(1+\nu)}\ln\left(\frac{r}{r_p}\right) - \frac{\sigma_s\nu}{G(1+\nu)}. \tag{12}$$

The average value of this radial elastic strain is defined as

$$\langle\varepsilon_r^{el}\rangle = \frac{\sigma_s(1-2\nu)}{G(1+\nu)}\left(\frac{r_0}{r_p - r_0}\ln\left(\frac{r_p}{r_0}\right) - 1\right) - \frac{\sigma_s\nu}{G(1+\nu)}. \tag{13}$$

According to relationship (4), the uniform radial elastic strain in the inclusion ($0 \leq r \leq r_p$) has the form

$$\varepsilon_r^{\text{el}} = \frac{\sigma_s(1-2\nu)}{G(1+\nu)}\ln\left(\frac{r_0}{r_p}\right). \tag{14}$$

Taking into account the elastic strains determined by relationships (13) and (14) and the inelastic dilatation of the inclusion, the dilatation δ^* can be represented in the following form:

$$\delta^* = \frac{r_0}{r_p}\delta - 3\frac{\sigma_s(1-\nu)}{G(1+\nu)}\left(1 - \frac{r_0}{r_p}\right). \tag{15}$$

From formulas (11) and (15), we find that the relative extent of the plastic zone can be described by the relationship

$$X = \frac{r_p}{r_0} = \frac{2}{9}\frac{G(1+\nu)\delta}{\sigma_s(1-\nu)} + \frac{2}{3}. \tag{16}$$

The sought expression for the volume fraction f_1, at which the boundary of the plastic zone reaches the outer surface ($r_p = R$), has the form

$$f_1 = X^{-3} = \left\{\frac{2}{9}\frac{G(1+\nu)\delta}{\sigma_s(1-\nu)} + \frac{2}{3}\right\}^{-3}. \tag{17}$$

By substituting relationship (11) into formula (10) and allowing for expression (5), we obtain

$$\begin{aligned}\sigma_0(r_0) &= -\frac{2}{3}\sigma_s(1 - X^3 f) - 2\sigma_s \ln X \\ &= \frac{2}{3}\sigma_s\left[\ln(f_1) + \frac{f}{f_1} - 1\right].\end{aligned} \tag{18}$$

Therefore, the stresses at the inclusion boundary in the volume fraction range $0 \leq f \leq f_1$ are determined by the relationships

$$\begin{gathered}\sigma_r = \sigma_\varphi = \sigma_0 = \frac{2}{3}\sigma_s\left[\ln(f_1) + \frac{f}{f_1} - 1\right], \\ 0 \leq r < r_0,\end{gathered} \tag{19}$$

$$\begin{gathered}\sigma_r = \sigma_\varphi - \sigma_s = \sigma_0 - \frac{2}{3}\sigma_s = \frac{2}{3}\sigma_s\left[\ln(f_1) + \frac{f}{f_1} - 1\right], \\ r = r_0 + 0.\end{gathered} \tag{20}$$

Note that the main results [relationships (6), (7), (19), (20)] were obtained under the assumption that the yield stress σ_s is constant, i.e., that the plasticity of the material is ideal. This assumption seems to be reasonable, because the accommodation plastic strain upon transformation does not exceed δ = 0.01–0.02 and, hence, can be disregarded from the standpoint of strain hardening. It is worth noting that the quantity δ and the elastic constants of the material affect the stresses only at small volume fractions of the inclusion ($0 \leq f \leq f_1$), because the parameter f_1 depends on these quantities.

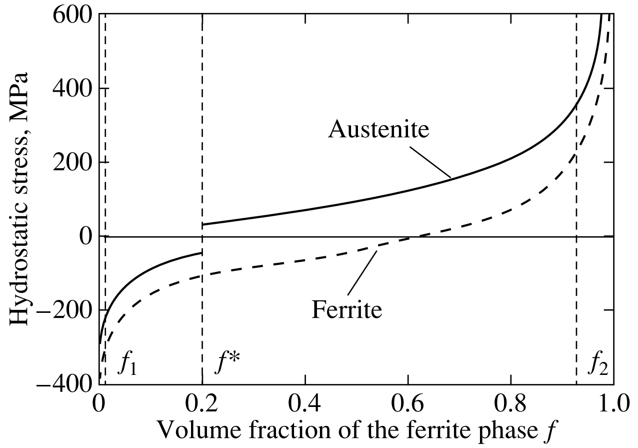

Fig. 3. Dependences of the hydrostatic phase stresses in ferrite (α phase) and austenite (γ phase) in the vicinity of the interface on the volume fraction of the ferrite.

When the volume fraction of the inclusion is large enough ($f > f_1$) for the plastic zone to reach the free surface, the stresses under consideration, according to expressions (6) and (7), at a given volume fraction f depend only on the yield stress of the matrix.

3. RESULTS OF CALCULATING THE PHASE STRESSES AND DISCUSSION

The stresses arising in the course of the transformation will be calculated from the formulas obtained in the previous section. At a volume fraction of ferrite in the range $0 \le f < f^* \approx 0.2$, when the austenite phase is continuous (Fig. 1a), the yield stress of austenite σ_s^γ should be used as σ_s in formulas (6), (7), (19), and (20). At $f^* < f \le 1$, isolated austenite regions appear to be embedded in the continuous ferrite matrix; i.e., the inelastic dilatation of inclusions changes the sign and becomes negative. In this case, it is necessary to replace σ_s by the yield stress of ferrite σ_s^α, to change the signs of all the stress components, and to use $1 - f$ (volume fraction of austenite) instead of f in the aforementioned formulas. As a result, the expressions for the phase stresses in the vicinity of the interface in the four characteristic ranges of volume fractions of ferrite take the following form:

$$\sigma_r^\alpha = \sigma_\varphi^\alpha = \sigma_0^\alpha = \frac{2}{3}\sigma_s^\gamma\left[\ln(f_1) + \frac{f}{f_1} - 1\right],$$
$$\sigma_r^\gamma = \sigma_\varphi^\gamma - \sigma_s^\gamma = \sigma_0^\gamma - \frac{2}{3}\sigma_s^\gamma \tag{21}$$
$$= \frac{2}{3}\sigma_s^\gamma\left[\ln(f_1) + \frac{f}{f_1} - 1\right]$$

for $0 \le f \le f_1$;

$$\sigma_r^\alpha = \sigma_\varphi^\alpha = \sigma_0^\alpha = \frac{2}{3}\sigma_s^\gamma\ln(f),$$
$$\sigma_r^\gamma = \sigma_\varphi^\gamma - \sigma_s^\gamma = \sigma_0^\gamma - \frac{2}{3}\sigma_s^\gamma = \frac{2}{3}\sigma_s^\gamma\ln(f) \tag{22}$$

for $f_1 \le f < f^*$;

$$\sigma_r^\gamma = \sigma_\varphi^\gamma = \sigma_0^\gamma = -\frac{2}{3}\sigma_s^\alpha\ln(1-f),$$
$$\sigma_r^\alpha = \sigma_\varphi^\alpha + \sigma_s^\alpha = \sigma_0^\alpha + \frac{2}{3}\sigma_s^\alpha = -\frac{2}{3}\sigma_s^\alpha\ln(1-f) \tag{23}$$

for $f^* \le f < f_2$; and

$$\sigma_r^\gamma = \sigma_\varphi^\gamma = \sigma_0^\gamma = -\frac{2}{3}\sigma_s^\alpha\left[\ln(1-f) + \frac{f - f_2}{f_2 - 1}\right],$$
$$\sigma_r^\alpha = \sigma_\varphi^\alpha + \sigma_s^\alpha = \sigma_0^\alpha + \frac{2}{3}\sigma_s^\alpha \tag{24}$$
$$= -\frac{2}{3}\sigma_s^\alpha\left[\ln(1-f) + \frac{f - f_2}{f_2 - 1}\right]$$

for $f_2 \le f \le 1$. The values of f_1 and $(1 - f_2)$ are determined from expression (17) at $\sigma_s = \sigma_s^\gamma$ and $\sigma_s = \sigma_s^\alpha$, respectively.

Now, we quantitatively estimate the phase stresses from the relationships derived. As follows from formulas (21)–(24) and (17), doing this requires that the yield stresses and the shear moduli of the phases in the temperature range of the $\gamma \longrightarrow \alpha$ transformation be determined. The flow stresses can be estimated from the Ashby deformation maps [7] for polycrystalline iron and the low-alloy steel. In the transition temperature range (700–800°C), we have $\sigma_s^\gamma \approx 100$ MPa and $\sigma_s^\alpha \approx 200$ MPa at strain rates of 10^{-4}–10^{-3} s^{-1}. Note that the local flow stresses of the phases can turn out to be higher than the aforementioned macroscopic yield stresses. Therefore, the case in point is the lower bound estimate. The shear moduli can be obtained from the experimental data on the temperature dependences of the Young modulus for ferrite and austenite [8]. At the Poisson ratio $\nu = 0.3$, we find the following shear moduli of the phases at 750°C: $G^\gamma = 5.7 \times 10^4$ MPa and $G^\alpha = 6.0 \times 10^4$ MPa. The volume effect of the transformation δ is assumed to be equal to 0.015 [1].

The volume fractions f_1 and f_2 calculated from formula (17) are equal to 1.3 and 94%, respectively. This means that the phase stresses can be calculated from relationships (22) and (23) virtually over the entire range of transformation fractions.

The evolution of the hydrostatic stresses in the vicinity of the interface in the course of the $\gamma \longrightarrow \alpha$ transformation is illustrated in Fig. 3. The jumps in the stresses at $f = f^*$ result from the use of the simplifying assumption regarding the spherical shape of ferrite regions up to their coalescence into the continuous matrix. However, it should be noted that the stress jump is pronounced for the austenite phase and insignificant for the ferrite phase. It can be seen from Fig. 3 that, at the initial stage, both phases are subjected to considerable hydrostatic compression. However, once the continuous ferrite matrix is formed, isolated austenite regions appear to be in the state of hydrostatic tension. During the transformation, the stresses increase and exceed the yield stress of ferrite at the final stage ($f > 0.8$). The hydrostatic stresses in ferrite remain compressive approximately half-way through the transformation and change sign only at $f \approx 0.6$. Note that significant gradients of hydrostatic stresses occur in the course of the transformation and can induce vacancy flows and, hence, additional relaxation of phase stresses. However, such effects call for separate consideration.

Let us evaluate how the phase stresses affect the effective driving force of the transformation $\Delta G^{*}_{\gamma\to\alpha}$ with due regard for the work A_σ done by the hydrostatic stresses in austenite due to the volume effect of the transformation. The effective driving force can be written in the following form:

$$\Delta G^{*}_{\gamma\to\alpha} = \Delta G^{\mathrm{ch}}_{\gamma\to\alpha} + A_\sigma = \Delta G^{\mathrm{ch}}_{\gamma\to\alpha} + \sigma_0^\gamma\delta, \qquad (25)$$

where $\Delta G^{\mathrm{ch}}_{\gamma\to\alpha}$ is the chemical driving force ($\Delta G^{\mathrm{ch}}_{\gamma\to\alpha} < 0$) and σ_0^γ is the hydrostatic stress in austenite in the vicinity of the interface. Taking into account the behavior of σ_0^γ during the transformation (the upper curve in Fig. 3), from analysis of expression (25), we can make the inference that the stresses under consideration retard the initial stage of the transformation ($f < f^*$) and, conversely, promote the transformation at the intermediate and final stages ($f > f^*$).

The magnitude of the effect can be estimated from the calculated data taken from [4] on the chemical driving forces in an alloy Fe + 2% Mn. At a cooling rate of 0.5 K/s, we have $\Delta G^{\mathrm{ch}}_{\gamma\to\alpha}(f = 0.1) \approx -31$ J/mol and $\Delta G^{\mathrm{ch}}_{\gamma\to\alpha}(f = 0.9) \approx -123$ J/mol. On the other hand, at $\delta = 0.015$, the works of the hydrostatic stresses at the corresponding volume fractions of ferrite are determined to be $A_\sigma(f = 0.1) \approx 22$ J/mol and $A_\sigma(f = 0.9) \approx 35$ J/mol. According to the above estimates, the relative contributions of the phase stresses to the effective driving force of the transformation ($A_\sigma/|\Delta G^{\mathrm{ch}}_{\gamma\to\alpha}|$) are approximately equal to 70 and 30% for ferrite volume fractions of 10 and 90%, respectively.

4. CONCLUSIONS

Thus, the phase stresses considered in this work can substantially affect the kinetics of the $\gamma \longrightarrow \alpha$ transformation and, therefore, should be taken into account in quantitative simulations of this transformation.

REFERENCES

1. B. Ya. Lyubov, *The Kinetic Theory of Phase Transformations* (Metallurgiya, Moscow, 1969) [in Russian].
2. A. Rizk and D. L. Bourell, Scr. Metall. **50**, 1321 (1982).
3. N. C. Goel, S. Sangal, and K. Tangri, Metall. Trans. A **16** (11), 2013 (1985).
4. A. T. W. Kempen, F. Sommer, and E. J. Mittemeijer, Acta Mater. **50**, 3545 (2002).
5. L. M. Kachanov, *Foundations of the Theory of Plasticity* (Nauka, Moscow, 1969; North-Holland, Amsterdam, 1971).
6. C. Teodosiu, *Elastic Models of Crystal Defects* (Springer-Verlag, Berlin, 1982; Mir, Moscow, 1985); in *Continuous Theory of Dislocations* (Inostrannaya Literatura, Moscow, 1963).
7. H. J. Frost and M. F. Ashby, *Deformation-Mechanisms Maps* (Pergamon, New York, 1982; Metallurgiya, Chelyabinsk, 1989).
8. *A Handbook of Physical Metallurgy: Steel*, Ed. by M. L. Bernshteĭn (Metallurgiya, Moscow, 1995), Vols. 1, 2 [in Russian].

Translated by O. Borovik-Romanova

Physics of the Solid State, Vol. 46, No. 11, 2004, pp. 2126–2133. Translated from Fizika Tverdogo Tela, Vol. 46, No. 11, 2004, pp. 2056–2063.
Original Russian Text Copyright © 2004 by Chkhartishvili.

Quasi-Classical Estimates of the Lattice Constant and Band Gap of a Crystal: Two-Dimensional Boron Nitride

L. S. Chkhartishvili
Georgian Technical University, ul. M. Kostava 77, Tbilisi, 0175 Georgia
e-mail: chkharti2003@yahoo.com

Received January 20, 2004

Abstract—The quasi-classical method for estimating the structural and energy parameters of crystals is justified. In the initial approximation, the charge-density and potential distributions are represented by step functions. As a result, the energy of the ground state of the crystal and the matrix elements of the secular equation determining its electronic structure can be expressed through finite sums. This approach makes it possible to avoid uncontrollable errors introduced in the truncation of infinite series, and the error of the approach itself does not exceed a few percent. The lattice constant $a = 2.64$ Å and the band gap $E_g = 6.22$ eV for two-dimensional boron nitride are determined by the quasi-classical method. *© 2004 MAIK “Nauka/Interperiodica”.*

1. INTRODUCTION

The development of theoretical approaches that do not require considerable computational effort but provide a reasonable accuracy in the prediction of physical parameters is particularly important for the study of materials that form different structural modifications. This is especially true for boron nitride. Boron nitride can exist in the form of diatomic molecules; two-dimensional nanotubes and fullerene-like structures; three-dimensional hexagonal (*h*-BN), rhombohedral (*r*-BN), cubic sphalerite-like (*c*-BN), and wurtzite-like (*w*-BN) crystals; and amorphized films. A number of structural and energy characteristics of BN molecules [1, 2] and *h*-BN [2, 3], *c*-BN [4], and *w*-BN [5] crystals were calculated by a new method based on the use of the quasi-classical approximation. In the present work, this approach was used to predict the lattice constant and the band gap of a two-dimensional infinite layer that has the lowest molar energy among the two-dimensional structures formed by boron nitride. Investigation of this hypothetical object is of special interest because the structures of *h*-BN and *r*-BN crystals are formed by similar layers and, moreover, fullerene molecules and nanotubes are bounded by flat or curved fragments of such a layer.

This paper consists of three sections. In Section 2, we justify the quasi-classical method. In Section 3, we calculate the binding energy and the density of states for a two-dimensional boron nitride crystal within the initial quasi-classical approximation and compare the estimated structural and energy parameters with the relevant data available in the literature for other modifications of boron nitride.

2. THE QUASI-CLASSICAL METHOD FOR CALCULATING THE CRYSTAL STRUCTURE AND ELECTRONIC STRUCTURE

2.1. Matter as a Quasi-Classical Electronic System

Since the advent of the Bohr model for a hydrogen atom, semiclassical models of light atoms have been constructed to advantage [6]. The effectiveness of this approach to the description of the periodic motion of electrons in small-sized molecules was demonstrated by Popa [7]. For many-electron systems, a reasonable accuracy can be achieved in terms of the self-consistent field approximation within which an extremum of the total energy is sought in the class of quasi-classical wave functions [8]. As is known, heavy atoms can be calculated in the framework of the density-functional theory using a quasi-classical expansion of the energy functional. A similar method appears to be appropriate for atomic clusters and condensed phases [9].

However, atomic, molecular, and crystal potentials do not satisfy the standard Wentzel–Kramers–Brillouin quasi-classical condition due to singularities at nuclear sites and electron shell effects. The success of the above approaches can be explained on the basis of the quasi-classical expressions obtained by Maslov [10] for the energies of bound electron states. It follows from these expressions that the exact and Wentzel–Kramers–Brillouin spectra are similar to each other irrespective of the potential smoothness at $2\Phi_0 R_0^2 \gg 1$, where Φ_0 and R_0 are the characteristic values of the potential and its effective range, respectively (hereafter, all relationships will be given in the atomic system of units).

Since atomic orbitals at long distances are characterized by an exponential decay, the use of the modified Thomas–Fermi models makes it possible to parametrize the electron density distribution in an atom by introducing the atomic radius $R < \infty$ (which is considerably larger than the Bohr radius, i.e., $R \gg 1$) such that, at larger distances, the electron density is assumed to be zero [11]. This is equivalent to the initial approximation in quasi-classical atomic models where the partial electron densities are ignored in classically forbidden regions. The potential $\Phi_i(r)$ of the effective field acting on the ith electron in the atom with the number $Z \geq 1$ can be represented in the form $\Phi_i(r) = (Z/R)F_i(r/R)/(r/R)$, where $0 \leq r \leq R$ is the distance from the center and $0 \leq F_i(r/R) \leq 1$ is the factor that characterizes screening of the nucleus by the other electrons. Consequently, we have $\Phi_0 \sim Z/R$ and $R_0 \sim R$, and the quasi-classicality condition for the electron energy spectrum of the atom takes the form $2ZR \gg 1$. Therefore, atoms and the molecules and crystals formed by the atoms are actually quasi-classical electronic systems in accordance with the Maslov criterion.

2.2. Quasi-Classical Parametrization of the Electron Density and Potential Distributions in an Atom

The potential energy of the ith electron (with energy $E_i < 0$ and orbital quantum number l_i) is equal to $-\Phi_i(r)$. Therefore, the radii r_i' and r_i'' of the classical turning points ($r_i' < r_i''$) can be found as the roots of the equation $E_i = -\Phi_i(r) + l_i(l_i + 1)/2r^2$ ($i = 1, 2, 3, \ldots, Z$).

Let $\tilde{\Phi}_i(r)$ be the potential of the field induced by the ith electron. Then, the potential of the field induced by the electron cloud of the atom can be written as the sum of the potentials $\tilde{\Phi}_i(r)$; that is,

$$\tilde{\Phi}(r) = \sum_{i=1}^{Z} \tilde{\Phi}_i(r). \tag{1}$$

The potential of the field acting on an arbitrary ith electron of the atom is equal to the sum of the potentials of the Coulomb field of the nucleus and the field induced by all the electrons of the atom, except for the potential of the field of the electron under consideration:

$$\begin{gathered} \Phi_i(r) = Z/r + \tilde{\Phi}(r) - \tilde{\Phi}_i(r), \\ i = 1, 2, 3, \ldots, Z. \end{gathered} \tag{2}$$

Now, we sum up these potentials over electrons. As a result, the terms independent of the number of the electron on the right-hand sides are multiplied by the total number Z of electrons in the atom and the sum of the potentials $\tilde{\Phi}_i(r)$ gives $\tilde{\Phi}(r)$. The solution of the obtained equation with respect to $\tilde{\Phi}(r)$ has the form

$$\tilde{\Phi}(r) = -\frac{1}{Z-1}\left(\frac{Z^2}{r} - \sum_{i=1}^{Z} \Phi_i(r)\right). \tag{3}$$

This relationship makes it possible to determine the potential energy $Z\tilde{\Phi}(r)$ of the interaction between the nucleus of the atom and the electron cloud. Since, in the ground state, their relative motion corresponds to a zero orbital quantum number, the radius of one classical turning point for this system is equal to zero and the radius $\tilde{r}$ of another classical turning point is the root of the equation $\tilde{E} = Z\tilde{\Phi}(r)$, where $\tilde{E}$ is the eigenvalue of the energy associated with the relative motion of the electron cloud and the nucleus.

The quasi-classical parametrization of the electron density and potential distributions in the atom can be performed in analytical form if the effective fields acting on the electrons are represented by Coulomb-like potentials $\Phi_i(r) = Z_i/r$, where $Z_i = n_i\sqrt{-2E_i}$ are the effective charges dependent on the principal quantum numbers n_i of the states. As a result, we obtain

$$\begin{aligned} r_i' &= \left(n_i - \sqrt{n_i^2 - l_i(l_i+1)}\right)/\sqrt{-2E_i}, \\ r_i'' &= \left(n_i + \sqrt{n_i^2 - l_i(l_i+1)}\right)/\sqrt{-2E_i}. \end{aligned} \tag{4}$$

In this case, the effective field of the interaction between the nucleus and the electron cloud also turns out to be a Coulomb-like field. Then, under the assumption that the nucleus has an infinite mass and, hence, is stationary (i.e., the reduced mass of the nucleus–electron cloud system is equal to the total mass of Z electrons in the atom), the radius of the turning point for the motion of the electron cloud with respect to the nucleus is given by the formula

$$\tilde{r} = \frac{2(Z-1)}{Z^2\left(Z^2 - \sum_{i=1}^{Z} Z_i\right)^2}. \tag{5}$$

The initial quasi-classical approximation implies that exponentially decaying partial electron densities are disregarded in the classically forbidden regions and that oscillations of these densities are ignored in classically allowed regions. As a result, the radial dependence of the direction-averaged partial charge density of the ith electron state in the atom is represented by a piecewise constant function, which is equal to zero in the classically forbidden regions:

$$\rho_i(r) = \begin{cases} 0, & r < r_i', \\ -3/4\pi(r_i''^3 - r_i'^3), & r_i' \leq r \leq r_i'' \\ 0, & r_i'' < r. \end{cases} \tag{6}$$

A similar averaging for the motion of the electron cloud as a whole with respect to the nucleus is equivalent to averaging the nuclear charge over a sphere of radius $\tilde{r}$; that is,

$$\tilde{\rho}(r) = \begin{cases} 3Z/4\pi\tilde{r}^3, & 0 \le r \le \tilde{r} \\ 0, & \tilde{r} < r. \end{cases} \tag{7}$$

Summation of similar contributions gives the distribution of the total density of the electric charge in the atom in the form of a step radial function,

$$\rho(r) = \tilde{\rho}(r) + \sum_{i=1}^{Z} \rho_i(r) = \rho_k, \qquad r_{k-1} \le r < r_k, \quad k = 1, 2, 3, \dots, q, \tag{8}$$

where ρ_k are constants determined from the radii of the classical turning points and r_k coincide with these radii. Here, $0 \equiv r_0 < r_1 < r_2 < \dots < r_q < r_{q+1} < \infty$, $q \le 2Z$ is the number of layers with uniform charge densities, and r_q plays the role of the quasi-classical atomic radius (the charge density is equal to zero at $r > r_q$). Mathematically, this representation is equivalent to the volume averaging in layers $r_{k-1} \le r < r_k$.

Next, we calculate the fields induced by the charged layers with densities ρ_k on the basis of the Gauss theorem and sum these fields. Then, the atomic potential can be written in the form of the continuously differentiable piecewise analytical function

$$\begin{gathered} \varphi(r) = a_k/r + b_k r^2 + c_k, \quad r_{k-1} \le r \le r_k, \\ a_k = \sum_{i=1}^{k-1} 4\pi\rho_i(r_i^3 - r_{i-1}^3)/3 - 4\pi\rho_k r_{k-1}^3/3, \\ b_k = -2\pi\rho_k/3, \\ c_k = \sum_{i=k+1}^{q} 2\pi\rho_i(r_i^2 - r_{i-1}^2) + 2\pi\rho_k r_k^2. \end{gathered} \tag{9}$$

However, since the energy of the electronic system is a single-valued functional of the electron density, it is expedient to approximate the above potential by a step function. This can be adequately performed by averaging over the volume:

$$\varphi(r) \approx \frac{3a_k(r_k^2 - r_{k-1}^2)}{2(r_k^3 - r_{k-1}^3)} + \frac{3b_k(r_k^5 - r_{k-1}^5)}{5(r_k^3 - r_{k-1}^3)} + c_k = \varphi_k, \qquad r_{k-1} \le r < r_k. \tag{10}$$

2.3. *Quasi-Classical Energy of a Crystal in the Ground State*

Let us assume that $\mathbf{d}_{(i)}$ are the basis vectors of a unit cell of a crystal. In this case, the point $\mathbf{d}_{(i)} + \mathbf{t}$ corresponds to the equilibrium position of the center of an (i)-type atom belonging to the unit cell with translational vector $\mathbf{t}$. Therefore, the total density of the nuclear and electronic charge in the atom and the total density of the potential of the field induced by this charge at the point $\mathbf{r}$ in the adiabatic approximation can be represented by the functions $\rho_{(i)}(\mathbf{r} - \mathbf{d}_{(i)} - \mathbf{t})$ and $\varphi_{(i)}(\mathbf{r} - \mathbf{d}_{(i)} - \mathbf{t})$. The potential energy of the (t)th atom of the central unit cell ($\mathbf{t} = 0$) can be calculated as 1/2 of the volume integral of the product of the corresponding charge density $\rho_{(i)}(\mathbf{r} - \mathbf{d}_{(i)})$ into the superposition of the potentials $\varphi_{(k)}(\mathbf{r} - \mathbf{d}_{(k)} - \mathbf{t})$ for all (k)th atoms of the crystal. The subsequent summation over the basis of the central unit cell with N atoms gives the potential energy of the cell. When calculating the static energy of the crystal (which is the system with Coulomb interaction) per unit cell, one more factor of 1/2 appears according to the virial theorem; that is,

$$E_{\text{stat}} = \frac{1}{4}\sum_{\mathbf{t}} \sum_{(i)=1}^{N} \sum_{(k)=1}^{N} \int d\mathbf{r}\, \rho_{(i)}(\mathbf{r} - \mathbf{d}_{(i)})\varphi_k(\mathbf{r} - \mathbf{d}_{(k)} - \mathbf{t}). \tag{11}$$

Let $r_{(i)j}$ ($j = 1, 2, 3, \dots, q_{(i)}$) be the outer radii of uniform layers in the (i)th atom ($q_{(i)}$ is the number of layers). Then, the volume of the intersection of the jth layer in the (i)th atom of the central unit cell with the lth layer in the (k)th atom of the cell displaced by the vector $\mathbf{t}$ is given by the formula

$$\begin{gathered} V_{(ik)jl}(r_{(ik)\mathbf{t}}) = V(r_{(i)j}, r_{(k)l}, r_{(ik)\mathbf{t}}) \\ + V(r_{(i)j-1}, r_{(k)l-1}, r_{(ik)\mathbf{t}}) - V(r_{(i)j}, r_{(k)l-1}, r_{(ik)\mathbf{t}}) \\ - V(r_{(i)j-1}, r_{(k)l}, r_{(ik)\mathbf{t}}). \end{gathered} \tag{12}$$

Here, $\mathbf{r}_{(ik)\mathbf{t}} = \mathbf{d}_{(k)} + \mathbf{t} - \mathbf{d}_{(i)}$ is the radius vector of the (i)th atom with respect to the (k)th atom and $V(R_1, R_2, D_{12})$ is the universal continuously differentiable piecewise analytical algebraic function determining the volume of the intersection of two spheres with radii R_1 and R_2 whose centers are spaced at D_{12} (this function was derived in an explicit form in [12] when formulating the problem regarding the quasi-classical calculation of the band structure of a crystal). By introducing the charge density $\rho_{(i)j}$ and the potential density $\varphi_{(i)j}$ in the atomic layers, the static energy of the unit cell of the crystal within the initial quasi-classical approximation can be written in the following form:

$$E_{\text{stat}} = \frac{1}{4}\sum_{\mathbf{t}} \sum_{(i)=1}^{N} \sum_{(k)=1}^{N} \sum_{j=1}^{q_{(i)}} \sum_{l=1}^{q_{(k)}} \rho_{(i)j}\varphi_{(k)l}V_{(ik)jl}(\mathbf{r}_{(ik)\mathbf{t}}). \tag{13}$$

If the interacting atoms are fixed at their sites (this is equivalent to the time averaging of their vibrations), the potential energy of the (i)th atom of the central unit cell displaced by the vector **t** from the equilibrium position is defined as

$$U_{(i)}(\mathbf{r}) = \frac{1}{2}\sum_{\mathbf{t}}{}' \sum_{(k)=1}^{N} \int d\mathbf{r}' \big(\rho_{(i)}(\mathbf{r}' - \mathbf{d}_{(i)} - \mathbf{r})\varphi_{(k)}(\mathbf{r}' - \mathbf{d}_{(k)} - \mathbf{t}) + \rho_{(k)}(\mathbf{r}' - \mathbf{d}_{(k)} - \mathbf{t})\varphi_{(i)}(\mathbf{r}' - \mathbf{d}_{(i)} - \mathbf{r})\big). \quad (14)$$

The prime on the summation sign indicates that the term with $\mathbf{t} = 0$ and $(k) = (i)$ is omitted. The above formula is symmetrized with respect to the contributions of interacting charges, because the approximations not related by the Poisson equation were used upon quasi-classical parametrization of the charge and potential densities.

The central-field approximation for the constituent atoms permits us to represent the aforementioned potential energy as the sum of the contributions that depend only on the squares of the distances from the point $\mathbf{r} + \mathbf{d}_{(i)}$ to the point $\mathbf{d}_{(k)} + \mathbf{t}$; that is,

$$U_{(i)}(\mathbf{r}) = \sum_{\mathbf{t}}{}' \sum_{(k)=1}^{N} U_{(ik)\mathbf{t}}(r_{(ik)\mathbf{t}}^2 - 2r_{(ik)\mathbf{t}}\mathbf{r} + r^2). \quad (15)$$

In order to estimate the energy of small-amplitude lattice vibrations, we expand each contribution into a power series of the variable parts of the arguments and retain only constant and linear terms. In these series, the terms responsible for the vibrations are as follows:

$$U_{(i)\mathrm{vibr}}(r) = \frac{1}{2}\sum_{\mathbf{t}}{}' \sum_{(k)=1}^{N} \frac{dU_{(ik)\mathbf{t}}(r_{(ik)\mathbf{t}})}{dr_{(ik)\mathbf{t}}} \frac{\mathbf{r}^2}{r_{(ik)\mathbf{t}}}. \quad (16)$$

In quasi-classical schemes, the pair potential energies $U_{(ik)\mathbf{t}}(r_{(ik)\mathbf{t}})$ are linear combinations of the functions $V(r_{(i)j}, r_{(k)l}, r_{(ik)\mathbf{t}})$, which determine the volumes of the intersection of the layers with uniform charge and potential densities in the interacting atoms. Consequently, the frequencies of lattice vibrations are expressed through the partial derivatives $\partial V(R_1, R_2, D_{12})/\partial D_{12}$. Specifically, if $M_{(i)}$ is the mass of the (i)th atom, the molar energy of zero-point vibrations in the crystal can be written in the form

$$E_{\mathrm{vibr}} = \frac{3}{2}\sum_{(i)=1}^{N} \sqrt{\sum_{\mathbf{t}}{}' \sum_{(k)=1}^{N} \sum_{j=1}^{q_{(i)}} \sum_{l=1}^{q_{(k)}} \frac{\rho_{(i)j}\varphi_{(k)l} + \rho_{(k)l}\varphi_{(i)j}}{2M_{(i)}r_{(ik)\mathbf{t}}} \frac{\partial V_{(ik)jl}(r_{(ik)\mathbf{t}})}{\partial r_{(ik)\mathbf{t}}}}. \quad (17)$$

2.4. Quasi-Classical Calculation of the Electronic Structure of a Crystal

In the initial quasi-classical approximation, the potentials $\varphi_{(\kappa)}(|\mathbf{r} - \mathbf{d}_{(\kappa)} - \boldsymbol{\tau}|)$ $[(\kappa) = 1, 2, 3, \ldots, N]$ of the atoms forming the crystal are expressed through radial step functions with centers at the lattice sites. The crystal potential

$$\varphi(\mathbf{r}) = \sum_{\boldsymbol{\tau}} \sum_{(\kappa)=1}^{N} \varphi_{(\kappa)}(|\mathbf{r} - \mathbf{d}_{(\kappa)} - \boldsymbol{\tau}|), \quad (18)$$

which is represented as their superposition, is a three-dimensional piecewise constant function. Here, (κ) and $\boldsymbol{\tau}$ are the indices of summation over the atoms of the unit cell and the unit cells of the crystal, respectively. In the same approximation, the basis functions for the LCAO (linear combination of atomic orbitals) method can be approximated by the square roots of the partial electron densities: $\psi_{(i)j}(|\mathbf{r} - \mathbf{d}_{(i)} - \mathbf{t}|) = \sqrt{-\rho_{(i)j}(|\mathbf{r} - \mathbf{d}_{(i)} - \mathbf{t}|)}$. These functions differ from zero only in the corresponding classically allowed regions $r'_{(i)j} \le |\mathbf{r} - \mathbf{d}_{(i)} - \mathbf{t}| \le r''_{(i)j}$ [$r'_{(i)j}$ and $r''_{(i)j}$ are the radii of the inner and outer classical turning points for the jth electron of the (i)th atom, respectively; $j = 1, 2, 3, \ldots, Z_{(i)}$; $Z_{(i)}$ is the charge number of the atom]. Undeniably, such a basis set does not represent the angular dependence and a sign-changing character of the atomic orbitals but provides the calculation of the electron density distribution in the atom within the initial quasi-classical approximation.

The matrix elements of the one-electron Hamiltonian H of the crystal

$$H_{(i)j(k)l}(\mathbf{p}) = -\frac{3}{4\pi}\sum_{\mathbf{t}}\sum_{\boldsymbol{\tau}}\sum_{(\kappa)=1}^{N}\sum_{\lambda=1}^{q_{(\kappa)}} \frac{\varphi_{(\kappa)\lambda}V_{(ik\kappa)jl\lambda}(r_{(ik)\mathbf{t}}, r_{(i\kappa)\boldsymbol{\tau}}, r_{(k\kappa)\mathbf{t}-\boldsymbol{\tau}})}{\sqrt{(r''^3_{(i)j} - r'^3_{(i)j})(r''^3_{(k)l} - r'^3_{(k)l})}} \exp(i\mathbf{p}\mathbf{t}) \quad (19)$$

between the Bloch sums of the aforementioned piecewise constant basis functions are reduced to the matrix elements of the potential energy of the electron $\varphi(\mathbf{r})$ and can be written as linear combinations of the volumes of the intersections of triads of the spheres centered at the lattice sites with radii equal to the radii of

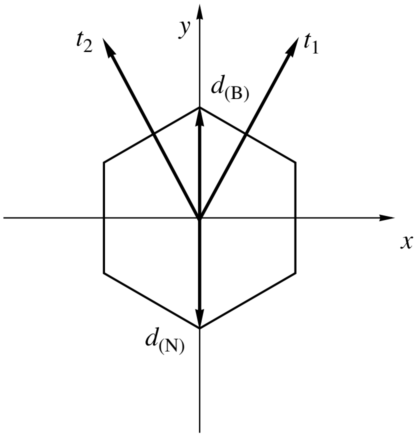

Fig. 1. Crystal structure of two-dimensional boron nitride.

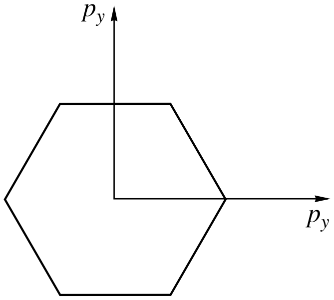

Fig. 2. The first Brillouin zone of two-dimensional boron nitride.

the classical turning points for particles in the atoms forming the crystal. Here, **p** is the electron quasi-momentum and

$$
\begin{aligned}
& V_{(ik\kappa)jl\lambda}(r_{(ik)\mathbf{t}}, r_{(i\kappa)\boldsymbol{\tau}}, r_{(k\kappa)\mathbf{t}-\boldsymbol{\tau}}) \\
&= V(r_{(i)j}, r_{(k)l}, r_{(\kappa)\lambda}, r_{(ik)\mathbf{t}}, r_{(i\kappa)\boldsymbol{\tau}}, r_{(k\kappa)\mathbf{t}-\boldsymbol{\tau}}) \\
&+ V(r_{(i)j}, r_{(k)l-1}, r_{(\kappa)\lambda-1}, r_{(ik)\mathbf{t}}, r_{(i\kappa)\boldsymbol{\tau}}, r_{(k\kappa)\mathbf{t}-\boldsymbol{\tau}}) \\
&+ V(r_{(i)j-1}, r_{(k)l}, r_{(\kappa)\lambda-1}, r_{(ik)\mathbf{t}}, r_{(i\kappa)\boldsymbol{\tau}}, r_{(k\kappa)\mathbf{t}-\boldsymbol{\tau}}) \\
&+ V(r_{(i)j-1}, r_{(k)l-1}, r_{(\kappa)\lambda}, r_{(ik)\mathbf{t}}, r_{(i\kappa)\boldsymbol{\tau}}, r_{(k\kappa)\mathbf{t}-\boldsymbol{\tau}}) \qquad (20) \\
&- V(r_{(i)j-1}, r_{(k)l}, r_{(\kappa)\lambda}, r_{(ik)\mathbf{t}}, r_{(i\kappa)\boldsymbol{\tau}}, r_{(k\kappa)\mathbf{t}-\boldsymbol{\tau}}) \\
&- V(r_{(i)j}, r_{(k)l-1}, r_{(\kappa)\lambda}, r_{(ik)\mathbf{t}}, r_{(i\kappa)\boldsymbol{\tau}}, r_{(k\kappa)\mathbf{t}-\boldsymbol{\tau}}) \\
&- V(r_{(i)j}, r_{(k)l}, r_{(\kappa)\lambda-1}, r_{(ik)\mathbf{t}}, r_{(i\kappa)\boldsymbol{\tau}}, r_{(k\kappa)\mathbf{t}-\boldsymbol{\tau}}) \\
&- V(r_{(i)j-1}, r_{(k)l-1}, r_{(\kappa)\lambda-1}, r_{(ik)\mathbf{t}}, r_{(i\kappa)\boldsymbol{\tau}}, r_{(k\kappa)\mathbf{t}-\boldsymbol{\tau}})
\end{aligned}
$$

is the volume of the intersection of the jth layer in the (i)th atom with the lth layer in the (k)th atom and the λth layer in the (κ)th atom of the unit cells, which are displaced by the vectors **t** and $\boldsymbol{\tau}$, respectively. In the above expressions, $V(R_1, R_2, R_3, D_{12}, D_{13}, D_{23})$ is a universal function that determines the volume of the intersection of three spheres with radii R_1, R_2, and R_3 whose centers are spaced at D_{12}, D_{13}, and D_{23}. This function is a continuously differentiable piecewise analytical combination of algebraic and inverse trigonometric functions (the corresponding geometric problem was solved in an explicit form in [13]).

The elements of the matrix S of the overlap integrals between the Bloch sums of the piecewise constant basis functions can be represented in the form

$$
\begin{aligned}
& S_{(i)j(k)l}(\mathbf{p}) \\
&= -\frac{3}{4\pi}\sum_{\mathbf{t}} \frac{V_{(ik)jl}(r_{(ik)\mathbf{t}})}{\sqrt{(r''^3_{(i)j} - r'^3_{(i)j})(r''^3_{(k)l} - r'^3_{(k)l})}} \exp(i\mathbf{p}\mathbf{t}). \qquad (21)
\end{aligned}
$$

Now, the dispersion laws $E = E(\mathbf{p})$ for the electron energy bands and the density of states can be determined by solving the secular equation $\det(H - ES) = 0$ with the use of the parameters $\rho_{(i)j}$ and $\varphi_{(i)j}$ for individual atoms as the initial approximation for these parameters in the self-consistent procedure.

It should be emphasized that, within the initial quasi-classical approximation, the matrix elements of the secular equation determining the electronic structure of the crystal and its ground-state energy are given by sums containing a finite number of nonzero terms due to the finiteness of atomic radii. For this reason, the

Quasi-classical parameters of the charge-density and potential distributions in boron and nitrogen atoms (in atomic units)

j	$r_{(\mathrm{B})j}$	$\rho_{(\mathrm{B})j}$	$\varphi_{(\mathrm{B})j}$	$r_{(\mathrm{N})j}$	$\rho_{(\mathrm{N})j}$	$\varphi_{(\mathrm{N})j}$
1	2.759×10^{-2}	$+5.687 \times 10^{4}$	2.105×10^{2}	9.446×10^{-3}	$+1.983 \times 10^{6}$	8.785×10^{2}
2	5.098×10^{-1}	-3.611	8.882	3.577×10^{-1}	-1.045×10	2.023×10
3	7.441×10^{-1}	-7.342×10^{-3}	3.653	5.498×10^{-1}	-1.939×10^{-2}	8.465
4	4.021	-1.028×10^{-2}	2.061×10^{-1}	2.909	-4.127×10^{-2}	5.097×10^{-1}
5	4.337	-2.941×10^{-3}	6.135×10^{-4}	3.204	-2.188×10^{-2}	3.993×10^{-3}

approach under consideration is free of the uncontrollable errors that arise in the truncation of infinite series.

3. CALCULATION OF STRUCTURAL AND ELECTRONIC CHARACTERISTICS FOR A TWO-DIMENSIONAL BORON NITRIDE CRYSTAL IN THE INITIAL QUASI-CLASSICAL APPROXIMATION

3.1. Crystal Structure of Two-Dimensional Boron Nitride and Quasi-Classical Parameters of Its Constituent Atoms

A two-dimensional boron nitride crystal is represented as a planar layer composed of regular hexagons with vertices alternately occupied by boron and nitrogen atoms (Fig. 1). In this crystal, $\mathbf{t}_1 = a(1/2, \sqrt{3}/2)$ and $\mathbf{t}_2 = a(-1/2, \sqrt{3}/2)$ are the basis vectors, where a is the lattice constant determined as the shortest distance between like atoms. The bond lengths between the adjacent unlike atoms are equal to $d = a/\sqrt{3}$. The unit cell contains one B atom and one N atom with radius vectors $\mathbf{d}_{(\mathrm{B})} = a(0, 1/\sqrt{3})$ and $\mathbf{d}_{(\mathrm{N})} = a(0, -1/\sqrt{3})$ with respect to the center of the corresponding hexagon. The first Brillouin zone of two-dimensional boron nitride is also hexagonal in shape (Fig. 2).

The quasi-classical parameters (necessary for calculations) for individual boron and nitrogen atoms were calculated within the scheme of Coulomb-like effective atomic potentials (see table). The quasi-classical radii were determined to be $R_{(\mathrm{B})} = 2.30$ Å and $R_{(\mathrm{N})} = 1.70$ Å.

3.2. Quasi-Classical Binding Energy of Two-Dimensional Boron Nitride

The molar binding energy E_{bind} for two-dimensional boron nitride in the initial quasi-classical approximation was calculated as the difference between the sum of the energies of individual boron and nitrogen atoms and the sum of the static and vibrational energies per unit cell. The calculated dependence of the binding energy on the lattice constant (Fig. 3) exhibits a maximum $E_{\mathrm{bind}} = 23.0$ eV at the lattice constant $a = 2.64$ Å, which should correspond to the equilibrium state for an isolated layer. The correction introduced by zero-point vibrations was estimated as $E_{\mathrm{vibr}} = 0.242$ eV.

It is expedient to analyze the correctness of these predictions (obtained in terms of the quasi-classical approach) by comparing them with the data available in the literature on the cohesion characteristics of *h*-BN layered crystals. As follows from the standard thermochemical data, the binding energy of *h*-BN is equal to 13.0 eV [14]. The binding energies of 14.5, 16.0, and 14.4 eV were determined from semiempirical calculations performed using two variants of the LCAO method and an approach based on a periodic small-sized cluster [15]. Within the model potential of a classical force field, the lower semiempirical estimate of 11.5 eV was obtained in [16]. In the framework of the density-functional theory, optimization of the structural parameters led to the theoretical binding energy of 12.5 eV [17]. Therefore, it should be expected that the molar binding energy for *h*-BN layered crystals lies in the range from 11.5 to 16.0 eV. The binding energy $E_{\mathrm{bind}} = 23.0$ eV obtained by the quasi-classical method for the isolated layer is considerably higher. However, when comparing these energies, it should be taken into account that interlayer bonds are substantially weaker than intralayer bonds and that each atom in layered boron nitride structures is involved in the formation of five bonds, of which only three bonds are intralayer bonds. Consequently, if the interlayer energy is ignored as compared to the intralayer energy, we can assume that the molar binding energy of similar modifications is equal to 3/5 of the molar binding energy of the isolated layer. With the use of our result (23.0 eV), we find the binding energy of 13.8 eV for layered boron nitride crystals. This energy is close to the midpoint of the aforementioned energy range. On the other hand, the vibrational energies of the isolated layer and layered crystals can be directly compared, because the atoms of the low-dimensional system can execute vibrations in three independent directions in the physical space. Our quasi-classical result $E_{\mathrm{vibr}} = 0.242$ eV for two-dimensional boron nitride agrees well with the semiempirical estimate of 0.225 eV for the energy of zero-point vibrations in *h*-BN [16] and coincides in order of magnitude with the estimate (0.35 eV) made from the theoretical phonon spectrum [17].

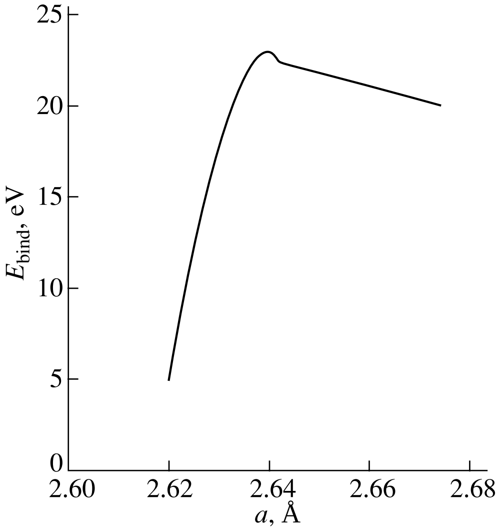

Fig. 3. Calculated dependence of the molar binding energy on the lattice constant for a two-dimensional boron nitride crystal in the quasi-classical approximation.

The equilibrium lattice constant determined for two-dimensional boron nitride within the initial quasi-classical approximation corresponds to the B–N bond length $d = 1.52$ Å. This bond length is in reasonable

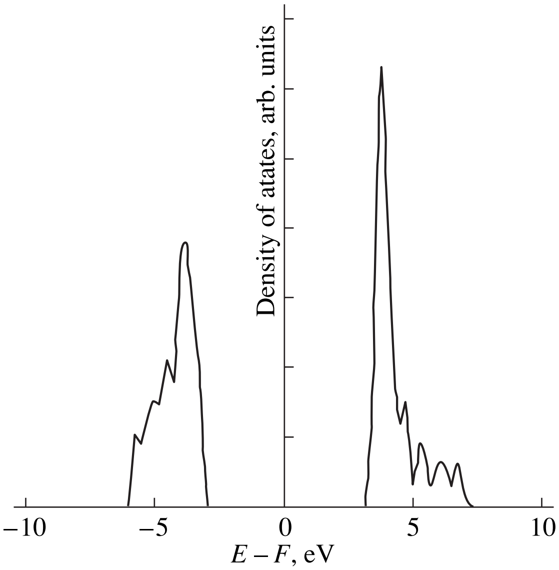

Fig. 4. Calculated density of states for a two-dimensional boron nitride crystal in the quasi-classical approximation.

agreement (a deviation of 4.6%) with the bond length $d = 1.45$ Å observed in layers of real *h*-BN crystals. At first glance, the surprising thing is that the result for the isolated layer is in better agreement (deviations of 2.6–3.8%) with the bond lengths in tetrahedrally coordinated modifications *c*-BN (1.57 Å) and *w*-BN (1.56, 1.58 Å). However, it is worth noting that, in some respects, two-dimensional boron nitride resembles three-dimensional crystals *c*-BN and *w*-BN: these structures do not contain interlayer bonds, which occur in the *h*-BN layered modification.

Owing to the finiteness of the energy sums, the initial quasi-classical approximation enabled us to determine the equilibrium bond length for an infinite boron nitride layer. It is of interest to compare this bond length with the results of *ab initio* calculations carried out with the use of several variants of the Hartree–Fock method and the density-functional theory for a planar molecule $B_{12}N_{12}$ consisting of seven six-membered rings [18]. This structure is a fragment of two-dimensional boron nitride, but the geometry of the fragment appears to be somewhat distorted because of finite sizes. As should be expected, the smallest deviations of the bond angles from an ideal value of 120° are observed for the bonds of the atoms forming the central hexagon: –(2.52°–2.65°) for the B atoms and +(2.52°–2.65°) for the N atoms. The corresponding bond lengths (1.52–1.54 Å, 1.55–1.58 Å) are also in good agreement with the quasi-classical result $d = 1.52$ Å obtained for an ideal infinite boron nitride layer.

3.3. Density of States for Two-Dimensional Boron Nitride

When calculating the electronic structure of two-dimensional boron nitride by the LCAO method in the initial quasi-classical approximation, the piecewise constant approximations of the 2*s* and 2*p* valence orbitals of the B and N atoms served as the basis set. The lattice constant was taken equal to 2.64 Å. Within the approximation under consideration, this value should correspond to the equilibrium state. The calculated densities of states in the valence and conduction bands are depicted in Fig. 4 with respect to the Fermi level. According to these results, two-dimensional boron nitride, like its three-dimensional crystalline modifications, is a dielectric: the band gap is determined to be $E_g = 6.22$ eV.

The calculated density of states for the isolated boron nitride layer should be compared with the corresponding data for the *h*-BN layered modification: the densities of states in the valence and conduction bands were calculated by the orthogonalized-plane-wave method [19], in the tight-binding approximation [20], by the full-potential linear augmented-plane-wave method [21], and in the framework of the local-density approximation with the use of orthogonalized LCAOs [22]. Moreover, the theoretical results were corrected with due regard for the experimental data on x-ray photoemission spectroscopy [23] and x-ray photoelectron spectroscopy [24]. In [2], the density of states for *h*-BN was also calculated by the quasi-classical method but with a different parametrization scheme. A comparison of the above results suggests that, in general terms, the density of states for two-dimensional boron nitride is identical to the density of states for *h*-BN crystals. However, the data available for *h*-BN three-dimensional crystals do not allow us to interpret specific features of the density of states for the two-dimensional boron nitride layer or to estimate characteristic energy ranges.

The calculated electronic structure of two-dimensional boron nitride can also be compared with the electronic structure of nanotubes, which are characterized by their own specific features. According to calculations, multiwall boron nitride nanotubes are also dielectrics [25]. For example, the band gap was estimated at 5.5 eV within the local-density approximation. Note that the band gap only slightly depends on the radii of curvature, the chirality, and the number of layers. One more class of boron nitride structures somewhat related to the isolated layer is represented by fullerene molecules B_mN_m, which are approximately spherical in shape and are faceted by flat rings comprising B and N atoms. For the $B_{12}N_{12}$, $B_{24}N_{24}$, and $B_{60}N_{60}$ fullerenes, the so-called HOMO–LUMO band gap, which is defined as the energy interval between the highest occupied molecular orbital and the lowest unoccupied molecular orbital, was calculated by the MNDO (modified neglect of diatomic overlap) method in [26]. The calculated HOMO–LUMO band gaps were equal to 7.98, 8.34, and 8.73 eV, respectively. Therefore, the inference can be made that, with an increase in the number *m* of atoms, when the angles between adjacent molecular faces increase, the HOMO–LUMO band gap is stabilized at approximately 9 eV. This estimate of the band gap for two-dimensional boron nitride is somewhat larger than that obtained in the present work. However, the former band gap should be overestimated, because, when changing over to the infinite periodic structure, the HOMO and LUMO levels are split into the valence and conduction bands, respectively. Furthermore, the error introduced in such an assignment of molecular states to crystalline states is associated with the fact that not only six-membered rings can serve as faces of the B_mN_m fullerenes.

In their recent work [27], Évarestov and Tupitsyn calculated the parameters of the electronic structure of two-dimensional boron nitride in the framework of the standard Hartree–Fock method, the Hartree–Fock method with inclusion of the weighting function in the exchange part of the Fock matrix, and the density-functional theory. The band gap is equal to 13.7 eV for both variants of the Hartree–Fock method and 4.30 eV in the case of the density-functional calculations. In [27], it was emphasized that the density-functional calculations systematically underestimate the band gap. This circumstance is most likely one of the two possible reasons for the discrepancy in the results. The second reason is that the value of 13.7 eV determined by the Hartree–Fock method seems to be extremely overestimated for the band gap in any boron nitride modification.

In conclusion, it should be noted that all the above calculations of the electronic structure of *h*-BN, boron nitride nanotubes, B_mN_m fullerenes, and the two-dimensional boron nitride layer were performed using the intralayer bond lengths *d* corresponding to the real *h*-BN structure. This bond length is approximately 5% shorter than the bond length obtained in the present work for two-dimensional boron nitride by the quasi-classical method. According to the Harrison interpolation scheme for energy parameters of solids, we can assume that $E_g \sim 1/d^2$. Then, substitution of the quasi-classical bond length leads to a decrease in the aforementioned estimates by ~10%.

REFERENCES

1. L. Chkhartishvili, D. Lezhava, O. Tsagareĭshvili, and D. Gulua, Tr. Akad. MVD Gruz., No. 1, 295 (1999).
2. L. Chkhartishvili, D. Lezhava, and O. Tsagareishvili, J. Solid State Chem. **154**, 148 (2000).
3. L. Chkhartishvili and D. Lezhava, Tr. Gruz. Tekh. Univ., No. 6, 87 (2001).
4. L. Chkhartishvili, J. Solid State Chem. **177**, 395 (2004).
5. L. Chkhartishvili, in *Proceedings of the 1st International Boron Symposium* (Dumlupinar Univ., Ankara, 2002), p. 139.
6. B. Bagchi and P. Holody, Am. J. Phys. **56**, 746 (1988).
7. A.-N. V. Popa, Rep. Inst. At. Phys. E **12**, 1 (1991).
8. K. M. Magomedov and P. M. Omarova, *Quasi-Classical Calculation of Electronic Systems* (Makhachkala, 1989) [in Russian].
9. M. Brack, Rev. Mod. Phys. (Part 1) **65**, 677 (1993).
10. V. P. Maslov, *The Perturbation Theory and Asymptotic Methods* (Mosk. Gos. Univ., Moscow, 1965) [in Russian].
11. W. Stich, E. K. U. Gross, P. Malzacher, and R. M. Dreizler, Z. Phys. A **309**, 5 (1982).
12. L. Chkhartishvili, Tr. Gruz. Tekh. Univ., No. 3(411), 45 (1996).
13. L. Chkhartishvili, Mat. Zametki **65**, 466 (2001).
14. *Selected Values of Chemical Thermodynamic Properties*, Ed. by D. D. Wagmann, W. H. Evans, V. B. Parker, J. Halow, S. M. Bairly, and R. H. Shumn (US Department of Commerce, National Bureau of Standards, Washington, 1968), Ser. 1, p. 270.
15. A. Zunger, J. Phys. C **7**, 76 (1974); J. Phys. C **7**, 96 (1974).
16. Ch. M. Marian, M. Gastreich, and J. D. Gale, Phys. Rev. B **62**, 3117 (2000).
17. K. Albe, Phys. Rev. B **55**, 6203 (1997).
18. D. L. Strout, J. Phys. Chem. A **104**, 3364 (2000).
19. M. S. Nakhmanson and V. P. Smirnov, Fiz. Tverd. Tela (Leningrad) **13**, 905 (1971) [Sov. Phys. Solid State **13**, 752 (1971)]; Fiz. Tverd. Tela (Leningrad) **13**, 3288 (1971) [Sov. Phys. Solid State **13**, 2763 (1971)].
20. J. Zupan, Phys. Rev. B **6**, 2477 (1972).
21. K. T. Park, K. Terakura, and N. Hamada, J. Phys. C **20**, 1241 (1987).
22. Y.-N. Xu and W. Y. Ching, Phys. Rev. B **44**, 7787 (1991).
23. J. Barth, C. Kunz, and T. M. Zimkina, Solid State Commun. **36**, 453 (1980).
24. D. J. Joyner and D. M. Hercules, J. Chem. Phys. **72**, 1095 (1980).
25. N. G. Chopra, R. J. Luyken, K. Cherrey, V. H. Crespi, M. L. Cohen, S. G. Louie, and A. Zettl, Science **269**, 966 (1995).
26. V. V. Pokropivny, V. V. Skorokhod, G. S. Oleinik, A. V. Kurdyumov, T. S. Bartnitskaya, A. V. Pokropivny, A. G. Sisonyuk, and D. M. Sheichenko, J. Solid State Chem. **154**, 214 (2000).
27. R. A. Évarestov and I. I. Tupitsyn, Fiz. Tverd. Tela (St. Petersburg) **44**, 1582 (2002) [Phys. Solid State **44**, 1656 (2002)].

Translated by O. Borovik-Romanova

Physics of the Solid State, Vol. 46, No. 11, 2004, pp. 2134–2138. Translated from Fizika Tverdogo Tela, Vol. 46, No. 11, 2004, pp. 2056–2063.
Original Russian Text Copyright © 2004 by Zatsepin, Cherkashenko, Kurmaev, Shamin, Fedorenko, Skorikov, Plastinin, Gavrilov, Medvedev, Cholakh.

LOW-DIMENSIONAL SYSTEMS AND SURFACE PHYSICS

X-ray Emission Study of the Electronic Structure of Nanocrystalline Al_2O_3

**D. A. Zatsepin*, V. M. Cherkashenko*, É. Z. Kurmaev*, S. N. Shamin*,
V. V. Fedorenko*, N. A. Skorikov*, S. V. Plastinin*, N. V. Gavrilov**,
A. I. Medvedev***, and S. O. Cholakh*****

**Institute of Metal Physics, Ural Division, Russian Academy of Sciences, ul. S. Kovalevskoĭ 18, Yekaterinburg, 620219 Russia*
e-mail: d_zatsepin@ifmlrs.uran.ru
***Institute of Electrophysics, Ural Division, Russian Academy of Sciences,*
ul. Komsomol'skaya 34, Yekaterinburg, 620016 Russia
****Ural State Technical University, ul. Mira 19, Yekaterinburg, 620002 Russia*

Received February 16, 2004

Abstract—Valence states of metal ions and the phase composition of nanocrystalline Al_2O_3 (of the original oxide and the oxide irradiated by high-energy Fe^+ ions) are studied by using x-ray emission Al $L_{2,3}$ and O $K\alpha$ spectra. It is established that the shape of the Al $L_{2,3}$ spectra strongly changes as one goes from the original (bulk) Al_2O_3 to nanocrystalline oxide, while the O $K\alpha$ spectra remain practically unchanged. Moreover, irradiation by high-energy Fe^+ ions results in slight additional changes in the x-ray spectral characteristics of the aluminum oxides under study. The obtained experimental data are compared with the results of theoretical calculations of the electronic structure of α and γ phases of Al_2O_3 performed using the LDA formalism. Using the results of x-ray spectral studies, electronic structure calculations, and x-ray diffraction analysis, it is shown that the revealed spectral differences between the nanocrystalline state of aluminum oxide and the bulk material can be interpreted as a phase transition from the α phase to the γ phase of Al_2O_3 with an addition of bayerite. © *2004 MAIK “Nauka/Interperiodica”.*

1. INTRODUCTION

In recent years, nanocrystalline materials have drawn attention from both fundamental and applied points of view, due to their unusual properties (high hardness, high electrical resistance, high specific heat, etc.) as compared to common bulk materials [1]. The existence of unusual properties of materials in the nanocrystalline state is usually associated with various size effects in nanoparticles. Another important feature of nanocrystalline materials is the possibility of substantially modifying their properties under the action of various external factors, since such materials are in the nonequilibrium state in some cases. The latter fact restricts industrial applications of these materials. In this respect, nanocrystalline oxides look most promising because of their higher chemical and thermal stability as compared to other nanomaterials; indeed, the structure and the grain size of nanocrystalline oxides do not change even after annealing at temperatures of about 600–800 K [2]. Aluminum oxide Al_2O_3 belongs to this group of materials.

To date, two widespread stable phases of Al_2O_3 are known: corundum α-Al_2O_3 and γ-Al_2O_3 defect spinel [3–5]. These phases can be transformed into each other, and this transformation strongly depends on the method of sample synthesis, the presence of foreign ions (impurities) in the lattice, and/or the presence of chemical catalysts and external factors [3]. Irradiation by charged particles is a convenient method for changing the phase structure of a material [6, 7]. Therefore, we can expect that, after irradiation by high-energy ions, the transition from α-Al_2O_3 to γ-Al_2O_3 or even the formation of lower forms of aluminum oxides can take place. Using CuO as an example, it has been shown that similar phase transitions are clearly seen in x-ray emission spectra [6, 7].

X-ray emission spectroscopy is an effective method of studying similar systems. This method allows one to determine charge (valence) states of ions and provides information on the partial densities of states of atomic components in the valence band of a compound, the changes in the character of chemical bonding, etc. In this paper, we report on a complete x-ray emission investigation of the valence states of metal ions and the phase structure of nanocrystalline Al_2O_3 (the original oxide and the oxide subjected to irradiation by high-energy iron ions). In addition, we describe calculations of the electronic structure of aluminum oxide in the framework of the LDA formalism [8]. Attention is mainly focused on the difference in x-ray spectra between the bulk and nanocrystalline states of aluminum oxide. The reasons and possible mechanisms of such spectral differences are discussed.

2. SAMPLE PREPARATION TECHNIQUE AND DESCRIPTION OF THE EXPERIMENT AND CALCULATIONS

Nanocrystalline Al_2O_3 powders were synthesized by the method of electric explosion of a metal aluminum wire in air with subsequent sedimentation in water [9]. As a reference sample, an α-Al_2O_3 single crystal was used.

Samples were irradiated by iron ions at the Institute of Electrophysics, Ural Division, Russian Academy of Sciences. An ion source of the MEVVA type [10] based on a vacuum arc with a cathode spot was used. This source operated in a periodic-pulse mode with a pulse duration of 0.4 ms and a pulse repetition frequency of 25 Hz (ion energy 30 keV, ion flux 10^{17} cm^{-2}, current density 3 mA/cm^{-2}).

X-ray emission Al $L_{2,3}$ spectra (valence transition Al $3d3s$–Al $2p_{3/2,1/2}$) of irradiated, nonirradiated, and reference aluminum oxide samples were measured using an ultrasoft x-ray emission spectrometer [11] (diffraction grating with 600 lines per millimeter having a bending radius of 2 m) and electron excitation with an energy resolution of 0.3 eV. X-ray emission O Kα spectra (electronic transition O $2p$–O $1s$) were obtained using a JEOL-733 electronic microanalyzer specially adapted for measurements of the fine structure of x-ray spectra [12]. The x-ray tube operated at 5 kV and 100 nA. In this case, the instrumental broadening of O $K\alpha$ spectra was approximately 0.5 eV.

X-ray diffractograms of the samples were taken using a DRON-4 diffractometer (Cu $K\alpha$ excitation) with a graphite monochromator. Interpretation of x-ray diffractograms and estimation of the phase composition were performed using the ASTM database and the PowderCell program. The Scherrer method was used to estimate the average grain size from the integral width of the (118) δ-Al_2O_3 reflection.

The band structure was calculated in the framework of the local density functional formalism (LDA) using the first-principles method of linearized MT orbitals in the tight-binding approximation (TB LMTO) [8]. The experimental crystal lattice parameters of α-Al_2O_3 and γ-Al_2O_3 [13, 14] were used. According to Verwey's data [14], γ-Al_2O_3 has a defect structure of inverted spinel with space group Fm-3m and lattice parameter $a = 3.95$ Å. The filling factors for aluminum atoms occupying crystallographically nonequivalent positions were 0.4665 and 0.0999. The unit cell contains 1.333 formula units (Al_2O_3). Since the simulation technique employed does not take into account the filling factors and cannot operate with nonintegral numbers of atoms per unit cell, calculations for γ-Al_2O_3 were performed for a model structure having the γ-Al_2O_3 symmetry; atoms occupied the same positions as in γ-Al_2O_3, but the unit cell contained three aluminum atoms and four oxygen atoms (therefore, there were 0.334 extra aluminum atoms per unit cell).

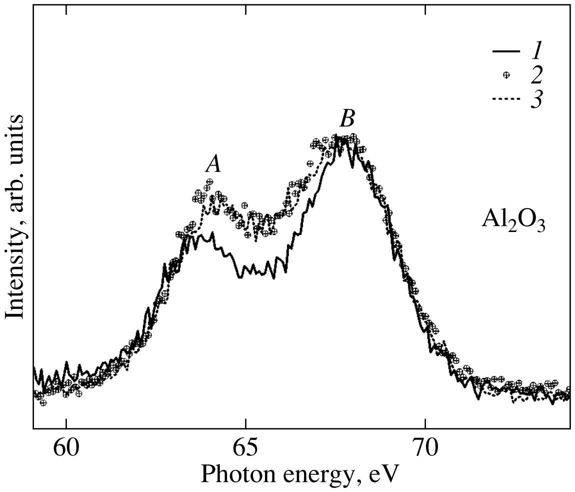

Fig. 1. X-ray Al $L_{2,3}$ emission spectra (XES) from (*1*) bulk α-Al_2O_3 (reference sample), (*2*) a 17-nm nanopowder of α-Al_2O_3, and (*3*) a 17-nm α-Al_2O_3 nanopowder irradiated by iron ions.

3. RESULTS AND DISCUSSION

It is well known that x-ray emission spectra of the valence band are related to electron transitions between the valence band and a core hole. Since the wave function of a core electron is strongly localized and the angular momentum symmetry is fixed, the x-ray spectra reflect the partial densities of states of the constituent atoms (due to the dipole selection rules). In our case, we measured x-ray Al $L_{2,3}$ and O $K\alpha$ emission spectra, which reflected the densities of Al $3d3s$ and O $2p$ states in the valence band, respectively.

Figure 1 shows x-ray emission Al $L_{2,3}$ spectra of α-Al_2O_3 (reference sample), of 17-nm nano-Al_2O_3, and of iron ion–irradiated 17-nm nano-Al_2O_3. Two bands located at 64 and 67.9 eV (denoted by *A* and *B*, respectively) are clearly seen in the spectra. The *A* band mainly reflects the contribution of Al *s* electrons to the valence band, and the *B* band reflects the mixture of aluminum *s* and *d* states [15]. On the whole, the shape of the spectrum and energy positions of the main lines in the Al $L_{2,3}$ spectrum of the reference sample are practically identical to those reported by Šimunek for α-Al_2O_3 [15]. In Fig. 1, we can see that the main distinction between the spectra of bulk α-Al_2O_3 and 17-nm nano-Al_2O_3 is the location of the *A* band at 64 eV; this band has a much higher intensity in the spectrum of 17-nm nano-Al_2O_3 than in the reference spectrum. The spectrum of 17-nm nano-Al_2O_3 irradiated by iron ions shows a similar behavior of the *A* band; however, the intensity of the *A* band is somewhat lower than in the spectrum of nonirradiated 17-nm nano-Al_2O_3.

Since the *A* band reflects the "pure" contribution of aluminum *s* states to the valence band, we can normalize x-ray emission Al $L_{2,3}$ spectra of samples by the spectral intensity of this band (Fig. 2) assuming that the degree of hybridization of the *d*–*s* states changes as one

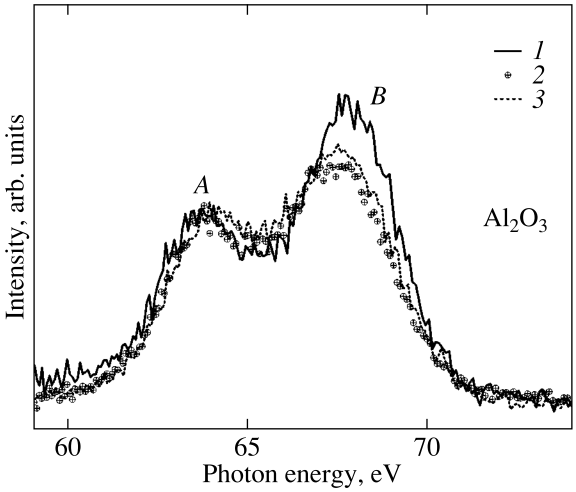

Fig. 2. X-ray Al $L_{2,3}$ emission spectra (normalized to the *A*-band intensity) from (*1*) bulk α-Al_2O_3 (reference sample), (*2*) a 17-nm α-Al_2O_3 nanopowder, and (*3*) a 17-nm α-Al_2O_3 nanopowder irradiated by iron ions.

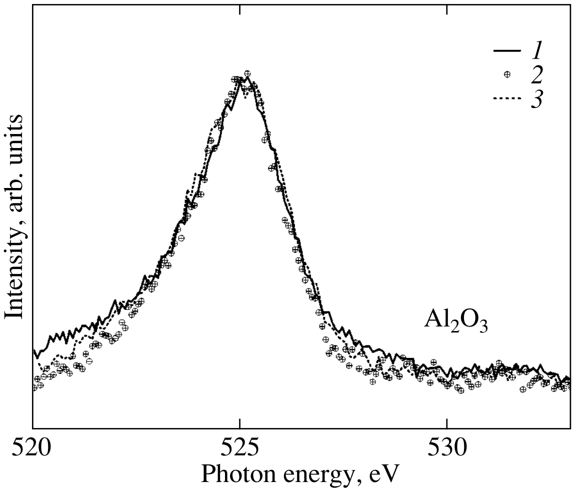

Fig. 3. X-ray O *K*α emission spectra from (*1*) bulk α-Al_2O_3 (reference sample), (*2*) a 17-nm α-Al_2O_3 nanopowder, and (*3*) a 17-nm Al_2O_3 nanopowder irradiated by iron ions.

goes from bulk α-Al_2O_3 to 17-nm nano-Al_2O_3. Here, the intensity of the (*d* + *s*)-like band in the x-ray Al $L_{2,3}$ emission spectrum is maximum for the reference α-Al_2O_3 sample, is medium for the irradiated sample, and becomes minimum for the spectrum of 17-nm nano-Al_2O_3. We did not reveal any significant changes in the x-ray emission *K*α spectra of oxygen for any samples (Fig. 3). This means that there is no difference in the 2*p* states of oxygen between the reference, original nanocrystalline, and irradiated nanocrystalline Al_2O_3 samples and the difference between the bulk (reference) and nanocrystalline aluminum oxide samples is only in the partial densities of *d*–*s* states of the metal.

One of the most probable reasons for the described behavior may be the formation of a different phase of aluminum oxide having a similar chemical composition in the nanocrystalline state. This phase is expected to be extremely stable, since only slight changes in the Al $L_{2,3}$ spectra of nanocrystalline samples are observed even after irradiation. At present, many of the structural modifications of Al_2O_3 are known: α, β, γ, δ, ρ, χ, η, and θ. However, only the α and γ phases of Al_2O_3 are considered independent, since in the absence of special chemical additives all other modifications of aluminum oxide are unstable and/or represent a mixture of phases [3]. Therefore, we can assume that a change in the intensity of the (*d* + *s*)-like band observed as we pass from the bulk to nanocrystalline state indicates the formation of the γ-Al_2O_3 phase. With this assumption, we can interpret a small variation in the intensity of the *B* band in the spectrum of the irradiated sample as the beginning of the reverse transition from the γ phase to α-Al_2O_3 (Fig. 2).

To check the above assumptions, we calculated the partial densities of *s* and *d* states of aluminum atoms for α and γ phases using the LDA formalism (Fig. 4). In Fig. 4, we see that the partial densities of states for γ-Al_2O_3 are shifted to the higher energy region of the band of occupied states as compared to the density of states of α-Al_2O_3. To perform calculations for the γ phase, we used a model Al_2O_3 structure (see the description of the calculations), which could be one of the reasons for the energy shift mentioned above. The top panel in Fig. 4 shows the (*d* + *s*) states for aluminum atoms. The peak in the density of states closest to the Fermi level in the α phase has a *d* character, whereas the peak located at 5 eV is formed by Al *s* states. As one goes from the α phase to the γ phase, the intensity of the *d* peak of aluminum states decreases sharply. At the same time, the intensity of the *s* peak does not change substantially. As a result, the intensity of the *d* peak in the density of (*d* + *s*) states for the γ phase is at least half its value in the α phase (top panel in Fig. 4). Therefore, we may conclude that the main difference between the electronic structures of the α and γ phases of Al_2O_3 consists in a different degree of hybridization of the *s* and *d* states of aluminum atoms, due to the smaller contribution of *d* states in the γ phase. This conclusion does not contradict the above-mentioned experimental results.

At the final stage, we performed an x-ray diffraction analysis of the original (nonirradiated) and irradiated samples. Figure 5 shows x-ray diffractograms of the original and iron ion–irradiated nanocrystalline Al_2O_3. From the diffractograms, it is seen that the original nanocrystalline sample consists of a mixture of aluminum oxide and aluminum hydroxide $Al(OH)_3$. The latter has bayerite and gibbsite structures (their main reflections are marked with the symbol β in the bottom panel in Fig. 5) and accounts for approximately 30% of the sample composition. The oxide component consists of a mixture of the γ and δ phases of Al_2O_3. X-ray dif-

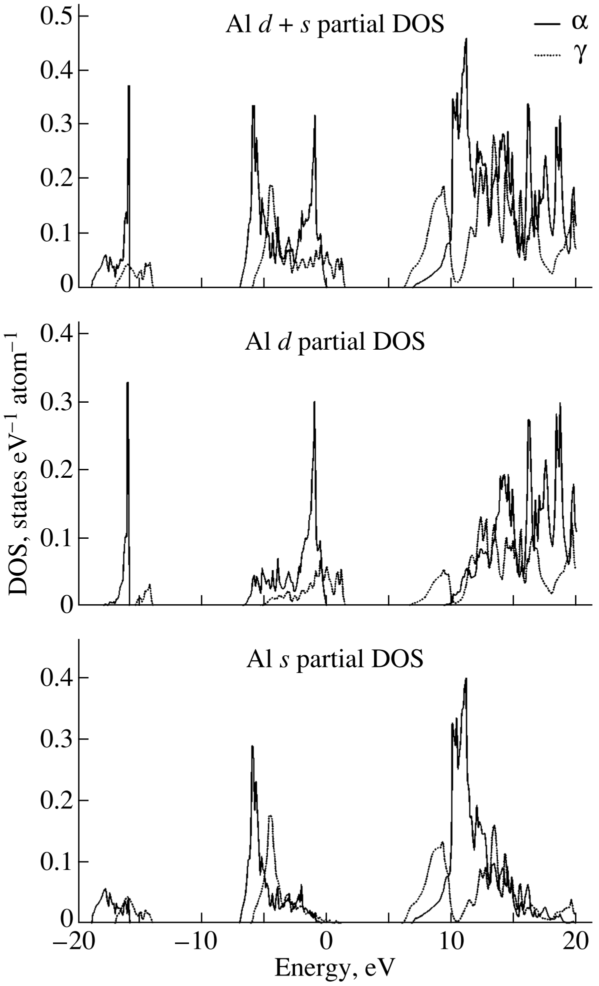

Fig. 4. Comparison of the partial densities of states for the α and γ phases of Al_2O_3 calculated in the framework of the LDA formalism.

fractograms of the γ-phase defect spinel structure (shown by symbol γ in Fig. 5) fully overlap the reflections from the tetragonal δ phase and can be separated only by simulation methods. The ratio of these phases is 1 to 1. The x-ray diffractogram of the irradiated sample (the upper panel in Fig. 5) differs from that for the original nanocrystalline Al_2O_3 only in the absence of the hydroxide lines; the remaining part of the diffractogram is very similar to the diffractogram of the nonirradiated Al_2O_3, and the ratio of γ and δ phases remains the same. Moreover, we should note that there are no traces of the high-temperature θ and α phases of Al_2O_3 in the diffractograms. The average grain size did not change after irradiation of the sample and remained the same (17 nm). Thus, the assumption that there is a transformation of the γ phase into the α phase in a nanocrystalline sample after irradiation is not confirmed by the x-ray diffraction data. The small change in the intensity of the *B* band mentioned above can be caused by the disappearance of the bayerite phase.

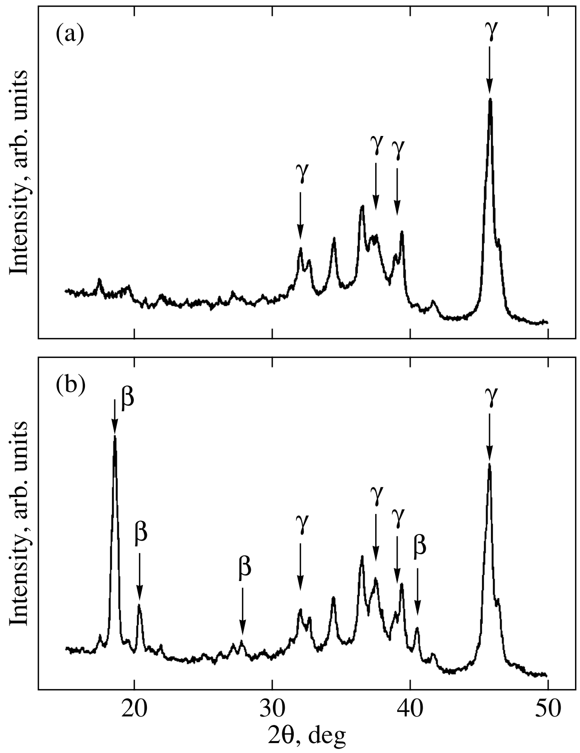

Fig. 5. X-ray diffractograms of (a) the original and (b) iron ion–irradiated 17-nm Al_2O_3 nanopowder.

From the above discussion, it is clear that the transition from the bulk to nanocrystalline state for Al_2O_3 is accompanied by the transformation of the α phase into the γ and, possibly, δ phase with a partial addition of bayerite. Irradiation by iron ions leads to the disappearance of bayerite, so that, in a finite sample, only low-temperature forms of Al_2O_3 are present. Thus, we may assume that the x-ray emission spectrum of the irradiated aluminum oxide is the spectrum of the “pure” γ phase of Al_2O_3. The results of our x-ray diffraction analysis agree well with the results of calculations in the framework of the LDA formalism and with the x-ray emission spectroscopy data.

4. CONCLUSIONS

We have studied the original nanocrystalline aluminum oxide Al_2O_3 and iron ion–irradiated Al_2O_3 using x-ray emission spectroscopy and x-ray diffraction. We have found that the transition from the bulk to nanocrystalline state is accompanied by the appearance of γ-Al_2O_3 and bayerite. Irradiation does not change the grain size and aluminum atom valence but results in the disappearance of the bayerite phase, so that there is a pure γ phase of Al_2O_3 in an irradiated sample. The results of our study agree well with the results of calculations of the electronic structure in the framework of the LDA formalism.

REFERENCES

1. A. I. Gusev and A. A. Rempel', *Nanocrystalline Materials* (Fizmatlit, Moscow, 2001) [in Russian].
2. Y. Ishida, H. Ichinose, T. Kizuka, and K. Suenaga, Nanostruct. Mater. **6** (1–4), 115 (1995).
3. N. A. Toropov, V. P. Barzakovskiĭ, I. A. Bondar', and Yu. P. Udalov, *Phase Diagrams of Silicate Systems* (Nauka, Leningrad, 1970) [in Russian].
4. I. P. Batra, J. Phys. C **15**, 5399 (1982).
5. Y.-N. Xu and W. Y. Ching, Phys. Rev. B **43**, 4461 (1991).
6. D. A. Zatsepin, V. R. Galakhov, B. A. Gizhevskii, E. Z. Kurmaev, V. V. Fedorenko, A. A. Samokhvalov, and S. V. Naumov, Phys. Rev. B **59**, 211 (1999).
7. B. A. Gizhevskii, V. R. Galakhov, D. A. Zatsepin, L. V. Elokhina, T. A. Belykh, E. A. Kozlov, S. V. Naumov, V. L. Arbuzov, K. V. Shal'nov, and M. Neumann, Phys. Solid State **44**, 1380 (2002).
8. O. K. Anderson, Phys. Rev. B **12**, 3060 (1975).
9. I. V. Beketov, Yu. A. Kotov, A. M. Murzakaev, O. V. Samatov, V. P. Volkov, R. Buhme, and G. Schumacher, Mater. Sci. Forum **225–227**, 913 (1995).
10. I. G. Brown, Rev. Sci. Instrum. **65**, 3061 (1994).
11. E. Z. Kurmaev, V. V. Fedorenko, S. N. Shamin, A. V. Postnikov, G. Wiech, and Y. Kim, Phys. Scr. T **41**, 288 (1992).
12. V. V. Fedorenko, V. R. Galakhov, L. V. Elokhina, L. D. Finkelstein, V. E. Naish, S. M. Butorin, E. J. Nordgren, A. K. Tyagi, U. R. K. Rao, and R. M. Iyer, Physica C (Amsterdam) **221**, 71 (1994).
13. H. Sawada, Mater. Res. Bull. **29** (2), 127 (1994).
14. E. J. W. Verwey, Z. Kristallogr. Kristallgeom. Kristallphys. Kristallchem. **91**, 317 (1935).
15. A. Šimunek and G. Wiech, Z. Phys. B **93**, 51 (1993).

Translated by I. Zvyagin

Physics of the Solid State, Vol. 46, No. 11, 2004, pp. 2139–2145. Translated from Fizika Tverdogo Tela, Vol. 46, No. 11, 2004, pp. 2069–2075.
Original Russian Text Copyright © 2004 by Orlov, Horváth, Potapov, Orlov, Ivin, Vdovin, Steinman, Fomin.

LOW-DIMENSIONAL SYSTEMS AND SURFACE PHYSICS

Electrical Characteristics and the Energy Band Diagram of the Isotype n-Si$_{1-x}$Ge$_x$/n-Si Heterojunction in Relaxed Structures

L. K. Orlov*, Zs. J. Horváth, A. V. Potapov*, M. L. Orlov***,**
S. V. Ivin*, V. I. Vdovin****, E. A. Steinman*****, and V. M. Fomin*****

** Institute for Physics of Microstructure, Russian Academy of Sciences, Nizhni Novgorod, 603950 Russia*
e-mail: Orlov@ipm.sci-nnov.ru
*** Research Institute for Technical Physics and Materials Science, Hungarian Academy of Sciences, Budapest, Hungary*
**** Nizhni Novgorod State University, Nizhni Novgorod, 603950 Russia*
***** Institute for Chemical Problems of Microelectronics, Bol'shoĭ Tolmachevskiĭ per. 5, Moscow, 109017 Russia*
****** Institute of Solid State Physics, Russian Academy of Sciences, Chernogolovka, Moscow oblast, 142432 Russia*

Received January 27, 2004; in final form, March 9, 2004

Abstract—The electrical characteristics of the relaxed isotype n-Si$_{1-x}$Ge$_x$/n-Si heterojunction are studied for the case of a misfit-dislocation network formed in the vicinity of the heterointerface. The data obtained are used to analyze the energy bands of the heterostructure. The band structure of the crystal near the interface is shown to be formed by a charge at lattice defects. The potential-barrier parameters are estimated by analyzing the temperature dependences of the J–U and C–U characteristics of the system. *© 2004 MAIK “Nauka/Interperiodica”.*

1. INTRODUCTION

The properties of relaxed silicon–germanium heterostructures containing a well-developed misfit-dislocation network in the bulk have been discussed recently in the literature. These heterostructures serve as base crystals for creating field-effect transistors with a two-dimensional silicon channel in a solid-solution layer, and they are being extensively studied [1]. In most works dealing with this problem, researchers studied the structural characteristics of Si$_{1-x}$Ge$_x$ buffers; the mechanisms of nucleation and multiplication of misfit dislocations, which form a dislocation network at the heterointerface; and the depth distribution of the dislocation density [2]. Recent practical interest in relaxed heterostructures has promoted the development of contactless nondestructive methods for controlling dislocations in layers by using mainly photo- and cathodoluminescence [3]. The light-emitting luminescence properties of plastically deformed Si/Si$_{1-x}$Ge$_x$ heterostructures [4] came to the attention of researchers due to the characteristic $D1$–$D4$ dislocation lines that are present in their photoluminescence spectra and whose intensity increases with dislocation density.

Among these spectral lines, the $D1$ line (0.804 eV) is of special interest (in particular, for optoelectronics), since it can be used to apply some IV–IV compounds in the optical spectral region (along with rare-earth elements and germanium nanoclusters in Si). However, despite the fact that dislocation lines in the photoluminescence spectra of Si/Si$_{1-x}$Ge$_x$ heterostructures have been extensively studied in recent years [5], the mechanism of dislocation-induced photoluminescence and the nature of each band in the spectra are still unknown. Moreover, the emissive power of all light-emitting silicon structures is still rather weak, which necessitates further detailed analysis of both the characteristics of these systems and the mechanisms of radiative recombination in them.

Many researchers are now discussing the potential of relaxed Si/Si$_{1-x}$Ge$_x$ heterostructures as possible light-emitting sources in silicon optoelectronics. It is difficult to solve the problem of creating effective emitters based on dislocation Si/Si$_{1-x}$Ge$_x$ structures because it is difficult to prepare high-quality diode matrices. For a structurally imperfect heterojunction, the matrices must have good injection properties and a low efficiency of nonradiative transitions at the heterointerface. The purpose of this work is to study the electrical characteristics of the isotype n-Si$_{1-x}$Ge$_x$/n-Si(100) heterojunction under the conditions of a high efficiency of electron–hole recombination through defect states in the vicinity of the heterointerface. Energy band diagrams of the relaxed heterojunction are also of interest; its barrier properties are most likely controlled by charge states in the region of a three-dimensional misfit-dislocation network rather than by a band discontinuity at the heterointerface, as is often suggested [6].

1063-7834/04/4611-2139$26.00 © 2004 MAIK “Nauka/Interperiodica”

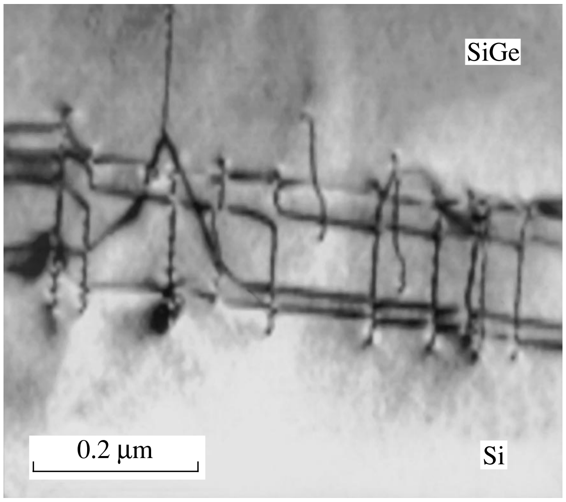

Fig. 1. Appearance of the $Si_{1-x}Ge_x$/Si heterointerface with a regular dislocation network.

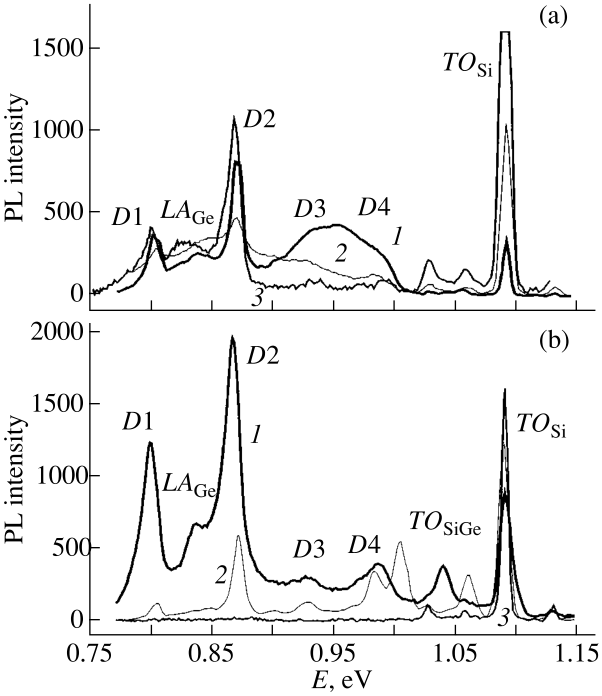

Fig. 2. Photoluminescence spectra recorded at 5 K from $Si_{1-x}Ge_x$/Si structures for various values of the solid-solution layer parameters: (a) d_{SiGe} = 0.6 μm and (*1*) $x = 0.11$, (*2*) 0.095, and (*3*) 0.06; (b) $x = 0.09$ and (*1*) d_{SiGe} = 1.2, (*2*) 0.9, and (*3*) 0.12 μm.

2. EXPERIMENTAL

$Si/Si_{1-x}Ge_x$ heteroepitaxial structures were grown using a modified method of molecular-beam epitaxy with a sublimating silicon source and gaseous germanium hydride source. This epitaxial method is described in detail in [7, 8]. Some properties of grown solid-solution layers are given in [9, 10]. The structures grown were relaxed; i.e., their thickness exceeded a critical thickness. The layers grown were 0.1–1μm thick, and the germanium content in them was lower than 20 at. %, which provided the conditions for plastic-deformation localization in the vicinity of the heterointerface. Near the heterointerface, a dense three-dimensional dislocation network was formed with a surface density of extended defects of 10^5–10^9 cm^{-2}. The density of threading dislocations in the solid-solution layer was estimated metallographically to be 10^4–10^5 cm^{-2}. The mechanisms of misfit-dislocation nucleation and multiplication at the $Si_{1-x}Ge_x$/Si heterointerface were discussed in [2, 10]. A characteristic transmission electron microscopy image of the $Si_{1-x}Ge_x$/Si heterointerface with a regular dislocation network is shown in Fig. 1.

3. RESULTS AND DISCUSSION

The photoluminescence spectra of the relaxed heterostructures contain traditional lines induced by the radiation of free excitons in both the silicon and $Si_{1-x}Ge_x$ layers (the exciton lines from the latter layers overlap with the *TO*-phonon replicas of radiative recombination in silicon and, hence, are often weakly pronounced) and additional, rather strong *D*1–*D*4 lines (Fig. 2), which are absent in the unrelaxed structures (Fig. 2b, curve *3*). The spectra were recorded at 5 K with a standard grating spectrometer with argon-laser excitation. A cooled germanium diode was used as a detector. In the heterostructures subjected to large plastic deformation ($h = xd_{SiGe} > 0.1$), the intensity of the *D*1–*D*4 lines exceeds the intensity of the *TO*-phonon replica of the radiative exciton recombination line from the silicon. Moreover, in some cases, the efficiency of the *D*1 and *D*2 lines, which are of most interest in optoelectronics, is fairly close to the radiation efficiency of erbium atomic complexes in silicon up to liquid-nitrogen temperature [4]. The nature of the spectral lines in question is related to the presence of dislocations in the material; however, the mechanisms and details of the radiative recombination at the frequencies of these lines are not completely understood. In particular, the nature of radiative-recombination centers is still unknown. It is most often related to localized states in dislocations having a certain configuration (*D*1, *D*2 lines) [6].

Since the nature of radiative recombination centers in dislocation structures is not fully understood, additional studies of localized states at heterointerfaces using electrophysical techniques are important. This problem becomes even more important in studying the electroluminescence characteristics in relaxed heterostructures and in using the effect of electroluminescence to develop silicon-based light-emitting devices.

In this work, we try to reveal the character of electrically active charge centers located in the vicinity of the dislocation network and their effect on the shape of energy band diagrams in the semiconducting heterostructure. In turn, the character of the energy bands determines the passage of current through the heterostructure and its injection properties. Preliminary Hall effect studies of the electrophysical properties of charge carriers in the relaxed structure indicate the appearance of an additional shunt layer (which often has purely *p*-type conduction) between the solid-solution layers and the silicon doped with donor impurities. The conclusion that a charged region exists in the vicinity of the dislocation network is also supported by *CU* profiling of structures during electrolytic etching of samples and by studying the structures by cathodoluminescence at different energies of exciting electron beams [3].

To measure the electrical characteristics of the relaxed heterojunction, we used a structure (no. 347) grown at 700°C by the method described above. The heterostructure contained an epitaxial $Si_{1-x}Ge_x$ ($x \approx 0.11$) layer of thickness $d_{SiGe} \approx 0.20$–0.25 μm grown through a buffer Si sublayer of thickness $d_{Si} \approx 0.5$–0.6 μm on a Si(100) wafer. According to the *CV* profiling data, the level of doping of the Si and $Si_{1-x}Ge_x$ layers was close to that [$N_2 \approx (2–3) \times 10^{16}$ cm^{-3}] of the sublimating silicon source (KÉM-0.1) in the device reactor. The Si wafer also had *n*- type conductivity (phosphorus concentration $N_1^+ = 1 \times 10^{19}$ cm^{-3}). The isotype n–n^+ junction height in silicon, $\Delta E_c^{(1)}$, can be estimated from the difference in the Fermi levels at the interface between the Si layer and the wafer and is found to be

$$\begin{aligned}\Delta E_c^{(1)} &= E_{c2}(n\text{-Si}) - E_{c1}(n^+\text{-Si}) \\ &= (kT/e)\ln\{N_1/N_2\} \approx 0.15 \text{ eV}.\end{aligned} \tag{1}$$

Figure 3 schematically shows the energy bands of the isotype n-$Si_{1-x}Ge_x$/n-Si/n^+-Si heterojunction at T = 300 K; its electrical characteristics will be described below.

The energy band discontinuity $\Delta E_{c,v}^{(2)}$ at the $Si_{1-x}Ge_x$/Si heterointerface, which is caused by the difference in the work functions, can be estimated from the difference between the band gaps in the silicon and solid-solution layer. This difference can easily be determined from, for example, the photoconductivity spectrum of this system. For the layers with $x = 0.1$, the optical spectra measured at room temperature give E_g(Si)–E_g($Si_{0.9}Ge_{0.1}$) ≈ 60 meV. According to [11, 12], this value corresponds to band discontinuities $\Delta E_c^{(2)} \le \pm 10$ meV for the conduction band and $\Delta E_v^{(2)} \approx 50$–$70$ meV for the valence band, depending on the elastic stresses at the heterointerface. However, experiments show that the barrier related to the conduction-band discontinuity at the heterointerface is substantially lower than the actual barrier of the isotype heterojunction.

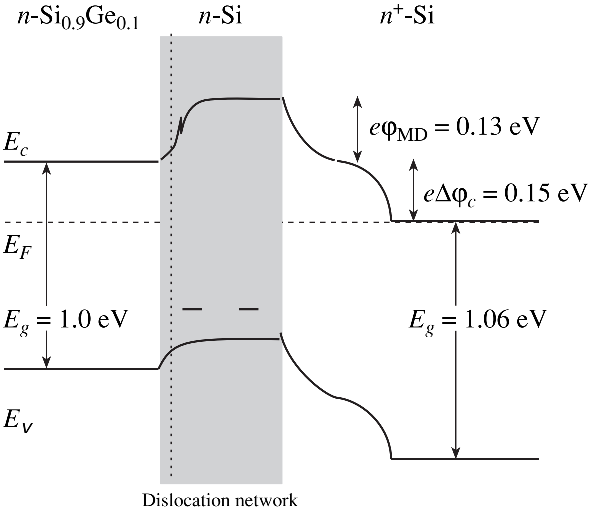

Fig. 3. Energy bands of the relaxed isotype n-$Si_{1-x}Ge_x$/n-Si/n^+-Si heterojunction.

The true height of the potential barrier that is formed by charge centers located on misfit dislocations in the vicinity of the heterojunction can be determined by studying the diode characteristics of the heterostructure. To study the potential barrier of the heterojunction, ohmic Al contacts having an area $S = 0.8 \times 0.8$ mm^2 were applied onto the $Si_{1-x}Ge_x$ layer from the outer and opposite surfaces of the structure treated in an $H_2SO_4 + H_2O_2$ etchant by using a special technology [13]. The forward and reverse branches of the current–voltage (J–U) characteristic measured on one of the mesa structures (no. 1E5) at various temperatures are shown in Fig. 4a (see also [14]).

Our attempt to describe the experimental characteristics of the isotype heterojunction using the simple traditional model of a single or double Schottky barrier (the Kanerva–Opdorp model [6, 15]) failed to yield satisfactory agreement between the calculated and experimental curves [16]. A problem is caused by the presence of leakage currents along threading dislocations that shunt the heterojunction. By taking this fact into account, we can adequately describe both the forward and reverse branches of the J–U characteristic using a barrier model with one type of charge carrier. For positive voltages at the upper contact, the dependence of the current on the applied voltage can be described to a high accuracy in terms of the thermal field emission model, according to which

$$J = J_0\{\exp[e(U - U_R)/nkT] - 1\}, \quad J = U_R/R, \tag{2}$$

or

$$U = JR + (nkT/e)\ln(J/J_0 + 1). \tag{3}$$

Here, R is the ballast resistance of the structure, which consists of the resistance of the ohmic contacts and the wafer resistance and is placed in series with the hetero-

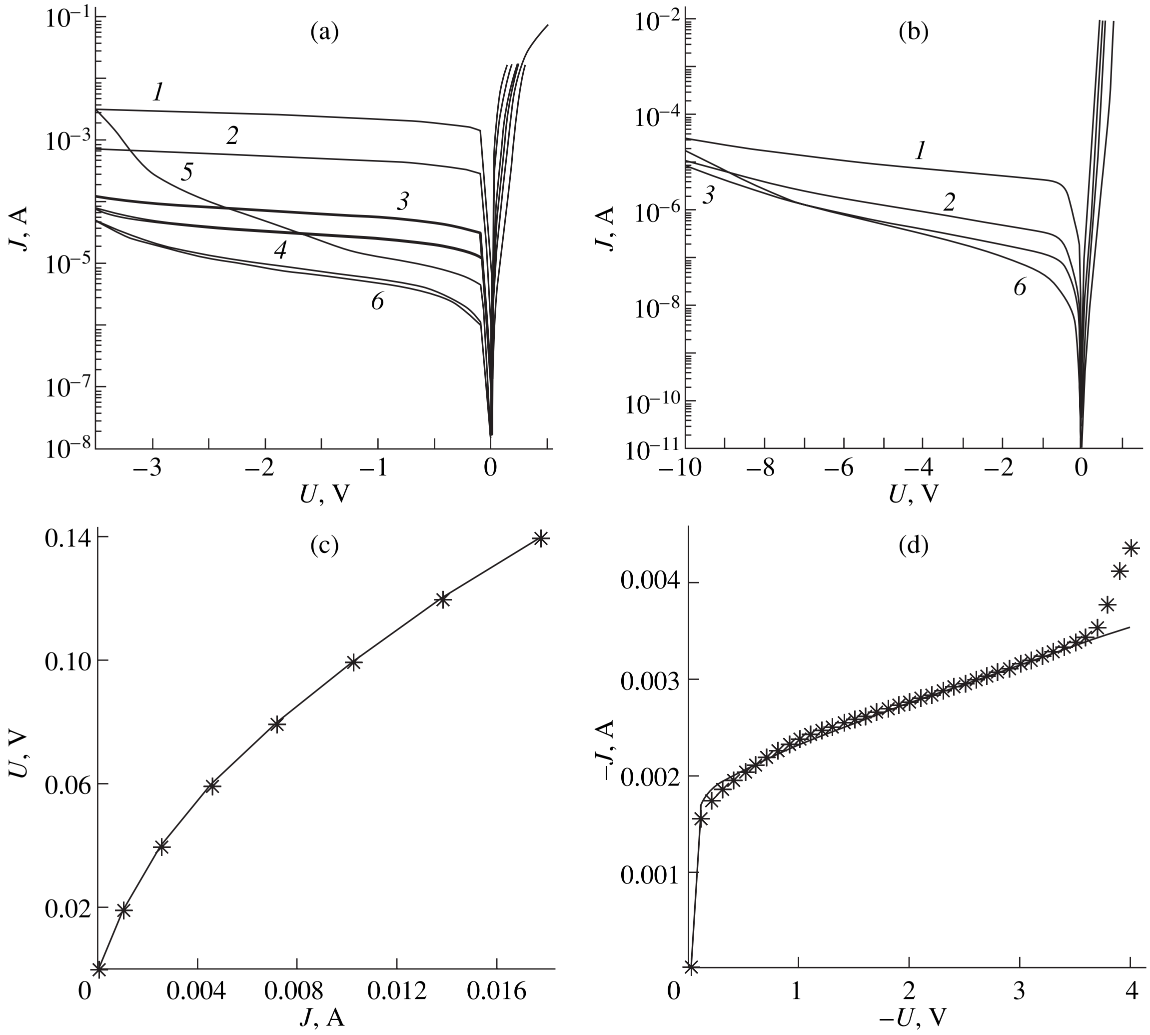

Fig. 4. J–U characteristic of a sample with an isotype n-$\mathrm{Si}_{1-x}\mathrm{Ge}_x$/$n$-Si/$n^+$-Si heterojunction and with (a) an ohmic Al contact (mesa structure 1E5) or (b) a Schottky contact (mesa structure 2C3) at various temperatures T: (*1*) 300, (*2*) 260, (*3*) 220, (*4*) 200, (*5*) 180, and (*6*) 100 K. (c, d) Experimental data at T = 300 K (points) and curves (solid lines) calculated by (c) Eq. (3) and (d) Eq. (4) using the parameters from Table 1 (Al contact, mesa structure 1E5).

junction; U_R is the voltage drop across the ballast resistor; and n is the imperfection coefficient of the potential barrier related to recombination currents in the heterojunction.

The reverse current in the structure (at $U < 0$) can be fairly accurately described by the relation

$$J = J_0[\exp(eU/nkT) - 1] - \sigma|U|^m, \tag{4}$$

where the second term is the stray current density that shunts the heterojunction along dislocations growing from the wafer into the layer. The surface density of such dislocations in both the wafer and the upper epitaxial layer was estimated metallographically to be 2×10^4–2×10^5 cm^{-2}.

For each experimental curve, we can determine the parameters R, J_0, and n for the forward current and the parameters σ and m for the reverse current by using the method of finite differences to fit theoretical dependences (3) and (4) to the corresponding experimental curves. The values of these parameters for mesa structure 1E5 in the temperature range 300–160 K are given in Table 1. Figures 4c and 4d show the forward and reverse branches of the J–U characteristic, respectively, measured on mesa structure 1E5 (Fig. 4a) at T = 300 K and the corresponding curves calculated by Eqs. (3) and (4) using the parameters given in Table 1.

An analysis of the J–U characteristic of the sample indicates that the values of each parameter vary from mesa to mesa in a certain range. For example, for the J–U characteristic measured at room temperature, J_0 varies in the range 1–15 mA, n varies in the range 1.0–1.5 (Table 2), R = 22–25 Ω for a series of mesa structures with $j = 0$, and R = 3.4–3.7 Ω for mesa structures with $j \neq 0$; m = 0.5–0.9, and σ = 0.0004–0.0011. The scatter of the diode parameters across the area of the structure is caused by both different contact areas and natural factors related to different densities of threading dislocations and misfit dislocations across the sample area, which has been confirmed by numerous studies using, e.g., photoluminescence and metallography.

Given J_0, we can estimate the potential-barrier height at the heterojunction. In particular, the application of the simplest formula for an emission model gives

$$\begin{aligned} J_0 &= A^*T^2\exp(-e\varphi_b/nkT) \\ &= 4\pi me(kT)^2h^{-3}S\exp(-e\varphi_b/nkT). \end{aligned} \tag{5}$$

Here, we assumed that $m_{\mathrm{Si}} \approx m_{\mathrm{SiGe}} = m = 0.26m_0$, where m is the effective conduction-electron mass. This relation, however, results in a strongly overestimated value (about 0.4 eV), since it does not take into account many factors that affect the heterojunction; these factors are taken into consideration in more complex models for a Schottky barrier that make allowance for the diffusion and generation–recombination components of the current density across the heterojunction.

A more accurate value for the contact potential difference $e\varphi_b$ can be obtained by analyzing the temperature dependence of J_0. The characteristic $J_0(T)$ dependence for mesa structure 1D9 is shown in Fig. 5a, where points I correspond to the values of J_0 obtained from the forward branch of the J–U characteristic, points II correspond to reverse currents measured at $U = -1$ V, and points III correspond to currents calculated by Eq. (5) at $A^* = 0.0225$ and $\varphi_b = 0.274$ eV.

A comparison of the curves in Fig. 5a shows that the calculated curves agree well with the experimental data at $T > 200$ K. In this range, the generation–recombination currents that specify the reverse current J_0 in the heterojunction are about an order of magnitude higher than the currents flowing along dislocations (which dominate at temperatures below 200 K). At $T < 200$ K, an increase in the bias voltage results not only in a leveling off of the reverse currents in the heterojunction (as shown in Fig. 4a) but also in an increase in the current J_0 because of a decrease in the barrier height, most likely, due to the freezing out of charge carriers at dislocations.

The Richardson constant A^* and the contact potential difference $e\varphi_b$ for mesa structure 1D9 and some others are listed in Table 3. A nonuniform dislocation-density distribution over the sample area is seen to cause a significant scatter of the potential-barrier heights at the heterointerface.

Let us estimate the position of the conduction-band bottom in the silicon sublayer with a dislocation network using the relation

$$\begin{aligned} N^+(\mathrm{Si})/N_{\mathrm{MD}}(\mathrm{Si}) &= \exp\{e(E_{c3}-E_{c1})/kT\} \\ &= \exp(e\varphi_b/kT). \end{aligned} \tag{6}$$

Table 1. Fitting parameters obtained from the J–U characteristics of the mesa 1E5–based structure depending on the measurement temperature

T, K	R, Ω	J_0, mA	n	m	$\sigma \times 10^6$
300	3.03	1.698	1.366	0.769	640
293	3.73	1.326	1.202	0.571	898
280	3.89	0.616	1.101	0.542	564
260	3.89	0.223	1.101	0.542	265
240	3.89	0.0639	1.101	0.542	112
220	3.89	0.0158	1.101	0.542	43.9
200	3.89	3.78×10^{-3}	1.101	0.542	26.8
180	3.89	9.45×10^{-4}	1.101	0.542	18.1
160	3.89	1.45×10^{-5}	1.101	0.542	14.2

Table 2. Saturation current and the imperfection coefficient at $T = 293$ K for various mesa structures

Parameter	Mesa structure						
	A0	B0	C0	D0	D9	E4	E5
J_0, mA	1.43	1.48	0.87	0.98	13.9	1.63	1.33
n	1.402	1.404	1.064	1.0	1.402	1.358	1.202

Table 3. Richardson constant, contact potential difference, and trap density in the dislocation network region

Mesa structure	A^*	$e\varphi_b$, eV	N_{MD}, cm^{-3}
1D9	0.0225	0.274	2.6×10^{14}
1E4	0.00682	0.215	2.5×10^{15}
1E5	0.00573	0.180	1.0×10^{16}
2C3	0.01663	0.85	3.0×10^{16}

The thickness of the buffer silicon layer is usually comparable to the thickness of the layer disturbed in the region of the dislocation network and to the electron shielding length. Therefore, the total barrier height φ_b is the sum of the barrier heights at the n-Si$_{1-x}$Ge$_x$/n-Si heterojunction and the n–n^+ junction in silicon, i.e., $\varphi_b = \varphi_{\mathrm{MD}} + \Delta\varphi_c$. The position of the conduction-band bottom in the barrier layer with respect to the Fermi level corresponds to φ_b and is given in Table 3 for various mesa structures. The conduction-band bottom rises because of electrons captured by traps localized in the region of plastic deformation and, therefore, determines the values of N_{MD}(Si) (the electron concentration near the dislocation network) listed in Table 3. The data from Table 3 indicate that the concentration of traps at dislocations in the heterojunction can vary within one or two orders of magnitude over the area of the structure (or from mesa to mesa).

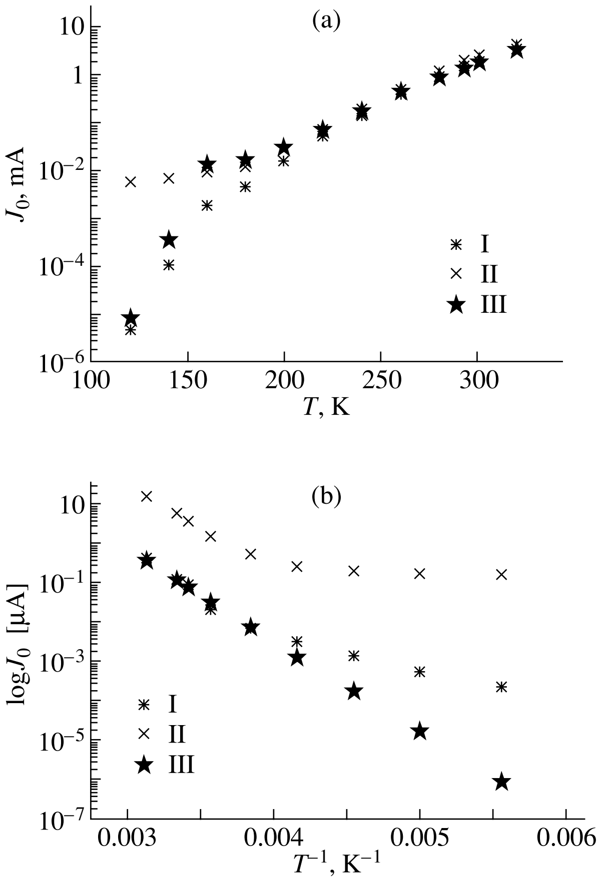

Fig. 5. Temperature dependences of the current J_0 in the J–U characteristics for (a) 1D3 and (b) 2E5 mesa structures with ohmic Al and Schottky contacts, respectively. (I) Values of J_0 obtained from the forward branch of the J–U characteristic; (II) reverse currents measured at (a) $U = -1$ and (b) -2 V; and (III) values of J_0 calculated by Eq. (5) at (a) $A^* = 0.0225$, $e\varphi_b = 0.274$ eV, and $n = 1.4$ and (b) $A^* = 0.0116$, $e\varphi_b = 0.85$ eV, and $n = 2$.

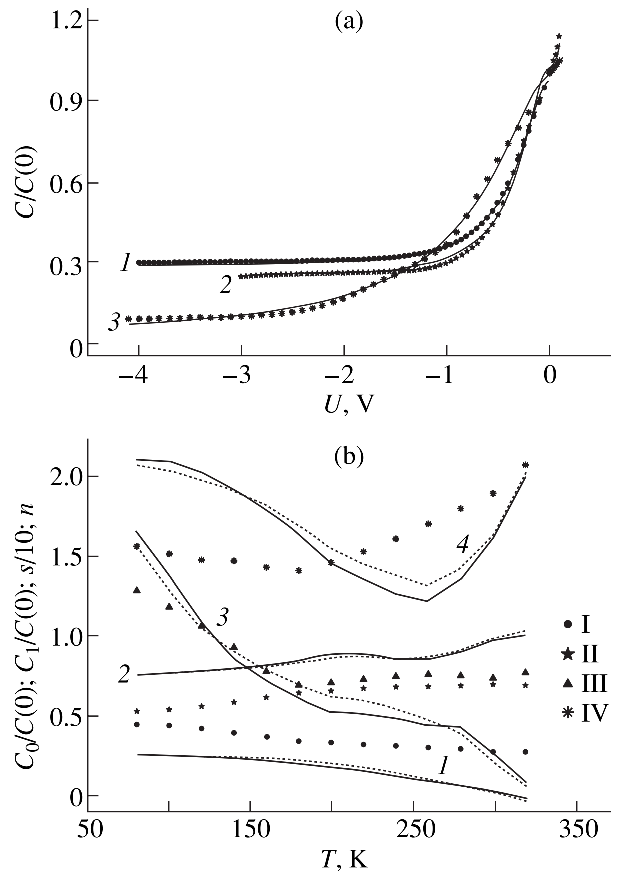

Fig. 6. (a) C–U characteristic at $T = 300$ K for (*1*) mesa structure 2C4 with a Schottky contact and mesa structures (*2*) 1D9 and (*3*) 1E4 with an ohmic Al contact. The solid lines are calculated by Eq. (7) using the parameters $C_0/C(0)$, $C_1/C(0)$, s, and n given in Table 4. (b) Temperature dependences of the J–U characteristic coefficients (*1*) $C_0/C(0)$, (*2*) $C_1/C(0)$, (*3*) s, and (*4*) n plotted for mesa structures 1D9 (solid lines) and 1E5 (dashed lines) and for mesa structure 2C4: (I) $C_0/C(0)$, (II) $C_1/C(0)$, (III) $s/10$, and (IV) n.

When analyzing the measured J–U characteristics, we assumed the nature of the contacts applied onto the outer side of the wafer according to a special technology to be ohmic. However, the possible appearance of a Schottky barrier at the Al/$Si_{1-x}Ge_x$ interface must not be ruled out. Measurements performed on this structure with an Al Schottky contact applied onto the upper layer of the $Si_{1-x}Ge_x$ solid solution showed a substantially different J–U characteristic of the system. The typical J–U characteristic for structure 347 with a Schottky contact is shown in Fig. 4b (see also [14]). The appearance of a barrier at the metal–semiconductor interface decreases reverse currents by several orders of magnitude and, simultaneously, increases the breakdown voltage for the structure. An analysis of the temperature dependences of the reverse current and J_0 (Fig. 5b) reveals that the reverse current is also determined by

Table 4. Fitting parameters of the C–U characteristic for several mesa structures measured at $T = 300$ K

Mesa structure	$C_0/C(U = 0)$	$C_1/C(U = 0)$	s	n
1D9	0.02233645	0.9676168	2.5934766	1.602602
1E4	0.00746530	0.99260988	1.6705343	1.606153
1E5	0.0171715	0.982764	1.9959967	1.6304558
2C4	0.2763548	0.69646187	7.34365559	1.8935072

currents flowing along dislocations [$J(U < -1) > J_0$] that pass through the structure and reach the outer surface.

The C–U characteristic of the structure has a typical form and is demonstrated in Fig. 6a for several mesa structures. The experimental dependences are described with high accuracy by the relation

$$C(U) = C_0 + C_1/(1 + sU^n). \tag{7}$$

The calculated $C(U)$ dependences are shown by solid lines in Fig. 6a. The corresponding values of the parameters C_0, C_1, s, and n are given in Table 4. It should be noted that we did not detect any features in the $C(U)$ dependences related to deep centers near the dislocation network for this structure at any temperatures. The temperature dependences of the coefficients C_0, C_1, s, and n are shown in Fig. 6b.

With a reverse bias, the decrease in the system capacitance is caused by the extension of the space-charge region (SCR) in the vicinity of the heterojunction. However, the voltage dependence of the capacitance for the heterostructure cannot be described by simple dependences of the type $C(U) \sim C_1/(U_b - U)^m$ with $m = 0.3$–0.5 that are typical of a simple barrier model. This is likely due to a more complex character of charging of centers located near the dislocation network and to the presence of currents that flow along dislocations and shunt this capacitance. As was shown above in analyzing the J–U characteristic, the voltage dependence of these currents is more complex than the Ohm law. An analysis of the values of C_0 at $U = 0$ and in the range of saturation of reverse currents allows certain conclusions to be drawn about the SCR width at a zero and a high negative bias voltage applied to the structure. For estimation, we use the simple relation

$$C(U) = S\varepsilon/W = 0.672 \times 10^{-14}/W(U), \tag{8}$$

where S is the contact area of the structure and $W(U)$ is the width of the SCR, which determines the measured value of the structure capacitance at a given voltage across the diode. In the case of ohmic contacts (mesa structure 1D9), we obtain the following values for $W(U)$ at $T = 300$ K: $W(0) = 0.067$ μm and $W(-4\text{ V}) = 0.85$ μm. At a zero bias voltage, the capacitance is determined by the region with a high resistance in the vicinity of the dislocation network (Fig. 3) and $W(0)$ gives the values of the actual width of a disturbed layer near the heterojunction. At a high negative bias voltage, the depletion layer expands over the whole width of the epitaxial structure, $W(-4\text{ V}) = d_{\text{SiGe}} + d_{\text{Si}} \approx 0.8$ μm. In the structure where the upper contact is a Schottky barrier (mesa structure 2C4), $W(0) = 0.27$ μm; that is, the SCR associated with the Schottky contact covers the entire solid-solution layer and the adjacent portion of the epitaxial Si layer with a dislocation network. At $U = -4$ V, we have $W(-4\text{ V}) = 0.9$ μm, which corresponds to the situation considered above, where the SCR covers the entire epitaxial structure.

ACKNOWLEDGMENTS

This work was supported by the Russian and Hungarian Academies of Sciences (project no. 15), ISTC (project no. 2372), and OTKA (project no. T035272).

REFERENCES

1. P. Waltereit, J. M. Fernandes, S. Kaya, and T. J. Thornton, Appl. Phys. Lett. **72** (18), 2262 (1998).
2. T. G. Yugova, V. I. Vdovin, M. G. Milvidskii, L. K. Orlov, V. A. Tolomasov, A. V. Potapov, and N. V. Abrosimov, Thin Solid Films **336** (1–2), 112 (1999).
3. X. L. Yuan, T. Sekiguchi, S. G. Ri, and S. Itol, in *Proceedings of DRIP X* (Batz-sur-Mer, France, 2003), p. 45.
4. L. K. Orlov, A. V. Potapov, N. L. Ivina, E. A. Steinman, and V. I. Vdovin, Solid State Phenom. **69–70**, 377 (1999).
5. É. A. Steinman, Doctoral Dissertation (Inst. of Solid-State Physics, Russian Academy of Sciences, Chernogolovka, 2002).
6. A. G. Milnes and D. L. Feucht, *Heterojunctions and Metal–Semiconductor Junctions* (Academic, New York, 1972; Mir, Moscow, 1975).
7. L. K. Orlov, A. V. Potapov, and S. V. Ivin, Zh. Tekh. Fiz. **70** (6), 102 (2000) [Tech. Phys. **45**, 770 (2000)].
8. L. K. Orlov, V. A. Tolomasov, and A. V. Potapov, in *Proceedings of Second Russian Symposium on Processes of Heat and Mass Transfer and Growth of Single Crystals and Thin-Filmed Structures*, Ed. by V. P. Ginkin (Obninsk, 1998), p. 288.
9. V. A. Tolomasov, L. K. Orlov, S. P. Svetlov, A. D. Gudkova, A. V. Kornaukhov, A. V. Potapov, and Yu. N. Drozdov, Kristallografiya **43** (3), 535 (1998) [Crystallogr. Rep. **43**, 493 (1998)].
10. L. K. Orlov, V. A. Tolomasov, A. V. Potapov, and V. I. Vdovin, Mater. Élektron. Tekh. **2**, 30 (1998).
11. E. P. O'Relly, Semicond. Sci. Technol. **4**, 121 (1989).
12. M. M. Rieger and P. Vogl, Phys. Rev. B **48** (19), 14276 (1993).
13. Zs. J. Horváth, M. Ádám, I. Szabó, M. Serényi, and Vo Van Tuyen, Appl. Surf. Sci. **190**, 441 (2002).
14. Zs. J. Horváth, L. K. Orlov, V. Rakovics, N. L. Ivina, A. L. Tóth, E. S. Demidov, Ferenc Riesz, V. I. Vdovin, and Z. Pászti, in *Proceedings of DRIP X* (Batz-sur-Mer, France, 2003), p. 107.
15. C. van Opdorp and N. K. J. Kanerva, Solid-State Electron. **10**, 401 (1967).
16. L. K. Orlov, Z. J. Horvath, N. L. Ivina, V. I. Vdovin, E. A. Steinman, M. L. Orlov, and Yu. A. Romanov, Opto-Electron. Rev. **11** (2), 85 (2003).

Translated by K. Shakhlevich

Physics of the Solid State, Vol. 46, No. 11, 2004, pp. 2146–2152. Translated from Fizika Tverdogo Tela, Vol. 46, No. 11, 2004, pp. 2076–2082.

Electrical Properties of Amorphous $(Co_{45}Fe_{45}Zr_{10})_x(Al_2O_3)_{1-x}$ Nanocomposites

Yu. E. Kalinin, A. N. Remizov, and A. V. Sitnikov

Voronezh State Technical University, Moskovskiĭ pr. 14, Voronezh, 394026 Russia

e-mail: kalinin@ns1.vstu.ac.ru

Received March 15, 2004

Abstract—The electrical properties of $(Co_{45}Fe_{45}Zr_{10})_x(Al_2O_3)_{1-x}$ granular nanocomposites have been studied. The concentration dependences of electrical resistivity are *S*-shaped (in accordance with the percolation theory of conduction) with a threshold at a metallic component concentration of ~41 at. %. An analysis of the temperature behavior carried out in the range 300–973 K revealed that structural relaxation and crystallization of the amorphous phase are accompanied by a decrease in the electrical resistivity of the composites above the percolation threshold and by its increase below the percolation threshold. For metallic phase concentrations $x < 41$ at. %, variable range hopping conduction over localized states near the Fermi level was found to be dominant at low temperatures (77–180 K). A further increase in temperature brings about a crossover of the conduction mechanism from Mott's law $\ln(\sigma) \propto (1/T)^{1/4}$ to $\ln(\sigma) \propto (1/T)^{1/2}$. A model of inelastic resonance tunneling over a chain of localized states of the dielectric matrix was used to find the average number of localized states involved in the charge transport between metallic grains. *© 2004 MAIK "Nauka/Interperiodica".*

1. INTRODUCTION

Extensive experimental effort is being devoted to the study of composite materials with metallic nanoparticles embedded in a dielectric matrix. The interest in these materials stems both from their application potential in electronics and from the possibilities they offer in addressing basic problems in solid-state physics. In particular, granular composites made up of ferromagnetic nanoparticles in a dielectric matrix possess unique physical properties, including giant magnetoresistance [1–3], a considerable magnetorefractive effect [4], good magnetooptical characteristics [5], high absorptivity of electromagnetic radiation in the RF and microwave ranges [6], a broad range of electrical resistivity variation, etc. [7–10].

On the scientific side, the interest in nanocomposites is spurred by the possibility of studying various quantum mechanisms of electrical conductivity, magnetization, and other properties over a broad range of compositions, both above and below the percolation threshold. For instance, above the percolation threshold, the metallic grains in a composite form a network through which metallic conduction sets in, with its magnitude being determined by the fractal structure of the conducting metallic-phase channels. Grains present in composites with a low metallic phase concentration are electrically insulated from one another in the matrix; therefore, the electrical conductivity in such composites is determined primarily by the dielectric component, while the question of the temperature behavior remains open in this case. Experimentally, the temperature dependence of electrical conductivity in this concentration range at low temperatures obeys, in most cases, the "one-half power law" [11]

$$\sigma \propto \exp(-T^{-1/2}), \tag{1}$$

which can be related to various mechanisms. In the model of activated tunneling (model of Sheng–Abeles), charge transport is assumed to occur by electron tunneling directly from one grain to another through dielectric barriers [12, 13] and Eq. (1) is treated as a manifestation of a Coulomb gap in the electron density of states on the grains [14]. The model of thermally activated hopping conduction assumes the one-half power law to be a consequence of the broad scatter in grain size, a feature characteristic of real composites [15]. In an attempt to account for the experimental relations, Lutsev invokes a theoretical model of inelastic tunneling [16, 17] by relating the one-half power law to resonance tunneling over a chain of localized states in an amorphous dielectric layer sandwiched between grains [18, 19]. In this conduction mechanism, one should expect the onset of variable range hopping conduction at lower temperatures [20]; it has indeed been observed in some composites [21, 22].

Our goal was to study the conduction mechanisms in $(Co_{45}Fe_{45}Zr_{10})_x(Al_2O_3)_{1-x}$ amorphous nanocomposites over a broad range of metallic phase concentrations and temperatures.

2. SAMPLES AND EXPERIMENTAL TECHNIQUES

Granular amorphous nanoclusters of a $Fe_{45}Co_{45}Zr_{10}$ alloy distributed randomly in an Al_2O_3 amorphous

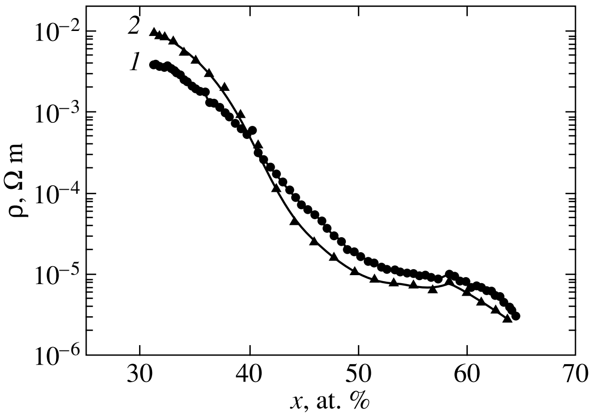

Fig. 1. Electrical resistivity of granular $(Co_{45}Fe_{45}Zr_{10})_x(Al_2O_3)_{1-x}$ composites plotted vs. metallic phase concentration x (*1*) in the original state and (*2*) after annealing at T = 400°C for 30 min.

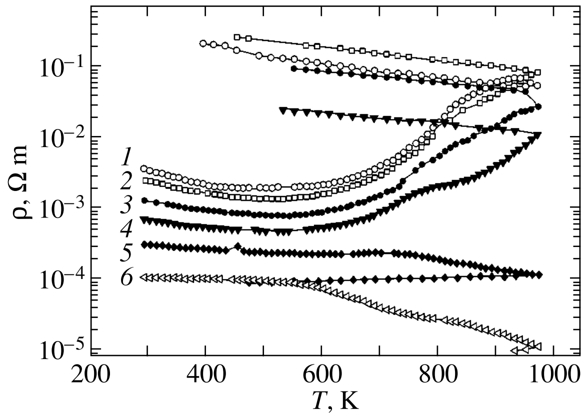

Fig. 2. Temperature dependences of the electrical resistivity of granular $(Co_{45}Fe_{45}Zr_{10})_x(Al_2O_3)_{1-x}$ composites measured at different metallic phase concentrations x: (*1*) 31.7, (*2*) 34, (*3*) 36.3, (*4*) 38.7, (*5*) 40.8, and (*6*) 43.7 at. %.

dielectric matrix were obtained by ion beam sputtering [23]. The choice of metallic grains of the complex composition $Fe_{45}Co_{45}Zr_{10}$ was motivated by the need to stabilize the amorphous structure of the ferromagnet (which is stable at room temperature). To favor the amorphous state, we added 10 at. % zirconium to ferromagnetic iron and cobalt atoms. In addition, the amorphous alloy $Fe_{45}Co_{45}Zr_{10}$ has a comparatively high saturation magnetostriction ($\lambda_s \approx 28 \times 10^{-6}$), which is an important factor for studies of the magnetoresistance and magnetooptical properties of composites. The material of the matrix (Al_2O_3) was chosen because it is thermally stable over a broad temperature range.

Metal–dielectric nanocomposites were deposited from a composite target, which was a cast base of a metal alloy of appropriate composition 270 × 80 × 20 mm in size with twelve aluminum oxide plates ~2 mm thick and ~9 mm wide fixed to its surface. The distance between the plates varied smoothly from 4 mm at one end of the target to 44 mm at the other. This composite target permitted fabrication, in one operational cycle, of composites over a broad range of concentrations of the metallic and dielectric components, depending on the position of the component relative to the substrates in the deposition chamber. The substrates were five glass-ceramic plates measuring 60 × 48 mm.

Using x-ray microprobe analysis, the composition of the composites was determined from five measurements made on different parts of the substrates, with subsequent polynomial extrapolation of the composition along the substrate length. The samples obtained by deposition were films 5- to 10-μm thick. The film thickness was measured with a MII-4 interferometer. The temperature dependence of electrical resistivity was studied using 2-mm-wide, 9-mm-long samples deposited on a glass-ceramic substrate.

Electrical resistivity measurements were carried out by the two-probe potentiometric method. A cryostat was employed to study the properties of the composites in the temperature interval 77–300 K. The absolute error of temperature measurement was ±1 K, and the relative error of electrical resistivity measurements was 0.5%.

3. EXPERIMENTAL RESULTS AND DISCUSSION

Figure 1 plots the dependence of electrical resistivity of $(Co_{45}Fe_{45}Zr_{10})_x(Al_2O_3)_{1-x}$ composites on the concentration of the metallic component at room temperature in the original state and after thermal treatment at T = 400°C for 30 min. When in the original state, an increase in x from 28 to 65 at. % causes the electrical conductivity of the systems under study to vary by more than three orders of magnitude (curve *1*). After treatment (curve *2*), the behavior of the electrical conductivity above and below $x \approx 41$ at. % follows different patterns; i.e., one can isolate a dielectric and a metallic region, a feature characteristic of percolation systems. Note that the thermal treatment brings about an increase in electrical resistivity for compositions below the percolation threshold and a decrease for compositions above the percolation threshold. The electrical resistivity of composites close to the percolation threshold is $\rho \sim 3 \times 10^{-4}$ Ω m and is determined by the fractal structure of metal-grain conducting channels. The reciprocal value of this electrical resistivity, $\sigma_{min} \sim 33.3$ Ω^{-1} cm^{-1}, may be considered the minimum metallic conductivity at the metal–insulator transition (the Anderson transition) for this system.

To study thermal stability of the amorphous state of the nanocomposites, temperature dependences of the electrical resistivity were measured (Fig. 2). In one group of composites (with the metallic phase content below the percolation threshold), the electrical resistivity varies only slightly over the range from room temperature to 750 K, while at higher temperatures it grows noticeably up to $T \approx 923$ K, with a subsequent small falloff. In the

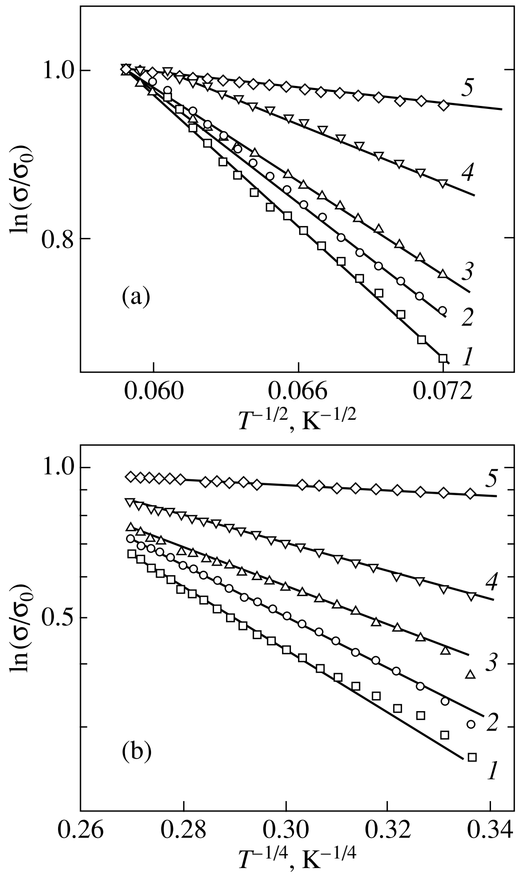

Fig. 3. Temperature dependences of electrical resistivity of $(Co_{45}Fe_{45}Zr_{10})_x(Al_2O_3)_{1-x}$ composites plotted in the coordinates (a) $\ln(\sigma/\sigma_0)$ vs. $(1/T)^{1/2}$ and (b) $\ln(\sigma/\sigma_0)$ vs. $(1/T)^{1/4}$ in the temperature regions (a) 180–290 K and (b) 80–180 K for different metallic phase concentrations x: (*1*) 31.7, (*2*) 34, (*3*) 36.3, (*4*) 37.3, and (*5*) 38.7 at. %.

crystalline state, such composites also have a negative temperature coefficient of electrical resistivity.

In another group of composites, whose metal content is in excess of 41 at. %, the electrical resistivity decreases slightly throughout the temperature range covered, with a sharper falloff in the region of the crystallization temperatures. Charge transport in this group occurs over the amorphous metallic phase forming a continuous network of inclusions in the dielectric matrix. The electrical resistivity of the composite is governed in this case by the concentration and structure of the metallic phase, as well as by the morphology of the composite as a whole. An increase in temperature gives rise to a decrease in the electrical resistivity of such composites as a result of structural relaxation and subsequent crystallization of the disordered structure, a feature characteristic of amorphous metal alloys.

Parameters of the $(Co_{45}Fe_{45}Zr_{10})_x(Al_2O_3)_{1-x}$ composites derived from temperature dependences of electrical conductivity

x, at. %	B, K (see Eq. (2))	$g(E_F)$, eV^{-1} cm^{-3}	R, nm (T = 100 K)
31.7	14.65^4	8.2×10^{20}	1.4
34	12.2^4	1.7×10^{21}	1.16
36.3	9.03^4	5.7×10^{21}	0.85
37.3	6.45^4	2.2×10^{22}	0.61

In an attempt to establish the mechanisms of electrical conductivity in the $(Co_{45}Fe_{45}Zr_{10})_x(Al_2O_3)_{1-x}$ composites below the percolation threshold, a study of the temperature dependences of electrical resistivity was made in the temperature interval 78–300 K and the results were plotted as $\ln(\sigma/\sigma_0)$ vs. $(1/T)^{1/4}$and $\ln(\sigma/\sigma_0)$ vs. $(1/T)^{1/2}$ graphs, where σ_0 is the room-temperature electrical conductivity. Our low-temperature studies showed that both the $\ln(\sigma/\sigma_0)$ vs. $(1/T)^{1/4}$ and $\ln(\sigma/\sigma_0)$ vs. $(1/T)^{1/2}$ plots of all the compositions studied exhibit a pronounced break at a temperature of 180 ± 10 K, which indicates a change in the mechanism of electrical conduction. It was established that, in the low-temperature region, the electrical conductivity obeys the one-fourth power law and, in the range 180–300 K, the one-half power law, as shown in Fig. 3.

The fact that Mott's law holds in the range 80–180 K implies that charge transport in the composites under study is dominated by variable-range electron hopping over localized states in a narrow energy band near the Fermi level, with the conductivity taking on the form [20]

$$\sigma = e^2 R^2 \nu_{ph} g \exp\left(-\frac{B}{T}\right)^{1/4}, \qquad (2)$$

where

$$B = \frac{1.66}{a^3 k g(E_F)}, \qquad (3)$$

e is the electronic charge, R is the hopping range, ν_{ph} is the spectral factor of the phonons involved in interaction, T is the absolute temperature, $g(E_F)$ is the density of states at the Fermi level, a is the electron wave-function localization length, and k is the Boltzmann constant.

Figure 3b was used to determine the values of the quantities B for four compositions of the composites, which were found to vary from 6.45^4 to 14.65^4 K (see table). Knowing B and assuming that $a \approx 0.8$ nm for the localization length, we obtain values for the density of states at the Fermi level $g(E_F)$ ranging from ~ 8.2×10^{20} to ~2.2×10^{22} eV^{-1} cm^{-3} for different compositions of the composites. The estimated densities of states are very high because localized states can derive not only from structural defects of the dielectric matrix but also from the matrix–grain boundaries. Note that, as the concentration of the metallic phase increases and approaches the percolation threshold, the density of states approaches the values characteristic of amorphous metal alloys. In particular, the Fermi level in amorphous alloys of transition metals with zirconium may fall at the maximum in the valence band density of states (primarily of the *d* states) and the density of states may amount to a few states/eV atom [24]. As the concentration of the dielectric phase grows, the density of states at the Fermi level is observed to decrease and to approach the values typical of amorphous semiconductors prepared by sputtering in the gas phase [25].

Using the expression [20]

$$R(T) = \frac{3}{8}aB^{1/4}T^{-1/4} \tag{4}$$

we estimated the carrier hopping range at a temperature of ~100 K (see table).

The average hopping range is about 1 nm and decreases with increasing metallic phase concentration. This trend correlates with the decrease in the grain separation.

The presence of localized states in the dielectric matrix should also affect the mechanism of conduction at higher temperatures where the $\ln\sigma \propto (1/T)^{1/2}$ law holds and where the phonon energy becomes important in the charge transport. Therefore, the temperature dependence of electrical conductivity in this temperature interval was described in terms of the model of inelastic resonance tunneling [16, 17] assuming the transport to occur over a finite number of channels with an average number of localized states $\langle n\rangle$; the number of these states was determined by the technique elaborated in [18, 19]. According to this model, the temperature dependence of conductivity in a channel containing *n* localized states is described by the power law

$$\sigma_n = P\left(\frac{\Lambda^2}{dc^5}\right)^{(n-1)/(n+1)}\frac{(ga^2n^2l)^nT^{\gamma_n}E^{\beta_n}}{al} \times \exp\left[\frac{-2l}{a(n+1)}\right], \tag{5}$$

where *a* is the radius of a localized state, *l* is the average separation between grains, $\gamma_n = n - 2/(n+1)$, $\beta_n = 2n/(n+1)$, *P* is a coefficient, Λ is a deformation potential constant, *d* is the density of the matrix material, *c* is the velocity of sound, *g* is the density of localized states, and *E* is the energy depth of a localized state in the barrier region. The average electrical conductivity between grains can be given by the sum of the conductivities over several channels:

$$\sigma^{(gr)} = \sum_n \sigma_n. \tag{6}$$

The total conductivity σ of a granular structure below the percolation threshold is determined by the tunneling conductivity between grains $\sigma^{(gr)}$ or (if the grains form finite conducting clusters) by the conductivity of the clusters and that between the clusters. Because the cluster conductivity is much higher than the tunneling conductivity, one can assume, as a first approximation, that the main contribution to the total σ of a granular structure in Eq. (6) in the temperature interval $[T_n, T_{n+1}]$ is due to one term, σ_n. This will result in a power-law dependence of σ on temperature determined by $\sigma^{(gr)}$ with $n = \langle n\rangle$ (the structure-averaged number of localized states in tunneling channels between grains), and the temperature dependence of the electrical conductivity will be described by the relation

$$\ln\sigma \propto -\left[\frac{2l}{\alpha}\ln\left(\frac{1}{g\alpha l^2T}\right)\right]^{1/2}. \tag{7}$$

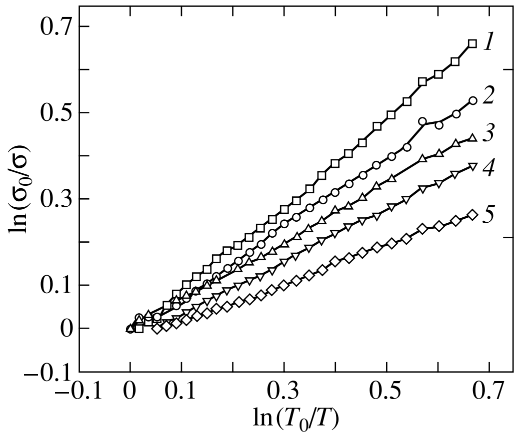

Fig. 4. Relative temperature dependences of the conductivity of $(Co_{45}Fe_{45}Zr_{10})_x(Al_2O_3)_{1-x}$ samples in original state plotted for different concentrations of the metallic phase *x*: (*1*) 31.7, (*2*) 34, (*3*) 36.3, (*4*) 37.3, and (*5*) 38.7 at. %.

By fitting the experimental $\sigma(T)$ curves by power-law relations with an exponent γ and using Eq. (1), it became possible to determine the average number of localized states $\langle n\rangle$ between the grains involved in electron transport over a granular structure at a given temperature as [18, 19]

$$\langle n\rangle = \frac{1}{2}[\gamma - 1 + (\gamma^2 + 2\gamma + 9)^{1/2}]. \tag{8}$$

Taking into account the power law in Eq. (5), the experimental $\sigma(T)$ dependences were plotted in $\ln(\sigma_0/\sigma)$ versus $\ln(T_0/T)$ coordinates with $T_0 = 300$ K (Fig. 4). An analysis of the experimental relations revealed that these data can be fitted to a power law within a fairly broad temperature interval (where the $\ln\sigma \propto (1/T)^{1/2}$ law holds). In this way, one could determine the exponent γ of the temperature dependences of conductivity and calculate the average number of localized states $\langle n\rangle$ in the tunneling channels between isolated conducting grain clusters from Eq. (8).

Calculations showed that the average number of localized states between grains decreases practically linearly as the metal fraction in the composite is

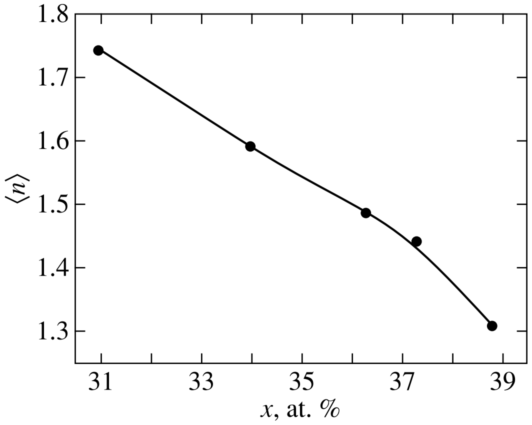

Fig. 5. Average number of localized states plotted vs. concentration of the metallic component for $(Co_{45}Fe_{45}Zr_{10})_x(Al_2O_3)_{1-x}$ composites in original state.

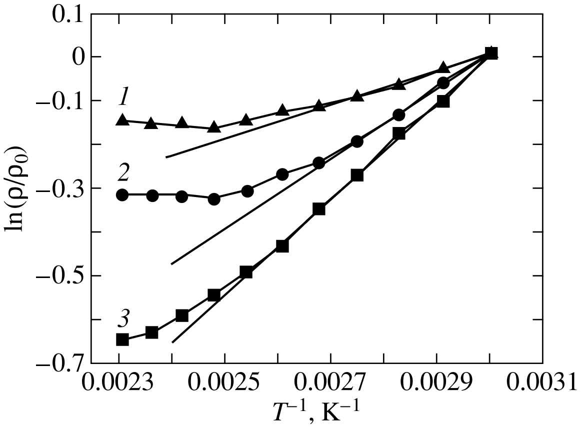

Fig. 6. Temperature dependences of electrical resistivity plotted in $\ln(\rho/\rho_0)$ vs. T^{-1} coordinates for $(Co_{45}Fe_{45}Zr_{10})_x(Al_2O_3)_{1-x}$ composites in the temperature interval 330–600 K for different concentrations of the metallic phase x: (*1*) 34, (*2*) 28, and (*3*) 23 at. %.

increased (Fig. 5). At high concentrations of the dielectric component in composites with an Al_2O_3 matrix, the values of $\langle n \rangle$ are almost the same as those for SiO_2-matrix composites [26]. For the conduction mechanism under consideration, the temperature dependence satisfying the one-half power law holds for T above a temperature T^* given by the relation [19]

$$\ln(T^* g a l^2) \approx -\left(\frac{l}{a}\right)^{1/3}. \tag{9}$$

Assuming $T^* \approx 180$ K (i.e., the temperature at which the mechanism of conduction crosses over from the $\ln\sigma \propto (1/T)^{1/4}$ to $\ln\sigma \propto (1/T)^{1/2}$ relation) and accepting $a \approx 0.8$ nm and $l \approx 2$ nm, we estimated the density of localized states as $g \approx 1.3 \times 10^{22}$ eV^{-1} cm^{-3}, which coincides, in order of magnitude, with the data obtained using Eq. (2).

An analysis of the temperature dependences of electrical resistivity of prepercolation composites presented in Fig. 1 revealed that, above room temperature, these dependences deviate from the one-half power law and become linear in $\ln(\rho/\rho_0)$ versus T^{-1} coordinates within a certain temperature interval, where ρ_0 is the electrical resistivity at $T = 333$ K (Fig. 6). By fitting the temperature dependences by the relation for thermally activated hopping conductivity

$$\rho = \rho_0 \exp\left(\frac{w}{kT}\right) \tag{10}$$

(where w is the hopping activation energy, which is on the order of the bandwidth of localized states) and determining the slope of the corresponding straight lines for the $(Co_{45}Fe_{45}Zr_{10})_x(Al_2O_3)_{1-x}$ composites under study (Fig. 6), we find $w = 0.030 \pm 0.005$, 0.066 ± 0.007, and 0.09 ± 0.01 eV for $x = 34$, 28, and 23 at. %, respectively. In this temperature interval, one can also use the inelastic resonance tunneling model and assign the deviation from the one-half power law to the switching of additional tunneling channels, which should give rise to an increase in electrical conductivity.

Thus, additional studies would be needed prior to drawing a convincing conclusion on the conduction mechanism operating in this temperature interval.

A further increase in temperature reveals a deviation from a linear course in the $\ln(\rho/\rho_0)$ versus (T^{-1}) dependence (Fig. 6), and ρ starts to grow slowly at $T > 600$ K (Fig. 2). This suggests that metal grains begin to affect charge transport. In these conditions, the conductivity in the matrix reaches the same order of magnitude as that in the grains and electron scattering from phonons becomes a dominant process in this temperature interval. For temperatures $T > 700$ K, structural relaxation followed by crystallization sets in in the amorphous structure of the composites, which gives rise to irreversible morphological changes and is accompanied by a strong increase in electrical resistivity.

Thus, at low and moderate temperatures, charge transport in prepercolation $(Co_{45}Fe_{45}Zr_{10})_x(Al_2O_3)_{1-x}$ composites is determined by the dielectric matrix, with the major conduction mechanisms being variable-range hopping and inelastic resonance tunneling over localized states near the Fermi level. The experimentally revealed high densities of localized states should be assigned to technological aspects of the fabrication of nanocomposites. The sample preparation procedure entails a partial oxidation of metal grains, which results in a deficiency of atomic oxygen in the dielectric matrix and in a predominant formation of Al_2O_y, where y may assume values less than 3. Hence, such a matrix abounds in defects at which an electron can become localized at low temperatures.

If structural defects in the amorphous dielectric matrix are responsible for the formation of localized states, thermal treatment should reduce the number of these states. To confirm this assumption, a series of iso-

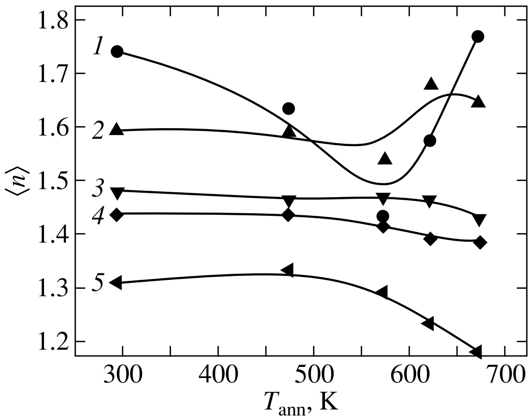

Fig. 7. Average number of localized states in $(Co_{45}Fe_{45}Zr_{10})_x(Al_2O_3)_{1-x}$ composites plotted vs. isothermal-annealing temperature for different metallic phase concentrations *x*: (*1*) 31.7, (*2*) 34, (*3*) 36.3, (*4*) 37.3, and (*5*) 38.7 at. %.

thermal anneals in a vacuum of $\sim 10^{-4}$ Torr for 30 min were carried out at temperatures *T* ranging from 293 to 893 K and Eq. (8) was used to calculate the average number of localized states $\langle n\rangle$ in the tunneling channels connecting isolated conducting clusters as a function of the anneal temperature.

Figure 7 plots the dependences of the average number of localized states $\langle n\rangle$ on the temperature of isothermal anneals of $(Co_{45}Fe_{45}Zr_{10})_x(Al_2O_3)_{1-x}$ composites determined for different compositions. Thermal treatment performed at temperatures of up to 550 K was found to reduce the average number of localized states between grains for all metallic phase concentrations. In composites with concentrations of the metallic phase $x < 37$ at. %, however, increasing the anneal temperature brings about an increase in $\langle n\rangle$. Such dependences of $\langle n\rangle$ on T_{ann} suggest the operation of two relaxation processes. One of them leads to a decrease in the average number of localized states $\langle n\rangle$, and the other, to an increase in $\langle n\rangle$. It is quite possible that the decrease in $\langle n\rangle$ is associated with the annealing of defects in the dielectric matrix, because the matrix is responsible for the localized states.

The simplest defect in covalently bonded structures is a dangling bond [27]. Point defects in an amorphous structure turn out to be more diverse than those in a crystal lattice. They may be simple (single dangling bonds) or more complex, combining several dangling bonds. At low temperatures of thermal treatment, defects in the amorphous structure may become annealed through decay of the complex defects into simpler species, with their subsequent migration to the grain–matrix interface, as shown schematically in Fig. 8. Defect migration toward interfaces at low temperatures is the dominant mechanism in the composites under study, and it leads to a fairly small decrease in the average number of localized states $\langle n\rangle$. As the annealing temperature is increased to above 700 K, structural relaxation followed by crystallization brings about irreversible changes in the morphology of the structure and a certain growth of the average number of localized states $\langle n\rangle$ in composites with a high concentration of the dielectric phase.

4. CONCLUSIONS

Thus, we have experimentally studied concentration and temperature dependences of the electrical conductivity of the $(Co_{45}Fe_{45}Zr_{10})_x(Al_2O_3)_{1-x}$ composites and determined the concentration of the components corresponding to the percolation threshold: $xc \approx 41$ at. %. The dominant mechanism of charge transport at metallic phase concentrations $x < 41$ at. % and low temperatures (77–180 K) was found to be variable-range hopping conduction over localized states near the Fermi level. A further increase in temperature results in a crossover of the conduction mechanism from Mott's law, $\ln\sigma \propto (1/T)^{1/4}$, to a dependence $\ln\sigma \propto (1/T)^{1/2}$. The model of inelastic resonance electron tunneling was applied to the $(Co_{45}Fe_{45}Zr_{10})_x(Al_2O_3)_{1-x}$ composites to

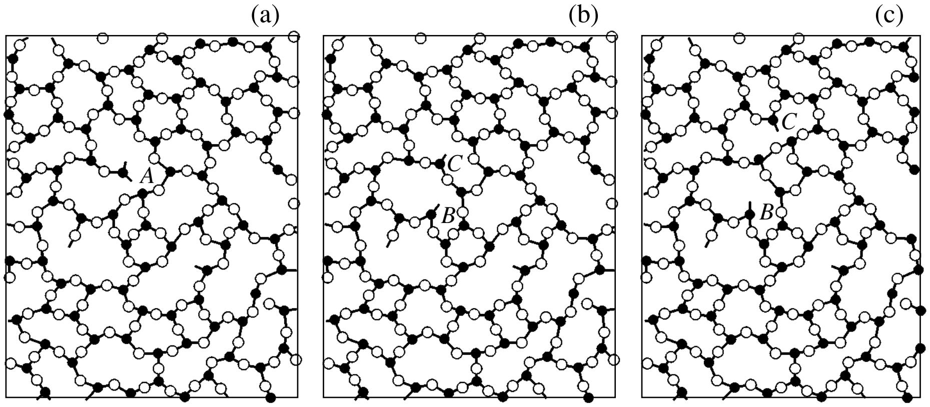

Fig. 8. Illustration of the decay of (a) defect *A* in an amorphous structure into (b) the simplest defects *B* and *C* and (c) the migration of defect *C* to the grain/matrix interface (schematic).

find the average number of localized states in the dielectric matrix between the metal grains involved in electron transport and its dependence on the temperature of isothermal annealing. It was established that increasing the thermal treatment temperature brings about a decrease in the average number of localized states in the dielectric matrix.

The studies of the temperature dependence of ρ in prepercolation composites at high temperatures revealed a strong growth of electrical resistivity long before the crystallization temperature is reached; this growth is caused by the merging of metal grains, an increase in the thickness of the dielectric spacers between grains, and a decrease in the average number of localized states between grains. The electrical resistivity of postpercolation composites decreases with increasing temperature as a result of the formation of additional conducting metallic channels and relaxation of the amorphous structure of the metallic phase.

ACKNOWLEDGMENTS

The authors are indebted to L.V. Lutsev for helpful discussions and valuable comments.

This study was supported by the Russian Foundation for Basic Research (project no. 03-02-96486) and the Ministry of Education of the Russian Federation.

REFERENCES

1. S. Honda, J. Magn. Magn. Mater. **165**, 153 (1997).
2. K. Yakushiji, S. Mitani, and K. Takanashi, J. Magn. Magn. Mater. **212**, 75 (2000).
3. N. Kobayashi, S. Ohnuma, T. Masumoto, and H. Fujimori, J. Appl. Phys. **90** (8), 4159 (2001).
4. I. V. Bykov, E. A. Gan'shina, A. B. Granovskiĭ, and V. S. Gushchin, Fiz. Tverd. Tela (St. Petersburg) **42** (3), 487 (2000) [Phys. Solid State **42**, 498 (2000)].
5. A. V. Kimel', R. V. Pisarev, A. A. Rzhevskiĭ, Yu. E. Kalinin, A. V. Sitnikov, O. V. Stogneĭ, F. Bentivegna, and Th. Rasing, Fiz. Tverd. Tela (St. Petersburg) **45** (2), 269 (2003) [Phys. Solid State **45**, 283 (2003)].
6. N. E. Kazantseva, A. T. Ponomarenko, V. G. Shevchenko, I. A. Chmutin, Yu. E. Kalinin, and A. V. Sitnikov, Fiz. Khim. Obrab. Mater., No. 1, 5 (2002).
7. O. V. Stogneĭ, Yu. E. Kalinin, A. V. Sitnikov, I. V. Zolotukhin, and A. V. Slyusarev, Fiz. Met. Metalloved. **91** (1), 24 (2001) [Phys. Met. Metallogr. **91**, 21 (2001)].
8. B. A. Aronzon, A. E. Varfolomeev, A. A. Likal'ter, V. V. Ryl'kov, and M. V. Sedova, Fiz. Tverd. Tela (St. Petersburg) **41** (6), 944 (1999) [Phys. Solid State **41**, 857 (1999)].
9. Yu. E. Kalinin, A. V. Sitnikov, O. V. Stognei, I. V. Zolotukhin, and P. V. Neretin, Mater. Sci. Eng. A **304–306**, 941 (2001).
10. H. R. Khan, A. Granovsky, F. Brouers, E. Ganshina, J. P. Clerc, and M. Kurmichev, J. Magn. Magn. Mater. **183**, 127 (1998).
11. J. C. Denardin, A. B. Pakhomov, M. Knobel, H. Liu, and X. X. Zhang, J. Phys.: Condens. Matter **12**, 3397 (2000).
12. B. Abeles, R. W. Cohen, and G. W. Cullen, Phys. Rev. Lett. **17**, 632 (1966).
13. P. Sheng, B. Abeles, and Y. Arie, Phys. Rev. Lett. **31** (1), 44 (1973).
14. E. Cuevas, M. Ortuño, and J. Ruiz, Phys. Rev. Lett. **71** (12), 1871 (1993).
15. E. Z. Meĭlikhov, Zh. Éksp. Teor. Fiz. **115** (4), 1484 (1999) [JETP **88**, 819 (1999)].
16. L. I. Glazman and K. A. Matveev, Zh. Éksp. Teor. Fiz. **94** (6), 332 (1988) [Sov. Phys. JETP **67**, 1276 (1988)].
17. L. I. Glazman and R. I. Shekhter, Zh. Éksp. Teor. Fiz. **94** (1), 292 (1988) [Sov. Phys. JETP **67**, 1462 (1988)].
18. L. V. Lutsev, T. K. Zvonareva, and V. M. Lebedev, Pis'ma Zh. Tekh. Fiz. **27** (15), 84 (2001) [Tech. Phys. Lett. **27**, 659 (2001)].
19. L. V. Lutsev, Yu. E. Kalinin, A. V. Sitnikov, and O. V. Stogneĭ, Fiz. Tverd. Tela (St. Petersburg) **44** (10), 1802 (2002) [Phys. Solid State **44**, 1889 (2002)].
20. N. F. Mott and E. A. Davis, *Electronic Processes in Non-Crystalline Materials* (Clarendon, Oxford, 1971; Mir, Moscow, 1974).
21. S. Weng, S. Moehlecke, and M. Strongin, Phys. Rev. Lett. **50** (22), 1795 (1983).
22. M. A. S. Boff, J. Geshev, J. E. Schmidt, W. H. Flores, A. B. Antunes, M. A. Gusmao, and S. R. Teixeira, J. Appl. Phys. **91** (12), 9909 (2002).
23. I. V. Zolotukhin, Yu. E. Kalinin, P. V. Neretin, A. V. Sitnikov, and O. V. Stogneĭ, Al'ternativ. Énerget. Ékol., No. 2, 7 (2002).
24. P. Olhafen, in *Glassy Metals II: Atomic Structure and Dynamics, Electronic Structure, Magnetic Properties*, Ed. by H. Beck and G. Güntherodt (Springer, Heidelberg, 1984; Mir, Moscow, 1986).
25. W. Heywang *et al.*, in *Amorphen und Polykristallinen Halbleiter*, Ed. by W. Heywang (Springer, Heidelberg, 1984; Mir, Moscow, 1987).
26. Yu. E. Kalinin, A. N. Remizov, A. V. Sitnikov, and N. P. Samtsova, Perspekt. Mater., No. 3, 62 (2003).
27. Yu. R. Zakis, *Defects in Vitreous State of Material* (Zinatne, Riga, 1984) [in Russian].

Translated by G. Skrebtsov

Physics of the Solid State, Vol. 46, No. 11, 2004, pp. 2153–2162. Translated from Fizika Tverdogo Tela, Vol. 46, No. 11, 2004, pp. 2083–2091.
Original Russian Text Copyright © 2004 by Averkiev, Berezovets, Mikhailova, Moiseev, Nizhankovskiĭ, Parfeniev, Romanov.

Energy Spectrum and Quantum Magnetotransport in Type-II Heterojunctions

**N. S. Averkiev[1], V. A. Berezovets[1, 2], M. P. Mikhailova[1], K. D. Moiseev[1],
V. I. Nizhankovskiĭ[2], R. V. Parfeniev[1], and K. S. Romanov[1]**
[1] *Ioffe Physicotechnical Institute, Russian Academy of Sciences, Politekhnicheskaya ul. 26, St. Petersburg, 194021 Russia*
e-mail: const@stella.ioffe.rssi.ru
[2] *International Laboratory of High Magnetic Fields and Low Temperatures, Wroclaw, Poland*

Received March 19, 2004

Abstract—Specific features of the energy spectrum of a separated type-II heterojunction in an external magnetic field are studied theoretically and experimentally. It is shown that, due to hybridization of the states of the valence band of one semiconductor and the conduction band of the other semiconductor at the heterointerface, there are level anticrossings, which produce quasigaps in the density of states in a nonzero magnetic field. The experimental results of magnetotransport studies for the GaInAsSb/*p*-InAs quaternary solid solutions with different doping levels are shown to agree well with the results of simulation, and specific features of the energy spectrum of separated type-II heterojunctions are established. *© 2004 MAIK "Nauka/Interperiodica".*

1. INTRODUCTION

Recently, heterostructures with separated type-II junctions, which are distinguished by the presence of an overlap in energy between the valence band of one of the contacting semiconductors and the conduction band of the other, have been intensively studied. A typical pair of the materials forming such a junction is InAs and GaSb [1].

The presence of the energy overlap results in the appearance of some specific features. For example, the fact that the mobile carriers are electrons on one side of the interface and holes on the other side should result in strong hybridization of the states of the conduction band of one semiconductor and of the valence band of the other. Band bending and deformation at the heterojunction bring about the formation of two two-dimensional potential wells on different sides of the interface, one for holes and the other for electrons. For example, for a GaSb–InAs heterojunction, a quantum well for holes is formed on the side of GaSb and a quantum well for electrons, on the side of InAs [2, 3]. In addition to single heterojunctions, structures consisting of two heterojunctions and a quantum well between them have also been widely studied [3]. A single type-II heterojunction with self-consistent quantum wells has analogous properties, but the specific form of the energy band bending near the heterointerface depends on the carrier concentration and can be changed by doping the contacting bulk materials.

A self-consistent calculation is necessary for exact quantitative description of the electronic structure of a separated type-II heterojunction. However, qualitative description of the character of hybridization and the positions of confinement energy levels can also be obtained by using simpler analytical models. In this study, we consider a single quantum well with infinitely high walls, which is divided into two parts for each of which the band parameters are constant (Fig. 1). Moreover, the band gaps are located such that there is an overlap between the valence band of one material (in our case, GaSb) and the conduction band of the other (InAs). For III–V semiconductors and their solid solutions forming heterojunctions of the type considered, the Kane model provides the most appropriate band diagram. In this model, we can take into account the boundary conditions and the actual values of the effective masses relatively simply (by integrating the original Hamiltonian). A magnetic field is included in this model in the standard way, by passing to generalized momenta and adding a term describing the g factor. In our calculation, we take into account only the electron g factor ($|g| = 10$) as the most essential.

The aim of this study is to calculate the energy spectrum of separated type-II heterojunctions both in a zero magnetic field and in a homogeneous magnetic field normal to the heterojunction plane and to compare the results with experimental data on magnetotransport in the GaInAsSb/InAs system using more consistent lattice parameters than those for the GaSb/InAs system.

2. MODEL

The energy structure of our model of the heterojunction is shown in Fig. 1. In our notation, the energy is measured from the midgap of one of the semiconductors forming the heteropair. The band gap of this semiconductor is 2Δ, and the band gap of the other is V_1–V_2, where V_1 is the upper and V_2 is the lower boundary of the band gap of the latter semiconductor. The layer thicknesses are a and b, respectively, and the overlap is

V_2–Δ. We describe the band structure of each of the semiconductor materials using the Kane model. For the bulk case, in the framework of the six-band Kane model with allowance only for terms linear in momentum, the Hamiltonian $\hat{H}$ describing the behavior of a free particle is the 6×6 matrix

$$\tilde{H} = \begin{pmatrix} \frac{E_g}{2} & 0 & \frac{\hat{R}_-}{\sqrt{2}} & \frac{2i\hat{R}_z}{\sqrt{6}} & \frac{\hat{R}_+}{\sqrt{6}} & 0 \\ 0 & \frac{E_g}{2} & 0 & \frac{\hat{R}_-}{\sqrt{6}} & \frac{2i\hat{R}_z}{\sqrt{6}} & \frac{\hat{R}_+}{\sqrt{2}} \\ \frac{\hat{R}_+}{\sqrt{2}} & 0 & -\frac{E_g}{2} & 0 & 0 & 0 \\ -\frac{2i\hat{R}_z}{\sqrt{6}} & \frac{\hat{R}_+}{\sqrt{2}} & 0 & -\frac{E_g}{2} & 0 & 0 \\ \frac{\hat{R}_-}{\sqrt{6}} & -\frac{2i\hat{R}_z}{\sqrt{6}} & 0 & 0 & -\frac{E_g}{2} & 0 \\ 0 & \frac{\hat{R}_-}{\sqrt{2}} & 0 & 0 & 0 & -\frac{E_g}{2} \end{pmatrix}, \quad (1)$$

Here, $\hat{R}_+ = \alpha(\hat{p}_y + i\hat{p}_x)$, $\hat{R}_- = \alpha(\hat{p}_y - i\hat{p}_x)$, $\hat{R}_z = \alpha\hat{p}_z$ ($\hat{p}_i$ are the projections of the momentum operator onto the corresponding coordinate axes), α is the Kane factor determining the values of the effective masses of electrons and light holes, and E_g is the band gap of the semiconductor (we choose the system of units in which $\hbar = c = 1$). The wave function is a six-component column. The eigenfunctions of the Hamiltonian (1) are

$$\psi_1 = \begin{pmatrix} a \\ 0 \\ \frac{\hat{R}_+}{\sqrt{2}\left(E + \frac{E_g}{2}\right)}a \\ -\frac{2i\hat{R}_z}{\sqrt{6}\left(E + \frac{E_g}{2}\right)}a \\ \frac{\hat{R}_-}{\sqrt{6}\left(E + \frac{E_g}{2}\right)}a \\ 0 \end{pmatrix}, \quad \psi_2 = \begin{pmatrix} 0 \\ b \\ 0 \\ \frac{\hat{R}_+}{\sqrt{6}\left(E + \frac{E_g}{2}\right)}b \\ -\frac{2i\hat{R}_z}{\sqrt{6}\left(E + \frac{E_g}{2}\right)}b \\ \frac{\hat{R}_-}{\sqrt{2}\left(E + \frac{E_g}{2}\right)}b \end{pmatrix}, \quad (2)$$

where *a* and *b* are functions of the coordinates *x*, *y*, and *z*. The equations for *a* and *b* are

$$\begin{aligned} \left[\frac{E_g^2}{4} - E^2 + \frac{\hat{R}_-\hat{R}_+}{2} + \frac{\hat{R}_+\hat{R}_-}{6} + \frac{2}{3}\hat{R}_z^2\right]a &= 0, \\ \left[\frac{E_g^2}{4} - E^2 + \frac{\hat{R}_-\hat{R}_+}{6} + \frac{\hat{R}_+\hat{R}_-}{2} + \frac{2}{3}\hat{R}_z^2\right]b &= 0. \end{aligned} \quad (3)$$

In the Kane model, the magnetic field is introduced by replacing the momentum operator $\hat{\mathbf{p}}$ by the generalized momentum operator $\hat{\pi} = \hat{\mathbf{p}} - e\mathbf{A}$, where **A** is the vector potential and *e* is the elementary charge. Since the vector potential depends on the coordinates, different projections of the vector π do not commute. Therefore, the operators $\hat{R}_-$ and $\hat{R}_+$ also do not commute in the presence of a magnetic field. In the case of zero magnetic field, the operators $\hat{R}_-$ and $\hat{R}_+$ commute and we can simplify Eqs. (3). They are reduced to one equation, which has the form

$$\left[\frac{E_g^2}{4} - E^2 + \frac{2}{3}\alpha^2\hat{p}^2\right]\alpha = 0. \quad (4)$$

Solutions to this equation are functions of the type $a = C\exp(i\mathbf{kr})$, where $\mathbf{k} = (p_x, p_y, k)$.

Now, we consider the case of a homogeneous magnetic field **B** directed along the *z* axis. The vector potential can be taken in the form $\mathbf{A} = \mathbf{e}_y xB$. Using Eqs. (2), the total wave functions can be found to be

$$\begin{aligned} |k, n, \uparrow\rangle &= \begin{pmatrix} |k, n\rangle \\ 0 \\ \frac{\alpha\beta\sqrt{n}}{\sqrt{2}\left(E + \frac{E_g}{2}\right)}|k, n-1\rangle \\ -\frac{2i\hat{R}_z}{\sqrt{6}\left(E + \frac{E_g}{2}\right)}|k, n\rangle \\ \frac{\alpha\beta\sqrt{n+1}}{\sqrt{6}\left(E + \frac{E_g}{2}\right)}|k, n+1\rangle \\ 0 \end{pmatrix}; \\ |k, n, \downarrow\rangle &= \begin{pmatrix} 0 \\ |k, n\rangle \\ 0 \\ \frac{\alpha\beta\sqrt{n}}{\sqrt{6}\left(E + \frac{E_g}{2}\right)}|k, n-1\rangle \\ -\frac{2i\hat{R}_z}{\sqrt{6}\left(E + \frac{E_g}{2}\right)}|k, n\rangle \\ \frac{\alpha\beta\sqrt{n+1}}{\sqrt{2}\left(E + \frac{E_g}{2}\right)}|k, n+1\rangle \end{pmatrix}, \end{aligned} \quad (5)$$

where $|k, n\rangle = \exp(ikz + ip_y y)\Psi_n(x - p_y/(eB))$ and Ψ_n is the wave function of the *n*th state of a one-dimensional harmonic oscillator.

The dispersion equations for these states are

$$\frac{E_g^2}{4} - E^2 + (\alpha\beta)^2\left(\frac{2}{3}n + \frac{1}{6}\right) + \frac{2}{3}k^2 = 0$$

for $|k, n, \uparrow\rangle$ and

$$\frac{E_g^2}{4} - E^2 + (\alpha\beta)^2\left(\frac{2}{3}n + \frac{1}{2}\right) + \frac{2}{3}k^2 = 0$$

for $|k, n, \downarrow\rangle$.

Now, we consider the quantum well in a zero magnetic field. As a boundary condition, we choose the continuity of the total wave function. To avoid complications with infinite barriers at the boundaries of the well, we attribute a finite band gap to the external regions (placing the midgap at $E = 0$) and then make the gap tend to infinity. Due to the axial symmetry in the plane of the well, we can set $p_x = 0$ without loss of generality. Then, the total wave function in the regions not containing heterointerfaces assumes the form

$$\psi_1 = \begin{pmatrix} a \\ 0 \\ \dfrac{\alpha p_y}{\sqrt{2}\left(E + \dfrac{E_g}{2}\right)}a \\ -\dfrac{2i\alpha p_z}{\sqrt{6}\left(E + \dfrac{E_g}{2}\right)}a \\ \dfrac{\alpha p_y}{\sqrt{6}\left(E + \dfrac{E_g}{2}\right)}a \\ 0 \end{pmatrix}, \quad \psi_2 = \begin{pmatrix} 0 \\ b \\ 0 \\ \dfrac{\alpha p_y}{\sqrt{6}\left(E + \dfrac{E_g}{2}\right)}b \\ -\dfrac{2i\alpha p_z}{\sqrt{6}\left(E + \dfrac{E_g}{2}\right)}b \\ \dfrac{\alpha p_y}{\sqrt{2}\left(E + \dfrac{E_g}{2}\right)}b \end{pmatrix}. \quad (6)$$

We note that spinors (6) are mutually orthogonal and, therefore, can be used to classify the states of the system. We also note that not all of the components of spinors (6) are linearly independent.

Due to the translational symmetry along the well, we can consider the wave function in each of the regions of the heterostructure as a state with a definite longitudinal momentum of the particle. Therefore, in each of the regions of the quantum well, it is natural to choose the component a as a superposition of two waves, $\exp[i(kz + py)]$ and $\exp[i(-kz + py)]$. Moreover, we should take into account that, in the region outside the well, there are only exponentially decaying solutions $\exp(-\kappa|z| + ipy)$.

After performing all the necessary calculations, we find the dispersion equation for the system:

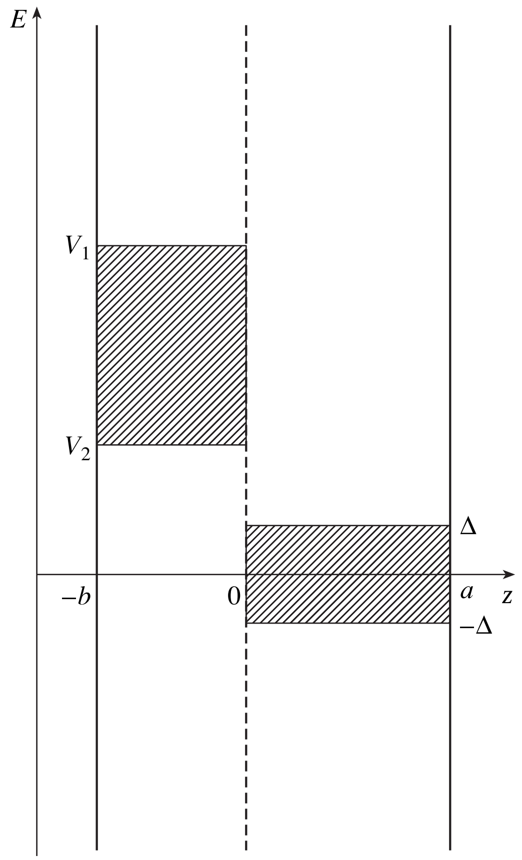

Fig. 1. Energy diagram of a type-II heterojunction consisting of two quantum wells with infinite walls. The vertical dashed line denotes the heterointerface, and the shaded regions correspond to the band gaps of the contacting semiconductors. The layer widths of the two semiconductors are a and b, and the band gaps are 2Δ and V_1–V_2, respectively.

$$\begin{gathered}
\left[\frac{2k}{E + \frac{E_g}{2}}\cos(ka) + \left(\frac{p}{E + \frac{E_g}{2}} + 2\sqrt{\frac{3}{2}}\right)\sin(ka)\right] \\
\times\left[\sin(sb)\left(\frac{4s^2 + p^2}{E - V_2} - 2\sqrt{\frac{3}{2}}p\right) - 4s\sqrt{\frac{3}{2}}\cos(sb)\right] \\
\times\frac{\beta}{E - V_2} + \frac{\alpha}{E + \frac{E_g}{2}} \qquad (7) \\
\times\left[\frac{2s}{E - V_2}\cos(sb) - \left(\frac{p}{E - V_2} - 2\sqrt{\frac{3}{2}}\right)\sin(sb)\right] \\
\times\left[\left(\frac{4k^2 + p^2}{E + \frac{E_g}{2}} + 2\sqrt{\frac{3}{2}}p\right)\sin(ka) - 4\sqrt{\frac{3}{2}}k\cos(ka)\right] = 0,
\end{gathered}$$

where k in the region $0 < z < a$ and s in the region $-b < z < 0$ are determined from Eq. (4) and α and β are the Kane coefficients in the regions $z < 0$ and $z > 0$, respectively.

We now turn to the case of a nonzero magnetic field perpendicular to the plane of the structure. In this case, as for $B = 0$, in different regions of the heterostructure, we choose the component a of the wave function to be a superposition of plane waves. However, in contrast to the case of zero magnetic field, where states with different electron spin projections do not mix, here the states $|n+1, \downarrow\rangle$ and $|n, \uparrow\rangle$ have the same symmetry and are mixed. Thus, each state is a superposition of "plane waves"

$$\begin{aligned}\psi = {} & A|k, n+1, \downarrow\rangle + B|-k, n+1, \downarrow\rangle \\ & + C|s, n, \uparrow\rangle + D|-s, n, \uparrow\rangle.\end{aligned}$$

Because the dispersion equations for the spinors are different, the wave vectors k and s are different, although there is a strict correspondence between them. The subsequent calculations include matching of the wave functions at the interfaces and making the band gaps outside the well tend to infinity. As a result, we obtain the dispersion equation

$$\mathrm{Det}\left\| \begin{array}{cc} A & B \\ C & D \end{array} \right\| = 0, \qquad (8)$$

where A, B, C, and D are 4th-order matrices

$$A = \left\| \begin{array}{cccc} \left(2 - \dfrac{2ik}{E - V_2}\right)e^{-ikb} & \left(2 + \dfrac{2ik}{E - V_2}\right)e^{ikb} & \dfrac{\alpha\sqrt{n+1}e^{-isb}}{E - V_2} & \dfrac{\alpha\sqrt{n+1}e^{isb}}{E - V_2} \\ \dfrac{\alpha\sqrt{n+1}e^{-ikb}}{E - V_2} & \dfrac{\alpha\sqrt{n+1}e^{ikb}}{E - V_2} & \left(2 - \dfrac{2is}{E - V_2}\right)e^{-isb} & \left(2 + \dfrac{2is}{E - V_2}\right)e^{isb} \\ 0 & 0 & 0 & 0 \\ 0 & 0 & 0 & 0 \end{array} \right\|;$$

$$B = \left\| \begin{array}{cccc} 0 & 0 & 0 & 0 \\ 0 & 0 & 0 & 0 \\ \left(2 + \dfrac{2ik}{E - \Delta}\right)e^{-i\kappa a} & \left(2 + \dfrac{2ik}{E - \Delta}\right)e^{-i\kappa a} & -\dfrac{\alpha\sqrt{n+1}e^{-i\sigma a}}{E - \Delta} & -\dfrac{\alpha\sqrt{n+1}e^{i\sigma a}}{E - \Delta} \\ -\dfrac{\alpha\sqrt{n+1}e^{-i\kappa a}}{E - \Delta} & -\dfrac{\alpha\sqrt{n+1}e^{i\kappa a}}{E - \Delta} & \left(2 + \dfrac{2i\sigma}{E - \Delta}\right)e^{i\sigma a} & \left(2 + \dfrac{2i\sigma}{E - \Delta}\right)e^{-i\sigma a} \end{array} \right\|;$$

$$C = \left\| \begin{array}{cccc} 1 & 1 & 0 & 0 \\ 0 & 0 & 1 & 1 \\ \dfrac{2ik}{E - V_2} & -\dfrac{2ik}{E - V_2} & -\dfrac{\alpha\sqrt{n+1}}{E - V_2} & -\dfrac{\alpha\sqrt{n+1}}{E - V_2} \\ \dfrac{\alpha\sqrt{n+1}}{E - V_2} & \dfrac{\alpha\sqrt{n+1}}{E - V_2} & -\dfrac{2is}{E - V_2} & \dfrac{2is}{E - V_2} \end{array} \right\|;$$

$$D = \left\| \begin{array}{cccc} -1 & -1 & 0 & 0 \\ 0 & 0 & -1 & -1 \\ \dfrac{2i\kappa}{E - \Delta} & -\dfrac{2i\kappa}{E - \Delta} & \dfrac{\alpha\sqrt{n+1}}{E - \Delta} & \dfrac{\alpha\sqrt{n+1}}{E - \Delta} \\ -\dfrac{\alpha\sqrt{n+1}}{E - \Delta} & -\dfrac{\alpha\sqrt{n+1}}{E - \Delta} & \dfrac{2i\sigma}{E - \Delta} & -\dfrac{2i\sigma}{E - \Delta} \end{array} \right\|.$$

Solutions to Eqs. (7) and (8) can be found only numerically.

In this model, there is no dispersion of heavy holes and, accordingly, there is no quantization of heavy hole levels in a magnetic field. Below, we discuss the results of the experiments in which the quantization of heavy holes can be of importance. To this end, we introduce quantization of heavy holes in the GaSb layer formally, attributing a quadratic dispersion law to them. We also assume that heavy holes of one material do not penetrate into the depth of the other.

We turn to the discussion of the results of simulation for the GaSb/InAs heterostructure. As an example, we consider a GaSb layer 100 Å thick and an InAs layer 150 Å thick, since approximately such dimensions of the confinement regions are realized experimentally. Figure 2 shows the electron and light hole dispersion curves calculated from Eq. (7) for the case of zero magnetic field. The band gap of GaSb is chosen to be 0.813 eV, the band gap of InAs is 0.415 eV, and the energy gap is 0.15 eV [4]. The effective masses are taken to be $m_e = m_{lh} = 0.025m_0$ and $m_{hh} = 0.41m_0$ in InAs and $m_e = m_{lh} = 0.045m_0$ and $m_{hh} = 0.4m_0$ in GaSb (m_0 is the free electron mass). The energy is measured from the midgap of the bulk InAs.

We see that the energy spectrum of the heterojunction outside the region of the overlap of the conduction band of InAs and the valence band of GaSb qualitatively coincides with the spectrum of a single quantum well with infinite walls. Spin splitting of quantum confinement levels is due to the noninvariance of the system with respect to the reflection in the *xy* plane. In contrast to the energy spectrum of a single quantum well, there is no band gap in the spectrum considered. This means that our heterojunction behaves like a semimetal.

We must also note that there are so-called “boundary” states in the spectrum (in Fig. 2, they are denoted by numerals *1*, *2*, *3*). These states appear in calculations for the Kane model. When using other boundary conditions, these states may be absent. For the first time, the presence of such states was indicated in [5]. Experimental detection of boundary states can serve as proof of the physical adequacy of the choice of the boundary conditions of the model. The dispersion laws for boundary states differ strongly from the dispersion laws for conventional states. We see that the energy of the boundary state designated by *2*, at zero longitudinal momentum, coincides with the top of the valence band of GaSb and, therefore, this state lies above the confinement levels for holes.

Near the region of the energy overlap of the bands, a number of anticrossings of the dispersion curves is observed. Comparing the calculations from Eq. (7) with the results of the study of boundary states, we can assert that states *2* and *3* are due to the presence of the heterointerface between InAs and GaSb and that state *1* is related to the well boundaries.

Figure 3 shows the magnetic field dependence of the positions of Landau levels calculated from Eq. (8) for the region of the energy overlap of the InAs conduction band and the GaSb band gap.

A specific feature of the behavior of the system in a magnetic field is the existence of quasigaps in the spectrum, where the density of levels sharply falls compared to the neighboring regions. Such a decrease in the density of states is caused by level anticrossings in a nonzero magnetic field.

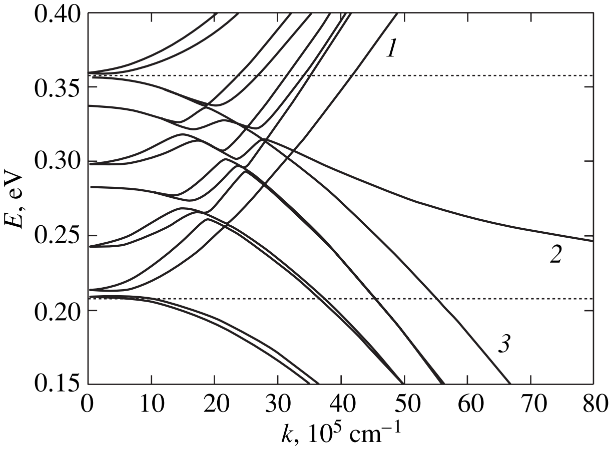

Fig. 2. Energy structure of a GaSb (100 Å)/InAs (150 Å) heterojunction in the region of overlap of the InAs conduction band and the GaSb valence band in the absence of a magnetic field with allowance for light holes and electrons only. Horizontal dashed lines denote the edges of the InAs conduction band and of the GaSb valence band.

The described results agree well with the results of simulation based on different models of quantum-confined structures [6–8].

3. COMPARISON WITH EXPERIMENTAL DATA

We compare the results of our theoretical calculations with the experimental data obtained for a GaInAsSb/InAs heterostructure, in which the In content in the quaternary solid solution determines the overlap of the valence band and the conduction band at the interface.

Earlier, an electronic channel with high mobility ($\mu >$ 50000–70000 cm^2/V s) was observed in single separated type-II heterojunctions, such as *p*-GaInAsSb/*p*-InAs, with self-consistent quantum wells at the heterointerface; its luminescence and magnetotransport properties have been studied in detail [9–12].

Layers of $Ga_{1-x}In_xAs_ySb_{1-y}$ solid solutions in the interval of compositions corresponding to an In content $0.08 < x < 0.16$ and to $y = x + 0.06$ with a good growth morphology were obtained by liquid-phase epitaxy on InAs (100) substrates. A melt solution was prepared from the pure components: atomic In and Sb of purity 5 and 3 N, respectively, and undoped binary compounds InAs and GaSb with intrinsic carrier concentrations $n = 2 \times 10^{16}$ cm^{-3} and $p = 5 \times 10^{16}$ cm^{-3}, respectively. The mismatch of the crystal lattice parameters between the epitaxial layer and the substrate was $\Delta a/a < 4 \times 10^{-4}$. The layer thickness was about 1.0 μm. The grown GaInAsSb layers were not inten-

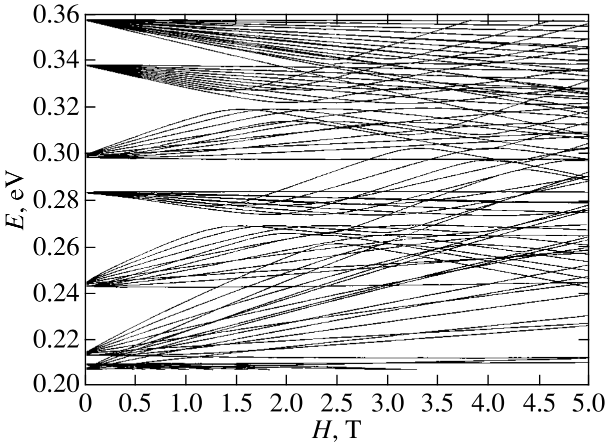

Fig. 3. Energy spectrum of Landau levels of electrons and light holes at the GaSb (100 Å)/InAs (150 Å) heterojunction in the region of overlap of the InAs conduction band and the GaSb valence band (from 0.207 to 0.357 eV).

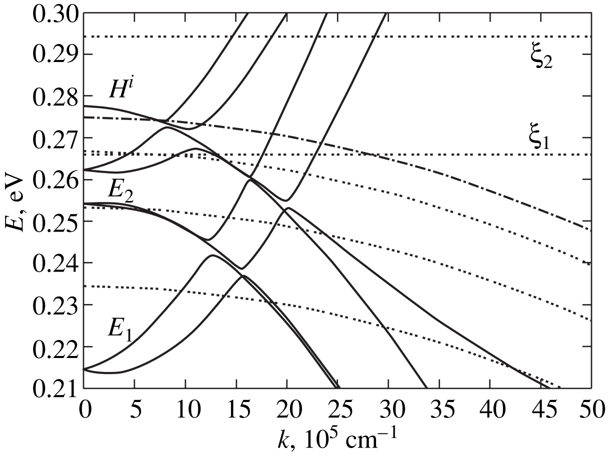

Fig. 4. Energy spectrum of the GaInAsSb (105 Å)/InAs (125 Å) heterojunction in the region of overlap of the InAs conduction band and the GaInAsSb valence band. The states of the interface holes are denoted by H^i, the states of heavy holes are shown by dashed lines, and electronic subbands are denoted by E_1 and E_2.

tionally doped and showed *p*-type conductivity with a hole concentration $p = 2 \times 10^{16}$ cm^{-3} at T = 77 K. Epitaxial GaInAsSb layers were prepared under the conditions of planar two-dimensional growth with planar interfaces sharp in composition. In such structures, planarity of the lower interface was determined by the roughness of the InAs (100) surface. The thickness of the transition layer at the $Ga_{0.84}In_{0.16}As_{0.22}Sb_{0.78}$/InAs interface was 10–12 Å.

For an In content of 16%, the overlap is 70 meV [13]. By doping the melt solution with donor impurities, the chemical potential can be shifted both into the overlap interval and to the region outside it. The energy structure of the *n*-$Ga_{0.84}In_{0.16}As_{0.22}Sb_{0.78}$/*p*-InAs heterojunction in a zero magnetic field calculated using Eq. (7) is shown in Fig. 4, where, in accordance with Fig. 1, $V_1 = 277.5$ meV, $V_2 = 907.5$ meV, $\Delta = 207.5$ meV, $a = 125$ Å, and $b = 100$ Å. Figure 4 also shows the positions of the Fermi levels (dashed lines ξ_1 and ξ_2) of the two samples under study, determined from Shubnikov–de Haas oscillations. We note that the dispersion law outside the anticrossing regions is actually parabolic, in spite of the fact that we kept only the linear terms in the Hamiltonian. The reason for this feature is that the energies considered (in the overlap region) are small compared to the band gaps of both semiconductors.

Figures 5 and 6 show Shubnikov–de Haas and Hall effect oscillation patterns (ρ_{xx}, ρ_{xy}) in the structures under study with different tellurium doping levels of the solid solution. The data reveal the existence of several periods of oscillations characteristic of a multisubband system of confinement levels. The oscillation pattern is analogous to that for a simple quantum well with two occupied confinement subbands, since in both figures two oscillation periods are observed in the fields up to 4 T. The transition to oscillations of ρ_{xy} and ρ_{xx} under the conditions of the quantum Hall effect (QHE) occurs in fields $B \geq 6$ T, where mainly the Landau levels of one subband remain.

For sample MK513/1 with a tellurium concentration in the solid solution $N_{Te} \cong 1 \times 10^{16}$ cm^{-3}, the minimum oscillation period is $\Delta_1 = 4.6 \times 10^{-2}$ T^{-1} (at temperature $T = 1.5$ K), from which we can calculate the electron concentration in the confinement subbands responsible for oscillations. Estimations give $n_{Ro} \cong 5.2 \times 10^{11}$ cm^{-2} (for one spin projection). Similarly, for sample MK527/4 with a tellurium concentration $N_{Te} \cong 1 \times 10^{17}$ cm^{-3}, using the minimal period of oscillations $\Delta_1 = 2.75 \times 10^{-2}$ T^{-1}, we can estimate the electron concentration to be $n_{Ro} \cong 8.8 \times 10^{11}$ cm^{-2} (also for one spin projection). Both of these values agree well with the results of measurements of the Hall coefficient in weak magnetic fields ($B \longrightarrow 0$), from which we obtain estimates $n_{Ro} \cong 3.4 \times 10^{11}$ cm^{-2} for sample MK513/1 and $n_{Ro} \cong 1.15 \times 10^{12}$ cm^{-2} for sample MK527/4.

Once the electron concentrations are known, we can calculate the position of the Fermi level by assuming that the dispersion law for the electron confinement subbands is close to parabolic. With the electron effective mass at the Fermi level in InAs taken to be $m_e^* = 0.03m_0$, we find that the Fermi energy for sample MK513/1 is $\xi \cong 54$ meV. Similarly, for sample MK527/4, the Fermi energy is estimated to be $\xi \cong 91.4$ meV. For these values of the Fermi energy in the presence of the overlap $\Delta E = 70$ meV between the conduction and valence bands, the Fermi level lies in the overlap region in sample MK513/1 and above this region in sample MK527/4.

Under the conditions of the quantum Hall effect, the maxima of ρ_{xx} correspond to the crossings of the Fermi

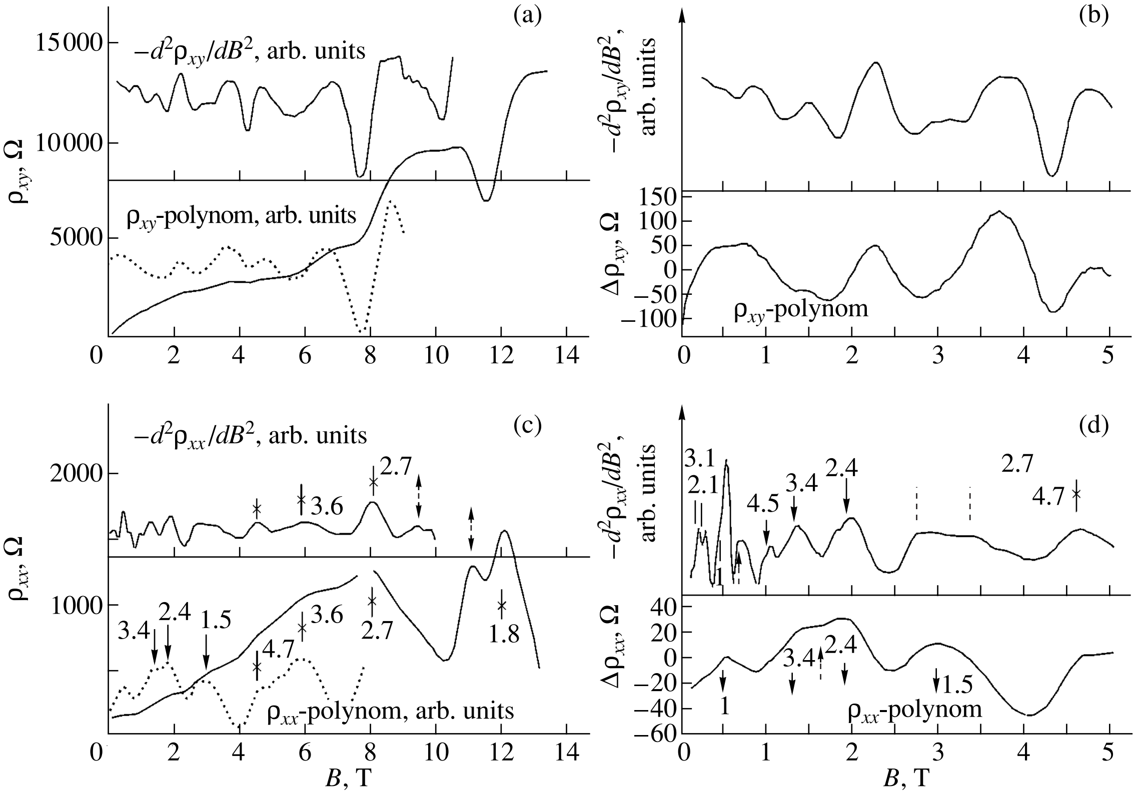

Fig. 5. Experimental magnetic field dependences of (a, b) the Hall resistance ρ_{xy} and (c, d) magnetoresistance ρ_{xx} for sample MK513/1 at $T = 1.5$ K ($\rho_0 = 136.2$ Ω, $R_{B\to 0} = 1.85 \times 10^7$ cm^2/Q, $R\sigma = 1.36 \times 10^5$ cm^2/V s). (b, d) Enlarged portions of the curves in (a) and (c) obtained from the experimental data for $\rho_{xy}(B)$ and $\rho_{xx}(B)$ by subtracting the smooth background (polynom) and doubly differentiating with respect to the field. Vertical lines denote different series of Shubnikov–de Haas oscillations and the transition region from one series to another. Numerals near curves correspond to the ratio of the positions of the maxima on the $1/B$ scale to the average period $\Delta(1/B)$ for a given series. A series of oscillations in weak fields $B < 1$ T with indices 1–3.1 corresponds to bulk Shubnikov–de Haas oscillations from a Te-doped ($\cong 1 \times 10^{16}$ cm^{-3}) epitaxial layer of the solid solution.

level with Landau levels. For both samples, we compared the maxima of ρ_{xx} with the crossings between the chemical potential and the calculated Landau levels under the assumption that the position of the chemical potential does not depend on the magnetic field applied to the structure. The best agreement between the model of a composite quantum well and the experimental data was achieved for the width of the electronic channel $a = 125$ Å and the width of the hole channel $b = 105$ Å. The band overlap at the interface was taken to be $\Delta E = 70$ meV; the band gap parameters for $Ga_{0.84}In_{0.16}Sb_{0.78}As_{0.22}$ and InAs were $E_g = 0.63$ and 0.41 eV, respectively; the effective masses of electrons and holes were $m_e = 0.023m_0$, $m_{lh} = 0.026m_0$, and $m_{hh} = 0.41m_0$ [4]; and the electron g factor was $|g| = 10$.

In Fig. 7, vertical lines correspond to the experimental maxima of ρ_{xx}, which arise at crossing of the extended states of the hybridized Landau levels of different subbands with the Fermi level for each of the subbands. The best agreement between the positions of the maxima of ρ_{xx} and the crossings of the chemical potential with Landau levels is achieved if we assume that the chemical potential is located in the interval 0.266–0.268 eV for sample MK513/1 and in the interval 0.293–0.295 eV for sample MK527/4. These values correspond to the following energy distances from the edges of the corresponding subbands denoted by E_1 and E_2 in Fig. 4: $\varepsilon_{F1} = 52.4$ meV and $\varepsilon_{F2} = 4.9$ meV for sample MK513/1 and $\varepsilon_{F1} = 80.4$ meV and $\varepsilon_{F2} = 30.9$ meV for sample MK527/4.

According to Fig. 4, two hole subbands for sample MK513/1 are partially filled, namely, the interface hole states and the first confinement subband of heavy holes (the energy distances from the edges of these subbands to the chemical potential level are $\varepsilon_F^i = 10.6$ meV and $\varepsilon_{1F}^h = 8.9$ meV, respectively). In fields of up to 5 T (Fig. 7a), the crossings of Landau levels of heavy and interface holes with the chemical potential are not seen in the experiment, since $\Omega_{\tau h} \ll 1$ for these carriers. Only the maxima of ρ_{xx} corresponding to the crossings of the chemical potential with Landau levels of electron subbands with positive and negative "pseudospin" projections are observed experimentally.

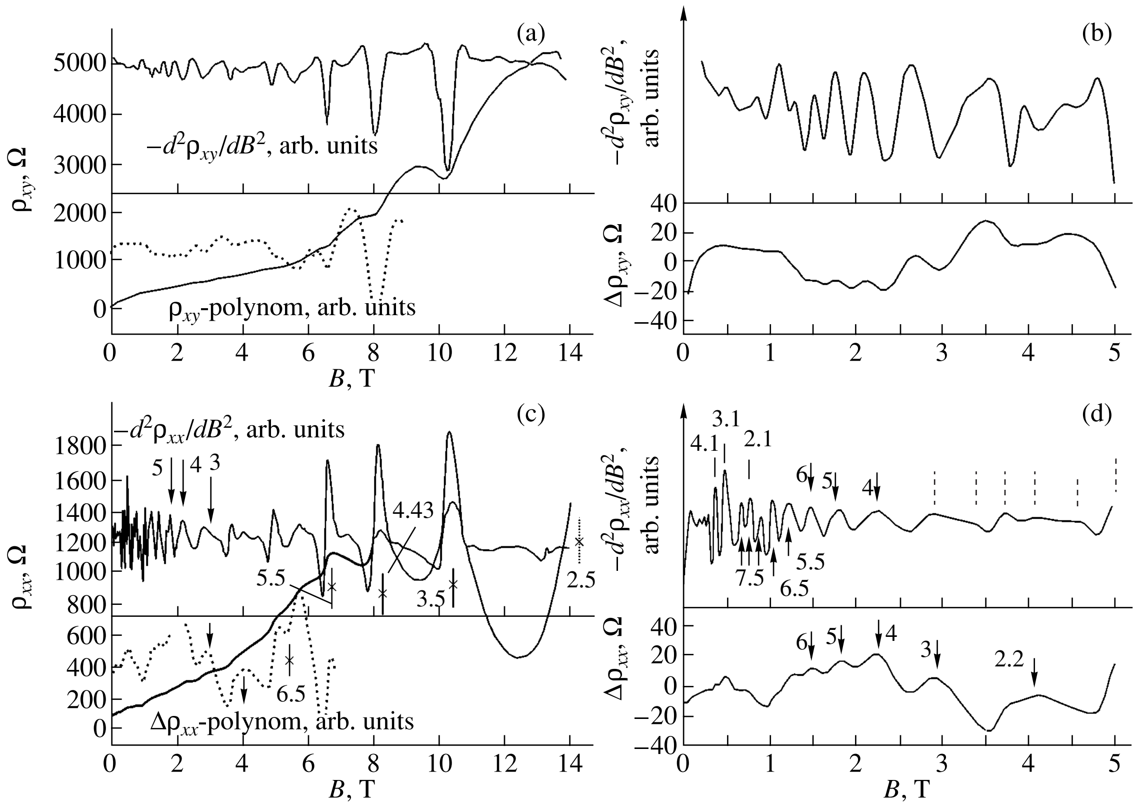

Fig. 6. Experimental magnetic field dependence of (a, b) the Hall resistance ρ_{xy} and (c, d) magnetoresistance ρ_{xx} for sample MK527/4 at $T = 1.5$ K ($\rho_0 = 91.4$ Ω, $R_{B\to 0} = 5.4 \times 10^6$ cm^2/Q, $R\sigma = 5.9 \times 10^4$ cm^2/V s). (b, d) On the right-hand side, enlarged parts of curves from (a) and (c) obtained from experimental curves by subtracting the smooth background and doubly differentiating with respect to the field are shown. Vertical lines with different indices and without indices denote different series of Shubnikov–de Haas oscillations and also the transition region from one series to another. Numerals correspond to the ratio of the positions of the maxima on the $1/B$ scale to the average period for a given series. A series of oscillations in weak fields $B \le 1$ T with indices 2.1–4.1 corresponds to bulk Shubnikov–de Haas oscillations from a Te-doped (~3×10^{16} cm^{-3}) epitaxial layer of the solid solution.

In fields of up to 1 T, both samples exhibit bulk Shubnikov–de Haas oscillations independent of the angle between the magnetic field **B** and the current **J** and related to doping of the Te layer of the solid solution (Figs. 5d, 6d). For sample MK527/4, these oscillations have indices 2.1, 3.2, and 4.1 (Fig. 6d), which correspond to an electron concentration of $n_{3D} \cong 1.2 \times 10^{16}$ cm^{-3} as determined from the period $\Delta(1/B)$. The 2.1 maximum overlaps oscillations of the two-dimensional electron subband with a positive pseudospin projection.

Thus, for both samples, the oscillations of the magnetoresistance (ρ_{xx}) are caused by all electron subbands that lie in the overlap region Δ. From the calculations, it follows that, for fields $B \ge 6$ T, the Fermi level for sample MK527/4 is crossed only by Landau levels having electronic character (Fig. 7a) and for sample MK513/1 by Landau levels having electronic and hole character. The presence of the contribution from hole confinement subbands to magnetoresistance accounts for the fundamental difference between samples MK513/1 and MK527/4. The minima of ρ_{xx} in sample MK527/4 lie below the minima of ρ_{xx} in sample MK513/1 with the same filling factor, since ρ_{xx} in sample MK513/1 is limited from below by the conductivity in hole states.

For the Hall resistance ρ_{xy} of sample MK513/1, the positions (on the magnetic field scale) of the QHE plateau are determined by electron Landau levels, whereas the monotonic part of ρ_{xy} substantially depends on the degree of filling of extended hole states and sharply decreases (by a factor of 3) as the temperature increases from 1.5 to 4 K.

It is seen in Fig. 7b that, for high-field magnetoresistance, the maxima of ρ_{xx} are observed as the Fermi level crosses the Landau levels of the deep electronic subband with both pseudospin projections. The anticrossings of the zeroth Landau level originating from the E_2 subband (Fig. 4) with the first Landau level of interface holes H_i result in the pinning of the chemical potential for $B > 10$ T at the zeroth Landau level of the E_2 subband. The additional maxima of ρ_{xx} in this field region plotted in Fig. 5c as a dotted line can be explained by the fact that Landau levels of heavy holes cross the chemical potential level simultaneously with an electron level.

A plateau of the QHE on the B dependence of ρ_{xy} occurs if the Fermi level lies between Landau levels when filling one confinement subband. In the presence of two subbands for electrons or for electrons and holes, giving different contributions to the background component of ρ_{xy} (B), the concentration in a subband changes when Landau levels of this subband (or of both subbands) cross the Fermi level from below; therefore, the plateau of QHE in ρ_{xy} is distorted (see the curves for ρ_{xy} in Figs. 5a and 6a in the QHE region, where the minima of ρ_{xy} are observed as electronic Landau levels cross the Fermi level). This effect is seen most clearly in sample MK513/1 (even at $T = 4.2$ K) at simultaneous crossing of the chemical potential by Landau levels of electrons and holes. Indeed, if the electron and hole Landau levels approaching the chemical potential are located close to the crossing, the density of extended states at the Fermi level increases, resulting in an increase in Hall conductivity σ_{xy} (a minimum in ρ_{xy}). This character of the crossings of the chemical potential with Landau levels of heavy holes is manifested as additional maxima of the magnetoresistance ρ_{xx} in the region 10–14 T, marked by dotted arrows in Fig. 5c. In higher fields ($B \geq 30$ T), an energy gap is formed between the lowest electron and hole Landau levels and a transition to intrinsic semiconductor conductivity occurs (in the absence of impurity states); in this case, the number of carriers occupying extended states at diverging Landau levels of electrons and holes decreases exponentially with increasing magnetic field at a given temperature.

4. CONCLUSIONS

Thus, we have for the first time experimentally established the features of the charge carrier spectrum in the region of overlap of the conduction and valence bands in a separated type-II heterojunction GaInAsSb/InAs on the basis of solid solutions enriched by GaSb. The appearance of energy gaps has been revealed resulting from anticrossings of the branches of the energy spectrum with different pseudospin projections both in zero and in nonzero magnetic fields. A simple analytical model of a type-II heterojunction was suggested, which describes well the experimental data on quantum magnetotransport in single GaInAsSb/p-InAs heterostructures.

A fundamental difference between quantum oscillations of magnetoresistance and the quantum Hall effect has been experimentally demonstrated for the cases where the chemical potential lies outside and inside the region of the energy band overlap at the heterointerface. It was shown that this difference is due to hybridization of states of the valence band of one semiconductor and the conduction band of the other in the overlap region.

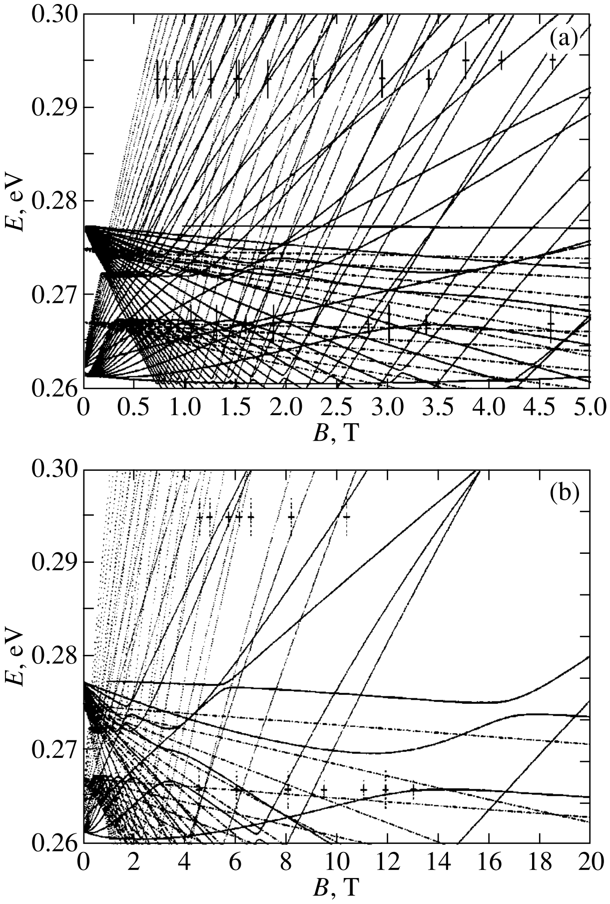

Fig. 7. Plots of the magnetic field dependence of Landau levels for two filled electron subbands, E_1 and E_2, as well as for the subband of boundary hole states H^i and two heavy hole subbands H_1^h and H_2^h in the field range from (a) 5 to (b) 20 T in the region of overlap of the bands near the edge of the valence band of the solid solution. Vertical lines of various lengths denote the positions of the maxima of ρ_{xx} of different series from Figs. 1c, 1d, 2c, and 2d, which are compared to the crossings of the chemical potential E_ξ with Landau levels of the E_1 and E_2 subbands. For sample MK513/1, the chemical potential is E_ξ = 267–266 meV, and for sample MK527/4, E_ξ = 293–295 meV. Short dashes for sample MK513/1 mark the positions of the maxima of ρ_{xx} from Fig. 5c at $B > 8$ T, related to the crossings of the electron and heavy hole Landau levels in the vicinity of E_ξ = 265 meV.

ACKNOWLEDGMENTS

This study was supported by the program of the Presidium of the Russian Academy of Sciences “Low-Dimensional Quantum Structures;” the Ministry of Industry, Science, and Technology of the Russian Federation; the division of physical sciences of the Russian Academy of Sciences; INTAS; the program for the Support of Leading Scientific Schools (no. NSh-2200.2003.2); and the Russian Foundation for Basic Research.

REFERENCES

1. M. Altarelli, Phys. Rev. B **28** (2), 842 (1983).
2. G. A. Sai-Halasz, L. Esaki, and W. A. Harrison, Phys. Rev. B **18** (6), 2812 (1978).
3. M. Altarelli, J. C. Maan, L. L. Chang, and L. Esaki, Phys. Rev. B **35** (18), 9867 (1987).
4. *Landolt–Bornstein. Numerical Data and Functional Relationships in Science and Technology. Physics of Group IV Elements and III-V Compounds* (Springer, New York, 1982), Vol. 17a.
5. R. A. Suris, Fiz. Tekh. Poluprovodn. (Leningrad) **20** (11), 2008 (1986) [Sov. Phys. Semicond. **20**, 1258 (1986)].
6. S. de-Leon, L. D. Shvartsman, and B. Laikhtman, Phys. Rev. B **60**, 1861 (1999).
7. E. Halvorsen, Y. Galperin, and K. A. Chao, Phys. Rev. B **61**, 16743 (2000).
8. A. Zakharova, S. T. Yen, and K. A. Chao, Phys. Rev. B **64**, 235332 (2001).
9. M. P. Mikhailova, K. D. Moiseev, V. A. Berezovetz, R. V. Parfeniev, N. L. Bazhenov, V. A. Smirnov, and Yu. P. Yakovlev, IEE Proc.: Optoelectron. **145** (5), 268 (1998).
10. K. D. Moiseev, M. P. Mikhailova, Yu. P. Yakovlev, I. Osval'd, É. Gulitsius, I. Pangrats, and T. Shimechek, Fiz. Tekh. Poluprovodn. (St. Petersburg) **37**, 1214 (2003) [Semiconductors **37**, 1185 (2003)].
11. K. D. Moiseev, V. A. Berezovets, M. P. Mikhailova, V. I. Nizhankovskii, R. V. Parfeniev, and Yu. P. Yakovlev, Surf. Sci. **482** (2), 1083 (2001).
12. V. A. Berezovets, M. P. Mikhailova, K. D. Moiseev, R. V. Parfeniev, Yu. P. Yakovlev, and V. I. Nizhankovskii, Phys. Status Solidi A **195** (1), 194 (2003).
13. T. I. Voronina, T. S. Lagunova, M. P. Mikhailova, K. D. Moiseev, A. E. Rozov, and Yu. P. Yakovlev, Fiz. Tekh. Poluprovodn. (St. Petersburg) **34** (2), 194 (2000) [Semiconductors **34**, 189 (2000)].

Translated by I. Zvyagin

Physics of the Solid State, Vol. 46, No. 11, 2004, pp. 2163–2170. Translated from Fizika Tverdogo Tela, Vol. 46, No. 11, 2004, pp. 2092–2098.
Original Russian Text Copyright © 2004 by Kalashnikova, Pavlov, Pisarev, Kalinin, Sitnikov, Rasing.

LOW-DIMENSIONAL SYSTEMS AND SURFACE PHYSICS

Optical and Magnetooptical Properties of CoFeB/SiO$_2$ and CoFeZr/Al$_2$O$_3$ Granular Magnetic Nanostructures

A. M. Kalashnikova*, V. V. Pavlov*, R. V. Pisarev*,
Yu. E. Kalinin, A. V. Sitnikov**, and Th. Rasing*****
**Ioffe Physicotechnical Institute, Russian Academy of Sciences, Politekhnicheskaya ul. 26, St. Petersburg, 194021 Russia*
e-mail: kalashnikova@mail.ioffe.ru
***Voronezh State Technical University, Moskovskiĭ pr. 14, Voronezh, 394026 Russia*
****NSRIM Institute, University of Nijmegen, Nijmegen, 6525 ED the Netherlands*

Received March 19, 2004

Abstract—The optical and magnetooptical properties of the new granular nanocomposites (CoFeB)/(SiO$_2$) and (CoFeZr)/(Al$_2$O$_3$), which are grains of amorphous ferromagnetic alloys embedded in dielectric matrices, have been studied. The dependence of the optical, magnetooptical, and magnetic properties of the nanocomposites on their qualitative and quantitative composition, as well as on the conditions of their preparation, was investigated. Spectra of the dielectric functions $\varepsilon = \varepsilon_1 - i\varepsilon_2$ were obtained by the ellipsometric method in the range 0.6–5.4 eV. Above 4.2 eV, the absorption coefficient of the (CoFeB)/(SiO$_2$) composites was found to be close to zero for all magnetic-grain concentrations. The polar Kerr effect measured at a photon energy of 1.96 eV in dc magnetic fields of up to 15 kOe reaches values as high as 0.25°–0.3° for these nanocomposites and depends only weakly on the conditions of preparation. On the other hand, the (CoFeZr)/(Al$_2$O$_3$) nanostructures reveal a considerable difference in the concentration dependences of the Kerr effect between samples prepared in a dc magnetic field and in zero field. *© 2004 MAIK “Nauka/Interperiodica”.*

1. INTRODUCTION

In recent years, there has been an increasing interest in the area of the physics of condensed matter that deals with investigating various structures on the nanometer and even smaller scales. Structures that are made up of grains a few nanometers in size embedded in nonmagnetic metallic or dielectric matrices are materials that border between classical physics of the solid state and nanophysics.

Interest in granular nanostructures has experienced explosive growth due to a number of their physical properties that have scientific significance and also application potential. Among them the magnetoresistance effect [1], inverse or positive magnetoresistance [2], spin-dependent electron tunneling, high dielectric losses in the microwave range [3], the anomalous Hall effect [4], and the large magnetorefractive effect [5] should be mentioned. A number of papers aimed at revealing and investigating possible correlations between the magnetic properties, magnetotransport, and linear and nonlinear optical and magnetooptical properties of granular nanostructures have appeared [5–7]. Particular attention centers presently on the behavior of nanostructures near the percolation threshold, because in this region the most pronounced changes in their characteristics are observed.

By studying the optical properties of materials, one can gain valuable information on their electronic structure, an approach widely employed in optics of the solid state. Magnetooptical phenomena (in particular, the Kerr and Faraday effects) can also yield information on the magnetic properties of materials. At the same time, certain features observed in the optical and magnetooptical properties of granular nanostructures are still not fully understood [8, 9].

Until recently, most studies of the properties of granular films dealt with crystalline grains of a metal or alloy. Nanocomposites with grains of amorphous materials have attracted less interest [10]. Compared to grains with crystal structure, amorphous grains have a lower anisotropy energy, whose magnitude noticeably affects the main magnetic properties of nanocomposites [11]; in some cases, this influence may become a favorable factor, for instance, for the manifestation of magnetoresistive properties [12]. This accounts for the increasing interest over the past several years in the magnetoresistive characteristics of such structures [2, 12], as well as in their properties in the microwave range [4].

As for the optical and magnetooptical properties of structures with amorphous grains, there are only a few reports on relevant studies. The steady-state and dynamic Kerr effects in (CoNbTa)/(SiO$_2$) nanocomposites are investigated in [13], where a correlation between the dynamic and steady-state magnetooptical properties of these structures was revealed. A study of the correlations between the magnetorefractive effect and magnetoresistance in (CoFeZr)/(SiO$_2$) is given in

Parameters of the nanocomposites under study

Series	Grain alloy	Matrix	Grain concentration, at. %	Preparation conditions
I-1	$Co_{41}Fe_{39}B_{20}$	SiO_2	From 34 to 68	Ar, $P_{Ar} = 8.0 \times 10^{-4}$ Torr
I-2	$Co_{41}Fe_{39}B_{20}$	SiO_2	From 34 to 68	Ar + N_2, $P_{N_2} = 1.8 \times 10^{-4}$ Torr
I-3	$Co_{41}Fe_{39}B_{20}$	SiO_2	From 34 to 68	Ar + O_2, $P_{O_2} = 2.8 \times 10^{-5}$ Torr
II-1	$Co_{45}Fe_{45}Zr_{10}$	Al_2O_3	From 21 to 54	Ar + O_2, $P_{O_2} = 2.8 \times 10^{-5}$ Torr
II-2	$Co_{45}Fe_{45}Zr_{10}$	Al_2O_3	From 21 to 54	Ar + O_2, $P_{O_2} = 2.8 \times 10^{-5}$ Torr; in-plane magnetic field, forced substrate cooling

[14]. A comparative investigation of the equatorial Kerr effect and magnetoresistance in SiO_2 matrices with embedded FeCoB, CoFeZr, and CoNbTa nanoparticles is discussed in [15].

We report here on a study of granular nanocomposites based on CoFeB and CoFeZr amorphous ferromagnetic alloys. Their optical and magnetooptical properties were investigated over a broad range of concentrations, both below and above the percolation threshold. We also investigated the effect of various conditions of nanocomposite preparation on their properties, namely, the presence of oxygen or nitrogen in the preparation process, the substrate temperature, and the magnetic field. We are not aware of any publications on either the spectra of dielectric functions of such granular structures or the polar Kerr effect.

2. EXPERIMENT

All samples were prepared by ion beam sputtering [10]. Two groups of nanostructures were investigated. Group I included structures based on grains of a $Co_{41}Fe_{39}B_{20}$ amorphous ferromagnetic alloy embedded in amorphous dielectric SiO_2 films. Nanocomposites of group II were films of amorphous dielectric Al_2O_3 with embedded nanograins of a $Co_{45}Fe_{45}Zr_{10}$ amorphous ferromagnetic alloy. The main characteristics of these groups are listed in the table. Samples of the first group differed in that part of them were prepared in an argon environment (subgroup I-1), while the other part was grown in an atmosphere with nitrogen (I-2) or oxygen (I-3). The magnetic-phase concentration varied from 34 to 68 at. %. Samples of the second group were fabricated in an argon or oxygen environment. Some of them were prepared in a dc magnetic field under forced cooling of the substrate (subgroup II-2), and the remainder, in zero magnetic field without forced cooling (I-1). The concentration of ferromagnetic grains in samples of this group varied from 21 to 54 at. %. The nanocomposite film thicknesses ranged from less than 1 μm for the (CoFeB)/(SiO_2) samples to 5–10 μm for (CoFeZr)/(Al_2O_3). The (CoFeB)/(SiO_2) films were deposited on glass substrates, and the (CoFeZr)/(Al_2O_3) films, on ceramic substrates. The ferromagnetic particles grew in size from 2 to 7 nm with increasing content of the magnetic phase. Such grain sizes are less than the typical critical diameters separating the superparamagnetic regime from the regime with blocked particles in granulated structures for specific temperatures and measurement times [11, 16]. Primary characterization of the samples was accomplished by measuring their electrical resistivity. Figure 1 shows the electrical resistivity of (CoFeB)/(SiO_2) structures as a function of grain concentration. This shape of the concentration dependences of electrical resistivity is typical of percolation systems [10].

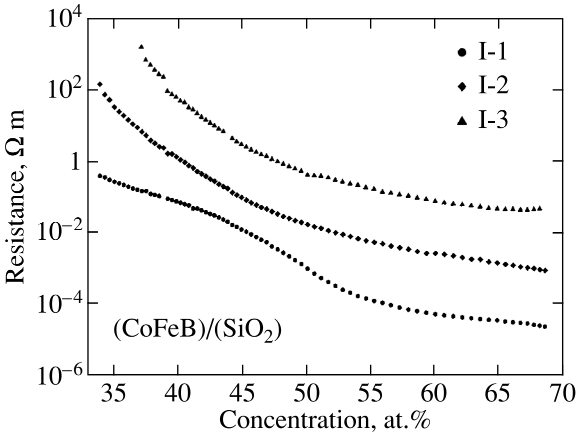

Fig. 1. Electrical resistivity of (CoFeB)/(SiO_2) nanocomposites plotted vs. grain concentration.

The optical properties of granular nanocomposites were studied by reflection ellipsometry. The choice of reflection geometry was motivated by the strong absorption in nanocomposites with high grain concentrations. The essence of the method, which is discussed in detail, e.g., in [17], consists in measuring the ellipsometric angles ψ and Δ. The physical meaning of these angles can be readily grasped from the main relation of reflection ellipsometry

$$\tan\psi \exp(i\Delta) = r_{pp}/r_{ss}, \qquad (1)$$

where $r_{pp}(r_{ss})$ is the amplitude reflectance for light polarized parallel (perpendicular) to the plane of incidence. Assuming the simplest model of a semi-infinite isotropic sample in a medium with a real refractive index of unity (air), the real and imaginary parts of the dielectric function $\varepsilon = \varepsilon_1 - i\varepsilon_2$, as well as the refractive index n and absorption index k [$(n - ik)^2 = \varepsilon$], can be determined from measured ellipsometric angles using the relation

$$\varepsilon = \sin^2\varphi\left[1 + \tan^2\varphi\left(\frac{1 - r_{pp}/r_{ss}}{1 + r_{pp}/r_{ss}}\right)^2\right], \tag{2}$$

where φ is the angle of incidence.

The ellipsometric angles ψ and Δ were measured on a spectroscopic ellipsometer at photon energies ranging from 0.6 to 5.4 eV. The spectral responses of the dielectric functions and of the indices of refraction and absorption were calculated from Eqs. (1) and (2).

A magnetooptical investigation of the nanocomposites was performed using the linear magnetooptical Kerr effect in polar geometry and the Faraday effect. These phenomena are of the same nature and consist in rotation of the plane of polarization and the appearance of ellipticity of the light reflected (in the case of the Kerr effect) from a medium magnetized perpendicular to the surface or of the light transmitted through such a medium (in the case of the Faraday effect). The angle of rotation of the plane of polarization is determined by both diagonal and off-diagonal elements of the permittivity tensor of the medium (in the isotropic case) [18]:

$$\hat{\varepsilon} = \begin{pmatrix} \varepsilon & -i\varepsilon_{xy}(M) & 0 \\ i\varepsilon_{xy}(M) & \varepsilon & 0 \\ 0 & 0 & \varepsilon \end{pmatrix}. \tag{3}$$

In particular, the rotation of the plane of polarization in the polar Kerr effect, θ_K, can be found from the relation

$$\theta_K = \frac{-B\varepsilon'_{xy} + A\varepsilon''_{xy}}{A^2 + B^2}, \tag{4}$$

where $\varepsilon_{xy} = \varepsilon'_{xy} + i\varepsilon''_{xy}$, $A = n^3 - 3nk^2 - n$, and $B = k^3 - 3kn^2 + k$.

In the case of transmitted light, the rotation of the plane of polarization is given by

$$\theta_F = -\frac{\pi l}{\lambda(n^2 + k^2)}(n\varepsilon'_{xy} - k\varepsilon''_{xy}), \tag{5}$$

where l is the layer thickness and λ is the wavelength of light.

Measurements were performed at photon energies of 1.96 and 2.54 eV (helium–neon and argon lasers) in a dc magnetic field of ±15 kOe applied perpendicular to the sample surface. The angle of rotation of the polarization plane θ of the light reflected from a magnetized sample was measured with a polarimeter setup (Fig. 2) using a modulation technique. All the studies were performed at room temperature.

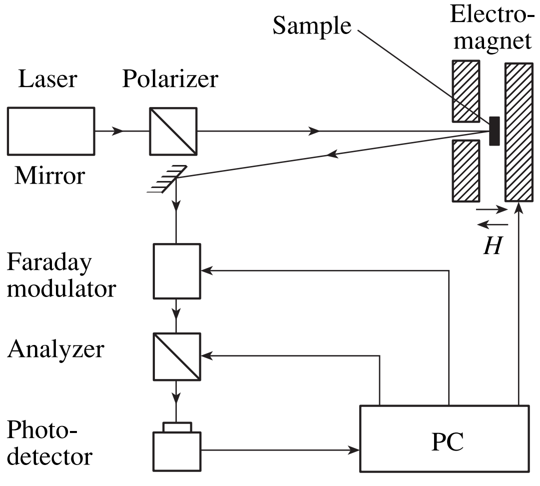

Fig. 2. Experimental setup for measurement of the magnetooptical Kerr effect. PC stands for computer.

3. RESULTS AND DISCUSSION

3.1. Optical Properties

Figure 3 plots spectral responses of the real and imaginary parts of the dielectric function of (CoFeB)/(SiO_2) nanocomposites with magnetic-phase concentrations below (35 at. %) and above (62 at. %) the percolation threshold. The absence of absorption at energies above 4.2 eV is a remarkable feature observed at all concentrations of the magnetic phase. The inset to Fig. 3 displays the dependences of the indices of refraction n and absorption k on the concentration of CoFeB nanograins at 3 eV. The refractive index for these nanostructures is $n \approx 1.5$ and does not depend on the magnetic phase concentration or photon energy. The absorption index k and the imaginary part of the dielectric function ε_2 undergo the most pronounced changes with increasing concentration in the energy range below 4.2 eV. The nonmonotonic pattern of the spectral response of the optical parameters observed at low energies should apparently be assigned to the interference occurring in nanocomposite films with a thickness less than 1 μm. This assumption is borne out by the fact that this effect is most clearly pronounced in samples with a low concentration of the magnetic phase (Fig. 3a) and, hence, with low absorption.

We calculated the spectral response of the dielectric functions for the CoFeB alloy from the spectral response of these functions obtained for the nanocomposite and available optical parameters of the matrix. The calculation was based on the effective-medium approximation [19] and showed that the increased transparency observed above 4.2 eV is accounted for by the properties of the alloy rather than of the nanocomposite (Fig. 4). The fact that the calculations performed

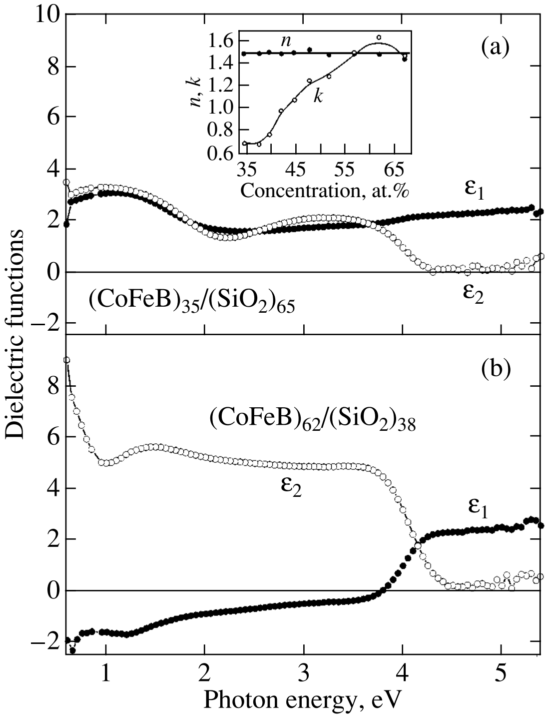

Fig. 3. Spectral response of the real (ε_1) and imaginary (ε_2) parts of the dielectric function for (CoFeB)/(SiO_2) nanocomposites (samples I-1) with a magnetic phase concentration of (a) 35 and (b) 62 at. %. Inset: concentration dependences of the refractive index *n* and absorption index *k* for (CoFeB)/(SiO_2) nanocomposites at a photon energy of 3 eV.

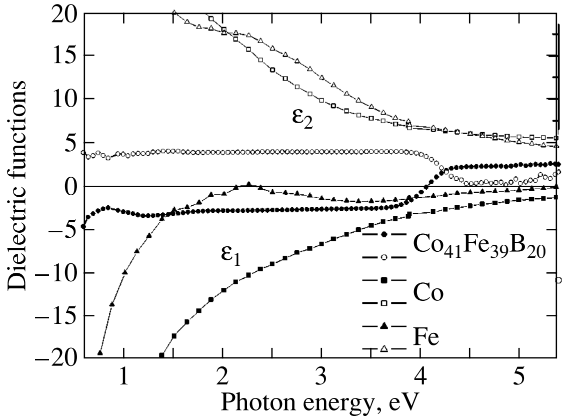

Fig. 4. Spectral response of the real, ε_1 (filled symbols), and imaginary, ε_2 (open symbols), parts of the dielectric function for a $Co_{41}Fe_{39}B_{20}$ alloy. Plotted for comparison are spectral responses for pure iron and cobalt [20].

for different magnetic phase concentrations yielded the same results corroborates the validity of the spectra displayed in Fig. 4.

The spectral and concentration relations of the (CoFeZr)/(Al_2O_3) nanocomposites followed a different pattern. Figure 5 presents graphs of the real and imaginary parts of the dielectric function obtained for nanocomposites of series II-1 and II-2 with a grain concentration of 51 at. %. It should be stressed that the absorption index of these nanocomposites does not vanish at any concentration of the magnetic phase, which sets this situation apart from the one observed in the (CoFeB)/(SiO_2) nanocomposites. This fact probably indicates that the matrix plays an essential role in forming the optical properties of a nanocomposite. Note that the spectral response of (CoFeZr)/(Al_2O_3) is more monotonic than that of (CoFeB)/(SiO_2) samples. The principal feature of the dielectric function spectral responses is a clearly pronounced structurization of spectra in the region of 3.5 eV at magnetic phase concentrations higher than 45 at. %. On the whole, the spectral responses of the dielectric functions of the nanocomposites prepared in a dc magnetic field under substrate cooling (samples II-2) and in zero field without cooling (II-1) are similar. In our opinion, the main difference lies in that the above-mentioned structurization of dielectric function spectra is more distinct in samples fabricated in zero field without cooling, which is demonstrated convincingly by Fig. 5. It should be pointed out that, in contrast to (CoFeB)/(SiO_2), the refractive index of the (CoFeZr)/(Al_2O_3) nanocomposites turns out to be dependent on photon energy, decreasing slightly with an increase in this energy, while remaining practically independent of concentration for the samples obtained in a magnetic field. Note that, at low energies, the spectra of nanocomposites II-1 are nonmonotonic, but this feature disappears as the particle concentration increases. We explain this feature in the same way as in the case of the (CoFeB)/(SiO_2) samples; namely, we assign it to interference. The smaller interference period in the samples of (CoFeZr)/(Al_2O_3) compared to that in the (CoFeB)/(SiO_2) nanocomposite correlates well with the larger thickness of the (CoFeZr)/(Al_2O_3) films. There is no interference, however, in samples II-2.

3.2. Magnetooptical Properties

Figure 6 displays concentration dependences of the Kerr effect obtained in a field of 15 kOe with a photon energy of 1.96 eV (solid lines) for the three types of (CoFeB)/(SiO_2) nanocomposites. Obviously, the presence of oxygen or nitrogen impurities does not have a noticeable effect on the maximum magnitude of the Kerr rotation angle, which is 0.25° for nanocomposites I-1 and I-2 and 0.3° for I-3. The concentration dependences also retain their general pattern for all samples. Note the presence of a sharp maximum at concentrations of 37, 40, and 37.5 at. % for samples I-1, I-2, and I-3, respectively. Because the percolation threshold for these nanocomposites was found to be about 46 at. % [12], the observed maximum is not related to percolation processes. This maximum lies in the range of magnetic-grain concentrations where the spectral responses of optical parameters behave nonmonotonically; there-

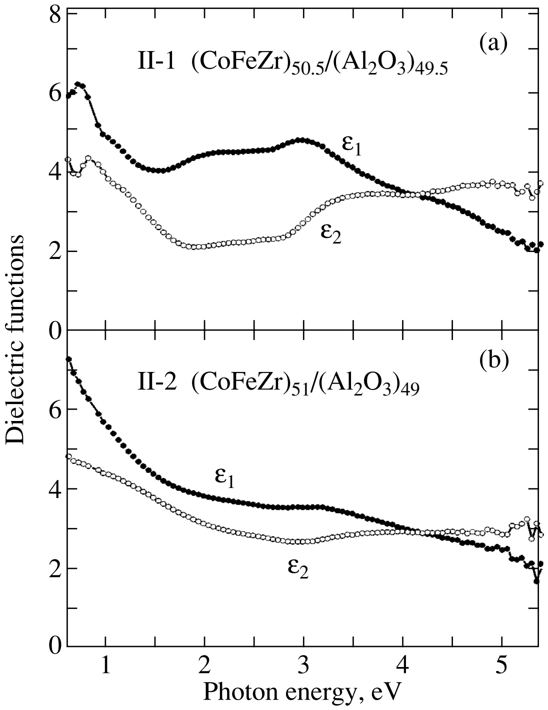

Fig. 5. Spectral response of the real, ε_1, and imaginary, ε_2, parts of the dielectric function for $(CoFeZr)/(Al_2O_3)$ nanocomposites obtained (a) without a magnetic field and cooling (II-1) and (b) in a magnetic field under cooling (II-2).

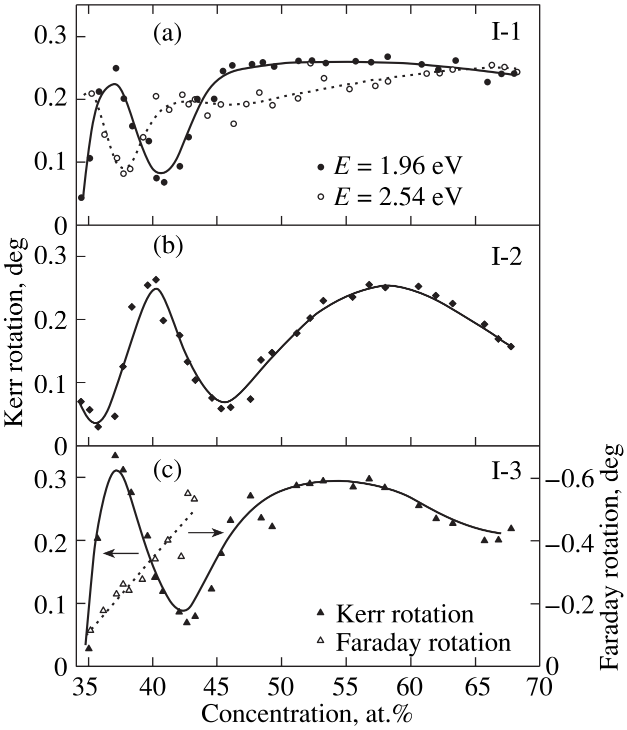

Fig. 6. Rotation of the plane of polarization plotted vs. magnetic grain concentration for $(CoFeB)/(SiO_2)$ nanocomposites in a magnetic field of 15 kOe. (a) Kerr rotation for series I-1 measured at a photon energy of 1.96 eV (solid line, filled symbols) and 2.54 eV (dashed line, open symbols); (b) Kerr rotation for series I-2 measured at a photon energy of 1.96 eV; and (c) Kerr rotation (solid line, dark symbols) and Faraday effect (dashed line, open symbols) for series I-3 measured at a photon energy of 1.96 eV.

fore, this behavior may originate from an interference phenomenon. The maximum is not associated with a change in an off-diagonal element of the permittivity tensor in Eq. (3), because the Faraday effect measured by us in this concentration range has the expected monotonic dependence on concentration (dashed line in Fig. 6c). Faraday rotation measurements could be performed only at magnetic-grain concentrations less than 42 at. % because of strong absorption of light setting in at higher concentrations.

The concentration dependence of the Kerr effect measured at a photon energy of 2.54 eV (dashed curve in Fig. 6a) is of the same character as the one observed for 1.96 eV but is shifted relative to the latter; in other words, the observed maximum is frequency-dependent and, thus, is not related to variation of the magnetic properties of the nanocomposites in the concentration range considered.

We calculated the concentration dependence of the rotation of the plane of polarization in reflection from a thin nanocomposite film (Fig. 7). The calculations were made in terms of the effective-medium approximation [21] using Eqs. (4) and (5) and included not only the Kerr effect for the ray reflected from the upper boundary of the nanocomposite film but also the Faraday effect for the ray transmitted through the film and reflected from the film/substrate interface. The calculated concentration dependence of the rotation of the plane of polarization revealed that interference effects do indeed give rise to a strong enhancement of the magnetooptical effect at low magnetic-grain concentrations. The above appears to provide a convincing argument for the observed nonmonotonic behavior of the

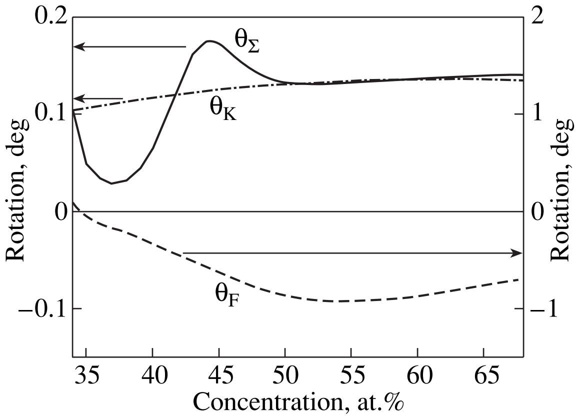

Fig. 7. Calculated concentration dependences of the Kerr rotation angle θ_K (dash-dotted line), Faraday rotation angle θ_F (dashed line), and total rotation angle θ_Σ (solid line).

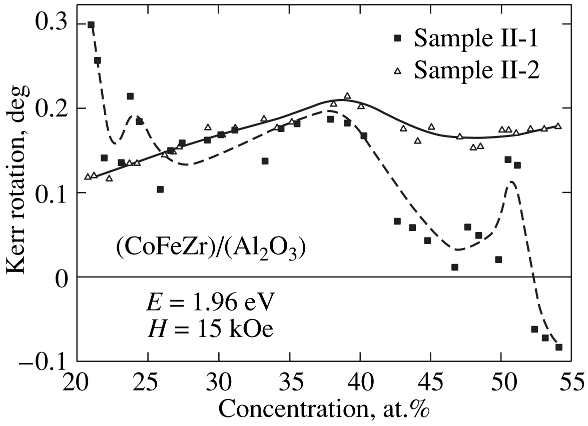

Fig. 8. Concentration dependences of the Kerr rotation for (CoFeZr)/(Al$_2$O$_3$) nanocomposites prepared in a dc magnetic field (samples II-2; solid line, open symbols) and without a magnetic field (samples II-1; dashed line, filled symbols).

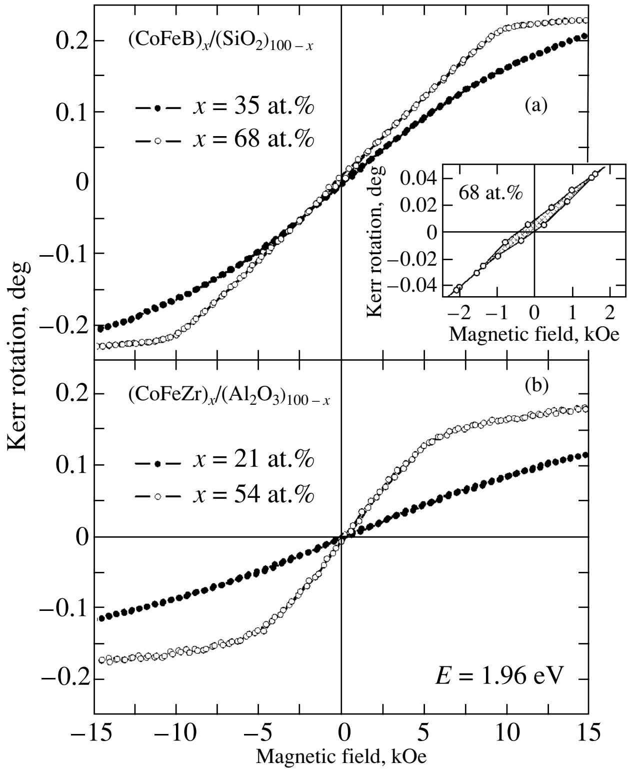

Fig. 9. Field dependences of the Kerr rotation obtained for nanocomposites with magnetic phase concentrations below and above the percolation threshold. (a) (CoFeB)/(SiO$_2$) and (b) (CoFeZr)/(Al$_2$O$_3$). Inset: hysteresis for a (CoFeB)$_{68}$/(SiO$_2$)$_{32}$ sample.

concentration dependences below the percolation threshold being closely related to the interference effect.

Another remarkable feature was revealed in the concentration dependences of the Kerr effect for the (CoFeZr)/(Al$_2$O$_3$) nanocomposites (Fig. 8). We believe the concentration dependence of the Kerr rotation for nanocomposites II-2, which has only one maximum near the percolation threshold, to be typical of nanocomposites. At the same time, samples II-1 reveal a reversal of sign of the effect at magnetic phase concentrations above 52 at. %. No such behavior is observed in nanostructures of the same composition but fabricated in a dc magnetic field under substrate cooling (samples II-2). As already mentioned, the optical spectra of these nanocomposites do not exhibit any radical differences; therefore, the observed difference in the magnetooptical properties may be assigned to a difference between the off-diagonal elements of the permittivity tensor in Eq. (3) for nanocomposites prepared in a magnetic field and without one.

It should be pointed out that the concentration dependences for samples II-1 reveal oscillations at low concentrations, which are not observed for samples II-2. This behavior reminds one of the case already discussed in connection with the optical properties of nanocomposites and is also related to interference effects.

3.3. Magnetic Properties

Figure 9 presents magnetic field dependences of the polar magnetooptic Kerr effect obtained on (CoFeB)/(SiO$_2$) and (CoFeZr)/(Al$_2$O$_3$) nanostructures for magnetic phase concentrations below and above the percolation threshold. The pattern of the field dependences measured at low concentrations (in particular, the absence of hysteresis and of saturation in a field of 15 kOe) is typical of an ensemble of superparamagnetic particles. Magnetization curves of a superparamagnet are described, similar to the case of a paramagnetic material, by the Langevin function [11] with the magnetic moment of a paramagnetic atom replaced by the magnetic moment of a grain given as a single-domain ferromagnetic particle:

$$\theta_{\mathrm{K}} = \theta_{\mathrm{K}}^{S}\left(\coth\left(\frac{\mu H}{k_{\mathrm{B}}T}\right)-\left(\frac{\mu H}{k_{\mathrm{B}}T}\right)^{-1}\right), \qquad (6)$$

where μ is the magnetic moment of the grain, H is the magnetic field strength, and T is the temperature.

Using function (6), we described the field dependences of the Kerr effect for all types of nanocomposites under study for concentrations below the percolation threshold. Thus, within this concentration region, these nanocomposites can be considered as an ensemble of noninteracting ferromagnetic single-domain particles with a negligible size dispersion for each concentration. At higher nanoparticle concentrations, the distances between the particles decrease, thus increasing the role of interactions between them and favoring the formation of clusters and chains, as a result of which the nanocomposites are no longer superparamagnets. The appearance of a weak hysteresis and saturation, which become particularly pronounced in nanocomposites I-1, supports the existence of ferromagnetism in the nanocomposites above the percolation threshold.

We used Eq. (6) to analyze the field dependences of the Kerr rotation for samples with grain concentrations below the percolation threshold. The analysis showed that an increase in the magnetic phase concentration brings about an increase in the magnetic moment of the grains, which is caused by their growth in size. The presence of oxygen or nitrogen impurities in the (CoFeB)/(SiO_2) nanocomposites affects the grain magnetic moment substantially by reducing it. Because hysteresis and saturation at high concentrations are more pronounced in samples that are free of impurities, one may conclude that the presence of impurities also weakens intergrain interaction.

4. CONCLUSIONS

The main results of our study of the optical, magnetooptical, and magnetic properties of (CoFeB)/(SiO_2) and (CoFeZr)/(Al_2O_3) nanocomposites can be summed up as follows.

(i) It has been established that, at photon energies above 4.2 eV, (CoFeB)/(SiO_2) nanocomposites are transparent, irrespective of the magnetic-grain concentration. The CoFeB alloy was also shown to be transparent in this energy region. The spectral responses of the dielectric functions of the (CoFeZr)/(Al_2O_3) composites are more smooth, with a distinct structure appearing in them only above the percolation threshold.

(ii) A feature has been revealed in the concentration dependences of the Kerr effect in (CoFeB)/(SiO_2) nanocomposites, both containing oxygen and nitrogen impurities and without them; this feature can be reliably related to interference effects.

(iii) The diagonal elements of the permittivity tensor of the medium for the (CoFeZr)/(Al_2O_3) composite samples prepared in a magnetic field and without one have similar spectra. Therefore, the observed difference in behavior of the concentration dependences of the Kerr rotation between the two types of (CoFeZr)/(Al_2O_3) nanocomposites suggests a substantial change in the off-diagonal elements of the permittivity tensor. More comprehensive information can be obtained from a study of the spectral response of the Kerr effect for these nanocomposites.

(iv) The maximum magnitude of the Kerr effect in a field of 15 kOe is 0.2°–0.3°. This should be compared with the saturated Kerr effect in pure Co and Fe, which is about 0.32° and 0.43°, respectively [22]. In all nanocomposites, the Kerr rotation reaches a maximum (if we neglect local interference maxima in the region of low concentrations) in the concentration region corresponding to the percolation threshold.

(v) Below the percolation threshold, the nanocomposites under study behave like superparamagnets with no appreciable dispersion in grain size. Above the percolation threshold, the interaction between grains plays a substantial part, with the presence of oxygen and nitrogen impurities reducing the strength of this interaction. Impurities also reduce the magnetic moment of the grains.

ACKNOWLEDGMENTS

This study was supported by the Russian Foundation for Basic Research (project no. 03-02-17575a), the Presidium of the Russian Academy of Sciences (program “Low-Dimensional Quantum Structures”), and the European program “Dynamics.”

REFERENCES

1. A. E. Berkowitz, J. R. Mitchell, M. J. Carey, A. P. Young, S. Zhang, F. E. Spada, F. T. Parker, A. Hutten, and G. Thomas, Phys. Rev. Lett. **68** (25), 3745 (1992).
2. A. S. Andreenko, V. A. Berezovets, A. B. Granovskiĭ, I. V. Zolotukhin, M. Inoue, Yu. E. Kalinin, A. V. Sitnikov, O. V. Stogneĭ, and T. Palevski, Fiz. Tverd. Tela (St. Petersburg) **45** (8), 1446 (2003) [Phys. Solid State **45**, 1519 (2003)].
3. L. V. Lutsev, N. T. Kazantseva, I. A. Tchmutin, N. G. Ryvkina, Yu. E. Kalinin, and A. V. Sitnikoff, J. Phys.: Condens. Matter **15** (22), 3665 (2003).
4. B. A. Aronzon, D. Yu. Kovalev, A. N. Lagar’kov, E. Z. Meĭlikhov, V. V. Ryl’kov, M. A. Sedova, N. Negre, M. Goiron, and J. Leotin, Pis’ma Zh. Éksp. Teor. Fiz. **70** (2), 87 (1999) [JETP Lett. **70**, 90 (1999)].
5. A. Granovskiĭ, V. Gushchin, I. Bykov, A. Kozlov, N. Kobayashi, S. Ohnuma, T. Masumoto, and M. Inoue, Fiz. Tverd. Tela (St. Petersburg) **45** (5), 868 (2003) [Phys. Solid State **45**, 911 (2003)].
6. T. V. Murzina, T. V. Misuryaev, A. A. Nikitin, O. A. Aktsipetrov, and J. Güdde, J. Magn. Magn. Mater. **258–259**, 99 (2003).
7. V. G. Kravets, D. Bozec, J. A. D. Matthew, and S. M. Thompson, Phys. Rev. B **65** (5), 054 415 (2002).
8. Wei Yang, Z. S. Jiang, J. H. Cai, Y. W. Du, R. J. Zhang, S. M. Zhou, and L. Y. Chen, J. Magn. Magn. Mater. **177–181**, 1289 (1998).
9. J. L. Menéndez, B. Bescós, G. Armelles, R. Serna, J. Gonzalo, R. Doole, A. K. Petford-Long, and M. I. Alonso, Phys. Rev. B **65** (20), 205413 (2002).
10. Yu. E. Kalinin, A. T. Ponomarenko, A. V. Sitnikov, and O. V. Stogneĭ, Fiz. Khim. Obrab. Mater., No. 5, 14 (2001).
11. C. P. Bean and J. D. Livingston, J. Appl. Phys. **30** (4), 120S (1959).
12. O. V. Stogneĭ, Yu. E. Kalinin, A. V. Sitnikov, I. V. Zolotukhin, and A. V. Slyusarev, Fiz. Met. Metalloved. **91** (1), 24 (2001) [Phys. Met. Metallogr. **91**, 21 (2001)].
13. A. V. Kimel’, R. V. Pisarev, A. A. Rzhevskiĭ, Yu. E. Kalinin, A. V. Sitnikov, O. V. Stogneĭ, F. Bentivegna, and Th. Rasing, Fiz. Tverd. Tela (St. Petersburg) **45** (2), 269 (2003) [Phys. Solid State **45**, 283 (2003)].
14. A. B. Granovskiĭ, I. V. Bykov, E. A. Gan’shina, V. S. Gushchin, M. Inoue, Yu. E. Kalinin, A. A. Kozlov,

and A. N. Yurasov, Zh. Éksp. Teor. Fiz. **123** (6), 1256 (2003) [JETP **96**, 1104 (2003)].

15. V. E. Buravtsova, E. A. Gan'shina, V. S. Gushchin, Yu. E. Kalinin, S. Pkhongkhirun, A. V. Sitnikov, O. V. Stogneĭ, and N. E. Syr'ev, Izv. Ross. Akad. Nauk, Ser. Fiz. **67** (7), 918 (2003).
16. X. Batlle and A. Labara, J. Phys. D **35** (6), R15 (2002).
17. R. M. Azzam and N. M. Bashara, *Ellipsometry and Polarized Light* (North-Holland, Amsterdam, 1977; Mir, Moscow, 1981).
18. R. V. Pisarev, in *Physics of Magnetic Dielectrics* (Nauka, Leningrad, 1981), Chap. 5, pp. 358–359 [in Russian].
19. R. W. Cohen, G. D. Coutts, and B. Abeles, Phys. Rev. B **8** (7), 3689 (1973).
20. P. B. Johnson and R. W. Christy, Phys. Rev. B **9** (12), 5056 (1974).
21. T. K. Xia, P. M. Hui, and D. Stroud, J. Appl. Phys. **67** (6), 2736 (1990).
22. G. S. Krinchik and V. A. Artem'ev, Zh. Éksp. Teor. Fiz. **53** (6), 1901 (1967) [Sov. Phys. JETP **26**, 1080 (1967)].

Translated by G. Skrebtsov

Physics of the Solid State, Vol. 46, No. 11, 2004, pp. 2171–2176. Translated from Fizika Tverdogo Tela, Vol. 46, No. 11, 2004, pp. 2099–2103.
Original Russian Text Copyright © 2004 by Krevchik, Marko, Grunin.

LOW-DIMENSIONAL SYSTEMS AND SURFACE PHYSICS

Magnetooptical Properties of a Molecular D_2^-– Ion in a Quantum Wire

V. D. Krevchik*, A. A. Marko*, and A. B. Grunin**
** Penza State University, Penza, 440024 Russia*
*** Penza State Pedagogical University, Penza, Russia*
e-mail: physics@diamond.stup.ac.ru

Received January 22, 2004; in final form, March 25, 2004

Abstract—In the framework of a model of zero-range potential, the problem of bound states of an electron in the field of two D0 centers (a two-center problem) in a semiconductor quantum wire is considered in the presence of a longitudinal magnetic field. It is shown that the magnetic field produces a significant shift of g and u terms and stabilizes the D_2^- states in quantum wires. It is found that, in the case of transverse polarization of light, the spectral dependence of the photoionization cross section of a D_2^- center exhibits the quantum-confined Zeeman effect with strongly pronounced oscillations of interference nature. © *2004 MAIK "Nauka/Interperiodica".*

1. INTRODUCTION

Experiments show [1] that, in low-dimensional systems under certain conditions, reactions of the type $D^0 + e \longrightarrow D^-$ are possible; as a result, neutral shallow donors bind an additional electron to form so-called D^- states. In the presence of a confinement potential, such states open new possibilities for studying correlation effects in low-dimensional systems [1]. In this study, we consider a situation where not all D^0 positions can be effectively filled by the electron transfer from the barrier. In this case, negative molecular ions D_2^- can be formed depending on the distance R between the D^- centers. We should note that the system of a weakly bound electron in the field of two identical potential centers is also encountered in alkali halide crystals [2], where it is called an M^- color center and is formed by an electron in the field of a neutral M center (two close F centers). It is known [3, 4] that a D^- center can be modeled by an electron in the field of a zero-range potential. We have shown previously [5, 6] that, by using the method of zero-range potential, we can obtain an analytical solution for the wave function and binding energy of an electron localized on a D^0 center and also investigate the impurity magnetoabsorption of light in a quantum wire (QW) with a parabolic confinement potential. Modeling of the negative molecular ion D_2^- and investigation of its magnetooptical properties in a QW are also of interest. Since the D_2^- system is symmetric with respect to its center, the electron states for a fixed distance R between the D^0 centers must be either symmetric (g terms) or antisymmetric (u terms). Obviously, the splitting of g and u terms, degenerate at large R, is determined by R and, as a consequence of lower dimensionality, by the parameters of the QW. A magnetic field applied along the QW axis plays the role of a variable parameter, which can be used to change the confinement geometry of the system and, hence, to control both the magnitude of the splitting and the energies of optical transitions [6].

The aim of this study is to trace, in the context of the model of zero-range potential, the evolution of terms with varying longitudinal magnetic field and also to investigate the structure of the magnetooptical spectrum of a QW related to electron optical transitions from the state of the g term to hybrid quantized states of the QW. We assume that the QW has the form of a circular cylinder whose base radius L is much smaller than its length L_z ($L \ll L_z$). To describe one-electronic states in a QW, we use a parabolic confinement potential

$$V(\rho) = \frac{m^*}{2}\omega_0^2\rho^2, \tag{1}$$

where $\rho \le L$; ρ, ϕ, and z are cylindrical coordinates; m^* is the effective electron mass; and ω_0 is the characteristic frequency of the confining potential of the QW.

For the vector potential $\mathbf{A}(r)$ of the magnetic field longitudinal with respect to the QW axis, we choose the symmetric gauge, so that $\mathbf{A} = (-yB/2, xB/2, 0)$. To describe the one-electron states (unperturbed by impurities) in a longitudinal magnetic field, we write the Hamiltonian of the model considered (in the cylindrical system of coordinates) as [6]

$$\hat{H} = -\frac{\eta^2}{2m^*}\left(\frac{1}{\rho}\frac{\partial}{\partial\rho}\left(\rho\frac{\partial}{\partial\rho}\right)+\frac{1}{\rho^2}\frac{\partial^2}{\partial\phi^2}\right) - \frac{i\eta\omega_B}{2}\frac{\partial}{\partial\phi}+\frac{m^*}{2}\left(\omega_0^2+\frac{\omega_B^2}{4}\right)\rho^2+\hat{H}_z. \tag{2}$$

1063-7834/04/4611-2171$26.00 © 2004 MAIK "Nauka/Interperiodica"

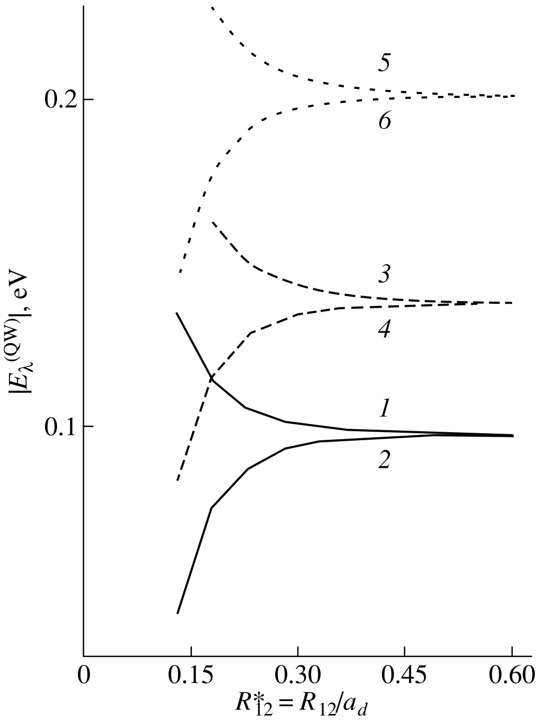

Fig. 1. Dependence of the electron binding energies on the distance between the D^0 centers at L = 65 nm, U_0 = 0.1 eV, and E_i = 0.01 eV for (*1*, *3*, *5*) the g term and (*2*, *4*, *6*) the u term; B is equal to (*1*, *2*) 0, (*3*, *4*) 10, and (*5*, *6*) 20 T.

Here, $\omega_B = |e|B/m^*$ is the cyclotron frequency, e is the elementary charge, and $\hat{H}_z = (-\eta^2/2m^*)\partial^2/\partial z^2$.

A two-center potential is modeled by a superposition of zero-range potentials of strengths $\gamma_i = 2\pi\eta^2/\alpha_i m^*$ (i = 1, 2):

$$V_\delta(r, R_1, R_2) = \sum_{i=1}^{2}\gamma_i\delta(r - R_i)[1 + (r - R_i)\nabla_r], \quad (3)$$

where $R_i = (\rho_i, \phi_i, z_i)$ are the coordinates of the D^0 centers and α_i is determined by the energy E_i of the electron state localized on the same D^- center in the bulk semiconductor.

The bound states in a one-dimensional system in the presence of a longitudinal magnetic field are considered in Section 2. Section 3 contains the results of calculating the photoionization cross section of a D_2^- center in a longitudinal magnetic field and the magnetic field–dependent impurity absorption.

2. TERMS OF A D_2^- MOLECULAR ION IN A LONGITUDINAL MAGNETIC FIELD

The electron wave function $\Psi_\lambda(r, R_1, R_2)$ localized at the D_2^- center and satisfying the Lippmann–Schwinger equation for the bound state can be written as a linear combination,

$$\Psi_\lambda(r, R_1, R_2) = \sum_{i=1}^{2} c_i\gamma_i G(r, r_i; E_\lambda), \quad (4)$$

where $G(r, r_i; E_\lambda)$ is the one-electron Green function corresponding to a source at the point r_i and to the energy $E_\lambda = -\eta^2\lambda^2/(2m^*)$ (E_λ is the bound state energy of an electron in the field of two D^0 centers in the presence of a longitudinal magnetic field and is measured from the bottom of the two-dimensional oscillator well) [5]. From the mathematical point of view, this two-center problem is reduced to finding nontrivial solutions of a homogeneous system of algebraic equations for the coefficients c_i [2], which leads to a transcendental equation for E_λ. In the case where $\gamma_1 = \gamma_2 = \gamma$, this equation is separated into two equations, which determine a symmetric (g term) and an antisymmetric (u term) electron state. With allowance for an explicit form of the one-electron Green function in a cylindrical system of coordinates [5] (the D^0 centers are located on the QW axis, $R_i = (0, 0, z_i)$), these equations can be written in the form

$$\frac{1}{\sqrt{\pi\beta}}\int_0^{+\infty}\frac{dt}{\sqrt{t}}\exp[-(\beta\eta^2 + w)t]$$
$$\times\left[\frac{1}{t} - 2w(1 - \exp(-2wt))^{-1}\right]\left(1 \pm \exp\left(-\frac{R_{12}^*}{4\beta t}\right)\right) \quad (5)$$
$$+ 2\sqrt{\eta^2 + \beta^{-1}w} - 2\eta_i = \pm\frac{2\sqrt{\pi\beta}}{R_{12}^*}\exp[-R_{12}^*\sqrt{\eta^2 + \beta^{-1}w}],$$

where the plus sign corresponds to symmetric states (g term) and the minus sign, to antisymmetric states (u term); $\eta^2 = |E_\lambda|/E_d$; $\beta = L^*/(4\sqrt{U_0})$; $U_0 = m^*\omega_0^2L^2/2$ is the amplitude of the confinement potential of the QW; $U_0^* = U_0/E_d$; $L^* = 2L/a_d$; $\eta_i^2 = |E_i|/E_d$; $w = \sqrt{1 + \beta^2 a^{*-4}}$; $R_{12}^* = R_{12}/a_d$; $R_{12} = |z_1 - z_2|$; and $a^* = a_B/a_d$ (a_d is the effective Bohr radius, E_d is the effective Bohr energy, and $a_B = \sqrt{h/(m^*\omega_0)}$ is the magnetic length).

The dependence of the terms on the magnetic field B for an InSb-based QW as obtained from Eqs. (5) is shown in Fig. 1 for the case of $E_\lambda < 0$ (binding energy $E_\lambda^{(QW)}$ of an electron localized at a D_2^- center in a QW is defined as $E_\lambda^{(QW)} = E_{0,0} + |E_\lambda|$, where $E_{0,0} = \eta\omega_0\sqrt{1 + \omega_B^2/(4\omega_0^2)}$ [5]). In Fig. 1, we see that, in the case of the g term, $\left|E_\lambda^{(QW)}\right| \longrightarrow \infty$ as $R_{12}^* \longrightarrow 0$; i.e., a sort of “falling to the center” is observed [27]. On the contrary, for a state with a smaller binding energy (u term), $\left|E_\lambda^{(QW)}\right|$ decreases as $R_{12}^* \longrightarrow 0$. Thus, with decreasing R_{12}^*, g and u terms (degenerate at $R_{12}^* \geq 1$) are split. In Fig. 1, we can also trace the evolution of the g and u terms as the magnetic field is varied (compare curves *1*, *2* and *5*, *6*): with increasing magnetic field, the binding energy of the D_2^- center grows and the conditions of existence of a g state become more restrictive (compare curves *1*, *5*). Figure 2 shows the magnetic field dependence of the splitting $|E_{\lambda g} - E_{\lambda u}|$ between the g and u terms. The sensitivity of the splitting to a magnetic field is important for experimental studies of the structure of the absorption band due to electron transitions between g and g states of the D_2^- center. We see that the magnetic field stabilizes D_2^- states in a QW. The possibility of controlling the energies of optical transitions in a magnetic field is of interest for the technology of laser structures and also for photodetectors with controlled sensitivity in the region of impurity optical absorption.

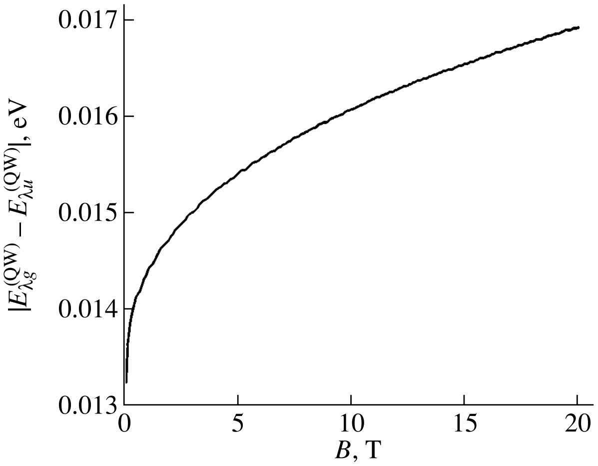

Fig. 2. Magnetic field dependence of the splitting between g and u terms for L = 65 nm, U_0 = 0.1 eV, E_i = 0.01 eV, and R_{12}^* = 0.25.

3. CALCULATION OF THE PHOTOIONIZATION CROSS SECTION OF A MOLECULAR ION D_2^-

Now, we consider the photoionization of the D_2^- center related to an electron optical transition from the g state of the QW to states of the quasidiscrete spectrum in a longitudinal magnetic field. The effective Hamiltonian of the interaction with the field of a light wave $\hat{H}_{\text{int}}^{(s)}$ in the case of longitudinal polarization $e_{\lambda s}$ (with respect to the direction of the magnetic field) is given by

$$\hat{H}_{\text{int}}^{(s)} = \lambda_0 \sqrt{\frac{2\pi\alpha^* h^2}{m^{*2}\omega}} I_0 \exp(iqr)(e_{\lambda s}, p), \tag{6}$$

where λ_0 is the local field factor, α^* is the fine structure constant including the permittivity ε, I_0 is the intensity of light, ω is the frequency of light, q is the wave vector, and p is the electron momentum operator. According to Eq. (4), the electron wave function in the g state of the D_2^- center can be written as

$$\Psi_g(\rho, z; z_1, z_2) = C\left\{\int_0^\infty \frac{dt}{\sqrt{t}} \exp[-(\beta\eta^2 + w)t]\right.$$
$$\times (1 - \exp[-2wt])^{-1} \exp\left[-\frac{\rho w(1 + e^{-2wt})}{4\beta a_d^2(1 - e^{-2wt})}\right] \tag{7}$$
$$\left.\times \left[\exp\left(-\frac{(z - z_1)^2}{4\beta a_d^2 t}\right) + \exp\left(-\frac{(z - z_2)^2}{4\beta a_d^2 t}\right)\right]\right\},$$

where z_1 and z_2 are the coordinates of the D^0 centers on the QW axis. The normalizing factor C is defined as

$$C = 2^{\frac{1}{4}} \pi^{-1} \beta^{-\frac{3}{4}} a_d^{-\frac{3}{2}} w^{\frac{5}{4}} \left[\zeta\left(\frac{3}{2}, \frac{\beta\eta^2}{2w} + \frac{1}{2}\right)\right.$$
$$+ \exp\left(-\frac{R_{12}^*}{2}(\eta^2 + \eta^{-2}\beta^{-1}w + 1)\right)\frac{\beta}{2w}\left(\frac{2\beta^{-1}w}{\eta^2 + \beta^{-1}w}\right.$$
$$\times {}_2F_1\left(1, \frac{\beta^2 + \beta^{-1}w}{2\beta^{-1}w}; 1 + \frac{\eta^2 + \beta^{-1}w}{2\beta^{-1}w};\right. \tag{8}$$
$$\left.\exp(-R_{12}^*\eta^{-2}\beta^{-1}w)\right) + (2\beta^{-1}w)^{-\frac{1}{2}}$$
$$\left.\left.\times \Phi\left(\exp(-R_{12}^*\eta^{-2}\beta^{-1}w), \frac{3}{2}, \frac{\eta^2 + \beta^{-1}w}{2\beta^{-1}w}\right)\right)\right]^{-\frac{1}{2}}.$$

Here, $\zeta(s, \nu)$ is the generalized zeta-function, ${}_2F_1(\alpha, \beta; \gamma; z)$ is the Gauss hypergeometric function, and $\Phi(z, s, \nu) = \sum_{n=0}^{\infty}(\nu + n)^{-s} z^n$ ($|z| < 1$, $\nu \neq 0, -1, -2, \ldots$) [8].

The matrix element $M_{fg}^{(s)}$ determines the oscillator strength of the dipole optical transition from the g state $\Psi_g(\rho, z; z_1, z_2)$ to states of the quasidiscrete spectrum of the QW $\Psi_{n, m, k}(\rho, \phi, z)$ and can be written as

$$M_{fg}^{(s)} = 2^{\frac{5}{2}} \pi \lambda_0 (\alpha^* I_0/\omega)^{\frac{1}{2}} \beta w^{-\frac{1}{2}} E_d a_d^3 C$$
$$\times \left[\frac{k(1 + \cos(kR_{12}))}{\beta\eta^2 + \beta a_d^2 k^2 + (2n + 1)w} + \frac{R_{12}}{2\beta a_d^2}\sin(kR_{12})\right. \tag{9}$$
$$\left. + i\left(\frac{R_{12}}{2\beta a_d^2}\cos(kR_{12}) - \frac{k\sin(kR_{12})}{\beta\eta^2 + \beta a_d^2 k^2 + (2n + 1)w}\right)\right],$$

where $n = 0, 1, 2, \ldots$ is the quantum number specifying Landau levels and k is the projection of the quasimomentum vector of an electron in the QW on the z axis. Applying a standard calculation procedure [6], the photoionization cross section in the dipole approximation can be found to be

$$\sigma_g^{(s)} = \sigma_0 w^{-1} C^2 \sum_{n=0}^{N} \left\{ 4X^{-3} f_n(X,\eta)\cos^2\left(\frac{R_{12}^*}{2} f_n(X,\eta)\right) + X^{-2}\frac{R_{12}^*}{2}\sin(R_{12}^* f_n(X,\eta)) + X^{-1}\frac{R_{12}^{*2}}{4f_n(X,\eta)} \right\}, \tag{10}$$

where $f_n(X, \eta) = \sqrt{X - \eta^2 - \beta^{-1}w(2n+1)}$, $X = \eta\omega/E_d$, $\sigma_0 = 2^6\pi^3\alpha^*\lambda_0 a_d^5$, and $N = [A]$ is the integer part of the number $A = \beta(X - \eta^2)/(2w) - 1/2$.

Figure 3 shows the spectral dependence of $\sigma_g^{(s)}$ calculated by using Eq. (10) for an InSb-based QW. We see that, for the longitudinal polarization of light, the magnetoabsorption spectrum contains resonant peaks with strongly pronounced oscillations, which are associated with the interference distribution (9). Simulation shows that the oscillation period increases linearly with decreasing distance between the D^0 centers and weakly depends on the magnetic field. The resonant peaks exhibit periodicity determined by the hybrid frequency $\Omega = \sqrt{4\omega_0^2 + \omega_B^2}$ and correspond to optical electron transitions from the g state of the D_2^- center to a state of the quasidiscrete spectrum of the QW with a magnetic quantum number $m = 0$. In a magnetic field, the absorption edge is shifted to the short-wave region of the spectrum (compare curves *1*, *2*). It is seen in Fig. 3 that, in the case of $B = 20$ T, this shift exceeds 0.05 eV and obeys the law $X_S = \eta_g^2 + \beta^{-1}w$. The oscillation amplitude appreciably decreases, and the period of the appearance of peaks increases. We consider the absorption of light by the system QW–D_2^- center in the case of $B \perp e_\lambda$ (e_λ is the unit vector of light polarization). The effective Hamiltonian of interaction with the field of an optical wave $\hat{H}_{\text{int}}^{(t)}$ in the cylindrical system of coordinates is written as

$$\hat{H}_{\text{int}}^{(t)} = -i\eta\lambda_0\sqrt{\frac{2\pi\eta^2\alpha^*}{m^{*2}\omega}}\, I_0 \exp(iq_z z)\Big[\cos(\theta-\phi)\frac{\partial}{\partial\rho} + \frac{1}{\rho}\sin(\theta-\phi)\frac{\partial}{\partial\phi} - \frac{i|e|B}{2\eta}\rho\sin(\phi-\theta)\Big], \tag{11}$$

where θ is the polar angle of the unit vector of transverse polarization $e_{\lambda t}$ in the cylindrical system of coordinates and $q = (0, 0, q_z)$.

In the dipole approximation, the matrix element $M_{fg}^{(s)}$ of the optical transition considered can be written as

$$M_{fg}^{(t)} = 2^2\pi\lambda_0\sqrt{\frac{\alpha^* I_0}{\omega}} E_d a_d^3 \beta^{\frac{1}{2}} C \exp(\mu i m\phi)\delta_{m,\pm 1}(n+1)^{\frac{1}{2}} \times \frac{[\beta\eta^2 + 2(n+1)w + m\beta a^{*-2} + \beta a_d^2 k^2]}{[\beta\eta^2 + (2n+1)w + \beta a_d^2 k^2][\beta\eta^2 + (2n+3)w + \beta a_d^2 k^2]}[1 + \exp(-ikR_{12}/2)]. \tag{12}$$

Calculating the matrix element in Eq. (12) involves calculation of an integral of the type

$$\int_0^{2\pi} \exp(-im\phi)\left(\cos(\theta-\phi)\frac{w(1+\exp(-2wt))}{\beta a_d^2(1-\exp(-2wt))} + \frac{i}{a_d^2}\sin(\phi-\theta)\right)d\phi \tag{13}$$

$$= \pi\exp(\mu i\theta)\delta_{m,\pm 1}\left(\frac{w(1+\exp(-2wt))}{\beta a_d^2(1-\exp(-2wt))} + \frac{m}{a_d^2}\right),$$

which determines the selection rules for the magnetic quantum number m. In Eq. (13), $\delta_{m,\pm 1}$ is the Kronecker delta, the minus sign in the exponent in $\exp(\mu i\theta)$ corresponds to $m = +1$, and the plus sign corresponds to $m = -1$. The photoionization cross section $\sigma_g^{(t)}$ of the D_2^- center in the case of transverse polarization of light (with respect to the direction of the magnetic field) in the dipole approximation can be written as

$$\sigma_g^{(t)} = \sigma_0 w^{-1} C^2 X \sum_{n=0}^{N}(n+1) \times \sum_{m=-1}^{1}\delta_{m,\pm 1}(f_{n,m}(X,\eta_g))^{-1/2} \times [\beta^2(X-(m+1)a^{*-2})(X-(m-1)a^{*-2})-1]^{-2} \times \cos^2\left(\frac{R_{12}^*}{4}\sqrt{f_{n,m}(X,\eta_g)}\right), \tag{14}$$

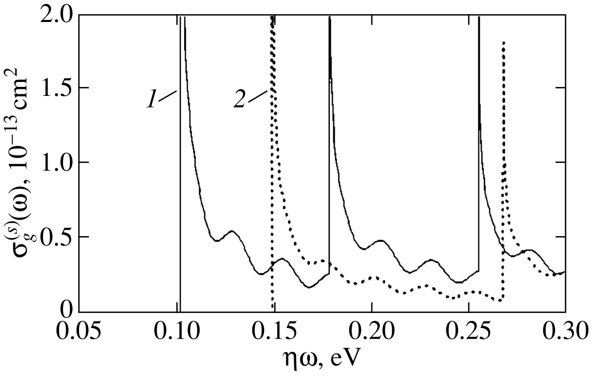

Fig. 3. Spectral dependence of the photoionization cross section of a D_2^- center in an InSb-based QW for $L = 65$ nm, $U_0 = 0.1$ eV, $E_i = 0.01$ eV, and $R_{12} = 16$ nm; B is equal to (*1*) 0 and (*2*) 20 T.

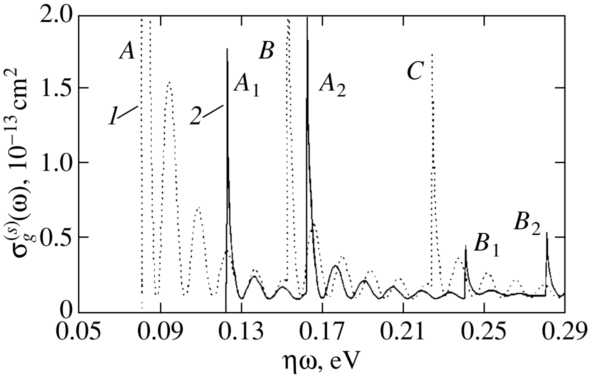

Fig. 4. Spectral dependence of the photoionization cross section of a D_2^- center in an InSb-based QW for transverse polarization of light calculated for $L = 65$ nm, $U_0 = 0.1$ eV, $E_i = 0.01$ eV, and $R_{12} = 16$ nm; B is equal to (*1*) 0 and (*2*) 20 T.

where $f_{n,m}(X, \eta_g) = X - \eta_g^2 - ma^{*-2} - \beta^{-1}w(2n + |m| + 1)$, $\sigma_0 = 2^7\pi^3\alpha^*\lambda_0^2 a_d^5$, and $N = [D]$ is the integer part of the number $D = \beta(X - \eta_g^2 + a^{*-2})/(2w) - 1$.

Figure 4 shows the spectral dependence of the photoionization cross section $\sigma_g^{(t)}$ of the D_2^- center calculated by Eq. (14) for an InSb-based QW. We can see that, in a magnetic field, the resonant peaks A and B (curve *1*) are split into doublets A_1, A_2 and B_1, B_2 (curve *2*). The intervals between the peaks in a Zeeman doublet are filled with oscillations of interference nature. The distance between the resonant peaks forming a doublet is equal to $\eta\omega_B$; i.e., it is determined by the cyclotron frequency. The doublets are located on the absorption curve with a period $\eta\Omega$. Simulation shows that the oscillation period in a doublet and between the doublets increases exponentially with decreasing distance between the D^0 centers and varies only slightly with magnetic field.

4. CONCLUSIONS

Our results have shown that a magnetic field applied along the QW axis acts as a variable parameter, which can be used to effectively control both the binding energy of D_2^- centers and their magnetooptical properties. This is important for creating photosensitive structures with controlled parameters. For a structure consisting of a set of QWs without tunnel coupling between them, the impurity magnetoabsorption coefficient $K^{(t)}(\omega)$ for transverse polarization can be obtained from Eq. (14) by averaging over all possible values of the parameter R_{12}^*. Taking into account that the contribution from large values of R_{12}^* is exponentially small, we can write

$$K^{(t)}(\omega) = \frac{1}{VL_c^*}\int_{2/\eta}^{1}\sigma_g^{(s)}(\omega, R_{12}^*)\exp(-(R_{12}^* - 2/\eta))$$
$$\times(1 - f_0(X - \eta))dR_{12}^*, \tag{15}$$

where V is the QW volume, L_c^* is the period of the structure given in units of the effective Bohr radius, $f_0(X, \eta) = 8\sqrt{\pi}(n_e a_d^3)\sqrt{\delta_T}\beta\omega^{-1}\sinh(\delta_T\beta^{-1}\omega)\exp(-\delta_T(X - \eta))$ is the quasiequilibrium distribution function for electrons in a QW [9], $\delta_T = E_d/(kT)$, and n_e is the electron concentration.

For an InSb-based QW, the spectral dependence of the impurity magnetoabsorption coefficient for light of transverse polarization in relative units, $K^{(t)}(\omega)/K_0$ (where $K_0 = \sigma_0/VL_c^*$, is shown in Fig. 5 for the optical

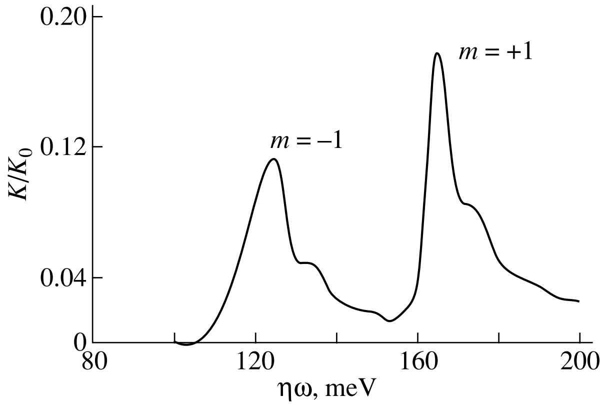

Fig. 5. Spectral dependence of the impurity magnetoabsorption for transverse polarization of light in relative units for the optical transition with the maximum oscillator strength ($n = 0$) in the case of an InSb-based QW for $L = 65$ nm, $U_0 = 0.1$ eV, $E_i = 0.01$ eV, $B = 20$ T, and $T = 7$ K.

transition with the maximum oscillator strength ($n = 0$). By comparing Figs. 4 and 5, we see that the resonant peaks A_1 and A_2 in the doublet (Fig. 4) are broadened into bands (Fig. 5); the oscillations in the doublet are also broadened. To estimate $K^{(t)}_{(-1;\,+1)}(\omega)$ in the doublet for an InSb-based QW, we used the following numerical values of the parameters (see Fig. 5): $L = 65$ nm, $U_0 = 0.1$ eV, $E_i = 0.001$ eV, $n_e = 1.4 \times 10^{16}$ cm^{-3}, $B = 20$ T, $T = 7$ K, and $L_c = 70$ nm. The result is $K^{(t)}_{(-1)}(\omega) \approx 3.6 \times 10^3$ cm^{-1} and $K^{(t)}_{(+1)}(\omega) \approx 5.4 \times 10^3$ cm^{-1} in the maxima corresponding to $m = -1$ and $m = +1$, respectively. In order of magnitude, these values are comparable to the absorption coefficient for direct interband transitions in a multiple quantum-well structure in the absence of a quantizing magnetic field [10].

REFERENCES

1. S. Huant and S. P. Najda, Phys. Rev. Lett. **65** (12), 1486 (1990).
2. Yu. N. Demkov and V. N. Ostrovskiĭ, *Zero-Range Potentials and Their Applications in Atomic Physics* (Leningr. Gos. Univ., Leningrad, 1975; Plenum, New York, 1988).
3. A. A. Pakhomov, K. V. Khalipov, and I. N. Yassievich, Fiz. Tekh. Poluprovodn. (St. Petersburg) **30** (8), 1387 (1996) [Semiconductors **30**, 730 (1996)].
4. V. D. Krevchik, R. V. Zaĭtsev, and V. V. Evstifeev, Fiz. Tekh. Poluprovodn. (St. Petersburg) **34** (10), 1244 (2000) [Semiconductors **34**, 1193 (2000)].
5. V. D. Krevchik and A. B. Grunin, Fiz. Tverd. Tela (St. Petersburg) **45** (7), 1272 (2003) [Phys. Solid State **45**, 1332 (2003)].
6. V. D. Krevchik, A. B. Grunin, A. K. Aringazin, M. B. Semenov, E. N. Kalinin, V. G. Mayorov, A. A. Marko, and S. V. Yashin, Hadronic J. **26** (1), 31 (2003).
7. L. D. Landau and E. M. Lifshitz, *Course of Theoretical Physics*, Vol. 3: *Quantum Mechanics: Non-Relativistic Theory*, 4th ed. (Nauka, Moscow, 1989; Pergamon, New York, 1977).
8. *Higher Transcendental Functions (Bateman Manuscript Project)*, Ed. by A. Erdelyi (McGraw-Hill, New York, 1953; Nauka, Moscow, 1973), Vols. 1, 2.
9. V. A. Geĭler, V. A. Margulis, and L. I. Filina, Zh. Éksp. Teor. Fiz. **113** (4), 1377 (1998) [JETP **86**, 751 (1998)].
10. A. Ya. Shik, Fiz. Tekh. Poluprovodn. (Leningrad) **20** (9), 1598 (1986) [Sov. Phys. Semicond. **20**, 1002 (1986)].

Translated by I. Zvyagin

Physics of the Solid State, Vol. 46, No. 11, 2004, pp. 2177–2182. Translated from Fizika Tverdogo Tela, Vol. 46, No. 11, 2004, pp. 2104–2108.
Original Russian Text Copyright © 2004 by Skryshevski.

POLYMERS AND LIQUID CRYSTALS

Energy Disorder in Polysilanes

Yu. A. Skryshevski
Institute of Physics, National Academy of Sciences of Ukraine, pr. Nauki 46, Kiev, 03028 Ukraine
e-mail: skrysh@iop.kiev.ua

Received December 23, 2003; in final form, March 25, 2004

Abstract—The absorption spectra ($T = 295$ K), photoluminescence spectra ($T = 5$– 295 K), and thermally stimulated luminescence curves (T = 5–295 K) of poly(di-*n*-hexylsilane) (*PDHS*), poly(methyl-*n*-hexylsilane) (*PMHS*), poly(methylcyclohexylsilane) (*PMCHS*), and poly(methylphenylsilane) (*PMPS*) films are measured. The results obtained are analyzed within the model of random hoppings of excitons and charge carriers over sites with a Gaussian distribution of the density of states. It is established that the variance parameters of the density-of-state functions of excitons and charge carriers characterize the energy disorder and depend on the chemical nature of side groups of the polymer, the conformation of segments of the main chain of the polymer macromolecule, and the temperature. At room temperature, the energy disorder in crystalline regions of the *PDHS* film is explained in terms of fluctuations in the number of monomer units in chain segments. In polymers with nonsymmetric side groups (such as *PMHS*, *PMCHS*, and *PMPS*), the disorder is more pronounced due to the formation of conformers in which silicon atoms occupy different positions in the chain. In the *PMPS* polymer, the disorder occurs through one more mechanism associated with fluctuations of the angle between the plane of the phenyl ring and the axis of the polymer segment due to mixing of σ- and π-electron states. *© 2004 MAIK "Nauka/Interperiodica".*

1. INTRODUCTION

Polysilanes of the general formula 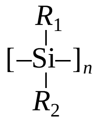 $[-\overset{\overset{R_1}{|}}{\underset{\underset{R_2}{|}}{\mathrm{Si}}}-]_n$ are organosilicon polymers in which the main chains of macromolecules consist of silicon atoms linked by σ bonds and R_1 and R_2 are side organic groups. These compounds are characterized by absorption and emission in the near-UV and visible spectral ranges [1–4], large quantum yields of photoluminescence (PL) [2] and photogeneration of charge carriers [3], the high mobility of holes [3, 5, 6], and nonlinear optical properties [2]. Polysilanes are materials used in the design of electrophotographic photoreceptors for xerography [6, 7] and photorefractive media [8]. Moreover, polysilane films have been widely used as transferring or light-emitting layers in different types of electroluminescent diodes [9–11].

The lowest lying excited state of the polysilane macromolecule is associated with the $^1(\sigma\sigma^*)$ transition of an electron delocalized along the segment of the main polymer chain. The polymer segments contain different numbers of monomer units and are separated by conformational defects that are formed when monomer units are rotated about silicon–silicon single bonds [2, 4]. The chain segments of the polymer also form transferring centers for holes [5, 6]. An increase in the number of monomer units and, correspondingly, in the length of the polymer segment leads to a decrease in the energy of the $^1(\sigma\sigma^*)$ transition and the ionization potential [2, 4, 12]. Therefore, polysilanes are disordered systems in which the distribution of energy states of excitons and charge carriers are characterized by density-of-state functions. It should be noted that the deviation of the number of monomer units in a polymer segment from the mean number is a random quantity. On this basis, in the model proposed by Bassler [6, 13–15], it is assumed that these functions can be represented by Gaussian distributions with the variance parameters σ_{ex} and σ_{cc} for excitons and charge carriers, respectively. The proper choice of this type of distribution function for polysilanes is also confirmed by the experimentally observed Gaussian shape of the absorption bands of these polymers [13, 16] and thermally stimulated luminescence (TSL) curves [11, 17].

It is known that the photophysical and transport properties of polysilanes depend on the conformation of the main chain of macromolecules and the chemical nature of the side groups [1–5]. In the present work, we revealed and analyzed a correlation between the chemical nature of side groups, the conformation of the main chain of the macromolecule, and the variance parameters σ_{ex} and σ_{cc}, which characterize the energy disorder in the polymer. For this purpose, we measured the absorption ($T = 295$ K) and photoluminescence ($T = 5$–295 K) spectra and thermally stimulated luminescence curves (T = 5–295 K) of poly(di-*n*-hexylsilane) (*PDHS*), poly(methyl-*n*-hexylsilane) (*PMHS*), poly(methylcyclohexylsilane) (*PMCHS*), and poly(methylphenylsilane) (*PMPS*) films.

1063-7834/04/4611-2177$26.00 © 2004 MAIK "Nauka/Interperiodica"

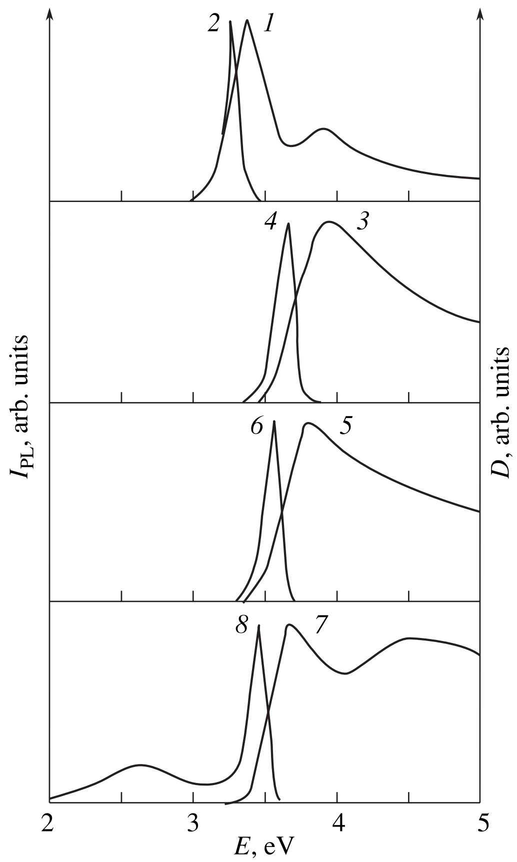

Fig. 1. (*1*, *3*, *5*, *7*) Absorption spectra and (*2*, *4*, *6*, *8*) photoluminescence spectra of (*1*, *2*) *PDHS*, (*3*, *4*) *PMHS*, (*5*, *6*) *PMCHS*, and (*7*, *8*) *PMPS* films at a temperature $T = 295$ K. Photoluminescence spectra were excited under exposure to light at a wavelength $\lambda_{ex} = 313$ nm.

2. SAMPLE PREPARATION AND EXPERIMENTAL TECHNIQUE

Polymer films a few micrometers thick were prepared by pouring toluene solutions of polymers (at a content of 3–5 wt %) onto fused silica substrates with subsequent drying at room temperature in air. The absorption spectra ($T = 295$ K) were recorded on a KSVU-23 spectrometric computer complex, and the photoluminescence spectra ($T = 5$–295 K) were measured on an SDL-1 spectrometer. The luminescence spectra were excited with the use of a DRSh-250-3 high-pressure mercury lamp through a filter transmitting a set of lines at the wavelength $\lambda_{ex} = 313$ nm for an excitation power density of less than 0.1 mW cm^{-2}. This made it possible to significantly reduce the photodestruction of the polymer films at high temperatures [11, 18, 19]. The low-temperature measurements were performed using an optical temperature-controlled flow nitrogen–helium cryostat with an automatic system for controlling and stabilizing the temperature.

Spectral characteristics of *PDHS*, *PMHS*, *PMCHS*, and *PMPS* films and the variance parameters of the density-of-state functions for excitons and charge carriers (all quantities are given in electron-volts)

Polymer	E_0^{ABS}	σ_{ex} (295 K)	$E_0^{ABS} - E_m^{PL}$	σ_{ex} (5 K)	σ_{cc}
PDHS	3.35	0.10	0.10	0.04	0.05
PMHS	3.86	0.15	0.19	0.04	0.06
PMCHS	3.76	0.12	0.17	0.07	0.09
PMPS	3.67	0.15	0.20	0.08	0.10

The thermally stimulated luminescence curves were measured as follows: the samples placed in the cryostat at a temperature $T = 5$ K were irradiated with a DRSh-500M mercury lamp at an excitation wavelength $\lambda_{irr} = 313$ or 365 nm for 60 s, were allowed to stand in the dark at this temperature until the isothermal recombination luminescence decayed, and were then heated at a constant rate of 0.15 K s^{-1}. The integrated intensity of thermally stimulated luminescence was measured on an automated setup with the use of an FÉU-106 photomultiplier operating in a photon-counting mode. In order to determine the activation energies of charge-carrier traps, continuous heating of the sample was modulated by weak temperature oscillations. The activation energies E_a in each thermal cycle were calculated from the relationship

$$E_a(T) = -d[\ln I_{TSL}(T)]/d(1/kT), \tag{1}$$

where $I_{TSL}(T)$ is the thermally stimulated luminescence intensity and k is the Boltzmann constant.

3. EXPERIMENTAL RESULTS

At $T = 295$ K, the absorption spectrum of the *PDHS* film (Fig. 1, curve *1*) consists of two bands with maxima at $E_m^{ABS} \approx 3.35$ and 3.91 eV. These bands are associated with the $^1(\sigma\sigma^*)$ transitions in chain segments that adopt *trans* planar and disordered conformations, respectively [2, 3]. Unlike the absorption spectrum of the *PDHS* films, the spectra of the *PMHS*, *PMCHS*, and *PMPS* films at $T = 295$ K contain only the band of the $^1(\sigma\sigma^*)$ transition with maxima at $E_m^{ABS} \approx 3.95$, 3.79, and 3.68 eV, respectively (Fig. 1, curves *3*, *5*, *7*) [3, 11, 19, 20]. Moreover, the spectrum of the *PMPS* film involves a band at $E_m^{ABS} \approx 4.51$ eV, which is assigned to the $^1(\pi\pi^*)$ transition in side phenyl groups. The shape of the lowest lying absorption bands for the studied polymers was approximated by the Gaussian function

$$D(E) \sim \exp[-(E_0^{ABS} - E)^2/(2\sigma_{ex}^2)], \tag{2}$$

where $D(E)$ is the optical density and E_0^{ABS} is the energy at the maximum of the Gaussian function. The parameters E_0^{ABS} and σ_{ex} (295 K) are listed in the table.

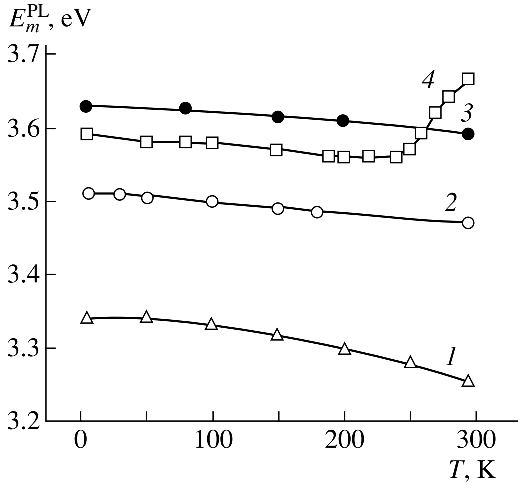

Fig. 2. Temperature dependences $E_m^{PL}(T)$ for (*1*) *PDHS*, (*2*) *PMPS*, (*3*) *PMCHS*, and (*4*) *PMHS* films.

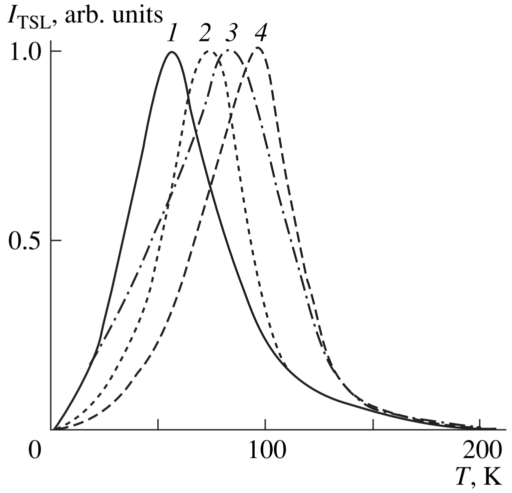

Fig. 3. Thermally stimulated luminescence curves for (*1*) *PDHS*, (*2*) *PMHS*, (*3*) *PMCHS*, and (*4*) *PMPS* films.

At $T = 295$ K, the photoluminescence spectra of the *PDHS*, *PMHS*, and *PMCHS* films ($\lambda_{ex} = 313$ nm) consist of one band at $E_m^{PL} \approx 3.25$, 3.67, and 3.59 eV with the half-widths $\Gamma_{ex} \approx 0.11$, 0.18, and 0.15 eV, respectively (Fig. 1, curves *2*, *4*, *6*). The photoluminescence spectrum of the *PMPS* film is composed of two bands, namely, a relatively narrow band ($\Gamma_{ex} \approx 0.19$ eV) at an energy $E_m^{PL} \approx 3.47$ eV and a broad band with a maximum at approximately 2.60 eV (Fig. 1, curve *8*). The bands in the spectra of the *PDHS*, *PMHS*, and *PMCHS* films and the narrow band in the spectrum of the *PMPS* film are bathochromically shifted with respect to the lowest lying band in the absorption spectra and correspond to the luminescence of excitons localized at long segments [11, 18, 19, 21]. The values of ($E_0^{ABS} - E_m^{PL}$) are presented in the table. The band with a maximum at approximately 2.60 eV in the spectrum of the *PMPS* film is associated with the luminescence of defects formed as a result of the cross-linking between polymer chains [11, 18, 22].

A decrease in the temperature in the range below room temperature leads to a shift in the maximum of the exciton photoluminescence band (Fig. 2), a decrease in the half-width of the band (at $T = 5$ K, $\Gamma_{ex} \approx$ 0.045, 0.047, 0.084, and 0.092 for the *PDHS*, *PMHS*, *PMCHS*, and *PMPS* films, respectively), and the appearance of a new broad band with a maximum at 2.99 eV in the spectrum of the *PMPS* film at $T < 40$ K. This band is assigned to the luminescence from the $^1(\sigma\pi^*)$ state, which is formed upon transfer of a π electron from a chain segment to the π^* orbital of the side phenyl group [11].

The thermally stimulated luminescence curves for the *PDHS*, *PMHS*, *PMCHS*, and *PMPS* films are broad asymmetric bands with maxima at temperatures $T_m \approx$ 55, 70, 85, and 95 K (Fig. 3) and coincide with those obtained earlier for the *PMCHS* [17] and *PMPS* [11, 17, 22] films. The activation energies of traps at the maximum of the thermally stimulated luminescence bands were determined by the fractional thermoluminescence technique: $E_m^{TSL} \approx 0.10$, 0.13, 0.19, and 0.21 eV for the *PDHS*, *PMHS*, *PMCHS*, and *PMPS* films, respectively.

4. DISCUSSION

Let us analyze the obtained results within the model of random hoppings of excitons and charge carriers over sites with a Gaussian distribution of the density of states [6, 13–15]. In the framework of this model, it is assumed that the hopping rate ν_{ij} between the ith and jth sites with the energies E_i and E_j depends only on parameters characterizing the overlap of the electron wave functions of the sites at an energy $E_j < E_i$. Moreover, an additional factor $\exp[-(E_j - E_i)/kT]$ is introduced into the expression for ν_{ij} at $E_j > E_i$. The fact that, unlike charge carriers, excitons have a finite lifetime is taken into account. In [6, 13–15], it was demonstrated that, at low temperatures, excitons and charge carriers relax to tail states and, with time, the distribution of the occupational density of states also takes a Gaussian shape with the variance parameters σ_{ex} and σ_{cc} equal to those for the density-of-state functions of excitons and charge carriers, respectively. The investigations performed in [13, 16] by selective spectroscopy revealed that the linewidth of the hole burned by a laser in an inhomogeneously broadened absorption band for a *PDHS* solution is equal to 0.5 meV at 1.4 K, the intensity of bands corresponding to the vibronic transitions in the photoluminescence spectra of *PDHS* and *PMPS* is relatively low, and the shift between the maxima of the absorption and photoluminescence bands for long segments of

PDHS does not exceed 1 meV. Therefore, the shape of the exciton photoluminescence band for polysilanes coincides with the shape of the occupational-density-of-state function of excitons and the following relationships hold in the limit $T \longrightarrow 0$ [13]:

$$\Gamma_{\mathrm{ex}} \approx 1.2\sigma_{\mathrm{ex}}, \tag{3}$$

$$(E_0^{\mathrm{ABS}} - E_m^{\mathrm{PL}}) \le 2\sigma_{\mathrm{ex}}. \tag{4}$$

At a finite temperature T_0, inequality (4) is also satisfied in the case when the dynamic equilibrium between excitons and phonons is not attained, i.e., at $\sigma_{\mathrm{ex}}(T_0)/kT_0 > 2$ [13].

It is known that the photoirradiation of polysilane films into the absorption band results in the generation of electron–hole pairs [3]. In the absence of impurities and defects with low ionization potentials, mobile charge carriers (holes) at low temperatures are localized at the longest segments of the main chain and exhibit an energy distribution described by the occupational-density-of-state function of charge carriers. Subsequent heating of the film in the dark leads to the thermal release of trapped holes, and their radiative recombination with electrons brings about the thermally stimulated luminescence. In order for the hole to be released from the trap and to reach a recombination center, it should be thermally activated to a transport energy E_{tr}. According to Hartenstein and Bassler [23], in the medium with a Gaussian distribution of the density of states, the energy E_{tr} is less than the energy corresponding to the maximum of the density-of-state function of excitons by σ_{cc}. By assuming that the activation energy at the maximum of the thermally stimulated luminescence band measured after photoirradiation of the sample at $T = 5$ K is equal to the difference between the energy corresponding to the maximum of the occupational-density-of-state function of charge carriers and the energy E_{tr} at $T \longrightarrow 0$, the parameter σ_{cc} can be determined from the formula [17]

$$\sigma_{\mathrm{cc}} = \frac{E_m}{[3\ln\ln(\Delta t/t_0)]^{1/2} - 1}. \tag{5}$$

Here, $\Delta t = 10^3$ s is the time between the photoirradiation of the sample and the measurement of the thermally stimulated luminescence curve and $t_0 \approx 10^{-13}$ s is the residence time of a charge carrier at a transport center [14, 15] in an energetically ordered medium.

The table presents the parameters $\sigma_{\mathrm{ex}}(5\text{ K})$ and σ_{cc} determined from the photoluminescence spectra and the thermally stimulated luminescence curves with the use of formulas (3) and (5), respectively. It can be seen from the table that the relationship $\sigma_{\mathrm{cc}} \approx 1.3\sigma_{\mathrm{ex}}(5\text{ K}) \approx 1.1\Gamma_{\mathrm{ex}}(5\text{ K})$ is satisfied for all the polymers. This indicates that uncontrollable impurities and structural defects in the studied samples do not substantially affect the parameters $\sigma_{\mathrm{ex}}(5\text{ K})$ and σ_{cc}. Note that the parameters σ_{cc} determined in the present work for the *PDHS*, *PMCHS*, and *PMPS* films by the thermally stimulated luminescence method are in good agreement with the analogous parameters (0.04, 0.08, and 0.09 eV, respectively) obtained in [6, 13] from the activation energies of hole mobility. On the other hand, the parameters $\sigma_{\mathrm{ex}}(5\text{ K})$ evaluated in the present work for the *PDHS* and *PMPS* films are approximately 1.3 times larger than those given in [13]. Most likely, this difference is associated with differences in the sample preparation conditions, because the absorption and photoluminescence spectra depend on the thickness, annealing temperature, and annealing time of films [2, 3, 19, 22, 24].

As can be seen from the table, an increase in the temperature from 5 to 295 K leads to an increase in the parameter σ_{ex}. This increase is explained by the broadening of the absorption and photoluminescence bands (see, for example, [1, 20, 21]). It is known that the temperature broadening of the bands of the exciton transitions is caused by the enhancement of the interaction between excitons and phonons [25, 26]. Slutsker *et al.* [27] investigated the mechanisms of reversible thermal deformation in flexible-chain and rigid-chain crystalline polymers and showed that, with an increase in the temperature, *trans–gauche* conformational transitions in macromolecules can occur in amorphous regions of the polymer in a devitrified state. Since the σ conjugation in polysilanes is determined by the overlap of the sp^3 orbitals of silicon atoms along the main chain, the energy of the $^1(\sigma\sigma^*)$ transition is very sensitive to changes in the conformation of the main chain [2–4]. Therefore, the additional temperature broadening of the absorption and photoluminescence bands of polymers in the devitrified state can be associated with the fluctuations in the energy of the $^1(\sigma\sigma^*)$ transition due to thermally induced rotations of monomer units about silicon–silicon single bonds upon the transformation of segments into a disordered conformation.

It can be seen from the data presented in the table that, in the *PDHS*, *PMHS*, *PMCHS*, and *PMPS* films at 295 K, dynamic equilibrium between excitons and phonons is not attained and $(E_0^{\mathrm{ABS}} - E_m^{\mathrm{PL}}) = (1.0\text{–}1.4)\sigma_{\mathrm{ex}}(295\text{ K})$; i.e., inequality (4) is satisfied. This implies that, in the polymers at room temperature, the coupling of excitons with phonons is weak and the bathochromic shift between the absorption and photoluminescence bands is associated with the exciton migration over the chain fragments [1–4, 13, 15]. It was previously demonstrated in [2, 3, 19, 20] that the location of the lowest lying absorption band at the maximum in the spectra of the *PDHS*, *PMHS*, *PMCHS*, and *PMPS* polymers depends on steric factors, which affect the conformation of the main chain and the number of monomer units in segments, and also on the mixing of states of the σ and π electrons in *PMPS*. Now, we dwell on the relation between the chemical nature of side groups in macromolecules, the conformation of chain segments, and the parameters $\sigma_{\mathrm{ex}}(295\text{ K})$ and $\sigma_{\mathrm{ex}}(5\text{ K})$.

As is known, the *PDHS* film has an amorphous–crystalline structure (upon deposition on an oriented substrate, the degree of crystallinity can be as high as 65% [24]) and the macromolecular chain at room temperature can exhibit a *trans* planar or disordered conformation [2, 3]. These two conformations are responsible for the absorption bands at $E_m^{\mathrm{ABS}} \approx 3.35$ and 3.91 eV, respectively (Fig. 1, curve *1*). In segments with the *trans* planar conformation, side *n*-hexyl groups are characterized by a crystal packing. The transition from the *trans* planar conformation to the disordered conformation occurs at $T \approx 315$ K and is associated with melting of the packing of side groups. Upon subsequent cooling of the film, the side groups begin to crystallize at $T \approx 300$ K. This results in the rotation of monomer units about the silicon–silicon bonds, the ordering of silicon atoms in the chain, and the formation of segments with the *trans* planar conformation. Therefore, the energy disorder in crystalline regions of the *PDHS* film at $T < 300$ K is caused only by the fluctuations of the number of monomer units in segments and the parameter σ_{ex}(295 K) has a minimum value (see table). When one *n*-hexyl group in each monomer unit is replaced by a methyl group, the van der Waals interaction between the side groups becomes weaker and the chain segments adopt a disordered conformation in the completely amorphous *PMHS* film, which at room temperature is in the devitrified state [20]. As a consequence, compared to the *PDHS* film, the *PMHS* film is characterized by larger fluctuations in the energy of the $^1(\sigma\sigma^*)$ transition due to the disordered positions of silicon atoms in the main chain of the macromolecule. This leads to an increase in the parameter σ_{ex}(295 K). On the other hand, when the side *n*-hexyl groups in the *PMHS* macromolecule are replaced by cyclohexyl or phenyl groups, the interaction between the side groups is enhanced and the chain conformation of the *PMCHS* and *PMPS* macromolecules becomes more ordered [19]. Note that both polymers at room temperature are in the vitreous state [6]. As a result, the parameter σ_{ex}(295 K) for the *PMCHS* polymer is smaller than that for the *PMHS* polymer. However, it can be seen from the table that the replacement of the side cyclohexyl groups in the *PMCHS* macromolecule by the phenyl groups is accompanied by an increase in the parameter σ_{ex}(295 K). Most likely, this is associated with the additional fluctuations in the energy of the $^1(\sigma\sigma^*)$ transition due to the mixing of states of σ and π electrons, because the efficiency of mixing depends substantially on the angle between the plane of the phenyl ring and the segment axis [28].

As can be seen from the data presented in the table, the decrease in the temperature of the *PDHS*, *PMPS*, and *PMCHS* films from 295 to 5 K results in a decrease in the parameter σ_{ex} by a factor of 1.7–2.5. In this case, the macromolecular conformations remain unchanged, because the dependences $E_m^{\mathrm{PL}}(T)$ exhibit a monotonic behavior (Fig. 2, curves *1*–*3*) and the hypsochromic shifts of the photoluminescence bands at the maximum upon cooling of the *PDHS* film from 295 to 5 K and the *PMPS* film from 295 to 95 K are close to the shifts in the maximum of the lowest lying absorption band [3, 21]. Consequently, the aforementioned decrease in the parameter σ_{ex} is most likely caused by the weakening of the exciton–phonon interaction with a decrease in the temperature. Unlike the dependences $E_m^{\mathrm{PL}}(T)$ for the *PDHS*, *PMPS*, and *PMCHS* films, this dependence for the *PMHS* film is nonmonotonic. Actually, the decrease in the temperature from room temperature to $T \approx 240$ K results in a bathochromic shift in the maximum of the photoluminescence band, whereas a further cooling to 5 K is attended by a hypsochromic shift in this maximum (Fig. 2, curve *4*). Yuan and West revealed that cooling of the *PMHS* film from room temperature to $T \approx 240$ K leads to a decrease in the intensity of the band at $E_m^{\mathrm{ABS}} \approx 3.95$ eV and to the appearance of a band at $E_m^{\mathrm{ABS}} \approx 3.81$ eV in the absorption spectra. The presence of the isosbestic point in the absorption spectra suggests that, in the given temperature range, segments of the main chain of the macromolecule undergo a thermally induced transition between two conformations. Since the parameters σ_{ex}(5 K) for the *PMHS* and *PDHS* films coincide with each other (see table), we can assume that the decrease in the temperature from room temperature to $T \approx 240$ K results in the formation of segments with an ordered *trans* planar conformation in the *PMHS* macromolecules, as is the case in the crystallization of side *n*-hexyl groups in *PDHS*. Therefore, upon cooling of the *PMHS* film from 295 to 5 K, the parameter σ_{ex} decreases to a greater extent (by a factor of approximately four) than that for the other polymers.

5. CONCLUSIONS

Thus, it was established that the distributions of the densities of states of excitons and charge carriers in the *PDHS*, *PMHS*, *PMCHS*, and *PMPS* films are described by a Gaussian function and the variance parameters of these distributions depend on the chemical nature of side groups of the polymer, the conformation of segments of the main chain of the polymer macromolecule, and the temperature. At room temperature, the energy disorder in crystalline regions of the *PDHS* film is caused by fluctuations in the number of monomer units in polymer segments. In the *PMHS*, *PMCHS*, and *PMPS* films, the disorder is more pronounced due to the formation of conformers in which silicon atoms occupy different positions in the chain. Moreover, in the *PMPS* films, the disorder occurs through one more mechanism associated with fluctuations of the angle between the plane of the phenyl ring and the axis of the polymer segment due to the mixing of states of σ and π electrons. It was demonstrated that the considerable decrease in the variance parameter σ_{ex} for the *PMHS* film with a decrease in the temperature in the range from 295 to 5 K can be associated with the transition of macromolecular chain segments to an ordered conformation.

REFERENCES

1. G. E. Johnson and K. M. McGrane, in *Photophysics of Polymers*, Ed. by C. E. Hoyle and J. M. Torkelson (Washington, 1987), ASC Symp. Ser., Vol. 358, pp. 499–515.
2. R. D. Miller and J. Michl, Chem. Rev. **89**, 1359 (1989).
3. M. Pope and C. E. Swenberg, *Electronic Processes in Organic Crystals and Polymers* (Oxford Univ. Press, New York, 1999), pp. 877–901.
4. N. Matsumoto, Jpn. J. Appl. Phys. **37**, 5425 (1998).
5. G. P. van Laan, M. de Haas, A. Hummel, H. Frey, and M. Moller, J. Phys. Chem. **100**, 5470 (1996).
6. P. M. Borsenberger and D. S. Weiss, *Organic Photoreceptors for Xerography* (Marcel Dekker, New York, 1998).
7. S. S. Badesha, M. Shanin, and D. M. Pai, US Patent No. 5,166,016 (1992).
8. S. M. Silence, J. C. Scott, E. J. Ginsburg, P. K. Jenkner, R. D. Miller, R. J. Twieg, and W. E. Moerner, J. Opt. Soc. Am. B **10**, 2306 (1993).
9. H. Suzuki, H. Meyer, S. Hoshino, and D. Haarer, J. Appl. Phys. **78**, 2684 (1995).
10. A. Fujii, K. Yoshimoto, M. Yosida, Y. Ohmori, K. Yoshino, H. Ueno, M. Kakimoto, and H. Kojima, Jpn. J. Appl. Phys. **35**, 3914 (1996).
11. S. Nespurek, A. Kadashchuk, Yu. Skryshevski, A. Fujii, and K. Yoshino, J. Lumin. **99**, 131 (2002).
12. R. G. Pitt, M. M. Bursey, and P. F. Rogerson, J. Am. Chem. Soc. **92**, 519 (1970).
13. A. Elschner, R. F. Mahrt, L. Pautmeier, H. Bassler, M. Stolka, and K. McGrane, Chem. Phys. **150**, 81 (1991).
14. H. Bassler, Phys. Status Solidi B **175**, 15 (1993).
15. H. Bassler, in *Disorder Effects on Relaxational Processes*, Ed. by R. Blumen (Springer-Verlag, Berlin, 1994), pp. 485–507.
16. A. Tilgner, H. P. Trommsdorff, J. M. Zeigler, and R. M. Hochstrasser, J. Chem. Phys. **96**, 781 (1992).
17. A. Kadashchuk, N. Ostapenko, V. Zaika, and S. Nespurek, Chem. Phys. **234**, 285 (1998).
18. Yu. A. Skryshevskii and A. Yu. Vakhnin, Fiz. Tverd. Tela (St. Petersburg) **43**, 569 (2001) [Phys. Solid State **43**, 589 (2001)].
19. Yu. A. Skryshevskii, Zh. Prikl. Spektrosk. **70**, 755 (2003).
20. C.-H. Yuan and R. West, Macromolecules **27**, 629 (1994).
21. M. Shimizu, S. Suto, T. Goto, A. Watanabe, and M. Matsuda, Phys. Rev. B **63**, 073403 (2001).
22. Yu. A. Skryshevski, Fiz. Tverd. Tela (St. Petersburg) **44**, 1705 (2002) [Phys. Solid State **44**, 1785 (2002)].
23. B. Hartenstein and H. Bassler, J. Non-Cryst. Solids **190**, 112 (1995).
24. K. Fukuda, T. Seki, and K. Ichimura, Macromolecules **36**, 2177 (2002).
25. V. L. Broude, E. I. Rashba, and E. F. Sheka, *Spectroscopy of Molecular Excitons* (Énergoizdat, Moscow, 1981) [in Russian].
26. É. A. Silin'sh, M. V. Kurik, and V. Chapek, *Electronic Processes in Organic Molecular Crystals: Localization and Polarization Phenomena* (Zinatne, Riga, 1998) [in Russian].
27. A. I. Slutsker, L. A. Laĭus, I. V. Gofman, V. L. Gilyarov, and Yu. I. Polikarpov, Fiz. Tverd. Tela (St. Petersburg) **43**, 1327 (2001) [Phys. Solid State **43**, 1382 (2001)].
28. K. Takeda, M. Fujino, K. Seki, and H. Inokuchi, Phys. Rev. B **36**, 8129 (1987).

Translated by O. Borovik-Romanova

Physics of the Solid State, Vol. 46, No. 11, 2004, pp. 2183–2184. Translated from Fizika Tverdogo Tela, Vol. 46, No. 11, 2004, pp. 2109–2110.
Original Russian Text Copyright © 2004 by Golovin, Ivanova, Lopatin, Nikolaev, Umrikhin.

FULLERENES AND ATOMIC CLUSTERS

The Influence of Low Doses of β Irradiation on the Conductivity of C_{60} Single Crystals

Yu. I. Golovin*, M. A. Ivanova*, D. V. Lopatin*, R. K. Nikolaev, and A. V. Umrikhin***
** Tambov State University, Internatsional’naya ul. 33, Tambov, 392622 Russia*
e-mail: lopatin@tsu.tmb.ru
*** Institute of Solid-State Physics, Russian Academy of Sciences, Chernogolovka, Moscow oblast, 142432 Russia*

Received March 18, 2004

Abstract—The electrical conductivity of C_{60} single crystals is found to increase by 55–120% under β irradiation with low doses. It is shown that this effect can be associated with multistage collision ionization of C_{60} molecules. *© 2004 MAIK “Nauka/Interperiodica”.*

1. INTRODUCTION

Investigation into the electrical conductivity of solids provides valuable information on the electronic subsystem and interaction of charge carriers with atoms of the material. The controlled introduction of radiation-induced defects into semiconductors makes it possible to change their electrical characteristics (such as the electrical conductivity; type of conduction; and concentration, mobility, and lifetime of charge carriers) over a wide range [1]. These methods are characterized by high efficiency, as shown by the development and extensive use of radiation technologies in electronics [2]. The study of the electrical properties of C_{60} single crystals and fullerene derivatives is an important problem, especially as these materials are promising for use in micro- and nanoelectronics [3]. Gordeev *et al.* [4] found that the energy of the HOMO–LUMO transition (and other molecular transitions) in the C_{60} fullerite changes under electron irradiation with energies ranging from 100 to 1000 eV. The purpose of the present work was to reveal and investigate the effect of β irradiation with low doses on the electrical conductivity of the C_{60} fullerite.

2. SAMPLES AND EXPERIMENTAL TECHNIQUE

The experiments were performed with C_{60} single crystals of high purity (99.95% C_{60}). The crystals were grown at the Institute of Solid-State Physics, Russian Academy of Sciences (Chernogolovka, Moscow oblast). The electric current I flowing through indium contacts served as a measure of conductivity. The indium contacts were fixed on one of the faces of the sample with silver paste. The dc voltage U applied to the indium contacts was equal to 50–70 V. In all measurements, the external resistance was considerably less than the electrical resistance of the sample, which was approximately equal to $\sim 10^9$ Ω for samples with characteristic linear sizes of 3–5 mm. The samples were exposed to β irradiation with the use of a radioactive source ^{90}Sr + ^{90}Y with activity $A_0 = 14.5$ MBq. The mean energy of electrons $\langle E \rangle$ was equal to 0.536 MeV. All measurements were carried out at room temperature.

3. RESULTS AND DISCUSSION

It was found that β irradiation affects the electrical conductivity of the C_{60} fullerite. In particular, the electrical conductivity of the sample irradiated with a fluence $F > 2 \times 10^9$ cm^{-2} increases by 55%. The dependence of the relative increase in the electric current $\Delta I/I$ on the irradiation time t is characterized by saturation at a time $t_{s1} \sim 12$ min after the onset of irradiation (see figure). After irradiation is ceased, the electric current relaxes to its initial value in a time $t_{r1} \sim 1$ h. If the same surface of the sample is repeatedly irradiated 20 h after the cessation of primary irradiation, the electrical conductivity increases by 120%. In this case, the times of

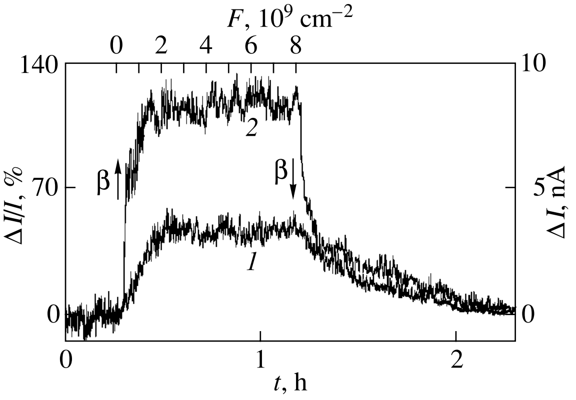

Dependences of the increment of the electric current ΔI on the irradiation time t and on the fluence F: (*1*) primary irradiation and (*2*) repeated irradiation after 20 h. Arrows indicate the instants of onset and termination of β irradiation.

1063-7834/04/4611-2183$26.00 © 2004 MAIK “Nauka/Interperiodica”

saturation and relaxation are t_{s2} ~ 9 min and t_{r2} ~ 1 h, respectively.

The basic effect due to interaction of fast electrons with the material is determined by the ionization of molecules and the formation of point defects. An increase in the electrical conductivity can be associated with multistage collision ionization of molecules in the lattice of the C_{60} crystals by relativistic electrons due to external excitation. Under these conditions, the energy of a conduction electron produced in the initial ionizing event is sufficiently high for subsequent ionization of C_{60} molecules. The increment of the electric current in this case is estimated as $\Delta I = A_0 ek\langle E\rangle/E_0 \sim 0.3 \times 10^{-8}$ A, where $e = 1.6 \times 10^{-19}$ C is the elementary charge, E_0 ~ 20 eV is an energy significantly exceeding the ionization energy of the fullerene molecule, and $k = 0.05$ is the coefficient accounting for the ratio of the number of particles impinging on the sample to the total number of particles emitted by the source. It can be seen that the calculated increment of the electric current lies within the range of experimental values $\Delta I = 10^{-8}$–10^{-9} A. However, the long times of rise and relaxation of the radiation-induced current cast some doubt on the fact that the observed increase in the electrical conductivity is caused only by multistage collision ionization of C_{60} molecules. Proper allowance must be made both for already existing deep-level trapping centers of free charge carriers and for new defects arising under β irradiation and also serving as traps for free charge carriers. It should be noted that, at the beginning of β irradiation, the trapping centers are generated and filled simultaneously. After β irradiation is ceased, the traps undergo thermal depletion. The larger increment of the electric current due to repeated irradiation can be explained in terms of radiation-induced defects persisting after the primary irradiation. The determination of the energy location of deep-lying levels and elucidation of the nature of radiation-induced defects in C_{60} single crystals call for further investigation.

ACKNOWLEDGMENTS

This work was supported by the Russian Foundation for Basic Research (project no. 02-02-17571) and the federal program “Fullerenes and Atomic Clusters.”

REFERENCES

1. V. A. Kozlov and V. V. Kozlovskiĭ, Fiz. Tekh. Poluprovodn. (St. Petersburg) **35** (7), 769 (2001) [Semiconductors **35**, 735 (2001)].
2. L. F. Zahkarencov and V. V. Kozlovski, in *Semiconductor Technology: Processing and Novel Fabrication Techniques* (Wiley, New York, 1997).
3. V. I. Trefilov, D. V. Shchur, B. P. Tarasov, Yu. M. Shul’ga, A. V. Chernogorenko, V. K. Pishchuk, and S. Yu. Zaginaĭchenko, *Fullerenes as a Basis for the Design of Materials in the Future* (ADEF, Kiev, 2001) [in Russian].
4. Yu. S. Gordeev, V. M. Mikushin, and V. V. Shnitov, Fiz. Tverd. Tela (St. Petersburg) **42** (2), 371 (2000) [Phys. Solid State **42**, 381 (2000)].

Translated by O. Moskalev